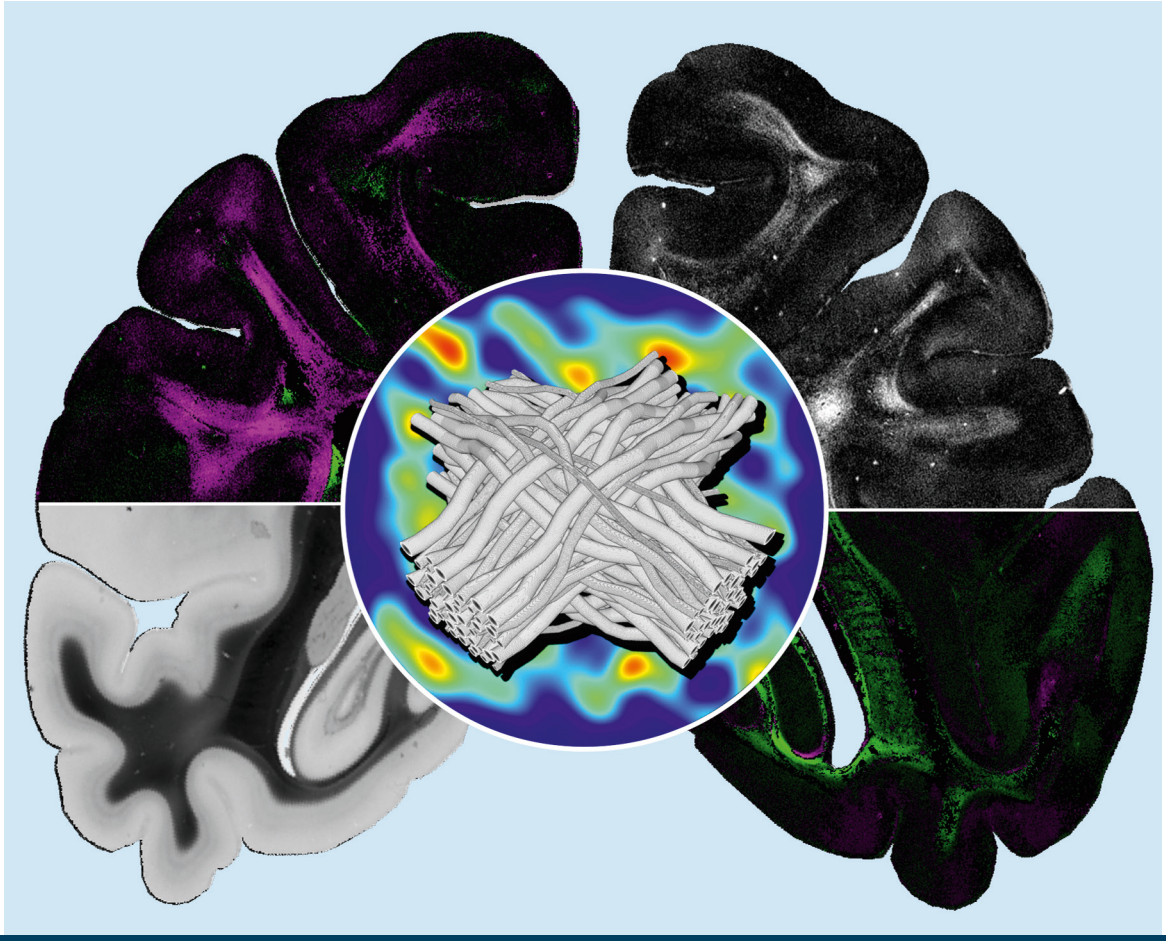

Finite-Difference Time-Domain Simulations Assisting to Reconstruct the Brain's Nerve Fiber Architecture by 3D Polarized Light Imaging

Miriam Menzel

Schlüsseltechnologien / Key Technologies
Band / Volume 188
ISBN 978-3-95806-368-6

Mitglied der Helmholtz-Gemeinschaft

JÜLICH
Forschungszentrum

Schriften des Forschungszentrums Jülich
Reihe Schlüsseltechnologien / Key Technologies Band / Volume 188

Forschungszentrum Jülich GmbH
Institut für Neurowissenschaften und Medizin
Strukturelle und funktionelle Organisation des Gehirns (INM-1)

Finite-Difference Time-Domain Simulations Assisting to Reconstruct the Brain's Nerve Fiber Architecture by 3D Polarized Light Imaging

Miriam Menzel

Schriften des Forschungszentrums Jülich
Reihe Schlüsseltechnologien / Key Technologies Band / Volume 188

ISSN 1866-1807 ISBN 978-3-95806-368-6

Bibliografische Information der Deutschen Nationalbibliothek.
Die Deutsche Nationalbibliothek verzeichnet diese Publikation in der
Deutschen Nationalbibliografie; detaillierte Bibliografische Daten
sind im Internet über http://dnb.d-nb.de abrufbar.

Herausgeber und Vertrieb:	Forschungszentrum Jülich GmbH Zentralbibliothek, Verlag 52425 Jülich Tel.: +49 2461 61-5368 Fax: +49 2461 61-6103 zb-publikation@fz-juelich.de www.fz-juelich.de/zb
Umschlaggestaltung:	Grafische Medien, Forschungszentrum Jülich GmbH
Druck:	Grafische Medien, Forschungszentrum Jülich GmbH
Copyright:	Forschungszentrum Jülich 2018

Schriften des Forschungszentrums Jülich
Reihe Schlüsseltechnologien / Key Technologies, Band / Volume 188

D 82 (Diss., RWTH Aachen University, 2018)

ISSN 1866-1807
ISBN 978-3-95806-368-6

Vollständig frei verfügbar über das Publikationsportal des Forschungszentrums Jülich (JuSER)
unter www.fz-juelich.de/zb/openaccess.

Abstract

The neuroimaging technique *Three-dimensional Polarized Light Imaging (3D-PLI)* reconstructs the brain's nerve fiber architecture by transmitting polarized light through histological brain sections and measuring their birefringence. Measurements have shown that the polarization-independent transmitted light intensity (*transmittance*) depends on the out-of-plane inclination angle of the nerve fibers. Furthermore, the optical anisotropy that causes the birefringence leads to polarization-dependent attenuation of light (*diattenuation*), which might provide additional information about the underlying fiber configuration. In this thesis, analytical considerations, supplementary measurements, and numerical simulations were performed to study the transmittance and diattenuation effects in more detail, and to develop ideas how the effects can assist the nerve fiber reconstruction with 3D-PLI. The propagation of the polarized light wave through the brain tissue was modeled by *Finite-Difference Time-Domain (FDTD)* simulations. Following a bottom-up approach, the simplest possible model was identified that describes the observed transmittance and diattenuation effects.

The experimental studies in this work have shown that the transmittance significantly decreases with increasing inclination angle of the fibers (by more than 50 %). The FDTD simulations could model this effect and show that the decrease in transmittance is mainly caused by polarization-independent light scattering in combination with the limited numerical aperture of the imaging system. Moreover, the simulations revealed that the transmittance does not depend on the crossing angle between horizontal fibers. Combining the simulation results with experimental data, it could be demonstrated that the transmittance can be used to distinguish between horizontal crossing and vertical fibers, which is not possible in standard 3D-PLI measurements.

To study the diattenuation of brain tissue, a measurement protocol has been developed that allows to measure the diattenuation even with a low signal-to-noise ratio: *Diattenuation Imaging (DI)*. The experimental studies in this work revealed that the diattenuation of brain tissue is relatively small (less than 10 %) and that it has practically no impact on the measured 3D-PLI signal. More importantly, it was demonstrated that there exist two different types of diattenuation that are specific to certain fiber configurations: in some brain regions, the transmitted light intensity becomes maximal when the light is polarized parallel to the nerve fibers (D^+), in other brain regions, it becomes minimal (D^-). The FDTD simulations could successfully model the diattenuation and show that diattenuation of type D^- is caused by anisotropic scattering of light which decreases with increasing time after tissue embedding, while diattenuation of type D^+ can be caused both by anisotropic scattering and by anisotropic absorption (dichroism). In addition, the simulations confirmed that steep fibers only show diattenuation of type D^+ and that the diattenuation also depends on the tissue composition. This makes Diattenuation Imaging a promising imaging technique that reveals different types of fibrous structures which cannot be distinguished with current imaging techniques.

Zusammenfassung

Das bildgebende Verfahren *Three-dimensional Polarized Light Imaging (3D-PLI)* rekonstruiert die Nervenfaserarchitektur des Gehirns, indem die Doppelbrechung von histologischen Hirnschnitten mit polarisiertem Licht gemessen wird. Vorausgehende Messungen haben gezeigt, dass die polarisationsunabhängige transmittierte Lichtintensität (*Transmittanz*) vom Neigungswinkel der Nervenfasern abhängt. Außerdem führt die optische Anisotropie, die die Doppelbrechung verursacht, zu einer polarisationsabhängigen Abschwächung des Lichts (*Diattenuation*), die zusätzliche Informationen über die zugrunde liegende Faserkonstellation liefern könnte. In dieser Arbeit wurden analytische Überlegungen, ergänzende Messungen und numerische Simulationen durchgeführt, um die Transmittanz- und Diattenuation-Effekte genauer zu untersuchen und Ideen zu entwickeln, wie die Effekte die Nervenfaserrekonstruktion mit 3D-PLI unterstützen könnten. Die Ausbreitung der polarisierten Lichtwelle durch das Hirngewebe wurde mit *Finite-Difference Time-Domain (FDTD)* Simulationen modelliert. Dabei wurde ein *Bottom-up*-Ansatz verfolgt, um das einfachste Modell zu finden, das die Transmittanz- und Diattenuation-Effekte beschreibt.

Die experimentellen Studien dieser Arbeit haben gezeigt, dass die Transmittanz mit zunehmendem Neigungswinkel der Nervenfasern signifikant abnimmt (um mehr als 50 %). Die FDTD Simulationen konnten diesen Effekt modellieren und zeigen, dass der Rückgang der Transmittanz hauptsächlich durch polarisationsunabhängige Lichtstreuung und die begrenzte numerische Apertur des Mikroskops zustande kommt. Außerdem haben die Simulationen ergeben, dass die Transmittanz bei horizontalen Fasern nicht von deren Kreuzungswinkel abhängt. Die Auswertung experimenteller Daten hat ergeben, dass die Transmittanz dazu genutzt werden kann, horizontal kreuzende von senkrechten Fasern zu unterscheiden, was mit derzeitigen 3D-PLI Messungen nicht möglich ist.

Zur Untersuchung der Diattenuation von Hirngewebe wurde ein Messprotokoll entwickelt, das die Diattenuation auch bei geringem Signal-Rausch-Verhältnis messen kann: *Diattenuation Imaging (DI)*. Die experimentellen Studien dieser Arbeit haben gezeigt, dass die Diattenuation des Hirngewebes relativ klein ist (weniger als 10 %) und dass sie praktisch keinen Einfluss auf das gemessene 3D-PLI Signal hat. Außerdem wurde gezeigt, dass es zwei verschiedene Arten von Diattenuation gibt, die für bestimmte Faserkonstellationen spezifisch sind: In einigen Gehirnregionen wird die transmittierte Lichtintensität maximal, wenn das Licht parallel zu den Nervenfasern polarisiert ist (D^+), in anderen Gehirnregionen wird sie minimal (D^-). Die FDTD Simulationen konnten die Diattenuation erfolgreich modellieren und zeigen, dass der D^--Effekt durch anisotrope Lichtstreuung verursacht wird, die mit zunehmender Zeit nach Eindeckung des Gewebes abnimmt, während der D^+-Effekt sowohl durch anisotrope Streuung als auch durch anisotrope Absorption (Dichroismus) verursacht werden kann. Außerdem bestätigten die Simulationen, dass steile Fasern nur den D^+-Effekt zeigen und dass die Diattenuation auch von der Gewebezusammensetzung abhängt. Das macht *Diattenuation Imaging* zu einem vielversprechenden bildgebenden Verfahren, das verschiedene Arten von Faserstrukturen sichtbar macht, die mit aktuellen bildgebenden Verfahren nicht unterscheidbar sind.

Acknowledgments

This doctoral thesis is part of an interdisciplinary research project. It has been carried out during the years 2015–2018 in the *'Fiber Architecture'* group of Dr. Markus Axer at the *Institute of Neuroscience and Medicine (INM-1)*, Forschungszentrum Jülich GmbH (FZJ), Germany – in close collaboration with the *Jülich Supercomputing Centre*. The thesis has been submitted to *RWTH Aachen University* to obtain a doctorate in physics.

The work in this thesis has been supported by the Helmholtz Association portfolio theme *'Supercomputing and Modeling for the Human Brain'* and by the European Union's Horizon 2020 Research and Innovation Programme under Grant Agreement No. 604102 and 720270 (*Human Brain Project*, SGA1). The computing time has been granted by the JARA-HPC Vergabegremium and VSR commission on the supercomputer *JURECA* [1] and the JARA-HPC Partition part of the supercomputer *JUQUEEN* [2] at Forschungszentrum Jülich. Besides research facilities, it was the help and support of many people that made this thesis possible in the first place.

First and foremost I would like to thank my thesis advisor and examiner, Prof. Kristel Michielsen (Jülich Supercomputing Centre, FZJ), for her continuous support throughout my doctoral studies, for her professional assistance, scientific input, insightful comments, and critiques. It has been an honor to be her first doctoral candidate. Despite her busy schedule, she found the time to answer all my questions and to discuss the progress of my thesis. She provided me with the *Maxwell Solver* without which the *Finite-Difference Time-Domain (FDTD)* simulations in Part IV would not have been possible.

At this opportunity, I also would like to thank Prof. Hans De Raedt (Zernicke Institute for Advanced Materials, University of Groningen, the Netherlands) who always participated in our scientific discussions. He put a lot of time and effort into further development of the software, assisted me with derivations in Sec. 10.1.2, and contributed a lot to my understanding of the involved physics and modeling.

My sincere thanks also go to my other thesis examiner, Prof. Katrin Amunts (director of the INM-1 at Forschungszentrum Jülich and of the C. and O. Vogt Institute of Brain Research at Heinrich Heine University Düsseldorf, Germany), for providing the funding, supporting me in my scientific career, and giving me interesting insights into the world of neuroscience. In her role as a leader of the *Human Brain Project*, she introduced me to interesting persons in the field and gave me the opportunity to attend many international conferences and events which has considerably broadened my scientific horizon.

Furthermore, I would like to thank Prof. Stefan Wessel (Institute for Theoretical Solid State Physics, RWTH Aachen University, Germany) who agreed on becoming another examiner of my thesis, for his time and helpful comments.

I also thank the rest of my thesis committee, Prof. Andreas Offenhäusser (director of the Institute of Complex Systems (ICS-8) and Peter Grünberg Institute (PGI-8), FZJ) and the chair Prof. Achim Stahl (director of the Physics Institute III B, RWTH Aachen University, Germany), for their time and their insightful comments and questions.

Of course, my thesis would not have been possible without the great support of my group leader, Dr. Markus Axer (INM-1, FZJ). Not only did he provide me with the opportunity to work in his *'PLI team'* on this interesting and challenging research project, he also helped me with his valuable advice and encouragement to plan and develop this thesis. He allowed me to realize my own ideas and always had a sympathetic ear for my questions and problems.

My special thanks also go to Prof. Francesco S. Pavone, Dr. Irene Costantini, and Dr. Ludovico Silvestri (*European Laboratory for Non-Linear Spectroscopy (LENS)*, University of Florence, Italy) for the good collaboration and the opportunity to work in their laboratory. During the two months of my research visit, Irene and Ludovico accompanied and supported me in analyzing their measurement data. Irene performed the *Two-Photon Fluorescence Microscopy (TPFM)* measurements and developed a technique to make myelinated axons autofluorescent which allowed me to study the transmittance of inclined nerve fibers in Sec. 8.3. She also helped me with proofreading Chap. 5.

My colleagues at the INM-1 also contributed a lot to the accomplishment of my thesis. First of all, I would like to thank Felix Matuschke for many helpful discussions about theory, physics, and modeling. He developed the *Fiber Growing Algorithm* and the *Volume Colliding Solver* which allowed me to generate more realistic nerve fiber constellations in Sec. 10.2 and to reproduce the experimental observations. He also helped me with programming issues and to create more complex fiber models for my thesis.

Furthermore, I am obliged to my former colleague Dr. Julia Reckfort for her contribution to the experimental diattenuation studies in Secs. 9.1 and 9.2.1. She performed most of the diattenuation measurements for the rat brain sections and co-authored our joint publication about *Diattenuation Imaging (DI)* [3]. Furthermore, she performed multiple measurements to characterize the *Large-Area Polarimeter (LAP)* in Secs. 7.1.1 and 7.2 and Appx. B.1 and B.3. On this occasion, I also would like to thank my Master student Hasan Köse who wrote his thesis about diattenuation measurements of vervet brain sections and developed a first measurement protocol. The results of his long-term measurements inspired me to study the time behavior of diattenuation in more detail in Sec. 9.3. I am also grateful to David Gräßel and Isabelle Mafoppa Fomat who spent a lot of their time with 3D-PLI and DI measurements and made the diattenuation measurements part of our measurement routine.

Moreover, I would like to thank Philipp Schlömer for processing the 3D-PLI measurements and generating the parameter maps (Sec. 4.4.1 and Chap. 8), for providing me with information about the *Polarizing Microscope* (Chap. 7 and Appx. B.1.1), and for assistance with the high-resolution diattenuation measurements with the prototypic polarizing microscope at *Taorad GmbH* in Aachen (Sec. 9.2.3).

Furthermore, I thank Martin Schober, Marcel Huysegoms, and Dr. Sascha Münzing for image registration (Sec. 8.2), Nicole Schubert for 3D visualization (Fig. 4.7), and Stefan Köhnen for programming issues.

I also would like to thank our laboratory people – Markus Cremer, Christian Rademacher, Patrick Nysten, Steffen Werner, and Sabina Klein – for their excellent technical assistance and the preparation of the histological brain sections.

Finally, I would like to thank the whole PLI team and the BDA group for their professional and moral support, the friendly working atmosphere, the diverting lunch breaks, the board games and cinema evenings, and for all the fun we have had in the last four years.

Last but not least, I would like to express my deep gratitude to my family and friends for all their love and encouragement throughout the preparation of my doctoral thesis. In particular, I would like to thank Daniel Weigand for his great support and patience. He spent a lot of his time with proofreading and discussing about my thesis and was always there for me. Thank you.

Contents

Chapter 1

Introduction

The brain is one of the most complex organs in our body: it contains about 100 billion neurons [4–7], which are each connected to 10,000 other nerve cells on average [6, 8]. Understanding the structure and function of the human brain remains one of the greatest challenges in neuroscience. In recent years, large international research projects like the *Human Brain Project (HBP)*[1] in Europe [9] or the *BRAIN Initiative*[2] in the US have been launched to take up that challenge.

To figure out how brain function emerges from its structural organization, it is necessary to study the neuronal connections, i. e. the nerve fiber architecture of the brain. Developing a detailed network model of the human brain, the so-called *connectome* [10, 11], helps to better understand neuro-degenerative diseases and to assist surgery. Simulations of the brain's circuitry could also inspire new computing technologies.

Decoding the human connectome is a multi-scale challenge, ranging from long-range inter-hemispheric fiber connections of several centimeters down to single axons (nerve fibers) with diameters of a few micrometers.

Neuro-Imaging Techniques at Different Scales To date, there exist various neuro-imaging techniques that investigate the brain's nerve fiber architecture at different scales (see Fig. 1.1).

Diffusion-weighted magnetic resonance imaging (dMRI)[3] – in particular *diffusion tensor imaging (DTI)* – is extensively used to reconstruct nerve fiber pathways in the brain [11, 12, 15]. It is at present the only method to map the nerve fibers of a whole human brain in vivo [12–14]. Due to motion artifacts and limited scan times, the spatial resolution is mostly limited to the millimeter scale [16–18]. In post-mortem brains, ultra-high magnetic fields and longer scan times can be used which enables higher resolutions, depending on the sample size: When measuring a whole human brain, fiber structures down to 0.7 mm can be examined [19]. For smaller samples like mouse or rat brains, the resolution can be in the order of a few dozen micrometers [12].

A big advantage of dMRI is that it allows to study the three-dimensional nerve fiber architecture without sectioning the brain. Another possibility to study the underlying tissue structure without sectioning is to use clearing methods [20–25] which make brain tissue transparent e. g. for *confocal laser scanning* [21, 23, 24] or *light-sheet microscopy* [20, 22, 26–28]. Other techniques that achieve in-depth information with high micrometer resolution are *Optical Coherence Tomography (OCT)* [29–31], *Two-Photon Fluorescence*

[1] `http://www.humanbrainproject.eu` (Status: 01.03.2018)
[2] `http://www.braininitiative.nih.gov` (Status: 01.03.2018)
[3] Diffusion-weighted magnetic resonance imaging (dMRI) measures the rate and the preferred direction of molecular diffusion, usually water, in the brain. As the diffusion is restricted by macroscopic structures, dMRI is able to visualize neuronal pathways [12–14].

Microscopy (TPFM) [28, 32–35], and reflectance microscopy techniques [36, 37], which do not require any clearing and can also be applied in vivo through a cranial window.

To study nerve fibers in anatomical detail, the brain is often sectioned into histological slices and the light transmitted through the brain section is analyzed. Staining techniques, which dye the fiber tracts after sectioning, make major fiber tracts visible [38]. With transmission electron microscopy, it is possible to achieve resolutions down to a few nanometers [39–42]. These microscopy techniques, however, are generally limited to 2D and cannot access the three-dimensional architecture of nerve fibers within the investigated sections.

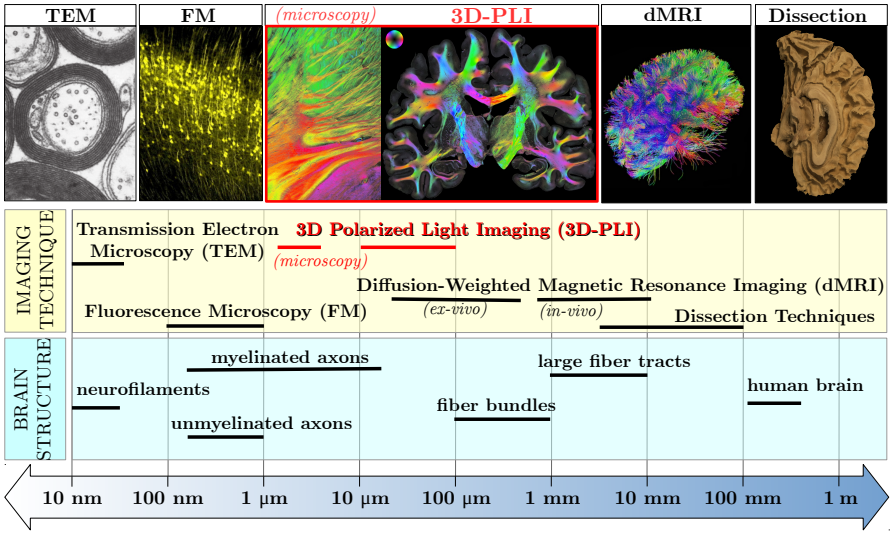

Fig. 1.1: Neuroimaging techniques used to access the brain's nerve fiber architecture at different scales: Transmission electron microscopy (TEM), fluorescence microscopy (FM), 3D Polarized Light Imaging (3D-PLI), diffusion-weighted magnetic resonance imaging (dMRI), and dissection techniques. The scale bars indicate the range of resolution for the different imaging techniques in comparison to the diameter of different brain structures (see also Sec. 3.1). The scale bars were derived from literature values and only provide an approximate order of magnitude. The images were taken from different sources with permission: TEM ([43] Fig. 4-7, Copyright Elsevier 2006), FM ([24] Fig. 4C, licensed under CC BY-NC-SA 3.0), 3D-PLI (INM-1, Forschungszentrum Jülich GmbH, Germany), dMRI ([11] Fig. 2d, licensed under CC BY-NC-ND 4.0), Dissection ([44] Fig. 9, Copyright Elsevier 2012).

3D Polarized Light Imaging In 2011, Axer *et al.*, a group of researchers in the Institute of Neuroscience and Medicine (INM-1) at *Forschungszentrum Jülich GmbH (FZJ)*, presented a novel approach to measure the three-dimensional nerve fiber architecture: *Three-dimensional Polarized Light Imaging (3D-PLI)* [45, 46]. The technique reconstructs the spatial pathways of nerve fibers in unstained histological brain sections with a resolution of a few micrometers, allowing to investigate long-range fiber bundles as well as single fibers [47, 48]. In this way, 3D-PLI serves as a bridging technology between the macroscopic and the microscopic scale.

Essential for the fiber reconstruction with 3D-PLI is the *birefringence* of the nerve fibers, which is mainly caused by the anisotropic structure of the surrounding myelin

sheaths [49, 50]. The brain is cut into sections of approx. 60 µm and placed in a polarimeter. By transmitting polarized light through the histological brain sections, the birefringence (axis of optical anisotropy) is measured, allowing to reconstruct the spatial orientations of the nerve fibers [51].

Although 3D-PLI is constantly being developed, the technique has certain limitations. One major problem are so-called *partial-volume effects*: As the brain sections are 60 µm thick, several nerve fibers are measured within the same volume element and only the predominant fiber direction is extracted. When fibers with different orientations are located on top of each other, the orientations of individual fibers cannot be accessed. Inhomogeneous fiber configurations (like crossing fibers or regions with varying fiber densities) influence the measured birefringence signal and thus the determined fiber orientations [52]. Especially challenging is the reconstruction of the so-called *inclination angle*, i. e. the out-of-plane orientation of the fibers. To date, there exist several approaches to improve the accuracy of the inclination angle:

- *Transmittance weighting:* Due to the large attenuation coefficient of the myelin sheaths, the polarization-independent transmitted light intensity (transmittance) is a measure of the myelin content in brain tissue. As myelin is mainly responsible for the measured birefringence signal, the myelin content influences the reconstructed fiber inclinations. To improve the fiber reconstruction, the measured birefringence signal is weighted by the transmittance [53]. However, the transmitted light intensity also depends on tissue composition, fiber orientation, and polarization (see later), which is not taken into account in this correction procedure.

- *Tilting:* With a tiltable specimen stage, the fiber orientations can be measured under slightly different angles, allowing a more precise determination of the fiber inclinations [54, 55]. However, the reconstruction of inhomogeneous fiber configurations is still challenging and the technique is currently only available for a polarimeter with pixel size ≥ 21 µm and not for microscopic resolution.

To improve the interpretation of the measured 3D-PLI signals and to enhance the reconstruction of the spatial fiber orientations, a multi-modal cross-validation with other techniques is needed. The main reconstructed fiber tracts can be compared to anatomical studies, but the exact orientation of individual fibers is unknown. So far, there exists no "phantom" that could serve as validation for 3D-PLI: Artificial tissue samples with a well-defined fiber architecture are not available because the birefringence of the myelin sheaths cannot be easily replicated. The extraction (or generation) of nerve fibers with well-defined orientations is also not feasible with the currently established methods.

The only possibility to validate the measured fiber orientations is to use alternative imaging methods with high in-depth resolution (e. g. OCT, TPFM or confocal/light-sheet microscopy combined with clearing) that allow to access the three-dimensional fiber architecture of the brain section. However, different measurement techniques require different tissue preparations so that either the measurements cannot be performed on the same sample or the tissue properties of the sample might change between the measurements. This makes a cross-validation between different techniques challenging. Recent studies [56] have shown that myelinated axons can be made auto-fluorescent and measured with TPFM (voxel size: $0.244 \times 0.244 \times 1$ µm). Thus, by measuring the same brain section with 3D-PLI and TPFM and comparing the reconstructed fiber orientations to the microscopic fiber architecture, the fiber orientations derived from 3D-PLI can be validated. However, the tissue preparation and the TPFM measurement require

a lot of time and effort so that the fiber orientations can only be validated in small brain regions.

A more efficient way to identify misinterpreted fiber orientations, is to better understand the physics behind the light-matter interactions and to derive general concepts of how the measurement and signal analysis of 3D-PLI can be improved. In recent years, numerical simulations (based on the Jones matrix calculus) have successfully been employed to model the 3D-PLI measurement and to validate the reconstructed fiber orientations [51, 52]. Comparing the known underlying fiber architecture of the simulation model to the fiber orientations derived from 3D-PLI helps to identify possible misinterpretations in the fiber reconstruction process. However, the employed simulation approach is based on linear optics and not suitable to model more complex light-matter interactions like scattering, so it cannot be used to study the transmittance or attenuation of light.

Transmittance and Diattenuation Experimental studies have demonstrated that the polarization-independent transmitted light intensity (*transmittance*) depends not only on the tissue composition (myelin content of the brain tissue), but also on the fiber inclination, which has an impact on the above-mentioned "transmittance weighting" and thus on the fiber orientations reconstructed by 3D-PLI. Therefore, it is important to study and understand this effect in more detail. If it is possible to identify a relation between the transmittance and the fiber inclination, it can be used as additional information to improve the fiber reconstruction with 3D-PLI. As the transmittance does not depend on the polarization of light, findings on the transmittance can also be useful for other transmission microscopy techniques which use unpolarized light.

The optical anisotropy that causes birefringence (anisotropy of refraction) also leads to *diattenuation* (anisotropy of attenuation) [57, 58]. As diattenuation leads to polarization-dependent attenuation of light, it might have an impact on the polarimetric measurement of 3D-PLI and consequentially affect the measured nerve fiber orientations. In other studies, diattenuation has been used to quantify tissue properties (e. g. thickness [59], concentration of glucose [60, 61]) and to distinguish between healthy and pathological tissue (cancerous tissue [62], burned/injured tissue [63, 64], tissue from eye diseases [59, 65]). Hence, diattenuation might also provide interesting structural information about the brain tissue and *Diattenuation Imaging (DI)* could be a useful extension to 3D-PLI. The experimental studies presented in this thesis (Chap. 9) show that the diattenuation effect is regionally specific and changes with increasing time after tissue embedding. To better understand where these differences and the time dependence come from and how to use DI as additional imaging technique, numerical simulations are needed.

Aims and Objectives The aim of this thesis is to learn more about the interaction of polarized light with brain tissue and to better understand the experimental observations (transmittance and diattenuation effects). For this purpose, analytical considerations, further experiments, and numerical simulations were performed. To investigate complex light-matter-interactions like scattering, transmittance, and diattenuation, *Finite-Difference Time-Domain (FDTD)* simulations were employed. The propagation of the polarized light wave through the brain tissue was modeled by approximating Maxwell's equations by so-called finite differences and the components of the electromagnetic field were computed in time and space. To better understand where the observed transmittance and diattenuation effects come from and what is needed to reproduce the experimental observations, a bottom-up approach was pursued: starting from a simpli-

fied model of the nerve fiber architecture, the model was made more and more complex until it is more comparable to the fiber architecture extracted from experimental measurements. Apart from modeling the observed effects, the thesis also aims at developing ideas how the measurement and signal analysis of 3D-PLI can be extended and optimized, i. e. how the accuracy and reliability of the reconstructed fiber orientations can be improved and how the measured signal can be related to a certain likelihood of fiber constellation. To obtain additional information about the fiber architecture, previously unconsidered effects (such as scattering and diattenuation) were taken into account.

Outline The focus of this thesis is to model and understand the observed transmittance and diattenuation effects. To study the effects' behavior in more detail and to make hypotheses where the effects come from, experimental studies were performed. To validate these hypotheses and to find a physical model for the effects, numerical simulations were performed. Therefore, the thesis consists of both experimental and simulation studies. The outline is as follows:

- **Part I (Theoretical Background):** Chapter 2 explains the physical principles (birefringence, diattenuation, etc.). Chapter 3 describes the structural and optical properties of brain tissue that are needed to analyze the measurements and to set up the simulation model.
- **Part II (Measurement & Simulation Techniques):** The polarimetric measurements (3D-PLI and DI) are described in Chap. 4. The TPFM technique which was used to validate the reconstructed fiber orientations and to generate a model for the nerve fiber architecture is presented in Chap. 5. The FDTD technique used for the simulations of the polarimetric measurements is introduced in Chap. 6.
- **Part III (Experimental Studies):** The optical systems used for the polarimetric measurements are characterized in Chap. 7. The experimental studies on the transmittance of inclined nerve fibers and on the diattenuation of brain tissue are presented in Chaps. 8 and 9.
- **Part IV (FDTD Simulation Studies):** Chapter 10 describes how the optical systems and the polarimetric measurements were modeled and discusses the simulation parameters in terms of their accuracy and computing time. Chapters 11 and 12 describe how the transmittance and diattenuation effects were simulated for various fiber configurations, from a simple hexagonal grid of fibers to more complex fiber constellations.
- **Part V (Discussion & Conclusion):** Chapter 13 compares the results from the experimental and simulation studies. Chapter 14 provides a conclusion and an outlook on future work.

Longer derivations and calculations can be found in Appx. A–D. A list of all used acronyms is given on pp. 243–244, a list of all used symbols on pp. 245–248. The definition of the most important terms can be looked up in an index at the very end of this thesis.

Parts of this thesis have already been published in [3, 51, 52, 56, 66–68]. On pp. 231–234, the publications and author contributions are listed in more detail. Throughout this thesis, all pre-publications and contributions from others (images, measurements, analysis, tools, etc.) are indicated by footnotes or separate notes.

Part I

THEORETICAL BACKGROUND

Chapter 2

Polarization Optics

This chapter introduces the theoretical background and physical principles that are relevant for this thesis: Section 2.1 describes the properties of the electromagnetic field, polarization, coherence, and diffraction. The following sections explain the optical tissue properties that are important for the polarimetric measurements: refraction and attenuation (Sec. 2.2), birefringence (Sec. 2.3), and diattenuation (Sec. 2.4). Section 2.5, finally, introduces the matrix calculus that was used for the analysis and modeling of the measured signals.

Sections 2.1 and 2.2 mostly focus on isotropic media, while Secs. 2.3 to 2.5 deal with anisotropic (uniaxial) media. A special focus was placed on plane monochromatic waves and on homogeneous, linear, and non-magnetic materials because they are of most interest in this thesis. Throughout this thesis, SI units are used. Parts of Secs. 2.4 and 2.5.2 have been published in Menzel *et al.* (2017) [3] Sec. 2.

2.1 Electromagnetic Field

In order to analyze the interaction of polarized light with brain tissue, it is necessary to understand the nature of light as an electromagnetic wave. Therefore, the properties of the electromagnetic field are discussed first. The explanations follow Born·Wolf [69] (Chaps. 1.1, 1.4), Demtröder [70] (Chaps. 7.1, 7.4, 7.5, 8.3), Hecht [71] (Chaps. 3.1.5, 3.2, 8.1), and Taflove·Hagness [72] (Chap. 3.2).

2.1.1 Maxwell's Equations

The *Maxwell equations* form the foundation of classical optics and are necessary for the study of light-matter interactions. In differential form, the four Maxwell equations read ([72] Sec. 3.2, [69] Sec. 1.1.1):

$$\vec{\nabla} \times \vec{E}(\vec{r},t) = -\frac{\partial \vec{B}(\vec{r},t)}{\partial t} - \vec{M}(\vec{r},t), \tag{2.1}$$

$$\vec{\nabla} \times \vec{H}(\vec{r},t) = \frac{\partial \vec{D}(\vec{r},t)}{\partial t} + \vec{J}(\vec{r},t), \tag{2.2}$$

$$\vec{\nabla} \cdot \vec{D}(\vec{r},t) = \rho_\mathrm{e}(\vec{r},t), \tag{2.3}$$

$$\vec{\nabla} \cdot \vec{B}(\vec{r},t) = \rho_\mathrm{m}(\vec{r},t), \tag{2.4}$$

where $\vec{E}$ and $\vec{H}$ are the *electric and magnetic fields*, $\vec{D}$ and $\vec{B}$ the *electric and magnetic flux densities*, $\vec{J}$ and $\vec{M}$ the *electric and equivalent magnetic current densities*, and ρ_e and ρ_m the *electric and magnetic charge densities*. The vector $\vec{\nabla}$ denotes the vector of

spatial partial derivatives and $\partial/\partial t$ the temporal partial derivative. All quantities are functions of space $\vec{r}$ and time t. The magnetic current and charge density (in blue) were only introduced for symmetry reasons (needed for the FDTD algorithm in Chap. 6); they are produced by magnetic monopoles which have not been found so far.

2.1.2 Material Equations

The *material equations* describe the behavior of a material under the influence of an electromagnetic field. They allow for a unique determination of the electromagnetic field vectors from a given distribution of currents and charges. The material equations for linear, isotropic, non-dispersive, and homogeneous materials[1] read ([72] Sec. 3.2):

$$\vec{D}(\vec{r},t) = \epsilon_0\, \epsilon_\mathrm{r}(\vec{r})\, \vec{E}(\vec{r},t) \equiv \epsilon(\vec{r})\, \vec{E}(\vec{r},t), \tag{2.5}$$

$$\vec{B}(\vec{r},t) = \mu_0\, \mu_\mathrm{r}(\vec{r})\, \vec{H}(\vec{r},t) \equiv \mu(\vec{r})\, \vec{H}(\vec{r},t), \tag{2.6}$$

$$\vec{J}(\vec{r},t) = \vec{J}_\mathrm{source}(\vec{r},t) + \sigma_\mathrm{e}(\vec{r})\, \vec{E}(\vec{r},t), \tag{2.7}$$

$$\vec{M}(\vec{r},t) = \vec{M}_\mathrm{source}(\vec{r},t) + \sigma_\mathrm{m}(\vec{r})\, \vec{H}(\vec{r},t). \tag{2.8}$$

Here, $\epsilon = \epsilon_0\epsilon_\mathrm{r}$ and $\mu = \mu_0\mu_\mathrm{r}$ are the *electric permittivity* and the *magnetic permeability* (the permittivity and permeability of the vacuum are denoted by ϵ_0 and μ_0, the relative permittivity and permeability by ϵ_r and μ_r), σ_e and σ_m the *electric conductivity* and the *equivalent magnetic loss*, and $\vec{J}_\mathrm{source}$ and $\vec{M}_\mathrm{source}$ the electric and magnetic current densities which act as independent sources of the electric and magnetic field energy.

The parameters ϵ, μ, and σ characterize the physical properties of a material. In anisotropic media, they become tensors (cf. Sec. 2.3). At a surface of discontinuity, boundary conditions need to be considered (see e. g. [69] Sec. 1.1.3).

2.1.3 Electromagnetic Waves

Light is an electromagnetic wave consisting of both electric and magnetic field components ($\vec{E}$ and $\vec{H}$) that oscillate perpendicularly to each other.

According to Maxwell's equations (2.1) and (2.2), the electric and magnetic field components are coupled: a time-varying electric field induces a magnetic field, and vice versa. In homogeneous, source-free media, the electric and magnetic field vectors obey the *wave equation* ([69] Sec. 1.2, see Appx. A.1 for derivation):

$$\nabla^2\vec{E} = \frac{1}{v^2}\frac{\partial^2}{\partial t^2}\vec{E}\,, \quad \nabla^2\vec{H} = \frac{1}{v^2}\frac{\partial^2}{\partial t^2}\vec{H}\,, \tag{2.9}$$

where v is the *phase velocity* of the electromagnetic wave, i. e. the rate at which the phase of the wave propagates in space. The phase velocity in a medium (v) and in vacuum (c) is given by ([69] Sec. 1.2):

$$v = \frac{1}{\sqrt{\epsilon\mu}}\,, \quad c = \frac{1}{\sqrt{\epsilon_0\mu_0}} = 299,792.458\,\frac{\mathrm{km}}{\mathrm{s}}. \tag{2.10}$$

The direction of phase propagation is defined by the *wave vector* $\vec{k}$ which is oriented perpendicularly to the surfaces of constant phase (*wave fronts*). The magnitude of the wave vector (*wave number*) is related to the phase velocity via:

[1] In general, the material equations are given in terms of the *polarization* $\vec{P}$ and the *magnetization* $\vec{M}$ of the material: $\vec{D} = \epsilon_0\vec{E} + \vec{P}$, $\vec{B} = \mu_0\,(\vec{H} + \vec{M})$.

$$k = \frac{\omega}{v} = \frac{2\pi}{\lambda_\mathrm{m}}, \tag{2.11}$$

where ω is the *angular frequency*, i. e. the angular change in unit time, and λ_m the wavelength in the medium (the wavelength in vacuum is denoted by λ).

In isotropic media, the wave vector $\vec{k}$ points in the direction of the energy flux, defined by the *Poynting vector* ([73] Sec. 28.3):

$$\vec{S}_\mathrm{E} = \vec{E} \times \vec{H}, \tag{2.12}$$

i. e. the electric field $\vec{E}$, the magnetic field $\vec{H}$, and the wave vector $\vec{k}$ form a right-handed orthogonal triad of vectors (see Appx. A.2). In anisotropic media, $\vec{k}$ and $\vec{S}_\mathrm{E}$ are not necessarily aligned (see Sec. 2.3.1).

The *intensity* of the light wave, i. e. the power transferred per unit area and unit time, is given by the time-averaged magnitude of the Poynting vector [69]: $I = \langle |\vec{S}_\mathrm{E}| \rangle$.

Plane Waves One simple solution to the wave equation are *plane waves*, i. e. the wave fronts are infinite parallel *planes of constant phase*.

A *plane monochromatic wave* that propagates through a homogeneous, isotropic, and non-attenuating medium in the direction of $\vec{k}$ is described by the complex electric field vector (cf. [70] Sec. 7.3):

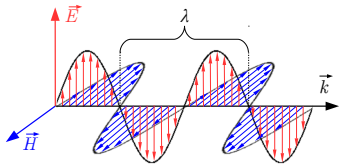

$$\vec{E}(\vec{r}, t) = \vec{E}_0 \, \mathrm{e}^{\mathrm{i}(\vec{k}\cdot\vec{r} - \omega t + \phi)}, \tag{2.13}$$

where ϕ denotes the *phase* and $\vec{E}_0$ the direction and amplitude of the electric field vector.

The intensity of a plane monochromatic wave is given by (cf. Appx. A.2):

$$I = \left\langle |\vec{S}_\mathrm{E}(\vec{r}, t)| \right\rangle \overset{(2.12)}{=} \left\langle \, |\vec{E}(\vec{r}, t)| \, |\vec{H}(\vec{r}, t)| \, \right\rangle \overset{(A.7),(2.10)}{=} \sqrt{\frac{\epsilon}{\mu}} \left\langle \, |\vec{E}(\vec{r}, t)|^2 \, \right\rangle \propto |\vec{E}_0|^2 \,. \tag{2.14}$$

The proportionality holds because ϵ and μ are material constants and the time average over the trigonometric functions in Eq. (2.13) yields a constant, e. g. $\langle \cos^2(x - \omega t) \rangle = \frac{1}{T} \int_0^T \cos^2(x - \omega t) \, \mathrm{d}t = \frac{1}{2}$, with $T = \frac{2\pi}{\omega}$ (cf. [70] Sec. 7.6).

2.1.3.1 Polarization of Light

The direction of the electric field vector $\vec{E}$ determines the *polarization state* of light. In anisotropic media, the polarization is determined by the direction of the electric flux density $\vec{D}$ (see Sec. 2.3.1).

Natural light is usually *unpolarized*, i. e. the direction of oscillation varies over time in an unpredictable manner. When the light is polarized, the direction of oscillation varies in a lawful manner. Depending on the shape that the vector $\vec{E}(\vec{r} = 0, t)$ describes in the plane perpendicular to $\vec{k}$, different polarization states can be distinguished ([70] Sec. 7.4), see Fig. 2.1:

- **linear polarization:** $\vec{E}$ always points in the same direction,
- **circular polarization:** $\vec{E}$ describes a circle (*right-handed* circular polarization: clockwise rotation; *left-handed* circular polarization: counter-clockwise rotation, when propagating towards the observer),
- **elliptical polarization:** $\vec{E}$ describes an ellipse.

Unpolarized light can be represented by an equal mixture of two opposite polarization states, e. g. horizontally and vertically linearly polarized light of equal intensity.

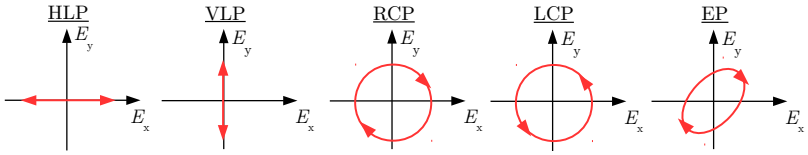

Fig. 2.1: Polarization states of light: horizontal/vertical linear polarization (HLP/VLP), right-/left-handed circular polarization (RCP/LCP), and elliptical polarization (EP). The figure shows the shape (in red) that $\vec{E}(\vec{r}=0,t)$ describes in the plane perpendicular to $\vec{k}$ ($\vec{k}$ points out of the image plane, towards the observer).

2.1.3.2 Coherence and Interference

The light sources used for the polarimetric measurements in this thesis emit mostly incoherent light, while the FDTD simulations can only model coherent light.

Spontaneously emitted light is *incoherent*, i. e. it consists of finite wave trains with randomly distributed phases that are completely uncorrelated. Light generated by stimulated emission (e. g. laser light) is *coherent*, i. e. the fluctuations of amplitudes and phases are correlated.

The maximum period of time during which the waves are coherent is called *coherence time*. The distance L_c that the light travels during the coherence time is called *coherence length* ([70] Sec. 10.1). The coherence length of monochromatic laser light can reach hundreds of meters. The higher the monochromacity of the light, the longer is the coherence length. The light sources used for the polarimetric measurements can be described by a Gaussian frequency spectrum. In this case, the coherence length[2] is given by ([74] Eq. 9):

$$L_\mathrm{c} = \frac{\hat{\lambda}^2}{\Delta\lambda}\sqrt{\frac{2\ln(2)}{\pi}}, \tag{2.15}$$

where $\hat{\lambda}$ is the peak wavelength and $\Delta\lambda$ the spectral bandwidth of the corresponding wavelength spectrum ($\Delta\lambda/\hat{\lambda}^2$ corresponds to the full width at half maximum of the Gaussian frequency spectrum).

The superposition of coherent waves leads to *interference*, i. e. the wave amplitude at a particular point is given by the vector sum of the amplitudes of the individual waves, which leads to interference patterns with alternating maxima and minima ([70] p. 307). Depending on the phase relationship, the resulting wave has a greater amplitude (*constructive* interference) or a lower amplitude (*destructive* interference) than the individual waves. The resulting intensity for plane monochromatic waves is given by: $I \propto |\sum_j \vec{E}_j|^2$. For incoherent light, no interference is observed. The intensity at a particular point in space is given by the sum of intensities of the individual waves: $I = \sum_j I_j \propto \sum_j |\vec{E}_j|^2$.

2.1.3.3 Diffraction

When light encounters a slit or another obstacle with dimensions comparable to the wavelength, the light is bent around the corners of the obstacle into the region of the

[2] Note that there exist different metrics of coherency so that coherence time and coherence length are not uniquely defined [74]. The given formula for L_c should therefore only be considered as an estimate of the coherence length.

geometrical shadow (*diffraction*). If the diffractive structure (of size W) is observed from a long distance ($\Delta L \gg W^2/\lambda$), the diffraction can be described by *Fraunhofer diffraction*. In the near field, it is described by *Fresnel diffraction* ([70] Sec. 10.6).

In the polarimetric measurements, the light wave is diffracted when passing through the finite aperture of the objective lens. The Fraunhofer diffraction pattern of a circular aperture with radius r is given by its Fourier transform (*Airy pattern*) ([70] p. 332):

$$I(\xi) = I_0 \left(\frac{2\, J_1(\xi)}{\xi} \right)^2, \quad \xi \equiv \frac{2\pi r}{\lambda_\mathrm{m}} \sin\theta, \tag{2.16}$$

where $J_1(\xi)$ is the Bessel function of the first kind of order one, θ the polar angular distance, and λ_m the wavelength in the medium. The first minimum occurs at: $\sin\theta \approx 0.61\,\lambda_\mathrm{m}/r$ (cf. Fig. 2.2).

Spatial Resolution Diffraction limits the spatial resolution. According to the *Rayleigh criterion*, two objects can just be resolved when the principal diffraction maximum of one object coincides with the first diffraction minimum of the other object [75]. Figure 2.2 shows the corresponding Airy patterns (cf. Eq. (2.16)) and the resulting intensity curve (in red) for incoherent light. The intensity between the principal maxima is about 26.5 % less than the maximum intensity, yielding a contrast $\mathcal{C} \approx 15.3\,\%$. Using this value as a reference, the resolution limits for two coherently (c) and incoherently (ic) illuminated object points that are observed with a microscope can be determined. The distance Δd between the two object points that can just be resolved by a microscope is given by ([69] pp. 466, 471):

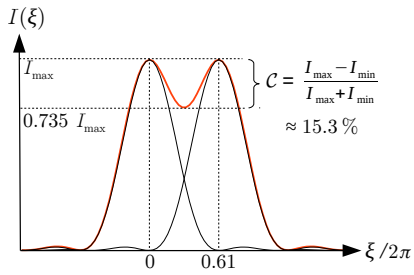

Fig. 2.2: Rayleigh criterion for two incoherent point sources with circular aperture

$$\Delta d_\mathrm{c} \approx 0.82\,\frac{\lambda}{\mathrm{NA}}, \quad \Delta d_\mathrm{ic} \approx 0.61\,\frac{\lambda}{\mathrm{NA}}, \tag{2.17}$$

where NA is the *numerical aperture* of the microscope objective which is defined by the refractive index n of the surrounding medium (see Sec. 2.2.1) and the maximum half-angle θ_max of the cone of light captured by the objective lens:

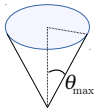

$$\mathrm{NA} = n\,\sin\theta_\mathrm{max}. \tag{2.18}$$

2.2 Refraction and Attenuation

When light propagates through a medium like brain tissue, the phase velocity and the wavelength of the light wave depend on the properties of the material, the frequency remains constant ([70] p. 224). At the boundary surface between two different media, the light therefore changes its direction of propagation under non-normal incidence (*refraction*, described in Sec. 2.2.1). At the same time, the light is attenuated when it passes through the medium due to absorption and/or scattering (described in Sec. 2.2.2).

2.2.1 Refraction and Reflection

Refractive Index The ratio of the phase velocity (or the wavelength) of light in vacuum and in the medium is defined by the *refractive index* ([70] Sec. 8.1):

$$n = \frac{c}{v} = \frac{\lambda}{\lambda_\mathrm{m}} \,. \tag{2.19}$$

The refractive index is related to the relative permittivity and permeability of the material via *Maxwell's formula* ([69] Sec. 1.2):

$$n = \sqrt{\epsilon_\mathrm{r} \mu_\mathrm{r}} \,. \tag{2.20}$$

For mostly non-magnetic materials like brain tissue, the refractive index is given by $\sqrt{\epsilon_\mathrm{r}}$.

In dispersive media, the refractive index depends on the wavelength of light in vacuum $n = n(\lambda)$.

Fresnel Equations The behavior of light between two media with different refractive indices is described by the *Fresnel equations* for transmission and reflection.

At the interface between two media with refractive indices n_1 and n_2, the incident light wave (with amplitude E) is partially refracted (i. e. transmitted with amplitude T) and partially reflected (with amplitude R), depending on the polarization of the light. The right-hand figure shows the refraction and reflection of the parallel (p) and perpendicular (s) components of the electric field of a plane wave in the *plane of incidence* (containing the wave vector $\vec{k}$ and the surface normal vector $\vec{n}$).

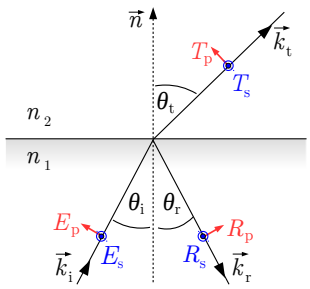

For non-magnetic linear isotropic materials, the *transmission*[3] and *reflection amplitudes* for p- and s-polarized light read [73]:

$$T_\mathrm{p} = \frac{2n_1 \cos(\theta_\mathrm{i})}{n_2 \cos(\theta_\mathrm{i}) + n_1 \cos(\theta_\mathrm{t})} E_\mathrm{p} \,, \qquad T_\mathrm{s} = \frac{2n_1 \cos(\theta_\mathrm{i})}{n_1 \cos(\theta_\mathrm{i}) + n_2 \cos(\theta_\mathrm{t})} E_\mathrm{s}, \tag{2.21}$$

$$R_\mathrm{p} = \frac{n_2 \cos(\theta_\mathrm{i}) - n_1 \cos(\theta_\mathrm{t})}{n_2 \cos(\theta_\mathrm{i}) + n_1 \cos(\theta_\mathrm{t})} E_\mathrm{p} \,, \qquad R_\mathrm{s} = \frac{n_1 \cos(\theta_\mathrm{i}) - n_2 \cos(\theta_\mathrm{t})}{n_1 \cos(\theta_\mathrm{i}) + n_2 \cos(\theta_\mathrm{t})} E_\mathrm{s} \,, \tag{2.22}$$

where θ_i is the angle of incidence and θ_t the angle of refraction (see above figure). The angle of reflection corresponds to the angle of incidence (*law of reflection*: $\theta_\mathrm{i} = \theta_\mathrm{r}$).

Snell's Law of Refraction The angles of incidence and refraction are related according to *Snell's law*:

$$n_1 \sin(\theta_\mathrm{i}) = n_2 \sin(\theta_\mathrm{t}) \,. \tag{2.23}$$

When the angle of refraction reaches $\theta_\mathrm{t} = 90°$, the light is *totally internally reflected* (see Appx. A.5), i. e. the light is captured within the first medium. If a third medium

[3] In contrast to many textbooks, the term "transmittance" (fraction of transmitted light) is not used here because it will be used in this thesis to refer to the polarization-independent transmitted light intensity obtained from the polarimetric measurements (cf. Sec. 4.4.1).

with higher refractive index is placed less than several wavelengths apart from the first medium, energy will be passed into the third medium (*frustrated total internal reflection*, [70] Sec. 8.4.6).

2.2.2 Absorption and Scattering

Absorption When the light wave interacts with the medium, part of the light is absorbed, i. e. the radiation power is transformed into other types of energy, e. g. heat. To account for absorption within the medium, a complex refractive index n' and a complex wave number k' are defined:

$$n' = n + \mathrm{i}\,\kappa, \tag{2.24}$$

$$k' = \frac{2\pi n'}{\lambda} = k + \mathrm{i}\,\frac{2\pi\kappa}{\lambda}. \tag{2.25}$$

Inserting k' in Eq. (2.13) yields (for a plane monochromatic wave propagating in the z-direction):

$$\vec{E}(z,t) = \vec{E}_0\ \mathrm{e}^{-\frac{2\pi\kappa z}{\lambda}}\ \mathrm{e}^{\mathrm{i}(kz-\omega t+\phi)} \equiv \vec{E}_0'(z)\ \mathrm{e}^{\mathrm{i}(kz-\omega t+\phi)}\,. \tag{2.26}$$

Thus, the imaginary part of the refractive index κ leads to an exponential decay. The intensity is proportional to the squared absolute value of the electric field amplitude (see Eq. (2.14)):

$$I(z) \propto |\vec{E}_0'(z)|^2 = |\vec{E}_0|^2\ \mathrm{e}^{-\frac{4\pi\kappa z}{\lambda}} \tag{2.27}$$

$$\Rightarrow I(z) = I_0\ \mathrm{e}^{-z\,K}\,. \tag{2.28}$$

This formula is known as the *Beer-Lambert law*, with I_0 being the *ingoing light intensity* and K being the *absorption coefficient* of the material ([70] p. 227):

$$K = \frac{4\pi\kappa}{\lambda}. \tag{2.29}$$

In dispersive media, the absorption depends on the wavelength of light in vacuum.

Scattering If the light is scattered[4] when passing through the medium, K has to be replaced by the *attenuation coefficient* μ_{att}, which is given by the sum of the absorption coefficient and the *scattering coefficient* $\mathcal{S}$:

$$\mu_{\mathrm{att}} = K + \mathcal{S} \quad \Rightarrow I(z) = I_0\ \mathrm{e}^{-z\,\mu_{\mathrm{att}}}. \tag{2.30}$$

2.3 Birefringence

This section introduces the principles of birefringence.[5] In 3D-PLI, the birefringence of brain tissue is measured to extract the spatial orientation of nerve fibers.

Birefringence is caused by orderly arranged molecules in a material (e. g. crystals) which lead to optical anisotropy. Birefringence might also be caused by orderly ar-

[4] In this thesis, scattering refers to everything that causes attenuation of light (in a particular direction) and that is not caused by absorption (i. e. energy transfer) of the light wave, e. g. scattering induced by multiple reflections or particle-particle collisions.

[5] In this thesis, the term "birefringence" always refers to linear birefringence.

ranged units of optically isotropic material with different refractive indices (e. g. layers of alternating refractive indices or long parallel cylinders) with dimensions larger than molecules, but smaller than the wavelength (*form birefringence*), cf. [69] p. 837.

In the following, the phenomenon of birefringence is described in more detail. The explanations follow Bergmann·Schäfer [76] (Chap. 4.5), Born·Wolf [69] (Chaps. 1.5, 15.1–15.3, 15.5.2), Demtröder [70] (Chaps. 7.4, 9.6.7), Hecht [71] (Chaps. 4.4, 8.4), Landau·Lifshitz [77] (Chap. 11), and Pedrotti [78] (Chap. 15.2). Note that the explanations do not necessarily hold for form birefringence. In this case, the reader is referred to related literature [69, 79–83].

2.3.1 Refractive Index Ellipsoid

In optically anisotropic media, the refractive index depends on the direction of propagation and on the polarization state of the incident light. In this case, the relative permittivity is given by a tensor $\tilde{\epsilon}_\mathrm{r}$ and Eq. (2.5) becomes: $\vec{D} = \epsilon_0 \tilde{\epsilon}_\mathrm{r} \vec{E}$, where $\vec{D}$ is oriented perpendicularly to the wave vector $\vec{k}$ and $\vec{E}$ is oriented perpendicularly to the Poynting vector $\vec{S}_\mathrm{E}$ (all vectors are coplanar, see right-hand figure, [70] Fig. 8.30). In case of non-absorbing media, all tensor elements are real; for media with no optical activity,[6] the tensor is symmetric.

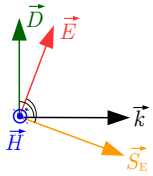

By choosing an appropriate coordinate system, the tensor $\tilde{\epsilon}_\mathrm{r}$ can be written in diagonal form (*principal axis transformation*) with diagonal entries $\epsilon_{\mathrm{r},i}$, where $n_i = \sqrt{\mu_\mathrm{r}\,\epsilon_{\mathrm{r},i}}$ are the refractive indices along the principal axes. The refractive index with respect to an arbitrary direction $\vec{n} = \{n_\mathrm{x}, n_\mathrm{y}, n_\mathrm{z}\}$ is defined by the so-called *refractive index ellipsoid* or *indicatrix* ([70] Sec. 8.5.2, see Appx. A.3 for derivation):

$$\frac{n_\mathrm{x}^2}{n_1^2} + \frac{n_\mathrm{y}^2}{n_2^2} + \frac{n_\mathrm{z}^2}{n_3^2} = 1. \tag{2.31}$$

For *uniaxial* birefringent materials like brain tissue (see Sec. 3.2.3), the index ellipsoid is given by a rotational ellipsoid (see Fig. 2.3) with one symmetry axis (*optic axis*) and two principal refractive indices:

- $n_\mathrm{o} \equiv n_1 = n_2$ (*ordinary* refractive index),
- $n_\mathrm{E} \equiv n_3$ (*extraordinary* refractive index).

The *birefringence* Δn of a material is defined as the difference between extraordinary and ordinary refractive index.[7] It is *positive* for $n_\mathrm{E} > n_\mathrm{o}$ and *negative* for $n_\mathrm{E} < n_\mathrm{o}$:

$$\Delta n \equiv n_\mathrm{E} - n_\mathrm{o}. \tag{2.32}$$

The birefringence of nerve fibers is negative with respect to the longitudinal fiber axis (see Sec. 3.2.3).

When light propagates through a uniaxial birefringent medium in the direction of $\vec{k}$, the plane through the center of the index ellipsoid perpendicular to $\vec{k}$ (*plane of constant phase* in gray) intersects the surface of the ellipsoid in an ellipse (green dotted line), see

[6] In media with optical activity, the polarization plane of linearly polarized light is rotated when it passes through the medium ([70] Sec. 8.6.5).

[7] In common literature, the principal extraordinary refractive index is denoted by n_e. In this thesis, it is denoted by n_E to distinguish it from the extraordinary refractive index $n_\mathrm{e}(\theta)$ which depends on the angle θ between the wave vector and the optic axis (see Eq. (2.33)).

Fig. 2.3a. The distance from the center to the border of the intersection curve in the direction of $\vec{D}$ indicates the (effective) refractive index that the electromagnetic wave experiences ([70] Sec. 8.5.2). Due to the birefringence, the light is split[8] into two waves with orthogonal linear polarization states (see Fig. 2.3b), which are defined by the vector of the electric flux density $\vec{D}$:

- **ordinary wave** (with refractive index n_o): $\vec{D}$ is oriented perpendicularly to the *principal plane* (containing the optic axis and the wave vector $\vec{k}$), i. e. perpendicularly to the optic axis projected onto the plane of constant phase. The ordinary wave obeys Snell's law of refraction for isotropic media, the velocity and the refractive index are independent of the direction of propagation ([70] Sec. 8.5.3).
- **extraordinary wave** (with refractive index $n_\mathrm{e}(\theta)$): $\vec{D}$ lies within the principal plane, parallel to the projection of the optic axis onto the plane of constant phase. The extraordinary wave can be refracted even at normal incidence, the velocity and the refractive index depend on the angle θ between $\vec{k}$ and the optic axis ([70] Sec. 8.5.3).

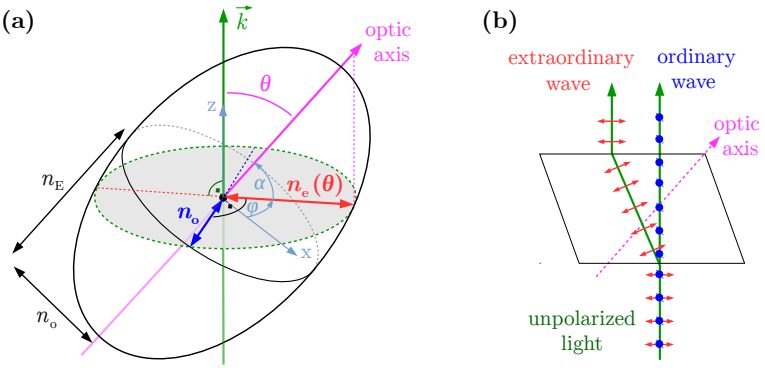

Fig. 2.3: (a) Rotational index ellipsoid of a positive uniaxial birefringent medium with $n_\mathrm{E} > n_\mathrm{o}$ (inspired by [70] Fig. 8.31a). The intersection curve (green dotted line) between the ellipsoid and the plane of constant phase (gray) defines the refractive index that a light wave with wave vector $\vec{k}$ experiences when it passes through the medium. The refractive index depends on the polarization, i. e. the direction of $\vec{D}$ in the plane of constant phase: In case of the extraordinary wave (with refractive index $n_\mathrm{e}(\theta)$), $\vec{D}$ lies parallel to the projection of the optic axis onto the plane of constant phase (red arrow). In case of the ordinary wave (with refractive index n_o), $\vec{D}$ lies perpendicularly to the optic axis and its projection (dark blue arrow). **(b)** Unpolarized light that passes through a birefringent medium is split into an ordinary wave (blue) and an extraordinary wave (red) with orthogonal linear polarization states. The ordinary wave obeys Snell's law, while the extraordinary wave is refracted even at normal incidence (adapted from [71] Fig. 8.19). The image plane shows the principal plane (spanned by the wave vector $\vec{k}$ and the optic axis).

The dependence of the extraordinary refractive index on the angle θ is given by (see Appx. A.3.1 for derivation):

[8] Light that is incident parallel to the optic axis is not split up because the refractive indices of ordinary and extraordinary wave are the same $\big(n_\mathrm{e}(\theta = 0°) = n_\mathrm{o}$, see Eq. (2.33)$\big)$.

$$n_{\mathrm{e}}(\theta) = \frac{1}{\sqrt{\frac{\cos^2\theta}{n_{\mathrm{o}}^2} + \frac{\sin^2\theta}{n_{\mathrm{E}}^2}}}\,. \tag{2.33}$$

In case of positive birefringence ($n_{\mathrm{E}} > n_{\mathrm{o}}$), the extraordinary refractive index becomes *minimal* for light that is incident parallel to the optic axis $\big(n_{\mathrm{e}}(\theta = 0°) = n_{\mathrm{o}}\big)$ and *maximal* for light that is incident perpendicularly to the optic axis $\big(n_{\mathrm{e}}(\theta = 90°) = n_{\mathrm{E}}\big)$. In case of negative birefringence ($n_{\mathrm{E}} < n_{\mathrm{o}}$), the situation is reversed.

More information about birefringence and the refractive index ellipsoid can be found in [70] (Sec. 8.5), [69] (Chap. 15), and [73] (Chap. 21).

2.3.2 Retardance

When light passes through a birefringent medium, it is split into an ordinary and an extraordinary wave. If the wave vector makes an angle θ with the optic axis, the phase velocities of these waves will be c/n_{o} and $c/n_{\mathrm{e}}(\theta)$, respectively. After passing through a birefringent medium of thickness d, the phase changes of ordinary and extraordinary wave are:

$$\phi_{\mathrm{o}} = k_{\mathrm{o}}\, d = \frac{2\pi n_{\mathrm{o}}\, d}{\lambda}, \tag{2.34}$$

$$\phi_{\mathrm{e}}(\theta) = k_{\mathrm{e}}(\theta)\, d = \frac{2\pi n_{\mathrm{e}}(\theta)\, d}{\lambda}. \tag{2.35}$$

The phase shift (*retardance*) of the extraordinary wave with respect to the ordinary wave is then ([70] Sec. 8.6.3):

$$\delta = \Delta\phi(\theta) = \phi_{\mathrm{e}}(\theta) - \phi_{\mathrm{o}} = \frac{2\pi d}{\lambda}\Big(n_{\mathrm{e}}(\theta) - n_{\mathrm{o}}\Big) \equiv \frac{2\pi d}{\lambda}\Delta n(\theta). \tag{2.36}$$

For materials with small birefringence like brain tissue ($|\Delta n| \ll n$), the retardance can be approximated as (see Appx. A.4.1 for derivation):

$$\delta \approx \frac{2\pi d}{\lambda}\,\Delta n\,\sin^2\theta. \tag{2.37}$$

2.3.3 Wave Retarders

Wave retarders introduce a phase shift between the two orthogonal polarization components of light, thus altering the state of polarization. They are usually made from uniaxial birefringent material with the optic axis lying parallel to the retarder surfaces, which induces a maximum retardance for normally incident light. Depending on the type of birefringence (positive or negative), the ordinary or the extraordinary wave travels faster; the corresponding axes are referred to as *fast* and *slow axes*, accordingly. Wave retarders are manufactured to work for a particular wavelength (*optimal working wavelength*) because the retardance δ depends on the wavelength (see Eq. (2.36)).

A wave plate that induces a retardance $\delta = \pi/2$ is called *quarter-wave retarder*. To generate circularly polarized light, a linear polarizer and a quarter-wave retarder are combined: if the polarizer axis (i. e. the direction of linear polarization) is oriented at +/- 45° with respect to the fast axis of the retarder, the resulting light will be right/left-handed circularly polarized ([70] Sec. 8.6.3).

2.4 Diattenuation

The anisotropy of a material that gives rise to birefringence (anisotropy of refraction) may also lead to *diattenuation*[9] (anisotropy of attenuation) [57, 58]. The anisotropic attenuation of light can be caused by anisotropic absorption (*dichroism* D_K) as well as by *anisotropic scattering* ($D_\mathcal{S}$) [57, 61, 69, 84, 85]. In this thesis, the diattenuation of brain tissue was investigated both in experimental studies (Chap. 9) and in numerical simulations (Chap. 12).

In diattenuating materials, the transmitted light intensity depends on the polarization state of the incident light: the transmitted light intensity becomes maximal (I_max) for light polarized in a particular direction and minimal (I_min) for light polarized in the corresponding orthogonal direction (for uniaxial systems). In this thesis, the direction of polarization (i. e. the azimuthal angle in the plane of constant phase) for which the transmitted light intensity becomes maximal is referred to as:

$$\varphi_\mathrm{D} \equiv \varphi\big(I = I_\mathrm{max}\big), \qquad 0 \leq \varphi_\mathrm{D} \leq \pi. \tag{2.38}$$

The *strength of the diattenuation*[10] is defined as [57, 85]:

$$|D| = \frac{I_\mathrm{max} - I_\mathrm{min}}{I_\mathrm{max} + I_\mathrm{min}}, \qquad 0 \leq |D| \leq 1. \tag{2.39}$$

The *average transmittance*, i. e. the fraction of unpolarized light that is transmitted through a sample, is given by [57]:

$$\tau = \frac{I_\mathrm{max} + I_\mathrm{min}}{2\,I_0}, \qquad 0 \leq \tau \leq 1, \tag{2.40}$$

with I_0 being the ingoing light intensity.

Instead of expressing the diattenuation in terms of the light intensity ($I = I_0\ \mathrm{e}^{-d\,\mu_\mathrm{att}}$) that is transmitted through a medium of thickness d, it can be written in terms of the corresponding attenuation coefficient μ_att. With $I_\mathrm{max} = I_0\ \mathrm{e}^{-d\,\mu_\mathrm{min}}$ and $I_\mathrm{min} = I_0\ \mathrm{e}^{-d\,\mu_\mathrm{max}}$, the above equations can be written in terms of the maximum and minimum attenuation coefficients μ_max and μ_min (see Appx. A.4.3.1):

$$|D| = \tanh\left(d\ \frac{\mu_\mathrm{max} - \mu_\mathrm{min}}{2}\right), \tag{2.41}$$

$$\tau = \mathrm{e}^{-d\,\frac{\mu_\mathrm{max}+\mu_\mathrm{min}}{2}}\ \cosh\left(d\ \frac{\mu_\mathrm{max} - \mu_\mathrm{min}}{2}\right). \tag{2.42}$$

2.4.1 Diattenuation and Birefringence with Shared Principal Axes

As diattenuation and birefringence are usually caused by the same anisotropic structure, the principal axes of diattenuation are usually coincident with the principal axes of birefringence [57]. The symmetry axis of the material corresponds to the optic axis (with direction angle φ and inclination angle $(90° - \theta)$ defined relative to the plane of constant phase, cf. Fig. 2.3a). The extraordinary (ordinary) wave is polarized parallel (perpendicularly) to the projection of the optic axis onto the plane of constant phase

[9] In this thesis, the term "diattenuation" refers to linear diattenuation.

[10] In the literature, this formula is simply referred to as "diattenuation" without absolute value signs. In this thesis, the formula is referred to as "strength of the diattenuation" with absolute value signs to enable the definition of a "signed diattenuation" ($D \gtrless 0$) in Sec. 2.4.1.

(see Sec. 2.3.1), i. e. in the direction φ ($\varphi + 90°$). The transmitted light intensity of the extraordinary (ordinary) wave is therefore denoted by $I_\parallel$ ($I_\perp$), accordingly,[11] and assumed to become extremal ($I_{\max}$ or $I_{\min}$). Thus, if the direction angle φ of the optic axis is known, a *signed diattenuation* can be defined instead of Eqs. (2.38) and (2.39):

$$D = \frac{I_\parallel - I_\perp}{I_\parallel + I_\perp}, \quad -1 \le D \le 1 \quad \begin{cases} D > 0 \;\Rightarrow \varphi_{\mathrm{D}} = \varphi, \\ D < 0 \;\Rightarrow \varphi_{\mathrm{D}} = \varphi + 90°, \end{cases} \tag{2.43}$$

where the absolute value of D corresponds to $|D|$ and the sign of D in combination with the direction angle φ of the optic axis defines φ_{D}. In other words, when D is positive ($I_\parallel > I_\perp$), the transmitted light intensity becomes maximal for the extraordinary wave which is polarized in the direction of $\varphi_{\mathrm{D}} = \varphi$. When D is negative ($I_\perp > I_\parallel$), the transmitted light intensity becomes maximal for the ordinary wave which is polarized in the direction of $\varphi_{\mathrm{D}} = (\varphi + 90°)$.

2.4.2 Dichroism

In the absence of anisotropic scattering, the diattenuation of a material is only caused by anisotropic absorption (dichroism: $D = D_{\mathrm{K}}$), i. e. the material absorbs light by different amounts depending on its polarization state ([69] Chap. 15.6).

Birefringence and dichroism can be regarded as two forms of appearance of the same phenomenon, which is that the complex refractive index n' of an anisotropic material depends on the polarization of the incident light: while the birefringence (anisotropic refraction) is caused by the real part of the refractive index (n) and influences the velocity of propagation, the dichroism (anisotropic absorption) is caused by the imaginary part of the refractive index (κ) and influences the absorption of light. Thus, birefringence and dichroism can be described by the real and imaginary parts of a complex retardance [69, 86]. To account for the analogy between birefringence and dichroism, the transmitted light intensities of ordinary and extraordinary wave are referred to as $I_{\mathrm{o}} = I_0\ \mathrm{e}^{-dK_{\mathrm{o}}} \equiv I_\perp$ and $I_{\mathrm{e}} = I_0\ \mathrm{e}^{-dK_{\mathrm{e}}} \equiv I_\parallel$, respectively, where $K_{\mathrm{o}} = 4\pi\kappa_{\mathrm{o}}/\lambda$ and $K_{\mathrm{e}} = 4\pi\kappa_{\mathrm{e}}/\lambda$ are the absorption coefficients that ordinary and extraordinary waves experience when passing through the material. With this definition, Eq. (2.43) can be written as (cf. Eq. (2.41)):

$$D_{\mathrm{K}} = \tanh\left(\frac{d}{2}\,(K_{\mathrm{o}} - K_{\mathrm{e}})\right) = \tanh\left(-\frac{2\pi d}{\lambda}\,(\kappa_{\mathrm{e}} - \kappa_{\mathrm{o}})\right) \equiv \tanh(-\delta_{\mathrm{K}}). \tag{2.44}$$

In materials like brain tissue where absorption and birefringence are small compared to the refractive index ($\kappa \ll n$ and $|\Delta n| \ll n$), the absorption of the ordinary wave (κ_{o}) is independent of the direction of propagation, while the absorption of the extraordinary wave ($\kappa_{\mathrm{e}}(\theta)$) depends on the angle θ between the wave vector and the optic axis (see Appx. A.3.2). In this case, the *dichroism* δ_{K} is approximately proportional to the retardance δ in Eq. (2.37) (see Appx. A.4.3.2):

$$\delta_{\mathrm{K}} \approx \frac{2\pi d}{\lambda}\Delta\kappa\,\sin^2\theta \quad \propto \quad \delta\,, \qquad \Delta\kappa \equiv \kappa_{\mathrm{E}} - \kappa_{\mathrm{o}}, \tag{2.45}$$

where κ_{E} is the imaginary part of the principal extraordinary refractive index.

[11] As diattenuation is also caused by anisotropic scattering, the anisotropic attenuation of light cannot necessarily be described in terms of an "attenuation ellipsoid". To avoid confusion with the refractive index ellipsoid (with principal axes n_{o} and n_{e}), the transmitted light intensities of the extraordinary and ordinary wave are here referred to as $I_\parallel$ and $I_\perp$ and not as I_{e} and I_{o}.

More information about the relationship between dichroism and birefringence can be found in Appx. A.4.3.3.

2.4.3 Linear Polarizers

Optical elements with high diattenuation can be used to create linearly polarized light. An ideal linear polarizer (*linear diattenuator*) fulfills $|D| = 1, \tau = 1/2$, i. e. the intensity of unpolarized light is reduced by one half.
Linear polarizers convert unpolarized light into linearly polarized light by transmitting all $\vec{E}$ oscillations in a certain direction $\varphi_\mathrm{D} = \varphi$ (corresponding to the axis of the polarizer) and blocking all $\vec{E}$ oscillations perpendicular to it (see right-hand figure, [70] Sec. 8.6.2). In general, the selectivity is not perfect ($|D| < 1$) and the transmitted light is not completely polarized.

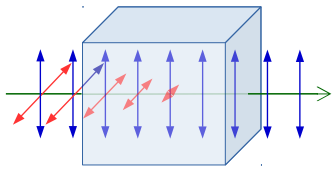

2.5 Matrix Calculus

In this section, the Jones and Müller-Stokes formalisms are introduced which allow for a mathematical description of polarized light. The Jones calculus is only applicable to completely polarized and coherent light and was used for the description of the FDTD simulations in Part IV. The more complex Müller-Stokes formalism is also suitable for the description of partially polarized and incoherent light and was used for the signal analysis of the polarimetric measurements introduced in Chap. 4.

The explanations follow Goldstein [73] (Chaps. 5, 6, 10), Demtröder [70] (Chap. 9.6.7), Chipman [85] (Chap. 22), Collett [87] (pp. 12–24, 57–60), Hecht [71] (Chap. 8.13), and Pedrotti *et al.* [78] (Chap. 14).

2.5.1 Jones Formalism

The Jones matrix formalism was first introduced by Jones in 1941 [88, 89] and describes the change in the polarization state of (completely polarized and coherent) light when passing through a set of optical elements. The polarization state of light is represented by a 2×1 vector (*Jones vector*), the optical elements are treated as a linear system represented by a 2×2 matrix (*Jones matrix*).

Jones vectors: The Jones vector is defined as normalized polarization vector (see Sec. 2.1.3.1):

$$\vec{J} = \frac{1}{|\vec{E}|} \begin{pmatrix} E_{0\mathrm{x}}\, \mathrm{e}^{\mathrm{i}\,\phi_\mathrm{x}} \\ E_{0\mathrm{y}}\, \mathrm{e}^{\mathrm{i}\,\phi_\mathrm{y}} \end{pmatrix}. \tag{2.46}$$

The Jones vectors of linearly polarized light (LP: $\phi_\mathrm{x} = \phi_\mathrm{y} \equiv 0$), right-/left-handed circularly polarized light (RCP/LCP: $E_{0\mathrm{x}} = E_{0\mathrm{y}} = |\vec{E}|/\sqrt{2}$, $\phi_\mathrm{x} - \phi_\mathrm{y} = \pm\pi/2$), and elliptically polarized light (EP) are thus given by [71, 87]:

$$\vec{J}_\mathrm{LP} = \begin{pmatrix} \cos\psi \\ \sin\psi \end{pmatrix}, \quad \vec{J}_\mathrm{RCP/LCP} = \frac{1}{\sqrt{2}} \begin{pmatrix} 1 \\ \pm\,\mathrm{i} \end{pmatrix}, \quad \vec{J}_\mathrm{EP} = \frac{1}{|\vec{E}|} \begin{pmatrix} E_{0\mathrm{x}} \\ E_{0\mathrm{y}}\, \mathrm{e}^{-\mathrm{i}\,\phi} \end{pmatrix}, \tag{2.47}$$

where ψ is the angle between the polarization vector $\vec{E}$ and the x-axis (in counter-clockwise direction).

Jones matrices: When an input beam described by the electric field vector $\vec{E}$ (Jones vector $\vec{J}$) passes an assembly of optical (polarizing) elements described by the Jones matrix J, the resulting output beam is:

$$\vec{E}' = J \cdot \vec{E}. \tag{2.48}$$

The Jones matrices for an ideal linear horizontal polarizer (P_x) and an ideal linear vertical polarizer (P_y) are given by:

$$P_\mathrm{x} = \begin{pmatrix} 1 & 0 \\ 0 & 0 \end{pmatrix}, \quad P_\mathrm{y} = \begin{pmatrix} 0 & 0 \\ 0 & 1 \end{pmatrix}. \tag{2.49}$$

A wave retarder which introduces a phase difference $\delta > 0$ between two orthogonal components of a light wave, i. e. a phase shift $\delta/2$ along the fast axis (x-axis) and $-\delta/2$ along the slow axis (y-axis), can be described by the Jones matrix:

$$M_\mathrm{ret} = \begin{pmatrix} \mathrm{e}^{\mathrm{i}\,\delta/2} & 0 \\ 0 & \mathrm{e}^{-\mathrm{i}\,\delta/2} \end{pmatrix}. \tag{2.50}$$

When an optical element (described by the Jones matrix J) is rotated counter-clockwise by an angle ξ, the rotated element is given by the matrix:

$$J(\xi) = R(\xi) \cdot J \cdot R(-\xi), \tag{2.51}$$

where the rotation matrix R is defined as:

$$R(\xi) = \begin{pmatrix} \cos\xi & -\sin\xi \\ \sin\xi & \cos\xi \end{pmatrix}. \tag{2.52}$$

2.5.2 Müller-Stokes Formalism

A drawback of the Jones calculus is that it is only applicable to completely polarized and coherent light. In the polarimetric measurements used in this thesis, the light is mostly incoherent and not completely polarized. For treating partially polarized as well as incoherent light, the more complex *Müller-Stokes formalism* has to be used. The Müller calculus allows for a complete mathematical description of polarized light and was first introduced by Müller in 1943 [90]. The polarization state of light is described by a 4×1 vector (*Stokes vector*), the optical elements of the setup are represented by a 4×4 matrix (*Müller matrix*).

Stokes vectors: The Stokes vector was first introduced by Stokes in 1852 [91] and is defined in terms of the electric field vector $\vec{E}$ via [85, 87]:

$$\vec{S} = \begin{pmatrix} S_0 \\ S_1 \\ S_2 \\ S_3 \end{pmatrix} = \begin{pmatrix} |E_\mathrm{x}|^2 + |E_\mathrm{y}|^2 \\ |E_\mathrm{x}|^2 - |E_\mathrm{y}|^2 \\ 2\,\Re(E_\mathrm{x}\,E_\mathrm{y}^*) \\ -2\,\Im(E_\mathrm{x}\,E_\mathrm{y}^*) \end{pmatrix} \equiv \begin{pmatrix} I \\ P_\mathrm{HLP} - P_\mathrm{VLP} \\ P_{45^\circ} - P_{-45^\circ} \\ P_\mathrm{RCP} - P_\mathrm{LCP} \end{pmatrix}, \quad S_0^2 \geq S_1^2 + S_2^2 + S_3^2. \tag{2.53}$$

The first Stokes parameter S_0 describes the total intensity I of the light beam, the second the predominance of horizontally over vertically linearly polarized light, the third the predominance of $+45°$ over $-45°$ linearly polarized light, and the fourth the predominance of right- over left-handed circularly polarized light (cf. Fig. 2.1). The Stokes vectors for these polarization states (linearly/circularly polarized light) are given by [87]:

$$\vec{S}_{\text{HLP/VLP}} = I_0 \begin{pmatrix} 1 \\ \pm 1 \\ 0 \\ 0 \end{pmatrix}, \quad \vec{S}_{\text{+/-45°}} = I_0 \begin{pmatrix} 1 \\ 0 \\ \pm 1 \\ 0 \end{pmatrix}, \quad \vec{S}_{\text{RCP/LCP}} = I_0 \begin{pmatrix} 1 \\ 0 \\ 0 \\ \pm 1 \end{pmatrix}. \tag{2.54}$$

In spherical coordinates, the Stokes vector is defined as [87]:

$$\vec{S} = \begin{pmatrix} I \\ I\,p\,\cos(2\psi)\,\cos(2\chi) \\ I\,p\,\sin(2\psi)\,\cos(2\chi) \\ I\,p\,\sin(2\chi) \end{pmatrix}, \quad p \equiv \frac{\sqrt{S_1^2 + S_2^2 + S_3^2}}{S_0}, \tag{2.55}$$

where I is the total intensity of the light beam, $p \in [0, 1]$ is the *degree of polarization*, and $\psi \in [0, \pi]$ and $\chi \in [-\pi/4, \pi/4]$ are the *spherical angles* which determine the orientation of the vector (S_1, S_2, S_3) in the *Poincaré sphere* (see Fig. 2.4), i. e. the (linear/circular) polarization of the light. For completely unpolarized light, the degree of polarization is zero ($p = 0$) and the Stokes vector simplifies to: $\vec{S}_{\text{unpol}} = (I, 0, 0, 0)^\top$.

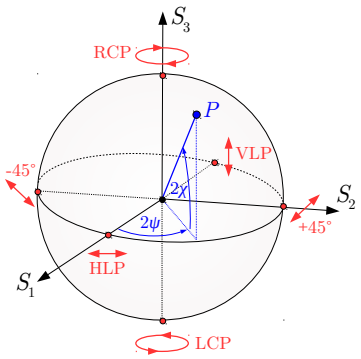

Fig. 2.4: Poincaré sphere used to represent polarized light (inspired by [87]): Every polarization state P is represented by a vector in Cartesian coordinates (S_1, S_2, S_3) or spherical coordinates (2ψ, 2χ). The length of the vector represents the degree of polarization $p \leq 1$ ($p = 0$ corresponds to the origin and $p = 1$ to the surface of the sphere). Linear polarization states lie on the equator, circular polarization states at the poles, elliptical polarization states everywhere else on the surface (see Fig. 2.1 for the definition of polarization states).

Müller matrices: The optical elements used in this thesis can be represented by a wave retarder and/or diattenuator. The Müller matrix for a general wave retarder and diattenuator (with retardance δ, diattenuation D, and average transmittance τ) is given by [57, 85]:

$$\mathcal{M}(\delta,\, D,\, \tau) = \tau \begin{pmatrix} 1 & D & 0 & 0 \\ D & 1 & 0 & 0 \\ 0 & 0 & \sqrt{1-D^2}\,\cos\delta & \sqrt{1-D^2}\,\sin\delta \\ 0 & 0 & -\sqrt{1-D^2}\,\sin\delta & \sqrt{1-D^2}\,\cos\delta \end{pmatrix}. \tag{2.56}$$

In this representation, it is assumed that the principal axes of birefringence and diattenuation are coincident and that their projections onto the xy-plane of the reference frame are aligned with the corresponding x- and y-axes. The fast axis of the retarder is chosen to be aligned with the x-axis. For materials with negative birefringence, the x-axis is oriented parallel to the projection of the optic axis onto the xy-plane. For $D > 0$ ($D < 0$), the axis of maximum (minimum) transmitted light intensity is aligned with the x-axis. These definitions will be used in all subsequent formulas and derivations.

A rotation in counter-clockwise direction by an angle ξ is described by the rotation matrix [85]:

$$R(\xi) = \begin{pmatrix} 1 & 0 & 0 & 0 \\ 0 & \cos(2\xi) & -\sin(2\xi) & 0 \\ 0 & \sin(2\xi) & \cos(2\xi) & 0 \\ 0 & 0 & 0 & 1 \end{pmatrix}. \tag{2.57}$$

The Müller matrix of a retarder and/or diattenuator rotated in counter-clockwise direction by an angle ξ is given by [85]:

$$\mathcal{M}(\xi,\, \delta,\, D,\, \tau) = R(\xi) \cdot \mathcal{M}(\delta,\, D,\, \tau) \cdot R(-\xi). \tag{2.58}$$

When an input beam described by a Stokes vector $\vec{S}$ passes an assembly of optical elements described by a Müller matrix $\mathcal{M}$, the resulting output beam is given by:

$$\vec{S}' = \mathcal{M} \cdot \vec{S}, \tag{2.59}$$

where the first entry of the resulting Stokes vector (S_0') describes the intensity of the output beam.

Chapter 3

Properties of Brain Tissue

In order to analyze the measurement results in Part III and to generate a proper simulation model in Part IV, the properties of brain tissue need to be known. This chapter provides a literature review about the structure (Sec. 3.1) and the optical properties (Sec. 3.2) of brain tissue. A special focus is placed on the dimensions of nerve fibers and the refractive indices of the different tissue components because these properties were used in Part IV to develop simulation models of the nerve fiber architecture. The general structure and the optical properties are mostly described for the human brain. If not otherwise stated, the properties also hold for brains from other mammals that were investigated in this thesis (vervet monkey, rat, and mouse).

3.1 Structure of Brain Tissue

The description of the brain structure follows Squire *et al.* [6] (Chaps. 1–3), Thieme [92] (Chaps. 1, 4), Zilles·Tillmann (Chap. 17) [93], and Kandel *et al.* [5] (Chaps. 1, 2, 4, 17). The description of the myelin structure follows Quarles *et al.* [43], Aggarwal *et al.* [94], Martenson [95], Morell *et al.* [96], and Hildebrand *et al.* [97]. Passages that refer to a certain textbook are labeled by separate bibliographic references.

The mammalian brain is a highly complex organ. It consists of the *cerebellum* ("little brain") and the larger *cerebrum* which is divided into two *hemispheres* (see Fig. 3.1a-b). Together with the spinal cord, the brain forms the *central nervous system (CNS)*. The morphological structure of brain tissue will be described in Sec. 3.1.1.

The primary components of the CNS are the nerve cells (*neurons*). An average human brain contains about 100 billion neurons [4–7] and even more *glial cells* [6, 8, 93] which protect and support the neurons, e. g. by supplying nutrients and aiding in recovery from neural injury [5, 92, 93]. On average, each neuron in the *cerebral cortex* (outer surface of the brain) is connected to 1000–10,000 other neurons [6, 8, 93].

Figure 3.1c shows the principal components of a neuron: The cell body (*soma*) is the metabolic center of the neuron, the tree-like *dendrites* receive incoming signals from neighboring neurons via synapses, and the long tubular *axon* transmits the signals encoded in electrical impulses to other neurons. Some axons are surrounded by a fatty, insulating layer – the so-called *myelin sheath* – which enhances the conduction speed.

The dimensions of the myelinated axons, the so-called *nerve fibers* [93], and the structure of the myelin sheath will be described in Secs. 3.1.2 and 3.1.3. For more detailed information about the brain's structure and function, the reader is referred to text books about neuroanatomy [5, 6, 93, 98].

3.1.1 Gray and White Matter

Morphologically, two major types of brain tissue are distinguished (see Fig. 3.1b): *gray matter (GM)* with a dark color and *white matter (WM)* with a lighter color.[1]

Gray matter contains mostly neuronal cell bodies as well as dendrites, synapses, unmyelinated axons, glial cells, and blood capillaries. Most of the gray matter is located at the outer surface of the brain, in the cerebral and cerebellar cortex [92]. But also inner parts of the brain – the sub-cortical nuclei such as the *thalamus* (see Fig. 3.1b) – contain islands of gray matter.

White matter is mainly composed of myelinated axons which connect different gray matter areas, but it also contains glial cells and blood capillaries. The characteristic white color is caused by the high content of lipids in the myelin sheath (see Sec. 3.1.3). White matter is located below the cortex and surrounds more deeply placed groups of gray matter [92]. A prominent white matter structure in the brain is the *corpus callosum* [99] which connects the two cerebral hemispheres (see Fig. 3.1b).

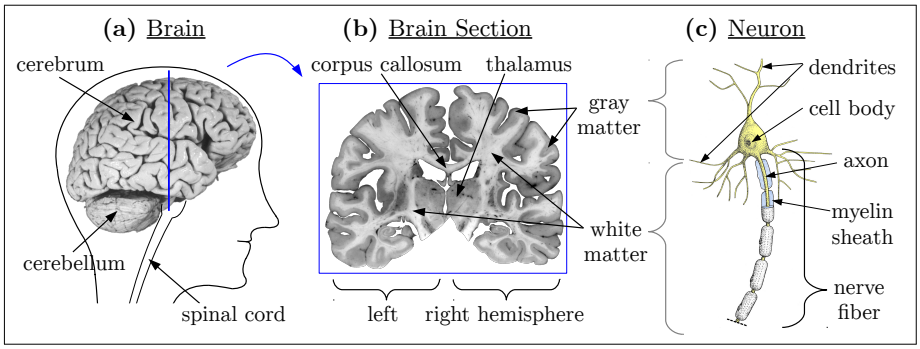

Fig. 3.1: Distinction of gray and white matter in the brain: **(a)** human brain, **(b)** coronal section through a formalin-fixated human brain, **(c)** nerve cell (neuron) consisting of a cell body, dendrites, and a nerve fiber (myelinated axon). The darker outer surface of the brain (gray matter) contains mostly nerve cell bodies and dendrites, while the brighter inner parts of the brain (white matter) contain mostly nerve fibers. (Copyright: INM-1, FZJ, Germany)

3.1.2 Nerve Fibers

Nerve fibers (myelinated axons) are mostly located in the white matter. Due to their strong birefringence (see Sec. 3.2.3), they show strong contrasts in 3D-PLI measurements.

Nerve fibers vary greatly in length: short-distance fibers are only 100 µm long, long-distance fibers reach lengths of up to 15 cm in the human brain [100]. The fiber diameter and the myelin sheath thickness increase with the fiber length [6] so that the conduction speed of the nerve impulses is maintained.

In the mammalian brain, the axon diameters differ by a factor of more than 100: some cortical axons are only 0.1 µm thick, while the diameter of axons in the optic nerve can be larger than 10 µm. Unmyelinated axons always have small diameters (less than 1 µm [97]). The diameters of myelinated axons in the human CNS range from 0.2 µm to 20 µm or even more [5, 7, 97, 100, 101]; the average diameter is rather small: Light

[1] Note that gray and white matter look different when transmitting light through the brain tissue: due to a higher attenuation coefficient (see Sec. 3.2.2), white matter appears darker than gray matter in the transmittance image (cf. Fig. 4.5a).

microscopy studies of the largest fiber bundle in the human brain – the corpus callosum – have shown that 80 % of the nerve fibers have diameters of 1 µm or below (median: 0.6–1 µm). Only 0.1 % (0.02 %) of the fibers have diameters larger than 3 µm (5 µm) [101, 102]. More recent electron microscopy studies[2] of various white matter regions in three human brains and one macaque brain yielded an average axon diameter of 0.5–0.8 µm [100]. Similar values were reported for the inner diameter of myelinated axons in the mouse brain measured with electron microscopy [41] and with in-vivo spectral reflectometry [103].

As a rule of thumb, the thickness of the myelin sheath contributes approximately one third to the overall fiber radius, thus providing optimal conduction speed [96]. Reported values for the *g-ratio* (the ratio of the axonal diameter to the total outer diameter of the nerve fiber) range from 0.5 to 0.85 [103]. The optimum g-ratio for the CNS was determined as 0.77 [104].

3.1.3 Myelin Sheath

Most axons in the CNS are myelinated [92, 97], especially in the white matter. The myelin sheath is an electrically insulating layer which increases the conduction speed of the nerve impulses by 10–100 times [6, 7]. It is synthesized by *oligodendrocytes* (a type of glial cells) which form extensions of their cytoplasmic membrane and spirally wrap them around up to 50 neighboring axons [43, 105], yielding stacks of densely packed cell membranes (see Fig. 3.2b). Depending on the fiber diameter, the myelin sheath segments (*internodes*) are between 150 µm and 1.5 mm [7, 97] (occasionally up to 3 mm [93]) long. They are separated at regular intervals by myelin-sheath gaps of about 1 µm [7, 41, 97] – the so-called *nodes of Ranvier* (see Fig. 3.2a). The electric impulses "jump" from one node of Ranvier to the next (*saltatory conduction*) [92], which increases the conduction speed of myelinated axons up to 100 m/s [5, 7].

The mature CNS myelin sheath consists of up to 160 compacted *lamellae* (two fused cell membranes) [97] which are each about 16 nm thick[3] [43, 95–97]: the cell membranes are about 5 nm thick [95, 107], the intracellular (*cytoplasmic*) and the extracellular space are about 3 nm [95, 107] (see Fig. 3.2c). The space between axon and myelin sheath (*periaxonal space*) is about the same size as the extracellular space in the CNS [97]. As the extracellular membranes are not fused [43], the extracellular spaces swell in aqueous solutions [95], like the glycerin solution used for the tissue embedding in 3D-PLI (see Sec. 4.1).

Figure 3.2c shows the molecular structure of the myelin sheath: Each cell membrane consists of a bimolecular layer of lipid molecules (70–85 %), the so-called *lipid bilayer*, and of different membrane proteins (15–30 %). The proteins are embedded in the bilayer, like the *proteolipid protein (PLP)*, or attached to the surface, like the *myelin basic protein (MBP)* [43, 94–96, 107, 108]. The lipid molecules are oriented radially around the axon, whereas the proteins are oriented tangentially with respect to the longitudinal axis of the axon [96]. The highly organized structure of the myelin sheath is responsible for the strong birefringence of myelinated axons (see Sec. 3.2.3).

More detailed information about the myelin formation and structure can be found in [43, 94, 109].

[2] Note that samples used for electron microscopy shrink during the preparation process so that the determined fiber diameters might differ from those observed in native tissue.

[3] In fixated and dehydrated tissue (used e. g. in electron microscopy), the lamellar spacing may shrink down to 8 nm [43, 95, 97]. The brain sections used in this thesis were fixated with formaldehyde and embedded in an aqueous glycerin solution (see Sec. 4.1) so that the shrinking can be neglected if the sections are measured directly after embedding [106].

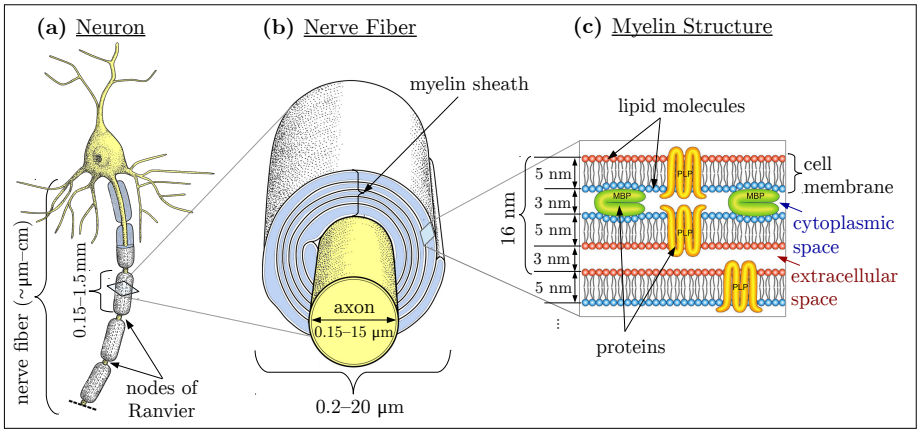

Fig. 3.2: Structure and dimensions of the CNS myelin sheath: **(a)** Nerve fibers consist of an axon (yellow) and a surrounding myelin sheath (blue) which is interrupted by nodes of Ranvier. **(b)** The myelin sheath is formed by extensions of oligodendrocytes which are spirally wrapped around the axon, yielding nearly concentric rings of densely packed cell membranes. For reasons of simplicity, the cell bodies of the oligodendrocytes are not shown. (Copyright: INM-1, FZJ, Germany) **(c)** Schematic representation of the myelin structure, consisting of bimolecular layers of lipids (red/blue) and membrane proteins (PLP/MBP). (Source: Aggarwal *et al.* [94] Fig. 2, Copyright (2012), with permission from Elsevier)

Table 3.1 summarizes the typical dimensions of nerve fibers in the brain (axon and myelin sheath).

	Value	Reference
fiber length	100 µm – 15 cm	[100]
internode distance	150 µm – 1.5 mm	[7, 97]
fiber diameter ($2r$)	(0.2 – 20) µm, (0.5 – 1) µm (avg./median)	[5, 97, 100, 101, 110], [100, 102, 103]
myelin sheath thickness (t_{sheath})	$\sim r/3$, (0.15 – 0.5) r	[96], [103]
lamella thickness	16 nm	[43, 95–97]
cell membrane thickness	5 nm	[92, 95]
cytoplasmic space	3 nm	[92, 95]
extracellular/periaxonal space	3 nm (swells in solution)	[43, 92, 95, 97]

Tab. 3.1: Dimensions of nerve fibers (myelinated axons) in the brain, assuming native tissue without fixation

3.2 Optical Properties of Brain Tissue

The optical properties of brain tissue influence the transmitted light intensity. In this thesis, measurements of the transmittance, birefringence, and diattenuation of brain tissue were used to derive tissue properties and structural information about the nerve fiber architecture. In order to analyze and model the polarimetric measurements correctly, the optical properties of the different tissue components need to be defined as precisely as possible.

The optical properties of brain tissue vary between different brain regions and strongly depend on the preparation of the tissue. The brain sections used for the polarimetric measurements in this thesis were formalin fixated, embedded in glycerin solution, and measured at peak wavelengths of 529 nm or 550 nm (see Secs. 4.1 and 7.1.1). Literature values are only given for fresh tissue or for fixated tissue prepared with other techniques. In many cases, the measurements were also performed with a different wavelength. Therefore, it is only possible to make rough estimates for the optical properties of the used brain sections.

Literature values for the refractive indices of the different tissue components are presented in Sec. 3.2.1. The attenuation properties of white and gray matter (absorption, scattering, and reflection) are described in Sec. 3.2.2. Finally, in Secs. 3.2.3 and 3.2.4, the birefringence and diattenuation of brain tissue are discussed.

3.2.1 Refraction

This section provides literature values and estimates for the refractive indices of the different tissue components in the investigated brain sections.

Gray and White Matter Table 3.2 lists various literature values for the refractive indices of gray matter (GM), white matter (WM), and different cells or cell components (like cytoplasm or cell membranes). The refractive indices in gray matter regions are similar to those of cells and cytoplasm: the values range from 1.35 to 1.39. The refractive index in a white matter region (corpus callosum) was determined as 1.41. The refractive indices of nerve fibers and cell membranes range from 1.46 to 1.48.

	n	λ [nm]	Sample	Meas. Technique	Ref.
GM	1.37	1310	thalamus (rat), 300 µm section, viable	OCT	[111]
	1.36	1310	hippocampus/cortex (rat), 300 µm section, viable	OCT	[111]
WM	1.41	1310	corpus callosum (rat), 300 µm section, viable	OCT	[111]
	1.46	546	sciatic nerves (rat), formalin fixed	imbibition technique[4]	[112]
Cell (Components)	1.36	580	airway smooth muscle cells (human), viable	phase-amplitude and confocal microscopy	[113]
	1.36 –1.39	633	HeLa cells (human) in culture medium	tomographic phase microscopy	[114]
	1.38	468	cytosol, living cells	fluorescence lifetime imaging microscopy	[115]
	1.35 –1.37	—	cytoplasm	—	[116]
	1.46 –1.48	468	plasma membrane, living cells	fluorescence lifetime imaging microscopy	[115]

Tab. 3.2: Literature values for the refractive indices n of gray matter (GM), white matter (WM), and cell components. The table lists the wavelengths λ, the samples, and the measurement techniques that were used to determine the refractive indices. The measurements were mostly performed at room temperature ($\sim 22\,^{\circ}\mathrm{C}$).

Embedding Solution The brain sections used for this thesis were pretreated with 4 % formaldehyde and 2 % dimethyl sulfoxide (DMSO), and embedded in a 20 % solution of glycerin (the preparation of the brain sections will be described in more detail in Sec. 4.1). Due to this preparation, the brain tissue is surrounded by a solution of 4 % formaldehyde, 2 % DMSO, 20 % glycerin, and 74 % distilled water.[5] The refractive indices for the different substances are listed in Tab. 3.3. With these literature values, the refractive index of the embedding solution was calculated for a wavelength of 589 nm: $n \approx 1.3659$. A measurement of the refractive index with a digital refractometer (*ATAGO*) at room temperature (22 °C) and $\lambda = 589\,\text{nm}$ yielded: $n = 1.3690 \pm 0.0003$.

The refractive index of the embedding solution could only be determined for a wavelength of 589 nm because most refractive indices are not given for other wavelengths. The polarimetric measurements described in Chap. 4 were performed with green light ($\lambda = 529\,\text{nm}$ and 550 nm). As the refractive index of water has similar values for smaller wavelengths (see Tab. 3.3), the refractive index of the embedding solution is presumably also about 1.37 for the wavelengths used in the polarimetric measurements.

	n	λ [nm]	Reference
Distilled Water	1.3375	486	[117], Tab. 1
	1.3348	546	[117], Tab. 1
	1.3330	589	[118] # 10039
Formaldehyde	1.3746	589	[118] # 4235
DMSO	1.4783	589	[118] # 3259
Glycerin	1.4746	589	[118] # 4484
Embedding Solution	1.3659	589	–

Tab. 3.3: Literature values for the refractive indices n of the different substances in the embedding solution, measured at a wavelength λ and a temperature of 20 °C. The refractive index of the embedding solution was computed from the values listed in the table for $\lambda = 589\,\text{nm}$, assuming 74 % distilled water, 4 % formaldehyde, 2 % DMSO, and 20 % glycerin.

Axon, Myelin, and Surrounding Tissue For the simulation studies in Part IV, the brain tissue is modeled by three tissue types with different refractive indices: axon (cytoplasm), myelin (lipids), and surrounding tissue (glycerin solution).

- **Axon:** The axon is filled with axoplasm which consists mostly of cytosol and cell organelles. The refractive index is expected to be similar to the refractive index of cytoplasm and gray matter which contains mostly unmyelinated axons ($n = 1.35$–1.39, see Tab. 3.2).

  Assuming a larger proportion of aqueous solution, the refractive indices of the axon and of the cytoplasmic spaces in the myelin sheath are assumed to correspond to the minimum refractive index in the given range:

$$n_{\text{ax}} = n_{\text{cyto}} = 1.35. \tag{3.1}$$

[4] The *imbibition technique* utilizes the form birefringence to measure the refractive index of an object: The object is embedded in a medium with refractive index n_{surr} and the birefringence is measured. When n_{surr} matches the refractive index of the object, the form birefringence vanishes and the measured birefringence becomes extremal ([81] pp. 26-28).

[5] These values are only rough estimates because it is not known how much formaldehyde and DMSO remain in the tissue.

- **Myelin:** The myelin sheath is composed of densely packed cell membranes and contributes about one third to the overall fiber diameter (see Secs. 3.1.2 and 3.1.3). Thus, the refractive index of the myelin layers can be estimated by the mean value of the refractive indices of nerve fibers and cell membranes ($n = 1.46$–1.48, see Tab. 3.2):

$$n_{\mathrm{m}} = 1.47. \tag{3.2}$$

  Depending on the protein composition, the refractive index of the myelin layers might be slightly larger ($n_{\mathrm{m}} \leq 1.5$ [103]).

  The above value for n_{m} only holds for tissue directly after embedding. After a while, the embedding glycerin solution (with $n = 1.37$) is expected to soak into the myelin layers, which reduces their effective refractive index.

- **Surrounding tissue:** The tissue surrounding the nerve fibers is composed of gray matter which contains cell bodies, unmyelinated axons, and blood capillaries ($n = 1.35$–1.39, see Tab. 3.2). Considering both the refractive index of gray matter and of the embedding solution ($n \approx 1.37$, see Tab. 3.3), the refractive index of the surrounding tissue is estimated as:

$$n_{\mathrm{g}} = 1.37. \tag{3.3}$$

  The subscript "g" indicates that the refractive index corresponds to the refractive index of the glycerin solution. As the extracellular spaces in the myelin sheath swell in aqueous solutions, they are assumed to be filled with glycerin and to have the same refractive index.

3.2.2 Attenuation

How much the light is attenuated when it passes through the brain section depends on the absorption and scattering coefficients of the respective tissue components.

Absorption In general, brain tissue has relatively small absorption coefficients. The absorption of white matter is slightly larger than for gray matter. Integrating-sphere measurements[6] of native human brain tissue (80–300 µm cryo-sections, rinsed from blood) yielded absorption coefficients (K) of about $0.1\,\mathrm{mm}^{-1}$ for white matter and $0.05\,\mathrm{mm}^{-1}$ for gray matter in a wavelength range of 500–550 nm (values estimated from [119] Figs. 5a and 6a and from [120] Figs. 2a and 3a). According to Eq. (2.29), this corresponds to:

$$\kappa_{\mathrm{WM}} \approx 4.4 \times 10^{-6}, \quad \text{for } \lambda = 550\,\mathrm{nm}, \tag{3.4}$$

$$\kappa_{\mathrm{GM}} \approx 2.2 \times 10^{-6}, \quad \text{for } \lambda = 550\,\mathrm{nm}. \tag{3.5}$$

As the brain sections used for this thesis were formalin fixated without washing out the blood, the absorption coefficients might differ from the above values.

The absorption coefficient of the embedding solution cannot be reliably determined because the values are not known for all contained substances. Spectroscopy measurements of pure water yielded absorption coefficients between $0.00005\,\mathrm{mm}^{-1}$ and $0.00007\,\mathrm{mm}^{-1}$

[6] The *integrating sphere* is commonly used to measure the absorption, scattering, and reflection of a sample. It consists of a hollow spherical cavity covered with a diffuse reflective coating so that light which is scattered in the interior of the sphere is evenly distributed over all angles.

for a wavelength range of 525–550 nm and a temperature of 25 °C [121, 122]. These values correspond to:

$$\kappa_{H_20} \approx 2 \times 10^{-9}, \quad \text{for } \lambda = 525\,\text{nm}, \tag{3.6}$$

$$\kappa_{H_20} \approx 3 \times 10^{-9}, \quad \text{for } \lambda = 550\,\text{nm}. \tag{3.7}$$

The absorption coefficient of the embedding solution is expected to have a similar order of magnitude ($\kappa_g \sim 10^{-9}$).

Scattering White matter has a higher scattering coefficient than gray matter. The integrating-sphere measurements mentioned above yielded scattering coefficients ($\mathcal{S}$) of about 40–50 mm^{-1} for white matter and about 10 mm^{-1} for gray matter in a wavelength range of 500–550 nm (values estimated from [119] Figs. 5b and 6b and from [120] Figs. 2a and 3a). Again, the scattering coefficients of the brain sections used for this thesis might differ from the above values due to another tissue preparation.

Reflectance White matter has a higher reflectance than gray matter. In-vivo measurements with a portable spectrometer during human surgery revealed that "the reflectance from gray matter is approximately 50 % or less than that from white matter" in a wavelength range of 650–800 nm [123]. For wavelengths between 500 nm and 600 nm, previous measurements of human brain tissue yielded relative levels of reflection between 40 % and 60 % for frontal white matter and between 20 % and 30 % for frontal gray matter (values estimated from [124] Fig. 5).

The literature values show that white matter has not only a larger refractive index than gray matter (see Tab. 3.2), but also a slightly larger absorption coefficient, a larger scattering coefficient, and a higher reflectance. Thus, white matter has a larger attenuation coefficient than gray matter, which explains why white matter appears darker in the transmittance images (cf. Fig. 4.5a). The large attenuation coefficient of white matter, especially the large scattering coefficient, is presumably caused by the highly anisotropic and layered structure of the myelin sheaths (see Sec. 3.1.3).

3.2.3 Birefringence

The optical anisotropy (birefringence) of brain tissue reflects the spatial orientation of the underlying nerve fibers. 3D-PLI measurements determine the birefringence of histological brain sections to reconstruct the three-dimensional nerve fiber architecture.

Birefringence is caused by highly ordered molecular or macroscopic structures (see Sec. 2.3). Primarily responsible for the birefringence of brain tissue are the myelin sheaths which surround most of the axons in the white matter. But there exist also other birefringent components like axonal neurofilaments[7], microtubules[8], proteins, and blood vessels.

The birefringence of the myelin sheath has already been described by Göthlin in 1913. He found that the myelin sheath exhibits positive uniaxial birefringence with radial optic

[7] Neurofilaments are essential for the velocity of nerve impulse conduction and for the radial growth of the axons during development. They have a diameter of about 10 nm; in myelinated axons, they are more numerous than microtubules [125].

[8] Microtubules are tubular polymers in the cytoplasm that maintain the structure of the cell and provide intracellular transport [126].

axes [49] caused by the highly ordered structure of the myelin sheath [95] (cf. Fig. 3.2). With respect to the longitudinal fiber direction, the birefringence is *negative* [51].

The neurofilaments and microtubules running along the length of the axon and the tangentially oriented proteins in the myelin sheath (cf. Sec. 3.1.3) lead to a *positive* uniaxial birefringence with respect to the longitudinal fiber direction [127–129]. The layered structure of the myelin sheath and the parallel arrangements of nerve fibers also lead to a positive (form) birefringence with respect to the longitudinal fiber direction [50]. The form birefringence of parallel layers and parallel cylinders embedded in a medium with different refractive index has already been described by Wiener in 1912 [79] and was used by de Campos Vidal *et al.* (1980) [112] to determine the refractive index of sciatic nerve fibers (see Tab. 3.2).

Various experimental and theoretical studies have shown that the overall birefringence of nerve fiber bundles is negative ($n_\mathrm{e} < n_\mathrm{o}$) and that the optic axis is oriented in the direction of the fiber bundle [49–51, 112]. As all other structures cause positive birefringence with respect to the longitudinal fiber direction, this suggests that the birefringence of nerve fibers is mainly caused by the lipid molecules in the myelin sheath.

In this thesis, the birefringence caused by the substructure of the myelin layers (e. g. lipid molecules) will be referred to as *molecular birefringence* in order to distinguish it from the birefringence caused e. g. by the layered structure of the myelin sheath.

The overall birefringence of the nerve fibers is dominated by molecular birefringence. A good effective model to describe the birefringence is a rotational refractive index ellipsoid (see Sec. 2.3.1) [45, 46].

The negative birefringence of the nerve fibers implies that light that is polarized in the direction of the fiber bundle (extraordinary wave polarized parallel to the optic axis, see Sec. 2.3.1) travels faster than light that is polarized perpendicularly to the fiber bundle, i. e. in the plane of the radial lipid molecules in the myelin sheath (ordinary wave polarized perpendicularly to the optic axis). Thus, a nerve fiber can be described as a wave retarder (cf. Sec. 2.3.3) with its fast axis oriented along the longitudinal fiber axis.

Due to their small dimensions, the birefringence of single myelin sheaths and of other birefringent components in the brain cannot easily be determined. Reported literature values for the birefringence of biological tissue are in the order of $|\Delta n| = 10^{-3}...10^{-2}$ [61].

As the birefringence of brain tissue is presumably small compared to its refractive index values ($n = 1.3$–1.5 [130], cf. Tab. 3.2), the formula in Eq. (2.37) can be used to estimate the retardance δ induced by the birefringent nerve fibers in a brain section: Choosing a coordinate system in which the light propagates in the z-direction and the brain section lies in the xy-plane, the angle θ between the direction of propagation (z-axis) and the optic axis (fiber axis) can be replaced by the out-of-plane fiber inclination angle $\alpha = 90° - \theta$ and the formula of the retardance can be written as:

$$\delta \approx \frac{2\pi d}{\lambda} \Delta n \, \cos^2 \alpha \,, \quad \Delta n = n_\mathrm{E} - n_\mathrm{o}. \tag{3.8}$$

where d is the thickness of the birefringent brain tissue and λ the wavelength of light in vacuum. In 3D-PLI, this formula is used to derive the inclination angles of the nerve fibers from the measured birefringence of brain sections (see Sec. 4.4.1).

3.2.4 Diattenuation

The anisotropy of brain tissue which causes birefringence also leads to diattenuation (see Sec. 2.4). The diattenuation of brain tissue is mainly caused by regular arrangements of nerve fibers [131] and by the specific anisotropic structure of the myelin sheaths: the layered myelin structure leads to multiple scattering which changes the polarization of the incident light and induces diattenuation [61].

There exist a broad range of studies that investigate the diattenuation of non-biological phantoms (polarizing filters [57, 132], Siemens star [58]) as well as biological tissue (collagen [133], tendon [134–136], muscle [135], heart [86, 136], skin [61, 63, 64, 137, 138], eye [60, 137], biopsy tissue [62, 139] of animals or humans). The diattenuation of nervous tissue has been studied for the retinal nerve fiber layer [59, 65, 140, 141] which only contains unmyelinated axons.

The diattenuation of the biological samples investigated in these studies has been reported to be much smaller than the birefringence of the samples ($|D| < 10\,\%$). The diattenuation of brain tissue and myelinated axons (nerve fibers) has not been addressed in other studies and will be discussed in Chap. 9.

As described in Sec. 2.4, diattenuation can be caused by anisotropic scattering as well as by anisotropic absorption (dichroism). In this thesis, diattenuation caused by regular fiber arrangements or myelin layers will be treated as anisotropic scattering. The *molecular diattenuation* of the nerve fibers, i. e. the diattenuation caused by the substructure of the myelin layers, will be modeled analogously to the molecular birefringence: as the molecular birefringence is well described by a rotational refractive index ellipsoid, the molecular diattenuation will effectively be treated as dichroism, described by the imaginary part of a complex refractive index (see Sec. 2.4.2). To explain the experimental observations in Chap. 9, both dichroism (described by an analytical model in Appx. A.4.2 and A.4.3) and anisotropic scattering (simulated by FDTD simulations in Chap. 12) need to be considered.

As the principal axes of dichroism are expected to be the same as for birefringence (the optic axis is oriented in the direction of the nerve fiber), the light absorption is assumed to become extremal when the light is polarized parallel or perpendicularly to the nerve fiber axis. As described in Sec. 2.4.2, the dichroism of brain tissue δ_K is approximately proportional to the retardance δ and depends on the inclination angle ($\alpha = 90° - \theta$) of the nerve fibers (see Eq. (2.45)):

$$\delta_\mathrm{K} \approx \frac{2\pi d}{\lambda} \Delta\kappa \cos^2\alpha \quad \propto \; \delta\,, \quad \Delta\kappa = \kappa_\mathrm{E} - \kappa_\mathrm{o}. \tag{3.9}$$

Thus, diattenuation caused by dichroism (see Eq. (2.44)) also depends on the fiber inclination (see Appx. A.4.3.2):

$$D_\mathrm{K} = \tanh\left(-\delta_\mathrm{K}\right) \approx \tanh\left(-\frac{2\pi d}{\lambda}\Delta\kappa \cos^2\alpha\right). \tag{3.10}$$

Because of $\delta_\mathrm{K} \propto \delta$, the magnitude of D_K is expected to be related to the measured retardation signal $|\sin\delta|$ (see Appx. A.4.3.3).

The inclination dependence of anisotropic scattering cannot be described by a simple model and was therefore investigated by means of simulation studies presented in Chap. 12.

Part II

MEASUREMENT & SIMULATION TECHNIQUES

Chapter 4

Polarimetric Measurements

This chapter introduces the different polarimetric measurements that were used in this thesis to study the birefringence and diattenuation of brain tissue: *Three-Dimensional Polarized Light Imaging (3D-PLI)*, *crossed polars (XP) measurement*, and *Diattenuation Imaging (DI)*. Parts of this chapter have been published in Menzel *et al.* (2017) [3] Secs. 1 and 3.

Birefringence as well as diattenuation can be measured by conventional *Müller-matrix polarimetry* [61, 85, 142–144] or by *polarization-sensitive optical coherence tomography (PS-OCT)* [145, 146]. While PS-OCT uses the interference of the backscattered light to provide a depth profile of the sample, Müller polarimetry measures the intensity of the transmitted light under a certain angle. Often, incomplete Müller polarimeters are used that measure the linear birefringence and diattenuation of a sample [57, 58]. For this thesis, combined measurements of linear[1] birefringence and diattenuation were performed with a polarimeter that analyzes the light transmitted through histological brain sections [45, 46].

The preparation of the brain sections is described in Sec. 4.1. The general measurement setup and signal processing are described in Secs. 4.2 and 4.3. Finally, in Sec. 4.4, the measurement setup and signal analysis are specified for the different polarimetric measurements (3D-PLI, XP, DI).

4.1 Preparation of Brain Tissue

The brains are prepared in the laboratory of the *Institute of Neuroscience and Medicine* (INM-1, Forschungszentrum Jülich, Germany) by the team of Markus Cremer. The brain sections investigated in this thesis were obtained from different species: human, monkey, rat, and mouse (see Fig. 4.1).[2] Due to the different brain sizes, the preparation of the sections differs between species. The preparation consists of several steps:

- **Fixation:** In order to prevent decay, the brain is fixated as soon as possible after death. The brain is removed from the skull (preferably within 24 hours) and immersed in a buffered solution of 4 % formaldehyde[3] for several weeks (human brain: 3 months, rat brain: 1–2 weeks).

[1] Circular birefringence and diattenuation are not considered because they are expected to contain little information about the tissue structure and to have no significant impact on the measured signals.

[2] All animal procedures are approved by the institutional animal welfare committee at the Forschungszentrum Jülich GmbH and are in accordance with European Union (National Institutes of Health) guidelines for the use and care of laboratory animals.

[3] The formaldehyde solution is prepared according to Lillie (1954) [147] and consists of diluted formalin, sodium hydrogen phosphate, and distilled water.

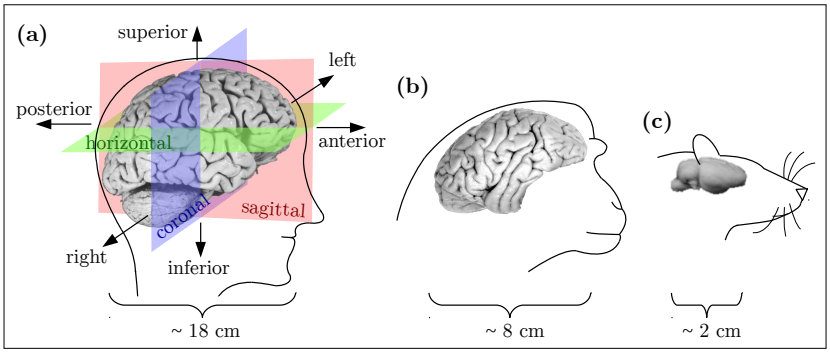

Fig. 4.1: The brain sections are obtained from different species with different brain sizes: **(a)** human, **(b)** vervet monkey, **(c)** rat or mouse. Subfigure (a) shows the anatomical planes (coronal, horizontal, sagittal) and the anatomical directions (anterior-posterior, superior-inferior, left-right) along which the brains are sectioned. The pictures of the brains were made at INM-1, FZJ, Germany.

- **Cryoprotection:** To avoid the development of ice crystals, the brain is first immersed in a solution of 10 % glycerin and then in a solution of 20 % glycerin for several days, respectively (human brain: > 3 weeks, rat brain: 7 days in total). To facilitate the penetration of glycerin into the cells, 2 % Dimethyl sulfoxide (DMSO) and 4 % formaldehyde are added.

- **Freezing:** After the treatment with the cryoprotectant, the brain is dipped in cooled isopentane for several minutes (human brain: > 30 min, rat brain: > 5 min). Sealed into an air-tight plastic bag, the brain is frozen down to -80 °C and can be stored for several months.

- **Sectioning:** The frozen brain is cut with a cryostat microtome (*Leica Microsystems*, Germany) at a temperature of -30 °C into sections of approx. 60 µm (see Fig. 4.2a).[4] The brain is cut along one of three mutually orthogonal, anatomical planes: *coronal*, *horizontal*, or *sagittal* (see Fig. 4.1a). A whole human brain yields 1,500–3,000 sections, depending on the brain size and cutting direction. As deformations of the tissue occur during the sectioning process, a picture of the brain block surface (*blockface image*) is taken every time before sectioning. A pattern of *ARTag markers* [148] (see Fig. 4.2a) helps to determine the position of the brain block in two-dimensional space and to create an undistorted reference volume [149].

- **Mounting:** After sectioning, the brain slice is mounted onto a cooled glass slide (see Fig. 4.2b) and embedded in a solution of 20 % glycerin. No histological staining is applied. The brain tissue is covered by a cover glass, sealed with lacquer, and weighted for several hours to prevent the development of air bubbles (see Fig. 4.2c). If not otherwise stated, the brain sections are measured 1–2 days after embedding to obtain optimal birefringence and diattenuation signals.

[4] A section thickness of approx. 60 µm (see Fig. 4.2a) turned out to be most suitable for the polarimetric measurements. A smaller section thickness would make the cutting and handling of whole brain cryosections difficult and the smaller signals would require a more precise imaging system. A larger section thickness, on the other hand, would lead to ambiguous signals so that tissue properties like the nerve fiber orientation cannot be reliably determined.

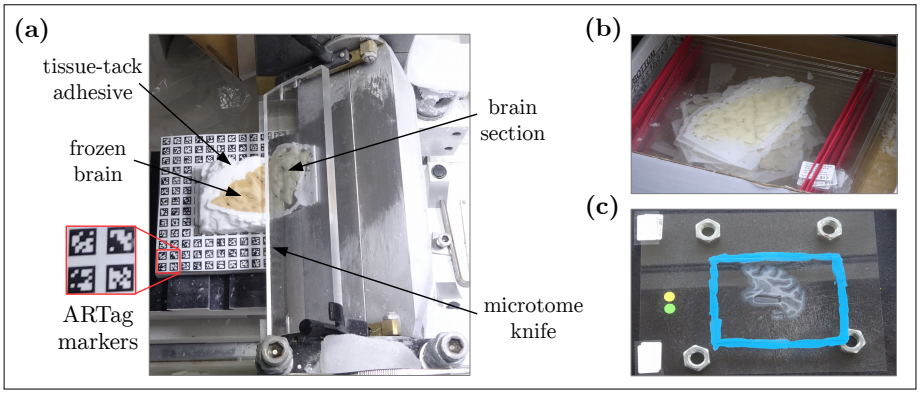

Fig. 4.2: Preparation of brain sections: **(a)** The frozen brain is attached to the object table with freezing glue (*tissue-tack*) and cut with a cryostat microtome into histological sections of about 60 µm thickness; the pattern of ARTag markers helps to determine the position of the brain block. **(b)** The brain sections are mounted on glass slides and stored at -80 °C. **(c)** The brain sections are embedded in 20 % glycerin solution, covered by a cover glass, sealed with lacquer, and weighted for several hours.

4.2 General Measurement Setup

The general measurement setup consists of a pair of two linear polarizers with orthogonal transmission axes, a quarter-wave retarder, and a specimen stage mounted between the polarizers. The fast axis of the retarder is oriented at $-45°$ with respect to the transmission axis of the first polarizer (cf. Fig. 4.3b). The sample is illuminated by a customized LED light source with green wavelength spectrum. The transmitted light intensity is recorded by a high-resolution CCD camera. During a measurement, the filters are rotated simultaneously around the stationary tissue sample. For each rotation angle $\rho = \{0°, 10°, ..., 170°\}$, an image is recorded which yields a series of 18 images.

In a standard 3D-PLI measurement [45, 46], this setup is used to measure the birefringence of brain tissue and to derive the spatial orientation of the nerve fibers from the measured retardation signal (described later in Sec. 4.4.1). The setup for measuring optical birefringence has already been described by Wood & Glazer (1980) [150, 151].

In the INM-1 laboratory, two state-of-the-art polarimeters are available (see Fig. 4.3) which enable polarimetric measurements with different optical resolutions and sensitivities: the *Polarizing Microscope (PM)* and the *Large-Area Polarimeter (LAP)* [45, 46]. In Chap. 7 and Appx. B, the optical resolution and the components of the optical systems will be characterized in more detail. This section provides a short overview of the employed polarimeters.

Polarizing Microscope (PM) The PM has a higher optical resolution than the LAP. The pixel size in object space is about 1.33 µm, which enables to map single axons and to disentangle complex fiber constellations in small brain areas. The custom-made microscope is equipped with a motorized specimen stage which performs a translational scan of the brain section. The sample is measured in tiles of 2.7×2.7 mm^2 which are put together after signal processing. To enable stitching, the tiles are measured with an overlap of approx. 30 % on all sides.

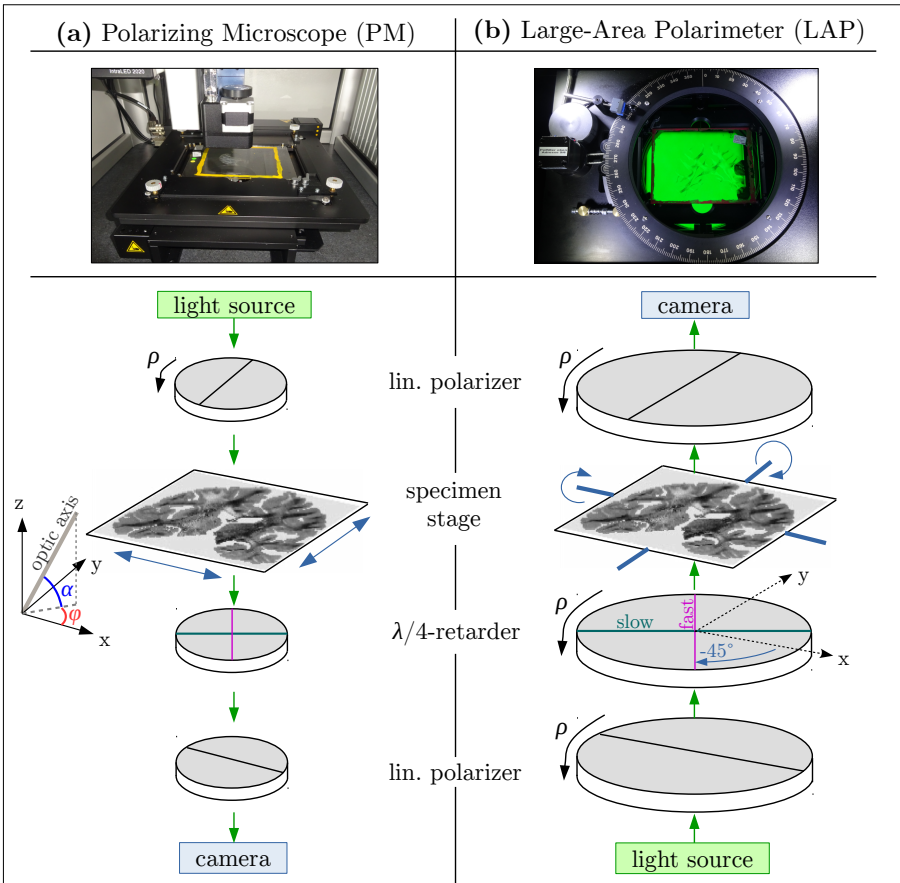

(a) Polarizing Microscope (PM)	(b) Large-Area Polarimeter (LAP)
px ≈ 1.33 µm	px ≥ 21 µm
$\lambda_{ill} = (550 \pm 5)$ nm, $\lambda_{ret} = 545$ nm	$\lambda_{ill} = (525 \pm 25)$ nm, $\lambda_{ret} = 568$ nm
high-quality, fixed filters	low-quality, removable filters
motorized specimen stage (tile-wise scan: 2.7 x 2.7 mm²)	tiltable specimen stage (max. 8° around two axes)
24 h scan time, 800 GB data	15 min scan time, 2 GB data

Fig. 4.3: Schematic setups of the employed polarimeters (PM and LAP), not to scale: The specimen stage with the brain section is placed between a pair of crossed linear polarizers and a quarter-wave retarder. During a measurement, the filters are rotated by discrete rotation angles ρ. In the PM, the light comes from above, only the first linear polarizer can be rotated, and the sample is measured tile-wise with a motorized specimen stage. In the LAP, the light is passed through the system from below, all filters can be rotated individually or be removed, and the specimen stage can be tilted around two axes. Further differences are the pixel size in object space (px), the illumination wavelength of the light source (λ_{ill}), the optimal working wavelength of the retarder (λ_{ret}), and the required time for scanning a whole human brain section ($\sim 18 \times 13\,\mathrm{cm}^2$). The displayed setups are used for 3D-PLI measurements (see Sec. 4.4.1) and measure the spatial orientation of the optic axis (fiber axis) of the sample, which is defined by the in-plane direction angle φ and the out-of-plane inclination angle α.

In contrast to the LAP, the filters cannot be removed, only the first polarizer can be rotated, and tilting of the sample is not possible. The PM can therefore only be used for standard 3D-PLI measurements. However, the filters are of much higher quality than in the LAP and the optimal working wavelength of the quarter-wave retarder ($\lambda_{\text{ret}} = 545\,\text{nm}$) matches approximately the wavelength of the incident light ($\lambda_{\text{ill}} = 550\,\text{nm} \pm 5\,\text{nm}$). The optical components of the PM will be characterized in Sec. 7.1 and Appx. B.1.1 in more detail.

Large-Area Polarimeter (LAP) The LAP enables single-shot imaging of brain sections up to 24 cm in diameter with a pixel size in object space between 21 µm and 64 µm. The in-house developed system is equipped with a specimen stage that can be tilted up to $\pm 8^\circ$ around two axes, allowing a more precise determination of the fiber inclination angle in 3D-PLI measurements (see Sec. 4.4.1). As all polarizing filters (polarizer, retarder, analyzer) can be rotated individually or be removed from the imaging system, the LAP can be used for a combined measurement of birefringence and diattenuation (see Sec. 4.4).

The polarizing filters in the LAP are of lower quality than in the PM and the wavelength of the incident light ($\lambda_{\text{ill}} = 525\,\text{nm} \pm 25\,\text{nm}$) does not perfectly match the optimal working wavelength of the retarder ($\lambda_{\text{ret}} = 568\,\text{nm}$) [152], which influences the measured signal and the derived tissue properties. The optical components and the non-ideal polarization properties of the LAP will be characterized in Secs. 7.1 and 7.2 and Appx. B.1.2 and B.3 in more detail.

4.3 General Signal Processing

During a standard measurement with the PM or the LAP, a series of 18 images is recorded (one image for each rotation angle of the polarizing filters). To derive the underlying tissue information, the image series is processed in several steps:

- **Image Calibration:** To compensate for inhomogeneities across the field of view, the images are calibrated. For each rotation angle of the filters, a set of 60 calibration images (without specimen) is taken and an averaged image is computed. The measured images of the specimen are divided by the corresponding averaged calibration image for each rotation angle and multiplied by the mode intensity of all calibration images [153]. To obtain a uniform background intensity after calibration, the intensity of the light source should not change between calibration and specimen measurements.[5]

- **Spatial Independent Component Analysis (ICA):** To enhance the signal-to-noise ratio for small signals and to reduce artifacts (like scratches, dirt, dust particles), the calibrated images are decomposed into statistically independent component maps. After decomposition, the tissue structures can be distinguished from interfering signal sources, which can then be discarded [153, 154]. Since the ICA removes artifacts induced by rotating filters, it is particularly suitable for the LAP in which all polarizing filters are rotated during a measurement.

[5] The calibration procedure only corrects for multiplicative errors in the measured light intensity (i. e. inhomogeneous illumination, absorption, detection sensitivity, etc.). Differences between presumed and actual polarization states (e. g. induced by a partially polarized light source, non-ideal polarization filters, or a polarization-sensitive camera as described in Sec. 7.2.2 and Appx. B.3.2) are not taken into account.

- **Discrete Harmonic Fourier Analysis:** The resulting series of $N = 18$ images is analyzed by means of a discrete harmonic Fourier analysis. The intensity values for each rotation angle $\rho_i \in \{0°, 10°, \ldots, 170°\}$ are described by a Fourier series for each image pixel:

$$I(\rho) = a_0 + \sum_{m=1}^{N/2} \Big(a_m \cos(m\rho) + b_m \sin(m\rho) \Big), \tag{4.1}$$

$$a_0 = \frac{1}{N} \sum_{i=1}^{N} I(\rho_i)\,, \quad a_m = \frac{2}{N} \sum_{i=1}^{N} I(\rho_i) \cos(m\rho_i)\,, \quad b_m = \frac{2}{N} \sum_{i=1}^{N} I(\rho_i) \sin(m\rho_i)\,. \tag{4.2}$$

  From the resulting Fourier coefficients $\{a_m, b_m\}$, the averaged transmitted light intensity ($\propto a_0$), the phase, and the amplitude of the measured birefringence or diattenuation signals are computed, which contain e. g. information about the spatial orientation of the nerve fibers within the brain tissue. The formulas to compute the parameter maps for the different polarimetric measurements will be introduced in Sec. 4.4.

- **Segmentation:** Objects outside the tissue are removed from the resulting parameter maps using a parallelized semi-automated seeded region growing algorithm [155] and manual masking.

- **Stitching:** For measurements with the PM, the different tiles need to be stitched together to regain the full field of view. An in-house developed software tool is used for the stitching. To avoid border effects caused by oblique illumination or lens artifacts, the overlapping of the tiles is chosen to be about 30 % of the side length of the tiles on all sides.

- **Registration:** As the polarimetric measurements are only able to analyze transmitted light, the brains are cut into histological sections to measure the underlying tissue properties. The cutting process might lead to tissue deformation and disruption. To regain the original three-dimensional volume, the parameter maps of several consecutive brain sections are registered onto each other, using the aligned blockface images (see Sec. 4.1) as undistorted reference volume.

  Image registration also becomes necessary when performing a pixel-wise comparison between parameter maps obtained from different polarimetric measurements or from measurements performed at different times. Due to the embedding in glycerin solution, the brain section might slightly move over time or when changing the measurement setup. Moreover, different types of filters introduce different parallax effects.

  The images are registered onto each other using in-house developed software tools based on the software packages *ITK*, *elastix*, and *ANTs* [156–160] which perform linear and non-linear transformations.

4.4 Signal Analysis for the Polarimetric Measurements

In the following, the signal analysis for the different polarimetric measurements (3D-PLI, XP, DI) is described in more detail. Parts of this section have been published in Menzel *et al.* (2017) [3] Sec. 3.

Figure 4.4a-c shows the setups for the polarimetric measurements. While the 3D-PLI and DI setups measure the birefringence and diattenuation of the sample, the XP measurement is used as a reference for the 3D-PLI and DI measurements to estimate the impact of diattenuation on the measured birefringence signal (see Sec. 9.1). While the 3D-PLI measurement can be performed both with the PM and the LAP (cf. Fig. 4.3), the XP and DI measurements can only be performed with the LAP because one or more filters need to be removed from the light path.

To simplify notation in the following, the signal analysis is only described for the setup of the LAP, which was used for the combined measurements of birefringence and diattenuation presented in Chap. 9. Although the setup of the PM is different from that of the LAP (only the first polarizer is rotated, the retarder is placed behind and not in front of the sample, see Fig. 4.3a), the signal analysis is analogous for the 3D-PLI measurement and the resulting formulas in Sec. 4.4.1 are the same.

To analyze the signals obtained from the three different kinds of measurement, an analytical expression of the transmitted light intensity is computed with the Müller-Stokes calculus (see Sec. 2.5.2). For this purpose, the optical components of the LAP are described by the Müller matrix $\mathcal{M}(\xi, \delta, D, \tau)$ of a rotating wave retarder and/or diattenuator as defined in Eqs. (2.56) to (2.58), with rotation angle ξ, retardance δ, diattenuation D, and average transmittance τ. To account for non-ideal optical properties of the filters (described later in Sec. 7.2.2), the polarizer and the analyzer are considered to be general diattenuators with rotation angles ρ and $(\rho + 90°)$, diattenuations $D_\mathrm{x} \approx 1$ and $D_\mathrm{y} \approx 1$, and average transmittances τ_x and τ_y, respectively. The quarter-wave retarder is considered as general retarder with rotation angle $(\rho - 45°)$, retardance $\gamma \approx \pi/2$, and average transmittance τ_Λ.

The retardance of the linear polarizers and the diattenuation of the retarder are not included in this model because the filter measurements of the LAP presented in Sec. 7.2.2 have shown that they can be neglected.

To account for birefringence as well as for a possible diattenuation of brain tissue, the brain section is described by the Müller matrix of a general wave retarder and diattenuator with retardance δ, diattenuation D, and average transmittance τ. The fast axis of the retarder and the axis of maximum[6] intensity transmittance are both assumed to be oriented along the fiber axis (see Secs. 3.2.3 and 3.2.4). The three-dimensional fiber orientation is defined in spherical coordinates by the in-plane direction angle φ and the out-of-plane inclination angle α (cf. Fig. 4.4h). Note that the Müller matrix describes only the net effect of the brain tissue and that the parameters (φ, δ, D, τ) do not necessarily correspond to local tissue properties.

With the above definitions and assumptions, the Müller matrices $\mathcal{M}(\xi, \delta, D, \tau)$ for the optical components of the LAP read:

$$\begin{aligned}
&\text{Polarizer:} && P_\mathrm{x}(\rho,\, D_\mathrm{x},\, \tau_\mathrm{x}) && \equiv\ \mathcal{M}(\rho, 0, D_\mathrm{x}, \tau_\mathrm{x}), && (4.3)\\
&\text{Retarder:} && \Lambda(\rho, \gamma, \tau_\Lambda) && \equiv\ \mathcal{M}(\rho - 45°, \gamma, 0, \tau_\Lambda), && (4.4)\\
&\text{Brain Tissue:} && M(\varphi,\, \delta,\, D,\, \tau) && \equiv\ \mathcal{M}(\varphi, \delta, D, \tau), && (4.5)\\
&\text{Analyzer:} && P_\mathrm{y}(\rho,\, D_\mathrm{y},\, \tau_\mathrm{y}) && \equiv\ \mathcal{M}(\rho + 90°, 0, D_\mathrm{y}, \tau_\mathrm{y}). && (4.6)
\end{aligned}$$

[6] The assumption that the axis of maximum intensity transmittance is oriented along the fiber axis is arbitrary. If the axis of *minimum* intensity transmittance is oriented along the fiber axis, the following considerations will still be valid when replacing the variable D by the variable $(-D)$.

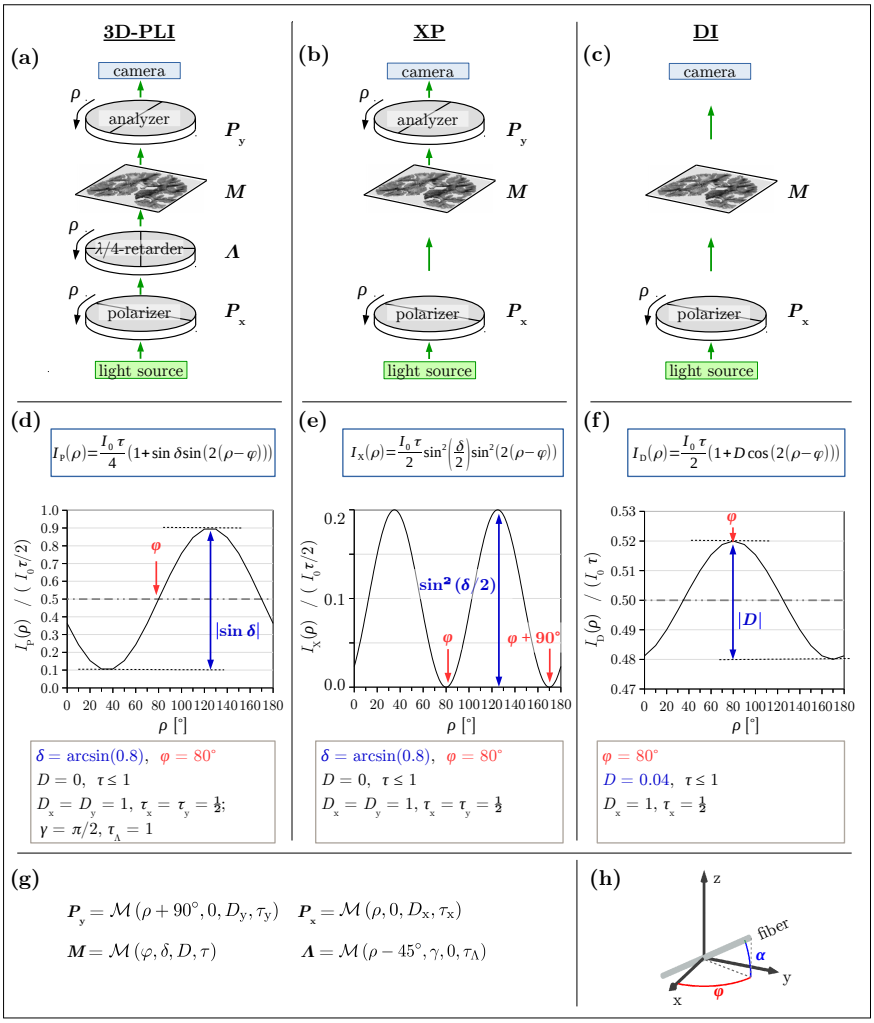

Fig. 4.4: (a-c) Schematic of the setups for the 3D-PLI, XP, and DI measurements for the LAP: For the 3D-PLI measurement (a), the brain section is placed between a pair of crossed linear polarizers (polarizer/analyzer) and a quarter-wave retarder. For the XP measurement (b), only the crossed linear polarizers are used while for the DI measurement (c) only the polarizer is used. For all measurement setups, the employed filters are rotated simultaneously by discrete rotation angles ρ around the stationary specimen. **(d-f)** Analytically computed normalized light intensity profiles for the different measurement setups, assuming a retardance $\delta = \arcsin(0.8)$, a fiber direction $\varphi = 80°$, and ideal filter properties ($D_x = D_y = 1$, $\tau_x = \tau_y = 1/2$; $\gamma = \pi/2$, $\tau_\Lambda = 1$): For the 3D-PLI and XP measurements, the diattenuation of the brain tissue was neglected ($D = 0$). For the DI measurement, the tissue diattenuation was assumed to be $D = 4\,\%$. The phase φ of the intensity profiles (in red) is a measure for the in-plane fiber direction, while the amplitude (in blue) is correlated to the out-of-plane fiber inclination. **(g)** The transmitted light intensities are calculated using the Müller-Stokes calculus, in which each optical element is represented by a Müller matrix $\mathcal{M}(\xi, \delta, D, \tau)$ as defined in Eqs. (2.56) to (2.58). **(h)** The three-dimensional fiber orientation is defined in spherical coordinates by the in-plane direction angle φ and the out-of-plane inclination angle α. A similar figure has been published in Menzel *et al.* (2017) [3] Fig. 2.

The transmitted light intensity is computed by multiplying the above matrices and evaluating the first entry of the resulting Stokes vector. To make the analytical expressions computable, camera and light source are assumed to be ideal: the light emitted by the LED is assumed to be completely unpolarized and the camera to be polarization-insensitive, i. e. light source and camera are both described by the Stokes vector for unpolarized light ($\vec{S}_\mathrm{L} = \vec{S}_\mathrm{c} = \vec{S}_\mathrm{unpol}$).

The following three sections describe the setups and signal analysis for the 3D-PLI, XP, and DI measurements. All parameters derived from the 3D-PLI measurement are denoted by an index "P", all parameters derived from the XP measurement by an index "X", and all parameters derived from the DI measurement by an index "D".

4.4.1 Three-Dimensional Polarized Light Imaging (3D-PLI)

The 3D-PLI technique has been introduced by Axer *et al.* (2011) [45, 46]. The measurement can be performed with the PM or the LAP, using all filters of the polarimeter (see Fig. 4.3). The setup allows to measure the retardance of the birefringent brain sections and to derive the spatial orientation of the nerve fibers [45, 46]: The polarizer and the quarter-wave retarder of the LAP transform the unpolarized light emitted by the light source into circularly polarized light which is then transformed into elliptically polarized light by the birefringent brain tissue. The amount of light that is transmitted through the analyzer depends on the orientation of the analyzer axis with respect to the optic axis of the brain tissue, indicating the predominant fiber orientation (φ, α) [51].

An analytical description of the transmitted light intensity can be derived by multiplying the matrices defined in Eqs. (4.3) to (4.6) and evaluating the first entry of the resulting Stokes vector (S'_0P):

$$\vec{S}'_\mathrm{P}(\rho) = P_\mathrm{y}\,(\rho,\, D_\mathrm{y},\, \tau_\mathrm{y}) \cdot M\,(\varphi,\, \delta,\, D,\, \tau) \cdot \Lambda\,(\rho, \gamma, \tau_\Lambda) \cdot P_\mathrm{x}\,(\rho,\, D_\mathrm{x},\, \tau_\mathrm{x}) \cdot \vec{S}_\mathrm{unpol} \tag{4.7}$$

$$\begin{aligned} \Rightarrow\quad I_\mathrm{P}(\rho) = \tau\,\tau_\mathrm{x}\,\tau_\mathrm{y}\,\tau_\Lambda\,I_0 \Big[& 1 + D_\mathrm{x}\,D_\mathrm{y}\,\sin\gamma\,\sin\delta\,\sqrt{1-D^2}\,\sin\big(2(\rho-\varphi)\big) \\ & - D_\mathrm{x}\,D_\mathrm{y}\,\cos\gamma\,\Big(\cos^2\big(2(\rho-\varphi)\big) + \sqrt{1-D^2}\,\cos\delta\,\sin^2\big(2(\rho-\varphi)\big)\Big) \\ & + D\,\big(D_\mathrm{x}\,\cos\gamma - D_\mathrm{y}\big)\cos\big(2(\rho-\varphi)\big)\Big], \end{aligned} \tag{4.8}$$

where I_0 denotes the intensity of the light source. Performing a discrete harmonic Fourier analysis on the acquired intensity signal yields:

$$I_\mathrm{P}(\rho) = a_\mathrm{0P} + a_\mathrm{2P}\,\cos(2\rho) + b_\mathrm{2P}\,\sin(2\rho) + a_\mathrm{4P}\,\cos(4\rho) + b_\mathrm{4P}\,\sin(4\rho), \tag{4.9}$$

$$a_\mathrm{0P} = \tau\,\tau_\mathrm{x}\,\tau_\mathrm{y}\,\tau_\Lambda\,I_0\,\left(1 - \frac{1}{2}D_\mathrm{x}\,D_\mathrm{y}\,\cos\gamma\,\left(1 + \sqrt{1-D^2}\,\cos\delta\right)\right), \tag{4.10}$$

$$a_\mathrm{2P} = \tau\,\tau_\mathrm{x}\,\tau_\mathrm{y}\,\tau_\Lambda\,I_0\,\left(D\,\big(D_\mathrm{x}\,\cos\gamma - D_\mathrm{y}\big)\,\cos(2\varphi) - \sqrt{1-D^2}\,D_\mathrm{x}\,D_\mathrm{y}\,\sin\gamma\,\sin\delta\,\sin(2\varphi)\right), \tag{4.11}$$

$$b_\mathrm{2P} = \tau\,\tau_\mathrm{x}\,\tau_\mathrm{y}\,\tau_\Lambda\,I_0\,\left(D\,\big(D_\mathrm{x}\,\cos\gamma - D_\mathrm{y}\big)\,\sin(2\varphi) + \sqrt{1-D^2}\,D_\mathrm{x}\,D_\mathrm{y}\,\sin\gamma\,\sin\delta\,\cos(2\varphi)\right), \tag{4.12}$$

$$a_\mathrm{4P} = -\frac{1}{2}\,\tau\,\tau_\mathrm{x}\,\tau_\mathrm{y}\,\tau_\Lambda\,I_0\,D_\mathrm{x}\,D_\mathrm{y}\,\cos\gamma\,\left(1 - \sqrt{1-D^2}\,\cos\delta\right)\cos(4\varphi), \tag{4.13}$$

$$b_\mathrm{4P} = -\frac{1}{2}\,\tau\,\tau_\mathrm{x}\,\tau_\mathrm{y}\,\tau_\Lambda\,I_0\,D_\mathrm{x}\,D_\mathrm{y}\,\cos\gamma\,\left(1 - \sqrt{1-D^2}\,\cos\delta\right)\sin(4\varphi). \tag{4.14}$$

The intensity signal $I_{\mathrm{P}}(\rho)$ is a measure of the fiber orientation as defined in Fig. 4.4h. In principle, the actual fiber direction angle φ could be derived from $(b_{4\mathrm{P}}/a_{4\mathrm{P}})$. However, this is not feasible because $a_{4\mathrm{P}}$ and $b_{4\mathrm{P}}$ are much smaller than $a_{2\mathrm{P}}$ and $b_{2\mathrm{P}}$ ($|\cos\gamma| \ll 1$, for a quarter-wave retarder with $\gamma \approx \pi/2$), resulting in a low signal-to-noise ratio. For the other Fourier coefficients, it is not possible to separate the actual fiber orientation (φ, α) from the polarization properties of the filters (D_{x}, D_{y}, γ) and from the diattenuation of brain tissue (D). In Sec. 9.1, the impact of the non-ideal polarization properties and the tissue diattenuation on the derived fiber orientations will be investigated in more detail. If the values for D_{x}, D_{y}, γ, and D were known pixel-wise, the actual fiber orientation could exactly be computed from the above Fourier coefficients (see Appx. C.1).

Standard 3D-PLI Analysis In the standard 3D-PLI analysis [45, 46, 51], the spatial fiber orientations (φ, α) are derived from the measured Fourier coefficients assuming ideal linear polarizers ($D_{\mathrm{x}} = D_{\mathrm{y}} = 1$, $\tau_{\mathrm{x}} = \tau_{\mathrm{y}} = 1/2$), an ideal quarter-wave retarder ($\gamma = \pi/2, \tau_\Lambda = 1$), and no diattenuation of brain tissue ($D = 0$). In this ideal case, the Fourier coefficients of order four vanish:

$$a_{0\mathrm{P}} = \frac{I_0\,\tau}{4}, \quad a_{2\mathrm{P}} = -\frac{I_0\,\tau}{4}\,\sin\delta\,\sin(2\varphi), \quad b_{2\mathrm{P}} = \frac{I_0\,\tau}{4}\,\sin\delta\,\cos(2\varphi), \tag{4.15}$$

and Eq. (4.8) simplifies to (see Fig. 4.4d):

$$I_{\mathrm{P}}(\rho) = \frac{I_0\,\tau}{4}\left(1 + \sin\delta\,\sin\big(2(\rho-\varphi)\big)\right). \tag{4.16}$$

The Fourier coefficients of order zero and two are used to derive different parameter maps (see Fig. 4.5a-c and Fig. 4.8a):

- **Transmittance ($I_{\mathrm{T,P}}$):** The transmittance represents the averaged transmitted light intensity over all rotation angles ρ of the filters and is computed from the Fourier coefficient of order zero:

  $$I_{\mathrm{T,P}} = 2\,a_{0\mathrm{P}}. \tag{4.17}$$

  The transmittance is divided by the transmittance obtained from measurements without brain tissue, yielding the *normalized transmittance* $I_{\mathrm{T,N}} \in [0, 1]$.

- **Direction (φ_{P}):** The direction describes the in-plane orientation angle of the fibers (cf. Fig. 4.4h, in red) and is computed from the phase of the intensity profile (Fig. 4.4d, in red):

  $$\begin{aligned}\varphi_{\mathrm{P}} &= \frac{\operatorname{atan2}(-a_{2\mathrm{P}}, b_{2\mathrm{P}})}{2} \quad \in\ [0, \pi) \\ &= \varphi,\end{aligned} \tag{4.18}$$

  where the function $\operatorname{atan2}(x, y)$ denotes the angle (in radian measure) between the positive x-axis and the point (x, y). The angle is positive for $y > 0$ and negative for $y < 0$.

- **Retardation (r_{P}):** The retardation is a measure of the birefringence of the brain tissue and is computed from the peak-to-peak amplitude of the intensity profile normalized by the transmittance $I_{\mathrm{P}}(\rho)/I_{\mathrm{T,P}}$ (Fig. 4.4d, in blue):

  $$r_{\mathrm{P}} \equiv |\sin\delta_{\mathrm{P}}| = \frac{\sqrt{a_{2\mathrm{P}}^2 + b_{2\mathrm{P}}^2}}{a_{0\mathrm{P}}}. \tag{4.19}$$

For a non-birefringent, diattenuating sample ($\delta = 0$, $D \neq 0$), the measured retardation corresponds to the diattenuation of the sample ($r_\mathrm{P} = |D|$), assuming ideal polarizing filters.

Determination of the Fiber Inclination (α_P) According to Eq. (3.8), the out-of-plane inclination angle α of the fibers (cf. Fig. 4.4h, in blue) is related to the retardation via: $\delta \propto \cos^2 \alpha$. As the retardance also depends on the illumination wavelength λ, the birefringence Δn, and the thickness d of the birefringent material, the fiber inclination angle cannot easily be extracted.

In a first step, the measured retardation r_P is normalized by the maximum measurable retardation $r_\mathrm{P,max}$, which is assumed to correspond to a region that is completely filled with horizontal[7] (birefringent) fibers [45]. From the normalized retardation, a modified inclination angle $\tilde{\alpha}_\mathrm{P}$ is computed:

$$\tilde{\alpha}_\mathrm{P} = \arccos\left(\sqrt{\frac{\arcsin(r_\mathrm{P})}{\arcsin(r_\mathrm{P,max})}}\right). \tag{4.20}$$

The determined inclination angle is always positive so that fibers with $\pm\alpha$ cannot be distinguished (*inclination-sign ambiguity*). To date, there exist several approaches to improve the determination of the fiber inclination angle:

- **Transmittance Weighting:** As gray matter regions contain less myelinated axons than white matter regions, the retardation signal in gray matter is much lower than in white matter, which leads to an overestimation of the fiber inclination. To improve the determination of the fiber inclination in gray matter, the maximum retardation value is determined both in white and in gray matter and the above normalization is performed for both regions separately.

  Local variations in the density of myelinated fibers also lead to a misinterpretation of the actual fiber inclination angle. As myelin has a high scattering coefficient (see Sec. 3.2.2), the transmittance is a good measure for the local myelin density and can be used to weight the retardation values [53].

  Although transmittance weighting improves the determination of the fiber inclination, it does not solve the inclination-sign ambiguity and the derived fiber orientations are not completely reliable because the transmittance also depends on other tissue properties like the fiber inclination (discussed later in Chap. 8).

- **Tilting:** The tilting stage of the LAP allows a more precise determination of the fiber inclination because the fiber orientations can be measured under slightly different angles [54, 55]. The 3D-PLI measurement is first performed with a flat tilting stage (as described in Secs. 4.2 and 4.3) and then repeated four times with a specimen stage that is tilted by $\pm 8°$ around the x- and y-axis, respectively, yielding 5×18 images in total. Before further signal processing, the image series obtained from the tilted measurements need to be "untilted", i. e. the perspective transformation needs to be inverted. As the fiber orientations were measured under slightly different angles for every tilting position, the sinusoidal profiles of the transmitted light intensity are slightly different. By performing a simultaneous least-squares fit to the intensity profiles of all oblique measurements for each

[7] In this thesis, the terms *horizontal* or *vertical* are used to describe the fiber orientation with respect to the section plane (xy-plane): horizontal fibers lie within the section plane ($\alpha \approx 0°$), whereas vertical fibers are oriented perpendicularly to it ($\alpha \approx 90°$). To describe fibers with small inclinations ($\alpha < 45°$) or large inclinations ($\alpha > 45°$), the terms *flat* or *steep* fibers are used, respectively.

image pixel, the fiber inclinations can be determined independently of the local myelin density [161]. Tilting also solves the inclination-sign ambiguity [162, 163]: considering the decrease in absolute inclination after tilting, fibers with positive and negative inclination can be distinguished.

However, the technique is currently not available for microscopic resolution, and the reconstruction of inhomogeneous fiber configurations is still challenging and subject of current research. For 3D-PLI measurements with the PM, transmittance weighting is so far the only possibility to improve the determined fiber orientations.

Figure 4.5d shows the inclination map of a coronal human brain section.

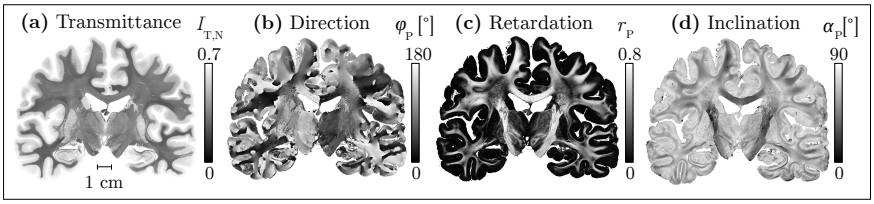

Fig. 4.5: Parameter maps of a coronal human brain section (cf. Fig. 3.1b) measured with the LAP (resolution: $64 \times 64 \times 60\,\mu m^3$): **(a)** normalized transmittance $I_{T,N}$, **(b)** in-plane direction angle φ_P, **(c)** retardation r_P, **(d)** out-of-plane inclination angle α_P. The measurements and the signal processing were performed at INM-1, FZJ, Germany.

Reconstruction of the Fiber Orientation The in-plane direction angle φ_P and the out-of-plane inclination angle α_P are combined to a three-dimensional unit vector which describes the spatial orientation of the nerve fibers (cf. Fig. 4.4h). The so-called *fiber orientation map (FOM)* encodes the fiber orientations in different colors (see Fig. 4.6).

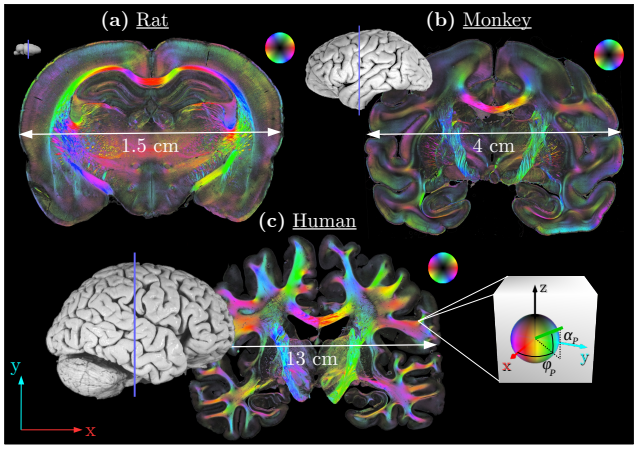

Fig. 4.6: Fiber orientation maps of coronal brain sections obtained from 3D-PLI measurements with the PM (a-b) and the LAP (c) for different species: **(a)** Wistar rat, **(b)** vervet monkey, and **(c)** human (cf. Fig. 4.5). The three-dimensional orientation of the nerve fibers within the brain sections is encoded in an HSV color scheme: the hue represents the in-plane fiber direction φ_P, the brightness value represents the out-of-plane fiber inclination α_P (orthogonal fibers with $\alpha_P = 90°$ appear in black). The fiber orientation (φ_P,α_P) was computed for each image pixel as described in Sec. 4.4.1. The measurements and the signal processing were performed at INM-1, FZJ, Germany and published in Zilles [47] (Copyright 2015, with permission from Elsevier).

The FOMs shown in this thesis are color-coded in a *Hue-Saturation-Value (HSV)* space: the hue represents the in-plane fiber orientation ($H = 2\,\varphi_P$), the brightness value represents the out-of-plane fiber orientation ($V = 1 - \alpha_P/90°$), and the saturation is set to the maximum ($S = 1$). In this color scheme (*HSV black*), regions with orthogonal fibers ($\alpha_P = 90°$) or low birefringence signals are represented in black.

To reconstruct the three-dimensional fiber architecture of a whole brain volume, the FOMs of several consecutive brain sections are registered onto each other (cf. Fig. 4.7a) and the fiber orientation vectors are combined to three-dimensional fiber tracts using tractography algorithms (cf. Fig. 4.7c).

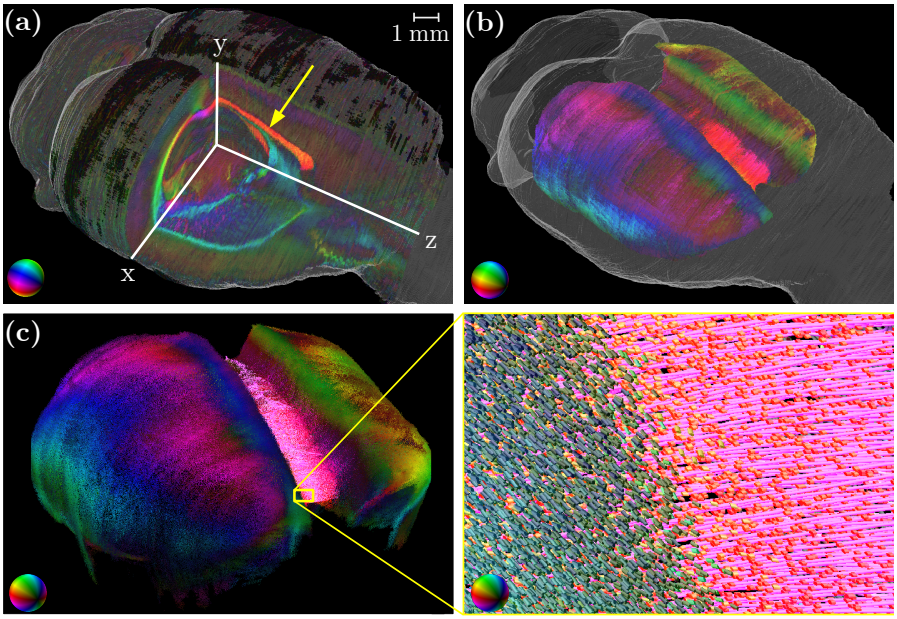

Fig. 4.7: 3D-reconstructed fiber orientations of a rat brain, obtained from 3D-PLI measurements with the LAP (resolution: $64 \times 64 \times 60\,\mu m^3$): **(a)** The fiber orientation maps (FOMs) of 455 coronal rat brain sections (cf. Fig. 4.6a) were registered onto each other in the z-direction as described in Sec. 4.3. The clipping-box view shows that the reconstructed fiber bundles (like the corpus callosum, yellow arrow) are consistent across several brain sections. **(b)** The region of the corpus callosum was masked in all FOMs for further evaluation. **(c)** The fiber pathways inside the corpus callosum were reconstructed by performing a fiber tractography with seed points on the sagittal plane. The zoomed-in region shows the fiber pathways that connect the two hemispheres (magenta). (Adapted from: Schubert *et al.* (2018) [164] Figs. 6a, 9 and 10a, licensed under CC BY 3.0)

4.4.2 Crossed Polars (XP) Measurement

The crossed polars (XP) measurement [165] allows the determination of the direction angle independently from D_x, D_y, γ, or D and can therefore be used as a reference for the actual fiber direction φ. However, the XP measurement cannot replace 3D-PLI because the direction angle can only be determined in a value range of $[0°, 90°)$ and the measurement gives no information about the fiber inclination α.

The setup for the XP measurement is similar to the 3D-PLI measurement, but it does not include the retarder (see Fig. 4.4b). Due to the 90°-orientation of polarizer and analyzer, a measurement without specimen would result in almost zero light intensity. A calibration as described in Sec. 4.3 is therefore not possible. Instead, the series of raw images obtained from the XP measurement is divided by the image of the light source and by the polarization-independent filter inhomogeneities of polarizer and analyzer (see Fig. 7.7a,b,d). As the filter inhomogeneities can only be determined for a circular region around the rotation center of the filters, the images obtained in the XP measurement need to be cropped to this region. The parallax effect induced by the analyzer is corrected before the calibration.

For the XP measurement, the transmitted light intensity (cf. Fig. 4.4e) and the corresponding Fourier coefficients read:

$$\vec{S}'_{\mathrm{X}}(\rho) = P_{\mathrm{y}}\left(\rho,\, D_{\mathrm{y}},\, \tau_{\mathrm{y}}\right) \cdot M\left(\varphi,\, \delta,\, D,\, \tau\right) \cdot P_{\mathrm{x}}\left(\rho,\, D_{\mathrm{x}},\, \tau_{\mathrm{x}}\right) \cdot \vec{S}_{\mathrm{unpol}} \tag{4.21}$$

$$\begin{aligned} \Rightarrow \quad I_{\mathrm{X}}(\rho) = \tau\, \tau_{\mathrm{x}}\, \tau_{\mathrm{y}}\, I_0 \Big[& 1 - D_{\mathrm{x}}\, D_{\mathrm{y}} + \left(1 - \sqrt{1 - D^2}\, \cos\delta\right) \sin^2\left(2(\rho - \varphi)\right) \\ & + D\left(D_{\mathrm{x}} - D_{\mathrm{y}}\right) \cos\left(2(\rho - \varphi)\right) \Big] \end{aligned} \tag{4.22}$$

$$\Rightarrow \quad I_{\mathrm{X}}(\rho) = a_{0\mathrm{X}} + a_{2\mathrm{X}}\, \cos(2\rho) + b_{2\mathrm{X}}\, \sin(2\rho) + a_{4\mathrm{X}}\, \cos(4\rho) + b_{4\mathrm{X}}\, \sin(4\rho), \tag{4.23}$$

$$a_{0\mathrm{X}} = \tau\, \tau_{\mathrm{x}}\, \tau_{\mathrm{y}}\, I_0 \left(1 - \frac{1}{2} D_{\mathrm{x}}\, D_{\mathrm{y}} \left(1 + \sqrt{1 - D^2}\, \cos\delta\right)\right), \tag{4.24}$$

$$a_{2\mathrm{X}} = \tau\, \tau_{\mathrm{x}}\, \tau_{\mathrm{y}}\, I_0\, D\left(D_{\mathrm{x}} - D_{\mathrm{y}}\right) \cos(2\varphi), \tag{4.25}$$

$$b_{2\mathrm{X}} = \tau\, \tau_{\mathrm{x}}\, \tau_{\mathrm{y}}\, I_0\, D\left(D_{\mathrm{x}} - D_{\mathrm{y}}\right) \sin(2\varphi), \tag{4.26}$$

$$a_{4\mathrm{X}} = -\frac{1}{2} \tau\, \tau_{\mathrm{x}}\, \tau_{\mathrm{y}}\, I_0\, D_{\mathrm{x}}\, D_{\mathrm{y}} \left(1 - \sqrt{1 - D^2}\, \cos\delta\right) \cos(4\varphi), \tag{4.27}$$

$$b_{4\mathrm{X}} = -\frac{1}{2} \tau\, \tau_{\mathrm{x}}\, \tau_{\mathrm{y}}\, I_0\, D_{\mathrm{x}}\, D_{\mathrm{y}} \left(1 - \sqrt{1 - D^2}\, \cos\delta\right) \sin(4\varphi). \tag{4.28}$$

For the XP measurement, one parameter map is computed (shown exemplary for a sagittal rat brain section in Fig. 4.8b):

- **Direction ($\boldsymbol{\varphi_{\mathrm{X}}}$):** The direction angle of the fibers is given by the minima of the intensity signal (see Fig. 4.4e, in red) and can be computed from the Fourier coefficients of order four via:

$$\begin{aligned} \varphi_{\mathrm{X}} &= \frac{\operatorname{atan2}\left(-b_{4\mathrm{X}}, -a_{4\mathrm{X}}\right)}{4} \quad \in [0, \pi/2) \\ &= \varphi \mod \pi/2. \end{aligned} \tag{4.29}$$

4.4.3 Diattenuation Imaging (DI)

To measure the diattenuation D of the brain tissue, only the polarizer is rotated below the stationary tissue sample (see Fig. 4.4c) [58]. For this setup, the transmitted light intensity (cf. Fig. 4.4f) and the corresponding Fourier coefficients read:

$$\vec{S}'_{\mathrm{D}}(\rho) = M\left(\varphi,\, \delta,\, D,\, \tau\right) \cdot P_{\mathrm{x}}\left(\rho,\, D_{\mathrm{x}},\, \tau_{\mathrm{x}}\right) \cdot \vec{S}_{\mathrm{unpol}} \tag{4.30}$$

$$\Rightarrow \quad I_{\mathrm{D}}(\rho) = \tau\, \tau_{\mathrm{x}}\, I_0 \left(1 + D\, D_{\mathrm{x}}\, \cos\left(2(\rho - \varphi)\right)\right) \tag{4.31}$$

$$\Rightarrow \quad I_{\mathrm{D}}(\rho) = a_{0\mathrm{D}} + a_{2\mathrm{D}}\,\cos(2\rho) + b_{2\mathrm{D}}\,\sin(2\rho), \tag{4.32}$$

$$a_{0\mathrm{D}} = \tau\,\tau_{\mathrm{x}}\,I_0, \tag{4.33}$$

$$a_{2\mathrm{D}} = \tau\,\tau_{\mathrm{x}}\,I_0\;\,D\,D_{\mathrm{x}}\,\cos(2\varphi), \tag{4.34}$$

$$b_{2\mathrm{D}} = \tau\,\tau_{\mathrm{x}}\,I_0\;\,D\,D_{\mathrm{x}}\,\sin(2\varphi). \tag{4.35}$$

From the determined Fourier coefficients, two parameter maps are computed (shown exemplary for a sagittal rat brain section in Fig. 4.8c):

- **Direction ($\boldsymbol{\varphi_{\mathrm{D}}}$):** The rotation angle for which the transmitted light intensity $I_{\mathrm{D}}(\rho)$ becomes maximal (see Fig. 4.4f, in red) is related to the direction angle of the fibers and can be computed from the Fourier coefficients of order two via:

$$\Rightarrow \quad \varphi_{\mathrm{D}} = \frac{\operatorname{atan2}\left(b_{2\mathrm{D}},\, a_{2\mathrm{D}}\right)}{2} \quad \in\ [0, \pi). \tag{4.36}$$

$$= \begin{cases} \varphi & , D > 0, \\ \varphi + \pi/2\,, & D < 0. \end{cases}$$

  As for the XP measurement, the determined direction angle does not depend on D_{x}, D_{y}, γ, or D.[8]

- **Measured Diattenuation ($|\mathscr{D}|$):** The amplitude of the normalized intensity profile (see Fig. 4.4f, in blue) is related to the diattenuation of the brain tissue and can be computed by combining all three Fourier coefficients:

$$\Rightarrow \quad |D_{\mathrm{D}}| = \frac{\sqrt{a_{2\mathrm{D}}^2 + b_{2\mathrm{D}}^2}}{D_{\mathrm{x}}\;a_{0\mathrm{D}}} \tag{4.37}$$

$$= |D| > 0.$$

  As the diattenuation of the polarizer (D_{x}) cannot be determined pixel-wise, $|D_{\mathrm{D}}|$ and D_{x} cannot be separated in a DI measurement. Therefore, the studies in Chap. 9 investigate the amplitude of the diattenuation signal:

$$|\mathscr{D}| \equiv |D_{\mathrm{D}}|\,D_{\mathrm{x}} > 0. \tag{4.38}$$

  To avoid confusion in the following, the symbol D is referred to as *tissue diattenuation* and the symbol $|\mathscr{D}|$ as *measured diattenuation*.

Figure 4.8 shows the parameter maps computed from the 3D-PLI measurement (transmittance $I_{\mathrm{T,P}}$, direction angle φ_{P}, retardation r_{P}), the XP measurement (direction angle φ_{X}), and the DI measurement (measured diattenuation $|\mathscr{D}|$, direction angle φ_{D}) for a sagittal rat brain section (section no. 175). The diattenuation in brain tissue is much smaller than the birefringence so that the measured diattenuation signal is much more sensitive to noise than the measured retardation signal. The impact of noise on the diattenuation signal and the impact of diattenuation on the 3D-PLI signal will be investigated in Chap. 9 in more detail.

[8] However, the direction angle φ_{D} obtained from the DI measurement is expected to be more error-prone than the direction angle φ_{X} obtained from the XP measurement because $a_{2\mathrm{D}}$ and $b_{2\mathrm{D}}$ are much smaller than $a_{4\mathrm{X}}$ and $b_{4\mathrm{X}}$ leading to a smaller signal-to-noise ratio (the amplitude of the diattenuation signal D is expected to be much smaller than the amplitude of the retardation signal $\sin^2(\delta/2)$, cf. Fig. 4.4e and f).

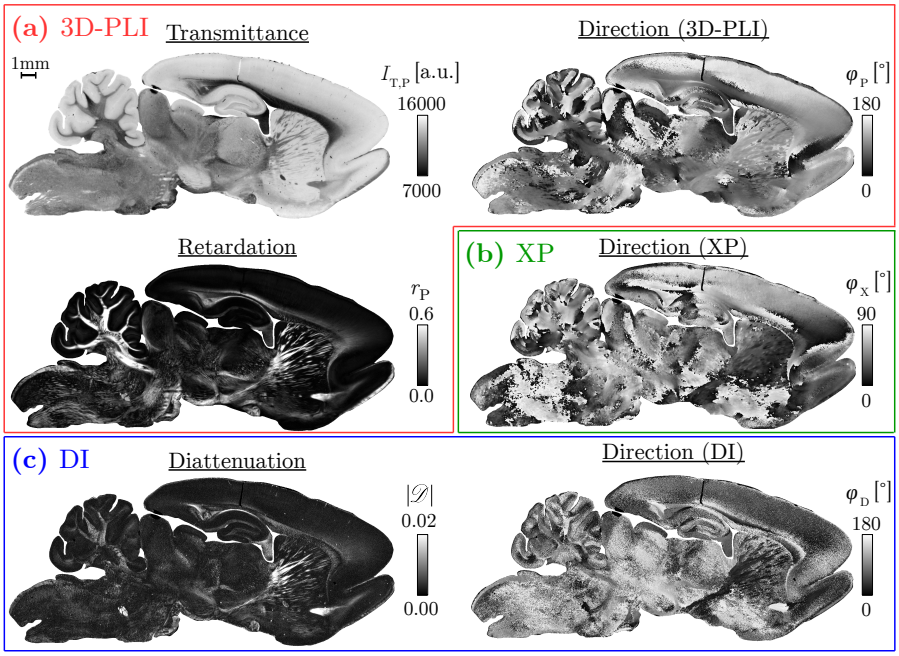

Fig. 4.8: Parameter maps of one sagittal rat brain section (section no. 175) obtained from 3D-PLI (a), XP (b), and DI (c) measurements with the LAP, as described in Secs. 4.4.1 to 4.4.3 (resolution in object space: 14 µm/px). A similar figure has been published in Menzel *et al.* (2017) Fig. 14.

Chapter 5

Two-Photon Fluorescence Microscopy (TPFM)

The imaging technique *Two-Photon Fluorescence Microscopy (TPFM)* uses non-linear two-photon excitation to achieve deep tissue penetration and reduced photodamage, allowing to image the three-dimensional structure of biological specimens with high in-depth resolution [166]. In 2016, Irene Costantini and colleagues from the *European Laboratory for Non-Linear Spectroscopy (LENS)* at the University of Florence, Italy, developed a technique to measure the three-dimensional architecture of myelinated axons with TPFM without using exogenous labeling. As the technique can be applied to brain sections that have previously been measured with 3D-PLI, it can be used to obtain detailed information about the underlying tissue structure and composition and to validate the reconstructed fiber orientations in 3D-PLI measurements [56, 167].

This chapter introduces the TPFM technique used to measure the fiber architecture of 3D-PLI brain sections: the preparation of the brain tissue (Sec. 5.1), the TPFM measurement (Sec. 5.2), and the signal analysis and image processing (Sec. 5.3). Parts of Sec. 5.2 have been published in Menzel *et al.* (2018a) [67].

5.1 Preparation of Brain Tissue

The brain sections were prepared for the 3D-PLI measurement as described in Sec. 4.1: the formalin-fixated brain was deeply frozen, cut into sections of about 60 µm thickness, embedded in a glycerin solution, and mounted on glass slides. After the 3D-PLI measurement at Forschungszentrum Jülich, the brain sections were sent to LENS, where the cover slips were removed. The brain sections were then placed in a Petri dish filled with *phosphate-buffered saline (PBS)* solution and gently washed for several months to remove the glycerin. The time of washing depends on the species and on the size of the brain section. After the washing, a new cover slip was placed on top of the brain section.

The washing of the glycerin-embedded brain sections is crucial for the TPFM measurements because it increases the autofluorescence of the myelin sheaths. The increased myelin autofluorescence is only observed for brain sections that have previously been embedded in glycerin – not for non-embedded tissue. Finding an explanation for this phenomenon is subject of ongoing research. Figure 5.1 shows on the left-hand side a TPFM image of a mouse brain section without washing (i. e. still embedded in glycerin) and on the right-hand side the same section after three weeks of washing with PBS. The autofluorescence, i. e. the contrast of myelinated axons increases notably (see arrows).

To validate that the measured autofluorescence signal is caused by the myelin sheaths, the same mouse brain section was measured with TPFM acquiring in the green channel

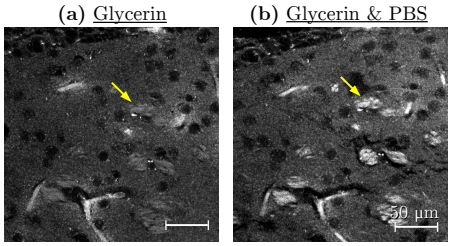

Fig. 5.1: TPFM image of nerve fiber bundles in a coronal mouse brain section: **(a)** embedded in glycerin, **(b)** after three weeks of washing with PBS. The contrast of myelinated axons increases notably (see arrows). (Source: Costantini *et al.* (2017) [56])

the signal from the autofluorescence without exogenous labeling (Fig. 5.2a) and in the red channel the signal from an exogenous dye specific for the myelin called *fluoromyelin* (Fig. 5.2b).[1] The colocalization of the signal (in yellow) demonstrates that the autofluorescent regions (green) and the regions labeled by fluoromyelin (red) are identical (Fig. 5.2c). Thus, the autofluorescence signal detected with TPFM is indeed produced by the myelin sheaths of the axons.

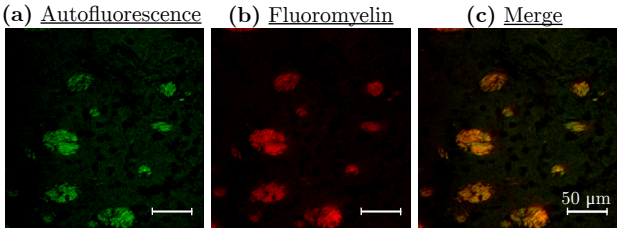

Fig. 5.2: Myelinated nerve fiber bundles in a coronal mouse brain section measured with TPFM: **(a)** autofluorescence signal without exogenous labeling, **(b)** fluoromyelin signal, **(c)** merge of the two channels suggesting that the measured autofluorescence signal is produced by the myelin sheaths surrounding the nerve fibers. (Courtesy of Irene Costantini [167])

5.2 Microscopic Measurement

Imaging Principle In conventional fluorescence microscopy, a fluorescent molecule (*fluorophore*) is excited from the electronic ground state to an excited state by absorbing a single photon (see Fig. 5.3a). This excitation process requires highly energetic photons, i. e. light with short wavelengths (e. g. ultraviolet). In TPFM, the fluorophore is excited by the simultaneous absorption of two less energetic photons (see Fig. 5.3b), i. e. light with longer wavelengths (near infrared). To enable this two-photon excitation, a high flux of photons is needed. As a result, the excitation only occurs in regions where the light is most concentrated (i. e. near the focal plane). The longer excitation wavelength also causes less tissue damage and less photobleaching so that in-vivo imaging with a penetration depth of several millimeters becomes possible [166]. However, due to the scanning system, the technique is limited to small volumes of interest – imaging a whole 3D-PLI section is very time consuming.

[1] The measurements were performed by Irene Costantini (LENS, University of Florence, Italy).

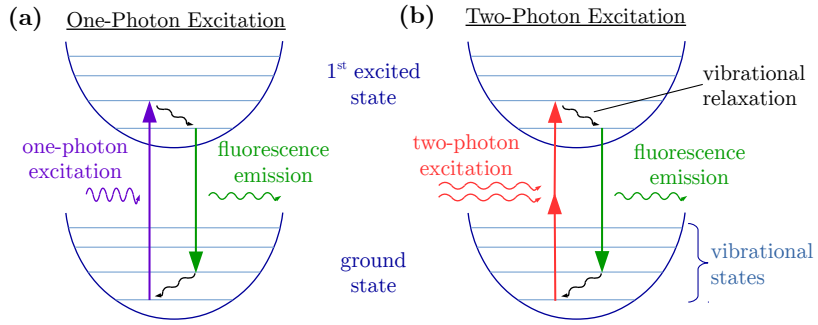

Fig. 5.3: Jablonski diagram of one-photon excitation (a) and two-photon excitation (b) (adapted from [166] Fig. 1)

Measurement Setup The TPFM measurements at LENS were performed with a custom-made system [28]. The microscope is equipped with a mode-locked titanium-sapphire (Ti:Sa) laser with a wavelength of 800 nm which is coupled into a scanning system based on a pair of galvanometric mirrors (GM), see Fig. 5.4. The laser is focused onto the sample by a water-immersion 25 × objective lens (*LD LCI Plan-Apochromat 25x/0.8 Imm Corr DIC M27*). The lateral displacement of the sample is realized by a motorized xy-stage (enabling tile-wise scanning of the sample). The axial displacement (along the z-axis) is realized by a closed-loop piezoelectric stage. The fluorescence signals are collected by two photomultiplier tubes (PMT), enabling to detect red fluorescence (e. g. caused by hemoglobin in blood cells) as well as green fluorescence (e. g. caused by nerve fibers) [56].

With this setup, a resolution of $0.244 \times 0.244 \times 1\,\mu m^3$ is achieved. The sample is measured in tiles of $250 \times 250\,\mu m^2$, with an overlap of 10 % to allow for stitching.

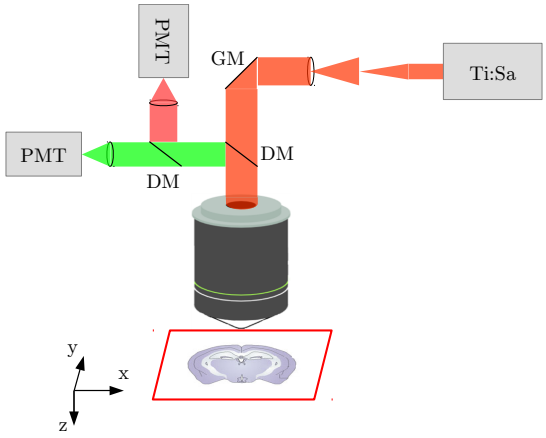

Fig. 5.4: Schematic drawing visualizing the TPFM measurement setup. The setup consists of a titanium-sapphire (Ti:Sa) laser, a pair of galvanometric mirrors (GM), dichroic mirrors (DM), photomultiplier tubes (PMT), a microscope objective, and a motorized specimen stage. (Courtesy of Irene Costantini)

5.3 Signal Analysis and Image Processing

To obtain a three-dimensional image of the sample, the measured tiles were stitched with the software *TeraStitcher*, a tool for fast and automatic 3D-stitching of microscopy images [168]. For a 3D-PLI brain section with 60 µm thickness, this results in a series of about 60 images. After stitching, the red fluorescence channel was subtracted from the green fluorescence channel to separate the autofluorescence of the myelin sheaths from the autofluorescence of the blood vessels in the red channel. The limited aperture of the lens causes diffraction which leads to blurring of the resulting images. To sharpen the contours and achieve a better resolution in the z-direction, the images were deconvolved, taking into account the point spread function of the objective lens (2.6 µm in the z-direction, 0.5 µm in the x- and y-direction). The deconvolution was performed with the *Huygens* software (Scientific Volume Imaging, the Netherlands, `http://svi.nl`), a processing package for fluorescence microscope images.

Figure 5.5 shows the resulting images for a coronal mouse brain section (left hemisphere). The image on the left shows the fiber orientation map measured with 3D-PLI. Specific areas (1–4) of the same brain section were subsequently measured with TPFM (3×3 tiles). Figures 5.5A and B show a zoom into the resulting three-dimensional architecture of the nerve fiber bundles. Applying a threshold and blurring to the TPFM image stack, the fiber bundles can be separated from the surrounding tissue (Fig. 5.5C). With 3D Structure Tensor Analysis [169], a vector field can be computed which reflects the orientations of the fiber bundles (cf. Figs. 5.5D and E) and which enables a direct comparison to the orientation vectors obtained from the 3D-PLI analysis.

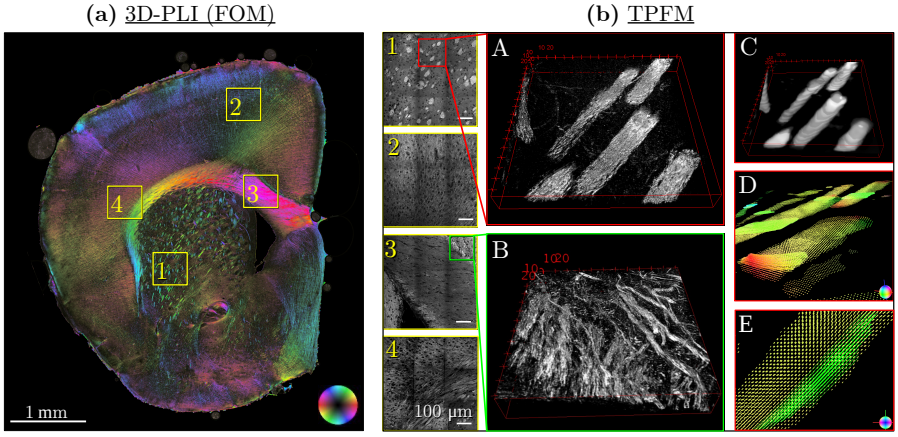

Fig. 5.5: Coronal section of the left hemisphere of a mouse brain measured with 3D-PLI (a) and with TPFM (b): The image on the left shows the fiber orientation map (FOM) measured with 3D-PLI (INM-1, FZJ, Germany). Specific areas (1–4) of the same brain section were subsequently measured with TPFM (3×3 tiles). Figures A and B show a zoom into the resulting image stack (Courtesy of Irene Costantini). Applying a threshold and blurring, the fiber bundles can be separated from the surrounding tissue (Fig. C). The extracted vector field (Figs. D and E) reflects the orientations of the fiber bundles (Courtesy of Nicole Schubert).

Chapter 6

Finite-Difference Time-Domain (FDTD) Simulation

Finite *Difference Time-Domain (FDTD)* algorithms are powerful tools for modeling the propagation of electromagnetic waves in arbitrary-shaped structures and allow the investigation of absorption and scattering of light. To model and better understand experimental observations in 3D-PLI and DI measurements and to make hypotheses for the experiment, the evolution of the electromagnetic field in brain tissue was solved by a massively parallel *3D Maxwell Solver* based on the FDTD method.

This chapter gives an introduction to the FDTD method. For a complete guidance on FDTD techniques and applications, the reader is referred to Taflove·Hagness [72].

As the name implies, the FDTD method computes the components of the electromagnetic field numerically by discretizing space and time and approximating Maxwell's curl equations by *finite differences*. The algorithm used in this study combines two different algorithms: the classical Yee algorithm (introduced in Sec. 6.1) and an unconditionally stable algorithm based on a product formula approach (introduced in Sec. 6.2). The software (simulation input and output) is described in Sec. 6.3.

The explanations follow Taflove·Hagness [72], De Raedt [170], De Raedt *et al.* [171], De Raedt·Michielsen [172], Kole [173], Shen [174], and Wilts [175]. Passages that refer to a certain textbook are labeled by separate bibliographic references. Parts of Sec. 6.1 have been published in Menzel *et al.* (2016) [66] Sec. 4.1. Parts of Secs. 6.3 and 6.4 have been published in Menzel *et al.* (2018a) [67].

6.1 Yee's Algorithm

The algorithm proposed by Yee in 1966 [176] represents one of the first FDTD techniques and is still very popular due to its accuracy, robustness, and flexibility ([72] p. 80). The algorithm computes the electromagnetic field components on staggered grids of space and time.

Discretization of Space The three-dimensional space is divided into a uniform cubic lattice of points, the so-called *Yee grid*[1] [176]. Each lattice point is assigned a component of the electromagnetic field such that each component of the magnetic field $\vec{H}$ is surrounded by four components of the electric field $\vec{E}$ and vice versa (see Fig. 6.1a). A sample is represented on the Yee grid by specifying the permittivity, permeability, and

[1] Depending on the purpose of the FDTD simulation and on the geometry of the simulated structure, alternative finite-difference grids can be used (see [72] Chap. 3.7). The choice of the grid influences the accuracy of the FDTD simulation.

conductivity of the material for each point in the corresponding sub-lattice. The spatial resolution is defined by the lattice spacing, i. e. the side length Δ of one unit cell in the Yee grid ([72] Sec. 3.6.1). The spatial discretization must be sufficiently fine in order to resolve the smallest geometric structure.[2]

Discretization of Time The propagation of the electromagnetic field in time is computed iteratively using a *leapfrog time-stepping scheme* ([72] Sec. 3.6.1), see Fig. 6.1b: The components of the $\vec{E}$-field at a given time t are computed from the values of the $\vec{H}$-field at time $(t - \Delta t/2)$ and from the values of the $\vec{E}$-field at time $(t - \Delta t)$, where Δt is a globally defined time step [170, 175]. The components of the $\vec{H}$-field at time $(t + \Delta t/2)$ are computed analogously from the values of the $\vec{E}$-field at time t and from the values of the $\vec{H}$-field at time $(t - \Delta t/2)$. The iteration of the $\vec{E}$-field and $\vec{H}$-field updates is repeated over and over again until the final time of the simulation is reached.

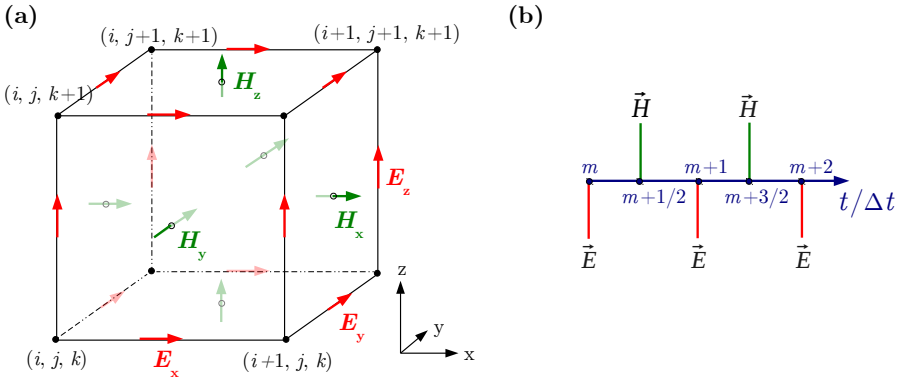

Fig. 6.1: (a) Unit cell of the cubic Yee grid: Each component of the magnetic field $\vec{H}$ is surrounded by four components of the electric field $\vec{E}$ and vice versa. (After: Yee [176] Fig. 1) **(b)** Illustration of the leapfrog time-stepping scheme. (After: Wilts [175] Fig. 1) (The figures have been published in Menzel *et al.* (2016) [66] Fig. 3b.)

Finite-Difference Approximation of Maxwell's Curl Equations In linear, isotropic, non-dispersive, lossy[3] materials, Maxwell's curl equations (2.1) and (2.2) read (using the material equations defined in Sec. 2.1.2):

$$\frac{\partial \vec{E}}{\partial t} = \frac{1}{\epsilon}\left[\vec{\nabla} \times \vec{H} - (\vec{J}_{\text{source}} + \sigma_{\text{e}}\vec{E})\right], \tag{6.1}$$

$$\frac{\partial \vec{H}}{\partial t} = -\frac{1}{\mu}\left[\vec{\nabla} \times \vec{E} + (\vec{M}_{\text{source}} + \sigma_{\text{m}}\vec{H})\right]. \tag{6.2}$$

The spatial and temporal derivatives of an arbitrary function $u^m_{i,j,k}$, evaluated at a discrete point in space $(i\,\Delta x, j\,\Delta y, k\,\Delta z)$ and at a discrete point in time $(m\,\Delta t)$, can be approximated by *second-order central differences* ([72] p. 62):

[2] The finite size of the Yee grid can generate artifacts like anisotropy, pseudo refraction, and imprecise cancellation of multiple scattered waves [72].

[3] Originally, the Yee algorithm was set up for lossless materials with $\sigma_{\text{e}} = \sigma_{\text{m}} = 0$, but can be generalized to lossy materials.

$$\frac{\partial u^m_{i,j,k}}{\partial x} = \frac{u^m_{i+\frac{1}{2},j,k} - u^m_{i-\frac{1}{2},j,k}}{\Delta x} + O\big[(\Delta x)^3\big], \tag{6.3}$$

$$\frac{\partial u^m_{i,j,k}}{\partial t} = \frac{u^{m+\frac{1}{2}}_{i,j,k} - u^{m-\frac{1}{2}}_{i,j,k}}{\Delta t} + O\big[(\Delta t)^3\big]. \tag{6.4}$$

The spatial derivatives with respect to y and z are analogous to Eq. (6.3). With these approximations, the electric and magnetic field components can be interleaved in space at intervals $\Delta/2$ and in time at intervals $\Delta t/2$, thus allowing the implementation of a leapfrog time-stepping algorithm. In Appx. D.1, the finite-difference approximation is shown exemplary for the x-component of the electric field.

Stability Criterion An algorithm is said to be *numerically stable* when a bounded input also yields a bounded output. An unstable FDTD algorithm generates results which increase *ad infinitum* as the time-stepping continues [173].

The Yee algorithm is stable when the *Courant stability bound* is fulfilled ([72] p. 154):

$$\Delta t \leq \frac{1}{c\sqrt{\frac{1}{(\Delta x)^2} + \frac{1}{(\Delta y)^2} + \frac{1}{(\Delta z)^2}}} \overset{(\Delta x, \Delta y, \Delta z = \Delta)}{\equiv} \frac{\Delta}{c\sqrt{3}}, \tag{6.5}$$

where Δt is the time step used in the FDTD simulation, c the velocity of light in free space, and Δ the Yee mesh size. Thus, a finer spatial discretization also requires a smaller time step in order to maintain numerical stability. The above inequality can be written as:

$$C \equiv \frac{c\sqrt{3}\,\Delta t}{\Delta} \leq 1, \tag{6.6}$$

where C denotes the normalized *Courant factor* ([72] p. 133).

As the numerical solution depends on the time step that is used for the integration of Maxwell's equations, the Yee algorithm is said to be *conditionally stable*, which might limit its use for certain applications. For the simulations presented in Part IV, a combination of the Yee algorithm and an *unconditionally stable* algorithm based on a product formula approach was used, which is described in the following.

6.2 Unconditionally Stable Algorithm (Product Formula Approach)

In the last decades, several unconditionally stable FDTD techniques have been developed (a state-of-the-art review is given by De Raedt [170]). The technique presented here uses a product formula approach to construct an unconditionally stable algorithm which computes the electromagnetic field components only with a slightly higher computational cost as compared to the conventional Yee algorithm.

The algorithm is a combination of several techniques: For the discretization of space, the conventional Yee grid is used and the spatial derivatives in Maxwell's equations are expressed by central-difference approximations (see Sec. 6.1). Instead of also discretizing time (as in the Yee algorithm) the formal solution of Maxwell's equations in matrix form is used to design an unconditionally stable algorithm based on the *Lie-Trotter-Suzuki product formula approach*, which is explained in the following. The explanations follow [174] (Secs. 2.1, 2.2).

Maxwell's curl equations (6.1) and (6.2) can be written in matrix form:

$$\frac{\partial}{\partial t}\begin{pmatrix}\sqrt{\mu}\,\vec{H}\\ \sqrt{\epsilon}\,\vec{E}\end{pmatrix} = \begin{pmatrix}-\frac{\sigma_\mathrm{m}}{\mu} & -\frac{1}{\sqrt{\mu}}\vec{\nabla}\times\frac{1}{\sqrt{\epsilon}}\\ \frac{1}{\sqrt{\epsilon}}\vec{\nabla}\times\frac{1}{\sqrt{\mu}} & -\frac{\sigma_\mathrm{e}}{\epsilon}\end{pmatrix}\begin{pmatrix}\sqrt{\mu}\,\vec{H}\\ \sqrt{\epsilon}\,\vec{E}\end{pmatrix} - \begin{pmatrix}\frac{1}{\sqrt{\mu}}\vec{M}_\mathrm{source}\\ \frac{1}{\sqrt{\epsilon}}\vec{J}_\mathrm{source}\end{pmatrix}, \tag{6.7}$$

where $\vec{E}$, $\vec{H}$, $\vec{J}_\mathrm{source}$, and $\vec{M}_\mathrm{source}$ are functions of $(\vec{r}, t)$.

For linear, isotropic, non-dispersive, lossless materials ($\sigma_\mathrm{e} = \sigma_\mathrm{m} = 0$) without electric or magnetic current sources ($\vec{J}_\mathrm{source} = \vec{M}_\mathrm{source} = 0$), this simplifies to:[4]

$$\frac{\partial}{\partial t}\Psi(t) = \mathcal{L}\,\Psi(t), \tag{6.8}$$

where $\Psi(t)$ and $\mathcal{L}$ are represented by:

$$\Psi(t) = \begin{pmatrix}\sqrt{\mu}\,\vec{H}\\ \sqrt{\epsilon}\,\vec{E}\end{pmatrix}, \quad \mathcal{L} = \begin{pmatrix}0 & -\frac{1}{\sqrt{\mu}}\vec{\nabla}\times\frac{1}{\sqrt{\epsilon}}\\ \frac{1}{\sqrt{\epsilon}}\vec{\nabla}\times\frac{1}{\sqrt{\mu}} & 0\end{pmatrix}. \tag{6.9}$$

The formal solution to Eq. (6.8) is given by:

$$\Psi(t) = \mathrm{e}^{t\mathcal{L}}\,\Psi(0) = \mathcal{U}(t)\,\Psi(0), \tag{6.10}$$

where $\mathcal{U}(t) = \mathrm{e}^{t\mathcal{L}}$ is the time evolution operator and $\Psi(0)$ the initial state of the electromagnetic field. The time evolution of the electromagnetic fields on the Yee grid can be described by: $\Psi(t + \Delta t) = \mathrm{e}^{\Delta t\,\mathcal{L}}\,\Psi(t) = \mathcal{U}(\Delta t)\,\Psi(t)$, with time step Δt.

As the matrix $\mathcal{L}$ is *skew-symmetric* ($\mathcal{L}^\mathrm{T} = -\mathcal{L}$), the matrix exponential is orthogonal $\left(\mathcal{U}(t)^\mathrm{T} = \mathcal{U}(t)^{-1}\right)$. Thus, the time evolution operator rotates the vector $\Psi(t)$ without changing its norm:

$$\begin{aligned}\langle\Psi(t)|\Psi(t)\rangle &= \langle\mathcal{U}(t)\,\Psi(0)\,|\,\mathcal{U}(t)\,\Psi(0)\rangle = \langle\Psi(0)\,|\,\mathcal{U}(t)^T\mathcal{U}(t)\,|\,\Psi(0)\rangle\\ &= \langle\Psi(0)\,|\,\Psi(0)\rangle \qquad (6.11)\\ \Leftrightarrow \|\Psi(t)\| &= \|\Psi(0)\|. \qquad (6.12)\end{aligned}$$

Hence, the algorithm is *unconditionally stable by construction*. In physical terms, the electromagnetic field energy, given by $\langle\Psi(t)|\Psi(t)\rangle$, is conserved [173].

The time evolution operator can be expressed by the series:

$$\mathcal{U}(t) = \mathrm{e}^{t\mathcal{L}} = \sum_{m=0}^{\infty}\frac{t^m}{m!}\,\mathcal{L}^m. \tag{6.13}$$

Usually, the matrix exponential cannot be calculated explicitly and an approximation has to be made. The here presented algorithm uses the *Lie-Trotter-Suzuki product formula* [177]:

$$\mathrm{e}^{t(\mathcal{L}_1+\ldots+\mathcal{L}_N)} = \lim_{m\to\infty}\left(\prod_{i=1}^{N}\mathrm{e}^{t\mathcal{L}_i/m}\right)^m. \tag{6.14}$$

[4] For the more general case of lossy materials with electric and magnetic current sources, the reader is referred to [170].

If the skew-symmetric matrix $\mathcal{L}$ can be decomposed into a sum of skew-symmetric matrices $\mathcal{L}_i$ of which the matrix exponential can be easily computed, the product formula approach can be used to construct an unconditionally stable algorithm.[5]

When the matrix $\mathcal{L}$ is decomposed into two skew-symmetric matrices $\mathcal{L}_1$ and $\mathcal{L}_2$ so that $\mathcal{L} = \mathcal{L}_1 + \mathcal{L}_2$, a second-order approximation for the time evolution operator reads:[6]

$$U(t) = \mathrm{e}^{t\mathcal{L}} \approx \mathrm{e}^{t\mathcal{L}_1/2}\ \mathrm{e}^{t\mathcal{L}_2}\ \mathrm{e}^{t\mathcal{L}_1/2}\,. \tag{6.15}$$

The error induced by this approximation is less than $\mathcal{O}(\Delta t^3)$ for any time step Δt [170].

More information on the decomposition of the matrix $\mathcal{L}$ and on the properties of $\mathcal{L}_1$ and $\mathcal{L}_2$ can be found in De Raedt [170] Chap. 18.4.

6.3 TDME3D Software

The simulation studies presented in Part IV were performed with the software *TDME3D*™ [178, 179], a massively parallel three-dimensional FDTD Maxwell Solver developed by Kristel Michielsen (Forschungszentrum Jülich GmbH, Germany) and Hans De Raedt (University of Groningen, the Netherlands), Copyright *EMBD* (European Marketing and Business Development BVBA).

The software solves Maxwell's equations for arbitrary-shaped objects that are illuminated by arbitrary incident plane waves and that consist of linear, isotropic[7], lossy materials with known permeability, permittivity, and conductivity. For this purpose, a combined algorithmic approach is used: For materials for which the light propagation is described by Eqs. (6.8) and (6.9) (in this study free space), Yee's algorithm (Sec. 6.1) is employed to compute (6.10). To compute the interaction of the light with the polarization of the material (in this study brain tissue), an unconditionally stable product formula approach (Sec. 6.2) is used. This results in a computationally efficient but conditionally stable algorithm (independent of the material parameters) to study the light propagation in brain tissue samples.

As solving Maxwell's equations for large three-dimensional objects is very complex and demanding on computing power (the Yee mesh needs to be sufficiently fine to resolve the geometric structure), the simulations were performed on *JUQUEEN* [2], a supercomputer at the Forschungszentrum Jülich GmbH, Germany, which provides a massively parallel computing architecture.

In the following, the input parameters and the output of the simulation tool are described.

Simulation Input It is possible to define various input parameters. Here, only the parameters that are relevant for the presented simulation studies are explained.

[5] If, for example, $\mathcal{L} = \mathcal{L}_1 + \mathcal{L}_2$ with $\mathcal{L}_1$ and $\mathcal{L}_2$ being skew-symmetric, the product formula approach will be unconditionally stable: $\left(\mathrm{e}^{t\mathcal{L}_1/m}\ \mathrm{e}^{t\mathcal{L}_2/m}\right)^{\mathrm{T}} = \left(\mathrm{e}^{t\mathcal{L}_1/m}\ \mathrm{e}^{t\mathcal{L}_2/m}\right)^{-1}$.

[6] $\mathrm{e}^{t\mathcal{L}_1/2}\ \mathrm{e}^{t\mathcal{L}_2}\ \mathrm{e}^{t\mathcal{L}_1/2} \overset{(6.13)}{=} \left(1 + \frac{t}{2}\mathcal{L}_1 + \frac{t^2}{2}\frac{\mathcal{L}_1^2}{4} + ...\right)\left(1 + t\mathcal{L}_2 + \frac{t^2}{2}\mathcal{L}_2^2 + ...\right)\left(1 + \frac{t}{2}\mathcal{L}_1 + \frac{t^2}{2}\frac{\mathcal{L}_1^2}{4} + ...\right)$
$= 1 + t(\mathcal{L}_1 + \mathcal{L}_2) + \frac{t^2}{2}\left(\mathcal{L}_1^2 + \mathcal{L}_2^2 + \mathcal{L}_1\mathcal{L}_2 + \mathcal{L}_2\mathcal{L}_1\right) + ... \overset{(6.13)}{\approx} \mathrm{e}^{t\mathcal{L}}$

[7] The optical properties of a material are defined by a (complex) refractive index that is independent of the polarization of the incident light, i. e. it is not feasible to model molecular birefringence or diattenuation of nerve fibers. Nevertheless, the simulation software is a valuable tool to study birefringence and diattenuation caused by the inner and outer fiber structure.

- **Light source:** The sample is continuously illuminated by a plane wave with a certain wavelength λ and direction of propagation (φ, θ). The light is coherent and completely polarized (linear/circular polarization).

- **Sample:** The geometry of the sample can be defined by various built-in functions (e. g. grid of cylinders/helices). It is possible to simulate dielectrics or metals (described by the *Drude*, *Debye*, or *Lorentz model*); the materials are specified by a (complex) refractive index. Furthermore, the user can specify the size of the simulation box (including absorbing boundaries) and the position of the detection planes before and behind the sample at which the reflected and transmitted light intensities are measured. The simulation volume should be chosen large enough to avoid boundary effects.

- **Discretization of space and time:** The spatial discretization of the simulation volume is determined by the *Yee mesh size* Δ. The mesh size should be sufficiently small to resolve all geometric structures and much smaller than the wavelength of the light ($\Delta \ll \lambda$). For light in the visible spectrum ($\lambda = 390$–$700\,\mathrm{nm}$), the mesh size should be $\Delta \leq 25\,\mathrm{nm}$. The temporal resolution of the simulation, the *time step* Δt, is determined by the Courant factor (Eq. (6.6)). A smaller value of the Courant factor increases the accuracy, but also leads to a longer computing time. A reasonable choice is $C = 0.8$. The duration of the simulation run is determined by the *number of periods*. One period is defined as the wavelength divided by the phase velocity of the electromagnetic wave. The number of periods that is needed to reach a stationary solution depends on the z-dimension of the simulation volume and on the characteristics of the sample.

- **Boundary conditions:** In order to reduce computing time, the simulation volume should be as small as possible, i. e. it should not be much larger than the structure to be simulated. The finite size of the simulation volume requires a proper choice of the boundary conditions in order to reduce artifacts. The simulation tool allows the implementation of two different types of boundary conditions:

  Periodic boundary conditions (PBC) imply that an object leaving the simulation volume on one side re-enters the simulation volume on the other side. PBC can be applied if the fiber configuration is periodic or translational invariant in the x/y-direction (i. e. in the plane perpendicular to the incident light); the use of PBC in the z-direction is not possible. In order to obtain an accurate solution, the periodic structure should not be too small.

  Uniaxial perfectly matched layer absorbing boundary conditions (UPML) are used in case PBC cannot be employed. The boundaries absorb light in order to suppress numerical reflections of outgoing waves, which would otherwise contribute to the transmittance or reflectance spectra. However, some of the light is always reflected back into the simulation volume (the amount of reflected light depends on the parameters of the UPML and on the angle under which the light impinges on the boundaries). As the algorithm computes the electromagnetic field in the whole simulation box, the scattering geometry should also be defined within the UPML regions. The cut-off-region for plane waves at the borders of the simulation volume is six times the reference wavelength.

  For the simulation studies in Part IV, UPML boundaries were used because they enable to model more complex, non-symmetric structures.

Simulation Output With the given input parameters, the Maxwell Solver simulates the evolution of the electromagnetic field within the given sample and thus allows the investigation of absorption and scattering of the electromagnetic wave. The reflected and transmitted light waves (i. e. the electromagnetic field measured at the detection planes in front of the sample and behind the sample) are given as a superposition of plane monochromatic waves $\vec{E}_k$ with different wave vectors $\vec{k}$ and amplitudes $\vec{E}_{0,k}$ (cf. real part of Eq. (2.13)), defined by a set of real vectors $\{\vec{A}_k, \vec{B}_k, \vec{k}\}$:

$$\vec{E}_k(\vec{r},t) = \vec{E}_{0,k}\,\cos(\vec{k}\cdot\vec{r}-\omega t+\phi) \tag{6.16}$$

$$= \underbrace{\vec{E}_{0,k}\,\cos\phi}_{\vec{A}_k}\,\cos(\vec{k}\cdot\vec{r}-\omega t) - \underbrace{\vec{E}_{0,k}\,\sin\phi}_{\vec{B}_k}\,\sin(\vec{k}\cdot\vec{r}-\omega t). \tag{6.17}$$

Note that every index k denotes a different wave vector $\vec{k}$ and is not related to the wave number $k = 2\pi/\lambda$ (the wavelength of the transmitted light waves is the same as for the ingoing light wave when the sample is surrounded by air).

6.4 Generation of Fiber Architectures

To study the polarimetric measurements of the brain sections with FDTD simulations, the spatial nerve fiber architecture of the brain tissue needs to be modeled.

The software TDME3D provides several built-in functions to generate various artificial fiber bundles, e. g. grids of helical tubes. The geometry of the grid is defined by grid vectors, enabling to generate, for example, hexagonal grids of fibers with different inter-fiber distances (cf. Sec. 10.2.1). The helix radius and the separation of the helix's loops can be defined by the user. To model more inhomogeneous fiber configurations, several sub-grids with different grid and helix parameters can be defined.

The nerve fiber architecture, however, is much more complex. Fibers are diversely distributed within bundles and typically do not follow simple geometric functions. Being converted to an image series of gray values, any three-dimensional fiber architecture can be used as input for TDME3D. To generate more realistic fiber bundles, Felix Matuschke (INM-1, Forschungszentrum Jülich, Germany) developed two algorithms that grow fibers without overlap and which are described in the following.

6.4.1 Fiber Growing Algorithm (FGA)

The *Fiber Growing Algorithm (FGA)* generates densely packed fiber bundles with small variations of fiber orientations. It consists of several steps:

1. A given number of circles (N fibers) with a user-defined distribution of radii r_n are randomly uniformly distributed in the xy-plane. Every circle is initialized with a random "speed" (maximum displacement of 0.1 µm per step) and a random direction in the xy-plane (see Fig. 6.2a).

2. The circles move with the given "speed" in the given direction. When two circles collide, the "speed" and direction of the circles change (assuming elastic collisions with particle mass r^2) until a solution is reached without overlapping circles in the xy-plane (see Fig. 6.2b).

3. To ensure well-distributed fibers, the last step is repeated 250 times before the circle positions are stored (see Fig. 6.2c). To grow the fibers in the z-direction, the

positions of the circle midpoints (x_n, y_n) are stored for the next i time steps with $z_i = i\,\Delta z$ ($\Delta z = 1\,\mu\text{m}$). The resulting list of coordinates ($x_{n,i}$, $y_{n,i}$, $z_{n,i}$) and the fiber radii r_n characterize the architecture of the generated fiber bundle in 3D (see Fig. 6.2d).

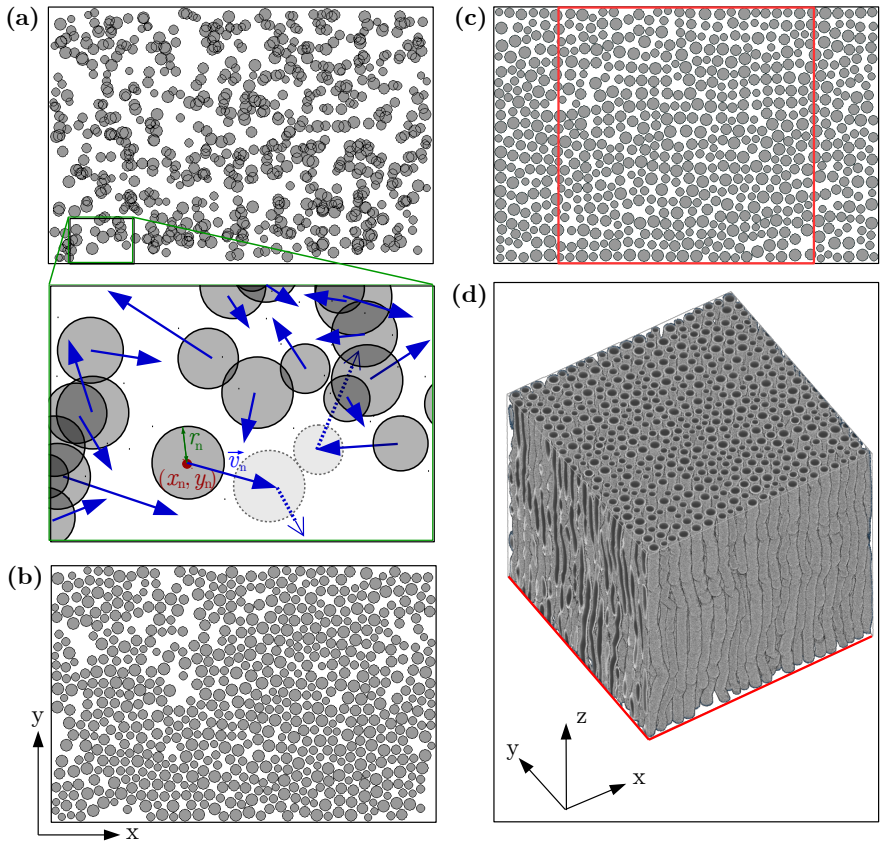

Fig. 6.2: Illustration of the Fiber Growing Algorithm: **(a)** A number of circles ($N = 700$) with a user-defined distribution of radii (uniform distribution with $r_n \in [0.5, 0.8]\,\mu\text{m}$) are randomly uniformly distributed in the xy-plane (in an area of $45 \times 30\,\mu\text{m}^2$). Every circle is initialized with a random speed $\vec{v}_n$; the circles collide assuming elastic collision (see circles with dashed lines). **(b)** The circles move around until a solution is reached without overlapping circles in the xy-plane. **(c)** The previous step is repeated 250 times until the position of the circles is stored. **(d)** To generate a 3D fiber volume ($30 \times 30 \times 30\,\mu\text{m}^3$), the position of the circles in the xy-plane (red square) is stored while incrementing the z-position by 1 µm per step.

The algorithm has several drawbacks: The cross-sections of the fibers in the xy-plane are always circular and there exists no collision control in 3D (between the z-steps). Therefore, the algorithm cannot be used to generate inhomogeneous fiber bundles with various fiber orientations or crossings.

6.4.2 Volume Colliding Solver (VCS)

The *Volume Colliding Solver (VCS)* is a more advanced algorithm that allows collision control in 3D (similar to [180, 181]). The algorithm takes an initial list of fiber midpoints and radii as input (e. g. randomly uniformly distributed fibers, generated by the Fiber Growing Algorithm), varies the fiber midpoints randomly, and changes the fiber course until no collisions are detected. The algorithm consists of several steps:

1. From the initial list of fiber midpoints ($x_{n,i}$, $y_{n,i}$, $z_{n,i}$) and radii (r_n), a first set of fibers (series of cylindrical fiber segments) is generated. The fiber segments are divided iteratively until the length of each segment is between 2–5 µm.

2. To each resulting fiber coordinate, a random displacement in x, y, z is added. The maximum displacement Ξ defines the degree of inhomogeneity of the resulting fiber bundle and can be specified by the user.

3. The resulting fiber segments are split or merged until the length of each segment is again between 2–5 µm.

4. To avoid sharp angles within fibers, the fiber coordinates are slightly changed such that the angle between adjacent fiber elements is less than 20°.

5. When the smallest distance between two fiber segments is smaller than the sum of their radii (detected collision, see Fig. 6.3 in red), every fiber coordinate is exposed to a small repelling force directed away from the other segment to avoid collision. A drag force between the segments ensures that the segments do not move too far apart from each other. The maximum fiber displacement per step is 0.1 µm.

6. The last three steps are repeated until no more collisions (i. e. overlapping fiber segments) are detected (cf. Fig. 6.3c).

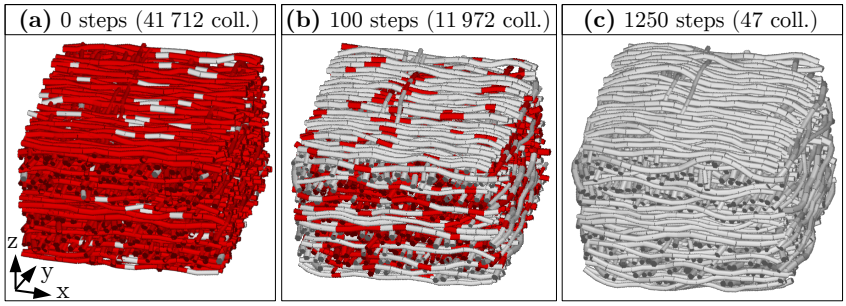

Fig. 6.3: Illustration of the Volume Colliding Solver for two perpendicularly crossing, interwoven fiber bundles (700 straight fibers generated by the FGA as in Fig. 6.2c, oriented alternately in the x- and y-direction): The fibers were divided into segments of 2–5 µm. The resulting fiber coordinates were assigned a random displacement (max. $\Xi = 1$ µm), ensuring that the maximum angle between adjacent segments was less than 20°. When a collision (overlap) between two segments was detected (in red), the segments were moved further apart and the previous step was repeated until no more collisions were detected. The figure shows the resulting fiber configuration and the number of detected collisions after 0, 100, and 1250 steps.

Part III

EXPERIMENTAL STUDIES

Chapter 7

Characterization of the Optical Systems

Before studying the transmittance and diattenuation of brain tissue (see Chaps. 8 and 9), the optical systems used for the polarimetric measurements were characterized: the Polarizing Microscope (PM) and the Large-Area Polarimeter (LAP) (cf. Sec. 4.2).

First, the general properties of the respective light sources and imaging systems were investigated for both optical systems (Sec. 7.1). Then, the properties of the polarizing filters in the LAP were studied (Sec. 7.2).

7.1 General Properties of the Optical Systems

The general properties of the polarimeters (setup, wavelength, pixel size) have already been described in Sec. 4.2. In this section, the properties of the employed light sources and imaging systems (objective lens, detector, optical resolution) are characterized in more detail. For reasons of clarity, only properties needed to analyze and model the experimental observations are described. Further information about the optical systems of PM and LAP (manufacturer information and exact specification of the optical elements) can be found in Appx. B.1.

7.1.1 Light Source

As described in Sec. 4.2, the sample is illuminated by green light generated by a light emitting diode (LED) which emits diffuse and mostly incoherent light (cf. Sec. 2.1.3.2). In the following, the wavelength spectra of the light sources and the illumination angles are specified for the PM and the LAP.

Wavelength spectrum The wavelength spectra of the light sources (see Fig. 7.1) were measured with a spectrometer (*CAS140CT*) from *Instrument systems*.[1] The measurements were performed for a duration of 30 minutes and wavelengths between 299 nm and 1100 nm in steps of 1 second and 0.8 nm [53].

- **PM:** The green light is generated by a single white LED combined with a bandpass filter. The wavelength spectrum has a peak wavelength at $\hat{\lambda} \approx 550\,\text{nm}$ and a full width at half maximum (FWHM) of about 9 nm (see Fig. 7.1a). Assuming a

[1] The measurements were performed by Christoph Zahren (Institute of Energy and Climate Research, Forschungszentrum Jülich, Germany) and evaluated by Julia Reckfort (Institute of Neuroscience and Medicine, Forschungszentrum Jülich, Germany) [53].

Gaussian frequency spectrum and using Eq. (2.15) with $\Delta\lambda = 9\,\text{nm}$, the coherence length is: $L_c \approx 22.33\,\mu\text{m}$.

- **LAP:** The light is generated by a panel of green LEDs. The wavelength spectrum ($\hat{\lambda} \approx 529\,\text{nm}$, FWHM $\approx 34\,\text{nm}$, see Fig. 7.1b) is much broader than for the PM, resulting in a smaller coherence length: $L_c \approx 5.47\,\mu\text{m}$ (computed from Eq. (2.15) with $\Delta\lambda = 34\,\text{nm}$).

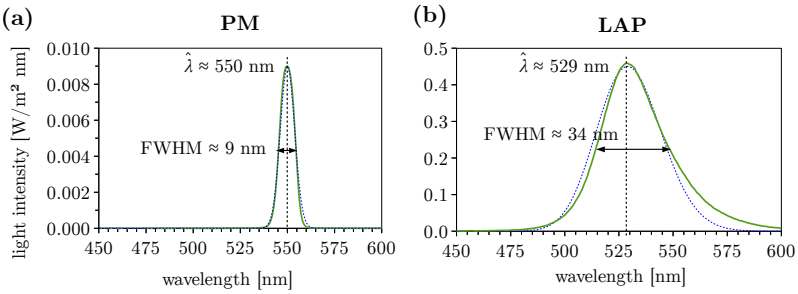

Fig. 7.1: The green curves show the wavelength spectra of the light sources (a) in the PM and (b) in the LAP (Adapted from Reckfort [53]). The blue dotted curves show the wavelength spectra resulting from a Gaussian fit to the corresponding frequency spectrum, using [74] Eq. (6) with $\lambda_0 \equiv \hat{\lambda}$ and $\Delta\lambda \equiv$ FWHM.

Illumination angles To ensure a homogeneous illumination, the sample is illuminated under different angles. The maximum angle of incidence $\theta_{\max}$ can be determined from the schematic figures shown in Fig. 7.2.

- **PM:** A Köhler illumination is used to generate a homogeneous illumination of the sample by defocussing the image of the LED light source in the object (and image) plane [55] (see Fig. 7.2a). The diameter of the light beam directly behind the Köhler illumination (and the polarizer) is about 6 mm. The distance to the sample is about 6 cm. Thus, the center of the sample is illuminated under angles smaller than: $\theta_{\max} = \arctan(3\,\text{mm}/6\,\text{cm}) \approx 2.86°$.
- **LAP:** A diffuser plate is placed behind the LED panel (see Fig. 7.2b) to generate a more uniform illumination. Figure 7.2b illustrates the positions of the optical elements in the LAP. The distance between sample and light source (LED panel with diffuser plate) is about: $(5 + 5 + 7 + 16)\,\text{cm} = 33\,\text{cm}$. The width of the LED panel is about 31 cm. Thus, the center of the sample is illuminated under angles smaller than: $\theta_{\max} = \arctan\big(15.5\,\text{cm}/33\,\text{cm}\big) \approx 25.16°$. The refraction of light at plane surfaces (e. g. polarizing filters) has been neglected in these calculations.

7.1.2 Objective Lens

Objective lenses focus the light rays to produce a real image and can be characterized by magnification and numerical aperture (Eq. (2.18)). They determine the optical resolution of the imaging system.

- **PM:** The microscope objective (*Nikon TL Plan Fluor EPI P 5x*) has a 5× magnification and a numerical aperture NA ≈ 0.15.

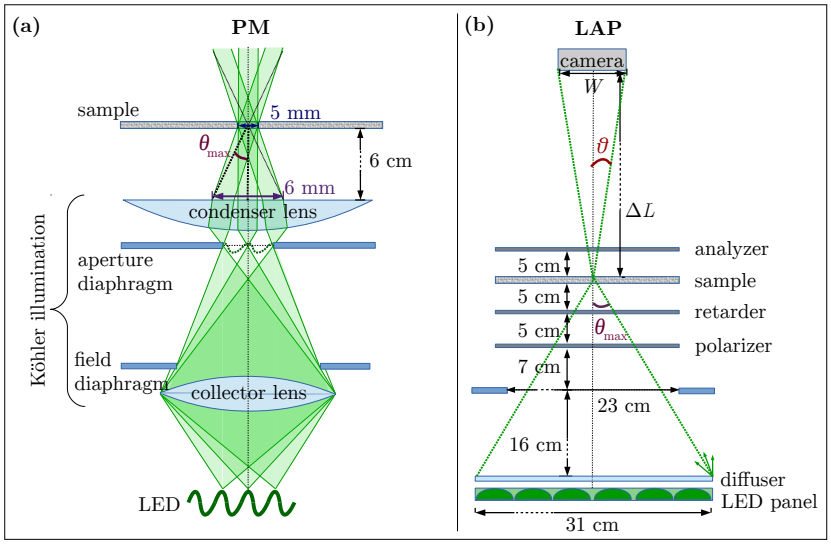

Fig. 7.2: Schematic figures (not to scale) illustrating the homogeneous illumination of the sample: **(a)** In the PM, a Köhler illumination is used to generate a homogeneous illumination of the sample. For reasons of simplification, the rotating bandpass filter and the polarizer in front of the sample (cf. Fig. B.1) are not included in the figure. **(b)** In the LAP, a diffuser plate is placed behind the LED panel to generate a homogeneous illumination of the sample. The homogeneous illumination in the PM and the LAP implies that the sample is illuminated under different angles. The maximum angle of incidence (with respect to the center of the sample) is denoted by θ_{max}, respectively. The refraction of light on plane surfaces (e. g. polarizing filters) has been neglected in the figures.

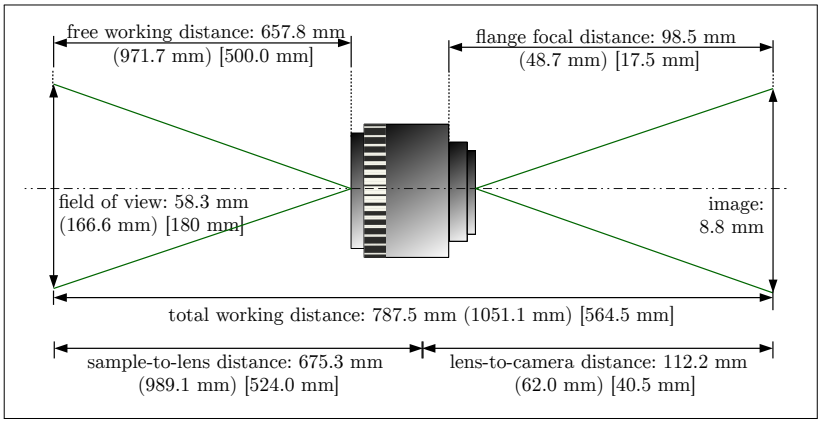

Fig. 7.3: Camera objective of the LAP (schematic system drawing, not to scale). The numbers have been computed with *MachVis 5.0.6* (lens calculator for *Qioptiq Machine Vision* lenses) by specifying the field of view and selecting a 2/3 inch sensor, a C-mount adapter, and modular focus. The numbers without brackets refer to the camera objective with higher resolution (*Apo-Rodagon-N90*), the numbers in brackets refer to the camera objectives with lower resolution (round brackets: *Apo-Rodagon-N50*; square brackets: *Lametar 2.8/25*). The *flange focal distance* refers to the distance from the mounting flange of the camera to the sensor plane.

- **LAP:** Three different camera objectives are used which enable different fields of view and different resolutions. For smaller samples (rat brains), the camera objective with the smallest field of view is used: *Apo-Rodagon-N90* (focal length: $f = 90.1\,\text{mm}$). For larger samples (vervet or human brains), the camera objectives with larger fields of view are used: *Apo-Rodagon-N50* ($f = 50.2\,\text{mm}$) and *Lametar 2.8/25* ($f = 25.0\,\text{mm}$). The *focal ratios* of the objectives, i. e. the ratio of the *focal length* f to the diameter W of the entrance pupil, were chosen to be the same for all objectives:

$$F = \frac{f}{W} = 8. \tag{7.1}$$

The effective numerical aperture of the camera objectives can be computed from the diameter of the entrance pupil $W = f/8$ and the sample-to-lens distance ΔL (cf. Fig. 7.2b):

$$\text{NA} = n \sin\vartheta = \sin\left(\arctan\left(\frac{W/2}{\Delta L}\right)\right) \overset{(7.1)}{=} \sin\left(\arctan\left(\frac{f}{16\,\Delta L}\right)\right), \tag{7.2}$$

using $n = 1$ (refractive index of vacuum). The sample-to-lens distance is the difference between the total working distance and the lens-to-camera distance (cf. Fig. 7.3). The total working distance and the lens-to-camera distance were computed from the respective fields of view using *MachVis 5.0.6*, a lens calculator for *Qioptiq Machine Vision* lenses (selecting a 2/3 inch sensor, a C-mount adapter, and modular focus), see Fig. 7.3. The resulting sample-to-lens distances (ΔL) were used to compute the numerical aperture (NA) of the camera objectives from Eq. (7.2). The results are summarized in Tab. 7.1.

	Apo-Rodagon-N90	Apo-Rodagon-N50	Lametar 2.8/25
focal length (f)	90.1 mm	50.2 mm	25.0 mm
field of view	58.3 mm	166.6 mm	180.0 mm
total working dist.	787.5 mm	564.5 mm	1051.1 mm
lens-to-camera dist.	112.2 mm	40.5 mm	62.0 mm
sample-to-lens dist. (ΔL)	675.3 mm	524.0 mm	989.1 mm
numerical aperture (NA)	0.0083	0.0032	0.0030
pixel size (2776×2080 px)	21 µm	60 µm	64 µm

Tab. 7.1: Properties of the camera objectives used for the LAP measurements (cf. Fig. 7.3)

7.1.3 Detector

The transmitted light intensities in the PM and LAP are recorded by a camera. The pixel size of the employed image sensor determines – together with the given field of view – the pixel size in object space that can be achieved by the imaging system.

- **PM:** The transmitted light intensity is detected by a monochrome *RETIGA-4000R* camera by *QImaging* which contains a *Kodak KAI-04022-ABA* image sensor (see Fig. 7.4a). The sensor consists of an interline transfer progressive scan CCD with 2048×2048 active pixels (see Fig. 7.4a). The active image size is $15.15 \times 15.15\,\text{mm}^2$. The light is collected by an array of spherical microlenses which focus the light onto subjacent photodiodes (see Fig. 7.4b). The effective pixel size in object space is about 1.33 µm.

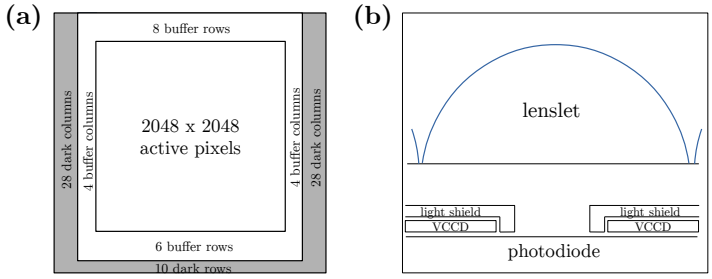

Fig. 7.4: CCD image sensor of the PM (Kodak KAI-04022-ABA): **(a)** device architecture (2048 × 2048 active pixels), **(b)** pixel architecture (square pixels with spherical microlens). The figures were drawn according to the data sheet from August 2015, Rev. 2, provided by *Semiconductor Components Industries, LLC.*[1]

- **LAP:** The transmitted light intensity is recorded by a different CCD camera (*AxioCam HRc* by *Carl Zeiss AG*). The size of the sensor is $8.9 \times 6.7\,\mathrm{mm}^2$ with a pixel size of 6.45 µm. The pixel architecture is not specified by the manufacturer. By moving the sensor along the vertical and horizontal axes (*microscanning*), the CCD basic resolution (1388×1040 pixels) can be increased up to 4164×3120 pixels. For standard 3D-PLI measurements, 2776×2080 pixels are used. Depending on the type and adjustment of the camera objective, this yields an effective pixel size in object space of about 21 µm, 60 µm, or 64 µm (cf. Tab. 7.1).

7.1.4 Optical Resolution

To characterize the optical resolution of the imaging systems, a *USAF-1951 resolution target* (military standard *MIL-STD-150A*) was measured[2] with the PM and the LAP, and the image contrast was determined for different spatial frequencies, i. e. different line widths (cf. Fig. 7.5).

USAF Resolution Target The target measured with the PM is a negative, high-resolution USAF-1951 target (R5000091235-13345) manufactured by *Edmund Optics GmbH*. The target measured with the LAP is a negative, low-resolution USAF-1951 target (R3L3S1N) manufactured by *Thorlabs GmbH*.

The USAF targets consist of a 1.5 mm thick soda-lime glass plate covered by a chromium layer of about 100 nm thickness which contains groups of equidistant lines. Each element within one group contains three horizontal and three vertical lines with a particular width l and spacing l (see Fig. 7.5a). The line width is related to the group number (G) and the element number (E) via:

$$l\,[\mathrm{mm}] = 2^{-\left(G+1+\frac{E-1}{6}\right)}. \tag{7.3}$$

The resulting line widths for group numbers 3 and 4 (low-resolution target) and group numbers 7 and 8 (high-resolution target) are listed in Tab. 7.2.

[1] `www.onsemi.com/pub/Collateral/KAI-04022-D.PDF` (Status: 01.03.2018)

[2] The measurements were performed by Julia Reckfort and David Gräßel (INM-1, Forschungszentrum Jülich, Germany).

Element	Group 3	4	...	7	8
1	62.50	**31.25**		3.91	**1.95**
2	55.68	**27.84**		3.48	**1.74**
3	49.61	**24.80**		3.10	1.55
4	44.19	22.10		2.76	1.38
5	39.37	19.69		**2.46**	1.23
6	**35.08**	17.54		**2.19**	1.10

Tab. 7.2: Width l (in µm) of one line in the USAF resolution target for different group numbers and elements. The line widths that were evaluated for the LAP (group numbers 3 and 4) and for the PM (group numbers 7 and 8) are highlighted in boldface. Line widths for which the three lines within one element cannot be distinguished are marked in red.

Measurement and Evaluation To compute the image contrast for different line widths, a 3D-PLI measurement (see Sec. 4.4.1) was performed on the USAF targets. From the transmittance images (cf. Figs. 7.5a,b), the horizontal and vertical line profiles were evaluated for different line widths. For each group of three lines, a centered region was selected (see yellow rectangles in Fig. 7.5b) and the intensity values were averaged along the axis perpendicular to the lines. The image contrast was computed from the average of the local minima ($\overline{I_{\min}}$) and the average of the local maxima ($\overline{I_{\max}}$) of the resulting line profile (see Fig. 7.5c) via:

$$\mathcal{C} = \frac{\overline{I_{\max}} - \overline{I_{\min}}}{\overline{I_{\max}} + \overline{I_{\min}}}. \tag{7.4}$$

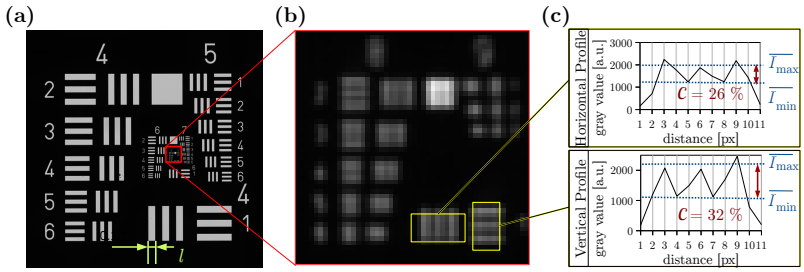

Fig. 7.5: USAF resolution target measured with the PM: **(a,b)** transmittance image, **(c)** horizontal and vertical line profiles evaluated for a line width $l = 1.95\,\mu\text{m}$ (group 8, element 1). The contrast $\mathcal{C}$ of the lines was computed by averaging the local minima ($\overline{I_{\min}}$) and the local maxima ($\overline{I_{\max}}$) of the intensity profile, and using Eq. (7.4).

Different positions of the USAF target on the specimen stage yield different line profiles because the camera position – and thus the position of the sensor pixels – changes with respect to the specimen stage. To determine the image contrast independently of the target position, the USAF chart was placed at 25 different positions on the specimen stage and the horizontal and vertical line profiles were evaluated for each of the 25 measurements. For the measurement with the LAP, the USAF resolution target was displaced by hand along the x- and y-axes of the specimen stage, using a ruler to align the borders of the target with the x- and y-axes. For the measurement with the PM, the USAF target was fixed and scanned in 5×5 tiles.

As the FDTD simulations described in Part IV were only performed for the smallest possible pixel size of the LAP (px = 21 µm), the LAP measurements were only performed for the objective lens with the highest possible resolution (Apo-Rodagon-N90).

For all measurements, it was ensured that the evaluated line profiles show three distinct peaks. For smaller line widths, some line profiles do not show a middle peak due to the small number of pixels per line. Line widths for which the three lines within one element could not be distinguished in all 25 measurements are marked in red in Tab. 7.2.

Beyond this resolution limit, four subsequent line widths were chosen for further evaluation (and later comparison with FDTD simulations, see Sec. 10.1.3). The line widths that were evaluated for the PM (group numbers 7 and 8) and for the LAP (group numbers 3 and 4) are highlighted in boldface in Tab. 7.2.

Results The contrast values of all evaluated line profiles (25 horizontal and 25 vertical profiles for 4 different line widths for PM and LAP) are displayed as histograms in Appx. B.2. The line profiles belonging to the median contrast values are shown in Fig. 7.6a. Figure 7.6b summarizes the median, minimum and maximum contrast values for all evaluated line widths. Note that the median (and not the average) values are shown to reduce the impact of possible outliers. Although horizontal and vertical line profiles yield different contrast values for some line widths (see Fig. B.2), they were both taken into account when computing the median contrast values to enable a comparison with the FDTD simulations in Sec. 10.1.3. (When modeling the optical resolution of the imaging systems, the lateral resolution was assumed to be the same in the horizontal and vertical direction.)

(a)

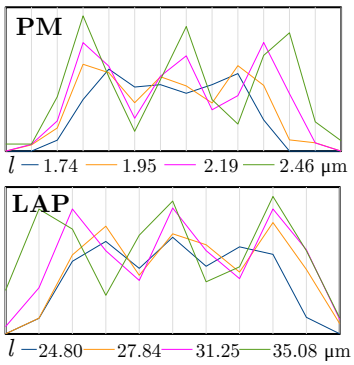

(b)

l [µm]	$\tilde{\mathcal{C}}$ [%]	$\mathcal{C}_{\min}$ [%]	$\mathcal{C}_{\max}$ [%]
1.74	10.5	9.1	15.9
1.95	26.1	22.4	33.2
2.19	47.6	42.9	54.3
2.46	68.7	61.6	71.5
24.80	16.1	12.7	18.9
27.84	27.8	20.7	31.9
31.25	39.5	33.3	43.8
35.08	48.8	46.0	54.9

Fig. 7.6: Horizontal and vertical line profiles evaluated from 25 measurements of a USAF resolution target with the PM and the LAP (with Apo-Rodagon-N90 objective) for different line widths l: **(a)** Line profiles belonging to the median contrast values $\tilde{\mathcal{C}}$. **(b)** Median, minimum and maximum contrast values of all evaluated line profiles (horizontal and vertical).

As expected, the contrast values decrease with decreasing line width. According to the Rayleigh criterion (see Sec. 2.1.3.3), the optical resolution limit is reached when the contrast between two lines becomes less than 15.3 % (cf. Fig. 2.2).[3] This criterion is fulfilled when the distance $2l$ between two lines becomes less than $\Delta d_{\mathrm{c}} \approx 0.82\,\lambda/\mathrm{NA}$ or $\Delta d_{\mathrm{ic}} \approx 0.61\,\lambda/\mathrm{NA}$ (see Eq. (2.17)).

[3] This model only considers the diffraction due to the circular aperture of the objective lens and does not take the diffraction of the grating and the finite line width into account as in Appx. D.7.

Due to the limited number of detector pixels, the contrast values of the measured line profiles are much less than the contrast values of analytically computed diffraction patterns. Instead of defining the resolution limit in terms of contrast, it is therefore assumed that the optical resolution limit is reached for line widths that show less than three peaks (see Tab. 7.2 in red). For the PM, this limit is reached for $l = 1.55\,\mu\text{m}$, which corresponds approximately to the optical resolution limit for coherent illumination ($l = \Delta d_\text{c}/2 \approx 0.41 \cdot 550\,\text{nm}/0.15 \approx 1.5\,\mu\text{m}$). For the LAP, this limit is reached for $l = 19.69\,\mu\text{m}$, which corresponds approximately to the optical resolution limit for incoherent illumination ($l = \Delta d_\text{ic}/2 \approx 0.305 \cdot 529\,\text{nm}/0.0083 \approx 19.4\,\mu\text{m}$). This is expected because the coherence length of the PM is much larger than the dimensions of the lines ($L_\text{c} \approx 22.33\,\mu\text{m} > 5\,l$), while the coherence length of the LAP is much smaller ($L_\text{c} \approx 5.47\,\mu\text{m} \ll l$), cf. Sec. 7.1.1.

7.1.5 Overview

Table 7.3 summarizes the general properties of the PM and the LAP that have been determined in the previous sections. For the LAP, the properties are only listed for the objective lens with the highest possible resolution (Apo-Rodagon-N90), which has been used for the FDTD simulations in Part IV.

	PM	LAP
wavelength spectrum	$\hat{\lambda} \approx 550\,\text{nm}$ FWHM $\approx 9\,\text{nm}$ $L_\text{c} \approx 22.33\,\mu\text{m}$	$\hat{\lambda} \approx 529\,\text{nm}$ FWHM $\approx 34\,\text{nm}$ $L_\text{c} \approx 5.47\,\mu\text{m}$
max. angle of incidence	$\theta_\text{max} \approx 2.86°$	$\theta_\text{max} \approx 25.16°$
numerical aperture	NA ≈ 0.15	NA ≈ 0.0083
detector	px $\approx 1.33\,\mu\text{m}$ (microlenses)	px $\approx 21\,\mu\text{m}$
optical resolution limit	$l = 1.55\,\mu\text{m}$	$l = 19.69\,\mu\text{m}$

Tab. 7.3: General properties of the PM and the LAP (with Apo-Rodagon-N90 objective): wavelength spectrum of the employed light source (peak wavelength $\hat{\lambda}$, full width at half maximum (FWHM), coherence length L_c), maximum angle of incidence θ_max relative to the surface normal of the specimen stage, numerical aperture (NA) of the objective lens, pixel size in object space (px), and maximum width of lines l that can no longer be distinguished by the imaging system

7.2 Filter Properties of the Large-Area Polarimeter

In the following, the properties of the polarizing filters in the LAP are described in more detail (polarization-independent inhomogeneities in Sec. 7.2.1, polarization properties in Sec. 7.2.2). More general filter properties and manufacturer information for the LAP can be found in Appx. B.1.2.

As the optical components of the PM cannot be measured individually, the characterization of the filter properties is only possible for the LAP. In any case, the filters in the PM are much smaller than in the LAP and therefore expected to be of better quality.

The subsequent sections have previously been published in Menzel *et al.* (2017) [3] Appx. A.

7.2.1 Polarization-Independent Inhomogeneities

One source for polarization-independent inhomogeneities in the LAP is a non-uniform illumination of the light source. Filter inhomogeneities introduced in the fabrication process can also cause inhomogeneities due to a non-uniform absorption of the light. In addition, the sensitivity of the CCD camera chip might not be exactly the same for all detector pixels.

The polarization-independent inhomogeneities of the LAP were investigated in separate measurements[4] of the light source and the filters (polarizer, retarder, analyzer), see Appx. B.3.1. The resulting images (averaged transmitted light intensities) and the corresponding histograms are shown in Fig. 7.7. Dust particles have been excluded from the analysis.

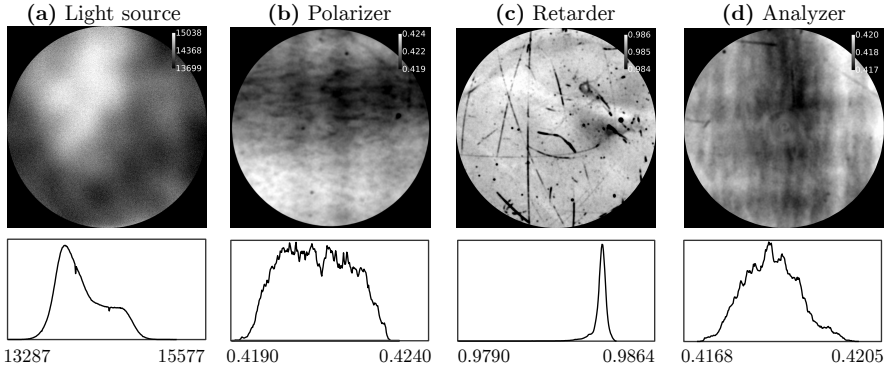

Fig. 7.7: Images and histograms of light source, polarizer, retarder, and analyzer. Note that the contrasts between images differ (the maximum measurable intensity values are depicted in white, the minimum values in black, respectively). The figure has been published in Menzel *et al.* (2017) [3] Fig. 12.

The light source (Fig. 7.7a) shows regions with varying light intensity. The maximum measurable image contrast (Eq. (7.4)) is about 8 %. The polarizer and analyzer (Fig. 7.7b,d) show patterns of large horizontal and vertical stripes, which are most likely caused by the stretching of the polymer foils during the fabrication process. The maximum measurable image contrast is about 0.59 % for the polarizer and about 0.44 % for the analyzer. The average transmittances of polarizer and analyzer ($\tau = (I_{\max} + I_{\min})/2$) are about 42 % ($\tau_x \approx 0.422$, $\tau_y \approx 0.419$). The quarter-wave retarder (Fig. 7.7c) shows several scratches, but is still quite homogeneous. The maximum measurable image contrast is about 0.38 % and the average transmittance about 98 % ($\tau_\Lambda \approx 0.983$).

The measurements have shown that the inhomogeneous illumination of the light source (8 % image contrast) is much more dominant than the polarization-independent inhomogeneities of the filters (0.4–0.6 % image contrast). In 3D-PLI and DI measurements, this can be compensated by performing an image calibration as described in Sec. 4.3. However, the image calibration can only correct for multiplicative errors in the measured light intensity (i. e. inhomogeneous illumination, absorption, detection sensitivity, etc.). Differences between presumed and actual polarization states (e. g. induced by a partially polarized light source, non-ideal polarization filters, or a polarization-sensitive camera as described in Sec. 7.2.2) are not taken into account.

[4]The measurements were performed by Julia Reckfort and Hasan Köse (INM-1, Forschungszentrum Jülich, Germany).

7.2.2 Polarization Properties

Apart from polarization-independent inhomogeneities, the polarization properties of the optical components in the LAP are expected to be non-ideal: The light emitted by the LED light source might not be completely unpolarized and the sensitivity of the camera might depend on the polarization of the incoming light. Furthermore, the degree of polarization of polarizer and analyzer (D_x and D_y) is expected to be less then 100 %. Previous studies have also shown that the working wavelength of the employed quarter-wave retarder is not optimally adapted to the illumination wavelength of the LED light source which induces a phase retardation γ that is not exactly equal to $\pi/2$ [152].

To estimate the partial polarization of the light source, the polarization sensitivity of the camera, and the non-ideal polarization properties of the filters, the polarization properties of the optical elements were fitted to the intensity curves obtained in various filter measurements (see Appx. B.3.2). As the polarization effects are non-multiplicative and influence each other, the polarization properties could only be determined as an average over the field of view.

The study was executed in two steps: First, the polarization properties were measured[5] with different filter setups. Second, the polarization parameters were estimated by fitting numerically computed light intensity profiles (obtained from modeling light source, camera, and filters as generalized Stokes vectors and Müller matrices) to the measured light intensity profiles by minimizing the sum of squared differences.

The Stokes parameters (Eq. (2.55)) of light source $\{p_\mathrm{L}, \psi_\mathrm{L}, \chi_\mathrm{L}\}$ and camera $\{p_\mathrm{c}, \psi_\mathrm{c}, \chi_\mathrm{c}\}$ were fitted for $D_\mathrm{x}, D_\mathrm{y} = \{0.9,\, 0.905,\, 0.91,\, \ldots,\, 1\}$ and $\gamma = \{0.4\,\pi, 0.405\,\pi, 0.41\,\pi, \ldots, 0.6\,\pi\}$. The parameter ranges were chosen such that the whole range of possible values is enclosed. The parameters D_x, D_y, and γ were not used as fit parameters to reduce computing time and to ensure a proper convergence of the algorithm.

The sum of squared differences (Eq. (B.2)) was found to be minimized for (see Tab. B.2 in Appx. B.3.2):

$$D_\mathrm{x} = 0.98, \quad D_\mathrm{y} = 0.97, \quad \gamma = 0.49\,\pi. \tag{7.5}$$

Thus, the employed linear polarizers have a similar degree of polarization which is slightly less than 100 %. The retardance of the quarter-wave retarder is slightly less than $\pi/2$ (probably due to the wavelength discrepancy between light source and retarder [152]).

Inserting the best fit parameters for $\{p_\mathrm{L}, \psi_\mathrm{L}, \chi_\mathrm{L}\}$ and $\{p_\mathrm{c}, \psi_\mathrm{c}, \chi_\mathrm{c}\}$ (see Tab. B.2) into Eq. (2.55) yields the following Stokes vectors for light source and camera (with $I = 1$):

$$\vec{S}_\mathrm{L} \approx \begin{pmatrix} 1 \\ -5 \times 10^{-3} \\ 8 \times 10^{-4} \\ -5 \times 10^{-7} \end{pmatrix}, \qquad \vec{S}_\mathrm{c} \approx \begin{pmatrix} 1 \\ 8 \times 10^{-3} \\ -1 \times 10^{-3} \\ -5 \times 10^{-4} \end{pmatrix}. \tag{7.6}$$

Hence, about 0.5 % of the ingoing light is vertically linearly polarized $\big(\arctan(S_{\mathrm{L},2}/S_{\mathrm{L},1})/2 \approx 86^\circ\big)$; the bigger part of the light is unpolarized. The camera has a small preference for horizontally linearly and left-handed circularly polarized light (0.8 % linear polarization oriented at 6° and 0.05 % left-handed circular polarization).

[5] The measurements were performed by Julia Reckfort and Hasan Köse (INM-1, Forschungszentrum Jülich, Germany).

Chapter 8

Transmittance of Inclined Nerve Fibers

The polarization-independent transmitted light intensity obtained in a 3D-PLI measurement (*transmittance*) shows how much the light is attenuated when propagating through the brain tissue. Especially for the PM, which has no tiltable specimen stage, the transmittance image is used to correct the measured birefringence signals for local variations in the fiber density (*transmittance weighting*, see Sec. 4.4.1).

3D-PLI measurements and anatomical studies suggest that the transmittance of brain sections depends not only on the tissue composition and fiber density, but also on the polarization of light (diattenuation, see Chap. 9) and on the out-of-plane inclination angle of the enclosed nerve fibers: regions with fibers oriented perpendicularly to the section plane show lower transmittance values than regions with horizontally oriented fibers, i. e. fibers lying within the section plane. The fiber inclination dependence of the transmittance influences the transmittance weighting, but also provides additional information about the fiber inclination and can help to improve the fiber reconstruction with 3D-PLI. Therefore, this effect is worth to be studied in more detail.

This chapter presents different experimental studies that investigate the inclination dependence of the transmittance: First, the transmittance was evaluated for flat and steep fiber configurations in brains cut along different anatomical planes (Sec. 8.1). To study the transmittance across several consecutive brain sections, the transmittance images were registered onto each other (Sec. 8.2). Finally, to quantitatively study the transmittance for different fiber inclinations, the inclination of fiber bundles was determined from TPFM measurements and compared to the transmittance values measured with 3D-PLI (Sec. 8.3). Parts of Secs. 8.1 to 8.3 have been published in Menzel *et al.* (2018a) [67].

The studies were performed on healthy brains obtained from different species: rat (*Wistar*, male, three months old), vervet monkey (African green monkey: *Chlorocebus aethiops sabaeus*, male, between one and two years old), and mouse (*C57BL/6*, male, six months old). All brains were obtained in accordance with legal and ethical requirements and prepared as described in Sec. 4.1. A 3D-PLI measurement with the PM was performed[1] on the histological brain sections (of about 60 µm thickness) and the normalized transmittance images ($I_{\mathrm{T,N}}$) were computed as described in Secs. 4.2, 4.3 and 4.4.1.

8.1 Transmittance of Flat and Steep Fiber Configurations

One possibility to study the transmittance of flat and steep fiber configurations is to compare brains that were cut along different anatomical planes (coronal, sagittal, and horizontal plane, cf. Fig. 4.1a).

[1] The 3D-PLI measurements were performed by David Gräßel and Isabelle Mafoppa Fomat and processed by Philipp Schlömer (INM-1, Forschungszentrum Jülich, Germany).

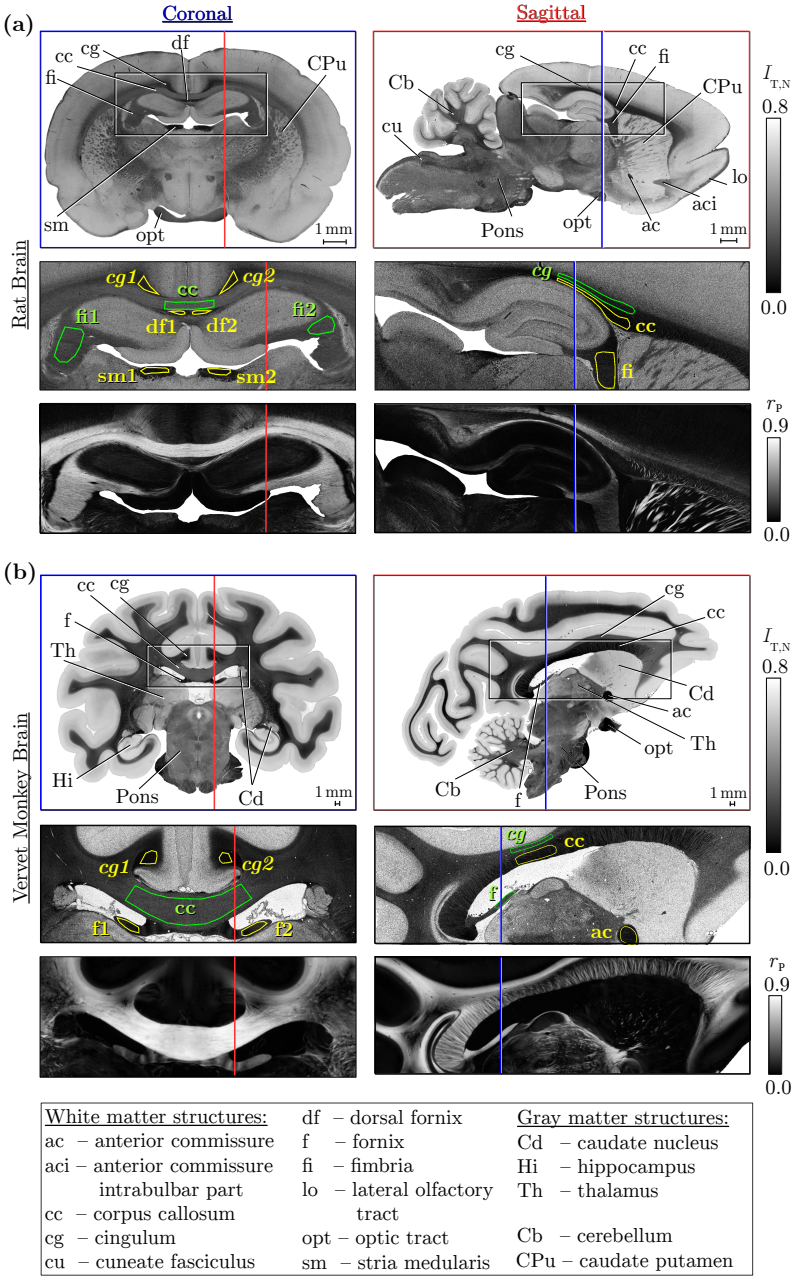

White matter structures:				Gray matter structures:	
ac	– anterior commissure	df	– dorsal fornix	Cd	– caudate nucleus
aci	– anterior commissure intrabulbar part	f	– fimbria	Hi	– hippocampus
		fi	– fimbria	Th	– thalamus
cc	– corpus callosum	lo	– lateral olfactory tract		
cg	– cingulum	opt	– optic tract	Cb	– cerebellum
cu	– cuneate fasciculus	sm	– stria medularis	CPu	– caudate putamen

Fig. 8.1: Coronal and sagittal sections through a rat brain (a) and a vervet monkey brain (b): The upper two rows show the normalized transmittance images ($I_{T,N}$), the third row shows the retardation images (r_P) obtained from 3D-PLI measurements with the PM. The images in the second and third row show an enlarged view of the region surrounded by a rectangle. The selected regions in yellow (green) belong to regions with steep (flat) fibers, which appear dark (bright) in the transmittance and retardation images. White and gray matter structures are labeled for reference. The figure has been published in Menzel *et al.* (2018a) [67] Fig. 1.

Figure 8.1 shows a rat brain (a) and a vervet monkey brain (b) cut along the coronal and the sagittal plane. The coronal (sagittal) section planes are indicated by blue (red) lines in the respective other brain section for reference. Selected white and gray matter structures are labeled according to rat [182–184] and vervet [47, 185, 186] brain atlases.

The transmittance images ($I_{T,N}$) were evaluated in white matter regions that have a relatively homogeneous tissue composition and predominantly contain *flat* fibers (fiber inclination $\alpha < 45°$, see areas surrounded in green) or *steep* fibers (fiber inclination $\alpha > 45°$, see areas surrounded in yellow). The approximate orientation of the fibers is known from the anatomy of the rat and the vervet brain as described in the atlases, and is confirmed by the retardation images ($|\sin\delta|$) shown below the transmittance images: regions with flat fibers (green) show larger retardation values than regions with steep fibers (yellow). In ambiguous cases like the *cingulum (cg)*, the underlying fiber architecture was determined from additional TPFM measurements of the brain section. As the sagittal plane is oriented perpendicularly to the coronal plane, the transmittance of a certain brain region can be evaluated for flat fibers in one section plane and for steep fibers in the other section plane.

Table 8.1 shows the averaged[2] transmittance values and the standard deviation for the evaluated green and yellow regions in Fig. 8.1. Regions belonging to the same fiber structure were evaluated together (e. g. df ≡ df1 ∪ df2). For better comparison, the values belonging to regions with flat (steep) fibers are surrounded by green (yellow) frames.

	Rat		Vervet	
Structure	Coronal	Sagittal	Coronal	Sagittal
ac	–	–	–	0.11 ± 0.04
cc	0.33 ± 0.16	0.09 ± 0.04	0.24 ± 0.09	0.11 ± 0.05
cg	*0.15 ± 0.06*	*0.18 ± 0.09*	*0.08 ± 0.02*	*0.24 ± 0.09*
df	0.10 ± 0.03	–	–	–
f	–	–	0.13 ± 0.06	0.26 ± 0.10
fi	0.25 ± 0.10	0.15 ± 0.07	–	–
sm	0.08 ± 0.03	–	–	–

Tab. 8.1: Mean transmittance values ($\overline{I_{T,N}}$) and standard deviation for the selected white matter regions in Fig. 8.1. For better comparison, the values are surrounded by frames in the same color. Regions with flat fibers (green) show larger transmittance values than regions with steep fibers (yellow). The fiber architecture in the cingulum (cg) might be inhomogeneous so that a distinction between flat and steep fibers is not straightforward. Therefore, the corresponding transmittance values are highlighted in italics. A similar table has been published in Menzel *et al.* (2018a) [67] Tab. 1.

In regions with flat fibers, the overall transmittance values are larger (green: $0.18 \leq \overline{I_{T,N}} \leq 0.33$) than in regions with steep fibers (yellow: $0.08 \leq \overline{I_{T,N}} \leq 0.15$). Two regions with flat and steep fibers which show large and small transmittance values in one section plane (coronal or sagittal), respectively, show the opposite behavior in the corresponding perpendicular section plane. Rat and vervet brains show a similar behavior. The difference is especially large when comparing the transmittance values in the corpus callosum (cc) and in the cingulum (cg): In the coronal brain sections, the transmittance values in

[2] In this thesis, the term *"averaged transmittance"* is used to describe the average over all evaluated pixel values in the transmittance image, and should not be confused with the *average transmittance* τ defined in Eq. (2.40).

the cingulum are about 55–67 % less than in the corpus callosum. In the sagittal brain sections, the transmittance values in the corpus callosum are about 50–54 % less than in the cingulum.

Figure 8.2a shows the transmittance images of a coronal, horizontal, and sagittal rat brain section. The enlarged views show the *caudate putamen (CPu)* – a region containing several nerve fiber bundles (*striatum fibers*) with different orientations.

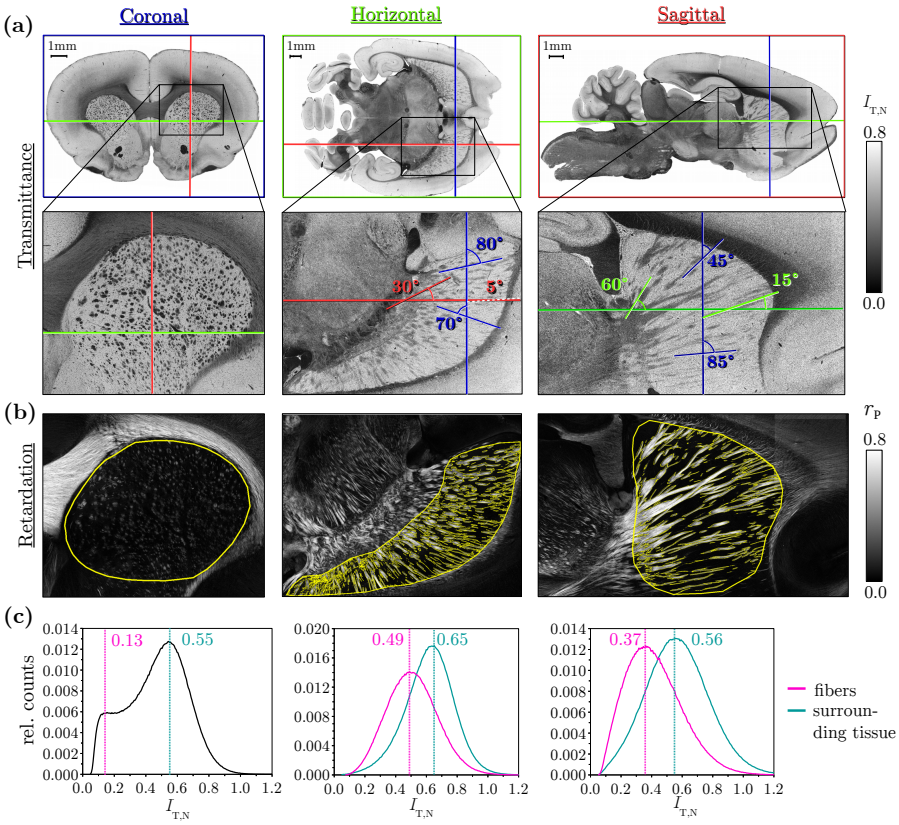

Fig. 8.2: (a) Normalized transmittance images of a coronal, horizontal, and sagittal rat brain section obtained from a 3D-PLI measurement with the PM. The colored lines indicate the section planes. The enlarged views show the region of the caudate putamen and the maximum and minimum angles under which the striatum fibers are oriented with respect to the section planes. **(b)** Retardation images of the enlarged views. The image contrast was used to select regions with fibers and with surrounding tissue in the caudate putamen (yellow). **(c)** Histograms of the transmittance values ($I_{T,N}$) for the selected fiber regions (pink) and the surrounding tissue (cyan) in the caudate putamen. For the coronal brain section, the retardation image cannot be used to separate the fibers from the surrounding tissue because the fibers are oriented almost perpendicularly to the image plane which leads to a small retardation signal and a small image contrast. Therefore, the histogram was computed over the whole selected region and the peak with lower (larger) transmittance was assumed to belong to fibers (surrounding tissue). The figure has been published in Menzel *et al.* (2018a) [67] Fig. 9.

The maximum and minimum inclination angles of the fibers within one section plane can be estimated from the orientation of the fibers in the other two section planes: while the coronal brain section (blue) contains mostly steep fibers with respect to the section plane ($45° \leq \alpha \leq 85°$), the horizontal (green) and sagittal (red) sections contain mostly flat fibers ($15° \leq \alpha \leq 60°$ and $5° \leq \alpha \leq 30°$, respectively). Note that the given angles for each section plane are only estimates obtained from the other two section planes and do not necessarily apply to all striatum fibers in the displayed brain sections.

Although all brain sections were prepared and measured according to the same protocol, the embedding of the tissue might not be exactly the same (e. g. the thickness of the embedding glycerin film might be different), which would cause differences in the measured absolute transmittance values. In addition, the brain sections were obtained from different brains so that the tissue properties might also be different. Therefore, a direct comparison between the transmittance values obtained from different brain sections is not possible. To still enable a comparison between the transmittance values of flat and steep fibers, the transmittance of the fibers was compared to the transmittance of the surrounding tissue for each brain section, assuming that the transmittance in the surrounding tissue (gray matter) does not show a strong inclination dependence.

To separate the striatum fibers from the surrounding tissue, the image contrast of the retardation images (Fig. 8.2b) was used (see yellow lines). Figure 8.2c shows the corresponding histograms of the transmittance evaluated in the regions with fibers (pink) and with surrounding tissue (cyan). For the coronal brain section which contains mostly steep fibers, the contrast in the retardation image is not large enough to separate the fibers from the surrounding tissue. The histogram was therefore computed for the whole caudate putamen (area surrounded by yellow line) and the peak with lower (larger) transmittance was assumed to belong to fibers (surrounding tissue).

The histograms show that the contrast (cf. Eq. (7.4)) between the peak transmittance values of surrounding tissue and flat fibers (horizontal and sagittal brain sections: $\mathcal{C} \approx 14$–$20\,\%$) is much lower than the contrast between the peak transmittance values of surrounding tissue and steep fibers (coronal brain section: $\mathcal{C} \approx 62\,\%$). Thus, the transmittance values of steep fibers are lower than the transmittance values of flat fibers.

However, the observed differences in the transmittance might not only be caused by the fiber inclination, but also by structural differences and tissue composition, e. g. a higher fiber density for steep fibers. To study the inclination dependence of the transmittance quantitatively, the exact underlying fiber architecture of the investigated brain section needs to be known (see Sec. 8.3).

8.2 3D-Reconstruction of Transmittance Images

So far, single brain sections from different specimens were compared to each other. A 3D-reconstructed volume of the right hemisphere of a vervet brain (occipital lobe) was used to study the transmittance across several consecutive brain sections. The volume consists of 234 coronal sections that were measured with 3D-PLI and registered onto each other[3] using in-house developed software tools based on the software packages *ITK*, *elastix*, and *ANTs* [156–160] which perform linear and non-linear transformations (see Sec. 4.3).

Figure 8.3 shows the 3D-reconstructed transmittance images along the coronal, horizontal, and sagittal plane (a-c) and a detail of the 3D-volume (d). The brain was cut

[3]The measurements were performed in the laboratory of the Institute of Neuroscience and Medicine (INM-1) at Forschungszentrum Jülich GmbH, Germany. The registration of the brain sections was performed by Martin Schober, Marcel Huysegoms, and Sascha Münzing.

along the coronal plane (xy-plane), the brain sections were registered onto each other from posterior to anterior (in the positive z-direction). The white arrows point to the *sagittal stratum* – a white matter structure that runs mostly perpendicularly to the image plane (along the z-direction), as can be seen in the horizontal and sagittal planes. The fiber structure appears darker than the background, as expected.

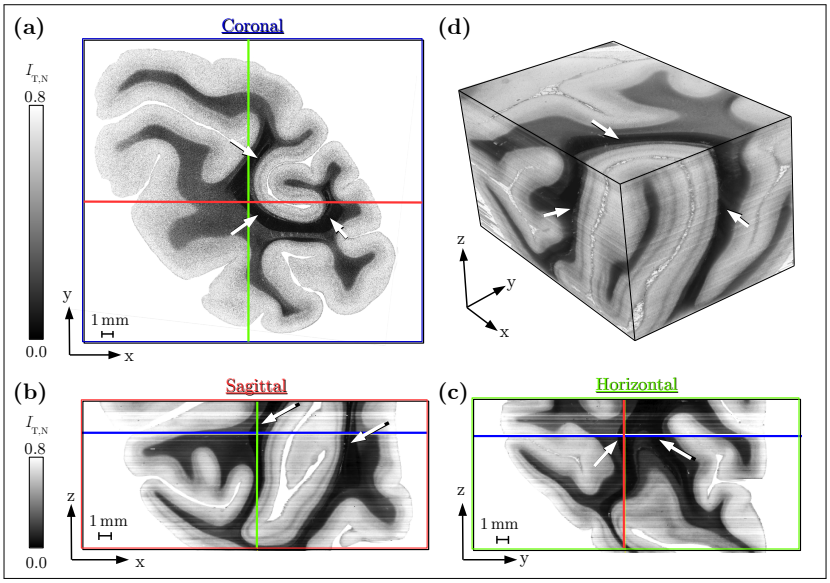

Fig. 8.3: 3D-reconstructed normalized transmittance images ($I_{T,N}$) of the right hemisphere of a vervet brain (234 consecutive brain sections from the occipital lobe) obtained from 3D-PLI measurements with the PM. The brain was cut along the coronal plane (xy-plane), the resulting brain sections were registered onto each other from posterior to anterior (in the positive z-direction). **(a-c)** 3D-volume shown along the coronal (xy), sagittal (xz), and horizontal (yz) plane. The colored lines indicate the position of the displayed xy-, xz-, and yz-planes. **(d)** Detail of the 3D-volume. The white arrows point to the sagittal stratum – a white matter structure with fibers that are mostly oriented perpendicularly to the image plane (along the z-direction) and which appears dark in the transmittance images. The figure has been published in Menzel *et al.* (2018a) [67] Fig. 2.

8.3 Transmittance vs. Fiber Inclination in TPFM Images

The studies presented in Secs. 8.1 and 8.2 show that the transmittance values in regions with vertical or steep fibers are lower than the transmittance values in regions with horizontal or flat fibers. However, the studies are only qualitative and do not take the exact tissue composition into account. To quantify how the transmittance depends on the fiber inclination, the same brain section was measured with 3D-PLI and with TPFM (as described in Chap. 5) to identify the underlying tissue structure.

The 3D-PLI measurement[4] was performed on a coronal section from the left hemisphere of a mouse brain (Fig. 8.4a shows the resulting fiber orientation map).

[4]The 3D-PLI measurement was performed in the laboratory of the Institute of Neuroscience and Medicine (INM-1) at Forschungszentrum Jülich, Germany.

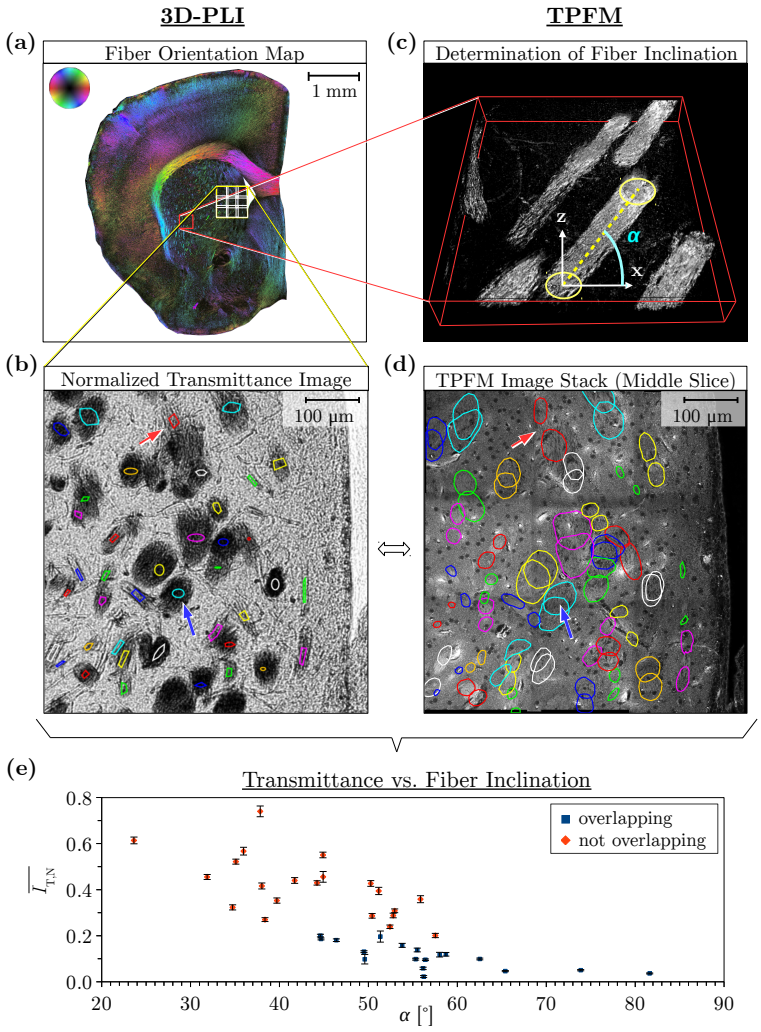

Fig. 8.4: Transmittance vs. fiber inclination: A coronal section from the left hemisphere of a mouse brain was measured both with 3D-PLI and with TPFM. The 3D-PLI measurement was performed with the PM as described in Chap. 4, the TPFM measurements were performed as described in Chap. 5 for a region of 3×3 tiles in the caudate putamen without washing out the glycerin: **(a)** fiber orientation map of the coronal mouse brain section, **(b)** normalized transmittance image of the selected region in the caudate putamen, **(c)** single tile of a contrast-enhanced TPFM image stack demonstrating the determination of the fiber inclination angle α, **(d)** middle slice of the TPFM image stack for the selected region in the caudate putamen, **(e)** averaged normalized transmittance values ($\overline{I_{T,N}}$) plotted against the determined fiber inclination angles α. The inclination angles of 40 fiber bundles were determined from the mid point positions of the cross-sections in the first and the last slice of the TPFM image stack (see colored shapes in Fig. d), the transmittance values were evaluated in the middle of the corresponding fiber bundles (see colored shapes in Fig. b). The blue (red) data points in the scatter plot belong to overlapping (not overlapping) regions that are (are not) completely filled with nerve fibers, see blue (red) arrows in Figs. b,d. The error bars indicate the standard error of the mean for the evaluated transmittance values. A similar figure has been published in Menzel *et al.* (2018a) [67] Fig. 10.

The TPFM measurements[5] were performed for a region of 3×3 tiles in the caudate putamen which contains relatively steep fiber bundles with different fiber inclination angles (see yellow square in Fig. 8.4a). To enhance the contrast of the myelinated axons, the glycerin solution is usually washed out before performing the TPFM measurement (see Sec. 5.1). However, the removal of the cover slip and the washing process might introduce tissue deformations which makes it difficult to directly compare the fiber architectures obtained from both measurements and influences the determined fiber inclinations. For this reason, the TPFM measurements were performed without washing out the glycerin and the fiber bundles were distinguished by hand from the surrounding tissue by means of the different tissue structure. The resulting TPFM image stacks were stitched together as described in Sec. 5.3 (Fig. 8.4d shows the middle slice).

To determine the inclination angle of the fibers, the cross-sections of the fiber bundles were determined in the first and the last slice of the TPFM image stack (see colored shapes in Fig. 8.4d). For each fiber bundle, the inclination angle α was computed from the mid points (xy-coordinates) of the corresponding cross-sections and from the thickness of the brain section in the z-direction (given by the number of slices in the TPFM image stack), cf. Fig. 8.4c. The corresponding transmittance values were evaluated in the middle of the fiber bundles (see colored shapes in Fig. 8.4b).

The fiber inclination and transmittance values were evaluated for 40 fiber bundles in the caudate putamen. The scatter plot in Fig. 8.4e shows the averaged transmittance values plotted against the determined fiber inclination angles. The values in blue belong to fiber bundles for which the cross-section of the bundle in the first and the last image of the image stack overlap, i. e. regions that can be considered to be completely filled with nerve fibers (see blue arrows in Fig. 8.4b,d). The values in red belong to fiber bundles without overlap, i. e. regions that are not completely filled with nerve fibers (see red arrows in Fig. 8.4b,d). As myelin has a large scattering coefficient, the attenuation of light increases with increasing fiber density, which leads to larger transmittance values for fiber bundles without overlap.

Although the values are broadly distributed, the scatter plot shows a clear tendency towards a decrease in transmittance with increasing fiber inclination, also in regions with similar myelin density (values in blue): while the transmittance values for flat fibers ($\alpha < 50°$) reach larger values ($0.1 < \overline{I_{\mathrm{T,N}}} < 0.2$), the transmittance values for steep fibers ($\alpha > 60°$) are small ($\overline{I_{\mathrm{T,N}}} < 0.05$).

8.4 Discussion

In this chapter, various experimental studies have been presented that evaluate how the transmittance of brain sections depends on the out-of-plane inclination angle α of the enclosed nerve fibers. To investigate the inclination dependence independently from the tissue composition and preparation, the studies were performed on various species, subjects, and brain sections. The studies show that the transmittance decreases significantly (by more than 50 %) with increasing fiber inclination.

To investigate the transmittance of flat fibers ($\alpha < 45°$) in comparison to steep fibers ($\alpha > 45°$), the transmittance values were evaluated in mutually orthogonal anatomical planes (see Sec. 8.1). This procedure has the advantage that the same structure (in different brains) can be studied for horizontal and vertical fiber orientations and that it is also possible to study larger structures (e. g. the corpus callosum) which fill the

[5] The TPFM measurements were performed by Irene Costantini in the European Laboratory for Non-Linear Spectroscopy (LENS) at the University of Florence, Italy.

whole section thickness. The study of brain structures along different anatomical planes clearly shows that flat fibers show larger transmittance values than steep fibers (the transmittance of steep and flat fibers in one anatomical plane shows the opposite behavior in the orthogonal plane). However, even when using TPFM measurements, the exact orientation of the fibers within the bulk tissue cannot be reliably determined. In addition, it is only possible to compare transmittance values within one brain section because different brain sections from different specimens might not be comparable due to different tissue structures and embedding.

As both scattering and absorption can contribute to the attenuation (transmittance) of light, differences in the transmittance values might not only be caused by different fiber inclinations, but also by a different tissue composition or density.

Myelin staining shows that regions like the cingulum (cg) or the stria medularis (sm) are less myelinated than the corpus callosum (cc) [53, 182]. Nevertheless, these regions show lower transmittance values in the coronal section plane than the corpus callosum (see Fig. 8.1a). This demonstrates that the differences in the transmittance values are rather caused by the orientation of the nerve fibers and not by tissue absorption.

The studies presented in Secs. 8.1 and 8.2 are only qualitative. To quantitatively study the inclination dependence of the transmittance, the fiber inclination angles and the tissue composition need to be known. The fiber inclination angle derived in a 3D-PLI analysis might be influenced by other factors such as the fiber density. Therefore, TPFM measurements were performed to determine the underlying tissue structure and the inclination angles of the fibers (see Sec. 8.3). However, the determination of the inclination angles is only reliable for distinct fiber bundles with similar tissue structures. As flat fiber bundles might not fill the whole section thickness, the transmittance values might be larger due to a lower myelin density. The inclination dependence of the transmittance can therefore only be studied for steep fiber bundles. In addition, the TPFM measurements and the determination of the fiber inclinations by hand are very time consuming, which makes it difficult to evaluate a large number of fiber bundles.

All studies have shown that the transmittance decreases with increasing fiber inclination. Steep fibers show much lower transmittance values (more than 50 % less) than flat fibers. The inclination dependence of the transmittance should therefore be considered in the transmittance weighting. However, to quantitatively describe the relationship between transmittance and fiber inclination, further studies are needed to obtain proper statistics.

As the transmittance does not depend on the polarization of light, the inclination dependence of the transmittance is also interesting for other imaging techniques which use unpolarized light.

To find an explanation for the observed effects and to model the inclination dependence of the transmittance, FDTD simulations were performed (see Chap. 11). The simulations account for scattering and (isotropic) absorption of light and can therefore be used to study the attenuation (transmittance) of light.

The anisotropic attenuation of light (diattenuation) will be studied in Chaps. 9 and 12.

Chapter 9

Diattenuation of Brain Tissue

Although there exist several studies that investigate the diattenuation of biological tissue [59–65, 86, 133–141] (see Sec. 3.2.4), the diattenuation of brain tissue and nerve fibers has not been addressed before.[1]

Diattenuation leads to polarization-dependent attenuation of light (see Sec. 2.4) and might therefore influence the birefringence values determined in a polarimetric measurement. The error induced by diattenuation has been investigated in various studies [58, 135, 137]. For the 3D-PLI measurement, the question arises to what extent the diattenuation of brain tissue influences the outcome of the polarimetric measurement and what the consequences are to the interpretation of the measured signal and the resulting nerve fiber orientations.

In other studies, diattenuation has been used to quantify tissue properties (e. g. thickness [59], concentration of glucose [60, 61]) and to distinguish between healthy and pathological tissue (cancerous tissue [62], burned/injured tissue [63, 64], tissue from eye diseases [59, 65]). Hence, diattenuation might also provide interesting structural information about the brain tissue and *Diattenuation Imaging (DI)* could be a useful extension to 3D-PLI.

In this chapter, various studies are presented that investigate the diattenuation of brain tissue, its impact on the measured 3D-PLI signal, and whether the diattenuation signal can be used to obtain additional information about the brain tissue structure.

For this purpose, brain sections of different species (mouse, rat, vervet, human) were prepared, measured, and analyzed as described in Chap. 4. To relate the measured diattenuation signal to the measured birefringence signal, 3D-PLI and XP measurements were performed in addition to the DI measurements. The XP measurements were used as a reference for 3D-PLI to study the impact of diattenuation on the derived fiber orientations. All measurements were performed with the LAP because it enables a combined measurement of 3D-PLI, XP, and DI without removing the brain section (cf. Fig. 4.4a-c). To account for the different numbers of employed filters, a different exposure time was chosen for each type of measurement. The images were recorded with the microscanning procedure of the camera sensor (see Sec. 7.1.3) yielding 4164×3120 pixels. As the signal-to-noise ratio of the XP (DI) measurement is lower than for the 3D-PLI measurement (cf. Fig. 4.8), the image of the brain section was recorded 10 (20) times for each filter position and averaged. After calibrating the images (see Sec. 4.3), a Fourier analysis was performed on the resulting image series and the parameter maps (transmittance $I_{\mathrm{T,P}}$, direction angles $\{\varphi_{\mathrm{P}}, \varphi_{\mathrm{X}}, \varphi_{\mathrm{D}}\}$, retardation r_{P}, and diattenuation $|\mathscr{D}|$) were computed from the Fourier coefficients as described in Secs. 4.4.1 to 4.4.3.

[1] A study about the diattenuation of brain tissue and its impact on 3D-PLI has been published in Menzel *et al.* (2017) [3].

To enable a pixel-wise comparison between the parameter maps, the Fourier coefficients of order zero $\{a_{0\mathrm{P}}, a_{0\mathrm{X}}, a_{0\mathrm{D}}\}$ were used to register the images of the 3D-PLI and XP measurements onto the images of the DI measurement (see Sec. 4.3).

To estimate the impact of diattenuation on the polarimetric measurements, a numerical study (Sec. 9.1) was performed prior to the experimental studies. The determined error estimates were then taken into account in the experimental studies to quantify the diattenuation of brain tissue and its impact on 3D-PLI: First, the diattenuation was investigated for various freshly embedded brain sections from different species (Sec. 9.2). To study how the diattenuation values change with increasing embedding time of the samples, some brain sections were measured multiple times over several weeks (Sec. 9.3).

Section 9.1 and parts of Secs. 9.2 and 9.4 have been published in Menzel *et al.* (2017) [3] Secs. 4 to 6. Parts of Secs. 9.2.2, 9.2.3 and 9.3 have been published in Menzel *et al.* (2018b) [68].

9.1 Impact of Diattenuation on the Polarimetric Measurements

The characterization of the filter properties in Sec. 7.2 has shown that the optical components of the LAP are not ideal: the light source emits slightly linearly polarized light, the camera is slightly sensitive to linearly and left-handed circularly polarized light, the retardance of the quarter-wave retarder does not perfectly match the illumination wavelength, and polarizer and analyzer have a degree of polarization of less than 100 %. As the diattenuation of brain tissue is expected to be small (see Sec. 3.2.4), the measured diattenuation signal might be influenced by these non-ideal polarization properties.

To predict the impact of the tissue diattenuation and the non-ideal polarization properties of the LAP on the reconstructed fiber orientations and the measured diattenuation, a numerical study was performed. By combining the analytical model from Sec. 4.4 and the polarization properties of the LAP defined in Eqs. (7.5) and (7.6), the errors on the measured fiber orientation and diattenuation were estimated for the 3D-PLI, XP, and DI measurements, using the formulas in Secs. 4.4.1 to 4.4.3 and assuming arbitrary fiber orientations and tissue diattenuations.

The numerical study has been published in Menzel *et al.* (2017) [3] Sec. 4. The complete results and more detailed information about the performed computations can be found in Appx. C.2.

Figure 9.1 shows the maximum predicted difference between the fiber direction angles $\{\varphi_{\mathrm{P}}, \varphi_{\mathrm{X}}, \varphi_{\mathrm{D}}\}$ obtained from 3D-PLI, XP, and DI measurements and the actual fiber direction φ plotted against the tissue diattenuation $D \geq 0$ for different fiber inclination angles α. For $D < 0$, the curves in Fig. 9.1a-c are rotated 180° around the origin, the curves in Fig. 9.1c obtain an additional shift by +90° along the y-axis. As the diattenuation values obtained from the LAP measurements in Secs. 9.2 and 9.3 are less than 5 %, the curves are only shown for $D \leq 0.05$.

When interpreting the numerical results for steep fibers ($\alpha > 60°$), it should be kept in mind that large deviations of the measured direction angle have only a small influence on the overall fiber orientation vector and that the diattenuation is expected to be small. For vertical fibers, the diattenuation approaches zero; the curves for $\alpha = 90°$ are only displayed as limiting cases.

The numerical study shows that the direction angle φ_{X} derived from the XP measurement is nearly independent from the diattenuation of brain tissue and from the polarization properties of the LAP. The angle deviates only slightly from the actual fiber direction φ for all tissue diattenuations and inclination angles $< 90°$. For $|D| \leq 5\,\%$,

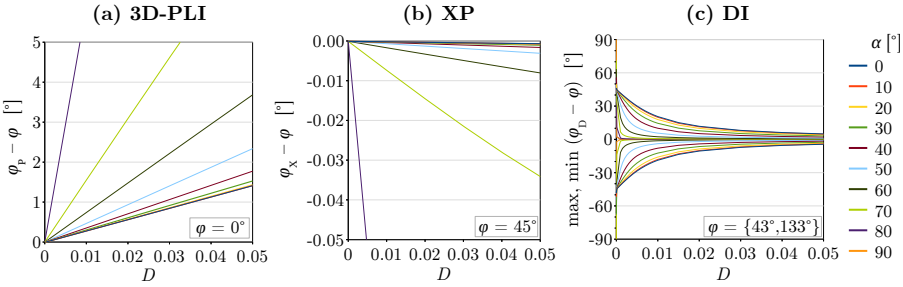

Fig. 9.1: Predicted impact of the non-ideal polarization properties of the LAP (Eqs. (7.5) and (7.6)) on the fiber direction angles $\{\varphi_P, \varphi_X, \varphi_D\}$ obtained from 3D-PLI, XP, and DI measurements (see Secs. 4.4.1 to 4.4.3). The maximum difference between $\{\varphi_P, \varphi_X, \varphi_D\}$ and the actual fiber direction angle φ is plotted against the tissue diattenuation $D \geq 0$ for different fiber inclinations α: (a) As the curves for different φ look identical, the curves are only shown for an assumed fiber direction $\varphi = 0°$. (b) The curves are shown for $\varphi = 45°$ for which $|\varphi_X - \varphi|$ becomes maximal. (c) The curves are shown for $\varphi = 43°$ (133°) for which the difference between φ_D and φ becomes maximal (minimal). For $D < 0$, the curves are rotated 180° around the origin, the curves in Fig. c obtain an additional shift by +90° along the y-axis. The figures are adapted from Menzel *et al.* (2017) [3] Figs. 3 to 5.

the absolute difference is less than 0.035° for $\alpha \leq 70°$ (see Fig. 9.1b). Hence, φ_X is a good reference value for the actual fiber orientation φ and can be used e. g. to determine $(\varphi_P - \varphi)$ from 3D-PLI and XP measurements and to estimate the impact of diattenuation on the fiber orientations derived in 3D-PLI.

In contrast to φ_X, the direction angles derived from the 3D-PLI and DI measurements (φ_P and φ_D) depend on the polarization properties and on the tissue diattenuation. Figure 9.1a shows that the absolute difference between φ_P and φ increases linearly with increasing absolute tissue diattenuation (for $|D| \leq 5\,\%$). For fibers with $\alpha \leq 60°$, the maximum difference is less than 3.7°. For steeper fibers, the difference is expected to be even smaller because the diattenuation values are expected to be small. The curves for the derived inclination angle α_P are shown in Appx. C.2.1: after correcting the inclination angle with the maximum retardation value (cf. Eq. (4.20)), the absolute difference between α_P and α is less than 11.2° for all inclination angles $< 90°$ and $|D| \leq 5\,\%$ (see Fig. C.1b). Thus, the diattenuation does not seem to have a large impact on the fiber orientations (φ_P, α_P) derived in a 3D-PLI analysis.

While the difference between φ_P and φ is mostly independent from φ and relatively small, the difference between φ_D and φ strongly depends on the actual fiber direction angle and becomes largest for small tissue diattenuations and flat fibers (see Fig. C.3c in Appx. C.2.3). This shows that φ_D is strongly influenced by the partially polarized light source and the polarization sensitivity of the camera. The direction angle φ_D derived from the DI measurement is broadly distributed around the actual fiber direction angle. The maximum absolute difference between φ_D and φ decreases with increasing D (see Fig. 9.1c): the difference is about 21° for $D = 1\,\%$ and about 5° for $D = 5\,\%$. For $D < 0$, there is an additional shift by +90°.

Figure C.3a in Appx. C.2.3 shows that the measured diattenuation $|\mathscr{D}|$ is also strongly influenced by the non-ideal polarization properties of the LAP: without tissue diattenuation ($D = 0$), the measured diattenuation reaches values up to $|\mathscr{D}| = 0.85\,\%$. To ensure that the measured diattenuation mostly corresponds to the actual tissue diattenuation, the experimental studies in Secs. 9.2 and 9.3 focus on values $|\mathscr{D}| > 1\,\%$. In this regime, the absolute difference between $|\mathscr{D}|$ and $|D|$ is expected to be less than 0.3 % for $|D| \leq 5\,\%$ (see Fig. C.3b in Appx. C.2.3).

9.2 Study on Freshly Embedded Brain Sections

To investigate the diattenuation of brain tissue and its impact on the measured 3D-PLI signal, an experimental study was performed on freshly embedded brain sections (one day after tissue embedding) from different species. First, a combined measurement of 3D-PLI, XP, and DI was performed on five rat brain sections (Sec. 9.2.1) to compare the measured diattenuation signal to the 3D-PLI signal and to relate the results to the predictions of the numerical study in Sec. 9.1. Brain sections from different species were then used to study the diattenuation signal for different fiber orientations (Sec. 9.2.2). Finally, the results were compared to diattenuation measurements with higher optical resolution, performed with a prototypic polarizing microscope realized on an optical bench (Sec. 9.2.3).

9.2.1 Diattenuation Signal Compared to 3D-PLI and XP Measurements

Five sagittal sections from the middle part of a healthy rat brain (*Wistar*, male, three months old) were selected for evaluation: sections no. 161, 162, 175, 177, and 185 (the brain was cut from right to left, all sections are located in the left hemisphere). The LAP measurements[2] (3D-PLI, XP, DI) were performed with the Apo-Rodagon-N90 objective (see Sec. 7.1.2), yielding an effective object-space resolution of 14 µm / px (for 4164×3120 pixels). The resulting parameter maps for section no. 175 have already been shown in Fig. 4.8. The diattenuation maps $|\mathscr{D}|$ of all five brain sections can be found in Fig. C.5a in Appx. C.4.

The signal analysis was performed for the complete rat brain sections. To ensure that the diattenuation signal is mainly caused by the brain tissue and not by the polarization properties of the LAP (cf. Sec. 9.1 and Appx. C.2.3), a special focus was placed on regions with $|\mathscr{D}| > 1\,\%$.

The content of this study has been published in Menzel *et al.* (2017) [3] Sec. 5.

9.2.1.1 Comparison of DI and 3D-PLI Signals

The five investigated rat brain sections accumulate in total to over 4,000,000 investigated pixels. The averaged diattenuation is about $(0.42 \pm 0.34)\,\%$. Regions with $|\mathscr{D}| > 1\,\%$ represent only 6 % of the tissue and yield an average of about $(1.42 \pm 0.43)\,\%$. The maximum measurable diattenuation signal ($|\mathscr{D}|_{\max} \approx 3.9\,\%$) was observed within the optic tract.

The measured diattenuation signal is much smaller than the measured retardation signal. Figure 9.2a shows the measured diattenuation $|\mathscr{D}|$ and the retardation r_P exemplary for the rat brain section no. 175, the anatomical regions were labeled in Fig. 8.1a for the corresponding transmittance image. Some regions with relatively high diattenuation values (e. g. aci and fibers in the CPu) also show high retardation values, some areas with low diattenuation values (e. g. gray matter regions) also show low retardation values. However, the strength of the diattenuation signal does not correlate with the strength of the retardation signal: The cyan (red) arrows indicate regions that show a larger contrast in the diattenuation (retardation) image. The yellow arrows indicate the region with the maximum diattenuation and retardation value in the displayed brain section, respectively. The largest diattenuation signal was measured within the anterior commissure intrabulbar part ($\overline{|\mathscr{D}|}(\mathrm{aci}) = 2.1\,\%$, $|\mathscr{D}|_{\max}(\mathrm{aci}) = 3.5\,\%$), while the

[2] The measurements were performed by Julia Reckfort and Hasan Köse (INM-1, Forschungszentrum Jülich, Germany).

largest retardation signal was measured within the cerebellum ($r_{\mathrm{P,max}}(\mathrm{cb}) = 0.78$) and not within the anterior commissure intrabulbar part ($r_{\mathrm{P,max}}(\mathrm{aci}) = 0.63$).

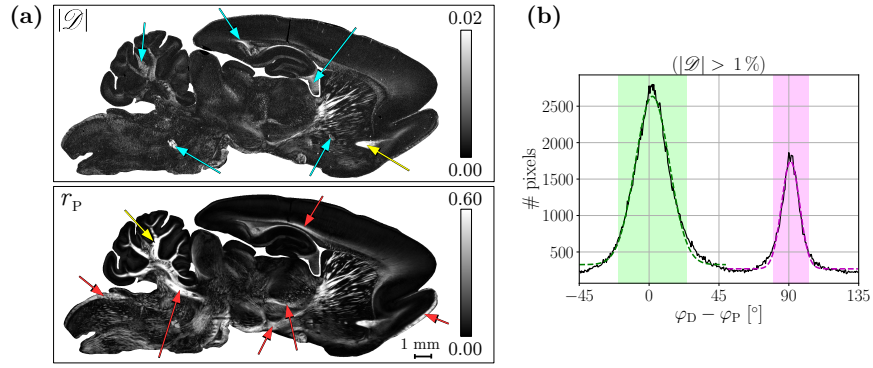

Fig. 9.2: Comparison of the amplitude (a) and phase (b) of DI signals $\{|\mathscr{D}|, \varphi_{\mathrm{D}}\}$ and 3D-PLI signals $\{r_{\mathrm{P}}, \varphi_{\mathrm{P}}\}$ obtained from LAP measurements (see Secs. 4.4.1 and 4.4.3) of five sagittal rat brain sections measured one day after tissue embedding with an effective object-space resolution of 14 µm/px: **(a)** Measured diattenuation $|\mathscr{D}|$ and retardation r_{P} shown exemplary for the rat brain section no. 175. The yellow arrows indicate the region with the maximum diattenuation and retardation value, respectively. The cyan (red) arrows indicate regions with larger contrast in the diattenuation (retardation) image. **(b)** Histogram showing the difference between the direction angles φ_{D} and φ_{P} for all investigated rat brain sections (bin width = 0.5°). Due to the 180°-periodicity, the data range has been reduced to $[-45°, 135°)$. To ensure that the diattenuation signal is mainly caused by the brain tissue and not by the non-ideal polarization properties of the LAP (cf. Appx. C.2.3) or other artifacts, only regions with $1 < |\mathscr{D}| < 4\,\%$ were used for evaluation. The highlighted regions show the 2σ-environments of the fitted Gaussian distributions: green (53.97 % of the selected pixels: $\mu = 2.1°, \sigma = 11.0°$), magenta (19.06 % of the selected pixels: $\mu = 91.1°, \sigma = 5.8°$). The figures have been adapted from Menzel *et al.* (2017) [3] Figs. 7a and 8.

A comparison of the direction angles φ_{D} and φ_{P} determined from the DI and 3D-PLI measurements reveals that the majority of the determined fiber directions are in good correspondence: the histogram of $(\varphi_{\mathrm{D}} - \varphi_{\mathrm{P}})$ in Fig. 9.2b shows a distinct peak around 0°, highlighted in green. The peak can be described by a Gaussian distribution with mean $\mu = 2.1°$ and standard deviation $\sigma = 11.0°$. In certain brain regions, the fiber direction derived from the DI measurement is shifted by 90°, see peak highlighted in magenta. The peak can be described by a Gaussian distribution with $\mu = 91.1°$ and $\sigma = 5.8°$.

The direction angle φ_{D} is computed from the maximum of the measured diattenuation signal (cf. Fig. 4.4f). According to Eq. (4.36), φ_{D} only corresponds to the actual fiber direction for $D > 0$. For $D < 0$, the actual fiber direction is given by the minimum of the diattenuation signal ($\varphi_{\mathrm{D}} = \varphi + 90°$). Thus, in some brain regions (green area), the transmitted light intensity becomes *maximal* when the light is polarized in the direction of the fibers. In other brain regions (magenta area), the transmitted light intensity becomes *minimal* when the light is polarized in the direction of the fibers.

For further investigation, all pixels belonging to the green highlighted area in Fig. 9.2b ($\varphi_{\mathrm{D}} - \varphi_{\mathrm{P}} \in [-19.9°, 24.1°]$) are denoted by D^+ and all pixels belonging to the area highlighted in magenta ($\varphi_{\mathrm{D}} - \varphi_{\mathrm{P}} \in [79.5°, 102.7°]$) are denoted by D^-. The angle ranges correspond to the 2σ-environments of the Gaussian peaks (the other direction angles cannot be clearly assigned to D^+ or D^-).

Figure C.5b in Appx. C.4 shows the regions of type D^+ and D^- for all five rat brain sections (for $|\mathscr{D}| > 1\,\%$). The type of diattenuation is specific for certain brain regions: some brain regions (ac, Cb, cu, opt, fi, part of cc) show diattenuation of type D^+, while other brain regions (aci, CPu, part of cg) show diattenuation of type D^- (cf. Figs. C.5 and 8.1a). This behavior is consistent across the investigated brain sections.

9.2.1.2 Uncertainties of DI and 3D-PLI Direction Angles as a Function of Diattenuation

To examine the accuracy of the determined fiber direction angles φ_D and φ_P, the direction angle φ_X was used as a reference for the actual fiber direction angle φ (cf. Sec. 9.1). While φ_P and φ_D have value ranges of $[0°, 180°)$, φ_X can only be determined in a value range of $[0°, 90°)$ (see Sec. 4.4.2). When being compared to φ_X, the direction angles φ_P and φ_D were therefore reduced to a value range of $[0°, 90°)$. In regions with small retardation values, the transmitted light intensity in the XP measurement is small due to the 90°-orientation of the linear polarizers (cf. Fig. 4.4e), leading to a low signal-to-noise ratio. Therefore, φ_X was only evaluated in regions with retardation values $r_\mathrm{P} > 0.1$ (see Appx. C.3).

Figure 9.3a,b shows $(\varphi_\mathrm{D} - \varphi_\mathrm{X})$ and $(\varphi_\mathrm{P} - \varphi_\mathrm{X})$ plotted against $|\mathscr{D}|$ for regions with retardation values $r_\mathrm{P} > 0.1$. In Appx. C.3, the same differences are plotted against r_P for regions with diattenuation $|\mathscr{D}| > 1\,\%$.

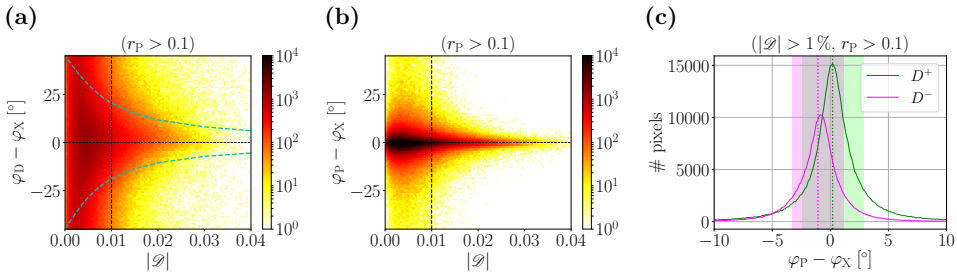

Fig. 9.3: Histograms of the direction angles $\{\varphi_\mathrm{P}, \varphi_\mathrm{D}, \varphi_\mathrm{X}\}$ determined from 3D-PLI, DI, and XP measurements with the LAP (see Secs. 4.4.1 to 4.4.3) for five sagittal rat brain sections measured one day after embedding with an effective object-space resolution of 14 µm/px: **(a)** 2D histogram showing the difference between φ_D and φ_X plotted against the measured diattenuation $|\mathscr{D}|$. The dashed cyan curves correspond to the maximum difference (pos./neg.) as predicted by the numerical study (see Fig. 9.1c, for $\alpha = 0°$). **(b)** 2D histogram showing the difference between φ_P and φ_X plotted against $|\mathscr{D}|$. The number of bins in the 2D histograms is 100 for both axes, respectively. The dashed vertical lines mark the region $(|\mathscr{D}| > 1\,\%)$ for which the diattenuation signal is expected to be mainly caused by the brain tissue and not by the non-ideal polarization properties of the LAP (cf. Appx. C.2.3). **(c)** Histogram showing the difference between φ_P and φ_X evaluated in regions (see Fig. C.5b) with diattenuation of type D^+ (green) and D^- (magenta) according to the angle ranges defined in Fig. 9.2b (bin width = 0.1°). The green and magenta dashed lines indicate the respective mean values: 0.19° for D^+ and −1.07° for D^-. The highlighted areas contain 75 % of the respective data: $[-2.45°, 2.84°]$ for D^+ and $[-3.27°, 1.13°]$ for D^-. To ensure a sufficient signal-to-noise ratio for φ_X, only regions with retardations $r_\mathrm{P} > 0.1$ were selected for evaluation (cf. Appx. C.3). The figures have been published in Menzel *et al.* (2017) [3] Figs. 10 and 11.

Due to the low signal-to-noise ratio of the diattenuation signal, the direction angle φ_D determined from the DI measurement is more error-prone than the direction angle φ_P determined from the 3D-PLI measurement (the distribution in Fig. 9.3a is much broader than in Fig. 9.3b). With increasing tissue diattenuation, the mean absolute differences between the determined direction angles (φ_D and φ_P) and the actual fiber direction (represented by φ_X) decrease.

The difference between φ_D and φ_X behaves as predicted by the numerical study: The mean absolute difference is large for regions with diattenuations $|\mathscr{D}| \leq 1\,\%$ and decreases with increasing diattenuation. The measured values for $(\varphi_D - \varphi_X)$ lie mostly between the dashed cyan lines in Fig. 9.3a, which indicate the maximum (positive/negative) difference between φ_D and φ as computed in the numerical study (see Fig. 9.1c).

The difference between the direction angles φ_P and φ_X shows a different pattern than for φ_D (see Fig. 9.3b). In regions with almost zero diattenuation, $(\varphi_P - \varphi_X)$ is very small. With increasing diattenuation ($0\,\% < |\mathscr{D}| < 0.5\,\%$), the distribution broadens rapidly. For $|\mathscr{D}| > 0.5\,\%$, the distribution narrows with increasing diattenuation. Taking into account that steep fibers are expected to have lower diattenuation values (cf. Sec. 9.1), these results are also in accordance with the predictions of the numerical study (see Fig. 9.1a): In regions with zero diattenuation, φ_P is equal to φ for all inclinations. In regions with small diattenuation values, contributions from fibers of all inclinations are expected, leading to a broad distribution of $(\varphi_P - \varphi)$. With increasing diattenuation, less contributions from steep fibers are expected, which causes the difference between φ_P and φ to become smaller.

For 75 % of the investigated rat brain pixels, $(\varphi_P - \varphi_X)$ lies within $[-3.2°, 2.49°]$. Thus, the diattenuation of the brain tissue can be neglected in the 3D-PLI analysis, as predicted by the numerical study.

Figure 9.3c shows the histograms of $(\varphi_P - \varphi_X)$, computed separately for regions with $|\mathscr{D}| > 1\,\%$ and diattenuation of types D^+ and D^-. On average, the fiber direction angle is slightly overestimated in regions of type D^+ (mean difference: 0.19°) and underestimated in regions of type D^- (mean difference: −1.07°).

This behavior has also been predicted by the numerical study: The diattenuation effect in regions of type D^- can be described by replacing the variable D in all analytical formulas by the variable $(-D)$, which causes the graphs in Fig. 9.1 to be rotated 180° around the origin. (The 90°-shift of $(\varphi_D - \varphi)$ is not visible for $(\varphi_D - \varphi_X)$ because the value range of φ_X is reduced.) As a consequence, the values for $(\varphi_P - \varphi)$ are expected to be positive for regions of type D^+ and negative for regions of type D^- (cf. Fig. 9.1a).

Thus, the experimental results are in good accordance with the numerical results when taking into account two different types of diattenuation, which can be described by a positive and a negative tissue diattenuation, cf. Eq. (2.43): D^+ ($D > 0$) and D^- ($D < 0$).

9.2.2 Diattenuation Signal for Different Species and Fiber Orientations

To study how the diattenuation signal and the regions of type D^+ and D^- depend on the underlying fiber architecture, the measurements[3] (3D-PLI, XP, DI) were performed on coronal and sagittal brain sections obtained from different species: mouse (*C57BL*, male, three months old, perfusion fixation[4]), rat (*Wistar*, male, three months old), and vervet monkey (African green monkey: *Chlorocebus aethiops sabaeus*, male, between one and

[3] The measurements of the mouse and vervet brains were performed by David Gräßel and Isabelle Mafoppa Fomat (INM-1, Forschungszentrum Jülich, Germany).

[4] The brain was fixated by perfusing paraformaldehyde solution through the circulatory system of the mouse so that the fixative reaches every corner of the natural vascular network.

two years old). The mouse and rat brains were measured with the Apo-Rodagon-N90 objective of the LAP with an effective object-space resolution of 14 µm / px. The vervet monkey brains were measured with the Apo-Rodagon-N50 objective (see Sec. 7.1.2) with 27 µm / px. Figure 9.4 shows the measured diattenuation $|\mathscr{D}|$ for (a) a coronal mouse brain section and a sagittal rat brain section (section no. 175) and (b) a coronal and sagittal vervet section (cf. Fig. 8.1).

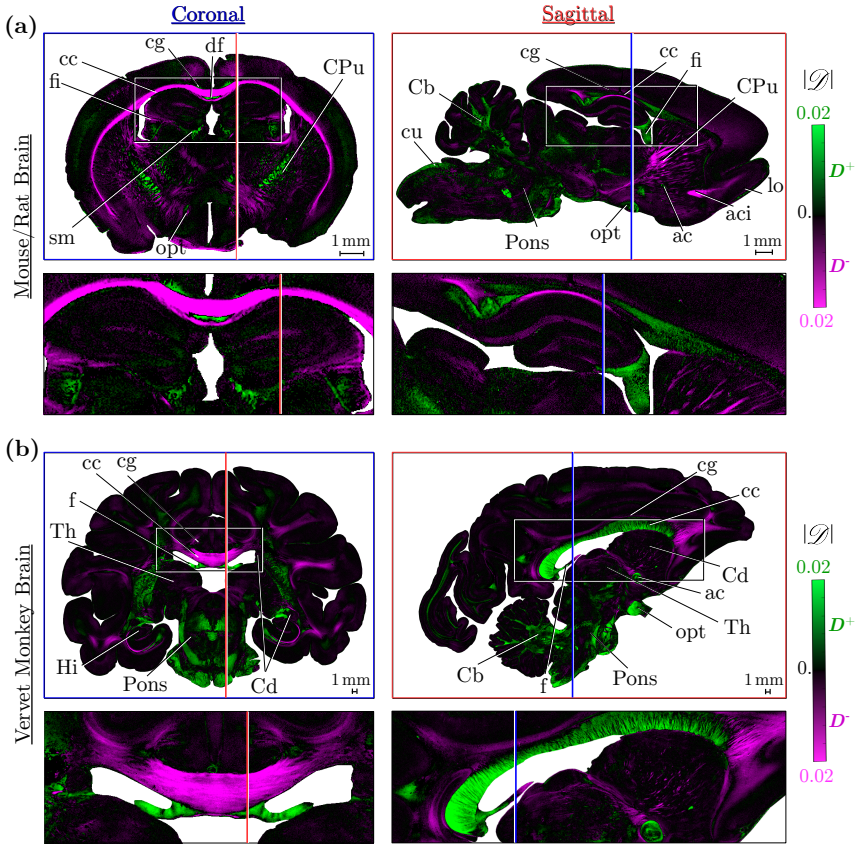

White matter structures:			df	– dorsal fornix	Gray matter structures:	
ac	– anterior commissure		f	– fornix	Cd	– caudate nucleus
aci	– anterior commissure intrabulbar part		fi	– fimbria	Hi	– hippocampus
			lo	– lateral olfactory tract	Th	– thalamus
cc	– corpus callosum					
cg	– cingulum		opt	– optic tract	Cb	– cerebellum
cu	– cuneate fasciculus		sm	– stria medularis	CPu	– caudate putamen

Fig. 9.4: Diattenuation images of coronal and sagittal sections **(a)** through a mouse brain (left) and a rat brain (right) measured with an effective object-space resolution of 14 µm/px and **(b)** through a vervet monkey brain measured with 27 µm/px, cf. Fig. 8.1. The measured diattenuation values $|\mathscr{D}|$ are shown in green for regions with diattenuation of type D^+ ($\varphi_D - \varphi_P \in [-20°, 20°]$) and in magenta for regions with diattenuation of type D^- ($\varphi_D - \varphi_P \in [70°, 110°]$). The values for $|\mathscr{D}|$, φ_D, and φ_P were obtained from 3D-PLI and DI measurements with the LAP (see Secs. 4.4.1 and 4.4.3) one day after tissue embedding. A similar figure has been published in Menzel *et al.* (2018b) [68] Fig. 2.

The diattenuation values are shown in green for regions with diattenuation of type D^+ ($\varphi_D - \varphi_P \in [-20°, 20°]$) and in magenta for regions with diattenuation of type D^- ($\varphi_D - \varphi_P \in [70°, 110°]$). The angle ranges account for the uncertainties of φ_D predicted by the numerical study ($\max|\varphi_D - \varphi| \approx 20°$ for $|\mathscr{D}| = 1\,\%$, cf. Fig. 9.1c).

In Fig. 8.1, the corresponding transmittance images were shown for the rat and the vervet brain sections, and regions with flat and steep fibers were marked in green and yellow, respectively. A comparison of Figs. 8.1 and 9.4 shows that regions of type D^- (magenta) mostly belong to regions with flat fibers (coronal: cc, fi; sagittal: aci, cg, CPu), while regions of type D^+ (green) mostly belong to regions with steep fibers (coronal: cg, df, sm, CPu; sagittal: cc, fi).

To study the inclination dependence of the diattenuation in more detail, regions with type D^+ and D^- were compared to the fiber inclination angles determined in a 3D-PLI analysis with tilting [55]. The 3D-PLI and DI measurements[5] were performed on another coronal section of the vervet brain with the Lametar 2.8/25 objective of the LAP (see Sec. 7.1.2) and an effective object space resolution of about 43 µm / px. Figure 9.5 shows the resulting diattenuation $|\mathscr{D}|$ and the inclination angle α_P. Regions with diattenuation of type D^+ ($\varphi_D - \varphi_P \in [-20°, 20°]$) and regions with steep fibers ($60° \leq \alpha_P \leq 90°$) are marked in green, regions with diattenuation of type D^- ($\varphi_D - \varphi_P \in [70°, 110°]$) and regions with flat fibers ($0° \leq \alpha_P \leq 30°$) are marked in magenta. For better comparison, only white matter regions were colorized.

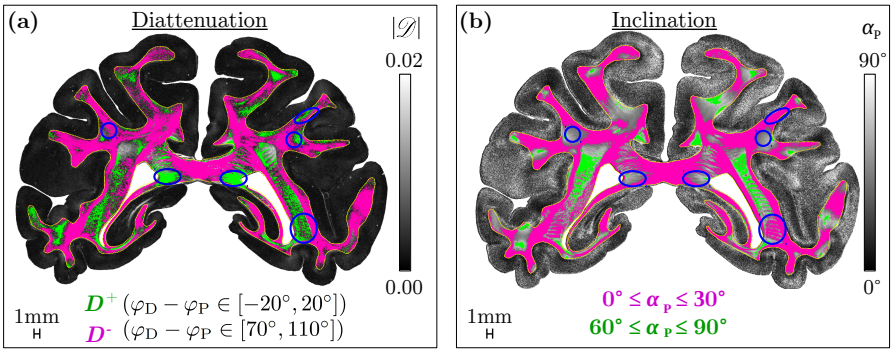

Fig. 9.5: Comparison of regions with different types of diattenuation (green: D^+, magenta: D^-) and regions with steep and flat fibers (green: $\alpha \geq 60°$, magenta: $\alpha \leq 30°$). The diattenuation $|\mathscr{D}|$ and the inclination angle α_P were computed from DI and 3D-PLI measurements performed with the LAP for a coronal section of a vervet monkey brain (cf. Fig. 9.4b) one day after tissue embedding with an effective object-space resolution of 43 µm/px. Regions with steep fibers ($\alpha \geq 60°$) mostly show diattenuation of type D^+, while fibers with lower inclination angles show both types of diattenuation (see areas surrounded in blue).

A comparison of the green and magenta regions in Fig. 9.5 shows that there exists no bidirectional relation between the type of diattenuation and the fiber inclination: while nearly all steep fibers ($\alpha \geq 60°$) show diattenuation of type D^+, fibers with lower inclination angles show both types of diattenuation (see areas surrounded in blue). Regions with type D^- are more likely to occur in regions with flat fibers ($\alpha < 30°$).

[5] The measurements were performed by Hasan Köse (INM-1, Forschungszentrum Jülich, Germany).

9.2.3 High-Resolution Diattenuation Measurement

As the filters in the PM cannot be removed, a routine measurement of the diattenuation is only possible with the LAP, which has a much lower optical resolution (px $> 20\,\mu m$) than the PM (px $\approx 1.33\,\mu m$). To still enable a diattenuation measurement at higher optical resolution, a prototypic polarizing microscope was used which is realized on an optical bench. The overall setup is the same as for the PM (see Fig. B.1), except that a diffuser is placed behind the LED light source and that the rotating polarizer is integrated in the Köhler illumination. The optical components are comparable to the PM (see Appx. B.1.1): The light source generates green light with a slightly different wavelength spectrum ($\lambda = 532\,nm$, FWHM $= 10\,nm$), the objective lens (*Nikon Plan Apo 4 x 0.2 NA*) has a slightly different magnification ($4\times$) and numerical aperture (NA $= 0.2$), and the camera (*SVS-Vistek EVO 4070*) contains an image sensor (*KAI-04070* by *Truesense Imaging*) with a slightly different size ($15.2 \times 15.2\,mm^2$) than in the PM. The pixel size in object space is about $1.8\,\mu m$. The setup and optical components were described in more detail by Wiese [55].

Directly after the LAP measurement of the coronal mouse brain section (see Fig. 9.4a), the brain section was measured with the prototypic polarizing microscope for three different areas of interest.[6] Due to a superior signal-to-noise ratio, repeated DI measurements were not necessary. Figure 9.6 shows the measured diattenuation $|\mathscr{D}|$ for all three areas as well as the regions of type D^+ and D^- for one selected area.

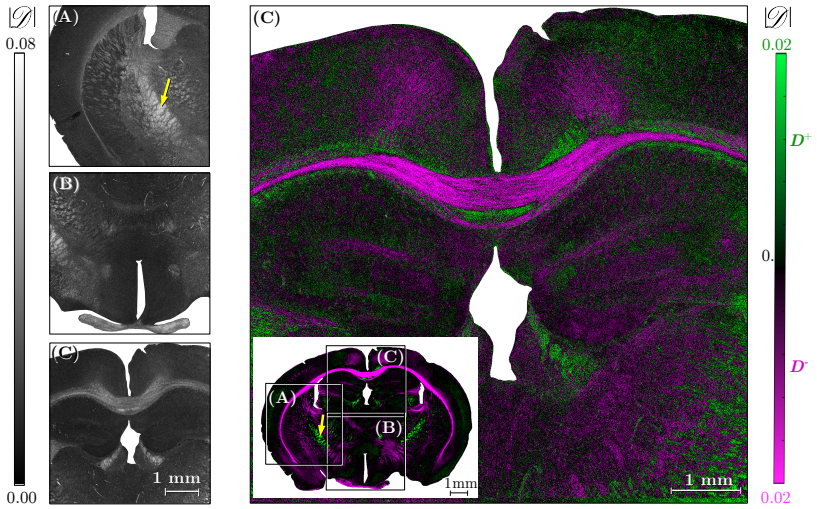

Fig. 9.6: Diattenuation images of a coronal mouse brain section (cf. Fig. 9.4a) obtained from DI and 3D-PLI measurements performed with the LAP (whole brain section) and with a prototypic polarizing microscope realized on an optical bench [55] (areas A–C). The LAP measurement was performed with an effective object-space resolution of $14\,\mu m\,/\,px$ one day after tissue embedding. The measurements with the microscope were performed with a pixel size of about $1.8\,\mu m$ two days after tissue embedding. The gray-scale images show the measured diattenuation $|\mathscr{D}|$, the colored images show the diattenuation values belonging to regions with diattenuation of type D^+ ($\varphi_D - \varphi_P \in [-20°, 20°]$, in green) and regions with diattenuation of type D^- ($\varphi_D - \varphi_P \in [70°, 110°]$, in magenta). The yellow arrows mark the maximum diattenuation measured by the polarizing microscope. The figure has been published in Menzel *et al.* (2018b) [68] Fig. 5.

[6] The measurements were performed at Taorad GmbH, Aachen, Germany, with the help of Philipp Schlömer (INM-1, Forschungszentrum Jülich, Germany).

The diattenuation images obtained from measurements with the prototypic polarizing microscope show more detailed structures than the diattenuation images obtained from the LAP measurements and the diattenuation values are much larger: While the maximum diattenuation value measured with the LAP is less than 5 % for all investigated brain sections and resolutions ($\geq 14\,\mu\text{m}\,/\,\text{px}$), the high-resolution diattenuation measurement yields values up to $|\mathscr{D}| = 9.9\,\%$ in a region of 10×10 pixels (see yellow arrow in Fig. 9.6A), single pixels in this region reach values up to 25 %. In the LAP measurement, the maximum pixel value in the same region (also marked by a yellow arrow) is only about $|\mathscr{D}| = 3.6\,\%$.

Nevertheless, both the low- and the high-resolution diattenuation images show similar features: high diattenuation values and diattenuation of type D^+ or D^- occur in similar regions, i. e. the same diattenuation effects are observed for different optical resolutions.

9.3 Long-Term Study

To obtain optimal birefringence and diattenuation signals, the brain sections are measured 1–2 days after embedding. While the retardation signal does not depend much on the embedding time (time after mounting the brain section, cf. Sec. 4.1), the transmittance of brain tissue fades out (cf. Fig. 9.7a,b). This suggests that the diattenuation signal (anisotropic attenuation of light) also changes with increasing embedding time.[7]

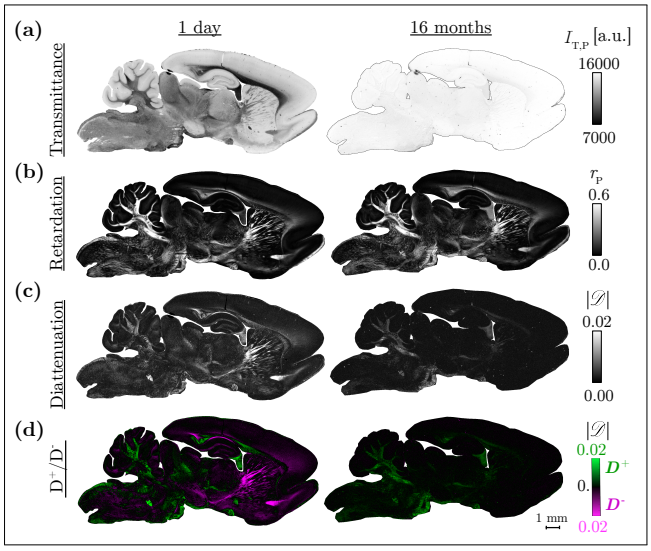

Fig. 9.7: Transmittance, retardation, and diattenuation images of a sagittal rat brain section (section no. 175) measured one day after tissue embedding and 16 months later with an effective object-space resolution of 14 µm/px. Due to the lack of contrast in the transmittance image, the tissue borders are surrounded by a black line. The values for $I_{T,P}$, r_P, and $|\mathscr{D}|$ were obtained from 3D-PLI and DI measurements with the LAP as described in Secs. 4.4.1 and 4.4.3. The colored images show the diattenuation values belonging to regions with diattenuation of type D^+ ($\varphi_D - \varphi_P \in [-20°, 20°]$, in green) and regions with diattenuation of type D^- ($\varphi_D - \varphi_P \in [70°, 110°]$, in magenta). Subfigure (a) has been published in Menzel *et al.* (2018a) [67] Fig. 14.

[7] Preliminary studies that investigate the diattenuation with increasing embedding time have been performed by Hasan Köse (INM-1, Forschungszentrum Jülich, Germany) as part of his Master thesis.

Figure 9.7 shows the parameter maps for the sagittal rat brain section no. 175 one day after tissue embedding (cf. Figs. 9.2 and 9.4a) and 16 months later. After 16 months, the regions with diattenuation of type D^- (magenta) have disappeared and only regions with diattenuation of type D^+ (green) are left.

To study the development of the diattenuation with increasing embedding time of the sample, a coronal vervet section (cf. Fig. 9.5) was measured 1, 8, 18, 22, 30, 37, 51, and 87 days after tissue embedding.[8] Figure 9.8a shows the colored diattenuation maps (D^+ in green, D^- in magenta) 8, 22, and 51 days after tissue embedding. The regions with diattenuation of type D^+ increase with increasing time after tissue embedding, while the regions with diattenuation of type D^- decrease. The yellow arrows mark a region that is already of type D^+ directly after tissue embedding (i), a region that is still of type D^- after 51 days (ii), and a region that changes from D^- to D^+ over time (iii). Figure 9.8b shows the corresponding values for $(\varphi_D - \varphi_P)$ and $|\mathscr{D}|$ for all eight measurements.

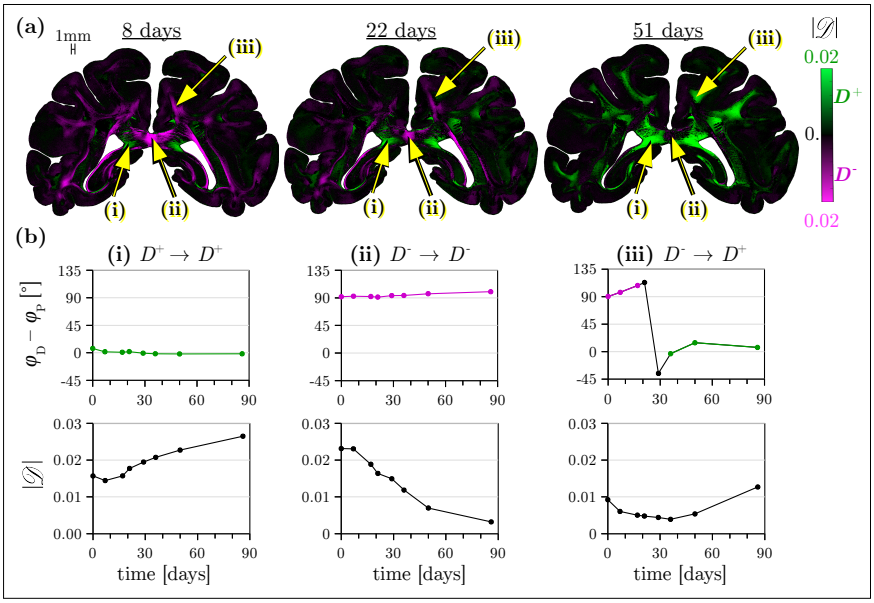

Fig. 9.8: (a) Diattenuation images of a coronal vervet section (cf. Fig. 9.5) measured 8, 22, and 51 days after tissue embedding with an effective object-space resolution of 43 µm/px. Diattenuation values $|\mathscr{D}|$ that belong to regions with diattenuation of type D^+ ($\varphi_D - \varphi_P \in [-20°, 20°]$) are shown in green, diattenuation values that belong to regions with diattenuation of type D^- ($\varphi_D - \varphi_P \in [70°, 110°]$) are shown in magenta. The values for $|\mathscr{D}|$, φ_D, and φ_P were determined from 3D-PLI and DI measurements with the LAP as described in Secs. 4.4.1 and 4.4.3. **(b)** Angle difference $(\varphi_D - \varphi_P)$ and measured diattenuation $|\mathscr{D}|$ evaluated exemplary for three different regions (see yellow arrows): a region that is already of type D^+ directly after tissue embedding (i), a region that is still of type D^- after 51 days (ii), and a region that changes from D^- to D^+ over time (iii). A similar figure has been published in Menzel *et al.* (2018b) [68] Fig. 3.

For regions that only show diattenuation of type D^+ (i) or D^- (ii), the phase of the diattenuation signal remains relatively constant. The strength of the diattenuation signal increases (i) or decreases (ii) with increasing time after tissue embedding. For

[8] The measurements were performed by Hasan Köse (INM-1, Forschungszentrum Jülich, Germany) as part of his Master thesis.

regions that change from type D^- to D^+ (iii), the phase changes from ($\varphi_D \approx \varphi_P + 90°$) to ($\varphi_D \approx \varphi_P$), while $|\mathscr{D}|$ first decreases and then increases after the phase change. This suggests that the observed diattenuation signal is generated by two opposite effects: one with positive sign ($D > 0$) and one with negative sign ($D < 0$).

In Fig. 9.9, the measured diattenuation $|\mathscr{D}|$ is compared to the measured retardation r_P, exemplary for a coronal section of a human temporal lobe (male, 87 years old) measured one day and three weeks after tissue embedding. The measurements were performed with the Apo-Rodagon-N50 objective of the LAP and an effective object-space resolution of about 40 µm/px.

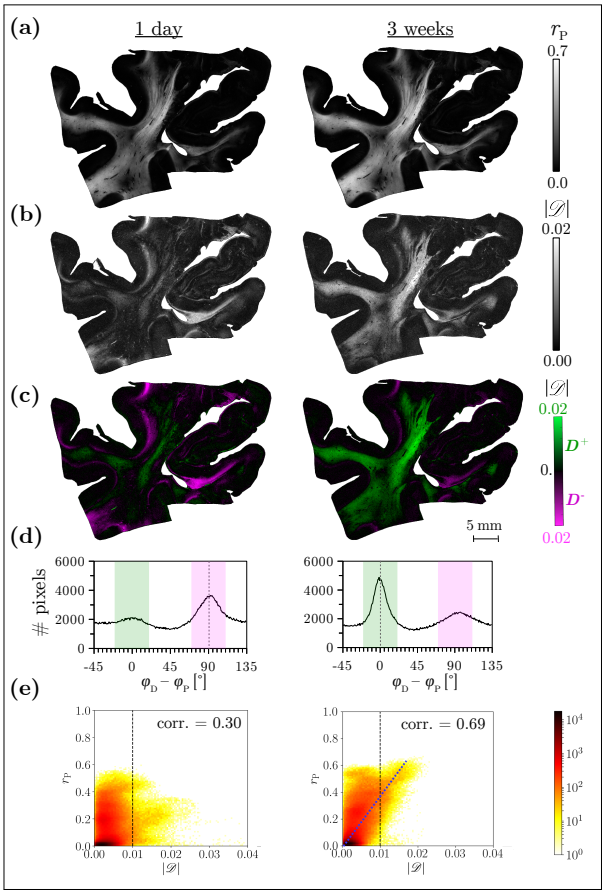

Fig. 9.9: (a-b) Retardation r_P and measured diattenuation $|\mathscr{D}|$ for a coronal section of a human temporal lobe measured one day and three weeks after tissue embedding with an effective object-space resolution of 40 µm/px. **(c-d)** Corresponding diattenuation images and ($\varphi_D - \varphi_P$) histograms in which the values belonging to regions with diattenuation of type D^+ ($\varphi_D - \varphi_P \in [-20°, 20°]$) are shown in green and diattenuation values that belong to regions with diattenuation of type D^- ($\varphi_D - \varphi_P \in [70°, 110°]$) are shown in magenta. The values for r_P, φ_P, $|\mathscr{D}|$ and φ_D were determined from 3D-PLI and DI measurements with the LAP as described in Secs. 4.4.1 and 4.4.3. **(e)** 2D histograms showing the retardation plotted against the measured diattenuation and the determined correlation coefficients (corr.). The dashed vertical lines mark the regions ($|\mathscr{D}| > 1\,\%$) for which the diattenuation signal is expected to be mainly caused by the brain tissue and not by the non-ideal polarization properties of the LAP (cf. Appx. C.2.3). The number of bins is 100 for both axes. Subfigures (b-d) have been published in Menzel *et al.* (2018b) [68] Fig. 6.

After three weeks, much more regions show diattenuation of type D^+ (green) and the main peak of $(\varphi_D - \varphi_P)$ is shifted from about 90° to 0°, as observed also for the other brain sections. In addition, the correlation between retardation and diattenuation increases: the correlation coefficient increases from about 0.3 to 0.7. This suggests that the birefringence of the nerve fibers and the diattenuation of type D^+ observed after long embedding time are caused by similar effects.

9.4 Discussion

In this chapter, the diattenuation of brain tissue and its impact on 3D Polarized Light Imaging have been investigated. The diattenuation was explored in numerical and experimental studies by performing three different types of measurements: 3D-Polarized Light Imaging (3D-PLI), crossed polars (XP) measurement, and Diattenuation Imaging (DI). The diattenuation signals were evaluated for different species, fiber orientations, and resolutions as well as for different times after tissue embedding. The studies revealed that there exist two different types of diattenuation that are regionally specific and partly depend on fiber orientation and embedding time.

Comparison between Numerical and Experimental Results The numerical study (see Sec. 9.1) estimated the impact of the non-ideal polarization properties of the LAP on the tissue measurements based on a thorough characterization of the optical components (in Sec. 7.2).

The general predictions of the numerical study were confirmed in the experimental studies (see Sec. 9.2.1): The uncertainties of the direction angles φ_D and φ_X as a function of diattenuation are compatible with the numerical results (cf. Figs. 9.3a and 9.1c). The experimental observation that the histogram of $(\varphi_P - \varphi_X)$ shows a positive mean for regions with diattenuation of type D^+ and a negative mean for regions with diattenuation of type D^- (see Fig. 9.3c) can be explained by a different sign of the tissue diattenuation D, as predicted by the numerical study (cf. Fig. 9.1a).

Thus, the experimental results are in good accordance with the numerical results when taking into account two different types of diattenuation (D^+ and D^-). This shows that the analytical description in Sec. 4.4 and the determined system parameters in Sec. 7.2.2 can be used to model the experimental measurements and to make general predictions.

Strength of the Diattenuation Signal The experimental studies (Secs. 9.2 and 9.3) quantified the diattenuation of brain tissue and its impact on 3D-PLI.

The diattenuation of the 60 µm thin brain sections was found to be relatively small: $|\mathscr{D}| < 5\,\%$ for measurements with the LAP (px ≈ 14–43 µm), $|\mathscr{D}| < 10\,\%$ for measurements with the prototypic polarizing microscope (px ≈ 1.8 µm). The order of magnitude is the same as reported in other biological tissues [60, 61, 134–136, 138]. As the signal-to-noise ratio for the microscopic measurement turned out to be much larger than for the LAP, future diattenuation measurements should be performed with higher optical resolution and with high-quality optical components.

In diattenuating brain tissue, the attenuation of light depends on the direction of polarization relative to the fiber axis, which leads to different transmittance values for nerve fibers with different inclinations. However, the diattenuation cannot explain the low transmittance values for steep fibers described in Chap. 8 because the difference in the transmittance values ($> 50\,\%$) is much larger than the measured diattenuation.

The study in Sec. 9.2.1.2 also showed that the diattenuation has only a small impact on the fiber orientations determined in 3D-PLI and that the diattenuation of brain tissue can be neglected in the 3D-PLI analysis.

Comparison of DI and 3D-PLI Signals Due to the low signal-to-noise ratio of the diattenuation signal measured with the LAP, the direction angle φ_D determined from the DI measurement is more error-prone than the direction angle φ_P determined from the 3D-PLI measurement (see Fig. 9.3a,b). The error decreases with increasing tissue diattenuation.

Despite the broad distribution of φ_D, the extremal transmittance is clearly correlated with the orientation of the nerve fibers (see Fig. 9.2b): In some brain regions, the transmitted light intensity becomes maximal when the light is polarized *parallel* to the fiber axes (described by D^+ or $D > 0$). In other brain regions, the transmitted light intensity becomes maximal when the light is polarized *perpendicularly* to the fiber axes (described by D^- or $D < 0$). Presumably, differences in the fiber composition or structure of these brain regions exist that cause the polarized light to be attenuated differently when passing through the brain tissue. These structural differences could concern the molecular composition of the fibers (more/less myelin, different lipid composition, etc.) as well as the macroscopic architecture of the fibers (long-range inter-cortical versus branching fibers, different inter-fiber distances, etc.).

In freshly embedded brain tissue, the distribution of regions with diattenuation of type D^+ and D^- is related to the fiber inclination (see Fig. 9.5): regions with steep fibers ($\alpha \geq 60°$) show almost exclusively diattenuation of type D^+, while both types D^+ and D^- occur in regions with non-steep fibers ($\alpha < 60°$).

The dependence of the diattenuation (D^+ and D^-) on the tissue structure and fiber inclination was investigated by means of FDTD simulations presented in Chap. 12.

Dichroism and Anisotropic Scattering for Samples with Increasing Embedding Time As described in Sec. 2.4, diattenuation can be caused by anisotropic absorption (dichroism D_K) as well as by anisotropic scattering (D_S). Analytical considerations in Appx. A.4.3 show that in regions where the diattenuation is only caused by dichroism ($D = D_K$), the diattenuation does not change its sign for different fiber inclinations (see Fig. A.1) and is expected to be approximately proportional to the retardation (for $r_P \leq 0.6$ or $|D_K| \leq 0.02$, see Fig. A.2).

In freshly embedded brain sections, there exist regions of both types D^+ and D^- (see Fig. 9.4) and the measured diattenuation and retardation signals show no distinct correlation (see Fig. 9.2a). With increasing time after tissue embedding, the fraction of D^+ regions grows and the correlation between measured diattenuation and retardation increases (see Sec. 9.3); the blue dotted line in Fig. 9.9e describes the predicted correlation between retardation and dichroism (cf. Fig. A.2, orange curve).

This suggests that the diattenuation is caused both by dichroism and by anisotropic scattering and that the scattering decreases with increasing time after tissue embedding, i. e. the diattenuation of old tissue samples is mainly caused by dichroism which is correlated with the retardation. A possible explanation for the decrease of scattering is that the glycerin solution in which the brain sections are embedded (see Sec. 4.1) soaks into the brain tissue and into the myelin sheaths of the nerve fibers, which leads to an equalization between the effective refractive indices of the myelin layers and the surrounding tissue and thus to a reduced scattering for old tissue samples. As this model does not include the molecular substructure, dichroism is not expected to change with

increasing embedding time – just as the birefringence of the nerve fibers (see Sec. 3.2.3 and Fig. 9.7b). The transmittance increases significantly with increasing embedding time (the attenuation vanishes, see Fig. 9.7a), which suggests that the transmittance is mostly caused by scattering outside the molecular substructure.

Transmittance and diattenuation caused by (anisotropic) scattering were further investigated by means of FDTD simulations presented in Part IV.

As anisotropic scattering is expected to decrease with increasing time after tissue embedding, the diattenuation of type D^+ observed in brain sections with long embedding time (see Fig. 9.7d) is presumably caused by anisotropic absorption (dichroism) with $D_\mathrm{K} > 0$. This means that the absorption becomes maximal (the transmitted light intensity becomes minimal) when the light is polarized perpendicularly to the fiber axis, i. e. in the plane of the radially oriented lipid molecules in the myelin sheath.

Although the diattenuation effect has practically no impact on the measured 3D-PLI signal, the diattenuation measurement is a valuable extension to 3D-PLI. By comparing the fiber directions extracted from 3D-PLI and DI, two different types of diattenuation effects can be distinguished that are specific to certain fiber architectures. The diattenuation effects are observed in different species, across several consecutive brain sections, and for different optical resolutions. The phase φ_D and amplitude $|\mathscr{D}|$ of the measured diattenuation signal can be used as imaging modalities providing different contrasts and structural information in addition to those obtained with 3D-PLI. Thus, Diattenuation Imaging is a promising imaging technique and reveals different types of fibrous structures that cannot be distinguished with current imaging techniques. The purpose of DI as additional imaging technique should be further investigated in the future.

Part IV

FDTD SIMULATION STUDIES

Chapter 10

Modeling

To model and explain the observed transmittance and diattenuation effects in 3D-PLI and DI (see Chaps. 8 and 9), a sophisticated simulation tool is needed. In previous studies [51, 52], the in-house developed simulation software *simPLI* was used to model the 3D-PLI measurement and signal analysis. However, the software is based on linear optics (Jones matrix multiplication) and cannot be used to investigate more complex effects like scattering. For this purpose, FDTD simulations (see Chap. 6) were used which model the propagation of the polarized light wave through brain tissue.

This chapter describes how FDTD simulations can be used to model the 3D-PLI and DI measurements: Section 10.1 explains the simulation of the polarimetric measurements, Sec. 10.2 introduces the geometries of the simulated fiber configurations, Sec. 10.3 describes the implementation in TDME3D and the parameters used for the simulations in the subsequent chapters, Sec. 10.4 evaluates the simulation parameters in terms of accuracy, and Sec. 10.5 provides a final discussion of the simulation model.

10.1 Simulation of the Polarimetric Measurements

This section describes how FDTD simulations were used to model the polarimetric measurements (3D-PLI and DI). Section 10.1.1 introduces the model of the optical systems, i. e. how the optical components of the employed polarimeters (PM and LAP) were modeled. Section 10.1.2 explains how the transmitted light intensities were derived from the electric field vectors computed by the Maxwell Solver (TDME3D). Finally, in Sec. 10.1.3, the simulation procedure was tested on a well-defined sample (USAF resolution target).

Parts of Secs. 10.1.1 and 10.1.2 have been published in Menzel *et al.* (2016, 2018a) [66, 67]. Section 10.1.2 has been published in Menzel *et al.* (2018a) [67] Note 3.

10.1.1 Model of the Optical Systems

When modeling the optical components of the polarimeters, the limitations of the software TDME3D need to be taken into account: the simulated light wave is completely polarized and coherent, the materials are characterized by isotropic refractive indices, and size and resolution of the simulated geometries are limited due to finite computing time.

Using completely polarized light for the simulations implies that the optical elements of the polarimeters are assumed to be ideal (unpolarized light source, ideal polarizing filters, no polarization-sensitivity of the camera). For the LAP, this assumption is reasonable because the non-ideal properties of the optical elements have only a small impact on the derived fiber orientation and diattenuation (in the regime of experimentally observed diattenuation values $1\,\% < D < 4\,\%$), as demonstrated in Sec. 9.1. The optical elements

of the PM are more ideal than for the LAP (the employed filters are smaller and of better quality), so that the impact of non-ideal optical elements is expected to be even smaller than for the LAP.

Although the order of the optical elements in the PM is different than in the LAP, the signal analysis is analogous. Therefore, only the setup of the LAP was considered in the simulations. For the simulation of 3D-PLI, all filters were considered (polarizer, quarter-wave retarder, analyzer), for the simulation of DI, only the first polarizer was considered.

The following paragraphs describe how the different optical elements of the polarimeters (PM/LAP) were modeled in the FDTD simulations (see also Fig. 10.1).

Light source The light source was modeled as a plane wave with a given wavelength and a certain direction of propagation (φ, θ). The light is coherent and completely polarized. To model the 3D-PLI measurement, the sample was illuminated by left-handed circularly polarized light (corresponding to the polarization state behind the first polarizer and the quarter-wave retarder). To model the DI measurement, the sample was illuminated by linearly polarized light with a certain direction of polarization (corresponding to the polarization state behind the rotating polarizer).

The LED used for the polarimetric measurements emits light with different wavelengths and angles of incidence (see Sec. 7.1.1). To model this incoherent and diffuse light source, several simulation runs were performed with different wavelengths λ and angles of incidence (φ, θ), and the resulting intensities were added incoherently.

The intensities for different wavelengths were weighted according to the wavelength spectrum of the respective light source (PM/LAP), see Fig. 7.1. The uniform illumination of the diffuse light source was modeled by equidistant angles of incidence, i. e. two neighboring light rays have the same polar angular difference Δ_θ. For light incident at a certain polar angle θ, the azimuthal angular distance Δ_φ between two neighboring rays is then given by (see Appx. D.2 for derivation):

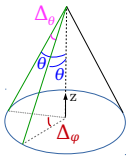

$$\Delta_\varphi = 2 \arcsin\left(\frac{\sin(\Delta_\theta/2)}{\sin(\theta)}\right). \qquad (10.1)$$

For example, the maximum angle of incidence in the PM is $\theta \approx 3°$, yielding $\Delta_\varphi \approx 60°$ for $\Delta_\theta = \theta = 3°$. Thus, to model the uniform diffuse light source of the PM, seven simulation runs are necessary: $\{\theta = 0°\}$, $\{\theta = 3°, \varphi = \{0°, 60°, \ldots, 300°\}\}$.

For most simulation studies, a different number η of φ-angles was chosen:

$$\varphi = \{0°, \Delta\varphi, \ldots (\eta - 1) \cdot \Delta\varphi\} \;\equiv\; \eta \times \Delta\varphi, \qquad \Delta\varphi = 360°/\eta. \qquad (10.2)$$

In this case, the resulting intensities for $\theta > 0°$ need to be weighted accordingly:

$$w = \frac{360°}{\Delta_\varphi \cdot \eta} = \frac{\Delta\varphi}{\Delta_\varphi}. \qquad (10.3)$$

The weighting for normally incident light ($\theta = 0°$) is $w = 1$. To obtain normalized intensity values, the weighted sum over all angles needs to be divided by $\sum w_i$.

By adding the intensities of several simulation runs with different wavelengths and angles of incidence, the light source was modeled by several wave pulses that have no constant phase difference or frequency, i. e. are not coherent to each other (cf. Sec. 2.1.3.3).

As it is not feasible to simulate all possible wavelengths and angles of incidence, the incoherent and diffuse light source could only be modeled to a certain extent.

Sample The optical properties of the sample are characterized by complex refractive indices, independent of polarization (see Sec. 6.3). The maximum sample size and the minimum mesh size are limited by computing time. For a mesh size $\Delta = 25\,\mathrm{nm}$, the maximum sample size is about $100^3\,\mu\mathrm{m}^3$.

Analyzer In a 3D-PLI measurement, a rotating polarizer (analyzer) is located behind the sample. The analyzer was represented by a rotated Jones matrix $R(\rho) \cdot P_\mathrm{y} \cdot R(-\rho)$ (see Eqs. (2.49) and (2.52)). As the matrix only acts on the projection of the electric field vector onto the xy-plane, it is also valid for non-normally incident (scattered) light.

Objective Lens In the experiment, the light is focused by a microscope (PM) or by a camera (LAP) objective consisting of several lenses (cf. Sec. 7.1.2 and Appx. B.1). To model the image formation, the optics of the imaging systems was represented by an effective objective lens, respectively. The lens was assumed to be ideal and both sample and detector were assumed to lie within the corresponding focal planes of the lens so that the propagation of the electromagnetic wave between specimen and camera detector could be neglected.

The numerical aperture (NA) of the lens was modeled by considering only waves with directions of propagation $\vec{k}$ that fulfill:

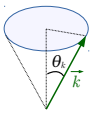

$$\theta_k \leq \arcsin(\mathrm{NA}). \tag{10.4}$$

In this way, only waves with low spatial frequencies contributed to the computed light intensity, leading to blurring of the resulting image.

To reduce sample size and computing time, the LAP-setup with the smallest pixel size ($\mathrm{px} = 21\,\mu\mathrm{m}$) was used for the simulations. To model the corresponding numerical aperture of the LAP ($\mathrm{NA} = 0.0083$), only k-vectors with angles $\theta_k \leq 0.48°$ were processed. For the PM ($\mathrm{NA} = 0.15$), only k-vectors with angles $\theta_k \leq 8.6°$ were processed.

Detector In the PM, the camera sensor contains an array of spherical microlenses which bundle the light onto subjacent photodiodes (see Fig. 7.4b). Each photodiode records the intensity of one particular image pixel. Assuming perfect microlenses and photodiodes that are completely covered by one microlens, respectively, the microlenses can be modeled by applying a moving average over the area of the microlens. Instead of taking the magnification and the physical size of the microlenses into account, the microlenses were modeled with a diameter corresponding to the pixel size of the PM in object space ($\mathrm{px} = 1.33\,\mu\mathrm{m}$), i. e. with radius $r_0 = \mathrm{px}/2 = 0.665\,\mu\mathrm{m}$. For the LAP, the pixel architecture is unknown and the simulations were therefore performed without microlenses ($r_0 = 0\,\mu\mathrm{m}$).

The finite size of the sensor pixels can be modeled by rasterizing the resulting light intensities with spacing $\Delta x = \mathrm{px}$. As the position of the sensor pixels is fixed with respect to the camera, a slightly different position of the sample leads to a different rasterizing and thus to slightly different intensities of the recorded image pixels. To still obtain the full image information, the transmitted light intensities were computed

without rasterizing unless the simulated images were directly compared to experimental data (see Sec. 10.1.3).

Figure 10.1 summarizes how the different optical elements of the polarimeters (PM/LAP) were modeled in the FDTD simulations.

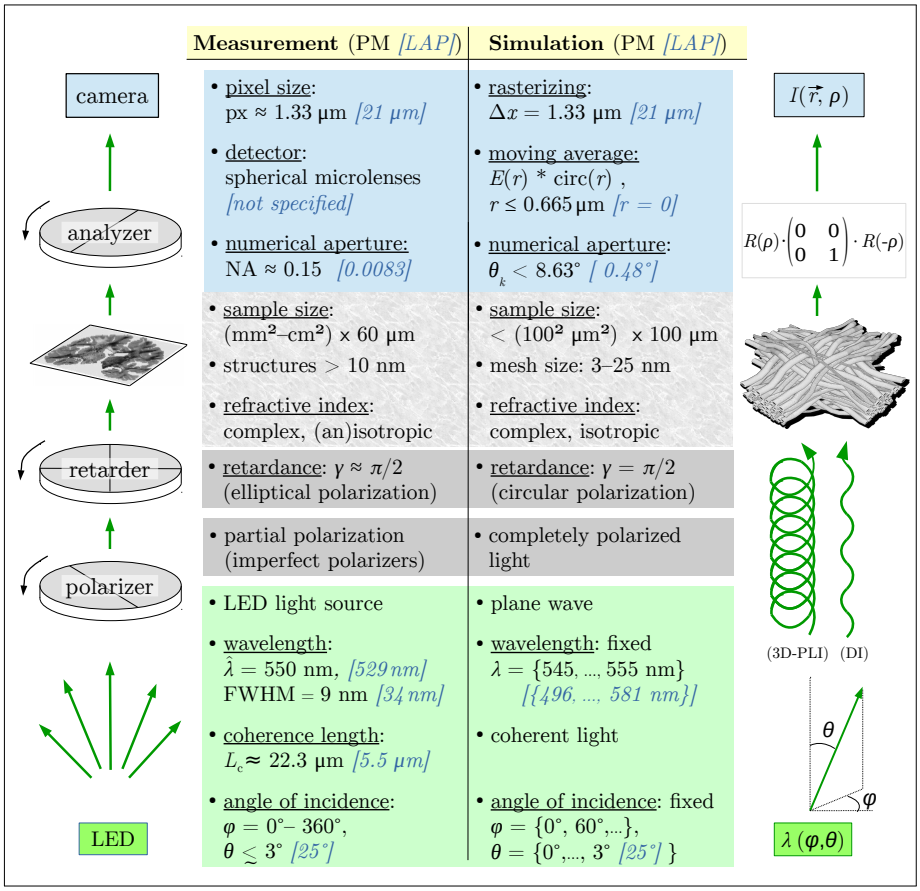

Fig. 10.1: Model of the optical systems (PM/LAP): On the left-hand side, the optical components of the polarimeters are characterized (cf. Tab. 7.3): light source (green), polarizer/retarder (dark gray), sample (light gray), objective lens/detector (blue). The figure shows the setup for the 3D-PLI measurement (for the DI measurement, retarder and analyzer are removed). The table and figure on the right-hand side show how the optical elements were modeled in the FDTD simulations: The incoherent and diffuse light source (LED) was modeled by performing several simulation runs with plane waves that have different wavelengths (λ) and angles of incidence (φ, θ). The modeled light source emits coherent light that is circularly or linearly polarized depending on the type of measurement (3D-PLI or DI). The tissue sample was represented by an artificial fiber architecture, the rotating analyzer by a rotated Jones matrix. A similar figure has been published in Menzel *et al.* (2018a) [67] Fig. 11.

Apparently, the Maxwell Solver is more suitable for modeling the optics of the PM than of the LAP: the PM has a narrower wavelength spectrum, less diffuse and more coherent light, and a smaller pixel size.

10.1.2 Computation of the Transmitted Light Intensities

This section describes how the vector data resulting from TDME3D was processed to model the 3D-PLI and DI measurements. The computation of the transmitted light intensities consists of several steps:

1.) Maxwell Solver: After passing the polarizing filters in front of the sample, the light wave is left-handed circularly polarized (3D-PLI) or linearly polarized (DI). The propagation of the light wave through the sample was computed by TDME3D. The resulting light wave is represented by a superposition of monochromatic plane waves with different wave vectors $\vec{k}$ and real amplitudes $\vec{E}_{0,k}$ (cf. Eq. (6.17)):

$$\vec{E}_k(\vec{r},t) = \vec{E}_{0,k}\,\cos(\vec{k}\cdot\vec{r}-\omega t+\phi) \tag{10.5}$$

$$\equiv \vec{A}_k\cos(\vec{k}\cdot\vec{r}-\omega t) - \vec{B}_k\sin(\vec{k}\cdot\vec{r}-\omega t), \tag{10.6}$$

with $\vec{A}_k = \vec{E}_{0,k}\cos\phi$ and $\vec{B}_k = \vec{E}_{0,k}\sin\phi$.

Note that every index k denotes a different wave vector $\vec{k}$ and is not related to the wave number $k = 2\pi/\lambda$ (the wavelength of the transmitted light waves is the same as for the ingoing light wave).

2.) Yee Shift: Before further processing, the electromagnetic field components were shifted in the x,y,z-direction to the middle of the corresponding Yee cell, respectively (cf. Fig. 6.1a):

$$E_{k,\mathrm{x}}(\vec{r},t): \quad y \mapsto y+\Delta y/2, \quad z \mapsto z+\Delta z/2, \tag{10.7}$$

$$E_{k,\mathrm{y}}(\vec{r},t): \quad x \mapsto x+\Delta x/2, \quad z \mapsto z+\Delta z/2, \tag{10.8}$$

$$E_{k,\mathrm{z}}(\vec{r},t): \quad x \mapsto x+\Delta x/2, \quad y \mapsto y+\Delta y/2, \tag{10.9}$$

where $\Delta x = \Delta y = \Delta z$ is the side length of the cubic Yee cell.

For each shift Δj in the direction $j = \{x, y, z\}$, the vector components $A_{k,i}$ and $B_{k,i}$ were recomputed as follows (see Appx. D.3 for derivation):

$$\breve{A}_{k,i} = A_{k,i}\cos(k_j\,\Delta j) - B_{k,i}\sin(k_j\,\Delta j), \tag{10.10}$$

$$\breve{B}_{k,i} = A_{k,i}\sin(k_j\,\Delta j) + B_{k,i}\cos(k_j\,\Delta j). \tag{10.11}$$

After performing the shifts specified in Eqs. (10.7) and (10.9), the resulting field vector is given by:

$$\vec{E}'_k(\vec{r},t) = \vec{A}'_k\cos(\vec{k}\cdot\vec{r}-\omega t) - \vec{B}'_k\sin(\vec{k}\cdot\vec{r}-\omega t), \tag{10.12}$$

with $\vec{A}'_k$ and $\vec{B}'_k$ being defined in Eqs. (D.16) to (D.21).

3.) Scattering Pattern: To study how much light is scattered under a certain angle (wave vector $\vec{k}$), the *scattering pattern* was computed, i. e. the intensity per wave vector (cf. Eq. (2.14)) normalized by the ingoing light intensity (I_0) per image pixel (px):

$$I_k = \frac{|\vec{E}'_{0,k}|^2}{I_0/(\#\,\mathrm{px})} = \frac{|\vec{A}'_k|^2 + |\vec{B}'_k|^2}{I_0/(\#\,\mathrm{px})}. \tag{10.13}$$

4.) Rotating Analyzer:

- **3D-PLI:** To model the 3D-PLI measurement, the electric field vector $\vec{E}'_k(\vec{r},t)$ was processed through a second linear polarizer (analyzer) rotated by angles ρ, yielding:

$$\vec{\tilde{E}}_k(\vec{r},t,\rho) = \vec{\tilde{A}}_k(\rho)\cos(\vec{k}\cdot\vec{r}-\omega t) - \vec{\tilde{B}}_k(\rho)\sin(\vec{k}\cdot\vec{r}-\omega t). \tag{10.14}$$

The x- and y-components of $\vec{\tilde{E}}_k(\vec{r},t,\rho)$ were computed by multiplying $\vec{E}'_k(\vec{r},t)$ with the Jones matrix of a rotated linear polarizer ($R(\rho)\cdot P_\mathrm{y}\cdot R(-\rho)$, cf. Sec. 2.5.1):[1]

$$\begin{aligned}\begin{pmatrix}\tilde{E}_{k,\mathrm{x}}(\vec{r},t,\rho)\\ \tilde{E}_{k,\mathrm{y}}(\vec{r},t,\rho)\end{pmatrix} &= \begin{pmatrix}\cos\rho & -\sin\rho\\ \sin\rho & \cos\rho\end{pmatrix}\begin{pmatrix}0 & 0\\ 0 & 1\end{pmatrix}\begin{pmatrix}\cos\rho & \sin\rho\\ -\sin\rho & \cos\rho\end{pmatrix}\begin{pmatrix}E'_{k,\mathrm{x}}(\vec{r},t)\\ E'_{k,\mathrm{y}}(\vec{r},t)\end{pmatrix}\\ &= \begin{pmatrix}\sin\rho\left(E'_{k,\mathrm{x}}(\vec{r},t)\,\sin\rho - E'_{k,\mathrm{y}}(\vec{r},t)\,\cos\rho\right)\\ -\cos\rho\left(E'_{k,\mathrm{x}}(\vec{r},t)\,\sin\rho - E'_{k,\mathrm{y}}(\vec{r},t)\,\cos\rho\right)\end{pmatrix}.\end{aligned} \tag{10.15}$$

The z-component was computed by applying Maxwell's equation in free space and assuming $\vec{\tilde{E}}_k(\vec{r},t,\rho) = \vec{\tilde{E}}_{0,k}(\rho)\ \mathrm{e}^{\mathrm{i}(\vec{k}\cdot\vec{r}-\omega t+\phi)}$ (plane monochromatic wave):[2]

$$\operatorname{div}\vec{\tilde{E}}_k(\vec{r},t,\rho) \;=\; 0 \quad\Leftrightarrow\quad \vec{k}\cdot\vec{\tilde{E}}_k(\vec{r},t,\rho) = 0 \tag{10.16}$$

$$\begin{aligned}\Leftrightarrow\ \tilde{E}_{k,\mathrm{z}}(\vec{r},t,\rho) &= -\frac{1}{k_\mathrm{z}}\left(k_\mathrm{x}\,\tilde{E}_{k,\mathrm{x}}(\vec{r},t,\rho) + k_\mathrm{y}\,\tilde{E}_{k,\mathrm{y}}(\vec{r},t,\rho)\right)\\ &\overset{(10.15)}{=} -\frac{k_\mathrm{x}\sin\rho - k_\mathrm{y}\cos\rho}{k_\mathrm{z}}\left(E'_{k,\mathrm{x}}(\vec{r},t)\,\sin\rho - E'_{k,\mathrm{y}}(\vec{r},t)\,\cos\rho\right).\end{aligned} \tag{10.17}$$

- **DI:** For the DI measurement, there are no polarizing filters behind the sample and no transformation is necessary. In this case holds: $\vec{\tilde{E}}_k(\vec{r},t,\rho) \equiv \vec{E}'_k(\vec{r},t)$.

5.) Objective Lens: As mentioned in Sec. 10.1.1, the objective lens was assumed to be ideal and both specimen and detector were assumed to lie within the corresponding focal planes of the lens. Thus, the propagation of the electromagnetic wave between sample and detector was neglected and $\vec{\tilde{E}}_k(\vec{r},t,\rho)$ was evaluated at the z-position of the detection plane behind the sample (defined as $z=0$):

$$\vec{r} = (r_\mathrm{x}, r_\mathrm{y}, 0)^\mathrm{T}. \tag{10.18}$$

To account for the numerical aperture (NA) of the objective lens, only k-vectors were processed that fulfill Eq. (10.4):

$$\theta_k = \arccos\left(\frac{k_\mathrm{z}}{\sqrt{k_\mathrm{x}^2+k_\mathrm{y}^2+k_\mathrm{z}^2}}\right) \le \arcsin(\mathrm{NA}). \tag{10.19}$$

[1] The Jones matrix formalism introduced in Sec. 2.5 assumes that the light is normally incident onto the optical elements represented by the Jones matrices. The Jones matrix of the linear polarizer can still be used for non-normally incident light because the polarizer acts only on the projection of the electric field vector (polarization vector) onto the xy-plane.

[2] Note that on the Yee grid (within the sample), $\operatorname{div}\vec{E}_k(\vec{r},t) = 0$ is not equivalent to $\vec{k}\cdot\vec{E}_k(\vec{r},t) = 0$ because $\vec{k}$ and $\vec{E}$ are only defined on the grid points (cf. Sec. 6.1).

6.) Detector Microlenses: As discussed in Sec. 10.1.1, the detector microlenses of the PM can be modeled by applying a moving average over the area of the microlens with radius $r_0 = 0.665\,\mu\text{m}$:

$$\breve{\vec{E}}_k(\vec{r},t,\rho) = \vec{\tilde{E}}_k(\vec{r},t,\rho) * \text{circ}(r)\ , \quad \text{circ}(r) = \begin{cases} \dfrac{1}{\pi\, r_0^2}\ , & r < r_0 \\ 0\ , & r \geq r_0. \end{cases} \tag{10.20}$$

7.) Intensity: In principle, the intensity detected by the camera sensor depends on the angle of incidence of the incident light: $I\,\cos\theta_k$. For the PM and the LAP, the numerical apertures are sufficiently small ($\text{NA} = \sin\theta_k \leq 0.15 \Leftrightarrow \cos\theta_k > 0.9886$). Thus, the angle dependence was neglected, which enables to represent the intensity $I(\vec{r},\rho)$ in 3D-PLI simulations as Fourier series in ρ, as described below.

With this assumption, the light intensity recorded by the camera is given by the absolute squared value of the electric field vector. To compute the intensity at a certain point $\vec{r}$ in the image plane, the electric field vectors were summed over $\vec{k}$ and averaged over time (see Appx. D.4 for derivation):

$$\begin{aligned} I(\vec{r},\rho) \propto |\vec{E}(\vec{r},\rho)|^2 \equiv\ & \frac{1}{T}\int_0^T \Big|\sum_{\vec{k}} \breve{\vec{E}}_k(\vec{r},t,\rho)\Big|^2\,\mathrm{d}t \\ \propto\ & \Big|\text{FT}^{-1}\Big\{\vec{\tilde{A}}_k(\rho) + \mathrm{i}\,\vec{\tilde{B}}_k(\rho)\Big\} * \text{circ}(r)\Big|^2, \end{aligned} \tag{10.21}$$

where FT^{-1} denotes the *inverse discrete Fourier transform*:

$$\text{FT}^{-1}\{f\} = \sum_{\vec{k}} f_{\vec{k}}\ \mathrm{e}^{\mathrm{i}\,\vec{k}\cdot\vec{r}}. \tag{10.22}$$

The *discrete Fourier transform (FT)* is defined analogously.

To save computing time, the convolution in Eq. (10.21) was replaced by a multiplication, making use of the *convolution theorem* (see Appx. D.5 for derivation):

$$I(\vec{r},\rho) \quad \propto \quad \Big|\text{FT}^{-1}\Big\{\Big(\vec{\tilde{A}}_k(\rho) + \mathrm{i}\,\vec{\tilde{B}}_k(\rho)\Big)\cdot \text{FT}\{\text{circ}(r)\}\Big\}\Big|^2 \tag{10.23}$$

$$\overset{(D.35)}{=} \Big|\text{FT}^{-1}\Big\{\Big(\vec{\tilde{A}}_k(\rho) + \mathrm{i}\,\vec{\tilde{B}}_k(\rho)\Big)\cdot 2\,\frac{J_1(r_0\,k_{\text{xy}})}{r_0\,k_{\text{xy}}}\Big\}\Big|^2, \tag{10.24}$$

where the function $J_1(x)$ is the Bessel function of the first kind of order one, with $k_{\text{xy}} \equiv \sqrt{k_{\text{x}}^2 + k_{\text{y}}^2}$ and $r_0 = 0.665\,\mu\text{m}$.

To simplify notation, the following abbreviations are defined:

$$\vec{\tilde{\mathcal{E}}}_k(\rho) \equiv \Big(\vec{\tilde{A}}_k(\rho) + \mathrm{i}\,\vec{\tilde{B}}_k(\rho)\Big)\cdot 2\,\frac{J_1(r_0\,k_{\text{xy}})}{r_0\,k_{\text{xy}}}, \qquad \vec{\tilde{\mathcal{E}}}(\vec{r},\rho) \equiv \text{FT}^{-1}\big\{\vec{\tilde{\mathcal{E}}}_k(\rho)\big\}, \tag{10.25}$$

$$\vec{\mathcal{E}}'_k \equiv \Big(\vec{A}'_k + \mathrm{i}\,\vec{B}'_k\Big)\cdot 2\,\frac{J_1(r_0\,k_{\text{xy}})}{r_0\,k_{\text{xy}}}, \qquad \vec{\mathcal{E}}'(\vec{r}) \equiv \text{FT}^{-1}\big\{\vec{\mathcal{E}}'_k\big\}. \tag{10.26}$$

The intensity is then given by:

$$I(\vec{r},\rho) \propto |\tilde{\mathcal{E}}_{\text{x}}(\vec{r},\rho)|^2 + |\tilde{\mathcal{E}}_{\text{y}}(\vec{r},\rho)|^2 + |\tilde{\mathcal{E}}_{\text{z}}(\vec{r},\rho)|^2. \tag{10.27}$$

- **3D-PLI:** The x- and y-components of the electric field vector $\vec{\tilde{E}}_k(\vec{r},t,\rho)$ behind the rotating analyzer were computed from $\vec{E}'_k(\vec{r},t) = \vec{A}'_k\cos(\vec{k}\cdot\vec{r}-\omega t) - \vec{B}'_k\sin(\vec{k}\cdot\vec{r}-\omega t)$ according to Eq. (10.15). As the equation is linear in the x- and y-components of $\vec{E}'_k(\vec{r},t)$, the x- and y-components of $\{\vec{A}'_k,\ \vec{B}'_k,\ \vec{\mathcal{E}}'_k\}$ are transformed to $\{\vec{\tilde{A}}_k(\rho),\ \vec{\tilde{B}}_k(\rho),\ \vec{\tilde{\mathcal{E}}}_k(\rho)\}$ according to the same equation. As the Fourier transform is independent from ρ, Eq. (10.15) also holds for the x- and y-components of $\vec{\mathcal{E}}'(\vec{r})$ and $\vec{\tilde{\mathcal{E}}}(\vec{r},\rho)$, yielding Fourier coefficients of order zero and two:

$$
\begin{aligned}
&|\tilde{\mathcal{E}}_\mathrm{x}(\vec{r},\rho)|^2 + |\tilde{\mathcal{E}}_\mathrm{y}(\vec{r},\rho)|^2 \\
&\overset{(10.15)}{=} \sin^2\rho\,|\mathcal{E}'_\mathrm{x}(\vec{r})|^2 + \cos^2\rho\,|\mathcal{E}'_\mathrm{y}(\vec{r})|^2 - \sin\rho\cos\rho\left(\mathcal{E}'_\mathrm{x}(\vec{r})\,\mathcal{E}'^{*}_\mathrm{y}(\vec{r}) + \mathcal{E}'^{*}_\mathrm{x}(\vec{r})\,\mathcal{E}'_\mathrm{y}(\vec{r})\right) \\
&= \underbrace{\frac{1}{2}\left(|\mathcal{E}'_\mathrm{x}(\vec{r})|^2 + |\mathcal{E}'_\mathrm{y}(\vec{r})|^2\right)}_{c_o} + \underbrace{\frac{1}{2}\left(|\mathcal{E}'_\mathrm{y}(\vec{r})|^2 - |\mathcal{E}'_\mathrm{x}(\vec{r})|^2\right)}_{c_2}\cos(2\rho) \\
&\quad \underbrace{-\frac{1}{2}\left(\mathcal{E}'_\mathrm{x}(\vec{r})\,\mathcal{E}'^{*}_\mathrm{y}(\vec{r}) + \mathcal{E}'^{*}_\mathrm{x}(\vec{r})\,\mathcal{E}'_\mathrm{y}(\vec{r})\right)}_{d_2}\sin(2\rho) \qquad (10.28) \\
&\equiv c_0(\vec{r}) + c_2(\vec{r})\,\cos(2\rho) + d_2(\vec{r})\,\sin(2\rho)\,, \qquad (10.29)
\end{aligned}
$$

where the trigonometric identities $\left(\cos^2 x = \frac{1}{2} + \frac{1}{2}\cos(2x),\ \sin x\cos x = \frac{1}{2}\sin(2x)\right)$ have been used.

Similar analytical calculations (see Appx. D.6) yield Fourier coefficients of orders zero, two, and four:

$$
\begin{aligned}
|\tilde{\mathcal{E}}_\mathrm{z}(\vec{r},\rho)|^2 = e_0(\vec{r}) &+ e_2(\vec{r})\,\cos(2\rho) + f_2(\vec{r})\,\sin(2\rho) \\
&+ e_4(\vec{r})\,\cos(4\rho) + f_4(\vec{r})\,\sin(4\rho)\,, \qquad (10.30)
\end{aligned}
$$

where $e_m(\vec{r})$ and $f_m(\vec{r})$ are functions of the inverse discrete Fourier transforms:

$$
X_\mathrm{x}(\vec{r}) \equiv \mathrm{FT}^{-1}\left\{\frac{k_\mathrm{x}}{k_\mathrm{z}}\mathcal{E}'_{k,\mathrm{x}}\right\}, \qquad X_\mathrm{y}(\vec{r}) \equiv \mathrm{FT}^{-1}\left\{\frac{k_\mathrm{y}}{k_\mathrm{z}}\mathcal{E}'_{k,\mathrm{x}}\right\}, \qquad (10.31)
$$

$$
Y_\mathrm{x}(\vec{r}) \equiv \mathrm{FT}^{-1}\left\{\frac{k_\mathrm{x}}{k_\mathrm{z}}\mathcal{E}'_{k,\mathrm{y}}\right\}, \qquad Y_\mathrm{y}(\vec{r}) \equiv \mathrm{FT}^{-1}\left\{\frac{k_\mathrm{y}}{k_\mathrm{z}}\mathcal{E}'_{k,\mathrm{y}}\right\}, \qquad (10.32)
$$

as described in Eqs. (D.46) to (D.50).

Thus, the transmitted light intensity $I(\vec{r},\rho)$ can be written in terms of a Fourier series:

$$
\begin{aligned}
I(\vec{r},\rho) \;\propto\; &|\tilde{\mathcal{E}}_\mathrm{x}(\vec{r},\rho)|^2 + |\tilde{\mathcal{E}}_\mathrm{y}(\vec{r},\rho)|^2 + |\tilde{\mathcal{E}}_\mathrm{z}(\vec{r},\rho)|^2 \\
&= a_0(\vec{r}) + a_2(\vec{r})\,\cos(2\rho) + b_2(\vec{r})\,\sin(2\rho) \\
&\quad + a_4(\vec{r})\,\cos(4\rho) + b_4(\vec{r})\,\sin(4\rho), \qquad (10.33) \\
a_0(\vec{r}) &\equiv c_0(\vec{r}) + e_0(\vec{r}), \quad a_2(\vec{r}) \equiv c_2(\vec{r}) + e_2(\vec{r}), \\
b_2(\vec{r}) &\equiv d_2(\vec{r}) + f_2(\vec{r}), \quad a_4(\vec{r}) \equiv e_4(\vec{r}), \quad b_4(\vec{r}) \equiv f_4(\vec{r})\,, \qquad (10.34)
\end{aligned}
$$

where the Fourier coefficients $a_m(\vec{r})$ and $b_m(\vec{r})$ are computed from the six inverse discrete Fourier transforms defined above: $\mathcal{E}'_\mathrm{x}(\vec{r})$, $\mathcal{E}'_\mathrm{y}(\vec{r})$, $X_\mathrm{x}(\vec{r})$, $X_\mathrm{y}(\vec{r})$, $Y_\mathrm{x}(\vec{r})$, $Y_\mathrm{y}(\vec{r})$.

For non-normally incident light ($k_\mathrm{x} \neq 0$ or $k_\mathrm{y} \neq 0$), the transmitted light intensity contains Fourier coefficients of order four (cf. Eqs. (10.30) to (10.32)). This explains the experimental observation that Fourier coefficients of order four also contain tissue information (see Appx. D.8) and suggests that these coefficients should also be taken into account when analyzing the 3D-PLI signal.

- **DI:** As there is no polarizing filter behind the sample, we can write $\vec{\tilde{\mathcal{E}}}(\vec{r}, \rho) = \vec{\mathcal{E}}'(\vec{r})$ and the intensity can directly be computed from the inverse discrete Fourier transform of $\vec{\mathcal{E}}'_k$ as defined in Eq. (10.26):

$$I(\vec{r}, \rho) \propto |\mathcal{E}'_\mathrm{x}(\vec{r})|^2 + |\mathcal{E}'_\mathrm{y}(\vec{r})|^2 + |\mathcal{E}'_\mathrm{z}(\vec{r})|^2. \tag{10.35}$$

Using Eq. (10.33) for 3D-PLI and Eq. (10.35) for DI, the light intensity was computed for arbitrary rotation angles ρ and normalized[3] by the ingoing light intensity per pixel:

$$I_\mathrm{N}(\vec{r}, \rho) = \frac{I(\vec{r}, \rho)}{I_0/(\#\,\mathrm{px})}. \tag{10.36}$$

For the polarimetric measurements, the measured light intensities are normalized by the light intensities measured without specimen to compensate for filter inhomogeneities (see Sec. 4.3). This image calibration could be modeled by performing an additional simulation run without sample. To save computing time, the simulated light intensities were simply normalized by I_0 (without considering the imaging system) and only relative values were used for the comparison between measured and simulated light intensities.

Implementation Figure 10.2 summarizes the most important steps of computing the transmitted light intensities for 3D-PLI and DI simulations (both for the PM and the LAP). The computation was carried out in *Python* (version 2.7.6) using the *NumPy* package (version 1.12.1) [187, 188]. To obtain the intensity at a certain pixel position (x,y), the inverse discrete Fourier transform was computed in two dimensions by means of the *Fast Fourier Transform (FFT)* [189]. To enable an efficient use of the FFT, the number of grid points in x and y (N_x and N_y) were set to be a multiple of 2:

$$N'_\mathrm{x} = 2^{m_\mathrm{x}} > N_\mathrm{x}, \tag{10.37}$$
$$N'_\mathrm{y} = 2^{m_\mathrm{y}} > N_\mathrm{y}. \tag{10.38}$$

Simulation Output Figure 10.3 shows the resulting images of a 3D-PLI and a DI simulation. The scattering pattern I_k shows the normalized intensity per k-vector, i. e. the intensity for different scattering angles $0° \leq \theta_k \leq 90°$. The white circles represent steps of $\Delta\theta_k = 10°$. To highlight the scattering peaks, the intensities are shown as log-plot and the scale was adapted to the maximum and minimum values. When simulating the PM measurement, only k-vectors within the inner circle ($\theta_k < 8.6°$) were included in the computation of the transmitted light intensity.

The Fourier coefficients ($a_{i,\mathrm{N}}$ and $b_{i,\mathrm{N}}$) were derived from a single 3D-PLI simulation according to Eqs. (10.34) and (10.36). Applying a standard 3D-PLI analysis (see Sec. 4.4.1), the parameter maps (transmittance, direction, retardation, and inclination) can be computed from the Fourier coefficients of order zero and two.

[3] A direct comparison between unnormalized light intensities is not always possible because the light intensity changes with the dimensions of the Yee grid and with the properties of the incident light.

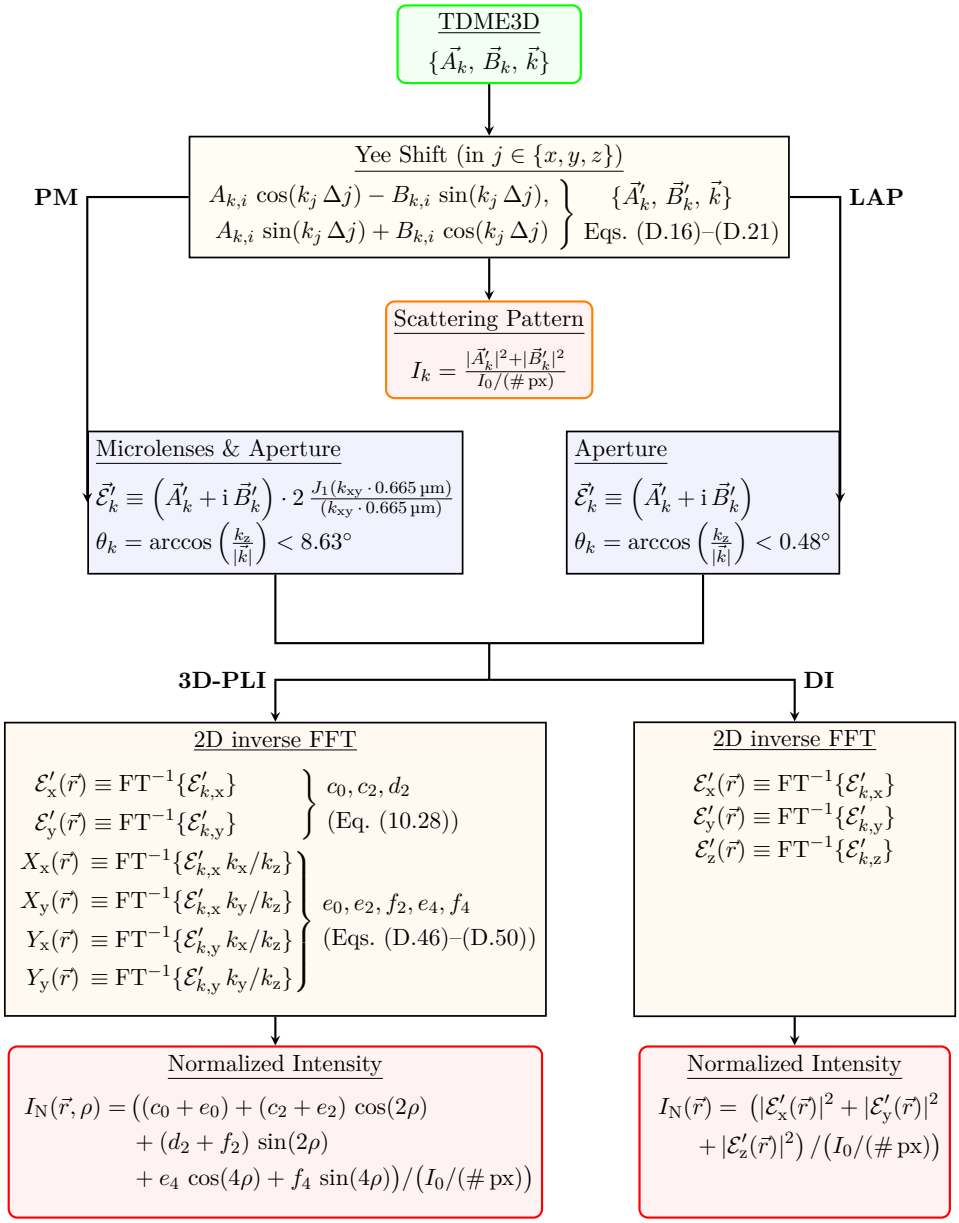

Fig. 10.2: Flow chart visualizing the computation of the transmitted light intensities for simulated 3D-PLI and DI measurements: The electromagnetic field components behind the sample (represented by a set of vectors $\{\vec{A}_k,\ \vec{B}_k,\ \vec{k}\}$, green box) are computed by TDME3D and shifted to the middle of the respective Yee cell. The spherical microlenses of the camera detector in the PM are modeled by applying a moving average over the area of the microlens with radius 0.665 µm, the numerical aperture of the imaging system (PM/LAP) is modeled by considering only waves with direction of propagation $\vec{k}$ that fulfill $\theta_k <$ arcsin(NA). Applying a 2D inverse discrete Fast Fourier Transform (FFT), the transmitted light intensities are computed and normalized by the ingoing light intensity I_0 per pixel (red boxes). Parts of this figure have been published in Menzel *et al.* (2018a) [67] Fig. 17.

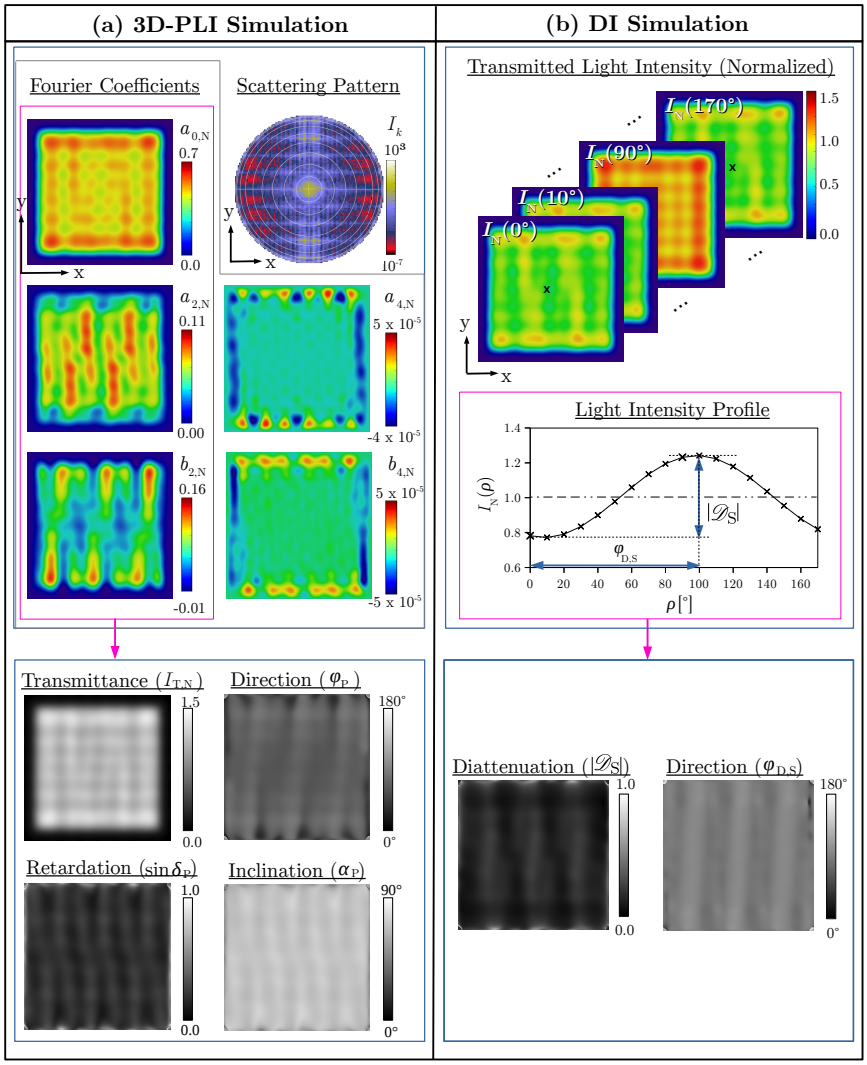

Fig. 10.3: Resulting images of a 3D-PLI and a DI simulation, shown exemplary for a hexagonal grid of aligned helical horizontal fibers (see Sec. 10.2.1 and Fig. 10.27). The simulations were performed for the imaging system of the PM with normally incident light and with the simulation parameters specified in Tab. 10.5. **(a)** The scattering pattern I_k was computed from the transmitted light intensity per k-vector according to Eq. (10.13). For the 3D-PLI simulation, the Fourier coefficients were computed from the normalized transmitted light intensity according to Eqs. (10.34) and (10.36). The parameter maps (transmittance, direction, retardation, and inclination) were computed from the Fourier coefficients of order zero and two, as described in Sec. 4.4.1 with $\alpha_P = \arccos(\sqrt{2\,\delta_P/\pi})$. **(b)** For the DI simulation, the transmitted light intensity was computed for linearly polarized light for different rotation angles $\rho = \{0°, 10°, \dots 170°\}$. The light intensity profile shows the intensity of the middle pixel (marked by a black "x"). The strength of the diattenuation $|\mathscr{D}_S|$ and the direction angle $\varphi_{D,S}$ were computed for each image pixel from the resulting light intensity profile by applying the same Fourier analysis as for the measured DI signal (see Sec. 4.4.3).

For the DI simulation, only one rotation angle can be simulated per simulation run. When modeling the DI measurement, the simulations need to be performed for all 18 rotation angles ($\rho = \{0°, 10°, \dots 170°\}$). In this case, the same analysis as in Sec. 4.4.3 can be applied to the computed light intensities. The strength of the simulated diattenuation signal $|\mathscr{D}_\mathrm{S}|$ and the corresponding phase $\varphi_\mathrm{D,S}$ are computed using Eqs. (4.36) and (4.37), assuming an ideal polarizer ($D_\mathrm{x} = 1$). Note that the index "S" is used to indicate that the FDTD simulations only account for diattenuation caused by anisotropic scattering.

Thus, the introduced simulation procedure is able to model both the 3D-PLI and the DI measurements, including all relevant parameter maps.

10.1.3 Simulation of the USAF Resolution Target

To test how well the simulation of the polarimetric measurements introduced in the previous sections can actually model the optical properties of the imaging systems, simulated and experimental data were compared for a well-defined sample – the USAF-1951 resolution target (see Sec. 7.1.4).

The geometric and optical properties of the USAF target were modeled both for the high- and the low-resolution targets that were measured with the PM and the LAP. For both samples, the normalized transmittance image ($I_\mathrm{T,N} \propto a_\mathrm{0,N}$) was computed from a simulated 3D-PLI measurement, as described in Sec. 10.1.2. To enable a direct comparison between simulation and experiment, the line profiles of the simulated transmittance images were determined for different detector pixel positions and the corresponding contrasts were compared to the contrasts of the measured line profiles (Figs. 7.6 and B.2) for different line widths.[4]

To figure out what is needed to efficiently model the optical properties of the PM and the LAP, the simulations were performed for light with different wavelengths and different angles of incidence (according to the wavelength spectrum and radiation of the respective light sources, cf. Sec. 7.1.1).

Section 10.1.3.1 introduces the simulation model of the high- and the low-resolution USAF targets. The simulation results and the comparison of simulated and measured line profiles are described in Sec. 10.1.3.2 for the PM and in Sec. 10.1.3.3 for the LAP.

10.1.3.1 Model of the USAF Resolution Target

The USAF targets used to determine the optical resolution of the PM and the LAP consist of a 1.5 mm soda-lime glass plate (substrate) covered by a thin chromium layer (coating), see Sec. 7.1.4. According to manufacturer information, the thickness of the chromium layer is about 100 nm for the high-resolution target (manufactured by *Edmund Optics GmbH*) and 120 nm for the low-resolution target (manufactured by *Thorlabs GmbH*). The chromium layers were simulated with the given thicknesses. To reduce computing time, the glass plate was simulated with a reduced thickness of 13.5 µm. As the thickness is still much larger than the wavelength, the simulation results are expected to be similar to simulations with 1.5 mm thick glass plate.

Figure 10.4 shows the dimensions of the simulation model. The model represents three lines of one element in the USAF resolution target: lines with width l (yellow), spacing l (yellow), and height $5\,l$ (cyan). The distance between the group of lines and the borders of the simulation volume is $4.5\,l$ (green). The x- and y-dimensions of the simulation

[4] Note that the values $a_\mathrm{0,N}$ obtained from a 3D-PLI simulation are derived for arbitrary rotation angles ρ, while the transmittance image obtained from a 3D-PLI measurement is computed by a discrete harmonic Fourier analysis over 18 different rotation angles.

volume ($14\,l$) were chosen to be as small as possible to reduce computing time, but large enough to avoid boundary effects when evaluating the contrasts of the line profiles. The targets were modeled for all evaluated line widths (cf. Tab. 7.2 in boldface): the x- and y-dimensions of the simulation model were scaled according to the line width, while the dimensions in the z-direction remained unchanged.

As the lateral resolution of the modeled imaging systems was assumed to be the same in the x- and y-direction, the simulations were only performed for the vertical lines of the USAF target. When comparing simulation and experiment, the contrasts of the simulated line profiles were compared to the measured contrasts determined both from horizontal and vertical line profiles.

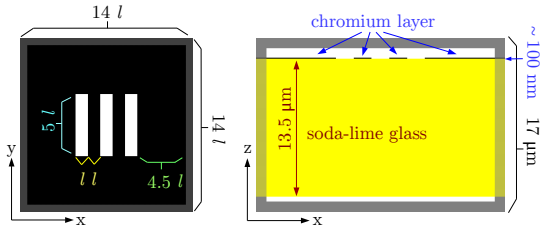

Fig. 10.4: Dimensions for the simulation model of the USAF target. The x- and y-dimensions of the simulation model scale according to the line width l, the dimensions in the z-direction remain unchanged. The simulation volume is surrounded by 1 µm thick UPML boundaries (gray).

The 3D-PLI measurement of the USAF target was simulated with TDME3D (see Sec. 6.3) using UPML boundaries. The glass substrate was modeled as a dielectric, while the chromium layer was modeled according to the polarization Drude model. The refractive indices and absorption coefficients of the glass and the chromium layer were chosen according to literature values (see Tab. 10.1), taking into account the different peak wavelengths ($\hat{\lambda}$) of the light sources in the PM and LAP (cf. Sec. 7.1.1). Note that the simulations were performed for slightly different wavelengths within the wavelength spectrum so that the real and imaginary parts of the refractive index (n, κ) might sightly differ from the values given in the table. Although small variations in the refractive indices might yield different total light intensities, the relative intensities (and thus the contrast of the line profiles) remain similar so that these differences were not considered in the simulations.

	PM ($\hat{\lambda} = 550\,\text{nm}$)	LAP ($\hat{\lambda} = 529\,\text{nm}$)	Reference
Substrate:	$n = 1.5251$	$n = 1.5263$	Rubin *et al.* (1985)
soda-lime glass	$\kappa = 2.20 \times 10^{-7}$	$\kappa = 1.75 \times 10^{-7}$	[190]
(1.5 mm thick)	$d = 13.5\,\mu\text{m}$	$d = 13.5\,\mu\text{m}$	
Coating:	$n = 2.7891$	$n = 2.6344$	Rakić *et al.* (1998)
chromium layer	$\kappa = 4.1976$	$\kappa = 4.1521$	[191]
($\approx 100\,\text{nm}$ thick)	$d = 100\,\text{nm}$	$d = 120\,\text{nm}$	

Tab. 10.1: The table shows the real and imaginary parts of the complex refractive index ($n' = n + \mathrm{i}\,\kappa$) as well as the thickness (d) of substrate and coating used to model the high- and low-resolution USAF targets for the PM and LAP measurements (for a peak wavelength $\hat{\lambda}$). The values for n and κ were derived from the data in the given references and by making use of the refractive index database (`https://refractiveindex.info`, © 2008–2017 Mikhail Polyanskiy).

10.1.3.2 Simulation of the PM Measurement

The USAF target was simulated for all line widths that were evaluated for the PM: $l = \{1.74, 1.95, 2.19, 2.46\}$ µm. The dimensions and refractive indices of the simulation model were chosen as in Fig. 10.4 and Tab. 10.1. All simulations were performed for a Yee mesh size of 25 nm, a Courant factor of 0.8, and 800 periods to ensure that the obtained simulation results are close to the stationary solution.

The 3D-PLI simulations were performed as described in Sec. 10.1.2, the transmittance ($a_{0,\mathrm{N}}$) images were computed for a numerical aperture NA = 0.15 and microlenses with a diameter of 1.33 µm.

To model the wavelength spectrum of the PM light source, the simulations were performed for different wavelengths: $\lambda = \{540, 545, 550, 555, 560\}$ nm. The resulting transmittance images were weighted according to the wavelength spectrum (see Fig. 10.5) and added together.

(a)

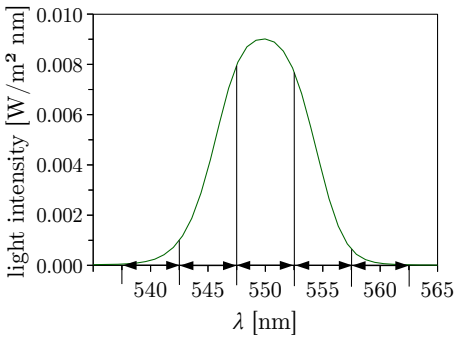

(b)

λ [nm]	area [%]
540	1.57
545	21.36
550	56.10
555	20.04
560	0.87

Fig. 10.5: Modeling the wavelength spectrum of the PM light source (cf. Fig. 7.1a): **(a)** The wavelength spectrum was sampled in steps of 5 nm. The area under the curve belonging to $\lambda = \{540, 545, 550, 555, 560\}$ nm was used to compute the contribution of these wavelengths to the spectrum. **(b)** The table lists the fractions of the total intensity for these wavelengths, which were used to compute the weighted sum of transmittance images representing the wavelength spectrum of the PM.

To model the diffuse light source of the PM (max. angle of incidence: $\theta_{\max} \approx 3°$, see Sec. 7.1.1), the simulations were performed for light with different angles of incidence: $\{\theta = 0°\}$, $\{\theta = 3°, \varphi = 6 \times 60°, 8 \times 45°\}$, cf. Eq. (10.2). The resulting transmittance images were weighted as described in Sec. 10.1.1 (using Eqs. (10.1) and (10.3) with $\theta = \Delta_\theta = 3°$) and added together. To simplify notation in the following, the simulation run for normally incident light is not explicitly mentioned and the short notation "$\eta \divideontimes \Delta\varphi$" is used to refer to the weighted sum of the simulation runs: $\{\theta = 0°\}$, $\{\theta = 3°, \varphi = \eta \times \Delta\varphi\}$, cf. Eq. (10.2).

Model of the Light Source Modeling the light source of the PM for all five wavelengths and all $8 \divideontimes 45°$ angles of incidence would require $5 \times 9 \times 4 = 180$ simulation runs for all four line widths. To find out how many simulation runs are really necessary, the transmittance images obtained from simulations with different wavelengths and angles of incidence were compared to each other, exemplary for a line width $l = 1.74$ µm.

For better comparison, the line profiles of the transmittance images were computed, i. e. the middle pixel in the y-direction evaluated along the x-direction (cf. white line

in Fig. 10.7b). To compare the simulation results independently of the detector pixel position, the line profiles were computed from the original transmittance images without downsampling, i. e. before taking the detector pixels into account.

Figure 10.6a shows the line profiles for normally incident light ($\theta = 0°$) simulated for different wavelengths ($\lambda = \{540, 545, 550, 555, 560\}$ nm). The line profiles for the other line widths are shown in Appx. D.9 in Fig. D.3a. The peak transmitted light intensities vary between wavelengths. The simulations for different line widths yield different peak intensities.

Figure 10.6b shows the line profiles for light with a wavelength $\lambda = 550$ nm simulated for different angles of incidence. The blue curve shows the line profile for normally incident light ($\theta = 0°$). The green, red, and cyan curves show the line profiles for diffuse light, computed from the weighted sum of several transmittance images with different angles of incidence $\{4 \divideontimes 90°, 6 \divideontimes 60°, 8 \divideontimes 45°\}$.

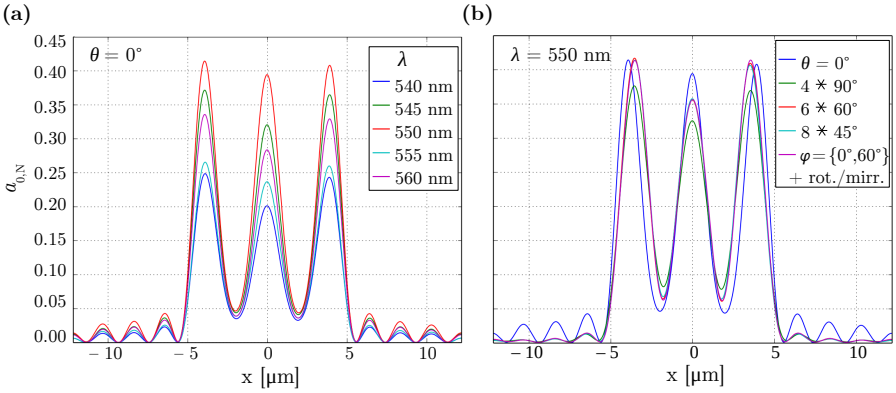

Fig. 10.6: Line profiles of the USAF target with line width $l = 1.74\,\mu$m (cf. Fig. 10.4) simulated for the optics of the PM. The line profiles show the middle pixel in the y-direction evaluated along the x-direction of the resulting transmittance images: **(a)** normally incident light with different wavelengths, **(b)** diffuse light with different angles of incidence and fixed wavelength ($\lambda = 550$ nm). The line profiles for diffuse light were generated by computing the weighted sum of the transmittance images obtained from several simulation runs with different angles of incidence, according to Eqs. (10.1) to (10.3). The notation $\eta \divideontimes \Delta\varphi$ indicates that the transmittance image was computed from the simulation runs: $\{\theta = 0°\}$, $\{\theta = 3°, \varphi = \eta \times \Delta\varphi\}$. While the first line profiles were generated from a complete range of azimuthal angles ($\varphi \in [0°, 360°)$), the line profile in magenta was generated from only three simulation runs: $\{\theta = 0°\}$, $\{\theta = 3°, \varphi = 0°\}$, and $\{\theta = 3°, \varphi = 60°\}$. The missing φ-angles were taken into account by rotating the resulting transmittance images by 180° or by flipping the images with respect to the x- or y-axes.

For diffuse light, the outer peaks move closer to the center. While $4 \divideontimes 90°$ yields a different line profile than $6 \divideontimes 60°$, the line profiles for $6 \divideontimes 60°$ and $8 \divideontimes 45°$ look almost identical. Thus, it is possible to model the diffuse light source by $6 \divideontimes 60°$ angles of incidence, which requires seven simulation runs.

To further reduce computing time, the diffuse light source was modeled by only three simulation runs: $\{\theta = 0°\}$, $\{\theta = 3°, \varphi = 0°\}$, and $\{\theta = 3°, \varphi = 60°\}$. The missing φ-angles were computed by exploiting the symmetry of the sample and the light source, i. e. by rotating the resulting transmittance images by 180° or by flipping the images with respect to the x- or y-axes. As the resulting line profile (magenta curve) is very

similar to the line profile obtained from $8 \times 45°$ angles of incidence, all other simulations for different wavelengths and line widths used only three simulation runs to model the diffuse light source.

Figure 10.7a shows the line profiles for diffuse light and different wavelengths for a line width $l = 1.74\,\mu\text{m}$. (The line profiles for the other line widths can be found in Appx. D.9 in Fig. D.3b.) The weighted sum over all five wavelengths (according to the table in Fig. 10.5b) yields a transmittance image that reflects both the diffuse light source of the PM and the wavelength spectrum. The yellow curve ("spectrum") in Fig. 10.7a shows the corresponding line profile, the image in Fig. 10.7b shows the transmittance image from which the line profile was generated (white dashed line). A similar transmittance image is obtained when summing only over three wavelengths ($\lambda = \{545, 550, 555\}\,\text{nm}$). This is expected because the outer wavelengths 540 and 560 nm make only a small contribution to the overall transmitted light intensity (see Fig. 10.5).

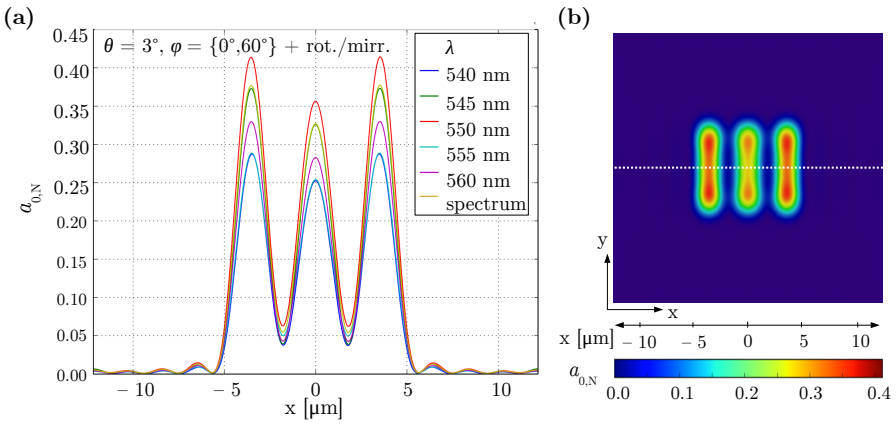

Fig. 10.7: USAF resolution target with line width $l = 1.74\,\mu\text{m}$ (cf. Fig. 10.4) simulated for the optics of the PM and diffuse light. The transmittance images were computed from three simulation runs with different angles of incidence ($\{\theta = 0°\}$, $\{\theta = 3°, \varphi = 0°\}$ $\{\theta = 3°, 60°\}$), and by 180°-rotation or flipping of the simulated transmittance images: **(a)** line profiles of the resulting transmittance images for different wavelengths λ, **(b)** transmittance image obtained from the weighted sum over all wavelengths (according to Fig. 10.5b). The corresponding line profile (white dashed line) is shown as yellow curve in subfigure (a).

The studies of the line profiles for $l = 1.74\,\mu\text{m}$ have shown that the light source of the PM can efficiently be modeled by summing over three wavelengths with three angles of incidence each. Thus, for all other line widths of the USAF target, the light source was modeled by only nine simulation runs instead of 45.

Comparison of Simulated and Measured Contrasts So far, the transmitted light intensities were evaluated without considering the detector pixels. To reproduce the line profiles obtained in the PM measurement (cf. Fig. 7.6a), the transmittance images need to be downsampled.

As described in Sec. 10.1.1, the finite detector pixels can be modeled by rasterizing the transmittance images with spacing $\Delta x = 1.33\,\mu\text{m}$ (along the x- and y-axes). To take different positions of the sample into account, the images were downsampled for all possible 53×53 raster origins with $\Delta = 25\,\text{nm}$: $(x_0, y_0) \in \{0, 25\,\text{nm}, \ldots, 1.325\,\mu\text{m}\}$.

Just as in the measurement (cf. Fig. 7.5), the line profiles were computed by selecting the pixels in a centered region ($-2\,l \leq y \leq 2\,l$) and averaging the corresponding intensity values along the y-axis. For all line profiles, the local minima and maxima were determined and the contrast was computed using Eq. (7.4).

Figure 10.8a shows the line profile of the transmittance image without downsampling (blue) and the line profiles of the downsampled transmittance images with minimum contrast (green) and maximum contrast (red), exemplary for a line width $l = 1.74\,\mu\text{m}$. The simulated contrast values ($\mathcal{C} = 48.3$–$65.1\,\%$) are much higher than the measured contrast values ($\mathcal{C} = 9.1$–$15.9\,\%$). This is also true for the other evaluated line widths (see non-bold numbers in Tab. 10.2).

More similar contrast values are obtained for all line widths when performing a moving average over an area of $2.66 \times 2.66\,\mu\text{m}^2$ (corresponding to 2×2 detector pixels in object space) before rasterizing the resulting transmittance image. The green and red curves in Fig. 10.8b show the resulting line profiles with minimum and maximum contrast values for $l = 1.74\,\mu\text{m}$. The simulated contrast values (Tab. 10.2 in boldface) are comparable to the measured contrast values (Tab. 10.2 in italics) for all evaluated line widths. For better comparison, the measured and simulated contrast values are represented in box-and-whisker diagrams (see Fig. 10.9) for all line widths.

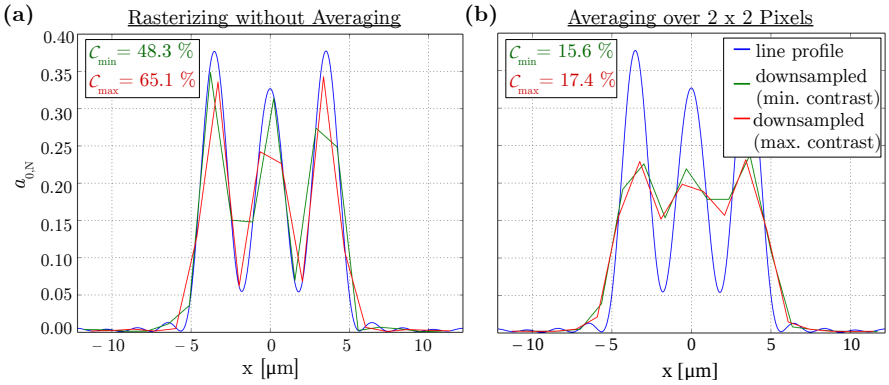

Fig. 10.8: Downsampled line profiles of the USAF resolution target (with line width $l = 1.74\,\mu\text{m}$) simulated for the optics of the PM. The blue curves show the line profiles of the original transmittance images without downsampling (cf. Fig. 10.7b). The green (red) curves show the downsampled line profiles with minimum (maximum) contrast, according to Eq. (7.4). **(a)** The downsampling was performed by rasterizing the transmittance image with spacing $\Delta x = 1.33\,\mu\text{m}$ along the x- and y-axes. **(b)** The downsampling was performed by applying a moving average over $2.66 \times 2.66\,\mu\text{m}^2$ before rasterizing the resulting image with spacing $1.33\,\mu\text{m}$.

Apparently, the model of the optical system described in Secs. 10.1.1 and 10.1.2 is not sufficient to model the optical resolution of the PM. The simulated contrast values of the USAF resolution target are much larger than the measured contrast values. Only when performing a moving average over 2×2 image pixels, the measured contrast values can be reproduced. Applying a moving average can be considered as an effective model for everything that is not taken into account in the current model of the optical system, e. g. additional lenses or the exact sensor architecture in the PM (cf. Appx. B.1.1).

l [µm]	$\tilde{\mathcal{C}}$ [%]	$\mathcal{C}_{\min}$ [%]	$\mathcal{C}_{\max}$ [%]
1.74	55.1	48.3	65.1
	16.2	**15.6**	**17.4**
	10.5	*9.1*	*15.9*
1.95	78.1	62.0	85.2
	31.9	**26.2**	**33.0**
	26.1	*22.4*	*33.2*
2.19	87.1	81.0	92.7
	46.8	**42.6**	**51.5**
	47.6	*42.9*	*54.3*
2.46	94.4	91.6	97.0
	65.0	**59.3**	**71.4**
	68.7	*61.6*	*71.5*
	• simulation without averaging • **simulation with averaging** • *measurement*		

Tab. 10.2: Median, minimum and maximum contrast values $\mathcal{C}$ of the USAF resolution target for different line widths l. The numbers in italics correspond to the contrast values obtained from 25 measurements with the PM (see Fig. 7.6b). The straight numbers correspond to the contrast values obtained from simulations of the USAF target for the optics of the PM. The downsampling was performed by rasterizing the transmittance image with spacing 1.33 µm along the x- and y-axes (non-bold numbers) or by applying a moving average over an area of $2.66 \times 2.66\,\mu\text{m}^2$ before rasterizing (bold numbers).

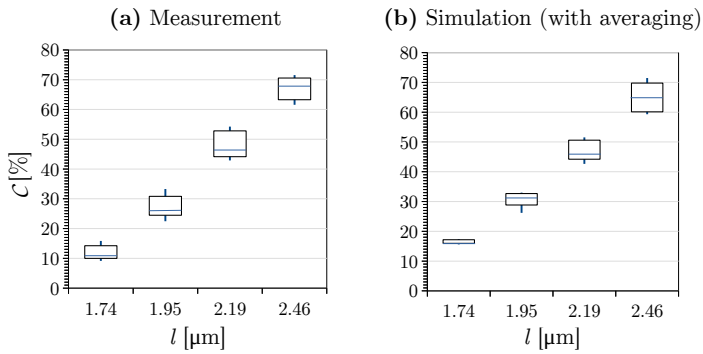

Fig. 10.9: Box-and-whisker diagrams for the contrast values of the USAF resolution target measured with the PM for different line widths l. The blue lines indicate the median contrast values, the boxes contain 25–75 % of the contrast values, the ends of the whiskers represent the minimum and maximum contrast values: **(a)** measured contrast values (see Tab. 10.2 in italics), **(b)** simulated contrast values (the downsampling was performed by applying a moving average over an area of $2.66 \times 2.66\,\mu\text{m}^2$ on the transmittance images and rasterizing with spacing $\Delta x = 1.33\,\mu\text{m}$ along the x- and y-axes, see Tab. 10.2 in bold).

As the average of the transmittance image is the same with and without averaging over 2×2 image pixels, the model of the optical system for the PM, described in Secs. 10.1.1 and 10.1.2, can still be used when comparing only average values between simulation and measurement.

10.1.3.3 Simulation of the LAP Measurement

The LAP light source has a much broader range of wavelengths and illumination angles than the light source of the PM (see Sec. 7.1.1).

To model the wavelength spectrum of the LAP light source, the transmitted light intensities were computed for different wavelengths $\lambda = \{496, \ldots, 581\}\,\text{nm}$ (see Fig. 10.10a) and weighted according to the wavelength spectrum (see Fig. 10.10b). The range of wavelengths was chosen such that the minimum and maximum wavelengths yield $1/16^{\text{th}}$ of the overall peak intensity.

(a)

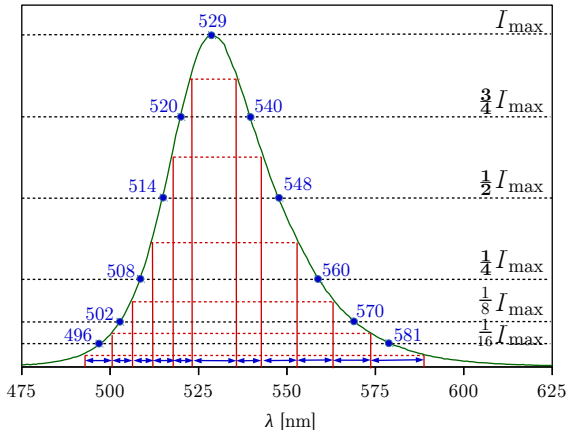

(b)

λ [nm]	area [%]
496	1.38
502	1.96
508	4.55
514	7.35
520	11.22
529	32.04
540	14.20
548	12.63
560	8.60
570	3.60
581	2.48

Fig. 10.10: (a) The wavelength spectrum of the LAP light source (see Fig. 7.1b) is less symmetric than the wavelength spectrum of the PM. Therefore, the spectrum was not sampled in equidistant steps, but with respect to the maximum intensity $I_{\max}$ of the peak wavelength. For this purpose, the wavelengths with intensities $\{1, 3/4, 1/2, 1/4, 1/8, 1/16\}\, I_{\max}$ were determined (blue numbers) and the wavelengths belonging to half of the intensity steps (red lines) were used to define borders around these wavelengths (blue arrows). The intensity steps were chosen such that the resulting wavelengths differ by 6–12 nm. The corresponding areas under the curve were used to compute the contribution of these wavelengths to the spectrum. **(b)** The table lists the fractions of the total intensity for these wavelengths, which were used to compute the weighted sum of transmittance images to model the wavelength spectrum of the LAP light source.

To model the diffuse light source of the LAP (max. angle of incidence: $\theta_{\max} \approx 25°$, see Sec. 7.1.1), the transmitted light intensities were computed for light with different angles of incidence $\theta = \{0°, \ldots, 25°\}$ and weighted by the angular distance between neighboring light rays.

Due to the large number of wavelengths and illumination angles, the light source of the LAP is computationally more intensive to model than the light source of the PM. In addition, the simulation volume of the USAF target needs to be much larger for the LAP. For the largest evaluated line width ($l = 35.08\,\mu\text{m}$), the simulation volume according to Fig. 10.4 would be about $490 \times 490 \times 17\,\mu\text{m}^3$, which is about 200 times larger than the largest simulation volume for the PM. In fact, the simulation volume needs to be even larger because the small numerical aperture of the LAP (NA = 0.0083) requires a sufficiently fine resolution in k-space. Even reducing the number of periods

(e. g. to 200 periods) would not make a simulation of the USAF target for the LAP in the same manner as for the PM feasible, especially when taking several wavelengths and angles of incidence into account. The model of the USAF target in Fig. 10.4 was therefore reduced to two dimensions.

2D Simulation Model The 3D model of the USAF target was reduced to 2D (xz-plane in Fig. 10.4) using periodic boundary conditions in the y-direction (cf. Sec. 6.3), i. e. the slits in the USAF target were approximated as infinitely long lines. This approximation is reasonable because the length of the slits ($5\,l \geq 124\,\mu\text{m}$) is much larger than the wavelength ($\lambda \leq 581\,\text{nm}$). Note that the light source was also restricted to 2D so that the angles of incidence were limited to the xz-plane ($\theta \geq 0°$, $\varphi \in \{0°, 180°\}$).

The dimensions of the simulation volume in the z-direction were chosen as in Fig. 10.4 (z = 17 µm, with 13.5 µm glass plate and 120 nm chromium layer). The dimensions in the x-direction were chosen to be much larger (x = 2600 µm) to achieve a sufficiently fine resolution in k-space ($\Delta\theta_k = 0.01°$). The refractive indices used for the LAP simulations are listed in Tab. 10.1. All simulations were performed for a Yee mesh size of 25 nm, a Courant factor of 0.8, and 800 periods. The transmittance ($a_{0,\text{N}}$) images, i. e. the 2D transmittance profiles, were computed from simulated 3D-PLI measurements as described in Sec. 10.1.2 for a numerical aperture NA = 0.0083 without microlenses.

Figure 10.11 shows the transmittance profiles for light with different wavelengths and angles of incidence, exemplary for a line width $l = 35.08\,\mu\text{m}$.

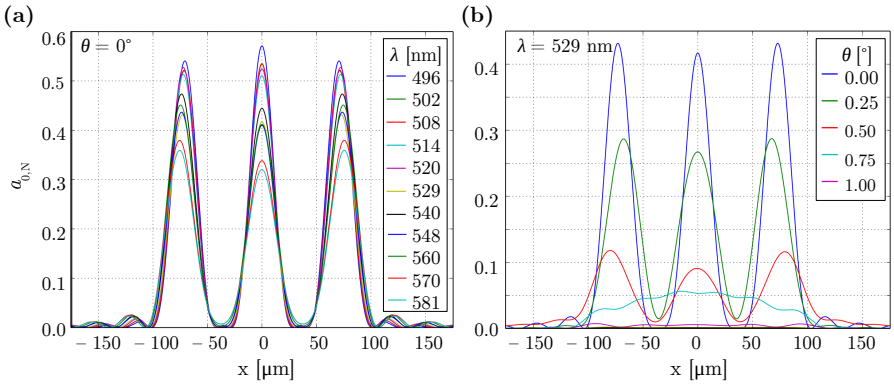

Fig. 10.11: Transmittance profiles obtained from 2D simulations of the USAF resolution target for the LAP (with line width $l = 35.08\,\mu\text{m}$): **(a)** normally incident light ($\theta = 0°$) with different wavelengths λ, **(b)** light with fixed wavelength ($\lambda = 529\,\text{nm}$) and different angles of incidence θ

Figure 10.11a shows the transmittance profiles for normally incident light ($\theta = 0°$) and different wavelengths. While the x-positions of the peaks are only slightly different, the peak intensities differ a lot between different wavelengths (they become maximal for $\lambda = 496\,\text{nm}$ and minimal for $\lambda = 581\,\text{nm}$).

Figure 10.11b shows the transmittance profiles for light with fixed wavelength ($\lambda = 529\,\text{nm}$) and different angles of incidence. With increasing θ, the peak intensities decrease and the peak widths increase. For $\theta \geq 0.75°$, there exist no three distinct peaks. For $\theta \geq 1°$, the transmitted light intensities ($a_{0,\text{N}}$) are almost zero.

Due to the small numerical aperture of the LAP, small changes in the angle of incidence make already a great difference in the resulting transmittance profiles. The small numerical aperture also implies that the discretization in k-space, which is caused by the finite x-size of the simulation volume, has a large impact on the simulation results. For this reason, the FDTD simulations should not only be performed for a broad range of different angles and wavelengths, but also for an increased x-size, which would require a lot of computing time. Therefore, the weighted sum over different wavelengths and angles of incidence was studied analytically.

Analytical Solution The USAF resolution target (three slits with width/spacing l) was modeled as a 1D grating (see Fig. 10.12) and the Fraunhofer diffraction pattern was computed analytically for different wavelengths λ and different angles of incidence θ.

The slits were considered to be a perfect grating with 100 % transmission within and 100 % extinction between the slits. The glass plate of the USAF target and the thickness of the chromium layer were neglected in this model. To apply the theory of Fraunhofer diffraction (see Sec. 2.1.3.3), it was assumed that the distance between the sample and the light source is much larger than l^2/λ and that the transmitted light intensity is detected in the far-field, i. e. in the back focal plane of the objective lens.

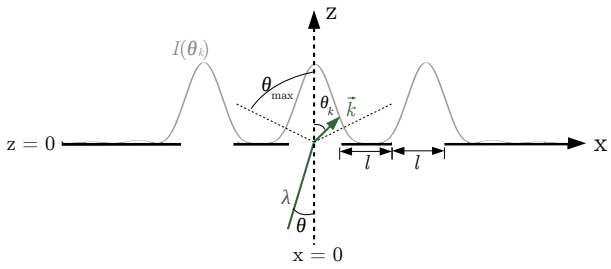

Fig. 10.12: 1D grating consisting of three slits with width and spacing l, representing the USAF resolution target for the LAP. The Fraunhofer diffraction pattern was computed for light with different angles of incidence θ and different wavelengths λ. The numerical aperture of the imaging system (NA) was taken into account by computing the transmitted light intensity $I(\theta_k)$ only from k-vectors with angles $\theta_k \leq \theta_{\max} = \arcsin(\mathrm{NA})$.

Under these assumptions, the complex amplitude U of a light wave with wavelength λ and angle of incidence θ that propagates through a 1D grating with $N = 3$ slits and line width l is given by (see Appx. D.7 for derivation):

$$U(\theta_k)_{\lambda,\theta,l} \propto \frac{2}{\lambda\, kp} \sin\left(k\, p\, \frac{l}{2}\right) \mathrm{e}^{2\,\mathrm{i}\,k\,p\,l} \left(\frac{1 - \mathrm{e}^{-6\,\mathrm{i}\,k\,p\,l}}{1 - \mathrm{e}^{-2\,\mathrm{i}\,k\,p\,l}}\right), \tag{10.39}$$

$$p \equiv \sin\theta_k - \sin\theta. \tag{10.40}$$

To account for the small numerical aperture of the LAP (NA = 0.0083), only k-vectors with angles $\theta_k \leq \arcsin(\mathrm{NA}) \approx 0.48°$ were considered. The transmitted light intensity in real space, i. e. the transmittance profile $I(x) \propto |U(x)|^2$, was computed from $U(\theta_k < 0.48°)$ via an inverse discrete Fourier transform in 1D:

$$I(x)_{\lambda,\theta,l} \propto \left|\mathrm{FT}^{-1}\left\{U(\theta_k < 0.48°)_{\lambda,\theta,l}\right\}\right|^2. \tag{10.41}$$

Figure 10.13 shows the analytically computed transmittance profiles for different wavelengths and angles of incidence, exemplary for a line width $l = 35.08\,\mu\text{m}$.

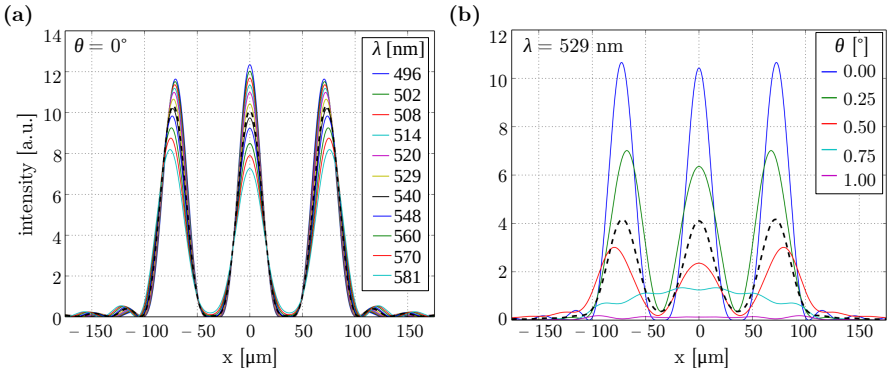

Fig. 10.13: Analytically computed transmittance profiles for the USAF resolution target of the LAP with line width $l = 35.08\,\mu\text{m}$ (Fraunhofer diffraction pattern of a 1D grating, see Appx. D.7): **(a)** normally incident light ($\theta = 0°$) with different wavelengths λ, **(b)** light with fixed wavelength ($\lambda = 529\,\text{nm}$) and different angles of incidence θ. The black dashed lines show the transmittance profiles obtained from the weighted sum over different wavelengths (according to Fig. 10.10b) and the weighted sum over different angles of incidence (same weighting for equidistant angles), respectively.

Figure 10.13a shows the transmittance profiles for normally incident light ($\theta = 0°$) and different wavelengths. With increasing wavelength, the peak intensities decrease continuously and the outer peaks move slightly further apart. The black dashed line shows the transmittance profile obtained from the weighted sum over all wavelengths (according to the table in Fig. 10.10b). The profile looks similar to the transmittance profile of the peak wavelength $\lambda = 529\,\text{nm}$ (yellow line).

Figure 10.13b shows the transmittance profiles for light with fixed wavelength ($\lambda = 529\,\text{nm}$) and different angles of incidence. The black dashed line shows the transmittance profile obtained by averaging all five angles of incidence. Compared to the transmittance profile for normally incident light, the contrast is reduced (the minimum intensity values between the peaks become larger).

Analytically computed and simulated transmittance profiles show exactly the same behavior for light with different angles of incidence (cf. Figs. 10.11b and 10.13b). The transmittance profiles for light with different wavelengths look different (cf. Figs. 10.11a and 10.13a). However, when being normalized to the peak intensity, analytically computed and simulated transmittance profiles look similar for different wavelengths. This suggests that the differences are mostly caused by the glass substrate and by the discretization in k-space which inevitably occurs in the 2D simulations due to the finite x-size of the simulation volume. As the normalized profiles of the 2D simulations look similar to the analytical ones, the k-discretization and the glass substrate seem to influence mostly the total light intensity and not the contrast of the lines. This demonstrates that the analytically computed Fraunhofer diffraction pattern can be used instead of the 2D simulations to model the transmitted light intensities for the USAF target measured with the LAP.

To consider the whole range of wavelengths and illumination angles of the LAP light source, the analytical transmittance profiles were computed for all combinations $\lambda =$

$\{496, \ldots, 581\}$ nm and $\theta = \{0°, 0.25°, \ldots, 25°\}$, weighted according to the wavelength spectrum (see Fig. 10.10b), and added together.

To compare the contrasts of the analytically computed transmittance profiles to the contrasts of the line profiles obtained from the LAP measurements (see Figs. 7.6 and B.2b), the transmittance profiles were downsampled. For this purpose, the transmittance profiles were convolved with a rectangle function of width $\Delta x = 21\,\mu$m (corresponding to the pixel size in object space) and sampled with spacing Δx for different sampling positions $x_0 = \{0,\ 25\,\text{nm},\ \ldots,\ 20.975\,\mu\text{m}\}$. Figure 10.14 shows the transmittance profiles for all evaluated line widths l after the convolution (blue curves) and the downsampled profiles with minimum (green) and maximum (red) contrast values. The contrasts $\mathcal{C}$ were computed by averaging the local minima and maxima of the downsampled profiles and using Eq. (7.4).

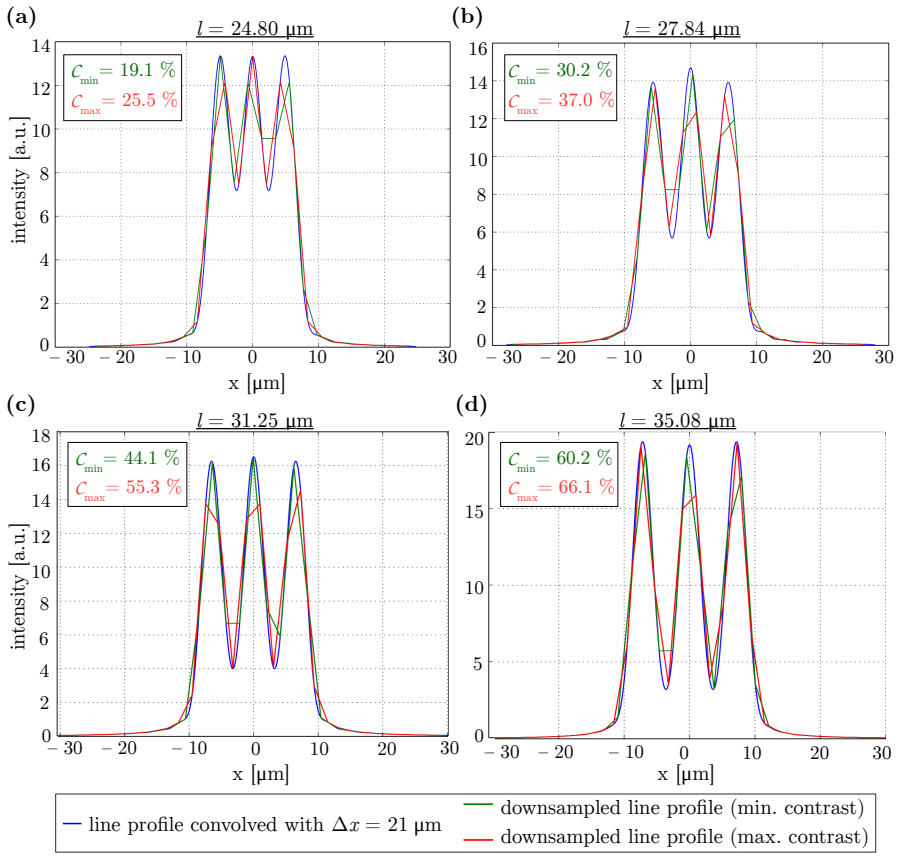

Fig. 10.14: Downsampled transmittance profiles of the USAF resolution target for different line widths l computed analytically from the Fraunhofer diffraction pattern of a 1D grating considering the optics of the LAP: The blue lines show the profiles after convolution with a rectangle function of width $\Delta x = 21\,\mu$m, the green (red) lines show the downsampled profiles with minimum (maximum) contrast values. The contrasts $\mathcal{C}$ were computed by averaging the local minima and maxima of the downsampled profiles and using Eq. (7.4).

As expected, the analytically computed contrast values decrease with decreasing line width. Table 10.3 shows the median, minimum and maximum contrast values for all evaluated line widths (bold numbers) in comparison to the measured contrast values (italic numbers).

l [µm]	$\tilde{\mathcal{C}}$ [%]	$\mathcal{C}_{\min}$ [%]	$\mathcal{C}_{\max}$ [%]
24.80	**21.4**	**19.0**	**25.5**
	16.1	*12.7*	*18.9*
27.84	**33.3**	**30.2**	**36.9**
	27.8	*20.7*	*31.9*
31.25	**53.1**	**44.1**	**55.3**
	39.5	*33.3*	*43.8*
35.08	**62.4**	**60.2**	**66.1**
	48.8	*46*	*54.9*
	• **analytical solution**		
	• *measurement*		

Tab. 10.3: Median, minimum and maximum contrast values $\mathcal{C}$ of the USAF resolution target for different line widths l. The numbers in italics correspond to the contrast values obtained from 25 measurements with the LAP (see Fig. 7.6b). The contrast values in bold were computed analytically from the Fraunhofer diffraction pattern of the USAF target (1D grating) for the LAP. Downsampling was performed by convolving the transmittance profiles with a rectangle function of width $\Delta x = 21\,\mu\text{m}$ and sampling with spacing Δx.

For better comparison, all measured and analytically computed contrast values are shown as box-and-whisker diagrams in Fig. 10.15.

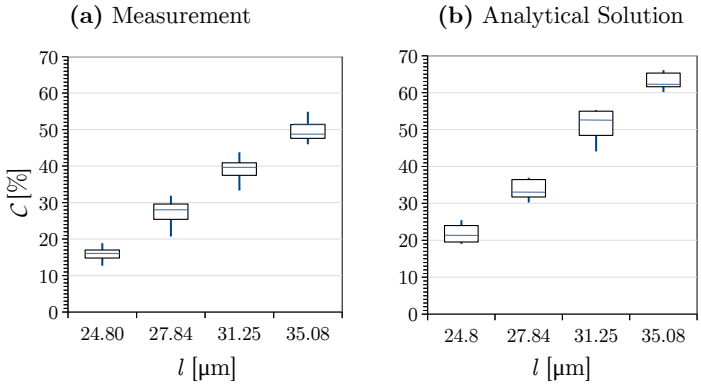

Fig. 10.15: Box-and-whisker diagrams for the contrast values of the USAF resolution target measured with the LAP for different line widths l. The blue lines indicate the median contrast values, the boxes contain 25–75 % of the contrast values, the ends of the whiskers represent the minimum and maximum contrast values: **(a)** measured contrast values (see Tab. 10.3 in italics), **(b)** analytically computed contrast values (see Tab. 10.3 in bold).

For all line widths, the analytically computed contrast values are slightly larger than the measured contrast values. For $24.8\,\mu\text{m} \leq l \leq 31.25\,\mu\text{m}$, the maximum measured contrast values correspond to the minimum contrast values obtained from the analytical solution. Thus, the analytical solution shows similar tendencies as the measurement.

In general, it can be noted that the optics of the PM is more suitable to be modeled with FDTD simulations than the optics of the LAP. Modeling the LAP light source requires a lot of simulation runs with different wavelengths and angles of incidence, and the optical resolution of the imaging system can only be studied analytically. While the optical resolution of the PM can efficiently be modeled by three different wavelengths and three angles of incidence each, yielding similar contrast values as in the measurement (see Fig. 10.9), the optical resolution of the LAP can only be investigated analytically and the resulting contrast values are less comparable to the measured contrast values, even when taking a broad range of wavelengths and illumination angles into account.

10.2 Geometries of the Simulated Fiber Configurations

This section introduces the fiber configurations that were used for the simulations of the transmittance and diattenuation effects presented in Chaps. 11 and 12.

To investigate which geometry parameters are responsible for the observed effects and to understand which parameters are needed to reproduce the experimental observations, a bottom-up approach was pursued: starting from a simple fiber configuration (hexagonal grid of straight fibers), the configurations were made more and more complex until they looked more comparable to realistic nerve fiber architectures.

The majority of myelinated axons in the brain have diameters of 1 µm or less (see Sec. 3.1.2). The fibers were therefore simulated with diameters of about 1 µm. This size is small enough to simulate a large number of fibers in a volume $< 100^3\,\mu m^3$ and large enough to include the inner fiber structure, e. g. the myelin sheath.

10.2.1 Hexagonal Grid of Fibers

Microscopy images of nerve fiber bundles show that the nerve fibers are densely packed and have similar inter-fiber distances[5], see Fig. 10.16a. In a first simple model, the fibers were therefore arranged on a hexagonal grid (densest circle packing) with equal inter-fiber distances, see Fig. 10.16b. The fiber diameters were chosen to be 1 µm and the inter-fiber-distances 0.4 µm, which allows to simulate also non-straight fibers without collision control.

The fiber geometries were generated with built-in functions of TDME3D (see Secs. 6.3 and 6.4) for different inclination angles. The configurations have different degrees of complexity: First, the fibers were simulated as straight cylinders. In a next step, the straight fibers were replaced by slightly undulated fibers described by a helix (see Fig. 10.17d) with small radius $r = 0.2\,\mu m$ and long stride $s = 9\,\mu m$ (see Fig. 10.17a). To break the symmetry, the fibers were arranged in four different groups (see different colors in Fig. 10.16b) and each group was assigned a different offset in the x-direction (0 µm, 2.25 µm, 4.5 µm, 6.75 µm), see Fig. 10.17b. To further increase disorder, the four groups were assigned four different strides ($s = 3\,\mu m$, 6 µm, 9 µm, 12 µm), see Fig. 10.17c.

[5] Note that inter-fiber distances might differ between native and fixated tissue.

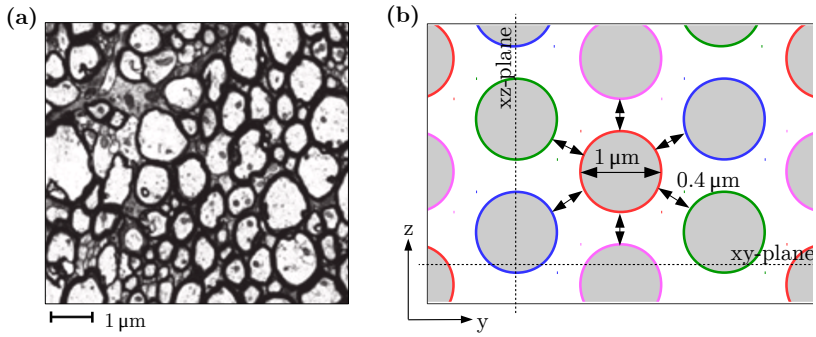

Fig. 10.16: (a) Electron microscopy photomicrograph of a nerve fiber bundle (pyramidal tract fibers) of a two-month-old rat (Adapted from: Xie *et al.* [192] Fig. 2b, Copyright (2014), with permission from Spandidos Publications). **(b)** Geometry of the hexagonal grid of simulated (straight horizontal) fibers (diameter: 1 µm, inter-fiber distance: 0.4 um). The different colors (blue, green, magenta, red) mark the four different groups of fibers used to realize different fiber geometries (cf. Fig. 10.17).

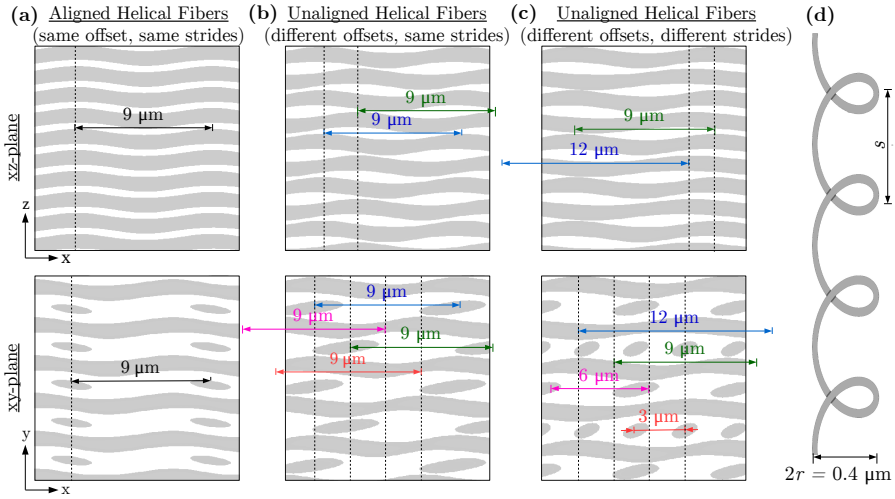

Fig. 10.17: Simulated geometries for the hexagonal grid of helical horizontal fibers: The fibers were arranged in a hexagonal grid (see Fig. 10.16b) with different offsets in the x-direction. All fibers follow a helix with radius $r = 0.2\,\mu m$ and stride s (d). In case of the aligned helical fibers (a), all fibers have the same offset and the same stride ($s = 9\,\mu m$). In case of the unaligned helical fibers, there exist four groups of fibers with different offsets (0 µm, 2.25 µm, 4.5 µm, 6.75 µm) and same strides (b) or with different offsets and different strides ($s = 3\,\mu m$, 6 µm, 9 µm, 12 µm) (c).

10.2.2 Bundle of Densely Grown Fibers

The fiber configurations presented in Sec. 10.2.1 are highly symmetric and periodic and can be described by simple geometric functions. Nerve fibers in brain tissue, however, are diversely distributed and do not follow simple geometric functions. To generate more realistic fiber bundles with densely packed fibers, the Fiber Growing Algorithm (FGA)

described in Sec. 6.4.1 was used. The algorithm generates bundles of densely grown fibers with similar fiber orientations and without collisions.

To generate a densely grown fiber bundle, $N = 700$ fibers (circles) were distributed in an area $x \times y = 45 \times 30\,\mu m^2$ with randomly uniformly distributed radii $r \in [0.5, 0.8]\,\mu m$. The average radius (0.65 µm) was chosen to be large enough to still enable the generation of bundles with larger fiber radius distributions (see Sec. 10.2.3.2). The number of fibers was chosen to be as large as possible so that the algorithm still finds a solution in a reasonable amount of time for $z = 45\,\mu m$. To generate fiber bundles with different inclination angles, the resulting bundle of densely grown fibers was rotated around the y-axis with respect to the center position and cropped to a volume of $30 \times 30 \times 30\,\mu m^3$.

As the algorithm only finds a solution for which the fibers do not intersect (in the xy-plane), fibers might still touch each other. As a consequence, the fiber architecture might not be correctly represented in the simulations because there is no boundary surface between touching fibers in the generated (discretized) fiber geometry. To avoid this problem, the fiber radii were reduced by 5 %, yielding fiber radii between 0.475 µm and 0.76 µm. To simplify notation in the following, the fiber radius r is given in terms of the initial radius (before reducing the radius by 5 %).

Figure 10.18a shows the geometry for the horizontal bundle of densely grown fibers.

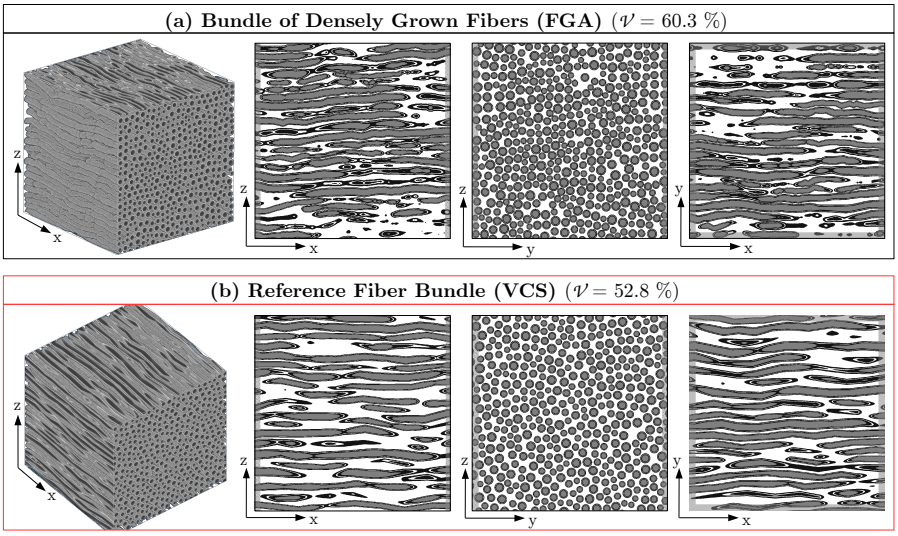

Fig. 10.18: 3D view and cross-sections through mid-planes for a horizontal fiber bundle: **(a)** bundle of densely grown fibers generated by the FGA, **(b)** reference fiber bundle generated by the VCS (see Sec. 10.2.3.1, with maximum displacement of fiber midpoints $\Xi = 1\,\mu m$). For both fiber bundles, 700 fibers with radii $r \in [0.5, 0.8]\,\mu m$ were generated in a volume of $45 \times 30 \times 45\,\mu m^3$ and cropped to a volume of $30 \times 30 \times 30\,\mu m^3$. Note that all fiber radii were reduced by 5 % to prevent fibers from touching each other. In addition to the geometry, the volume fraction $\mathcal{V}$ is given (i. e. the volume filled by fibers divided by the total volume).

As the bundle of densely grown fibers was generated from a random distribution of circles with random initial displacements, it is not feasible to give a complete description of the geometry. To characterize the geometry of the underlying fibers, the *volume fraction* and the *fiber orientation dispersion* were determined for the generated fiber bundles.

The volume fraction $\mathcal{V}$ is a measure of how densely the fibers are packed within the generated fiber bundle. It is given by the volume filled by fibers divided by the total volume ($30 \times 30 \times 30\,\mu m^3$). For all inclination angles $\alpha = \{0°, 10°, \ldots, 90°\}$, the volume fraction was determined to be between 60.2 % and 60.6 %, i. e. the bundles of densely grown fibers all have a similar fiber density.

The fiber orientation dispersion is a measure of how the fibers are distributed within the volume, i. e. how the orientation of individual fibers differs from the predominant direction of growing. It is given by the vector angle differences between the local orientation vectors of the fiber segments (i. e. the vectors between two neighboring fiber midpoints) and the predominant orientation of the fiber bundle (direction of growing). The blue curve in Fig. 10.19 shows the corresponding histogram for the bundle of densely grown fibers. To account for different lengths of fiber segments, the vector angle difference was weighted by the fraction of the total fiber length, i. e. the vector length divided by the total length of fibers in the volume. To compute the fiber orientation dispersion independently of the inclination angle, the fiber volume was evaluated before cropping ($45 \times 30 \times 45\,\mu m^3$). The fiber orientation dispersion for the bundle of densely grown fibers follows a Rayleigh distribution[5] (dashed line) with mode around 10°.

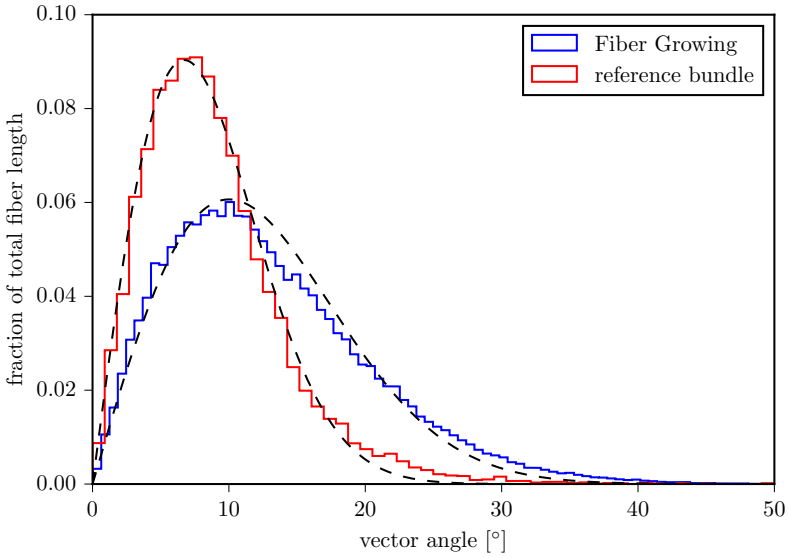

Fig. 10.19: Fiber orientation dispersion for the bundle of densely grown fibers generated by the FGA (blue histogram, cf. Fig. 10.18a) and for the reference fiber bundle generated by the VCS with radii $r \in [0.5, 0.8]\,\mu m$ and a maximum displacement of fiber midpoints $\Xi = 1\,\mu m$ (red histogram, cf. Fig. 10.18b). The dashed lines show Rayleigh distributions[5] with mode σ fitted to the histograms with a least square fit (blue histogram: $\sigma = (10.00 \pm 0.06)°$; red histogram: $\sigma = (6.71 \pm 0.03)°$).

[5]The Rayleigh distribution with mode σ is fitted with a least square fit: $\frac{x}{\sigma^2}\, e^{-x^2/(2\sigma^2)}$

10.2.3 Complex Fiber Bundles

The bundle of densely grown fibers contains fibers with similar orientations and similar radii. More complex fiber configurations containing fibers with different orientations and radii or crossing fibers were generated by the Volume Colliding Solver (VCS) described in Sec. 6.4.2. To still enable a comparison with the simulation results of the bundle of densely grown fibers, the initial list of fiber midpoints and radii (step 1 in Sec. 6.4.2) was computed with the FGA (700 straight fibers distributed in an area of $40 \times 30\,\mu m^2$, cf. Sec. 10.2.2). To generate a bundle with similar properties as the bundle of densely grown fibers, the same distribution of fiber radii was used ($r \in [0.5, 0.8]\,\mu m$) and the maximum displacement of the fiber midpoints (step 2 in Sec. 6.4.2) was chosen to be $\Xi = 1\,\mu m$. In the following, this configuration is referred to as the *reference fiber bundle*. Figures 10.18 and 10.19 show the geometry and the fiber orientation dispersion of the reference fiber bundle (in red) in comparison to the bundle of densely grown fibers. The subsequent sections describe how different parameters of the reference fiber bundle were varied to obtain different fiber configurations.

10.2.3.1 Different Fiber Orientation Distributions

To generate bundles with different fiber orientation distributions, the maximum displacement Ξ of the reference fiber bundle was varied: $\Xi = \{0,\ 1,\ 2.5,\ 5,\ 7.5,\ 10\}\,\mu m$. Figure 10.20 shows the resulting fiber bundles for different Ξ. The volume fraction $\mathcal{V}$ of the fibers decreases (almost) linearly with increasing Ξ, from about 60 % to 33 %.

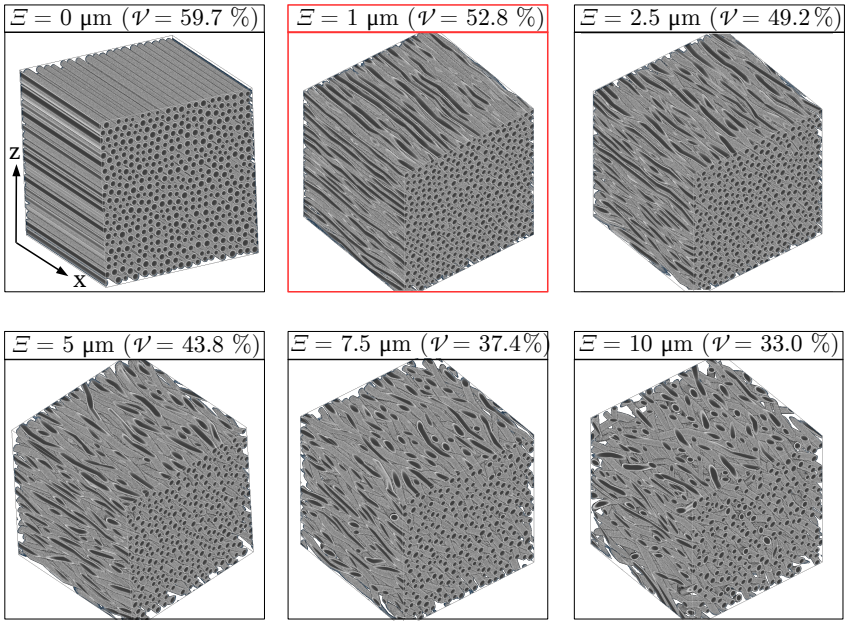

Fig. 10.20: Horizontal fiber bundle ($30 \times 30 \times 30\,\mu m^3$) with fiber radii $r \in [0.5, 0.8]\,\mu m$ and different fiber orientation distributions (i. e. different maximum displacements Ξ of fiber midpoints) generated by the VCS. The volume fraction $\mathcal{V}$ of the fibers decreases with increasing Ξ. The red frame highlights the reference fiber bundle (cf. Fig. 10.18b).

The histograms of the fiber orientation dispersion follow a Rayleigh distribution (see Fig. 10.21a), the mode of the distributions increases (almost) linearly with increasing Ξ (see Fig. 10.21b).

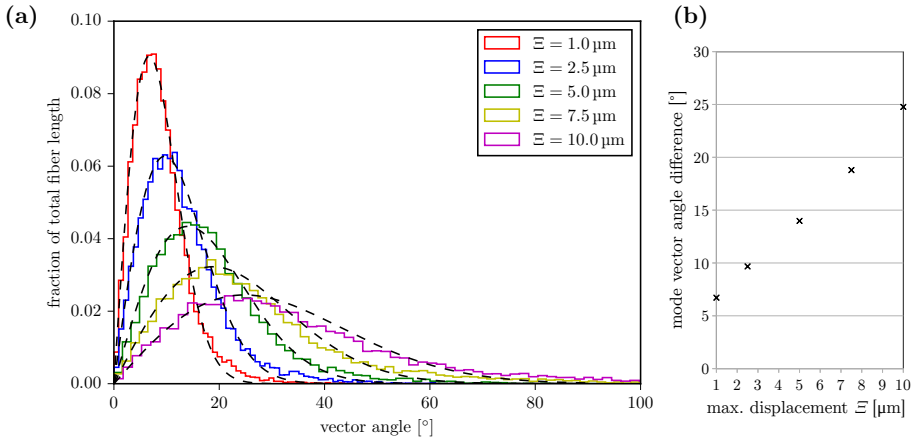

Fig. 10.21: Fiber orientation dispersion for bundles with different maximum displacements Ξ of fiber midpoints (cf. Fig. 10.20): **(a)** Histograms of the vector angle differences between the local fiber orientation vectors and the predominant fiber orientation (x-axis). The red histogram belongs to the reference fiber bundle (cf. Fig. 10.18b). The dashed lines show the fitted Rayleigh distributions with mode σ. The relative error of all fitted mode values is below 0.9 %. **(b)** Mode angle difference (σ) for different maximum displacements Ξ.

This demonstrates that the maximum displacement of fiber midpoints (Ξ) is a good parameter to characterize the fiber orientation distribution of the fiber bundle.

10.2.3.2 Different Fiber Radius Distributions

To generate fiber bundles with different fiber radius distributions, the reference fiber bundle was initialized with the same average radius ($r_{\text{avg}} = 0.65\,\mu\text{m}$) and different (randomly uniform) radius distributions: $\Delta r = r_{\max} - r_{\min} = \{0, 0.1, 0.2, 0.3, 0.4, 0.5, 0.6, 0.7\}\,\mu\text{m}$. The average radius was chosen to be large enough so that the minimum radius for $\Delta r = 0.7\,\mu\text{m}$ ($r_{\min} = 0.3\,\mu\text{m}$) is still reasonable (cf. Sec. 3.1.2).[6]

Figure 10.22 shows the resulting fiber bundles for different Δr. The volume fraction is similar for different fiber radius distributions ($\mathcal{V} = 52.0$–$53.6\,\%$).

The histograms of the fiber orientation dispersion follow a Rayleigh distribution with similar mode values ($\sigma = 6.7$–$7.1°$), see Fig. 10.23.

[6] Recall that all fiber radii were reduced by 5 % to prevent fibers from touching each other.

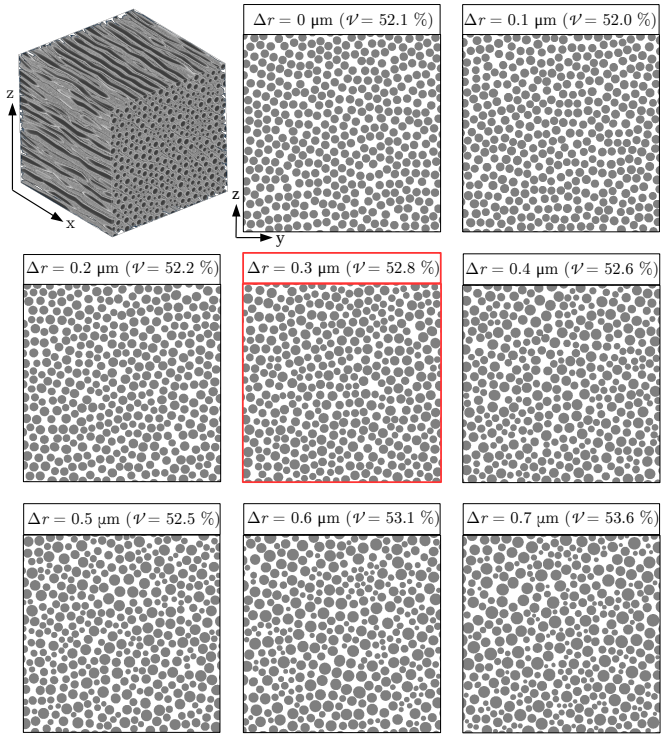

Fig. 10.22: Horizontal fiber bundle ($30 \times 30 \times 30\,\mu m^3$) with an average fiber radius of 0.65 µm and different fiber radius distributions ($\Delta r = r_{max} - r_{min}$) generated by the VCS. The maximum displacement of fiber midpoints is $\Xi = 1\,\mu m$. The figure shows cross-sections through the yz-mid-plane for different fiber radius distributions. The red frame highlights the reference fiber bundle (cf. Fig. 10.18b), which is also shown as 3D image. The volume fraction $\mathcal{V}$ of the fibers is similar for different Δr.

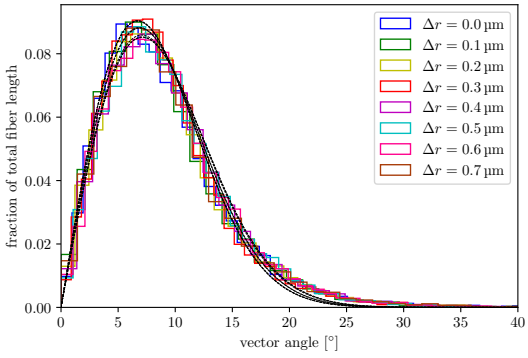

Fig. 10.23: Fiber orientation dispersion for bundles with an average fiber radius of 0.65 µm and different fiber radius distributions ($\Delta r = r_{max} - r_{min}$, cf. Fig. 10.22). The dashed lines show the fitted Rayleigh distributions with mode σ = 6.7–7.1°. The relative error of all fitted mode values is mostly below 0.6 %.

10.2.3.3 Different Scales

To generate bundles with different fiber sizes, the reference fiber bundle was scaled by factors of 1, 2, 2.5, 3, 4, and 5, yielding bundles with fiber radii from $r \in [0.5, 0.8]\,\mu m$ to $r \in [2.5, 4.0]\,\mu m$. After scaling, the fiber volume was again cropped to a volume of $30 \times 30 \times 30\,\mu m^3$.

Figure 10.24 shows the resulting fiber bundles for different scaling factors. The volume fractions of the fiber bundles are similar for scaling factors 1 to 4 ($\mathcal{V} = 52.8$–$53.7\,\%$). For a scaling factor of 5, the volume fraction is slightly less ($\mathcal{V} = 50.8\,\%$).

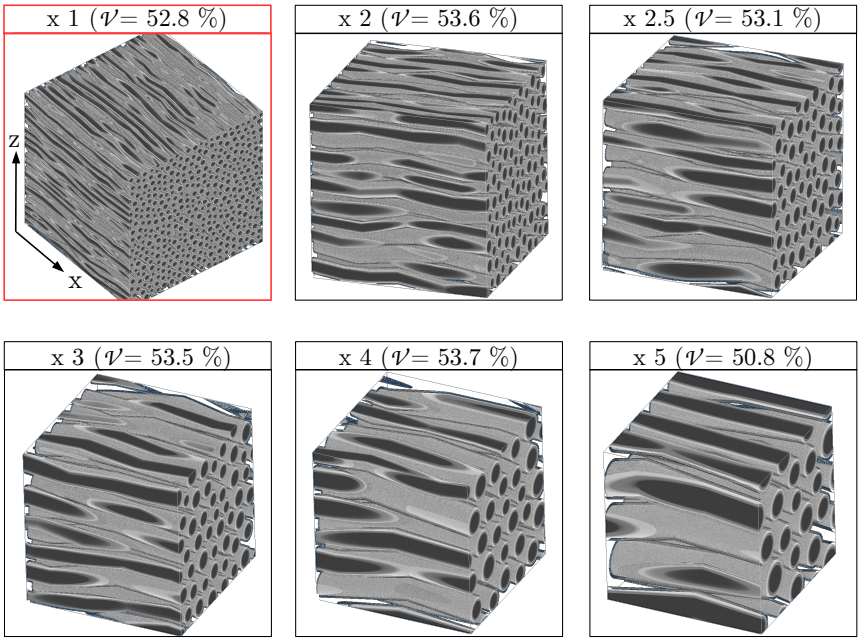

Fig. 10.24: Horizontal fiber bundle generated by the VCS with different scaling factors in a volume of $30 \times 30 \times 30\,\mu m^3$. The volume fraction $\mathcal{V}$ of the fibers is similar for scaling factors 1 to 4. For a scaling factor of 5, it is slightly smaller. The red frame highlights the reference fiber bundle without scaling (cf. Fig. 10.18b).

10.2.3.4 Different Fiber Crossing Angles

To generate fibers with different crossing angles, a bundle of straight fibers oriented in the x-direction (with $N = 700$ and $r \in [0.5, 0.8]\,\mu m$) was generated with the FGA, as described at the beginning of Sec. 10.2.3.

To generate two separate crossing fiber bundles, the bundle of straight fibers was divided in an upper and a lower bundle of thickness $z/2$, respectively. The upper bundle was rotated around the z-axis about the center position by an angle $+\chi/2$, the lower bundle was rotated by an angle $-\chi/2$, resulting in two separate bundles with crossing angle χ (cf. Fig. 10.25a).

Crossing fiber bundles in the brain are not always separated. Often, the fiber bundles are interwoven and form a complex meshwork. Therefore, fiber crossings were also simulated for interwoven bundles. For this purpose, each fiber layer in the z-direction

of the straight fiber bundle was rotated alternately by $\pm\chi/2$ (cf. Fig. 10.25b). Both the separate and the interwoven fiber bundles were generated with different crossing angles $\chi = \{0°, 15°, \ldots, 90°\}$.

To study fiber crossings in all spatial directions, three mutually orthogonal, interwoven fiber bundles were generated. For this purpose, the straight fiber bundle (oriented in the x-direction) was divided in three types of alternating layers: one layer was rotated $+45°$ around the z-axis, one $-45°$ around the z-axis, and one $+90°$ around the y-axis, yielding two horizontal fiber bundles in the xy-plane and one vertical fiber bundle oriented along the z-axis.

The resulting bundles of straight crossing fibers were used as input for the VCS for all three models of crossing fibers. To obtain a similar fiber orientation dispersion as for the bundle of densely grown fibers, the maximum displacement of the fiber midpoints in the VCS was chosen to be $\Xi = 1\,\mu m$. For fibers with zero crossing angle ($\chi = 0°$), the reference fiber bundle was used (cf. Fig. 10.18b).

Figure 10.25a,b shows at the bottom the resulting separate and interwoven fiber bundles exemplary for a crossing angle $\chi = 30°$ and $\chi = 60°$. Figure 10.25c shows the three mutually orthogonal fiber bundles.

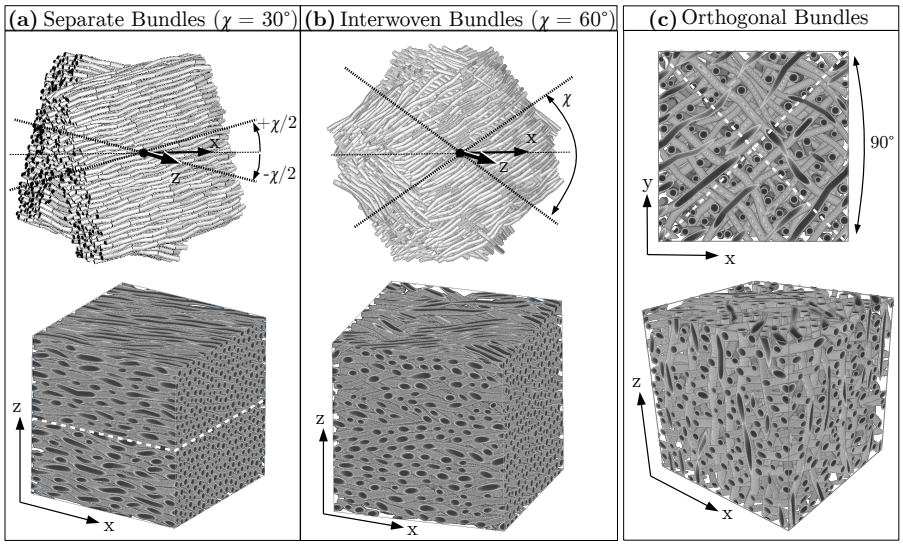

Fig. 10.25: (a-b) Separate and interwoven fiber bundles with crossing angle χ: The upper figures show the bundles generated by the VCS. The lower figures show the bundles after being cropped to a volume of $30 \times 30 \times 30\,\mu m^3$. The white dotted line indicates the border between the upper and lower bundle of the separate crossing fibers. For $\chi = 0°$, the bundles correspond to the reference fiber bundle (cf. Fig. 10.18b). **(c)** Three mutually orthogonal, interwoven fiber bundles generated by the VCS and cropped to a volume of $30 \times 30 \times 30\,\mu m^3$. The white dotted lines indicate the main directions of the two horizontal fiber bundles in the xy-plane, the third fiber bundle is oriented in the z-direction. All fibers were generated with radii $r \in [0.5, 0.8]\,\mu m$ and a maximum displacement of fiber midpoints $\Xi = 1\,\mu m$. The figure has been published in Menzel *et al.* (2018a) [67] Fig. 15.

The volume fraction of the orthogonal fiber bundles is $\mathcal{V} \approx 31.6\,\%$. Table 10.4 shows the volume fraction of the separate and interwoven fiber bundles for different crossing angles. The volume fraction of the separate fiber bundles is similar for different crossing

angles ($\mathcal{V} \approx 48.5$–$49.0\,\%$). The volume fraction of the interwoven fiber bundles slightly decreases with increasing crossing angle (from $\mathcal{V} \approx 46.5\,\%$ for $\chi = 15°$ to $\mathcal{V} \approx 40\,\%$ for $\chi = 60$–$90°$).

χ [°]	Separate Bundles	Interwoven Bundles
0	49.0 %	49.0 %
15	48.9 %	46.5 %
30	48.5 %	44.1 %
45	48.7 %	41.1 %
60	48.8 %	40.6 %
75	48.9 %	40.5 %
90	48.6 %	39.6 %

Tab. 10.4: Volume fraction of separate and interwoven fiber bundles with crossing angle χ

10.3 Implementation of the Fiber Configurations in TDME3D

This section describes how the fiber configurations were implemented in TDME3D in order to simulate the transmittance and diattenuation effects in Chaps. 11 and 12. The dimensions and refractive indices of the fibers are motivated in Sec. 10.3.1. All other parameters used for the simulation with TDME3D are introduced in Sec. 10.3.2. Finally, in Sec. 10.3.3, the simulation parameters are discussed in terms of computing time. Parts of Secs. 10.3.1 and 10.3.2 have been published in Menzel *et al.* (2018a) [67].

As computing time is always limited, it is necessary to find a compromise between computing time and accuracy. The accuracy of the chosen simulation parameters will be evaluated in the subsequent Sec. 10.4.

10.3.1 Model of the Nerve Fibers

In order to model and better understand the observed transmittance and diattenuation effects of brain tissue, the structure of the nerve fibers and of the surrounding myelin sheaths needs to be considered.

The myelin sheath surrounds most of the axons in the white matter (see Sec. 3.1.3). Figure 10.26b shows again the layered structure of the myelin sheath: it consists of alternating layers of cell membranes (lipid bilayers of about 5 nm thickness) and cytoplasmic or extracellular space (of about 3 nm thickness). The effective refractive indices n of the layers are given by literature values of cytoplasm, lipids, and glycerin solution (see Eqs. (3.1) to (3.3)). As the extracellular membranes are not fused and swell in water (see Sec. 3.1.3), it is assumed that the extracellular space is filled with the glycerin solution used for embedding the brain sections (cf. Sec. 4.1).

Due to limited resources, the molecular substructure of the layers cannot be included in the simulation model, i. e. molecular birefringence or diattenuation (see Secs. 3.2.3 and 3.2.4) need to be described by an effective analytical model instead. Simulating all layers requires Yee mesh size of at most 3 nm, which would consume a lot of computing time. As computing time is limited, a simplified model was used to represent the myelin sheath (see Fig. 10.26c): Each cell layer (two lipid bilayers with separating cytoplasm) was considered as one *myelin layer* with an effective refractive index $n_\mathrm{m} = 1.47$ (blue), the extracellular space was considered to be filled with glycerin solution (*glycerin layer*) with a refractive index $n_\mathrm{g} = 1.37$ (yellow). Assuming that the extracellular space increases when being embedded in glycerin, the myelin and glycerin layers were assumed

to contribute 3/4 and 1/4 to the overall myelin sheath thickness t_{sheath}, respectively. The refractive index of the cytoplasmic layer was neglected in this model.

As mentioned in Sec. 3.1.3, the myelin sheath thickness contributes approximately one third to the overall fiber radius r. Hence, the myelin sheath thickness was chosen to be $t_{\text{sheath}} = 0.35\,r$ and the radius of the inner axon $r_{\text{ax}} = 0.65\,r$. The refractive index of the axon was chosen to be $n_{\text{ax}} = 1.35$ (green), as motivated in Sec. 3.2.1. The myelin sheath was modeled as double myelin layers with thickness $t_{\text{m}} = 3/7\,t_{\text{sheath}}$ each and a single glycerin layer with thickness $t_{\text{g}} = 1/7\,t_{\text{sheath}}$ separating the myelin layers. The nodes of Ranvier and the small space between axon and myelin sheath, the so-called *periaxonal space* (see Sec. 3.1.3), were neglected in this model.

For the 3D-PLI and DI simulations in Chaps. 11 and 12, all fibers were simulated with double myelin layers and with the refractive indices given above. The surrounding medium was assumed to be homogeneous with a refractive index $n_{\text{surr}} = n_{\text{g}} = 1.37$ (yellow), which corresponds to the refractive index of gray matter as well as to the refractive index of the surrounding glycerin solution (see Sec. 3.2.1).

In Sec. 10.4.2, the accuracy of the model of double myelin layers will be discussed by comparing the simulation results for fibers with different numbers of myelin layers.

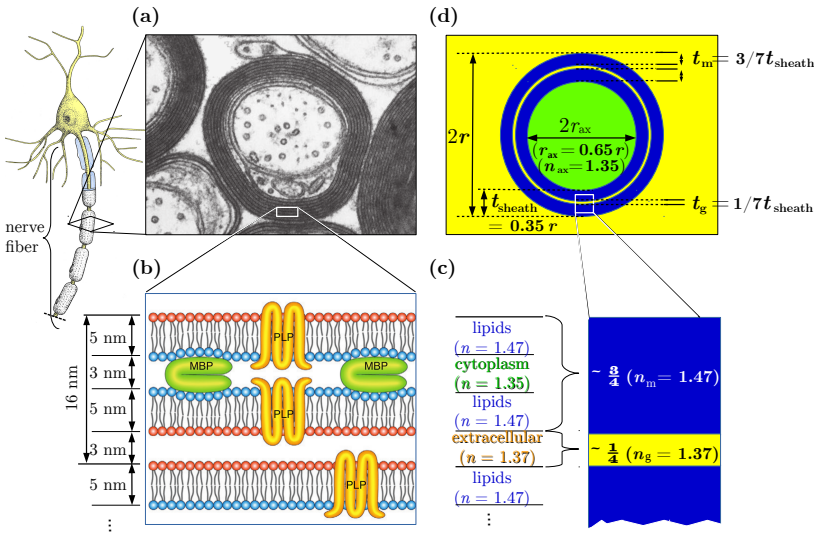

Fig. 10.26: Modeling nerve fibers: **(a)** Electron micrograph of nerve fibers in the CNS (Source: Quarles *et al.* [43] Fig. 4–7, Copyright (2006), with permission from Elsevier). **(b)** Schematic representation of the myelin structure (cf. Fig. 3.2c), consisting of several lipid bilayers (5 nm thick cell membranes) interrupted by proteins (MBP/PLP) with a cytoplasmic and extracellular space of about 3 nm (Source: Aggarwal *et al.* [94] Fig. 2, Copyright (2012), with permission from Elsevier). **(c)** Each cell layer (two lipid bilayers with separating cytoplasm) is considered as one "myelin layer" with an effective refractive index $n_{\text{m}} = 1.47$ (blue), the extracellular space is considered to be filled with glycerin solution ("glycerin layer") with a refractive index $n_{\text{g}} = 1.37$ (yellow). The myelin and glycerin layers are assumed to contribute 3/4 and 1/4 to the overall myelin sheath thickness t_{sheath}, respectively. **(d)** Nerve fibers are modeled with double myelin layers with thickness $t_{\text{m}} = 3/7\,t_{\text{sheath}}$ each and a single separating glycerin layer with thickness $t_{\text{g}} = 1/7\,t_{\text{sheath}}$. The myelin sheath thickness contributes approximately one third to the overall fiber radius ($t_{\text{sheath}} = 0.35\,r$). The inner axon is modeled with a refractive index $n_{\text{ax}} = 1.35$. A similar figure has been published in Menzel *et al.* (2018a) [67] Fig. 16.

10.3.2 System Parameters

For the implementation in TDME3D, different input parameters need to be specified (see Sec. 6.3). The following list describes the system parameters that were used for simulating the fiber configurations in the subsequent chapters.

- **Boundary conditions:** To enable the simulation of complex and non-symmetric fiber configurations, all simulations were performed with UPML absorbing boundaries (cf. Sec. 6.3). The boundaries were chosen to be 1 µm thick: thick enough to prevent light from being reflected back into the simulation volume and thin enough to let the majority of light pass through the sample.

- **Volume sizes:** The sample size should be large enough to contain all relevant geometric features and small enough to reduce computing time. All fiber configurations were generated in a volume $x \times y \times z = 30 \times 30 \times 30\,\mu\text{m}^3$. The sample thickness is relatively thin compared to the 60 µm thick brain sections used for the polarimetric measurements and the field of view is relatively small (it contains only about 22 pixels for the PM and about one pixel for the LAP with the high-resolution objective). However, the sample size is sufficient to study the transmittance and diattenuation for various fiber configurations. In Sec. 10.4.4, the accuracy of the simulation results will be investigated for different sample sizes.

  As described in Sec. 4.1, all brain sections are embedded in glycerin solution so that they float between glass slide and cover slip. To account for this, 0.5 µm thick layers of glycerin solution (with refractive index $n_\text{g} = 1.37$) were added at the bottom and on top of the sample, yielding a total medium with dimensions $x \times y \times z = 30 \times 30 \times 31\,\mu\text{m}^3$ (see Fig. 10.27).

  The dimensions of the simulation box were chosen to be $x \times y \times z = 30 \times 30 \times 35\,\mu\text{m}^3$ to leave some space for light source and detection planes. The light source (emitting a plane monochromatic wave) was placed outside of the UPML boundaries and in front of the sample at $z = 1.2\,\mu\text{m}$ (see green dashed line in Fig. 10.27). The detection planes at which the reflected and transmitted light waves are recorded were placed just in front of and behind the sample at $z = 1.5\,\mu\text{m}$ and $z = 33.5\,\mu\text{m}$, respectively (see red dashed lines in Fig. 10.27).

- **Discretization of space and time:** All simulations were performed for 200 periods with Courant factor $C = 0.8$. The Yee mesh size was chosen to be $\Delta = 25\,\text{nm}$, which corresponds to the maximum possible mesh size for light in the visible spectrum. The mesh size is just large enough to account for the double myelin layers of the fibers (the glycerin layer for fibers with 0.5 µm radius is only 25 nm thick). A larger number of periods and a smaller mesh size would increase the accuracy of the simulation results, but also the computing time (cf. Sec. 10.3.3). Sections 10.4.2 and 10.4.3 will discuss the simulation results for different numbers of periods and different mesh sizes.

- **Material properties:** Every medium in the sample was simulated as dielectric with real refractive index (cf. Fig. 10.27): axon (green, $n_\text{ax} = 1.35$), myelin layers (blue, $n_\text{m} = 1.47$), glycerin layer and surrounding medium (yellow, $n_\text{g} = n_\text{surr} = 1.37$). As the absorption coefficients of brain tissue are small (cf. Sec. 3.2.2), they were neglected in the simulations. Simulation runs with and without absorption will be compared in Sec. 10.4.2.

All simulation parameters used for the TDME3D simulations in Chaps. 11 and 12 are summarized in Tab. 10.5. The properties of the light source (wavelength, direction of propagation, and polarization) were specified for each simulation run individually and are therefore not listed in the table.

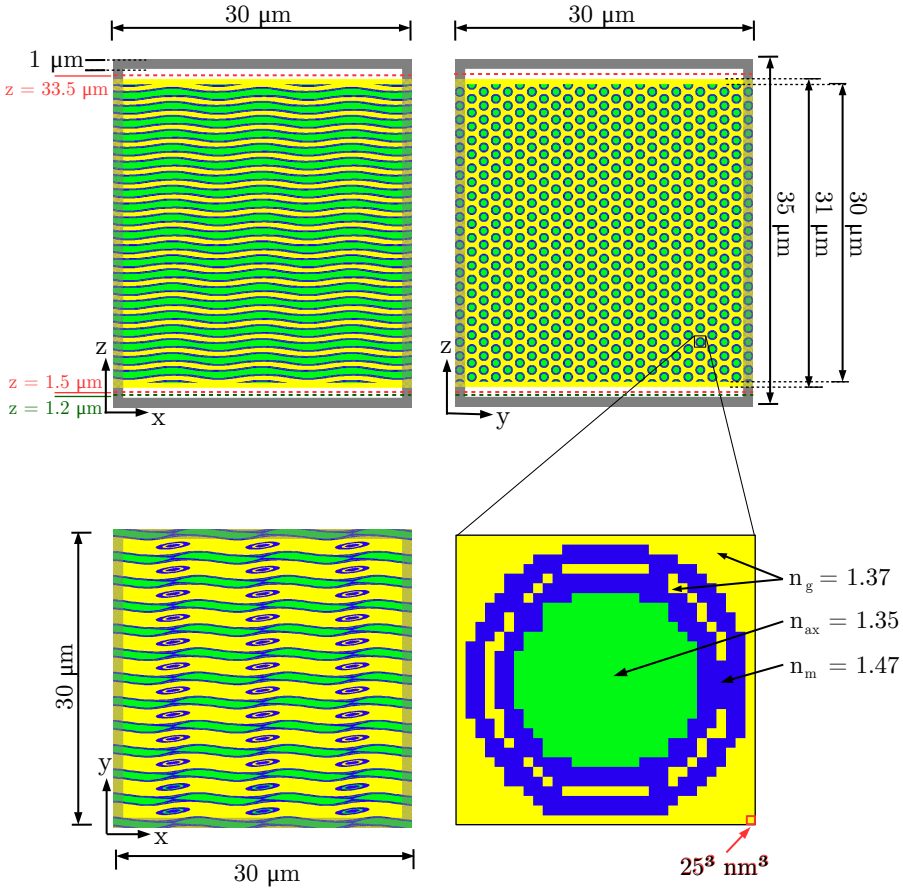

Fig. 10.27: Dimensions of the simulation box used for simulating the fiber configurations by TDME3D in Chaps. 11 and 12, shown exemplary for the hexagonal grid of aligned helical horizontal fibers (see Sec. 10.2.1). All fiber configurations were simulated in a volume of $30 \times 30 \times 30\,\mu m^3$, surrounded by a medium with dimensions $30 \times 30 \times 31\,\mu m^3$ and a refractive index $n_g = 1.37$ (yellow). The sample was placed in a simulation box of $30 \times 30 \times 35\,\mu m^3$, surrounded by 1 µm thick UPML boundaries (gray). The fibers were modeled with double myelin layers (see Fig. 10.26d), i. e. two myelin layers (blue, $n_m = 1.47$) with separating glycerin layer (yellow, $n_g = 1.37$) surrounding the inner axon (green, $n_{ax} = 1.35$). The Yee mesh size was chosen to be $\Delta = 25\,nm$ for all simulations. The light source (green dashed line) was placed in front of the sample at position $z = 1.2\,\mu m$. The detection planes which record the reflected and transmitted light waves (red dashed lines) were placed between light source and sample at position $z = 1.5\,\mu m$, and behind the sample at position $z = 33.5\,\mu m$.

General Simulation Parameters	
• Yee mesh size:	$\Delta = 25\,\text{nm}$
• Courant factor:	$C = 0.8$
• number of periods:	200
• MPI grid:	$16 \times 16 \times 16$
• core hours:	~ 4700 (built-in), ~ 7000–8000 (user-defined)
• wall time:	$\sim$ 1:08 h (built-in), $\sim$ 1:45–2:00 h (user-defined)
• min. memory required:	$\sim 150\,\text{GB}$ (built-in), ~ 260–$360\,\text{GB}$ (user-defined)
Simulation Box	
• volume:	$x \times y \times z = 30 \times 30 \times 35\ \mu\text{m}^3$
• boundaries:	UPML (1 µm thick)
Surrounding Medium	
• dimensions:	$x \times y \times z = 30 \times 30 \times 31\ \mu\text{m}^3$
• refractive index:	$n_{\text{surr}} = 1.37$
Fiber Configuration	
• volume:	$x \times y \times z = 30 \times 30 \times 30\ \mu\text{m}^3$
• fiber radius:	$r \sim 0.5\,\mu\text{m}$
• axon:	$r_{\text{ax}} = 0.65\,r, \quad n_{\text{ax}} = 1.35$
• myelin sheath:	$t_{\text{sheath}} = 0.35\,r = t_{\text{m}} + t_{\text{g}} + t_{\text{m}}$
• double myelin layers:	$t_{\text{m}} = \frac{3}{7}\,t_{\text{sheath}}, \quad n_{\text{m}} = 1.47$
• single glycerin layer:	$t_{\text{g}} = \frac{1}{7}\,t_{\text{sheath}}, \quad n_{\text{g}} = 1.37$

Tab. 10.5: Simulation parameters (see Sec. 6.3) used for simulating the fiber configurations by TDME3D in Chaps. 11 and 12. The fibers were modeled with radius r and double myelin layers with thicknesses t and refractive indices n (see Fig. 10.26c,d). The fiber configurations were generated in a volume of $30 \times 30 \times 30\,\mu\text{m}^3$, surrounded by a medium with dimensions $30 \times 30 \times 31\,\mu\text{m}^3$ and a refractive index of 1.37 (glycerin solution). The sample was placed in a simulation box of $30 \times 30 \times 35\,\mu\text{m}^3$, surrounded by 1 µm thick UPML boundaries (see Fig. 10.27). Apart from dimensions and refractive indices, the table also lists more general simulation parameters and the expenses of one simulation run (using built-in functions or user-defined fiber constellations, see Sec. 10.3.3). The properties of the light source (wavelength, direction of propagation, and polarization) are not listed in the table because they were specified for each simulation run individually. A similar table has been published in Menzel *et al.* (2018a) [67] Tab. 2.

Simulation of the Polarimetric Measurements The simulations of the 3D-PLI and DI measurements were performed as described in Sec. 10.1: For the 3D-PLI simulation, left-handed-circularly polarized light was used, for the DI simulation, linearly polarized light. Depending on whether the imaging system of the PM or the LAP was modeled, the simulations were performed for different (peak) wavelengths ($\lambda = 550\,\text{nm}$ or $529\,\text{nm}$).

To save computing time, most simulations were performed for normally incident light ($\theta = 0°$). To model diffuse light, four additional simulation runs were performed with $\varphi = \{0°, 90°, 180°, 270°\}$ and $\theta = 3°$ (PM) or $\theta = 0.5°$ (LAP), and weighted as described in Eqs. (10.1) to (10.3). In Sec. 10.4.6, the simulation results for diffuse light will be discussed for different angles of incidence.

For the DI simulation, each rotation angle $\rho \in \{0°, 10°, \ldots, 170°\}$ of the polarizer requires a separate simulation run (with light polarized in the direction ρ). To save computing time, the diattenuation was approximated by D_{S} which is computed from only two simulation runs (with light polarized in the direction ρ_i and $\rho_i + 90°$). When

aligning the longitudinal symmetry axis of the sample (projected onto the xy-plane) with the x-axis of the system, D_S can be computed from the transmitted intensity of light polarized along the x- and y-axes (analogously to Eq. (2.43)):

$$D_\mathrm{S} \equiv \frac{I_\mathrm{x} - I_\mathrm{y}}{I_\mathrm{x} + I_\mathrm{y}}, \quad -1 \leq D_\mathrm{S} \leq 1 \quad \begin{cases} D^+ : D_\mathrm{S} > 0 \;\Leftrightarrow\; \varphi_\mathrm{D,S} \approx 0°, \\ D^- : D_\mathrm{S} < 0 \;\Leftrightarrow\; \varphi_\mathrm{D,S} \approx 90°. \end{cases} \tag{10.42}$$

This definition allows to directly relate the simulated diattenuation to the measured diattenuation and to regions of type D^+ or D^- (cf. Chap. 9): Positive diattenuation values ($D_\mathrm{S} > 0 \Leftrightarrow I_\mathrm{x} > I_\mathrm{y}$) correspond to regions of type D^+ (the transmitted light intensity becomes maximal when the light is polarized parallel to the fibers, i. e. in the x-direction). Negative diattenuation values ($D_\mathrm{S} < 0 \Leftrightarrow I_\mathrm{x} < I_\mathrm{y}$) correspond to regions of type D^- (the transmitted light intensity becomes maximal when the light is polarized perpendicularly to the fibers, i. e. in the y-direction).

The magnitude of D_S is related to the strength of the simulated diattenuation signal ($|D_\mathrm{S}| \approx |\mathscr{D}_\mathrm{S}|$), while the sign approximately indicates the phase $\varphi_\mathrm{D,S}$ (cf. Fig. 10.3b). For uniaxial systems with single optic axis holds equality.

In Sec. 10.4.1, the diattenuation images will be compared for a simulation with all 18 rotation angles and for a simulation with only $\rho = 0°$ and $\rho = 90°$.

10.3.3 Estimation of Computing Time

The computing time needed for simulating a sample with TDME3D increases linearly with the number of grid points (given by the volume size divided by the Yee mesh size), the number of periods, and the number of simulation runs. Between 2015 and 2017, 14–19 million core hours per year have been granted on the supercomputer JUQUEEN at Forschungszentrum Jülich GmbH, Germany. For the presented simulation studies, a large number of simulations was necessary: Various fiber configurations were simulated for various wavelengths and angles of incidence. Beforehand, various test runs were needed to identify interesting effects.

A combined simulation of 3D-PLI and DI (yielding transmittance and diattenuation images) requires at least three simulation runs: one for 3D-PLI (with circularly polarized light), and at least two for DI (with linearly polarized light along x and y). For the simulation parameters defined in Tab. 10.5 (Yee mesh size of 25 nm, simulation volume of $30 \times 30 \times 35\,\mu\mathrm{m}^3$, 200 periods, MPI grid of $16 \times 16 \times 16$), a single simulation run requires between 4700 and 8000 core hours: Using built-in functions in TDME3D (hexagonal grid of fibers), consumes about 4700 core hours (wall time $\approx$ 01:08 h, min. memory required $\approx$ 150 GB). Importing a user-defined fiber constellation as text file (fiber bundles generated by the FGA or VCS), consumes about 7000–8000 core hours because generating the medium from the text file requires additional computing time (wall time $\approx$ 1:45 h–2:00 h, min. memory required $\approx$ 260–360 GB).

In Chaps. 11 and 12, different fiber configurations were simulated for different inclination angles and diffuse light to study the transmittance and diattenuation effects. The transmittance and diattenuation curves were computed for 10 different inclination angles. In the case of normally incident light, one 3D-PLI measurement and two DI measurements were performed. In the case of diffuse light, four additional simulation runs were performed per simulation run ($\varphi = \{0°, 90°, 180°, 270°\}$). Computing the transmittance and diattenuation curves for a user-defined fiber bundle and diffuse light requires already $3 \times 10 \times 5 \times 8000 = 1.2$ million core hours.

Thus, it is necessary to find a compromise between computing time and accuracy to enable the simulation of various fiber configurations. In the subsequent section, the chosen simulation parameters will be evaluated in terms of their accuracy.

10.4 Evaluation of Simulation Parameters

The simulation model introduced in Sec. 10.3 is a great simplification of the experimental situation. The simulated results might therefore differ a lot from the measured results. As the FDTD simulations are too complex, conventional error estimation is not possible. To still estimate the accuracy of the simulation results, the hexagonal grid of aligned helical horizontal fibers (see Sec. 10.2.1 and Fig. 10.27) was simulated for different simulation parameters. This fiber geometry was chosen because it is well-defined and horizontal fibers are expected to produce the strongest birefringence and diattenuation signals. In certain cases, the simulation parameters were also evaluated for more complex fiber configurations, e. g. a bundle of densely grown fibers (see Sec. 10.2.2) or crossing fibers (see Sec. 10.2.3.4). As the simulation studies in the subsequent chapters were mostly performed for the imaging system of the PM, only the optics of the PM was considered for evaluation (peak wavelength $\hat{\lambda} = 550\,\text{nm}$, NA $= 0.15$, $r_0 = 0.665\,\mu\text{m}$, cf. Sec. 10.1.1).

The transmittance and diattenuation images were studied for different simulation parameters: different sampling angles of the diattenuation signal (Sec. 10.4.1), different numbers of myelin layers (Sec. 10.4.2), different numbers of periods (Sec. 10.4.3), different sizes of the simulation volume (Sec. 10.4.4), different wavelengths (Sec. 10.4.5), and different angles of incidence (Sec. 10.4.6). Parts of Secs. 10.4.2.1 and 10.4.2.2 have been published in Menzel *et al.* (2018a) [67] Note 4.

To estimate the impact of the simulation parameters on the simulation results, only one simulation parameter was varied while all other simulation parameters were chosen as in Sec. 10.3 (see Fig. 10.27 and Tab. 10.5). If not otherwise stated, the simulations were performed for normally incident light with a wavelength of 550 nm.

To estimate the accuracy of the resulting transmittance and diattenuation images, the *absolute relative difference between the mean values (ARDM)* and the *relative mean absolute difference (RMAD)* between the images were computed:

$$\text{ARDM} \equiv \left| \frac{\langle \text{image} \rangle - \langle \text{ref.image} \rangle}{\langle \text{ref.image} \rangle} \right|, \tag{10.43}$$

$$\text{RMAD} \equiv \frac{\langle |\text{image} - \text{ref.image}| \rangle}{|\langle \text{ref.image} \rangle|}. \tag{10.44}$$

In this notation, the "image" refers to the transmittance or diattenuation image for which the absolute relative difference is computed (obtained e. g. from simulation runs with different Yee mesh sizes). The "reference image" is the transmittance or diattenuation image used for comparison (obtained e. g. from the simulation run with minimum mesh size). The symbol $\langle\rangle$ represents the average over all image pixels.

The simulation studies in Chaps. 11 and 12 mostly investigate the mean values of the transmittance and diattenuation images. Therefore, the ARDM is a direct measure for the accuracy of these simulation results, while the RMAD is a measure for the reliability of the ARDM as an error estimate.

10.4.1 Different Sampling of the Diattenuation Signal

Figure 10.3b in Sec. 10.1.2 shows the transmitted light intensities and parameter maps for the hexagonal grid of aligned helical horizontal fibers oriented in the x-direction obtained from a simulated DI measurement with 18 rotation angles. The strength of the diattenuation $|\mathscr{D}_S|$ and the direction angle $\varphi_{D,S}$ were computed for each image pixel from the amplitude and phase of the sinusoidal light intensity profile (see Fig. 10.28a in blue and green). To save computing time, $|\mathscr{D}_S|$ and $\varphi_{D,S}$ were approximated in the subsequent simulation studies by D_S which is computed from only two simulation runs (light polarized along the x- and y-axes) according to Eq. (10.42) (see Fig. 10.28a in red). Figure 10.28b shows the resulting diattenuation images and corresponding histograms obtained from 18 simulation runs (blue) and from only two simulation runs (red).

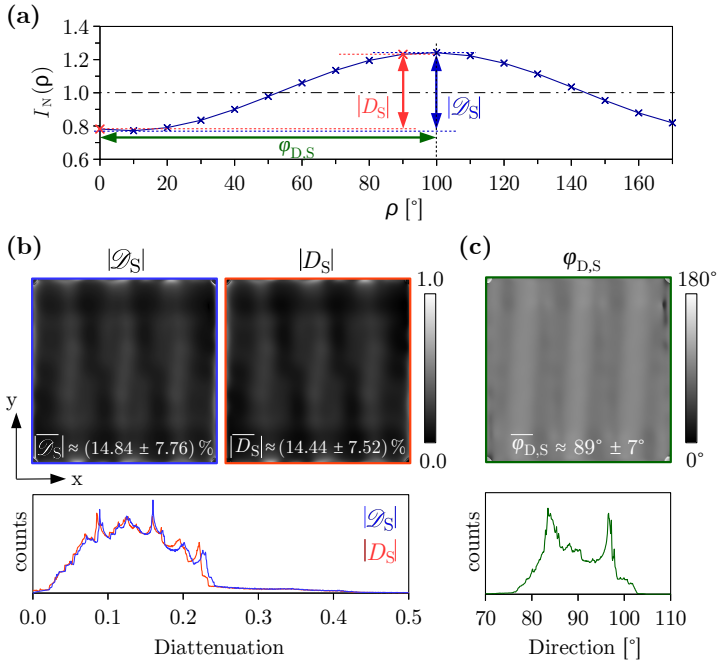

Fig. 10.28: DI simulation for the hexagonal grid of aligned helical horizontal fibers (cf. Fig. 10.3b) for the optics of the PM: **(a)** normalized transmitted light intensity $I_N(\rho)$ evaluated at the middle image pixel for 18 simulation runs with rotation angles ρ, **(b)** images and histograms representing the strength of the diattenuation signal, **(c)** image and histogram of the direction angle. The strength of the diattenuation signal $|\mathscr{D}_S|$ (blue) and the phase $\varphi_{D,S}$ (green) were computed for each image pixel from the amplitude and maximum of the sinusoidal light intensity profile. To save computing time, the strength of the diattenuation was approximated by $|D_S|$ (red) which was computed from only two simulation runs with light polarized along the x-axis ($\rho = 0°$) and along the y-axis ($\rho = 90°$), according to Eq. (10.42).

The histograms show a similar distribution of diattenuation values. The overall diattenuation values $|D_S|$ obtained from only two simulation runs are a bit smaller than the diattenuation values $|\mathscr{D}_S|$ obtained from a simulation with 18 rotation angles

($\overline{|\mathscr{D}_S|} \approx 14.8\,\%$, $\overline{|D_S|} \approx 14.4\,\%$). The relative difference between the two diattenuation images is about 2.7 %, both for ARDM and RMAD.

Figure 10.28c shows the direction angle $\varphi_{D,S}$ for each image pixel and the corresponding histogram. Most direction angles are between 80° and 100°, the average value is about 89°. Thus, the diattenuation of the sample is negative for practically all image pixels (cf. Eq. (10.42)).

The light intensity profile $I_N(\rho)$ is sinusoidal for each image pixel (cf. Fig. 10.28a) and on average (see Fig. 10.29a). As the position of the maximum is close to 90° for each image pixel ($\varphi_{D,S} \approx 80$–$100°$), the amplitude $|\mathscr{D}_S|$ of the sinusoidal signal is similar to the amplitude $|D_S|$ computed from light polarized along the x-axis ($\rho = 0°$) and along the y-axis ($\rho = 90°$). Further simulations of the hexagonal grid of aligned helical fibers have shown that the light intensity profile is not only sinusoidal for horizontal fibers, but also for inclination angles $\alpha > 0°$. The position of the maximum is close to 90° (for $\alpha < 45°$) or close to 0° (for $45° \leq \alpha < 90°$) with a maximum deviation of 10°. The inclination dependency of the diattenuation signal will be studied in more detail in Chap. 12.

Thus, the diattenuation can approximately be computed from only two simulation runs with polarization parallel and perpendicular to the fibers instead of performing 18 simulations for all different rotation angles of the polarizer. The resulting diattenuation values are only slightly underestimated. In the following DI simulations, the diattenuation signal $\{|\mathscr{D}_S|, \varphi_{D,S}\}$ was therefore approximated by D_S which was computed from only two simulation runs using Eq. (10.42).

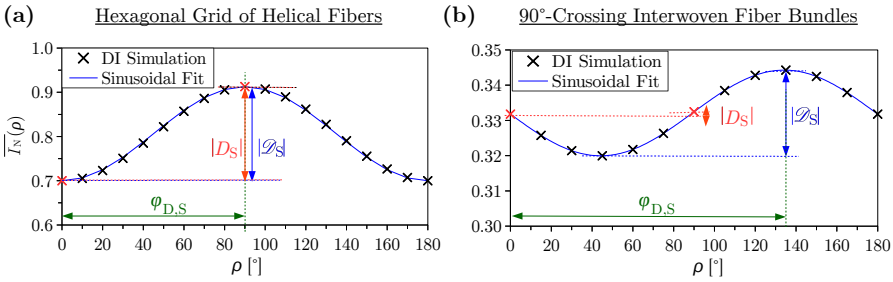

Fig. 10.29: Averaged transmitted light intensity $\overline{I_N}(\rho)$ obtained from a simulated DI measurement for the optics of the PM with 18 rotation angles ρ (crosses) fitted by a sinusoidal curve (blue line). The strength of the diattenuation $|\mathscr{D}_S|$ (blue arrow) and the direction angle $\varphi_{D,S}$ (green arrow) are computed from the amplitude and maximum of the sinusoidal curve. To save computing time, $|D_S|$ (red arrow) is computed from the transmitted intensity of light polarized along the x-axis ($\rho = 0°$) and along the y-axis ($\rho = 90°$) (red crosses): **(a)** hexagonal grid of aligned helical horizontal fibers (see Fig. 10.27), **(b)** 90°-crossing interwoven fiber bundles (cf. Fig. 10.25b with $\chi = 90°$).

This approximation is only reasonable when the orientation of the fiber configuration is well defined and when its projection onto the xy-plane is oriented along the x-axis. For fiber configurations with several principal orientations such as crossing fibers, the position of the maximum and minimum transmitted light intensities might not correspond to $\rho = 0°$ and $\rho = 90°$ (cf. Fig. 10.29b). In such a case, more than two simulation runs are necessary to determine the correct phase and amplitude of the light intensity profile.

10.4.2 Different Numbers of Myelin Layers

As described in Sec. 3.1.3, the nerve myelin sheath is composed of many thin layers with different thicknesses and refractive indices. Modeling all these layers requires a small Yee mesh size ($\Delta \leq 3\,\text{nm}$). When simulating configurations with several fibers, such small mesh sizes are not feasible because the computing time increases with the number of grid points. For this reason, the simulations were mostly performed for a larger mesh size ($\Delta = 25\,\text{nm}$) and the myelin sheath was modeled with only two layers (cf. Figs. 10.26 and 10.27).

To estimate the impact of the reduced number of myelin layers on the simulation results, a straight single fiber with reduced simulation volume was simulated for different numbers of myelin layers and for a realistic model of the myelin sheath. The hexagonal grid of aligned helical horizontal fibers – in the following called *hexagonal bundle* – was simulated for up to three myelin layers. More layers were not feasible because the mesh size needs to be small enough to resolve the myelin layers, which cannot be simulated with the given computing resources. To estimate the impact of discretization, fibers with two myelin layers were also simulated for larger mesh sizes. To estimate the impact of absorption, the hexagonal bundle was simulated with and without complex refractive indices.

The different models of the myelin sheath used for the simulations are described in Sec. 10.4.2.1. The transmittance and diattenuation values obtained from the 3D-PLI and DI simulations are presented in Sec. 10.4.2.2 both for the single fiber and the hexagonal bundle. In Sec. 10.4.2.3, a more complex fiber bundle (bundle of densely grown fibers) was simulated for double myelin layers with $\Delta = 12.5\,\text{nm}$ and 25 nm.

10.4.2.1 Model of the Myelin Sheath

Figure 10.30a shows the dimensions of the simulation volume used to simulate the straight single fiber which was modeled as a cylinder. The dimensions of the surrounding medium (yellow) and the simulation box were chosen to be $x \times y \times z = 10 \times 10 \times 3\,\mu\text{m}^3$ and $10 \times 10 \times 6\,\mu\text{m}^3$, including the 1 µm thick UPML boundaries (gray). The dimensions for the hexagonal grid of aligned helical horizontal fibers are shown in Fig. 10.27.

All fibers were modeled with a diameter of 1 µm, consisting of an inner axon (green) with a diameter of 0.65 µm and a surrounding myelin sheath with thickness $t_{\text{sheath}} = 0.175\,\mu\text{m}$ (cf. Fig. 10.26d). The myelin sheath was simulated for different numbers L of myelin layers (blue), separated by $(L-1)$ glycerin layers (yellow), see Fig. 10.30b. As motivated in Fig. 10.26c, the glycerin layer thickness was chosen to be three times thinner than the myelin layer thickness ($t_{\text{m}} = 3\,t_{\text{g}}$):

$$t_{\text{sheath}} = L\,t_{\text{m}} + (L-1)\,t_{\text{g}} = 3L\,t_{\text{g}} + (L-1)\,t_{\text{g}} \tag{10.45}$$

$$\Leftrightarrow t_{\text{g}} = \frac{t_{\text{sheath}}}{4L-1}, \quad \text{for } L \geq 2. \tag{10.46}$$

To create a "realistic" model of the myelin sheath (see Fig. 10.26b), 22 lipid layers of 5 nm thickness (blue) were separated by 3 nm thick alternating layers of cytoplasm (green) and extracellular space filled with glycerin solution (yellow), yielding a myelin sheath model consisting of 43 thin layers, see zoomed-in region in Fig. 10.30b.

The Yee mesh size was chosen to be small enough to resolve all geometric features. For most samples, the mesh size was chosen to be one third of the glycerin layer thickness: $\Delta = t_{\text{g}}/3$. Fibers with two myelin layers ($L = 2$) were also simulated for larger mesh sizes ($\Delta = t_{\text{g}}/2 = 12.5\,\text{nm}$ and $\Delta = t_{\text{g}} = 25\,\text{nm}$). The realistic myelin sheath was simulated for $\Delta = t_{\text{g}} = 3\,\text{nm}$.

The single fiber was simulated for all numbers of myelin layers and mesh sizes shown in Fig. 10.30b. Due to the larger simulation volume, the hexagonal bundle was only simulated for $L = \{0, 1, 2\}$ with $\Delta = \{12.5, 25\}$ nm and for $L = 3$ with $\Delta = 8$ nm.

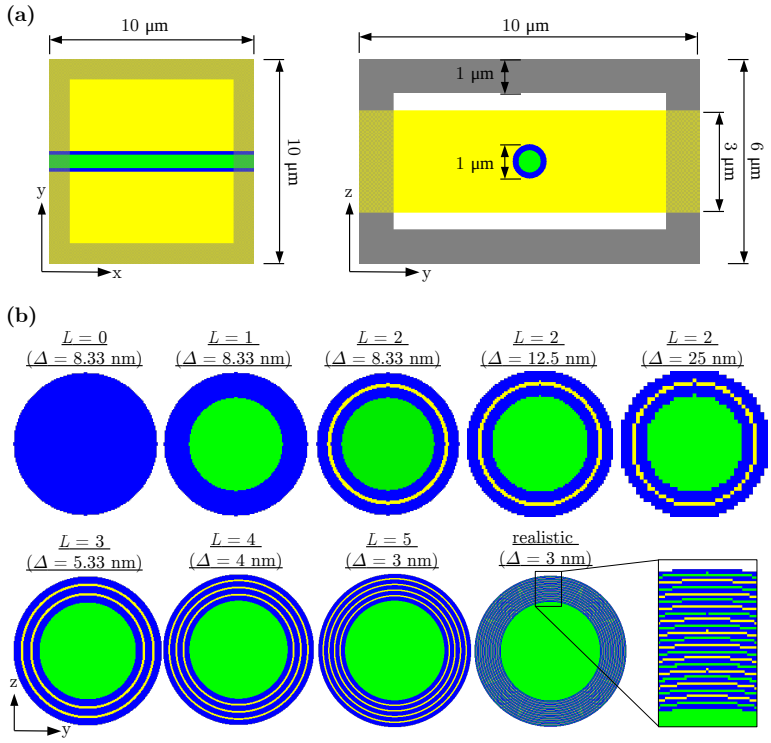

Fig. 10.30: Model of the myelin sheath for different numbers of myelin layers: **(a)** Dimensions of the simulation volume used to simulate a straight single fiber. **(b)** Cross-section through fibers with different numbers L of myelin layers and different Yee mesh sizes Δ. All fibers were modeled with a diameter of 1 µm, consisting of an inner axon (green) with a diameter of 0.65 µm and a surrounding myelin sheath with a thickness of 0.175 µm. The myelin sheath is composed of alternating layers of myelin (blue) and glycerin (yellow), the myelin layers are three times thicker than the glycerin layers (the glycerin layer thickness is defined by the number of myelin layers, see Eq. (10.46)). The realistic model of the myelin sheath contains 22 layers of 5 nm thick cell membranes (blue), interrupted by 3 nm thick alternating layers of cytoplasm (green) and glycerin solution (yellow), yielding a myelin sheath composed of 43 thin layers. The refractive indices are 1.35 for the axon/ cytoplasm (green), 1.37 for the glycerin solution (yellow), and 1.47 for the myelin layers (blue). A motivation of the myelin sheath model and the refractive indices can be found in Fig. 10.26. A similar figure has been published in Menzel *et al.* (2018a) [67] Fig. 18a-b.

Most simulations were performed with real refractive indices. The refractive indices for axon/cytoplasm (green: $n_{\mathrm{ax}} = 1.35$), myelin (blue: $n_{\mathrm{m}} = 1.47$), and glycerin (yellow: $n_{\mathrm{g}} = 1.37$) were chosen as in Sec. 10.3.1. To study the impact of absorption, the hexagonal bundle $\{L = 2,\ \Delta = 25\,\mathrm{nm}\}$ was also simulated with complex refractive indices. The corresponding imaginary parts of the refractive indices were chosen as in Sec. 3.2.2: $\kappa_{\mathrm{ax}} = \kappa_{\mathrm{H_2O}} = 3 \times 10^{-9}$, $\kappa_{\mathrm{m}} = \kappa_{\mathrm{WM}} = 4.4 \times 10^{-6}$, and $\kappa_{\mathrm{g}} = \kappa_{\mathrm{GM}} = 2.2 \times 10^{-6}$, assuming that the absorption of cytoplasm is similar to that of water, the absorption

of myelin similar to that of white matter, and the absorption of the surrounding tissue (everything outside the nerve fibers) similar to that of gray matter.

10.4.2.2 Single Fiber and Hexagonal Grid of Aligned Helical Fibers

Transmittance The transmittance images obtained from simulations with and without absorption are almost identical (RMAD $< 0.0015\,\%$). To keep the simulation model as simple as possible, all subsequent simulations were performed without absorption, i. e. with real refractive indices.

Figure 10.31 shows on the left-hand side the normalized transmittance images $a_{0,\mathrm{N}}$ obtained from 3D-PLI simulations of the straight single fiber and of the hexagonal grid of aligned helical horizontal fibers (hexagonal bundle) for different numbers L of myelin layers and different Yee mesh sizes Δ (with respect to the glycerin layer thickness t_g). The graphs on the right-hand side show the corresponding transmittance profiles, i. e. the middle pixels of the normalized transmittance images evaluated along the y-axis (white dashed lines). The profiles with non-italic labels belong to the displayed transmittance images. Note that the transmittance images for $L = \{0, 1, 2\}$ shown in Fig. 10.31a belong to fibers with the same small mesh size $\Delta = t_\mathrm{g}/3 = 8.33\,\mathrm{nm}$, while the transmittance image surrounded by a red frame belongs to fibers with double myelin layers and a mesh size $\Delta = t_\mathrm{g} = 25\,\mathrm{nm}$ (used for the simulations in the following chapters).

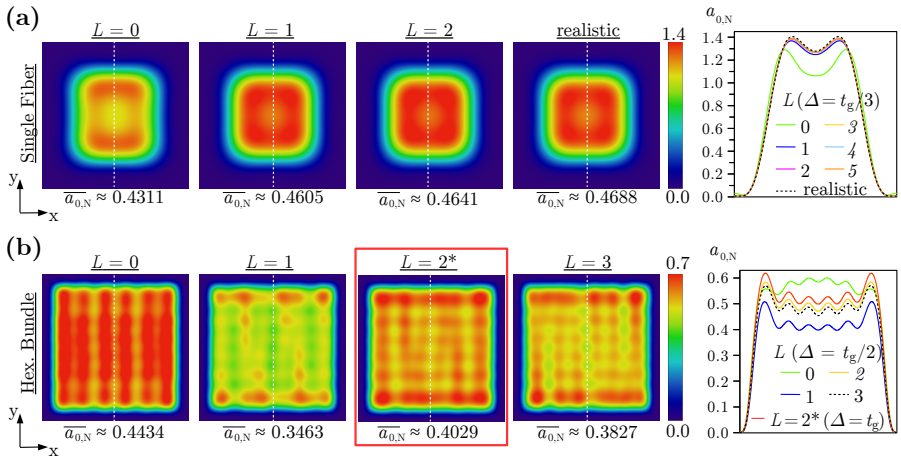

Fig. 10.31: Transmittance images $a_{0,\mathrm{N}}$ and profiles obtained from 3D-PLI simulations with different numbers L of myelin layers and different Yee mesh sizes Δ for the optics of the PM: **(a)** straight single fiber (cf. Fig. 10.30a), **(b)** hexagonal grid of aligned helical horizontal fibers (hexagonal bundle, cf. Fig. 10.27). The images on the left-hand side show the normalized transmittance images and the corresponding average values $\overline{a_{0,\mathrm{N}}}$. The graphs on the right-hand side show the transmittance profiles (middle image pixels evaluated along the y-axis, see white dashed lines). The profiles with non-italic labels belong to the displayed transmittance images. For the single fiber, the mesh size is one third of the glycerin layer thickness ($\Delta = t_\mathrm{g}/3 = 8.33\,\mathrm{nm}$) for $L = \{0, 1, 2\}$ and $\Delta = t_\mathrm{g} = 3\,\mathrm{nm}$ for the realistic myelin sheath, see Fig. 10.30b. For the hexagonal bundle, the mesh size is half of the glycerin layer thickness ($\Delta = 12.5\,\mathrm{nm}$ for $L = \{0, 1, 2\}$). The star and the red frame highlight the transmittance image obtained from a simulation with double myelin layers and a mesh size $\Delta = t_\mathrm{g} = 25\,\mathrm{nm}$, which is used for the simulations in the subsequent chapters (cf. Tab. 10.5). Subfigure (a) has been published in Menzel *et al.* (2018a) [67] Fig. 18c.

For the single fiber, the transmittance images with single and double myelin layers look similar to the one with the realistic myelin sheath. For the hexagonal bundle, the transmittance images with double myelin layers look much more similar to the one with three myelin layers than the one with single myelin layer.

For a better comparison of the transmittance images, the relative differences (ARDM and RMAD) were computed with respect to the reference transmittance image (single fiber: realistic myelin sheath with $\Delta = 3\,\text{nm}$, hexagonal bundle: three myelin layers with $\Delta = 8\,\text{nm}$), see Fig. 10.32. The values surrounded in red belong to fibers with double myelin layers and 25 nm mesh size (used for the simulations in the subsequent chapters).

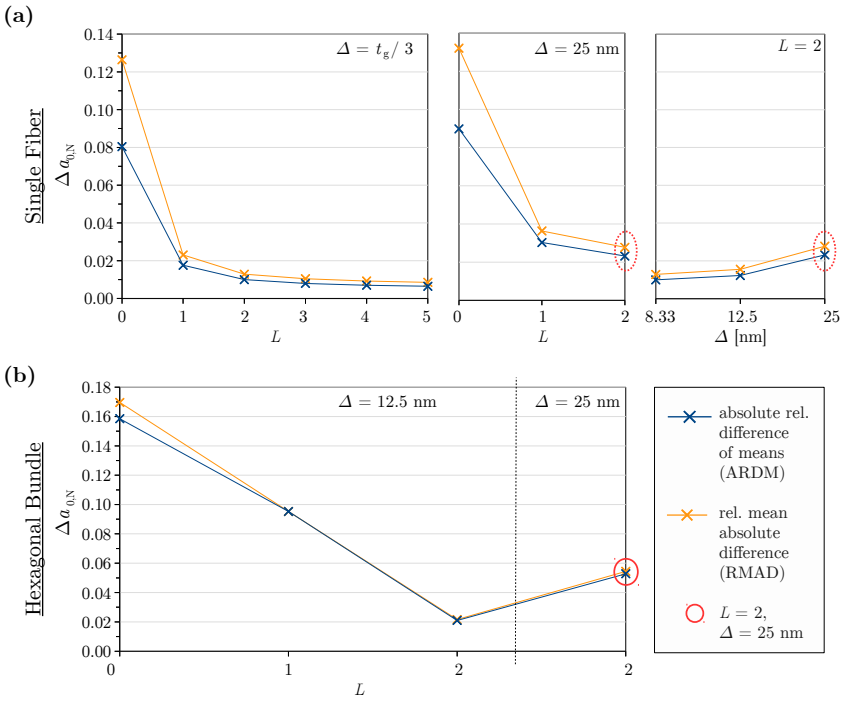

Fig. 10.32: Relative differences between the transmittance images $a_{0,\text{N}}$ (with different numbers L of myelin layers and different Yee mesh sizes Δ, cf. Fig. 10.30b with glycerin layer thickness t_g) and the reference transmittance image (with maximum number of myelin layers and minimum mesh size) obtained from 3D-PLI simulations for the optics of the PM: **(a)** straight single fiber (cf. Fig. 10.30a) with realistic myelin sheath as reference, **(b)** hexagonal grid of aligned helical horizontal fibers (hexagonal bundle, cf. Fig. 10.27) with three myelin layers as reference ($L = 3$, $\Delta = 8\,\text{nm}$). The absolute relative difference of means (ARDM) was computed using Eq. (10.43), the relative mean absolute difference (RMAD) was computed using Eq. (10.44). The values surrounded in red belong to fibers with double myelin layers ($L = 2$) and 25 nm mesh size, which were used for the simulations in Chaps. 11 and 12 (cf. Tab. 10.5). Subfigure (a) has been published in Menzel *et al.* (2018a) [67] Fig. 18d.

For the single fiber (see Fig. 10.32a), the absolute relative differences are largest without myelin layer and become much less for a single myelin layer. A fiber with two or more myelin layers and a mesh size $\Delta = t_\text{g}/3$ yields similar transmittance values as the fiber with realistic myelin sheath. With increasing mesh size, the relative differences

increase. For a fiber with double myelin layers and a mesh size $\Delta = 12.5\,\text{nm}$ (25 nm), the differences are: ARDM $\approx 1.2\,\%$ (2.3 %) and RMAD $\approx 1.6\,\%$ (2.8 %). For a mesh size of 25 nm, the differences are still smaller than for a fiber without or with a single myelin layer.

For the hexagonal bundle (see Fig. 10.32b), the absolute relative differences between the transmittance values for fibers without or with single/double myelin layers ($\Delta = 12.5\,\text{nm}$) and the transmittance values for fibers with three myelin layers ($\Delta = 8\,\text{nm}$) decrease with increasing number of myelin layers. For a larger mesh size of 25 nm, the differences increase. For fibers with double myelin layers and a mesh size $\Delta = 12.5\,\text{nm}$ (25 nm), the differences are: ARDM $\approx 2.1\,\%$ (5.3 %) and RMAD $\approx 2.2\,\%$ (5.4 %). The differences for fibers with double myelin layers and $\Delta = 25\,\text{nm}$ are still less than for fibers with single myelin layer and $\Delta = 12.5\,\text{nm}$. In comparison to fibers with realistic myelin sheaths, these differences are probably underestimated.

Diattenuation The diattenuation images D_S obtained from simulations with and without absorption are very similar (RMAD $< 0.0032\,\%$). All subsequent simulations were therefore performed with real refractive indices.

Figure 10.33 shows the diattenuation images and profiles for the straight single fiber and the hexagonal grid of aligned helical horizontal fibers (hexagonal bundle) for different numbers of myelin layers and different Yee mesh sizes.

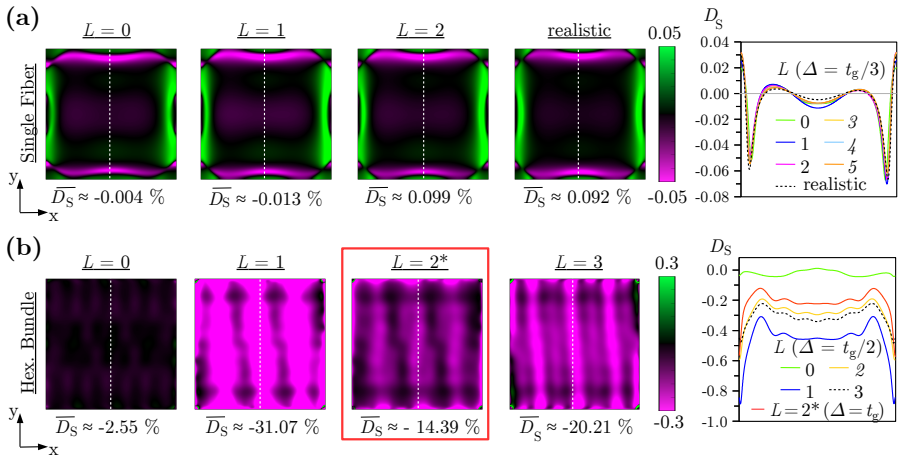

Fig. 10.33: Diattenuation images D_S and profiles obtained from DI simulations with different numbers L of myelin layers and different Yee mesh sizes Δ for the optics of the PM: **(a)** straight single fiber (cf. Fig. 10.30a), **(b)** hexagonal grid of aligned helical horizontal fibers (hexagonal bundle, cf. Fig. 10.27). The images on the left-hand side show the diattenuation images and the corresponding average values $\overline{D_S}$. The graphs on the right-hand side show the diattenuation profiles (middle image pixels evaluated along the y-axis, see white dashed lines). The profiles with non-italic labels belong to the displayed diattenuation images. For the single fiber, the mesh size is one third of the glycerin layer thickness ($\Delta = t_\text{g}/3 = 8.33\,\text{nm}$) for $L = \{0, 1, 2\}$ and $\Delta = t_\text{g} = 3\,\text{nm}$ for the realistic myelin sheath, see Fig. 10.30b. For the hexagonal bundle, the mesh size is half of the glycerin layer thickness ($\Delta = 12.5\,\text{nm}$ for $L = \{0, 1, 2\}$). The star and the red frame highlight the diattenuation image obtained from a simulation with double myelin layers and a mesh size $\Delta = t_\text{g} = 25\,\text{nm}$, which is used for the simulations in the subsequent chapters (cf. Tab. 10.5).

The diattenuation images for the single fiber show areas with positive and negative values. The averaged diattenuation values are small ($|\overline{D_S}| < 1\,\%$) and change from negative values (for $L \leq 1$) to positive values (for $L \geq 2$). The diattenuation values for the hexagonal bundle are mostly negative. The averaged diattenuation value for fibers with three myelin layers ($\overline{D_S} \approx -20.2\,\%$) is strongly underestimated for fibers without myelin sheath and overestimated for fibers with single myelin layer.

Figure 10.34 shows the relative differences (ARDM and RMAD) of the diattenuation images, with the reference image being the image with maximum number of myelin layers and minimum mesh size (single fiber: realistic myelin sheath with $\Delta = 3\,\text{nm}$, hexagonal bundle: $L = 3$ with $\Delta = 8\,\text{nm}$).

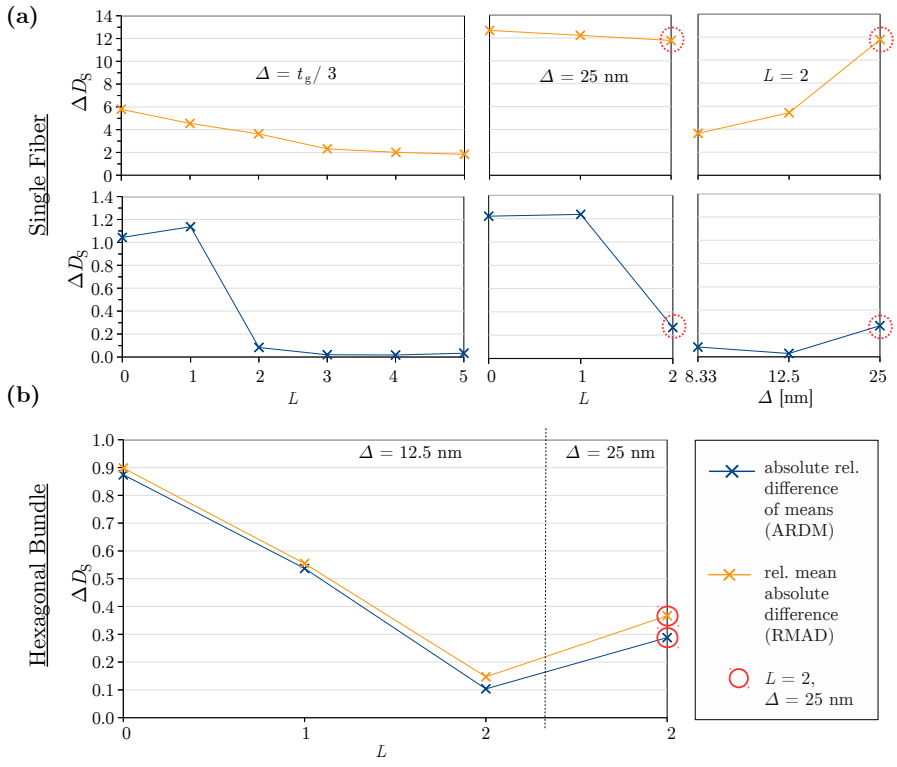

Fig. 10.34: Relative differences between the diattenuation images D_S (with different numbers L of myelin layers and different Yee mesh sizes Δ, cf. Fig. 10.30b with glycerin layer thickness t_g) and the reference diattenuation image (with maximum number of myelin layers and minimum mesh size) obtained from DI simulations for the optics of the PM: **(a)** straight single fiber (cf. Fig. 10.30a) with realistic myelin sheath as reference, **(b)** hexagonal grid of aligned helical horizontal fibers (hexagonal bundle, cf. Fig. 10.27) with three myelin layers as reference ($L = 3$, $\Delta = 8\,\text{nm}$). The absolute relative difference of means (ARDM) was computed using Eq. (10.43), the relative mean absolute difference (RMAD) was computed using Eq. (10.44). The values surrounded in red belong to fibers with double myelin layers ($L = 2$) and 25 nm mesh size, which were used for the simulations in the subsequent chapters (cf. Tab. 10.5).

Due to the small diattenuation values, the relative mean absolute differences (RMAD) for the single fiber are very large (see Fig. 10.34a in orange) and cannot be used for comparison. The absolute relative difference of the mean values (ARDM) for mesh sizes $\Delta = t_g/3$ is about 8.3 % for double myelin layers and about 2–3 % for a fiber with more myelin layers. For double myelin layers, the difference changes with increasing mesh size: ARDM $\approx$ 2.8 % (26.6 %) for $\Delta = 12.5\,\text{nm}$ (25 nm). The differences for a fiber without myelin layers or a single myelin layer are much larger.

For the hexagonal bundle, the relative differences (ARDM and RMAD) show a similar behavior. For fibers with double myelin layers and $\Delta = 12.5\,\text{nm}$ (25 nm), the differences are: ARDM $\approx$ 10.4 % (28.8 %) and RMAD $\approx$ 14.7 % (36.7 %). As fibers with double myelin layers yield very different diattenuation values than fibers with three myelin layers, a hexagonal bundle with realistic myelin sheaths would probably yield even more different results.

10.4.2.3 Bundle of Densely Grown Fibers

Figure 10.35 shows the transmittance and diattenuation images for the horizontal bundle of densely grown fibers (cf. Fig. 10.18a) simulated with double myelin layers and a Yee mesh size of 25 nm and 12.5 nm.

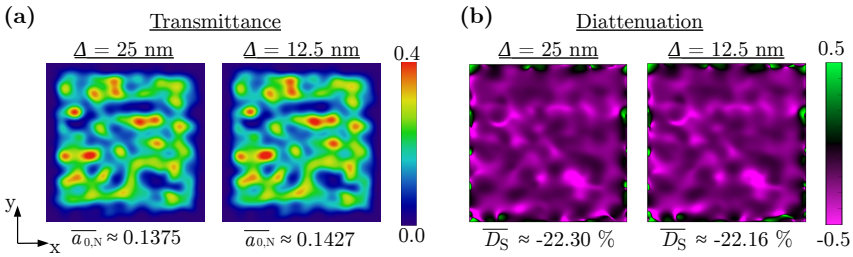

Fig. 10.35: Transmittance images $a_{0,N}$ (a) and diattenuation images D_S (b) of a horizontal bundle of densely grown fibers (see Fig. 10.18a) simulated for the optics of the PM with double myelin layers, normally incident light ($\theta = 0°$), and Yee mesh size Δ. The 3D-PLI and DI simulations were performed as described in Sec. 10.3. For $\Delta = 25\,\text{nm}$, the simulation parameters defined in Tab. 10.5 were used. For $\Delta = 12.5\,\text{nm}$, an MPI grid of $32 \times 32 \times 32$ was chosen, consuming about 205 700 core hours.

Although the transmittance and diattenuation images look very similar for $\Delta = 25\,\text{nm}$ and $\Delta = 12.5\,\text{nm}$, there exist pixel-wise differences (transmittance: RMAD $\approx$ 63.1 %, diattenuation: RMAD $\approx$ 50.6 %). The absolute relative differences between the average values are much less (transmittance: ARDM $\approx$ 3.8 %, diattenuation: ARDM $\approx$ 0.6 %). The averaged diattenuation values are much more similar than those of the hexagonal bundle (transmittance: ARDM $\approx$ 3.11 %, diattenuation: ARDM $\approx$ 20.55 %). Thus, for more complex fiber configurations, simulations with 25 nm Yee mesh size might already give a good estimate not only for the averaged transmittance, but also for the averaged diattenuation values.

Due to limited computing resources, the following simulations were performed for fibers with double myelin layers and 25 nm mesh size. In exceptional cases, a mesh size of 12.5 nm was considered, especially when interpreting simulated diattenuation results.

10.4.3 Different Numbers of Periods

The simulations in Chaps. 11 and 12 were performed for 200 periods with Courant factor $C = 0.8$. To study how the number of periods influences the stability and accuracy of the simulation results, the 3D-PLI and DI simulations for the hexagonal grid of aligned helical horizontal fibers (cf. Fig. 10.27) were performed with 100, 200, 400, and 600 periods. The resulting transmittance images $a_{0,\mathrm{N}}$ and diattenuation images D_S were compared to the images obtained with 600 periods.

After 600 periods, a steady-state solution is reached (the intensity of the wave function does not change with increasing number of periods). Figure 10.36 shows the relative differences (ARDM and RMAD) for the transmittance and diattenuation images (with 600 periods as reference).

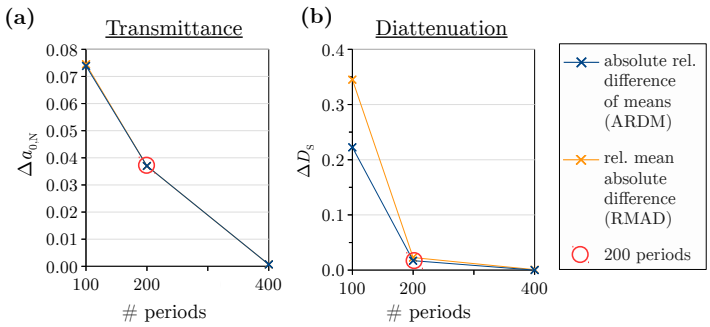

Fig. 10.36: Relative differences between simulations with 100, 200, and 400 periods and a simulation with 600 periods for the hexagonal grid of aligned helical horizontal fibers (cf. Fig. 10.27 and Tab. 10.5) for the optics of the PM: **(a)** difference between transmittance images $a_{0,\mathrm{N}}$, **(b)** difference between diattenuation images D_S. The absolute relative difference of means (ARDM) was computed using Eq. (10.43), the relative mean absolute difference (RMAD) was computed using Eq. (10.44). The values surrounded in red belong to simulations with 200 periods, which were used for the simulations in the subsequent chapters.

The differences decrease with increasing number of periods. For 200 (400) periods, the differences are: ARDM $\approx$ RMAD $\approx 3.7\,\%$ ($0.07\,\%$) for the transmittance images, and ARDM $\approx 1.7\,\%$ ($0.01\,\%$) and RMAD $\approx 2.3\,\%$ ($0.08\,\%$) for the diattenuation images.

Thus, simulations with 400 periods yield almost the same results as simulations with 600 or more periods. A good compromise between computing time and accuracy are 200 periods which yield an estimated error of $3.7\,\%$ or less.

10.4.4 Different Volume Sizes

To reduce computing time, the fiber configurations in Chaps. 11 and 12 were simulated for a reduced simulation volume of $30 \times 30 \times 30\,\mu\mathrm{m}^3$. To estimate the impact of the volume boundaries on the simulation results, the hexagonal grid of aligned helical horizontal fibers (cf. Fig. 10.27) was simulated for larger volumes of $40 \times 40 \times 30\,\mu\mathrm{m}^3$ and $50 \times 50 \times 30\,\mu\mathrm{m}^3$. To ensure a stable solution for larger sample sizes and enable a direct comparison, all simulations were performed with 400 periods.

Figure 10.37 shows the resulting transmittance and diattenuation images. The middle areas with size $15 \times 15\,\mu\mathrm{m}^2$ show similar patterns. The averaged transmittance values for the small volume ($30 \times 30\,\mu\mathrm{m}^2$) and the large volume ($50 \times 50\,\mu\mathrm{m}^2$) are similar

(ARDM ≈ 0.2 %). The absolute relative difference between the corresponding averaged diattenuation values is also small (ARDM ≈ 0.5 %). A pixel-wise comparison (RMAD) is not possible due to the different image sizes.

Thus, the reduced simulation volume of $30 \times 30 \times 30\,\mu m^3$ can be used to study the transmittance and diattenuation effects.

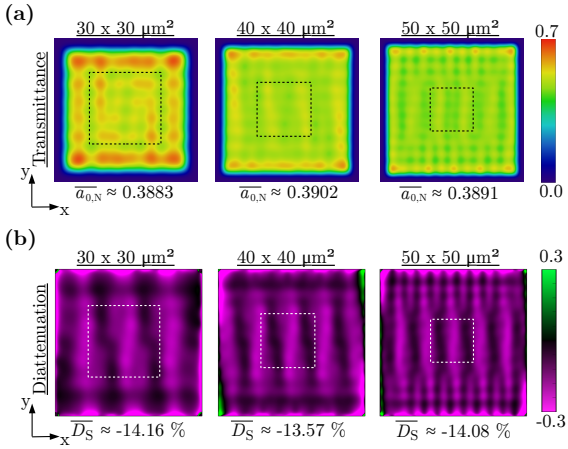

Fig. 10.37: Transmittance images $a_{0,N}$ (a) and diattenuation images D_S (b) of a hexagonal grid of aligned helical horizontal fibers (cf. Fig. 10.27) computed from simulations with different volume sizes in the xy-plane for the optics of the PM. All simulations were performed with 400 periods to ensure a stable solution for larger sample sizes. The dashed lines mark the middle area with size $15 \times 15\,\mu m^2$.

10.4.5 Different Wavelengths

The wavelength spectrum of the PM (see Fig. 7.1a) contains slightly different wavelengths ($\hat{\lambda} = 550\,nm$, FWHM = 9 nm). The study of the USAF resolution target in Sec. 10.1.3.2 has shown that the transmitted light intensities might differ for different wavelengths. To study how to model the PM light source for a configuration of fibers, the 3D-PLI and DI simulations for the hexagonal grid of aligned helical horizontal fibers were performed with $\lambda = \{540, 545, 550, 555, 560\}$ nm and the transmitted light intensities were summed over different numbers of wavelengths, weighted according to the table in Fig. 10.5b.

Figure 10.38 shows the transmittance $a_{0,N}$ and diattenuation D_S images and line profiles obtained from the weighted sum over one, three, and five wavelengths. Figure 10.39 shows the averaged transmittance and diattenuation values obtained for the different wavelengths as well as the values obtained from the weighted sum over the whole wavelength spectrum (orange stars).

As the contribution of the outer wavelengths ($\lambda = 540\,nm$ and 560 nm) to the spectrum are small (cf. Fig. 10.5b), the weighted sums over three and five wavelengths yield similar results, especially for the transmittance images. The values obtained from a single simulation with wavelength $\lambda = 550\,nm$ are different (see Fig. 10.38 in red). The averaged transmittance and diattenuation values differ for different wavelengths (see Fig. 10.39 in blue): they become maximal for $\lambda = 540\,nm$ and minimal for $\lambda = 555\,nm$. The absolute relative differences between the mean values for a single wavelength (1 ×)

and the weighted sum over the wavelength spectrum (5 ×) are ARDM ≈ 1.5 % for the transmittance and 17.1 % for the diattenuation. Thus, the diattenuation is much more susceptible for differences in the wavelength than the transmittance and should – in certain cases – also be studied for three different wavelengths.

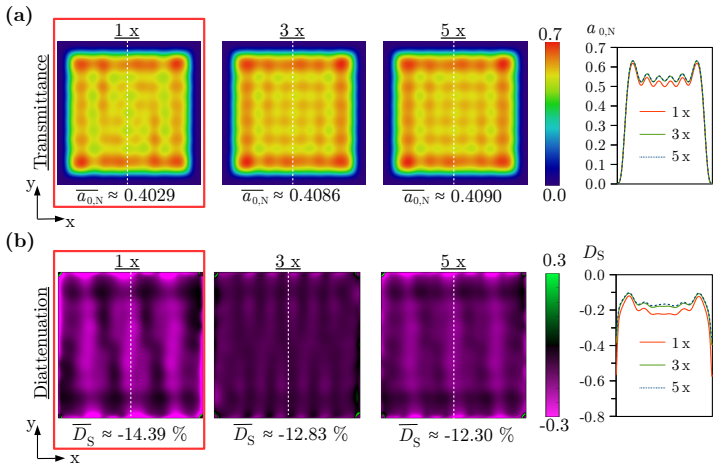

Fig. 10.38: Transmittance $a_{0,N}$ (a) and diattenuation D_S (b) of a hexagonal grid of aligned helical horizontal fibers (cf. Fig. 10.27 and Tab. 10.5) computed as the weighted sum over different numbers of simulation runs with different wavelengths: $\lambda = 550\,\text{nm}$ (1 ×), $\lambda = \{545, 550, 555\}\,\text{nm}$ (3 ×), and $\lambda = \{540, 545, 550, 555, 560\}\,\text{nm}$ (5 ×) weighted according to the wavelength spectrum of the PM (see Fig. 10.5b). The images on the left-hand side show the transmittance and diattenuation images and the respective average values, the graphs on the right-hand side show the corresponding line profiles (middle image pixels evaluated along the y-axis, see white dashed lines). The red frame marks the images obtained from simulations with a wavelength $\lambda = 550\,\text{nm}$, which was used for most simulations in the subsequent chapters.

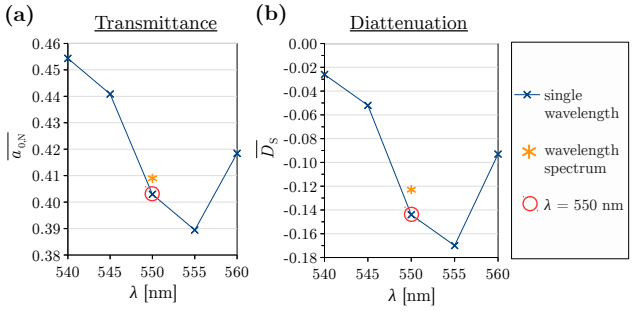

Fig. 10.39: Averaged transmittance values $\overline{a_{0,N}}$ (a) and averaged diattenuation values $\overline{D_S}$ (b) of a hexagonal grid of aligned helical horizontal fibers (cf. Fig. 10.27 and Tab. 10.5) computed for different wavelengths λ (blue) for the optics of the PM. The orange star marks the values obtained for the wavelength spectrum of the PM, i. e. the weighted sum over the transmitted light intensities obtained for $\lambda = \{540, 545, 550, 555, 560\}\,\text{nm}$, weighted according to Fig. 10.5b. The values surrounded in red were obtained from simulations with a wavelength $\lambda = 550\,\text{nm}$, which was used for most simulations in the subsequent chapters.

10.4.6 Different Angles of Incidence

In the PM, the sample is illuminated by slightly different angles of incidence, see Sec. 7.1.1. To save computing time, most simulations in the following chapters were performed for normally incident light. The USAF simulations in Sec. 10.1.3.2, however, have shown that diffuse light might yield different transmitted light intensities. To study how many angles of incidence are needed to efficiently model the PM light source, the simulations of the hexagonal grid of aligned helical fibers (cf. Fig. 10.27 and Tab. 10.5) were performed for light with different angles of incidence (θ, φ).

Figure 10.40 shows the images and line profiles of the transmittance $a_{0,\mathrm{N}}$ and diattenuation D_S for normally incident light ($\theta = 0°$) and diffuse light ($\{\theta = 0°\}$, $\{\theta = 3°$, $\varphi = \eta \times \Delta\varphi\}$, with $\eta \in \{4, 6, 8, 12\}$, $\Delta\varphi = 360°/\eta$) computed from the weighted sum over simulation runs with different angles of incidence, according to Eqs. (10.1) to (10.3) with $\theta = \Delta_\theta = 3°$. Just as in Sec. 10.1.3.2, the weighted sum is referred to as "$\eta \divideontimes \Delta\varphi$" to simplify notation.

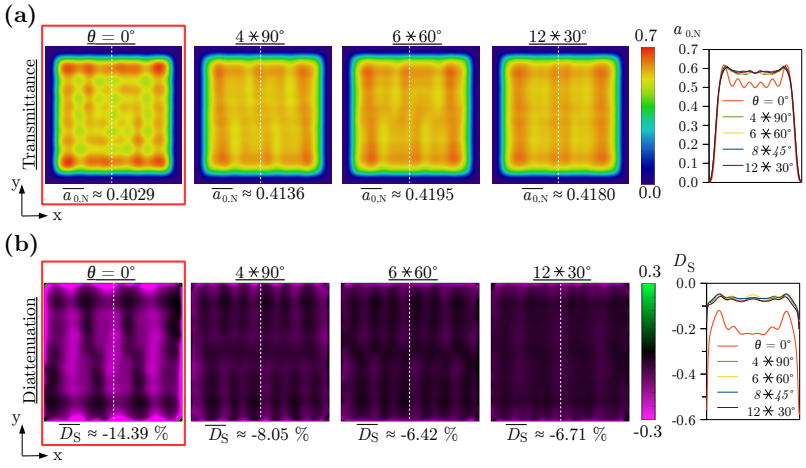

Fig. 10.40: Transmittance $a_{0,\mathrm{N}}$ (a) and diattenuation D_S (b) of a hexagonal grid of aligned helical horizontal fibers (cf. Fig. 10.27 and Tab. 10.5) computed as weighted sum over different angles of incidence for the optics of the PM: normally incident light ($\theta = 0°$) and diffuse light ($\{\theta = 0°\}$, $\{\theta = 3°$, $\varphi = \eta \times \Delta\varphi\}$), referred to as $\eta \divideontimes \Delta\varphi$, with weighting according to Eqs. (10.1) to (10.3). The images on the left-hand side show the transmittance and diattenuation images and the respective average values, the graphs on the right-hand side show the corresponding line profiles (middle image pixels evaluated along the y-axis, see white dashed lines). Line profiles with non-italic labels belong to the displayed images. The red frame marks the images obtained from simulations with normally incident light, which was used for most simulations in the subsequent chapters.

The transmittance and diattenuation values for normally incident light differ a lot from the values for diffuse light.

For better comparison, Fig. 10.41a,b shows the relative differences (ARDM and RMAD) between the transmittance and diattenuation images with $12 \divideontimes 30°$ as reference. The differences between normally incident and diffuse light are especially large for the diattenuation images. For normally incident light, the relative differences are larger than 100 %. For diffuse light with $4 \divideontimes 90°$ angles, the differences are still 20.0 % (ARDM) and 31.5 % (RMAD), they become less for more angles of incidence.

Figure 10.41c shows the averaged diattenuation values for $\theta = 3°$ plotted against the angle φ. The diattenuation values become minimal for $\varphi \in \{0°, 180°\}$ and maximal for $\varphi \in \{90°, 270°\}$. Thus, the diffuse light source needs to be represented by at least $4 \ast 90°$ angles.

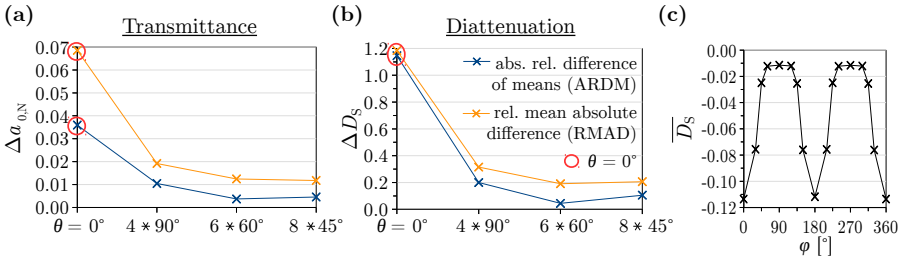

Fig. 10.41: (a-b) Relative differences between simulations with different angles of incidence (normally incident light ($\theta = 0°$) and diffuse light ($\{\theta = 0°\}$, $\{\theta = 3°,\ \varphi = \eta \times \Delta\varphi\}$), referred to as $\eta \ast \Delta\varphi$) and a simulation with $12 \ast 30°$ for the hexagonal grid of aligned helical horizontal fibers (cf. Fig. 10.27 and Tab. 10.5) for the optics of the PM: (a) difference between transmittance images $a_{0,N}$, (b) difference between diattenuation images D_S. The weighting was performed according to Eqs. (10.1) to (10.3). The absolute relative difference of means (ARDM) was computed using Eq. (10.43), the relative mean absolute difference (RMAD) was computed using Eq. (10.44). The values surrounded in red belong to simulations with normally incident light ($\theta = 0°$), which was used for most simulations in the subsequent chapters. **(c)** Averaged diattenuation values $\overline{D_S}$ for different angles of incidence ($\theta = 3°$, φ).

Figure 10.42 shows the transmittance and diattenuation images for the horizontal bundle of densely grown fibers (cf. Fig. 10.18a) simulated with normally incident and diffuse light ($4 \ast 90°$).

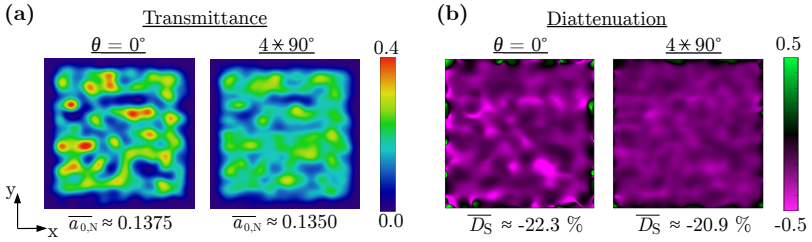

Fig. 10.42: Transmittance images $a_{0,N}$ (a) and diattenuation images D_S (b) of a horizontal bundle of densely grown fibers (see Fig. 10.18a) simulated for the optics of the PM for normally incident light ($\theta = 0°$) and diffuse light ($\{\theta = 0°\}$, $\{\theta = 3°,\ \varphi = 4 \times 90°\}$), referred to as $4 \ast 90°$, with weighting according to Eqs. (10.1) to (10.3). The 3D-PLI and DI simulations were performed as described in Sec. 10.3 with the simulation parameters specified in Tab. 10.5.

Although the images for normally incident and diffuse light show pixel-wise differences (transmittance: RMAD $\approx 19.9\,\%$, diattenuation: RMAD $\approx 26.9\,\%$), the absolute relative differences between the average values (transmittance: ARDM $\approx 1.8\,\%$, diattenuation: ARDM $\approx 6.7\,\%$) are much less than for the hexagonal bundle.

Thus, for more complex configurations, simulations with normally incident light might already give a good estimate for the averaged transmittance and diattenuation values.

10.5 Discussion

In this chapter, a framework has been developed that allows to model 3D-PLI and DI measurements by FDTD simulations: the optical components of the employed polarimeters (PM and LAP) are modeled and the transmitted light intensities of the polarimetric measurements are derived by processing the electric field vectors obtained from the Maxwell Solver. A comparison of simulated and experimental data for a well-defined sample (USAF resolution target) has shown that the light source of the imaging system can sufficiently be modeled by a few numbers of wavelengths and angles of incidence, and that the simulations are more suitable to model the optics of the PM. In addition, a simplified nerve fiber model has been developed (double myelin layers) and the simulation parameters have been evaluated by means of accuracy and computing time.

In the subsequent Chaps. 11 and 12, the developed simulation model will be used to study the transmittance and diattenuation for different fiber configurations.

Limitations of the Simulation Model When interpreting the simulation results, the limitations of the simulation model need to be taken into account.

First of all, the molecular substructure of the myelin layers cannot be included in the simulation model because memory is limited and the software TDME3D does not allow to specify anisotropic refractive indices. As the transmittance is not much influenced by the substructure (cf. Sec. 9.4), it can be investigated quantitatively by FDTD simulations as described in Chap. 11. The diattenuation can only be investigated qualitatively: the DI simulations in Chap. 12 only model the diattenuation caused by anisotropic scattering outside the molecular substructure, the molecular diattenuation was described by an effective analytical model of dichroism instead (see Sec. 3.2.4).

Second, the simulations can only be performed for completely polarized and coherent light. The incoherent and diffuse light source was modeled by a weighted sum over simulation runs with different wavelengths and angles of incidence (see Sec. 10.1.1), neglecting dispersion. Due to limited computing resources, the number of simulation runs is limited so that the light source can only be modeled to a certain extent. The limited computing time also implies that simulations can only be performed for small sample sizes and that possible boundary effects need to be considered when interpreting the simulation results.

Because of these limitations, the Maxwell Solver is more suitable for modeling the imaging system of the PM than of the LAP:

The light source of the PM has a much narrower wavelength spectrum, more coherent light, and smaller illumination angles than the LAP (cf. Sec. 7.1.1) and can therefore be modeled more efficiently. While the polarizing filters in the LAP are non-ideal (cf. Sec. 7.2) and the wavelength mismatch of the retarder generates light that is not perfectly circularly polarized, especially for larger angles of incidence, the polarizing filters in the PM are more ideal so that a simulation with completely polarized light is a good approximation. In addition, the pixel size in the PM ($px \approx 1.33\,\mu m$) is much smaller than in the LAP ($px \geq 21\,\mu m$) so that the underlying fiber architecture can also be resolved in small simulation volumes of $30 \times 30 \times 30\,\mu m^3$. Finally, the optical resolution of the simulated imaging system could be tested for the PM on a model of the USAF resolution target (cf. Sec. 10.1.3.2), while the imaging system of the LAP could only be tested analytically (cf. Sec. 10.1.3.3).

As the FDTD simulations are more suitable for modeling the imaging system of the PM, the evaluation of the simulation parameters in Sec. 10.4 and most of the simulation studies in the subsequent chapters were only performed for the PM.

Averaging The purpose of the FDTD simulations is to study the transmittance and diattenuation effects observed in 3D-PLI and DI measurements. To this end, the simulation results should rather describe the overall effects and not depend on details in the fiber architecture or on the detector pixel position. Therefore, the simulation studies in the subsequent chapters mostly deal with averaged values of the transmittance and diattenuation images.

The simulations of the USAF target in Sec. 10.1.3.2 have shown that the optical resolution of the PM can only be modeled when performing a moving average over 2×2 image pixels. As the average of the images is the same with and without averaging over 2×2 pixels, the model of the optical system described in Secs. 10.1.1 and 10.1.2 can still be used for the PM simulations.

Accuracy of the Simulation Results FDTD simulations are deterministic: the same input always yields the same output. There exist several reasons why the simulated results might differ from the experimental results:

In order to use the simulation results to make general statements about a certain fiber configuration, it is necessary to repeat the simulations with slightly different geometry parameters to ensure that the simulated effects do not depend on the very details of the simulated geometry (e. g. the exact course of a single fiber within a fiber bundle). As the FDTD simulations are computationally very intense, it is not possible to repeat the simulations many times with randomly generated parameters to obtain sufficient statistics for a proper error estimation. This problem is comparable to the experimental situation: due to the limited number of body donors and time consuming tissue preparation, it is to date not possible to study the same brain structure in many different brains.

In addition, the simulation model is a great simplification of the experimental situation, which induces systematic errors. The simplifications are not only due to the limitations of the simulation software and the limited computing time (see above), but also due to imprecise or unavailable knowledge about the structural and optical tissue properties (cf. Sec. 3.2) which makes the generation of a realistic fiber model (ground truth) impossible.

To still estimate the accuracy of the simulation results in Chaps. 11 and 12, individual simulation parameters were varied while the other parameters remained unchanged (see Sec. 10.4). By comparing the simulation results of a more complex model to the simulation results of the simplified model, the stability and reliability of the model was investigated. As the simulation results cannot be compared to the ground truth, the estimated accuracies are only rough estimates.

The studies in Sec. 10.4 have shown that simulations with larger sample sizes and more periods yield similar results as a simulation with $30 \times 30 \times 30\,\mu m^3$ sample size and 200 periods (see Secs. 10.4.3 and 10.4.4). Thus, the simulations in the subsequent chapters were performed for this volume size and number of periods.

As simulations with and without absorption yield comparable results, the simulations were performed with real refractive indices to simplify the simulation model. The simulated transmittance effects in Chap. 11 are therefore only caused by attenuation of light due to scattering and not due to tissue absorption.

Simulations with different wavelengths yield different results, especially for the diattenuation (see Sec. 10.4.5). For this reason, the DI simulations in Chap. 12 were in exceptional cases also performed for three different wavelengths ($\lambda = \{545, 550, 555\}$ nm).

Simulations with normally incident and diffuse light also yield different results, especially for the diattenuation and simple fiber configurations (see Sec. 10.4.6). For more complex configurations, normally incident light might already give a good estimate. To ensure stable results especially for the simulated diattenuation, the simulations were in interesting cases also performed for diffuse light ($\{\theta = 0°\}$, $\{\theta = \theta_{\max}, \varphi = 4 \times 90°\}$).

The number of myelin layers has the largest impact on the accuracy of the simulation results (see Sec. 10.4.2). Due to limited computing resources, a comparison between simulations with double myelin layers and simulations with realistic myelin sheath is only possible for a single fiber. While the simulated transmittance values are still comparable for different numbers of myelin layers, the simulated diattenuation values for double myelin layers and a mesh size of 25 nm differ by more than 25 % from the realistic case. For the hexagonal grid of aligned helical fibers, the difference is about 30 % when comparing the results to a model with three myelin layers and smaller mesh size. In comparison to the realistic case, the difference is expected to be even larger. For a mesh size of 12.5 nm, the difference can be reduced by about one half. For a more complex fiber configuration (bundle of densely grown fibers), the averaged diattenuation values for simulations with 25 nm and 12.5 nm mesh size differ by only 0.6 % (see Sec. 10.4.2.3). In exceptional cases, the DI simulations were performed for a reduced mesh size. When interpreting the simulated diattenuation results, it should be considered that a reduced number of myelin layers also leads to a reduced form birefringence and reduced scattering.

In addition, the cubic Yee grid used for the FDTD simulations is not optimal for the cylindrical geometry of the nerve fibers (curved surfaces are approximated by staircases). In future studies, it should be tested whether alternative meshes (e. g. hexagonal grids) are more suitable and reduce discretization artifacts.

The simulated transmittance values can in principle be considered to be more reliable than the simulated diattenuation values: While the simulated diattenuation was only approximately computed by D_{S} and does not account for anisotropic absorption (dichroism), the transmittance can exactly be computed from only one simulation run and the influence of a possible anisotropy of the refractive index is negligible. In addition, for the selected simulation parameters, the accuracy of the simulated transmittance values is expected to be higher than the accuracy of the simulated diattenuation values.

Chapter 11

Transmittance of Simulated Fiber Configurations

This chapter studies the transmittance of various simulated fiber configurations in order to model and better understand the observed transmittance effects described in Chap. 8.

The measurements in the experimental studies were executed with the PM, which has a narrow wavelength spectrum and small angles of incidence. If not otherwise stated, the simulations were therefore performed for a single wavelength $\lambda = 550\,\text{nm}$ and normally incident light with a Yee mesh size $\Delta = 25\,\text{nm}$. In interesting cases, the simulations were repeated for other wavelengths ($\lambda = \{545, 555\}\,\text{nm}$), a smaller mesh size ($\Delta = 12.5\,\text{nm}$), and different angles of incidence ($\theta = 3°$, $\varphi = \{0°, 90°, 180°, 270°\}$) to demonstrate the robustness of the simulated transmittance effects. The fiber configurations were simulated according to the geometries defined in Sec. 10.2. The implementation of the fiber configurations in TDME3D was described in Sec. 10.3, the simulation parameters were specified in Tab. 10.5.

To study the transmittance and the impact of scattering, the 3D-PLI measurements were simulated as described in Sec. 10.1 and the transmittance images and scattering patterns were computed for all simulated fiber configurations. The scattering patterns were computed according to Eq. (10.13). The transmittance images were computed by determining the Fourier coefficients of order zero $a_{0,\text{N}}(\vec{r})$ from the normalized transmitted light intensity profiles $I_\text{N}(\vec{r}, \rho)$, cf. Eqs. (10.33) and (10.36). To study the effect of the numerical aperture, the transmittance images were not only computed for the imaging system of the PM (numerical aperture: NA = 0.15, microlenses: $r_0 = 0.665\,\mu\text{m}$), but also for the case without lenses (NA = 1, $r_0 = 0\,\mu\text{m}$). As the approximation $I \approx I \cos\theta_k$ is not valid for NA = 1, the resulting transmittance images do not represent any measurement results and were only used as a reference.

To model and understand the inclination dependence of the transmittance described in Sec. 8.3, various fiber bundles were simulated for different inclination angles (Sec. 11.1). To explore how the transmittance depends on the fiber structure and organization, horizontal fiber bundles with different fiber properties (different fiber orientations, radii, myelin sheath thicknesses, refractive indices, and sizes) were simulated (Sec. 11.2). Finally, the transmittance was studied for horizontal crossing fiber configurations with different crossing angles and compared to the transmittance of vertical fiber configurations (Sec. 11.3).

Parts of Secs. 11.1.2, 11.1.3, 11.3 and 11.4 have been published in Menzel *et al.* (2018a) [67].

11.1 Transmittance of Inclined Fiber Bundles

The experimental studies in Chap. 8 have shown that the transmittance decreases with increasing inclination angle of the nerve fibers. To model this phenomenon, the scattering patterns and transmittance images were computed for different simulated fiber bundles (oriented along the x-axis) with different inclination angles[1] (rotated around the y-axis): $\alpha = \{0°, 10°, \ldots, 90°\}$. If not otherwise stated, the simulations were only performed for normally incident (non-diffuse) light with a wavelength of 550 nm and a mesh size of 25 nm to save computing time. To better understand which geometric features are responsible for the observed effects, the inclination dependence of the transmittance was first studied for simple fiber configurations (hexagonal grid of fibers in Sec. 11.1.1) before looking at more complex models (bundle of densely grown fibers in Sec. 11.1.2 and inhomogeneous fiber bundles in Sec. 11.1.3).

11.1.1 Hexagonal Grid of Fibers

The hexagonal grid of fibers was generated for different fiber geometries as described in Sec. 10.2.1: straight fibers, aligned helical fibers, unaligned helical fibers with same strides, and unaligned helical fibers with different strides. Figure 11.1a shows the cross-sections through the xz-mid-plane of the corresponding fiber models that were used for the simulation by TDME3D. All simulations were performed with normally incident light.

Figure 11.1b shows the resulting scattering patterns I_k exemplary for some inclination angles $\alpha = 0°, 30°, 60°, 90°$. The corresponding transmittance images can be found in Appx. D.10.

Both transmittance images and scattering patterns show certain symmetries and periodicities caused by the underlying fiber configurations. The scattering patterns show distinct peaks: the lower the symmetry of the simulated bundle, the higher the number of peaks. For intermediate inclination angles ($30° \leq \alpha < 60°$), more light is scattered in the direction of the fibers (i. e. in the positive x-direction), especially for less symmetric fiber bundles (unaligned helical fibers with different strides).

To study the inclination dependence of the transmittance, the average value of the transmittance images ($\overline{a_{0,\mathrm{N}}}$) was plotted against the fiber inclination (α) for the different fiber geometries of the hexagonal grid (see Fig. 11.2).

The resulting transmittance curves show multiple local minima and do not follow a smooth curve. In the case of straight and aligned helical fibers (Fig. 11.2a,b), the averaged transmittance for flat fibers ($\alpha \leq 30°$) depends less on the numerical aperture (NA) than for steeper fibers ($\alpha > 40°$). For the imaging system of the PM (NA = 0.15), the averaged transmittance values for horizontal and vertical fibers are similar. While straight fibers show minimum transmittance values at $\alpha = 10°$ and 50°, the transmittance for aligned helical fibers only becomes minimal at $\alpha = 50°$. In the case of unaligned helical fibers (Fig. 11.2c,d), the averaged transmittance depends for all inclination angles on the numerical aperture. For NA = 0.15, the averaged transmittance values for vertical fibers are lower than for horizontal fibers. In the case of unaligned helical fibers with different strides (Fig. 11.2d), the averaged transmittance decreases

[1] The inclination of a fiber bundle is defined by the principal (average) orientation of the fibers within the bundle, i. e. horizontal or vertical bundles contain fibers with an average inclination of $\alpha \approx 0°$ or $\alpha \approx 90°$, respectively. The inclination angles of single fibers (or fiber segments) might of course differ from the overall inclination of the fiber bundle.

with increasing inclination angle so that the transmittance of vertical fibers is much less than the transmittance of horizontal fibers.

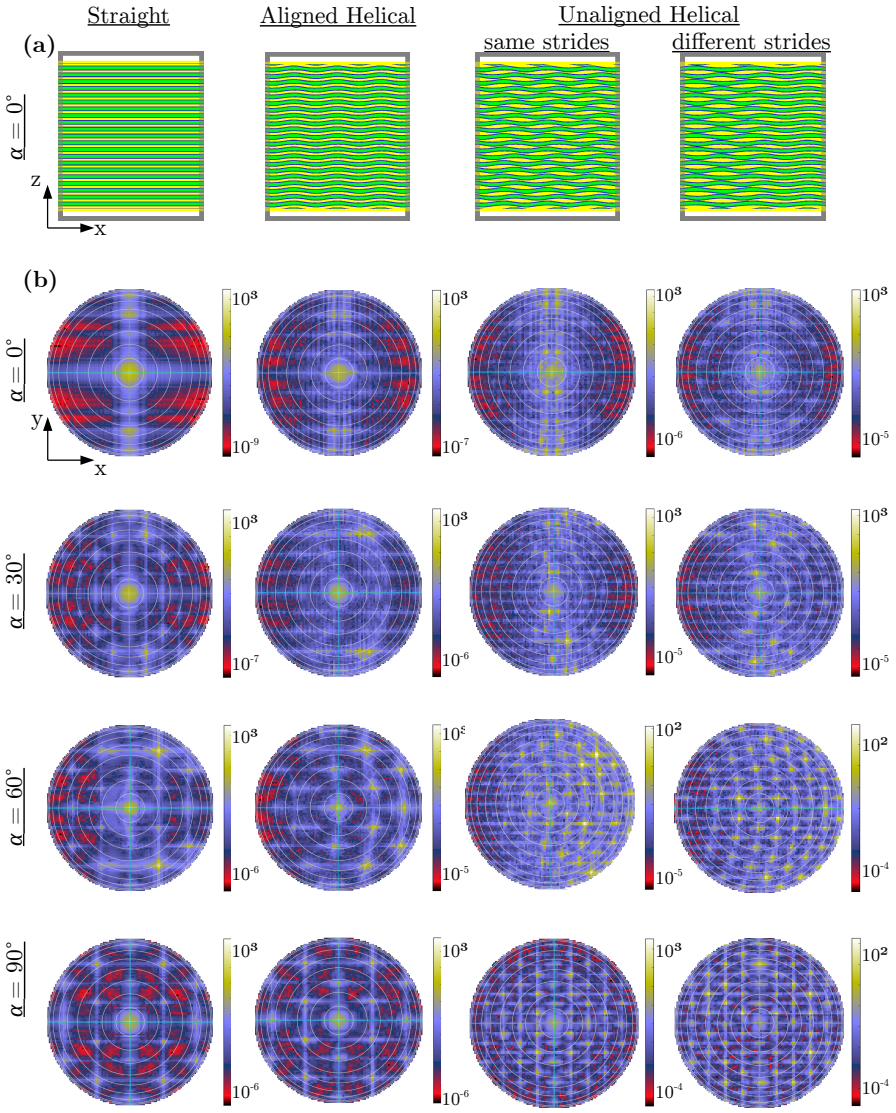

Fig. 11.1: (a) Cross-sections through the xz-mid-plane of a hexagonal grid of fibers simulated by TDME3D with different geometries (cf. Sec. 10.2.1): straight fibers, aligned helical fibers, unaligned helical fibers with same strides, and unaligned helical fibers with different strides. **(b)** Scattering patterns (I_k) computed from a simulated 3D-PLI measurement of the hexagonal grid of fibers with different geometries and different inclination angles α (for normally incident light with $\lambda = 550\,\text{nm}$ and simulation parameters specified in Tab. 10.5). Note that the value ranges differ between images.

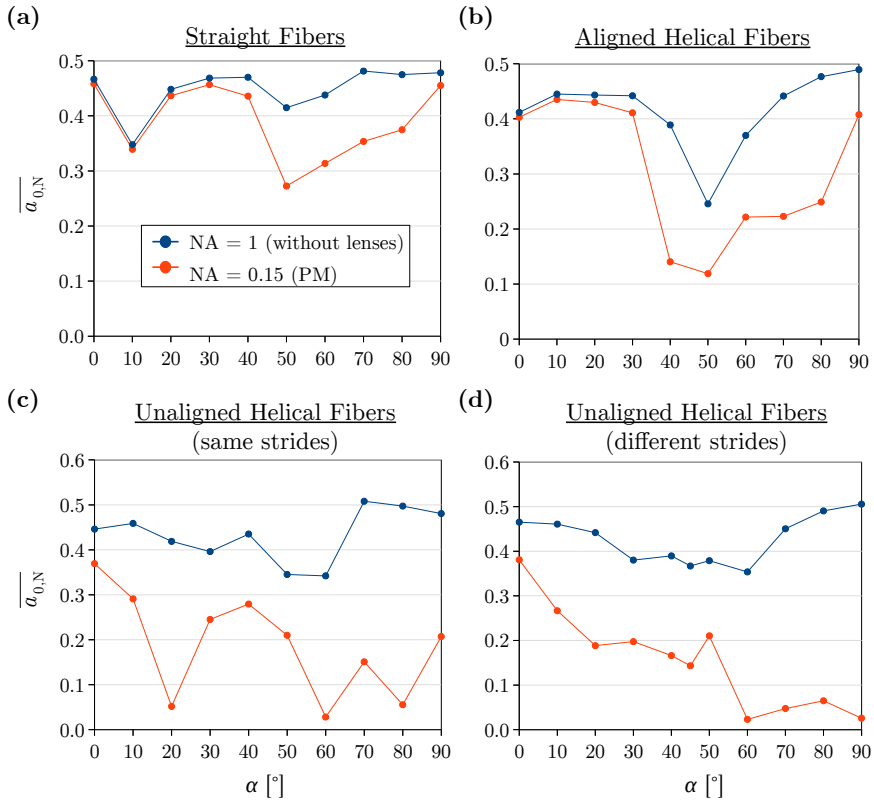

Fig. 11.2: Averaged transmittance $\overline{a_{0,N}}$ plotted against the fiber inclination angle α for a hexagonal grid of fibers with different geometries (cf. Sec. 10.2.1): (a) straight fibers, (b) aligned helical fibers, (c) unaligned helical fibers with same strides, (d) unaligned helical fibers with different strides. The red/blue lines correspond to the transmittance images that were computed for normally incident light with $\lambda = 550\,\text{nm}$ and simulation parameters specified in Tab. 10.5 for the imaging system of the PM/without lenses.

11.1.2 Bundle of Densely Grown Fibers

Even in the case of unaligned helical fibers with different strides, the transmittance images of the hexagonal grid of fibers show some artifacts due to grid symmetries. To break the symmetry and make the fiber bundle more realistic, a bundle of densely grown fibers (see Sec. 10.2.2) was simulated for different inclination angles. Figure 11.3a shows (exemplary for an inclination angle of 45°) a 3D view and cross-sections through the mid-planes of the fiber model that was used for the simulation by TDME3D.

Figure 11.3b shows the resulting transmittance images $a_{0,N}$ for some inclination angles $\alpha = \{0°, 20°, \dots 80°\}$ and the scattering patterns for all inclination angles. The images show less symmetries and periodicities than the hexagonal grid of fibers. The maximum and minimum transmittance values are broadly distributed over the transmittance images and the scattering patterns show no distinct peaks.

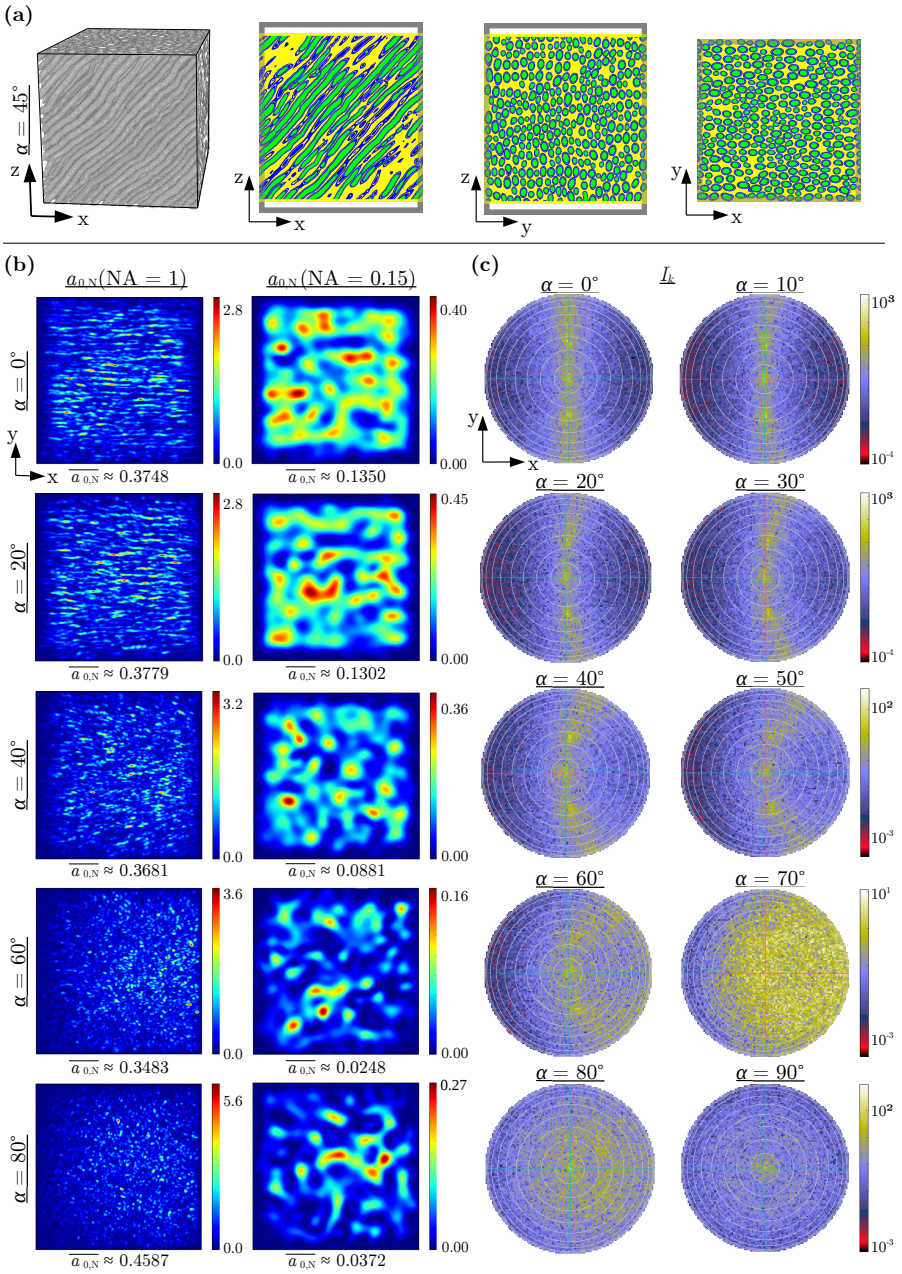

Fig. 11.3: (a) 3D view and cross-sections through mid-planes for the bundle of densely grown fibers (cf. Sec. 10.2.2) simulated by TDME3D with an inclination angle of $\alpha = 45°$. **(b,c)** Transmittance images ($a_{0,N}$) and scattering patterns (I_k) computed from a simulated 3D-PLI measurement for different fiber inclination angles α (for normally incident light with $\lambda = 550\,\text{nm}$ and simulation parameters specified in Tab. 10.5). The transmittance images were computed for the imaging system of the PM (with numerical aperture NA = 0.15) and for the case without lenses (NA = 1). Note that the value ranges differ between images. A similar figure has been published in Menzel *et al.* (2018a) [67] Fig. 12.

For flat fibers, the light is mostly scattered under angles perpendicular to the principal axis of the fiber bundle (i. e. along the y-axis). For intermediate inclination angles, the light is scattered more and more in the direction of the fibers (i. e. in the positive x-direction). For an inclination angle of 70°, the light is broadly scattered in almost all directions.

The blue and red lines in Fig. 11.4a show the corresponding transmittance curves, i. e. the average values of the transmittance images ($\overline{a_{0,\mathrm{N}}}$) plotted against the inclination angle (α). To enable a better comparison between horizontal and vertical fibers, the lower figure shows the transmittance curves divided by the averaged transmittance of the horizontal fiber bundle ($\alpha = 0°$), respectively.

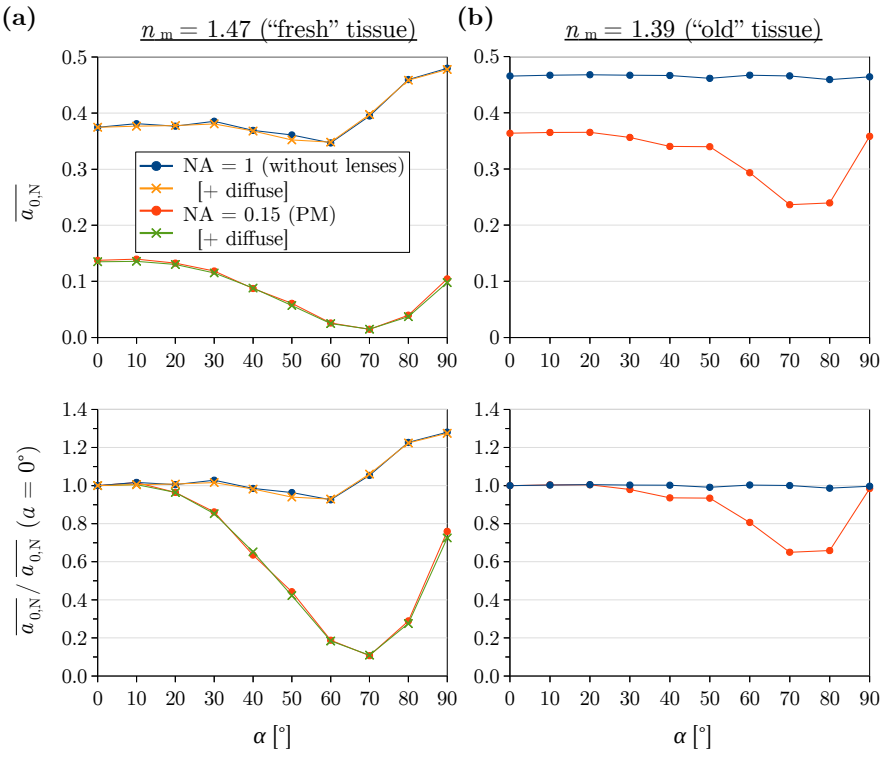

Fig. 11.4: Averaged transmittance $\overline{a_{0,\mathrm{N}}}$ plotted against the fiber inclination angle α for a bundle of densely grown fibers (cf. Sec. 10.2.2): **(a)** The refractive index of myelin corresponds to given literature values of lipids ($n_\mathrm{m} = 1.47$). **(b)** The refractive index of myelin is reduced ($n_\mathrm{m} = 1.39$) to model tissue with long embedding time. The red and green lines correspond to the transmittance images that were computed for the imaging system of the PM. The blue and yellow lines correspond to the transmittance images that were computed without lenses. In addition to normally incident light (blue and red lines), the transmittance curves in (a) are also shown for diffuse light (yellow and green lines) with angles of incidence $\{\theta = 0°\}$ and $\{\theta = 3°,\ \varphi = \{0°, 90°, 180°, 270°\}\}$, weighted according to Eqs. (10.1) to (10.3). To enable a better comparison between horizontal and vertical fibers, the lower figures show the transmittance curves normalized by the averaged transmittance of the horizontal fiber bundle, respectively. A similar figure has been published in Menzel *et al.* (2018a) [67] Fig. 13a-b.

The transmittance curves are much smoother than the curves for the hexagonal grid of fibers (cf. Fig. 11.2). The averaged transmittance decreases with decreasing numerical aperture. For NA = 0.15, the transmittance decreases significantly between $\alpha = 30°$ and $\alpha = 70°$. The transmittance for fibers with 70° inclination is about 90 % less than the transmittance for horizontal fibers. For steeper fibers, the transmittance values increase, but are still less than for the horizontal case – as observed in the 3D-PLI measurement.

Simulations with different wavelengths ($\lambda = \{545, 550, 555\}$ nm) and a smaller Yee mesh size ($\Delta = 12.5$ nm) yield very similar transmittance curves (see Fig. D.8a in Appx. D.11). Therefore, all subsequent simulations were performed for $\lambda = 550$ nm and $\Delta = 25$ nm.

Diffuse Light So far, normally incident light ($\theta = 0°$) was used for the simulations. To see whether the results are also valid for a diffuse light source, the simulations were repeated for light with non-normal incidence, considering the illumination angles in the PM ($\{\theta = 0°\}$, $\{\theta = 3°, \varphi = \{0°, 90°, 180°, 270°\}\}$). The transmittance images were computed from the weighted sum of the resulting light intensities according to Eqs. (10.1) to (10.3).

The resulting transmittance curves are shown in Fig. 11.4a (yellow and green lines). Apparently, the curves for normally incident and diffuse light are very similar. The maximum relative difference between the averaged transmittance values is less than 9 % (for $\alpha = 50°$). Therefore, all subsequent simulations were performed with normally incident light, which reduces the computing time by 80 %.

Long Embedding Time The refractive indices used for the simulations have been derived in Sec. 3.2.1, assuming that the brain tissue is measured one day after tissue embedding (in the following referred to as *"fresh"* tissue). Over time, the glycerin solution (with refractive index $n_g = 1.37$) presumably soaks into the myelin sheaths, which reduces the effective refractive index of myelin ($n_m = 1.47$). To study the transmittance effect for brain tissue that is measured a long time after tissue embedding (in the following referred to as *"old"* tissue), the simulations were repeated with a reduced myelin refractive index ($n_m = 1.39$).

Figure 11.4b shows the resulting transmittance curves. The transmittance values are much higher than for "fresh" tissue (with $n_m = 1.47$), i. e. the fiber bundle becomes more transparent. For NA = 0.15, about 36 % of the light is transmitted for horizontal fibers (in the case of "fresh" tissue, it is less than 14 %). In addition, the minimum transmittance value is shifted to slightly larger inclination angles (between $\alpha = 70°$ and 80°). The minimum transmittance is only about 35 % less than the transmittance for horizontal fibers (in the case of "fresh" tissue, it is about 90 % less). Another difference is that the transmittance for horizontal and vertical fibers is almost the same.

11.1.3 Inhomogeneous Fiber Bundles

The bundle of densely grown fibers contains fibers with similar orientations. To see whether the decrease in transmittance can be reproduced for more inhomogeneous fiber constellations, two fiber bundles generated by the VCS (see Sec. 10.2.3) were simulated with normally incident light for different inclination angles: a fiber bundle with very different fiber radii ($\Delta r = 0.7$ µm, cf. Fig. 10.22) and a fiber bundle with very different fiber orientations ($\Xi = 10$ µm, cf. Fig. 10.20).

Figure 11.5 shows the resulting transmittance curves. The curves for the bundle with broad fiber radius distribution ($\Delta r = 0.7$ µm, $\Xi = 1$ µm) look similar to the curves for

the bundle of densely grown fibers (with $\Delta r = 0.3\,\mu m$), cf. Fig. 11.5a and 11.4a. The curves for the bundle with broad fiber orientation distribution ($\Delta r = 0.3\,\mu m$, $\Xi = 10\,\mu m$) look different: while the transmittance in Fig. 11.4a becomes minimal at $\alpha = 70°$ and the averaged transmittance for vertical fibers is only about 25 % less than for horizontal fibers, the transmittance values in Fig. 11.5b decrease monotonically with increasing fiber inclination and become minimal for vertical fibers (the transmittance for vertical fibers is more than 80 % less than for horizontal fibers).

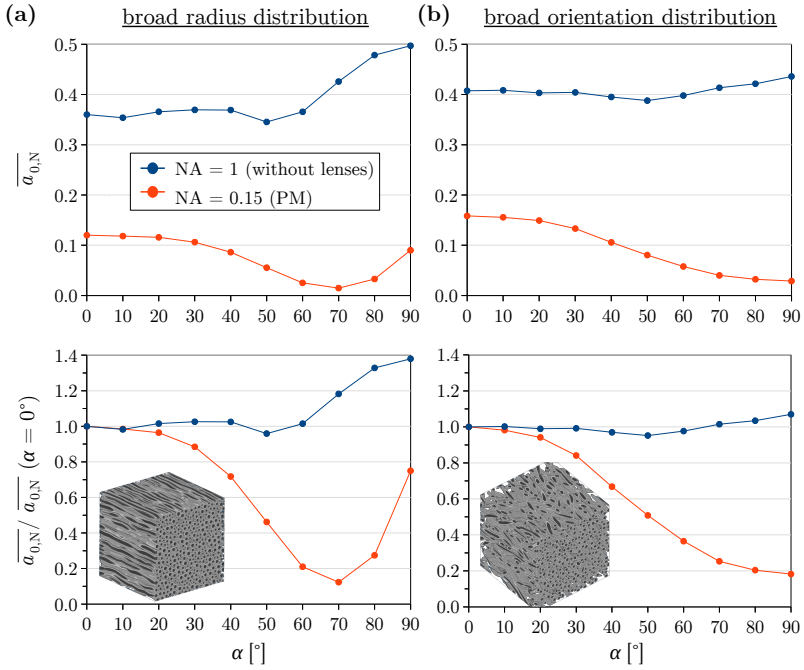

Fig. 11.5: Averaged transmittance $\overline{a_{0,N}}$ plotted against the fiber inclination angle α for inhomogeneous fiber bundles: **(a)** bundle with broad fiber radius distribution ($\Delta r = 0.7\,\mu m$, see Sec. 10.2.3.2), **(b)** bundle with broad fiber orientation distribution ($\Xi = 10\,\mu m$, see Sec. 10.2.3.1). The red/blue lines correspond to the transmittance images that were computed for normally incident light for the imaging system of the PM/without lenses. To enable a better comparison between horizontal and vertical fibers, the lower figures show the transmittance curves normalized by the averaged transmittance values of the horizontal fiber bundle, respectively. Subfigure (b) has been published in Menzel *et al.* (2018a) [67] Fig. 13c.

11.2 Transmittance of Horizontal Fiber Bundles with Different Fiber Properties

To study in more detail how the transmittance depends on the fiber configuration and structure, the transmittance was computed for horizontal fiber bundles with different fiber properties (different fiber orientations, fiber radii, myelin sheath thicknesses, refractive indices, and fiber sizes). To enable a comparison with the simulation results in

Sec. 11.1, the fiber bundles were generated with the VCS by varying the fiber properties of the reference fiber bundle (Fig. 10.18b) as described in Sec. 10.2.3.

For all simulated fiber bundles, the scattering patterns and transmittance curves were computed. The scattering patterns and averaged transmittance values belonging to the reference fiber bundle are highlighted with a red frame and a star, respectively. All simulations were performed with normally incident (non-diffuse) light with a wavelength of 550 nm and a mesh size of 25 nm.

11.2.1 Different Fiber Orientation Distributions

Figure 11.6b shows the scattering patterns for horizontal fiber bundles with different fiber orientation distributions, i. e. bundles generated with different maximum displacements Ξ in the VCS (cf. Fig. 10.20). With increasing fiber orientation distribution, the scattering broadens.

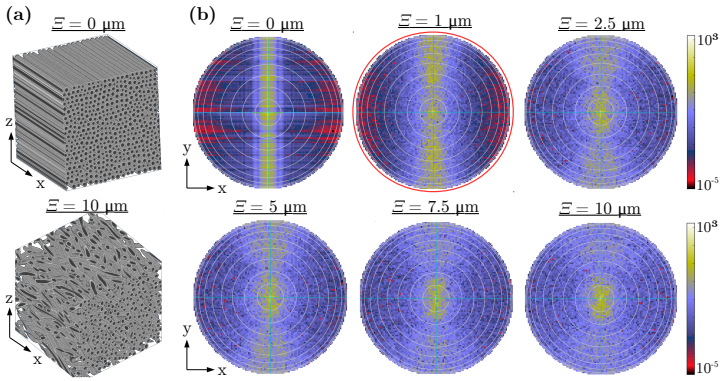

Fig. 11.6: (a) 3D views and **(b)** scattering patterns (I_k) for horizontal fiber bundles with different fiber orientation distributions (i. e. bundles generated with different maximum displacements Ξ in the VCS, cf. Fig. 10.20). The red frame highlights the scattering pattern of the reference fiber bundle (see Fig. 10.18b).

Figure 11.7 shows the corresponding transmittance curves for NA = 1 and 0.15. For NA = 0.15, the transmittance values for non-straight fibers ($\Xi > 0$) are similar.

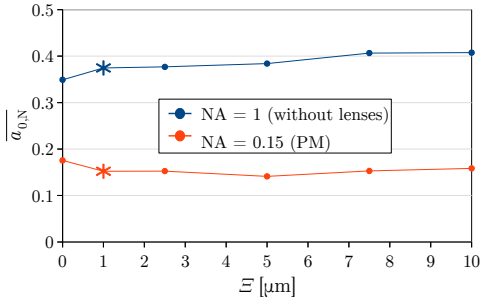

Fig. 11.7: Averaged transmittance $\overline{a_{0,N}}$ of a horizontal fiber bundle plotted against the fiber orientation distribution (i. e. the maximum displacement Ξ used to generate the bundle by the VCS, cf. Fig. 10.20). The red/blue lines correspond to the transmittance images that were computed for the imaging system of the PM/without lenses. The stars mark the values for the reference fiber bundle (cf. Fig. 10.18b).

11.2.2 Different Fiber Radius Distributions

Figure 11.8b shows the scattering patterns for bundles with equal average fiber radius ($r_{avg} = 0.65\,\mu m$) and different fiber radius distributions $\Delta r = r_{max} - r_{min}$ (cf. Fig. 10.22). The scattering patterns look similar for different Δr: the light is scattered in directions perpendicular to the predominant fiber orientation (i. e. along the y-axis).

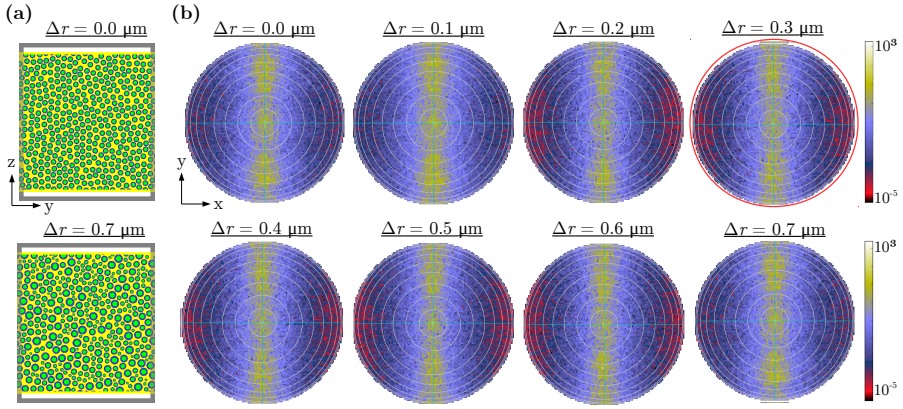

Fig. 11.8: (a) Cross-sections through yz-mid-plane and **(b)** scattering patterns (I_k) for horizontal fiber bundles with equal average fiber radius ($r_{avg} = 0.65\,\mu m$) and different fiber radius distributions $\Delta r = r_{max} - r_{min}$ (see Fig. 10.22). The red frame highlights the scattering pattern of the reference fiber bundle (see Fig. 10.18b).

Figure 11.9 shows the corresponding transmittance curves for NA = 1 and 0.15. For NA = 0.15, the averaged transmittance decreases with increasing fiber radius distribution. The averaged transmittance value for fibers with very different fiber radii ($\Delta r = 0.7\,\mu m$) is about 25 % less than the averaged transmittance value for fibers with same radii ($\Delta r = 0$).

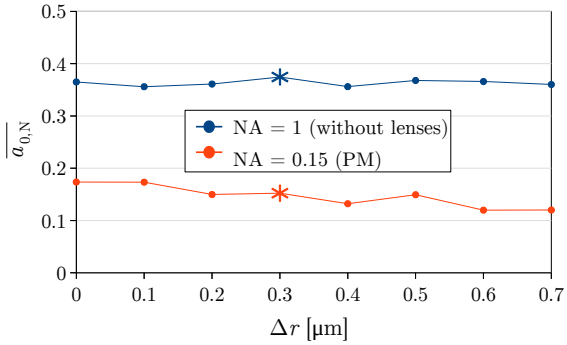

Fig. 11.9: Averaged transmittance $\overline{a_{0,N}}$ of a horizontal fiber bundle with equal average fiber radius ($r_{avg} = 0.65\,\mu m$) plotted against the fiber radius distribution $\Delta r = r_{max} - r_{min}$ (cf. Fig. 10.22). The red/blue lines correspond to the transmittance images that were computed for the imaging system of the PM/without lenses. The stars mark the values for the reference fiber bundle (cf. Fig. 10.18b).

11.2.3 Different Myelin Sheath Thicknesses

To study the effect of the myelin sheath thickness on the transmittance, the reference fiber bundle was simulated with different myelin sheath thicknesses (relative to the fiber radius r): $t_{\text{sheath}} = \{0, 0.2, 0.3, 0.4, 0.5, 0.6\}\, r$. The relative thicknesses of the two myelin layers ($t_{\text{m}} = \frac{3}{7}\, t_{\text{sheath}}$) and of the separating glycerin layer ($t_{\text{g}} = \frac{1}{7}\, t_{\text{sheath}}$) were not changed.

Figure 11.10b shows the scattering patterns for different myelin sheath thicknesses. The scattering patterns look similar for different t_{sheath}: the light is scattered in directions perpendicular to the predominant fiber orientation (i. e. along the y-axis). For thinner myelin sheaths, the scattering angles become smaller.

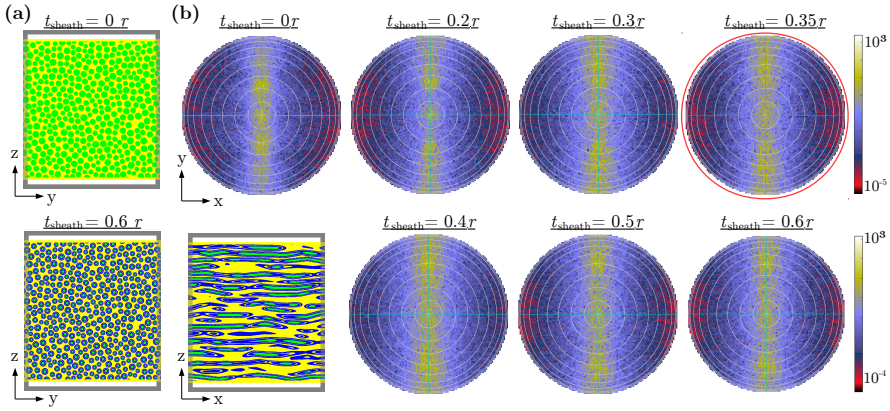

Fig. 11.10: (a) Cross-sections through yz(xz)-mid-planes and **(b)** scattering patterns (I_k) for a horizontal fiber bundle (see Fig. 10.18b) with different myelin sheath thicknesses t_{sheath} (in terms of the fiber radius r). The red frame highlights the scattering pattern belonging to the myelin sheath thickness that was used for all other simulations in this chapter ($t_{\text{sheath}} = 0.35\, r$). Note that the value ranges differ between upper and lower images.

Figure 11.11 shows the corresponding transmittance curves for NA = 1 and 0.15.

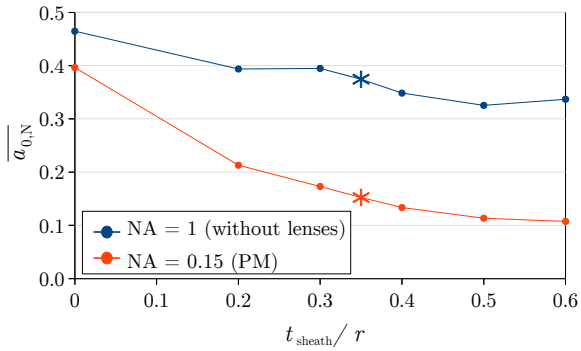

Fig. 11.11: Averaged transmittance $\overline{a_{0,\text{N}}}$ of a horizontal fiber bundle (see Fig. 10.18b) plotted against the myelin sheath thickness t_{sheath} relative to the fiber radius r. The red/blue lines correspond to the transmittance images that were computed for the imaging system of the PM/without lenses. The stars mark the myelin sheath thickness that was used for all other simulations in this chapter ($t_{\text{sheath}} = 0.35\, r$).

For NA = 0.15, the averaged transmittance strongly decreases with increasing myelin sheath thickness. The averaged transmittance value for fibers with a thick myelin sheath ($t_{\text{sheath}} = 0.6\,r$) is about 75 % less than the averaged transmittance value for unmyelinated fibers ($t_{\text{sheath}} = 0$).

11.2.4 Different Myelin Refractive Indices

With increasing time after embedding the brain section (cf. Sec. 4.1), the surrounding glycerin solution presumably soaks into the myelin sheaths, which causes the effective refractive index of myelin ($n_{\text{m}} = 1.47$) to become more similar to the refractive index of the surrounding tissue ($n_{\text{surr}} = 1.37$). To study how the transmittance changes with increasing embedding time of the tissue sample, the reference fiber bundle was simulated for different myelin refractive indices n_{m} between 1.47 and 1.37.

Figure 11.12 shows the resulting scattering patterns for different myelin refractive indices. The light is scattered in directions perpendicular to the predominant fiber orientation (i. e. along the y-axis). When the refractive index of myelin becomes similar to the one of the surrounding glycerin solution, the scattering angles become smaller.

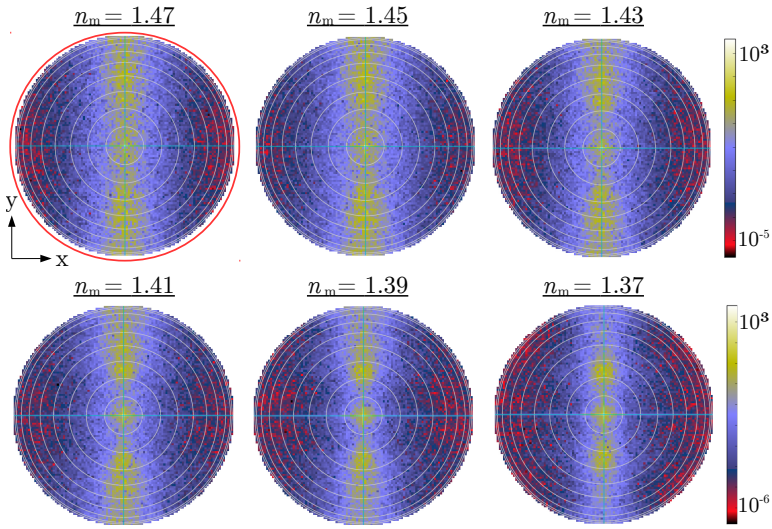

Fig. 11.12: Scattering patterns (I_k) for a horizontal fiber bundle (see Fig. 10.18b) with different myelin refractive indices n_{m}. The red frame highlights the scattering pattern belonging to the myelin refractive index of tissue directly after embedding ($n_{\text{m}} = 1.47$) that was used for all other simulations in this chapter. Note that the value ranges differ between upper and lower images.

Figure 11.13 shows the corresponding transmittance curves for NA = 1 and 0.15. With decreasing n_{m} (i. e. when the refractive indices of myelin and surrounding glycerin solution become more similar with increasing time after tissue embedding), the averaged transmittance values increase and the transmittance curves for NA = 1 and NA = 0.15 become more similar.

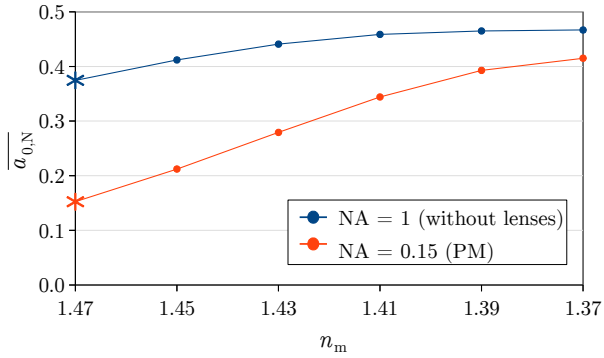

Fig. 11.13: Averaged transmittance $\overline{a_{0,N}}$ of a horizontal fiber bundle (see Fig. 10.18b) plotted against the myelin refractive index n_m. The red/blue lines correspond to the transmittance images that were computed for the imaging system of the PM/without lenses. The stars mark the myelin refractive index of tissue directly after embedding ($n_m = 1.47$) that was used for all other simulations in this chapter.

11.2.5 Different Scales

So far, the simulations were performed with small fiber diameters around 1 µm. To study how the transmittance depends on the size of the fibers, the reference fiber bundle was scaled by factors of 1, 2, 2.5, 3, 4, and 5, cropped to a volume of $30 \times 30 \times 30\,\mu m^3$, and discretized into voxels of $25^3\,nm^3$ (see Fig. 10.24).

Figure 11.14 shows the resulting scattering patterns for different scaling factors. The light is scattered in directions perpendicular to the predominant fiber orientation (i. e. along the y-axis). The scattering increases with increasing scaling factor.

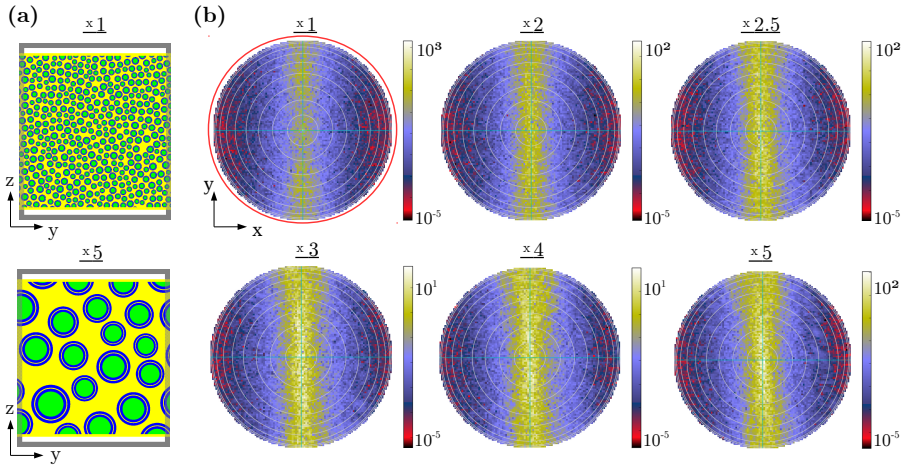

Fig. 11.14: (a) Cross-sections through yz-mid-plane and **(b)** scattering patterns (I_k) for a horizontal fiber bundle with different scaling factors (see Fig. 10.24). The red frame highlights the scattering pattern belonging to the reference bundle without scaling. Note that the value ranges differ between images.

Figure 11.15 shows the corresponding transmittance curves for NA = 1 and 0.15. For NA = 0.15, the averaged transmittance decreases with increasing scaling factor, i. e. with increasing size of the fibers, up to 60 % (for a scaling factor of 4).

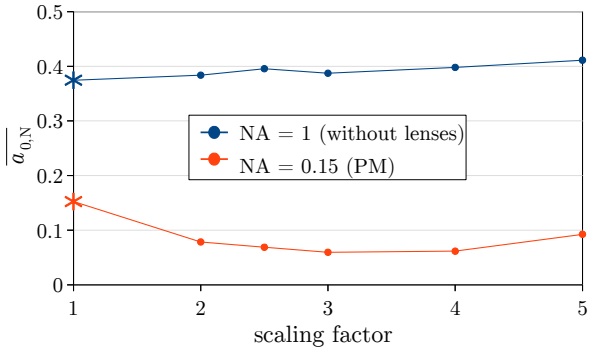

Fig. 11.15: Averaged transmittance $\overline{a_{0,N}}$ of a horizontal fiber bundle (see Fig. 10.24) plotted against the scaling factor. The red/blue lines correspond to the transmittance images that were computed for the imaging system of the PM/without lenses. The stars mark the values for the reference fiber bundle without scaling.

11.3 Transmittance of Horizontal Crossing vs. Vertical Fibers

As both the birefringence and the diattenuation of horizontal 90°-crossing and vertical fibers are small, these fiber configurations cannot easily be distinguished in a standard 3D-PLI or DI measurement. The simulation results in Sec. 11.1, however, suggest that horizontal fibers have higher transmittance values than vertical fibers. To investigate whether the transmittance can be used to distinguish between horizontal crossing and vertical fibers, the transmittance of horizontal crossing fibers was studied for different crossing angles and the results were compared to the transmittance of vertical fibers.

The horizontal crossing fibers were generated as separate and interwoven fiber bundles with different crossing angles $\chi = \{0°, 15°, \ldots, 90°\}$ as described in Sec. 10.2.3.4. For $\chi = 0°$, the reference fiber bundle (see Fig. 10.18b) was used. The vertical fiber bundle was generated by rotating the reference fiber bundle by 90°.

Figures 11.16b and 11.16c show the transmittance images ($a_{0,N}$) and the scattering patterns (I_k) for the 90°-crossing fibers (separate and interwoven bundles with $\alpha = 0°$) and for the vertical fibers with $\alpha = 90°$. Both the transmittance images and the scattering patterns look similar for separate and interwoven 90°-crossing fiber bundles. The averaged transmittance values for the interwoven fiber bundles are a bit larger than those for the separate fiber bundles. For NA = 0.15, the averaged transmittance of the vertical fiber bundle is lower than for the horizontal crossing fibers and the scattering pattern looks different.

Figure 11.17 shows the scattering patterns for the vertical fibers and the horizontal crossing fibers (separate and interwoven bundles) for different crossing angles $\chi = \{0°, 30°, 60°, 90°\}$. The scattering patterns for separate and interwoven crossing fiber bundles look similar for all crossing angles. The underlying fiber configuration, i. e. the crossing angle of the fibers, is clearly visible in all scattering patterns. The scattering

patterns of the horizontal crossing fibers look clearly different from the scattering pattern of the vertical fibers.

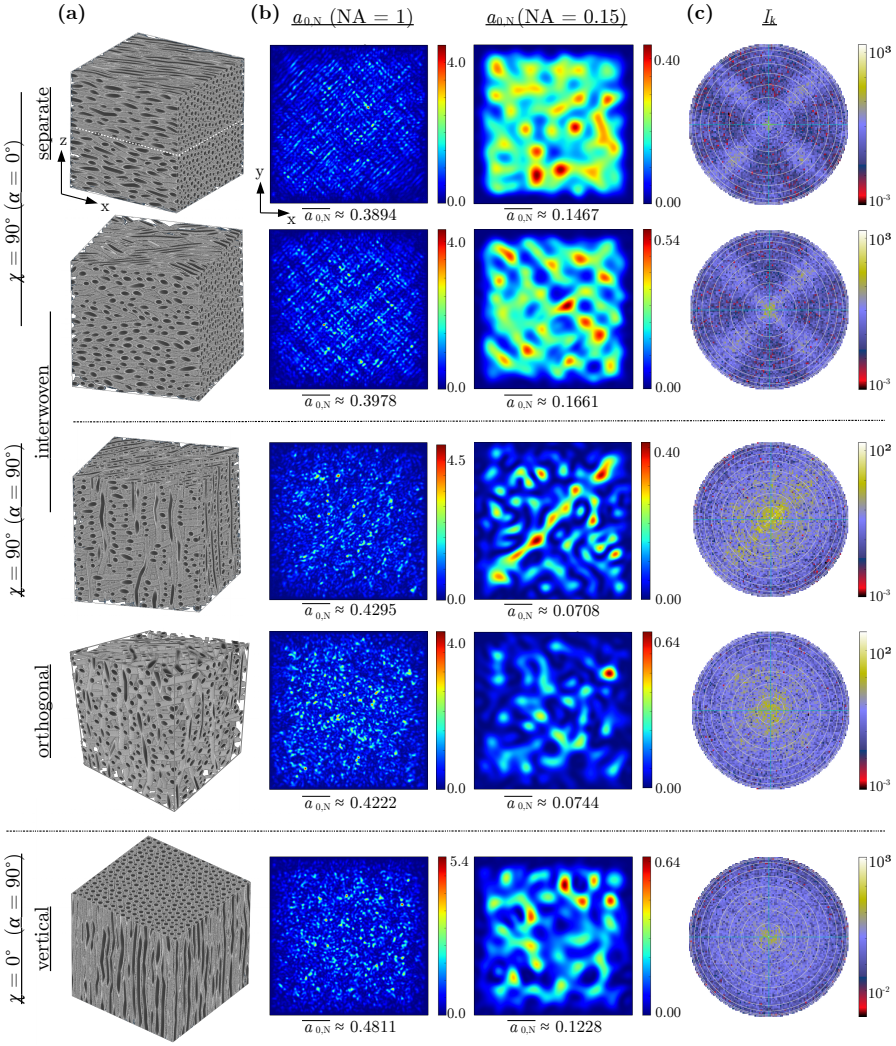

Fig. 11.16: (a) 3D views, **(b)** transmittance images ($a_{0,N}$), and **(c)** scattering patterns (I_k) for 90°-crossing fibers (separate and interwoven bundles, cf. Sec. 10.2.3.4), orthogonal fiber bundles (see Fig. 10.25c), and vertical fibers (reference fiber bundle, cf. Fig. 10.18b). The interwoven fibers were simulated for two horizontal fiber bundles with $\alpha = 0°$ (oriented along $\varphi = \pm 45°$) as well as for a horizontal fiber bundle ($\varphi = +45°$) and a vertical fiber bundle with $\alpha = 90°$. The transmittance images were computed from a simulated 3D-PLI measurement for the imaging system of the PM (with numerical aperture NA = 0.15) and for the case without lenses (NA = 1). Note that the value ranges differ between images. Parts of this figure have been published in Menzel *et al.* (2018a) [67] Fig. 4a-b.

To enable a direct comparison between horizontal crossing and vertical fibers, the interwoven 90°-crossing fibers were rotated 90° around the principal axis of one fiber bundle with $\varphi = 45°$, yielding a horizontal bundle oriented along $\varphi = 45°$ and a vertical fiber bundle with $\alpha = 90°$ (see Fig. 11.16, third row). The transmittance images and the scattering pattern differ a lot from those of the horizontal 90°-crossing fibers (see Fig. 11.16, second row). For NA = 0.15, the averaged transmittance is much lower.

The forth row in Fig. 11.16 shows the transmittance images and scattering pattern for three mutually orthogonal, interwoven fiber bundles (see Fig. 10.25c). The fiber configuration is similar to the horizontal 90°-crossing, interwoven fiber bundles, but one third of the fibers is oriented in the z-direction. This configuration also leads to much lower transmittance values for NA = 0.15.

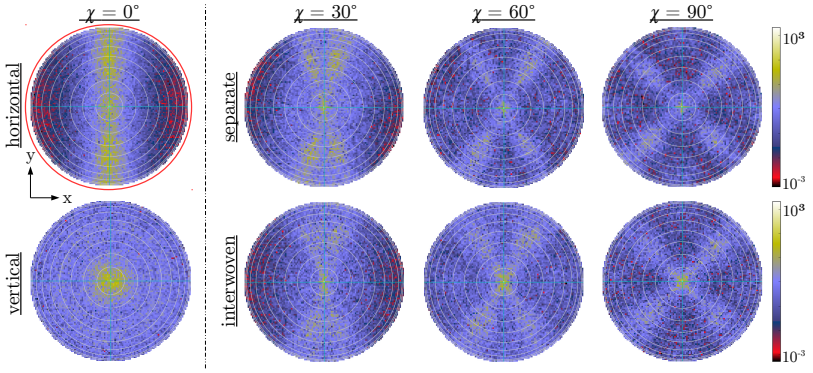

Fig. 11.17: Scattering patterns (I_k) for vertical fibers and horizontal crossing fibers (separate and interwoven fiber bundles) with different crossing angles χ (cf. Fig. 11.16). The red frame highlights the scattering pattern of the horizontal reference fiber bundle (see Fig. 10.18b). Parts of this figure have been published in Menzel *et al.* (2018a) [67] Fig. 4a.

The solid curves in Fig. 11.18 show the averaged transmittance values of the horizontal crossing fibers (separate and interwoven bundles) for different crossing angles, simulated for the imaging system of the PM (NA = 0.15). The densely dotted lines show the averaged transmittance values for various fiber constellations that contain vertical or steep fibers: the vertical reference fiber bundle in magenta, the three mutually orthogonal fiber bundles in cyan, the interwoven 90°-crossing fibers with one horizontal and one vertical fiber bundle in dark green (see last three rows in Fig. 11.16), a vertical fiber bundle with broad fiber orientation distribution in blue (cf. Fig. 10.20, with $\Xi = 10\,\mu m$), and fiber bundles with broad fiber radius distribution (cf. Fig. 10.22, with $\Delta r = 0.7\,\mu m$) and inclinations of 90° (orange) and 70° (light green).

The transmittance curves of horizontal crossing fibers are similar for separate and interwoven fiber bundles. While the averaged transmittance of the separate crossing fibers corresponds more or less to the averaged transmittance of the horizontal reference fiber bundle (marked with a star at $\chi = 0°$), the transmittance values of the interwoven crossing fibers slightly increase with increasing crossing angle (by max. 11 %).

For all simulated fiber bundles that contain vertical or steep fibers, the averaged transmittance values (densely dotted lines) are less than for the horizontal crossing fibers (solid lines). For interwoven crossing fibers, the transmittance value is reduced by more than one half when one of the fiber bundles is oriented along the z-direction (see green lines) or when the horizontal crossing fibers are combined with a vertical fiber bundle

(orthogonal fiber bundles). For fibers with broad fiber orientation distribution or steep fibers with $\alpha = 70°$, the difference between the transmittance values is especially large: the transmittance is about 80–90 % less than for the horizontal crossing fibers.

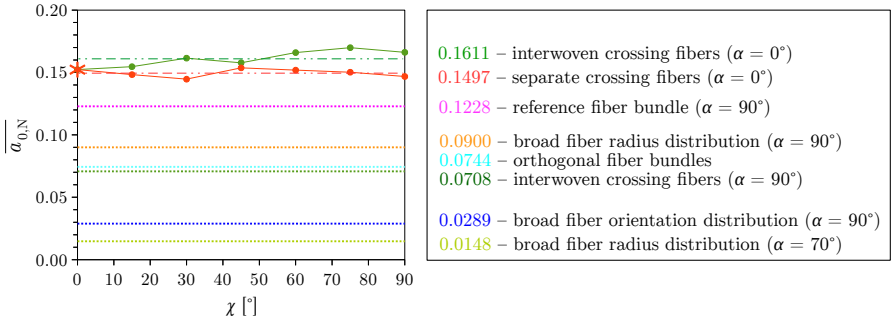

Fig. 11.18: The solid lines show the averaged transmittance values $\overline{a_{0,N}}$ of horizontal crossing fibers (separate and interwoven bundles, cf. Sec. 10.2.3.4) plotted against the crossing angle χ, simulated for the imaging system of the PM. The red star marks the averaged transmittance of the horizontal reference fiber bundle (cf. Fig. 10.18b). The densely dotted lines show the averaged transmittance values for fiber constellations that contain vertical or steep fibers: the vertical reference fiber bundle (cf. Fig. 10.18b), fiber bundles with broad fiber radius distribution (cf. Fig. 10.22, with $\Delta r = 0.7\,\mu m$) and inclinations $\alpha = 90°$ and $70°$, three mutually orthogonal fiber bundles (see Fig. 10.25c), the interwoven 90°-crossing fibers with one horizontal and one vertical fiber bundle (see third row in Fig. 11.16a), and a vertical fiber bundle with broad fiber orientation distribution (cf. Fig. 10.20, with $\Xi = 10\,\mu m$). A similar figure has been published in Menzel *et al.* (2018a) [67] Fig. 4d.

11.4 Discussion

The experimental studies in Chap. 8 have shown that the transmittance of brain sections decreases with increasing inclination angle of the enclosed nerve fibers. To study how the transmittance depends on the fiber inclination angle and on the tissue composition, the transmittance and scattering patterns have been simulated in this chapter for various fiber configurations with different inclination angles and fiber properties.

The transmittance is a measure of how much the light is attenuated when it passes through the brain tissue, i. e. it depends on (isotropic and anisotropic) tissue absorption and scattering. The absorption coefficients in brain tissue are small (see Sec. 3.2.2) and the diattenuation study in Chap. 9 has shown that the anisotropic absorption (dichroism) is also small ($D_K < 5\,\%$). Therefore, tissue absorption was neglected when modeling the observed transmittance effects. The increased transparency of tissue samples with long embedding time (see Fig. 9.7a) also suggests that the transmittance is mainly caused by scattering outside the molecular substructure of the myelin layers (see Sec. 9.4). As TDME3D is able to model (isotropic and anisotropic) light scattering of fiber configurations and myelin layers, the transmittance effect can be investigated quantitatively in terms of FDTD simulations.

Transmittance vs. Fiber Inclination The inclination dependence of the transmittance was studied for hexagonal grids of fibers as well as for more complex fiber bundles (bundle of densely grown fibers and inhomogeneous fiber bundles), see Sec. 11.1.

Although the hexagonal grid of fibers shows artifacts due to grid symmetries, the transmittance curves (Fig. 11.2) already show some features of the more complex fiber bundles: The transmittance curve for the aligned helical fibers shows a global minimum at $\alpha = 50°$ (the transmittance curve for the bundle of densely grown fibers shows a global minimum at $\alpha = 70°$, cf. Fig. 11.4a). In the case of unaligned helical fibers, the transmittance decreases with decreasing numerical aperture (also for horizontal fibers). For different strides, the averaged transmittance value decreases with increasing inclination angle (just as for the bundle with broad fiber orientation distribution, cf. Fig. 11.5b).

The transmittance curves for the bundle of densely grown fibers and for more inhomogeneous fiber bundles (see Figs. 11.4a and 11.5) are much smoother than those for the hexagonal grid of fibers. A comparison of the transmittance curves for NA = 1 and NA = 0.15 shows that the decrease in transmittance with increasing fiber inclination is caused by the limited numerical aperture of the microscope objective in the PM. The camera only detects light with small scattering angles ($\theta_k < 8.6°$). For steep fibers, the light is scattered almost uniformly in all possible directions (cf. Fig. 11.3c) so that the transmitted light intensity recorded by the camera becomes minimal. The DI simulations in Chap. 12 will show that this effect is mainly caused by isotropic and not by anisotropic scattering (diattenuation) because linearly polarized light shows a similar decrease in the transmitted light intensity, independently of the direction of polarization (see Fig. 12.3b).

For better comparison, Fig. 11.19 shows the normalized transmittance curves for the bundle of densely grown fibers ("fresh" tissue with $n_\mathrm{m} = 1.47$ and "old" tissue with $n_\mathrm{m} = 1.39$, cf. Fig. 11.4) and the normalized transmittance curves for more inhomogeneous fiber bundles (broad fiber radius/orientation distribution, cf. Fig. 11.5) in one plot (for NA = 0.15).

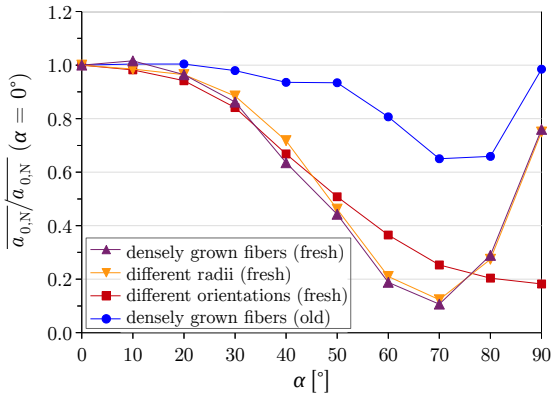

Fig. 11.19: Averaged transmittance $\overline{a_{0,\mathrm{N}}}$ plotted against the inclination angle α for various fiber bundles simulated for the imaging system of the PM with normally incident light and single wavelength (see Secs. 11.1.2 and 11.1.3): a bundle of densely grown fibers (for "fresh" and "old" tissue), a bundle with broad fiber radius distribution ($\Delta r = 0.7\,\mu\mathrm{m}$), and a bundle with broad fiber orientation distribution ($\Xi = 10\,\mu\mathrm{m}$). The transmittance curves were normalized by the averaged transmittance of the horizontal fiber bundle, respectively.

Bundles with similar fiber orientations (densely grown fibers and different radii) yield similar transmittance curves (purple and orange lines); the inclination angle for minimum transmittance ($\alpha = 70°$) corresponds to the critical angle of total internal reflection of

the myelin sheath ($\theta_c = 66.7$–$68.7°$, see Appx. A.5). This also holds for "old" tissue (blue line), for which the critical angle of total internal reflection is slightly larger ($\theta_c = 76.2$–$80.3°$, see Appx. A.5). Total internal reflection would cause the light to be captured within the myelin sheaths, which would provide a classical explanation why the light intensity detected by the camera is minimal for fiber inclinations $\theta_c \leq \alpha < (90° - \theta_k)$. However, it should be noted that the myelin sheath thickness is smaller than the wavelength so that the observed effects cannot necessarily be explained in terms of geometrical optics.

While the transmittance curves of bundles with similar fiber orientations show a minimum at steep inclination angles ($\alpha = 70$–$80°$), the transmittance curve of the bundle with broad fiber orientation distribution (red line) decreases monotonically with increasing inclination angle and becomes minimal for vertical fibers. The fiber orientation dispersion (magenta histogram in Fig. 10.21a) shows that the mode angle difference between the local fiber orientation vectors and the predominant orientation of the fiber bundle is about 25°. Thus, a vertical fiber bundle contains many fibers with inclination angles between 60° and 70°, which explains why the minimum transmittance is shifted to larger inclination angles.

For "fresh" tissue (with $n_m = 1.47$), the minimum transmittance values are similar for all types of bundles: the transmittance for steep fibers is up to 80–90 % less than the transmittance for flat fibers. For "old" tissue (with $n_m = 1.39$), the transmittance is only reduced by about a third.

Slightly different wavelengths, a smaller Yee mesh size, and different angles of incidence yield similar simulation results (for the bundle of densely grown fibers, see Fig. D.8a). This shows that the simulation results do not depend on details in the simulated imaging system and can be considered as stable.

With the FDTD simulations, the inclination dependence of the transmittance could be investigated in more detail and the relationship between transmittance and inclination angle could be studied for different fiber architectures. This knowledge can help to obtain additional information about the fiber inclination.

Transmittance vs. Embedding Time The simulations in Sec. 11.2.4 show that the transmittance increases with decreasing myelin refractive index n_m (see Fig. 11.13). This suggests that the transmittance of brain tissue increases with increasing embedding time of the tissue sample, assuming that the embedding glycerin solution soaks into the myelin sheaths of the nerve fibers and that the effective refractive index of myelin becomes more similar to the refractive index of the surrounding tissue.

Transmittance vs. Homogeneity The simulation results presented in Sec. 11.2 show that the transmittance depends not only on the fiber inclination and the refractive index of the myelin sheath, but also on the homogeneity of the simulated fiber bundles: The transmittance of horizontal fibers decreases with increasing myelin sheath thickness and fiber size (see Figs. 11.11 and 11.15). It also decreases for a larger distribution of fiber radii (see Fig. 11.9), but much less. All these effects are significantly weaker than the observed inclination dependence of the transmittance.

The transmittance images obtained in a 3D-PLI measurement are used to correct the retardation images of the PM for varying myelin densities (transmittance weighting). The simulations have shown that the transmittance depends not only on the amount of myelin in the measured brain section, but also on the fiber inclination and – to some

extent – on the tissue homogeneity. These effects should be taken into account in the transmittance weighting.

Transmittance of Horizontal Crossing vs. Vertical Fibers The simulations of crossing fibers in Sec. 11.3 have shown that the transmittance for horizontal fibers is mostly independent of the crossing angle (see solid curves in Fig. 11.18). This is also in accordance with the finding that the transmittance of horizontal fibers does not depend much on the fiber orientation distribution (see Fig. 11.7).

As the transmittance of horizontal crossing fibers is similar to the transmittance of horizontal parallel fibers, the transmittance of horizontal crossing fibers is also expected to be larger than the transmittance of steep fibers due to the inclination dependence of the transmittance. The simulations in Sec. 11.3 have shown that the transmittance for vertical fibers is significantly less than for horizontal crossing fibers, especially for bundles with broad fiber orientation distribution. For bundles with similar fiber orientations, the transmittance becomes minimal for steep fibers with an inclination of 70° (see Fig. 11.18). Also for the same fiber configuration (interwoven 90°-crossing fibers), the transmittance values become much lower when one of the fiber bundles is oriented along the z-direction and not in the xy-plane.

In standard 3D-PLI and DI measurements, horizontal crossing and steep fibers cannot easily be distinguished because they both yield similar birefringence and diattenuation values. The transmittance could help to distinguish between these fiber configurations.

A decrease in transmittance is also observed when combining two horizontal crossing fiber bundles with a vertical fiber bundle (see orthogonal fiber bundles in Figs. 11.16 and 11.18). Thus, it is not only possible to distinguish horizontal crossing from vertical fibers, but also to detect vertical fibers within fiber crossings, which cannot be achieved by the current 3D-PLI analysis even when using a tiltable specimen stage [161].

Horizontal crossing and vertical fibers do not only yield different transmittance values, they also yield different scattering patterns. When studying the scattering pattern of a sample, it is even possible to determine the crossing angle of the fibers within one measured tissue voxel (see Fig. 11.16). Apparently, the scattering pattern contains valuable information about the underlying fiber configuration which cannot be accessed in a standard 3D-PLI or DI measurement. The scattering pattern could be measured e. g. by means of dark-field microscopy or simply by changing the position of the light source or the camera with respect to the sample and measuring the intensity of light scattered under a certain angle.

Chapter 12

Diattenuation of Simulated Fiber Configurations

This chapter studies the diattenuation of various simulated fiber configurations in order to model and better understand the diattenuation effects described in Chap. 9. As TDME3D can only assign an isotropic complex refractive index to a medium (see Sec. 6.3), the molecular diattenuation, i. e. the diattenuation caused by the substructure of the myelin layers (e. g. lipid molecules), was described by an effective analytical model of dichroism (D_K, see Sec. 3.2.4), while the FDTD simulations model the diattenuation caused by anisotropic scattering ($D_\mathcal{S}$) of all other structures. The simulation results presented in this chapter should therefore always be considered in addition to a possible dichroism of brain tissue (cf. Sec. 9.4).

The considerations and simulations in Chap. 10 have shown that TDME3D is more suitable to model the optical system of the PM than of the LAP. To save computing time, most of the simulations were therefore performed for the system parameters of the PM, i. e. for normally incident light with a wavelength of 550 nm, a mesh size of 25 nm, and a numerical aperture of 0.15. In interesting cases, the simulations were repeated for other wavelengths ($\lambda = \{545, 555\}$ nm), a smaller mesh size ($\Delta = 12.5$ nm), and different angles of incidence ($\theta = 3°$, $\varphi = \{0°, 90°, 180°, 270°\}$) to demonstrate the validity of the simulated diattenuation effects.

As the polarizing filters of the PM cannot be removed, a routine diattenuation measurement is only possible for the LAP which has a lower resolution than the PM. Measurements with a prototypic polarizing microscope (see Sec. 9.2.3), however, suggest that the observed diattenuation effects are similar at higher resolution. To show that the simulated diattenuation effects for the PM are similar for the LAP, additional simulations were performed for the system parameters of the LAP. This chapter only presents the simulation results for the PM. The full study for the LAP can be found in Appx. D.12.

The diattenuation was computed from a simulated DI measurement (see Sec. 10.1). If not otherwise stated, the diattenuation was approximated by D_S which is computed from only two simulation runs with light polarized along the x-axis (I_x) and light polarized along the y-axis (I_y), as described in Sec. 10.3.2:

$$D_\mathrm{S} = \frac{I_\mathrm{x} - I_\mathrm{y}}{I_\mathrm{x} + I_\mathrm{y}}, \tag{12.1}$$

where the x-axis corresponds to the longitudinal symmetry axis of the fibers in the xy-plane. Apart from the diattenuation image D_S, the averaged diattenuation value $\overline{D_\mathrm{S}}$ and the standard deviation $\sigma_\mathrm{D,S}$ were computed for all simulated fiber configurations. To facilitate the comparison with the experimental results, positive diattenuation values $D_\mathrm{S} > 0$ were marked in green (representing regions of type D^+) and negative diattenuation values $D_\mathrm{S} < 0$ were marked in magenta (representing regions of type D^-).

The simulations of the diattenuation effect were performed for the same fiber configurations as the simulations of the transmittance effect in Chap. 11. The geometries of the simulated fiber configurations have been characterized in Sec. 10.2. The implementation of the fiber configurations in TDME3D was described in Sec. 10.3, the simulation parameters were specified in Tab. 10.5.

The structure of this chapter is analogous to Chap. 11: The diattenuation was first studied on simulated fiber configurations with different inclination angles (Sec. 12.1). Then, the diattenuation was investigated for a horizontal fiber bundle with different fiber properties (Sec. 12.2). Finally, the diattenuation of horizontal crossing fibers was compared to the diattenuation of vertical fibers (Sec. 12.3). Parts of Secs. 12.1.2, 12.1.3 and 12.2 have been published in Menzel *et al.* (2018b) [68].

12.1 Diattenuation of Inclined Fiber Bundles

The experimental studies in Sec. 9.2.2 suggest that the diattenuation effect depends to some extent on the inclination angle of the nerve fibers in the measured brain section. To better understand this phenomenon, the diattenuation images were computed for different simulated fiber bundles (oriented along the x-axis) with different inclination angles (rotated around the y-axis): $\alpha = \{0°, 10°, \ldots, 90°\}$. If not otherwise stated, the simulations were only performed for normally incident (non-diffuse) light with a wavelength of 550 nm and a Yee mesh size of 25 nm to save computing time.

To investigate which geometric features are responsible for the observed diattenuation effects, the inclination dependence of the diattenuation was first studied for simple fiber configurations (hexagonal grid of fibers in Sec. 12.1.1) before looking at more complex models (bundle of densely grown fibers in Sec. 12.1.2 and inhomogeneous fiber bundles in Sec. 12.1.3).

12.1.1 Hexagonal Grid of Fibers

Figure 12.1b shows the diattenuation images D_S for a hexagonal grid of aligned helical fibers (cf. Fig. 10.27) with different inclination angles.

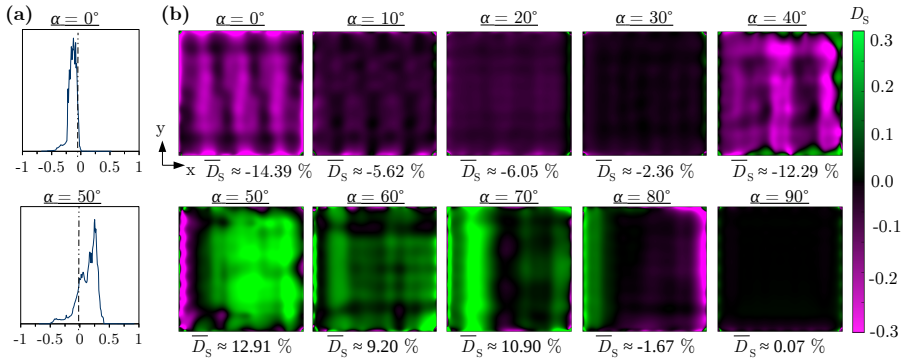

Fig. 12.1: (a) Histograms and **(b)** diattenuation images D_S for a hexagonal grid of aligned helical fibers with different inclination angles α. The diattenuation was computed for the imaging system of the PM for normally incident light with $\lambda = 550$ nm and simulation parameters specified in Tab. 10.5. Positive diattenuation values (representing regions of type D^+) are displayed in green, negative diattenuation values (representing regions of type D^-) are displayed in magenta.

Depending on the inclination angle, the diattenuation is positive or negative: for flat fibers ($\alpha \leq 40°$) the diattenuation is mostly negative (magenta), for steeper fibers ($50° \leq \alpha \leq 70°$) it becomes mostly positive (green), and for vertical fibers the diattenuation values are positive as well as negative. The histograms in Fig. 12.1a show that the diattenuation values are broadly distributed around the average value $\overline{D_S}$ with standard deviations $\sigma_{D,S}$ between 0.05 and 0.2.

Figure 12.2 shows the averaged diattenuation values $\overline{D_S}$ plotted against the inclination angle for different geometries of the hexagonal grid (cf. Sec. 10.2.1): (a) straight fibers, (b) aligned helical fibers, (c) unaligned helical fibers with same strides, and (d) unaligned helical fibers with different strides.

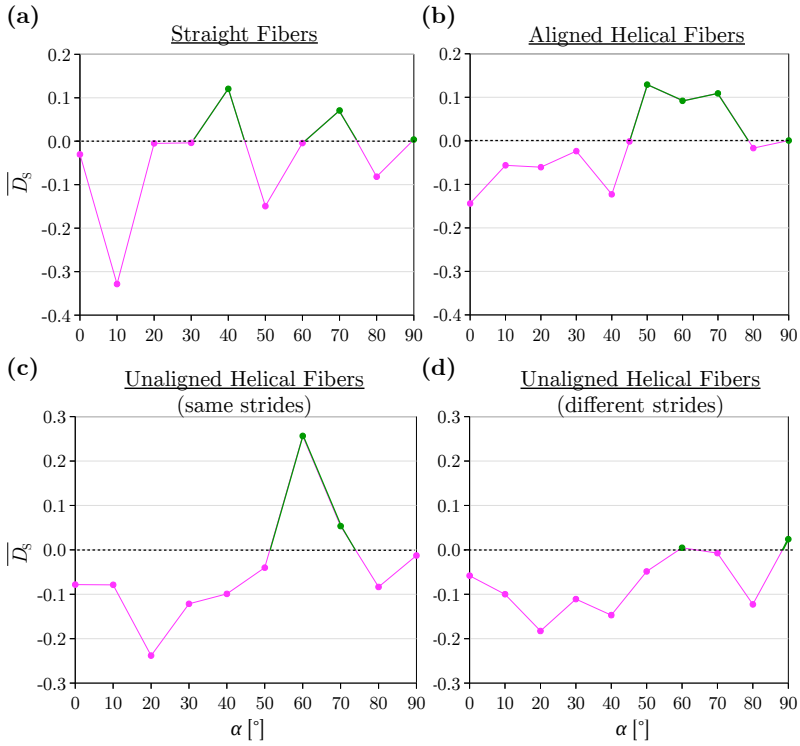

Fig. 12.2: Averaged diattenuation $\overline{D_S}$ plotted against the fiber inclination angle α for a hexagonal grid of fibers with different geometries (cf. Sec. 10.2.1): (a) straight fibers, (b) aligned helical fibers, (c) unaligned helical fibers with same strides, and (d) unaligned helical fibers with different strides. The diattenuation curves were computed for the imaging system of the PM with normally incident light and $\lambda = 550\,\text{nm}$.

While the averaged diattenuation values for straight fibers alternate between positive and negative values for different inclination angles, the other geometries show a transition from negative to positive diattenuation values. For aligned helical fibers, the averaged diattenuation is negative for flat fibers ($\alpha < 45°$) and positive for steep fibers ($45° < \alpha < 80°$) with maximum values $|\overline{D_S}| < 15\,\%$. The diattenuation for vertical fibers ($\alpha \geq 80°$) is much less ($|\overline{D_S}| < 1.7\,\%$). The negative diattenuation for unaligned helical fibers is slightly stronger than for aligned helical fibers (about max. $-24\,\%$ for same strides and

−18 % for different strides). While the diattenuation for unaligned helical fibers with same strides becomes positive for steep fibers (about +26 % for $\alpha = 70°$), it remains mostly negative for different strides.

12.1.2 Bundle of Densely Grown Fibers

To study the inclination dependence of the diattenuation for a more realistic fiber bundle, the DI measurement was simulated for a bundle of densely grown fibers (see Sec. 10.2.2) for different inclination angles. Figure 12.3a shows the (normalized) transmitted light intensities I_x and I_y for the horizontal fiber bundle. Figure 12.3b shows the averaged transmitted light intensities $\overline{I_x}$ and $\overline{I_y}$ plotted against the inclination angle α.

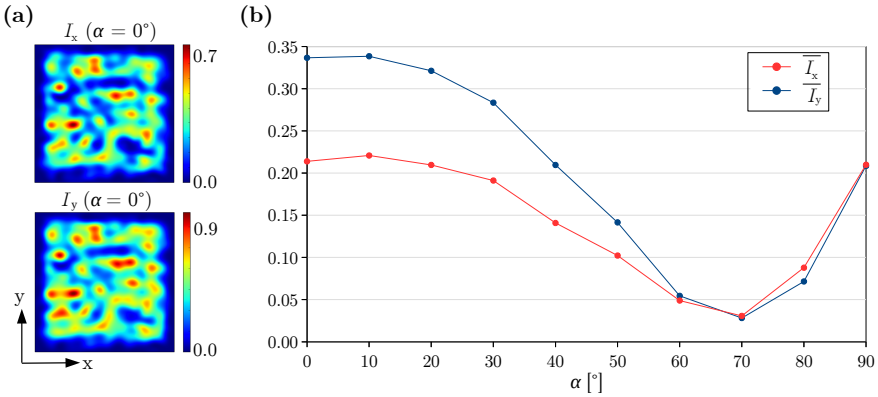

Fig. 12.3: (a) Normalized transmitted light intensities for the horizontal bundle of densely grown fibers obtained from a DI simulation for the imaging system of the PM ($\lambda = 550\,\text{nm}$, NA = 0.15) with rotation angles $\rho = 0°$ and $\rho = 90°$, i. e. with light polarized along the x-axis (I_x) and with light polarized along the y-axis (I_y). **(b)** Averaged transmitted light intensities $\overline{I_x}$ and $\overline{I_y}$ plotted against the inclination angle α of the fiber bundle. Subfigure (b) has been published in Menzel *et al.* (2018a) [67] Fig. 19a.

For flat fibers ($\alpha < 60°$), the transmitted light intensity is maximal when the light is polarized perpendicularly to the direction of the fiber bundle ($I_y > I_x$). For steep fibers ($\alpha > 70°$), the transmitted light intensity is maximal when the light is polarized parallel to the direction of the fiber bundle ($I_x > I_y$). The difference between I_x and I_y decreases with increasing inclination angle. The curves show a similar behavior as the transmittance curve for the bundle of densely grown fibers (cf. Fig. 11.4a for NA = 0.15).

Figure 12.4b shows the diattenuation images $\left(D_S = (I_x - I_y)/(I_x + I_y)\right)$ for the bundle of densely grown fibers with different inclination angles. Regions with maximum and minimum diattenuation values are more homogeneously distributed than for the hexagonal grid of fibers. The diattenuation is mostly negative (magenta) for fibers with small inclination angles ($\alpha \leq 50°$) and becomes more positive (green) for steeper fibers ($\alpha > 60°$). The histograms in Fig. 12.4a show that the diattenuation values are almost symmetrically distributed around the average value ($-22\,\% \pm 12\,\%$ for $\alpha = 0°$ and $-17\,\% \pm 19\,\%$ for $\alpha = 50°$). Thus, the average $\overline{D_S}$ and the standard deviation $\sigma_{D,S}$ are good parameters to describe the diattenuation images.

The solid curve in Fig. 12.5a shows the corresponding averaged diattenuation values $\overline{D_S}$ plotted against the inclination angle. For flat fibers ($\alpha \leq 50°$), the averaged diattenuation is between $-17\,\%$ and $-22\,\%$. For fibers with larger inclination angles, the diattenuation values increase and finally reach positive values (max. $+10\,\%$ for $\alpha = 80°$). For vertical fibers ($\alpha = 90°$), the averaged diattenuation is approximately zero.

Simulations with different wavelengths ($\lambda = \{545, 550, 555\}\,\text{nm}$) and a smaller Yee mesh size ($\Delta = 12.5\,\text{nm}$) yield very similar diattenuation curves (see Fig. D.8b in Appx. D.11). Therefore, all subsequent simulations were performed for $\lambda = 550\,\text{nm}$ and $\Delta = 25\,\text{nm}$.

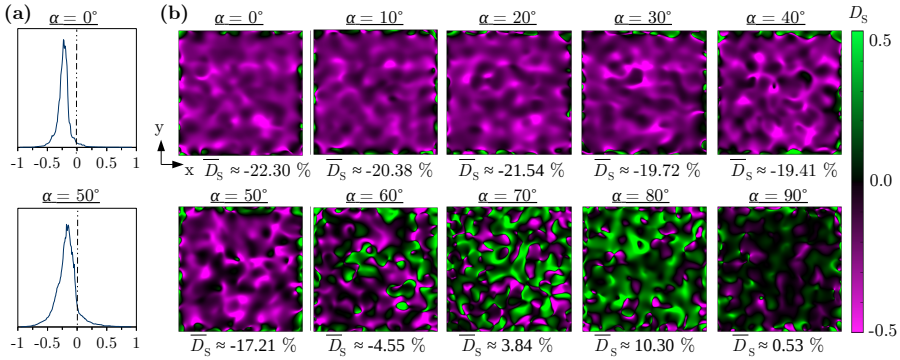

Fig. 12.4: (a) Histograms and **(b)** diattenuation images D_S for a bundle of densely grown fibers with different inclination angles α. The diattenuation was computed for the imaging system of the PM for normally incident light with $\lambda = 550\,\text{nm}$ and simulation parameters specified in Tab. 10.5. Positive diattenuation values (representing regions of type D^+) are displayed in green, negative diattenuation values (representing regions of type D^-) are displayed in magenta. The figure has been published in Menzel *et al.* (2018b) [68] Fig. 7.

Diffuse Light So far, the simulations were only performed for normally incident light. To investigate whether the same diattenuation effects can also be observed for non-normal incidence, the simulations were repeated for the diffuse light source of the PM ($\{\theta = 0°\}$, $\{\theta = 3°,\ \varphi = \{0°, 90°, 180°, 270°\}\}$, weighted according to Eqs. (10.1) to (10.3)). The densely dotted curve in Fig. 12.5a shows the resulting diattenuation curve. The absolute averaged diattenuation values are a bit smaller than for normally incident light (between $-15\,\%$ and $-21\,\%$ for $\alpha \leq 50°$, and $+8\,\%$ for $\alpha = 80°$), but the diattenuation curves are still similar. To save computing time, all other simulations were therefore only performed for normally incident light.

Long Embedding Time To model the diattenuation effect for brain tissue measured a long time after tissue embedding (referred to as "old" tissue), the simulations were repeated with a reduced myelin refractive index ($n_m = 1.39$) to account for glycerin solution soaking into the myelin sheaths. The dash-dotted curve in Fig. 12.5a shows the resulting diattenuation curve. The inclination dependence of the diattenuation is similar to the one for brain tissue measured directly after embedding (referred to as "fresh" tissue), but the absolute averaged diattenuation values are much smaller (about $-2.3\,\%$ for $\alpha \leq 40\,\%$ and max. $+1.6\,\%$ for $\alpha = 80°$).

Comparison between PM and LAP To save computing time, most simulations were performed for the system parameters of the PM. To investigate whether the inclination dependence of the diattenuation D_S is similar for the LAP, the simulations were repeated for the system parameters of the LAP both for normally incident and diffuse light. As discussed in Chap. 10, the diffuse and incoherent light source of the LAP can be modeled by several simulation runs with different wavelengths ($\lambda = \{496, \ldots, 581\}$ nm) and different angles of incidence ($\theta_{max} < 25°$, $\varphi = \eta \times \Delta\varphi$). Additional simulations of the LAP with NA = 0.0083 (see Appx. D.12) show that the simulated diattenuation values D_S for the horizontal bundle of densely grown fibers are similar for different wavelengths and different angles of incidence. Due to the small numerical aperture, most of the transmitted light intensity is generated by light with angles $\theta \leq 0.5°$. Thus, the simulations of the LAP were only performed for the peak wavelength ($\lambda = 529$ nm) and both for normally incident light and diffuse light with angles $\{\theta = 0°\}$, $\{\theta = 0.5°$, $\varphi = \{0°, 90°, 180°, 270°\}\}$, weighted according to Eqs. (10.1) to (10.3). The resulting diattenuation curves are shown in Fig. 12.5b.

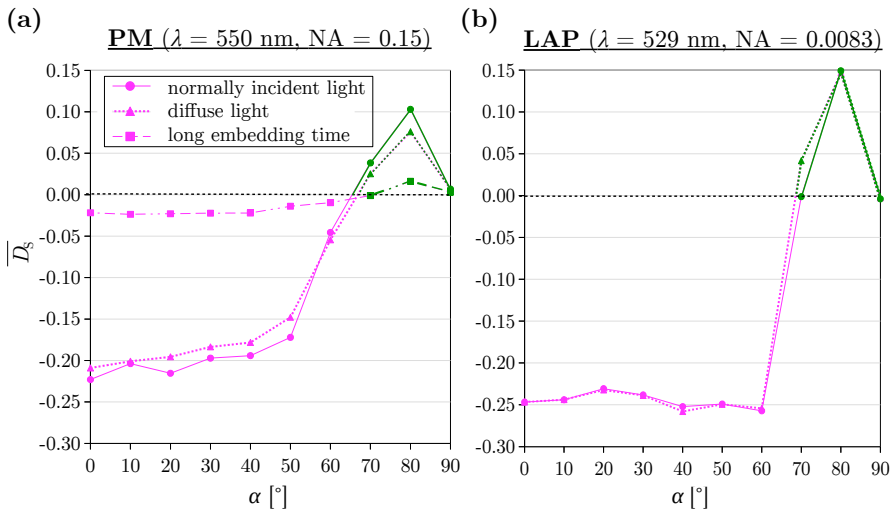

Fig. 12.5: Averaged diattenuation $\overline{D_S}$ plotted against the fiber inclination angle α for the bundle of densely grown fibers (cf. Sec. 10.2.2). The diattenuation curves were computed for the imaging system of the PM (a) and of the LAP (b) with $\Delta = 25$ nm. The solid and densely dotted curves were computed for normally incident and diffuse light ($\{\theta = 0°\}$, $\{\theta = \theta_{max}$, $\varphi = \{0°, 90°, 180°, 270°\}\}$, weighted according to Eqs. (10.1) to (10.3)), respectively, assuming a measurement directly after tissue embedding ($n_m = 1.47$). The diffuse light for the PM was computed with $\theta_{max} = 3°$, the diffuse light for the LAP with $\theta_{max} = 0.5°$. The dash-dotted curve was computed for normally incident light assuming a measurement long time after tissue embedding ($n_m = 1.39$).

The diattenuation curves are similar to those obtained for the system parameters of the PM. The absolute averaged diattenuation values $\overline{D_S}$ are larger (about $-25\,\%$ for $\alpha \leq 60\,\%$ and max. $+15\,\%$ for $\alpha = 80°$) and the transition to positive diattenuation values is more abrupt. As the diattenuation curves for the PM and the LAP are similar, all other simulations of the DI measurement were only performed for the system parameters of the PM and for normally incident light to save computing time.

12.1.3 Inhomogeneous Fiber Bundles

To study the diattenuation effect on more inhomogeneous fiber bundles, a fiber bundle with a broad fiber radius distribution ($\Delta r = 0.7\,\mu m$, cf. Fig. 10.22) and a fiber bundle with a broad fiber orientation distribution ($\Xi = 10\,\mu m$, cf. Fig. 10.20) were generated by the VCS and the DI simulations were performed for different inclination angles of the bundles.

The resulting diattenuation curves are shown in Fig. 12.6. The curves for the bundle with broad fiber radius distribution ($\Delta r = 0.7\,\mu m$, $\Xi = 1\,\mu m$) look similar to the curves for the bundle of densely grown fibers (with $\Delta r = 0.3\,\mu m$), cf. the solid lines in Figs. 12.6 and 12.5a. The negative diattenuation is a bit stronger (max. $-26\,\%$ for $\alpha = 0°$) and the positive diattenuation is a bit weaker (max. $+8\,\%$ for $\alpha = 80°$).

For the bundle with broad fiber orientation distribution ($\Delta r = 0.3\,\mu m$, $\Xi = 10\,\mu m$), the negative diattenuation for flat fibers and the positive diattenuation for steep fibers are much weaker (max. $-12\,\%$ for $\alpha = 0°$ and $+1.2\,\%$ for $\alpha = 80°$).

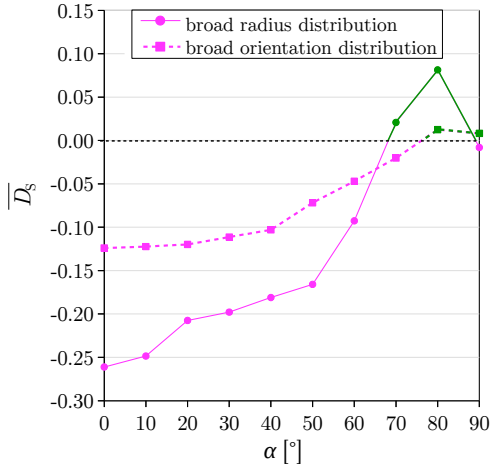

Fig. 12.6: Averaged diattenuation $\overline{D_S}$ plotted against the fiber inclination angle α for a bundle with broad fiber radius distribution ($\Delta r = 0.7\,\mu m$, $\Xi = 1\,\mu m$, cf. Fig. 10.22) and a bundle with broad fiber orientation distribution ($\Delta r = 0.3\,\mu m$, $\Xi = 10\,\mu m$, cf. Fig. 10.20). The diattenuation curves were computed for the imaging system of the PM with normally incident light.

12.2 Diattenuation of Horizontal Fiber Bundles with Different Fiber Properties

To study in more detail how the strength of the diattenuation signal depends on the fiber configuration and structure, the DI measurement was simulated for horizontal fiber bundles with different fiber properties (different fiber orientations, fiber radii, myelin sheath thicknesses, myelin refractive indices, and fiber sizes). The fiber bundles were generated with the VCS by varying the fiber properties of the reference fiber bundle (Fig. 10.18b). For all simulated fiber bundles, the averaged diattenuation value $\overline{D_S}$ was computed and plotted against the varied fiber parameter (see Fig. 12.7). The diattenuation values be-

longing to the reference fiber bundle are marked by a star in the diattenuation curves. All simulations were performed for the system parameters of the PM and with normally incident light with $\lambda = 550\,\text{nm}$ and $\Delta = 25\,\text{nm}$.

12.2.1 Different Fiber Orientation Distributions

Figure 12.7a shows the diattenuation curve for horizontal fiber bundles with different fiber orientation distributions, i. e. bundles generated with different maximum displacements Ξ in the VCS (cf. Fig. 10.20). The negative diattenuation becomes weaker with increasing Ξ: the averaged diattenuation $\overline{D_\text{S}}$ increases from about $-22\,\%$ for $\Xi = 1\,\mu\text{m}$ to about $-12\,\%$ for $\Xi = 10\,\mu\text{m}$. Note that the volume fraction increases linearly with increasing Ξ (see Fig. 10.20).

12.2.2 Different Fiber Radius Distributions

Figure 12.7b shows the diattenuation curve for horizontal fiber bundles with equal average fiber radius ($r_\text{avg} = 0.65\,\mu\text{m}$) and different fiber radius distributions $\Delta r = r_\text{max} - r_\text{min}$ (cf. Fig. 10.22). The averaged diattenuation $\overline{D_\text{S}}$ becomes more negative with increasing Δr (from about $-20\,\%$ for $\Delta r = 0$ to about $-26\,\%$ for $\Delta r = 0.7\,\mu\text{m}$).

12.2.3 Different Myelin Sheath Thicknesses

To study the effect of the myelin sheath thickness on the diattenuation, the reference fiber bundle was simulated with different myelin sheath thicknesses t_sheath relative to the fiber radius r (the relative thicknesses of the two myelin layers and the separating glycerin layer remained the same): $t_\text{sheath} = \{0, 0.2, 0.3, 0.4, 0.5, 0.6\}\,r$.

Figure 12.7c shows the resulting diattenuation curve for different myelin sheath thicknesses. With increasing myelin sheath thickness, the diattenuation $\overline{D_\text{S}}$ becomes more negative (from about $-23\,\%$ for $t_\text{sheath} = 0.2\,r$ to about $-29\,\%$ for $t_\text{sheath} = 0.6\,r$). For unmyelinated fibers ($t_\text{sheath} = 0$), the averaged diattenuation is still negative, but relatively small ($\overline{D_\text{S}} \approx -1.25\,\%$).

12.2.4 Different Myelin Refractive Indices

To study how the diattenuation changes with increasing embedding time of the tissue sample (i. e. when the embedding glycerin solution soaks into the myelin sheaths of the nerve fibers and the refractive indices of myelin and surrounding tissue equalize), the reference fiber bundle was simulated for different myelin refractive indices n_m between 1.47 (corresponding to the refractive index of lipids and used for all previous simulations) and 1.37 (corresponding to the refractive index of the embedding glycerin solution).

Figure 12.7d shows the resulting diattenuation curve for different myelin refractive indices. The negative diattenuation approaches zero with decreasing myelin refractive index (from about $-21.7\,\%$ for $n_\text{m} = 1.47$ to about $-0.7\,\%$ for $n_\text{m} = 1.37$).

12.2.5 Different Scales

To study how the diattenuation depends on the size of the fibers, the reference fiber bundle was scaled by factors of 1, 2, 2.5, 3, 4, and 5, cropped to a volume of $30 \times 30 \times 30\,\mu\text{m}^3$, and discretized into voxels of $25^3\,\text{nm}^3$ (see Fig. 10.24).

Figure 12.7e shows the resulting diattenuation curve for different scaling factors. The negative diattenuation becomes weaker with increasing scaling factor. For scaling factors

of 1 and 2, the averaged diattenuation is $\overline{D_S} < -20\,\%$. For a scaling factor of 5, the averaged diattenuation is only about $-8\,\%$.

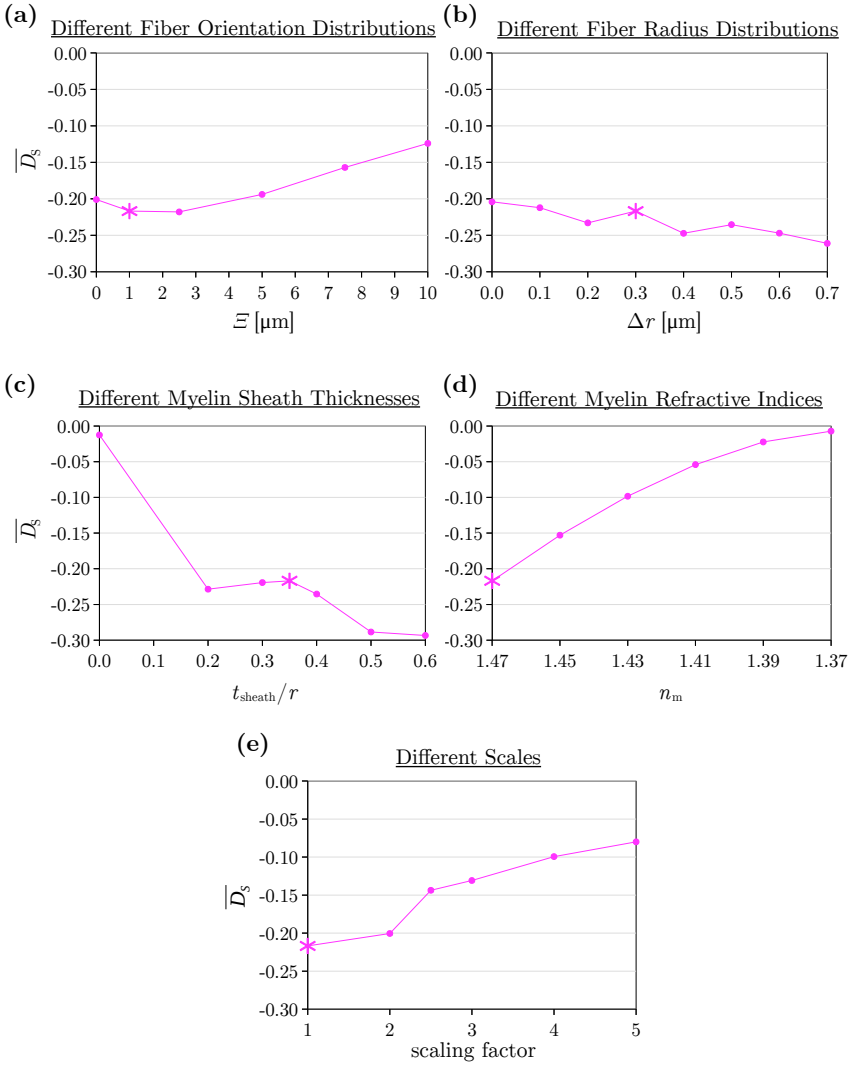

Fig. 12.7: Averaged diattenuation $\overline{D_S}$ for horizontal fiber bundles with different fiber properties (cf. Sec. 10.2.3): **(a)** different fiber orientation distributions, i. e. different maximum displacements Ξ (see Fig. 10.20), **(b)** different fiber radius distributions $\Delta r = r_{\max} - r_{\min}$ (see Fig. 10.22), **(c)** different myelin sheath thicknesses t_{sheath} relative to the fiber radius r (cf. Fig. 11.10a), **(d)** different myelin refractive indices n_{m}, **(e)** different scaling factors (see Fig. 10.24). The bundles were generated with the VCS by varying the fiber properties of the horizontal reference fiber bundle (see Fig. 10.18b). The diattenuation values belonging to the reference fiber bundle are marked by a star. The diattenuation curves were computed for the imaging system of the PM with normally incident light and $\lambda = 550\,\mathrm{nm}$, $\Delta = 25\,\mathrm{nm}$. Similar subfigures (b-e) have been published in Menzel *et al.* (2018b) [68] Fig. 8.

12.3 Diattenuation of Horizontal Crossing vs. Vertical Fibers

Just like the transmittance, the diattenuation was also investigated for vertical fibers and horizontal crossing fibers (separate and interwoven bundles) with different crossing angles $\chi = \{15°, 30°, \ldots, 90°\}$ (cf. Sec. 10.2.3.4).

As the crossing fibers are oriented along two principal directions ($\varphi = \pm\chi/2$) in the xy-plane, the value for D_S, which is derived from light polarized along the x-axis ($\rho = 0°$) and from light polarized along the y-axis ($\rho = 90°$), might not be a good approximation for the diattenuation of the crossing fibers (cf. Fig. 10.29b in Sec. 10.4.1). The transmitted light intensity $I_N(\rho)$ was therefore computed for at least four rotation angles ($\rho = \{0°, 45°, 90°, 135°\}$). From the resulting Fourier coefficients a_0, a_2, and b_2 (computed from Eq. (4.2) with $N = 4$), the strength $|\mathscr{D}_S|$ and the phase $\varphi_{D,S}$ of the simulated diattenuation signal were determined using Eqs. (4.36) and (4.37).

The averaged transmitted light intensities $\overline{I_N(\rho)}$ of the separate and interwoven fiber bundles follow a sinusoidal curve for all crossing angles. Figure 12.8 shows the resulting values for $|\mathscr{D}_S|$ and $\varphi_{D,S}$ plotted against the crossing angle χ of the fibers (magenta lines). For reference, the averaged diattenuation value of the vertical fiber bundle is shown as a green dotted line in Fig. 12.8a.

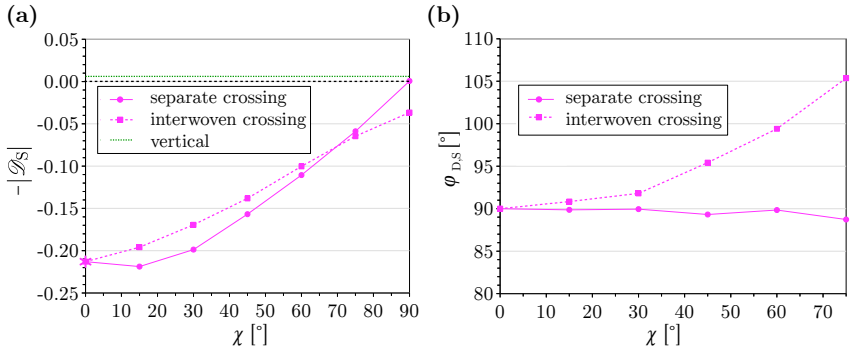

Fig. 12.8: Simulated diattenuation signal for horizontal crossing fibers (separate and interwoven bundles, cf. Sec. 10.2.3.4) for different crossing angles χ (magenta lines): The strength $|\mathscr{D}_S|$ (a) and the phase $\varphi_{D,S}$ (b) of the diattenuation signal were computed from a Fourier analysis of the averaged transmitted light intensity $\overline{I_N(\rho)}$ with $\rho = \{0°, 45°, 90°, 135°\}$ using Eqs. (4.36) and (4.37). The green dotted line shows the averaged diattenuation of the vertical reference fiber bundle (see Fig. 10.18b). The value for the horizontal reference fiber bundle is marked by a magenta star. The simulations were performed for the imaging system of the PM with normally incident light and $\lambda = 550\,\text{nm}$, $\Delta = 25\,\text{nm}$.

For separate fiber bundles, the phase of the diattenuation signal does not change a lot with the crossing angle ($\varphi_{D,S} \approx 90°$, for $\chi \leq 75°$). For interwoven fiber bundles, the phase increases with increasing crossing angle ($\varphi_{D,S} \approx 90°$ for $\chi = 15°$, $\varphi_{D,S} \approx 105°$ for $\chi = 75°$), see Fig. 12.8b. For 90°-crossing fibers, the phase is about 18° for separate bundles and 134° for interwoven bundles.

As the simulated diattenuation is rather negative ($45° < \varphi_{D,S} < 135°$), the values for $|\mathscr{D}_S|$ are shown with a negative sign (see Fig. 12.8a). The strength of the diattenuation signal $|\mathscr{D}_S|$ decreases with increasing crossing angle, both for the separate and interwoven fiber bundles. While the diattenuation is almost zero for the vertical fiber bundle and for 90°-crossing separate bundles, it is about $-3.7\,\%$ for 90°-crossing interwoven bundles.

12.4 Discussion

The experimental studies in Chap. 9 have shown that brain tissue exhibits two different types of diattenuation (D^+ and D^-) which are regionally specific and depend on fiber inclination and embedding time. To model and better understand these effects, the diattenuation signal has been investigated in this chapter by means of FDTD simulations for various fiber configurations with different inclination angles and fiber properties.

As discussed in Sec. 2.4, diattenuation can be caused by anisotropic absorption (dichroism D_K) as well as by anisotropic scattering ($D_\mathcal{S}$). The experimental studies suggest that both D_K and $D_\mathcal{S}$ contribute to the measured diattenuation of brain tissue (see Sec. 9.4). As the simulation model does not include the molecular substructure of the myelin layers, molecular diattenuation was described by an analytical model of dichroism instead (see Sec. 3.2.4). Diattenuation caused by other structures (like fiber configurations or myelin layers) was treated as anisotropic scattering and studied by the FDTD simulations presented in this chapter.[1] As TDME3D is not designed to model dichroism and there exists no analytical description of anisotropic scattering, both effects were treated separately, neglecting mutual interdependencies. In contrast to the transmittance effect, it is therefore only possible to gain a qualitative understanding of the combined diattenuation effect. When comparing the simulation results to experimental data, it should also be kept in mind that most simulations were performed for the imaging system of the PM while the diattenuation was measured with the LAP.

Analytical considerations in Appx. A.4.3 have shown that the dichroism of brain tissue is approximately proportional to the retardance (see Eq. (3.9)). The long-term study in Sec. 9.3 suggests that the dichroism causes positive diattenuation $D_\mathrm{K} > 0$ (maximum absorption for light polarized in the plane perpendicular to the fibers, i. e. in the plane of the myelin lipids). Thus, D_K is expected to become maximal for horizontal in-plane fibers and to decrease with increasing fiber inclination angle (see Fig. A.1).

The diattenuation caused by anisotropic scattering ($D_\mathcal{S}$) was studied by FDTD simulations presented in this chapter. For fiber configurations with one principal orientation (oriented along the x-axis when projected onto the xy-plane), the amplitude and phase of the diattenuation signal $\{|\mathscr{D}_\mathrm{S}|, \varphi_\mathrm{D,S}\}$ were approximated by D_S which is computed from only two simulation runs with light being polarized along the x- and y-axes of the sample ($|D_\mathrm{S}| \approx |\mathscr{D}_\mathrm{S}|$, $D_\mathrm{S} > 0\,(D^+) \Rightarrow \varphi_\mathrm{D,S} \approx \varphi_\mathrm{P}$, $D_\mathrm{S} < 0\,(D^-) \Rightarrow \varphi_\mathrm{D,S} \approx \varphi_\mathrm{P} + 90°$).

Diattenuation vs. Fiber Inclination The inclination dependence of D_S was studied for hexagonal grids of fibers as well as for more complex fiber bundles (bundle of densely grown fibers and inhomogeneous fiber bundles), see Sec. 12.1.

The hexagonal grids of fibers show artifacts due to symmetries (the diattenuation curves show several local minima and maxima), but they also show some features of the more complex fiber bundles: For aligned helical fibers, the averaged diattenuation $\overline{D_\mathrm{S}}$ is negative for flat fibers and positive for steep fibers – just as for the bundle of densely grown fibers (cf. Figs. 12.2b and 12.5a). When breaking the symmetry by introducing different offsets with respect to the fiber position, the diattenuation curves become a bit more similar to the one of the more complex fiber bundles: While the bundle of unaligned helical fibers (with same strides) has averaged diattenuation values between $-18\,\%$ and $-24\,\%$ for inclination angles $\alpha \leq 40°$ and about $+26\,\%$ for $\alpha = 60°$ (see Fig. 12.2c), the

[1] In the following, the term *"anisotropic scattering"* will only be used to describe diattenuation caused by structures included in the simulation model (i. e. no molecular substructures), while *"dichroism"* refers to the effective model used to describe diattenuation caused by everything else that is not included in the simulation model (e. g. lipid molecules).

bundle of densely grown fibers and the bundle with broad fiber radius distribution have averaged diattenuation values between −17 % and −26 % for inclination angles $\alpha \leq 50°$ and about +10 % for $\alpha = 80°$ (see solid curves in Figs. 12.5a and 12.6). The averaged diattenuation for the bundle of unaligned helical fibers with different strides (Fig. 12.2d) remains mostly negative – just as for the bundle with broad fiber orientation distribution (see dashed curve in Fig. 12.6).

The simulations of the more complex fiber bundles (Secs. 12.1.2 and 12.1.3) have shown that the averaged diattenuation $\overline{D_S}$ is negative for non-steep fibers, positive for steep fibers, and almost zero for vertical fibers. For bundles with similar orientations (densely grown fibers and different radii), the values range from $\overline{D_S} \approx -26\,\%$ to 10 % (see solid curves in Figs. 12.5 and 12.6). For bundles with very different fiber orientations, the range is much narrower ($\overline{D_S} \approx -12.4\,\%$ to 1.2 %, see dashed curve in Fig. 12.6). For "old" tissue with reduced myelin refractive index ($n_m = 1.39$), the values are even smaller ($\overline{D_S} \approx -2.2\,\%$ to 1.6 %, see dash-dotted curve in Fig. 12.5a).

To estimate the combined diattenuation effect of D_S and D_K, Fig. 12.9 shows the corresponding diattenuation curves D_S in direct comparison to the dichroism D_K plotted against the fiber inclination angle α: For regions with non-steep fibers ($\alpha < 65°$), both types D^+ and D^- might be observed, depending on whether $D_S < 0$ or $D_K > 0$ dominates. Regions with steep fibers should only show diattenuation of type D^+ because both D_S and D_K are positive. As expected, regions with vertical fibers ($\alpha = 90°$) show small diattenuation values ($|D_S|, |D_K| \ll 1$).

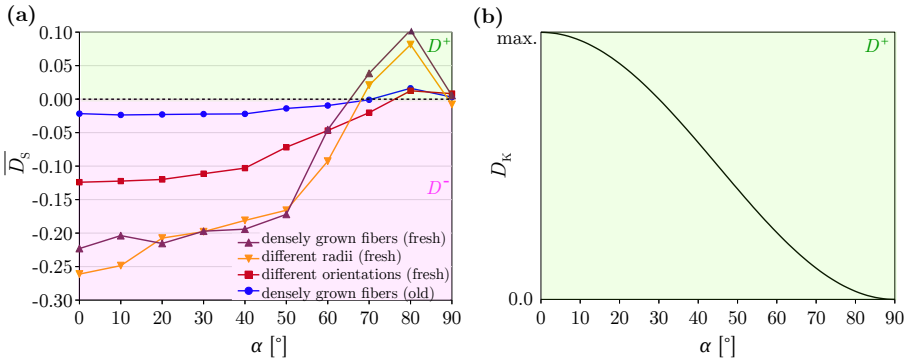

Fig. 12.9: (a) Diattenuation caused by anisotropic scattering ($\overline{D_S}$) plotted against the inclination angle α for various fiber bundles simulated for the imaging system of the PM with normally incident light and $\lambda = 550\,\text{nm}$, $\Delta = 25\,\text{nm}$ (see Secs. 12.1.2 and 12.1.3): a bundle of densely grown fibers (for "fresh" tissue with $n_m = 1.47$ and "old" tissue with $n_m = 1.39$), a bundle with broad fiber radius distribution ($\Delta r = 0.7\,\mu\text{m}$), and a bundle with broad fiber orientation distribution ($\Xi = 10\,\mu\text{m}$). **(b)** Diattenuation caused by anisotropic absorption (dichroism D_K) plotted against the inclination angle α, computed analytically using $D_K = \tanh(0.05\,\cos^2\alpha)$ (see Appx. A.4.3.2). Positive diattenuation values (representing type D^+) are shown on a green background, negative diattenuation values (representing type D^-) are shown on a magenta background.

Different angles of incidence yield similar diattenuation curves for the bundle of densely grown fibers – both for the imaging system of the PM and of the LAP (see Fig. 12.5). As slightly different wavelengths and a smaller Yee mesh size also yield comparable results

(see Fig. D.8b), the simulation results do not depend on details in the simulated imaging system and can be considered as stable.

As the simulated diattenuation curves for the PM and the LAP are similar, the simulation results can be used to make predictions for diattenuation measurements with the LAP as well as for diattenuation measurements with the prototypic polarization microscope.

The transmitted light intensities I_x and I_y show a similar inclination dependence as the transmittance obtained from 3D-PLI simulations (cf. Figs. 12.3b and 11.4a). This confirms that the observed inclination dependence of the transmittance is mainly caused by isotropic scattering and not by anisotropic scattering (diattenuation).

Diattenuation vs. Embedding Time With increasing time after embedding the brain section, the surrounding glycerin solution presumably soaks into the myelin sheaths of the nerve fibers which reduces the effective refractive index of myelin. The simulations for different myelin refractive indices (Sec. 12.2.4) confirm the assumption that anisotropic scattering $|D_{\mathcal{S}}|$ decreases with increasing time after tissue embedding (when the difference between the refractive indices decreases). As dichroism $D_K > 0$ is expected to be less time-dependent than scattering, the net observed diattenuation is expected to become more positive with increasing embedding time of the tissue samples.

Diattenuation of Horizontal Crossing vs. Vertical Fibers The simulations of horizontal 90°-crossing and vertical fibers have shown that these fiber configurations cannot be distinguished by means of their diattenuation values, especially in the case of two separate crossing bundles: the diattenuation images are similar and the averaged diattenuation values are almost zero. The strength of the simulated diattenuation signal for horizontal crossing fibers shows a similar behavior with respect to the crossing angle as the dichroism D_K (see Appx. A.4.4). The total diattenuation is therefore expected to follow a similar function and to approach zero with increasing crossing angle.

The phase of the simulated diattenuation signals shows a different behavior for separate and interwoven crossing fiber bundles. For separate crossing fibers, the phase ($\varphi_{D,S} \approx 90°$) is mostly independent of the crossing angle: the transmitted light intensity becomes maximal for light polarized along the y-axis and minimal for light polarized along the x-axis, i. e. the diattenuation signal is symmetric with respect to the main fiber directions $\varphi = \pm\chi/2$. For interwoven crossing fibers, the phase increases with increasing crossing angle: for 90°-crossing fibers ($\varphi_{D,S} \approx 134°$), the transmitted light intensity becomes maximal for light polarized along one fiber axis ($\varphi = -\chi/2$) and minimal for light polarized along the other fiber axis ($\varphi = +\chi/2$), i. e. the diattenuation signal is not symmetric with respect to the main fiber directions. This suggests that the diattenuation for interwoven crossing fibers depends on details in the underlying fiber configuration (e. g. on the orientation of the first fiber layer). In order to distinguish separate from interwoven crossing fiber bundles by means of their diattenuation signal, the diattenuation of interwoven crossing fibers needs to be studied in more detail to better understand how the phase of the signal is affected by the underlying fiber architecture.

Diattenuation vs. Homogeneity The simulations in Sec. 12.2 have shown that the diattenuation caused by anisotropic scattering depends on the fiber structure and organization. The negative diattenuation values $\overline{D_S}$ for horizontal fiber bundles become stronger with increasing distribution of fiber radii and with increasing myelin sheath

thickness (see Fig. 12.7b,c). They become weaker with increasing fiber size and with increasing distribution of fiber orientations (see Fig. 12.7a,e). (Note that the latter effect might also be caused by a decreasing volume fraction.) Thus, the diattenuation of type D^- is expected to be especially large if the brain tissue is measured directly after embedding and if it contains regions with horizontal fiber bundles that consist of relatively straight fibers with different fiber radii (and small average fiber radius) surrounded by thick myelin sheaths.

This suggests that Diattenuation Imaging can be used to obtain information about the structure and composition of brain tissue which cannot be obtained with other imaging techniques like 3D-PLI.

Part V

DISCUSSION & CONCLUSION

Chapter 13

Comparison of Experimental and Simulation Studies

In this chapter, the results from the experimental studies in Part III are compared to the results from the FDTD simulation studies in Part IV. The findings of the simulation studies are used to explain the effects observed in the experimental studies and to make predictions which are then validated on experimental data. Moreover, it is demonstrated how the predictions can be used to improve the analysis of the measurements. The studies concerning the transmittance effect (Chaps. 8 and 11) are discussed in Sec. 13.1. The studies concerning the diattenuation effect (Chaps. 9 and 12) are discussed in Sec. 13.2. The chapter ends with an overall discussion in Sec. 13.3.

Parts of Sec. 13.1 have been published in Menzel *et al.* (2018a) [67]. Parts of Sec. 13.2 have been published in Menzel *et al.* (2018b) [68].

13.1 Transmittance Effect

The experimental studies in Chap. 8 have shown that the transmittance of brain sections measured with 3D-PLI decreases with increasing out-of-plane inclination angle α of the enclosed nerve fibers. The measured transmittance of steep fibers ($\alpha > 45°$) is more than 50 % less than the transmittance of flat fibers ($\alpha < 45°$). Although this effect has clearly been demonstrated in various measurements (Secs. 8.1 to 8.3), the experimental data is not sufficient to raise any statistics. It can only serve as an indication for the inclination dependence of the transmittance and cannot be used for quantitative comparisons.

The FDTD simulations revealed that the decrease in transmittance is caused by isotropic scattering of light which increases with increasing fiber inclination: due to the finite aperture of the objective lens in the imaging system, scattering reduces the light intensity detected by the camera and thus the measured transmittance (see Sec. 11.4). In the following paragraphs, the findings of the simulation studies are compared to the findings of the experimental study.

Transmittance vs. Fiber Inclination The simulations were able to reproduce the observed inclination dependence of the transmittance when modeling the nerve fibers with double myelin layers (cf. Sec. 10.3.1) and with slightly different fiber diameters and orientations (e. g. bundle of densely grown fibers, cf. Sec. 10.2.2). Figure 13.1 compares the scatter plot from the combined 3D-PLI/TPFM measurement (averaged normalized transmittance plotted against the nerve fiber inclination, cf. Fig. 8.4e) to the simulated transmittance curves for the bundle of densely grown fibers and for a bundle with very different fiber orientations (cf. dark purple and red lines in Fig. 11.19). Note that Figs.

13.1a and b can only be compared qualitatively because the measured and simulated light intensities were normalized in different ways and the TPFM measurements were performed for ca. 50 µm thick brain sections while the simulations were only performed for a volume thickness of 30 µm due to limited computing time.

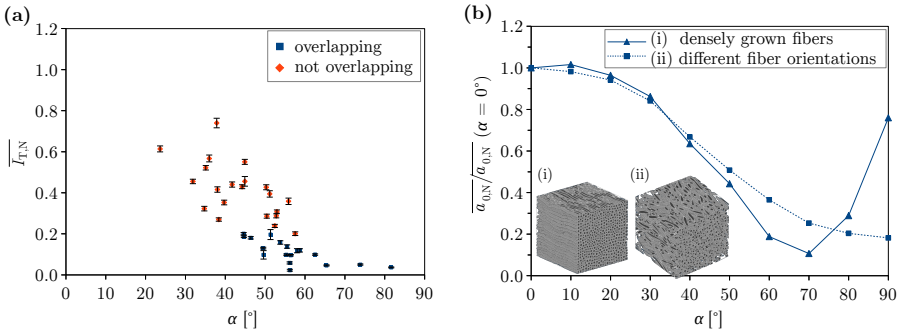

Fig. 13.1: (a) Averaged normalized transmittance $\overline{I_{T,N}}$ determined from a 3D-PLI measurement with the PM plotted against the inclination angle α of fiber bundles in the caudate putamen determined from a TPFM measurement of a coronal mouse brain section (cf. Fig. 8.4e). Transmittance values derived from regions that are mostly filled with fibers, i. e. with a similar myelin density, are highlighted in blue. **(b)** Averaged normalized transmittance $\overline{a_{0,N}}$ plotted against the fiber inclination angle for a bundle of densely grown fibers (i) and a bundle with broad fiber orientation distribution (ii) simulated for the imaging system of the PM, cf. Fig. 11.19. For better comparison, the transmittance curves were normalized by the averaged transmittance values of the horizontal bundles, respectively.

The simulated transmittance curves show a similar behavior as the measured transmittance values in the scatter plot, especially for the bundle with different fiber orientations. The simulation results are also consistent with the measured transmittance values of flat and steep fibers in Sec. 8.1: the simulated transmittance of steep fiber bundles is up to 80–90 % less than the transmittance of flat fiber bundles.

Transmittance vs. Embedding Time The simulations do not only model the observed inclination dependence of the transmittance, they also provide an explanation for the increasing transparency of tissue samples with increasing embedding time (cf. Fig. 9.7a): Assuming that the surrounding glycerin solution soaks into the myelin sheaths of the nerve fibers with increasing time after tissue embedding, the high refractive index of myelin becomes more similar to the lower refractive index of the surrounding tissue. The simulations show that the transmittance increases with decreasing myelin refractive index (see Fig. 11.13), i. e. the brain section becomes more transparent with increasing time after tissue embedding.

Transmittance vs. Homogeneity The simulations in Secs. 11.2.3 and 11.2.5 suggest that the transmittance decreases not only with increasing fiber inclination, but also with increasing fiber size and myelin sheath thickness. As the fiber dimensions cannot easily be determined, these predictions cannot be validated by experimental data.

Transmittance of Horizontal Crossing Fibers The FDTD simulations cannot only be used to explain the observed transmittance effects. They can also be used to make predictions for the experiment.

The simulations of a horizontal fiber bundle with different fiber orientation distributions (Sec. 11.2.1) and the simulations of crossing fiber bundles with different crossing angles (Sec. 11.3) suggest that the transmittance for flat fibers is mostly independent of the crossing angle between the fibers. This prediction was verified in experimental measurements of a crossing fiber region:

Figure 13.2b shows the transmittance and retardation images for the optic chiasm of a hooded seal – a region that contains fibers with crossing angles of about 90° in the image plane (cf. Fig. 13.2c). While the retardation values in the region with crossing fibers (region B) are broadly distributed between small and large values (the birefringence signals of crossing fibers cancel out), the transmittance values in this region show a similar distribution as in a region with mostly parallel fibers (region A), see histograms in Fig. 13.2d. The peak transmittance value of region B is lower than in region A because the number of fibers in the crossing region (two crossing bundles) is larger than in the region with parallel fibers (one bundle). Thus, the transmittance depends on the tissue density, but not on the crossing angles of the fibers – as predicted by the simulation.

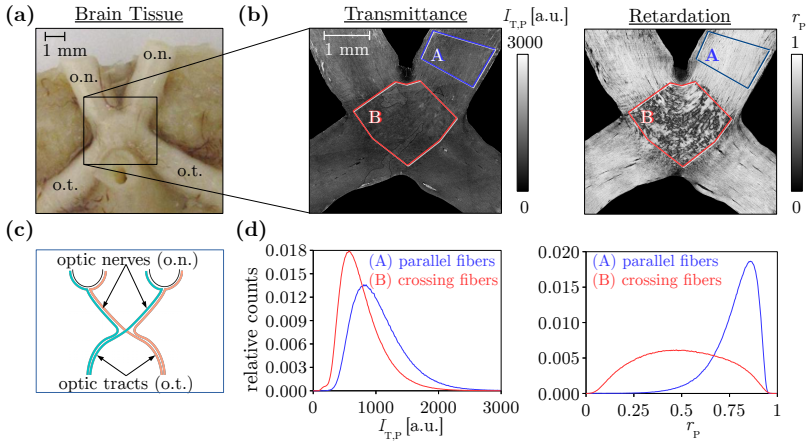

Fig. 13.2: Optic chiasm of a hooded seal: **(a)** brain tissue before sectioning, **(b)** transmittance and retardation images of the middle brain section obtained from 3D-PLI measurements with the PM, **(c)** schematic drawing of the optic chiasm consisting of optic tract (o.t.) and optic nerves (o.n.), **(d)** normalized histograms of the transmittance and retardation images for a region with mostly parallel fibers (blue) and a region with nearly 90°-crossing fibers (red). More information about the sample can be found in Dohmen *et al.* [52] (Figs. (a) and (c) were adapted from Figs. 1B and 5B0). The figure has been published in Menzel *et al.* (2018a) [67] Fig. 5.

Combined Analysis of Transmittance and Retardation The FDTD simulations in Chap. 11 suggest that the transmittance of brain tissue can be leveraged to obtain additional information about the underlying nerve fiber architecture and to improve the 3D-PLI analysis: as the transmittance depends on the fiber inclination and not on the in-plane crossing angle of the fibers, it should be possible to distinguish between horizontal crossing and vertical fiber configurations.

So far, the transmittance images are only used for transmittance weighting and as a reference for tissue segmentation. The three-dimensional orientation of the nerve fibers is computed from the retardation and direction images (cf. Sec. 4.4.1). By this means, regions with vertical fibers, regions with horizontal crossing fibers, and regions with a low myelin density (e. g. gray matter regions with a small number of myelinated axons) cannot be distinguished from each other because they all yield small retardation values. Figure 13.3 demonstrates how a combined analysis of retardation ($r_\mathrm{P} \equiv |\sin\delta_\mathrm{P}|$) and transmittance ($I_\mathrm{T,N}$) allows to distinguish between these fiber configurations.

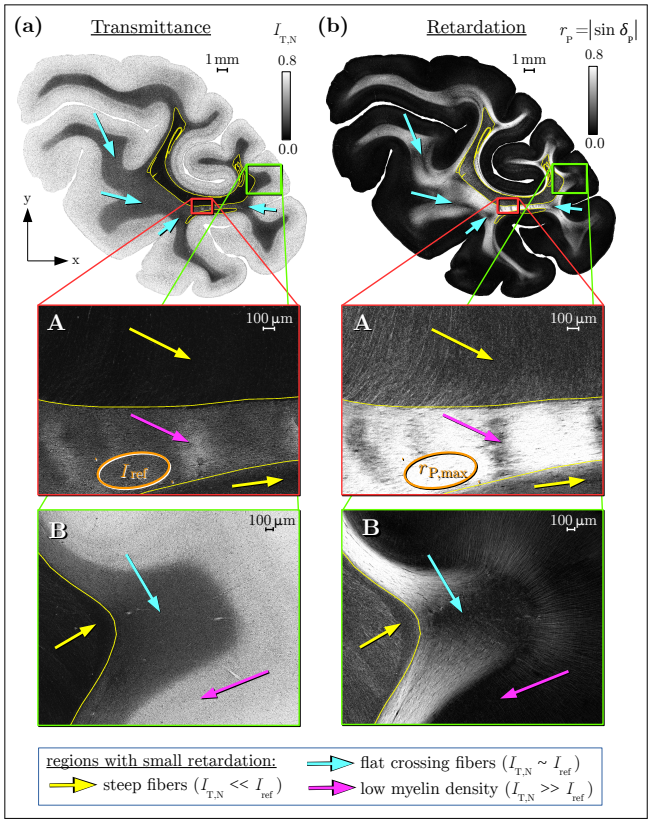

Fig. 13.3: Normalized transmittance image ($I_\mathrm{T,N}$) and retardation image ($r_\mathrm{P} \equiv |\sin\delta_\mathrm{P}|$) of a coronal section through the right hemisphere of a vervet brain (cf. Fig. 8.3a). The images demonstrate how a combined analysis of retardation and transmittance images can help to distinguish between horizontal crossing fibers and vertical fibers: The transmittance in the region with maximum retardation (orange ellipse) is used as a threshold value ($I_\mathrm{ref} \equiv I_\mathrm{T,N}(r_\mathrm{P,max})$). Regions with small retardation values and notably lower transmittance values ($I_\mathrm{T,N} \ll I_\mathrm{ref}$, yellow arrows and regions surrounded by a yellow line) are expected to contain vertical (steep) fibers. Regions with small retardation values and similar transmittance values ($I_\mathrm{T,N} \approx I_\mathrm{ref}$, cyan arrows) are expected to contain horizontal (flat) crossing fibers. Regions with small retardation values and larger transmittance values ($I_\mathrm{T,N} > I_\mathrm{ref}$, magenta arrows) belong to regions with low myelin density, i. e. regions with a large amount of unmyelinated axons or surrounding tissue. The figure has been published in Menzel *et al.* (2018a) [67] Fig. 6.

As the transmittance depends on absorption, the region with maximum absorption was determined as a reference: The retardance of brain tissue increases with decreasing fiber inclination and with increasing thickness of birefringent tissue components ($\delta_\mathrm{P} \propto d\,\Delta n\,\cos^2\alpha$, cf. Eq. (3.8)). Assuming that a brain section contains all possible nerve fiber configurations, the region with maximum retardation signal $r_\mathrm{P,max}$ (orange ellipse) is therefore expected to contain mostly horizontal parallel fibers ($\alpha \approx 0°$) with a high fiber density (max. $d\,\Delta n$). Due to the high fiber density, the region is also expected to cause a maximum of absorption. Regions with even lower transmittance values are therefore expected to contain steep fibers which increase the scattering and thus the attenuation of light.

By comparing the transmittance values ($I_\mathrm{T,N}$) of regions with small retardation values to the transmittance of the region with maximum retardation ($I_\mathrm{ref} \equiv I_\mathrm{T,N}(r_\mathrm{P,max})$), the regions can therefore be classified into three categories (see Fig. 13.3):

- $I_\mathrm{T,N} \ll I_\mathrm{ref}$: regions with notably lower transmittance values are expected to contain vertical fibers (see yellow arrows and regions surrounded by a yellow line),
- $I_\mathrm{T,N} \sim I_\mathrm{ref}$: regions with similar transmittance values are expected to contain horizontal crossing fibers (see cyan arrows),
- $I_\mathrm{T,N} \gg I_\mathrm{ref}$: regions with notably larger transmittance values have a lower myelin density (see magenta arrows).

For regions with slightly lower or larger transmittance values, an unambiguous classification is not possible. Provided that the region with maximum retardation has the largest tissue absorption, lower transmittance values can only be caused by steep fibers. Similar transmittance values, however, could also be caused by a small number of steep fibers, and larger transmittance values could be caused by a small number of horizontal crossing fibers (or a smaller number of steep fibers). A classification by means of retardation and transmittance values can therefore only serve as an indication of the underlying fiber architecture and should always be considered in addition to individual tissue characteristics.

A comparison with brain atlases and 3D-reconstructed images (cf. Fig. 8.3) shows that the classification of regions in Fig. 13.3 (coronal vervet section) is reasonable. Thus, by including the transmittance image in the 3D-PLI analysis,[1] the reconstruction of the brain's nerve fiber architecture can significantly be improved without need for additional measurements.

This example demonstrates that FDTD simulations are not only a valuable tool to explain and model the effects observed in 3D-PLI measurements, but also to make predictions and to improve the measurement procedure and analysis.

13.2 Diattenuation Effect

Diattenuation can be caused by anisotropic absorption (dichroism) and by anisotropic scattering (see Sec. 2.4). The experimental studies in Chap. 9 have shown that brain tissue exhibits two different types of diattenuation which are regionally specific and depend on the time after embedding the tissue sample: In some regions, the transmitted light intensity becomes maximal when the light is polarized in the direction of the nerve

[1] As the transmittance depends on the tissue preparation, the combined analysis of transmittance and retardation should only be performed section-wise.

fibers (D^+). In other regions, it becomes maximal when the light is polarized perpendicularly to the nerve fibers (D^-). The fraction of regions with diattenuation of type D^- decreases with increasing time after tissue embedding.

To model and better understand the observed diattenuation effects, the anisotropic scattering ($D_{\mathcal{S}}$) was studied by means of FDTD simulations in Chap. 12. The dichroism D_{K} was described by an analytical model, assuming that dichroism only causes positive diattenuation and does not depend on the embedding time (see Appx. A.4.3).

Diattenuation vs. Fiber Inclination The experimental studies in Sec. 9.2.2 have shown that freshly embedded brain tissue with non-steep fibers ($\alpha < 60°$) show both types of diattenuation, while steep fibers mostly show diattenuation of type D^+ (cf. Fig. 9.5).

The simulations of densely grown and inhomogeneous fiber bundles in Secs. 12.1.2 and 12.1.3 confirmed that two types of diattenuation (D^+ and D^-) can be observed and that the diattenuation depends indeed on the fiber inclination: regions with non-steep fibers ($\alpha < 65°$) show both types D^+ and D^- (depending on whether $D_{\mathrm{K}} > 0$ or $D_{\mathcal{S}} < 0$ dominates), regions with steep fibers ($65° < \alpha < 90°$) are expected to only show type D^+ because both $D_{\mathcal{S}}$ and D_{K} are positive, and regions with vertical fibers ($\alpha \approx 90°$) show small diattenuation values (see Fig. 13.4a).

To directly compare the predictions of the simulation studies to the experimental data, the diattenuation maps of a coronal vervet brain section (measured 8 days and 51 days after tissue embedding, cf. Fig. 9.8a) were evaluated in regions with different fiber inclinations (see Fig. 13.4b). The fiber inclinations (shown in Fig. 13.4c) were determined from a 3D-PLI measurement with tilting (cf. Fig. 9.5b). In order to better compare the regions of type D^+ and D^- to the fiber inclination, the brain sections on the right only show the white matter regions without any weighting. Regions of type D^+ and regions with fiber inclinations $> 65°$ are shown in green, while regions of type D^- are shown in magenta.

As predicted by the simulation studies, regions with steep fibers ($\alpha_{\mathrm{P}} > 65°$) only show diattenuation of type D^+: nearly all green regions in Fig. 13.4c are also green in Fig. 13.4b (see red circles). Regions with lower fiber inclinations show both types D^+ and D^- (see yellow circles). Regions with flat fiber inclinations are most likely to show diattenuation of type D^- (see cyan circles).

All these observations can be explained by the combined model of analytically computed and simulated diattenuation curves (the dashed vertical lines in Fig. 13.4a mark the inclination angles of the evaluated regions). However, the magnitude of D_{K} can only be estimated and the magnitude of D_{S} depends on details of the underlying fiber architecture that cannot easily be determined (e. g. $|D_{\mathrm{S}}|$ decreases with increasing fiber orientation distribution, see dark purple and red curves in Fig. 13.4a). Thus, without additional information about the underlying fiber structure and architecture, the model cannot clearly predict whether D_{K} or D_{S} dominates in a certain brain region. This makes a classification into regions of type D^+ or D^- difficult for non-steep fibers.

Diattenuation vs. Embedding Time The experimental studies in Sec. 9.3 have shown that the diattenuation of type D^- decreases with increasing time after tissue embedding. Figure 13.4b shows that this behavior also depends on the fiber inclination: In regions with steep fibers, which are already of type D^+ for freshly embedded tissue, the strength of the measured diattenuation $|\mathscr{D}|$ does not change much with the embedding time (see red circles). In regions with intermediate fiber inclinations, the diattenuation of type D^- decreases with increasing time after tissue embedding (magenta regions turn

into green) and the diattenuation of type D^+ increases (dark green regions turn into brighter green, see yellow circles). Regions with flat fiber inclinations might still show diattenuation of type D^- for tissue samples with long embedding time, but the strength of the diattenuation becomes much less (see cyan circles).

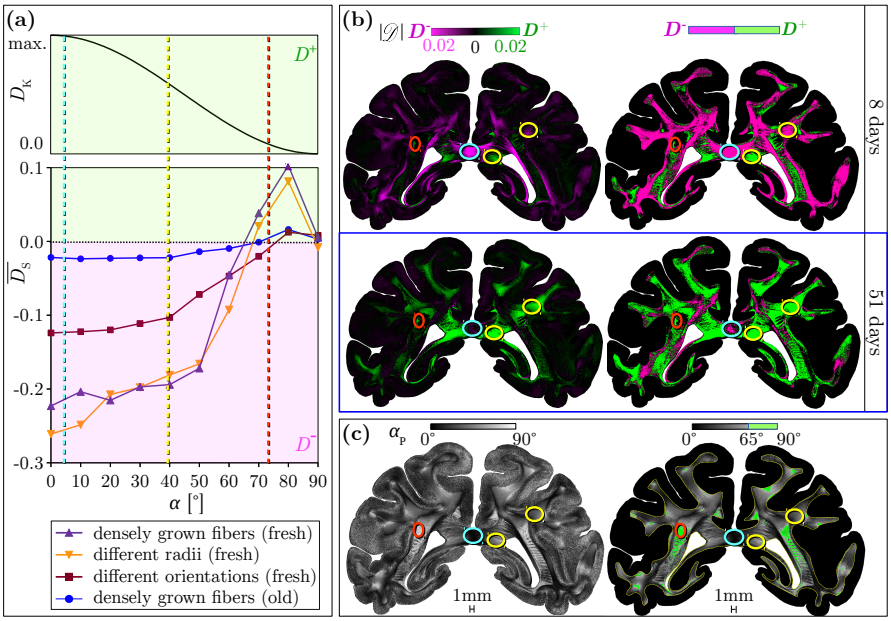

Fig. 13.4: **(a)** Diattenuation caused by anisotropic absorption (dichroism D_K) and by anisotropic scattering (D_S) plotted against the inclination angle α. The curve for D_K was computed analytically, the curves for D_S were computed from FDTD simulations for a bundle of densely grown fibers ("fresh" and "old" tissue), a bundle with broad fiber radius distribution, and a bundle with broad fiber orientation distribution for the optics of the PM (adapted from Fig. 12.9). Positive diattenuation values (representing type D^+) are shown on a green background, negative diattenuation values (representing type D^-) are shown on a magenta background. **(b)** Diattenuation images of a coronal vervet brain section measured 8 and 51 days after tissue embedding (adapted from Fig. 9.8a). Diattenuation values $|\mathscr{D}|$ that belong to regions with diattenuation of type D^+ ($\varphi_D - \varphi_P \in [-20°, 20°]$) are shown in green, diattenuation values that belong to regions with diattenuation of type D^- ($\varphi_D - \varphi_P \in [70°, 110°]$) are shown in magenta, regions that cannot clearly be assigned are shown in black. The images on the left were weighted with the measured diattenuation $|\mathscr{D}|$, the images on the right show the regions of type D^+ and D^- in the white matter without any weighting. **(c)** Corresponding inclination angles α_P obtained from a 3D-PLI measurement with tilting (cf. Fig. 9.5b). The image on the right only shows the inclination angles in the white matter and regions with $\alpha_P > 65°$ are marked in green. The dashed vertical lines in (a) and the colored circles in (b) and (c) highlight regions with flat, intermediate, and steep fiber inclinations: $\alpha = 5°$ (cyan), $\alpha = 40°$ (yellow), and $\alpha = 75°$ (red). A similar figure has been published in Menzel *et al.* (2018b) [68] Fig. 4C-D.

The FDTD simulations provide an explanation for this behavior: The simulations in Sec. 12.2.4 (cf. dark purple and blue curves in Fig. 13.4a) revealed that anisotropic scattering $|D_S|$ decreases with increasing time after tissue embedding, assuming that the embedding glycerin solution soaks into the myelin sheaths of the nerve fibers and reduces

the difference between the effective refractive indices (cf. transmittance vs. embedding time). Assuming in addition that dichroism ($D_K > 0$) does not depend much on the embedding time of the sample, this explains why the fraction of regions with diattenuation of type D^- decreases with increasing time after tissue embedding.

Strength of the Diattenuation Signal The diattenuation of brain tissue was found to be relatively small: the maximum diattenuation values measured with the LAP are less than 5 % (see Secs. 9.2 and 9.3). The FDTD simulations for the bundle of densely grown fibers yield larger diattenuation values (max. $D_S \approx 15\,\%$ for the simulated optics of the LAP, see Fig. 12.5b, without taking $D_K > 0$ into account). However, the diattenuation values are expected to become much less when considering a bundle with broad fiber orientation distribution (max. $D_S \approx 1.25\,\%$, see dark red curve in Fig. 13.4a) and the diattenuation also depends on other tissue properties like fiber size, radius distribution, or myelin sheath thickness (see Secs. 12.2.2, 12.2.3 and 12.2.5). Taking these effects into account, the diattenuation caused by anisotropic scattering D_S is compatible with the small diattenuation values observed in the experiment.

Measurements with a prototypic polarizing microscope (see Sec. 9.2.3) have shown that imaging systems with higher optical resolution reach diattenuation values up to 10 %. These values are in accordance with the maximum diattenuation values obtained from DI simulations for the optics of the PM (max. $D_S \approx 10\,\%$, see Fig. 13.4a).

The simulated diattenuation curves for the PM and the LAP show a similar behavior (see Fig. 12.5). This agrees with the experimental observation that the measurements with the LAP and with the prototypic polarization microscope yield similar diattenuation effects (the maximum diattenuation values and diattenuation of type D^+ or D^- occur in the same brain regions, cf. Fig. 9.6).

Diattenuation vs. Homogeneity The simulations of horizontal 90°-crossing and vertical fibers (see Sec. 12.3) are compatible with the experimental observation that these fiber constellations cannot be distinguished by means of their diattenuation values.

The FDTD simulations of horizontal fiber bundles with different fiber properties (see Sec. 12.2) suggest that the diattenuation of type D^- is especially large in regions with horizontal fiber bundles that consist of relatively straight fibers with different fiber radii (and small average fiber radius) surrounded by thick myelin sheaths. This explains why regions like the corpus callosum show large negative diattenuation values in coronal brain sections (see Figs. 9.4a and 9.6C). However, to really compare the predictions of the simulation studies to experimental data, the exact underlying tissue structure needs to be known (like the fiber radius distribution or myelin sheath thickness), which would require additional microscopy studies.

The FDTD simulations do not only give an explanation for the observed diattenuation effects and correctly model the behavior of D^+ and D^- regions for different fiber inclinations and embedding times. They also confirm that the diattenuation depends on the fiber structure and organization and can be used to obtain additional information about the structure and composition of brain tissue. This makes Diattenuation Imaging a valuable technique in extension to 3D-PLI.

13.3 Overall Discussion

This chapter provided a cross-validation of the experimental and simulation studies in Parts III and IV. The comparison of experimental and simulation results in Secs. 13.1 and 13.2 has shown that the simulations cannot only be used to model and explain the transmittance and diattenuation effects in brain tissue, but also to make valuable predictions and to improve the measurement procedure and analysis.

The experimental studies in Chap. 8 clearly show that the transmittance decreases with increasing fiber inclination. In future studies, the transmittance values and the corresponding inclination angles should be evaluated for a larger number of fiber bundles, especially in regions with flat fibers, to obtain better statistics and to enable a more profound comparison between experimental and simulated data (cf. Fig. 13.1).

The diattenuation measurements with the LAP have a low signal-to-noise ratio which makes a clear distinction between regions of type D^+ and D^- difficult in regions with low diattenuation signals. To obtain more reliable diattenuation values, future measurements should be performed with higher optical resolution and better optical components (cf. measurements with prototypic polarizing microscope in Sec. 9.2.3). To learn more about how the diattenuation (D^+ and D^-) is related to the underlying tissue structure, additional measurements (e. g. electron microscopy studies) are needed that provide information such as the fiber radius or the myelin sheath thickness.

Concerning the simulation results, it should be noted that the FDTD simulations are more suitable to study the transmittance than the diattenuation of brain tissue: The transmittance is mostly determined by isotropic tissue properties and was measured with the PM. The diattenuation, however, was mostly measured with the LAP and can only be partly modeled by TDME3D because the diattenuation is not only caused by regular fiber configurations or myelin layers, but also by the molecular substructure of the myelin layers which cannot be included in the simulation model (cf. Sec. 10.5). In addition, the simulated diattenuation values turned out to be more sensitive to small changes in the simulation model than the simulated transmittance values (cf. Sec. 10.4), and the simulated diattenuation values were only approximately computed from only two simulation runs while the transmittance is a direct result of the Fourier transform (cf. Sec. 10.1.2).

Despite these limitations, both the transmittance and the diattenuation of brain tissue could successfully be modeled and explained by the simulation studies.

Following a bottom-up approach (starting from a straight cylindrical fiber and ending with more complex fiber configurations), it was possible to identify the simplest possible model that describes the observed effects: the transmittance as well as the diattenuation effects were reproduced when modeling the nerve fibers with double myelin layers and with slightly different radii and orientations (bundle of densely grown fibers). This shows that a relatively simple fiber model can already reproduce the observed transmittance and diattenuation effects, but it is necessary to break the symmetry by slightly random variations of the fiber direction.

While the simulation results for the hexagonal grid of helical fibers are especially sensitive to changes in wavelength, Yee mesh size, and angle of incidence, the simulations for the bundle of densely grown fibers yield similar results for different wavelengths, mesh sizes, and angles of incidence (cf. Appx. D.11). The simulation results for slightly different fiber radii or slightly different refractive indices are also similar. This demonstrates

that the simulation results do not depend on details in the simulation model and can be regarded as stable and reliable.

The dependence of the transmittance and diattenuation on the embedding time of the sample can be explained by the same model: the surrounding glycerin solution soaks into the myelin sheaths, which causes the effective refractive index of myelin to become more similar to the refractive index of the surrounding solution. Under this assumption, the simulations were able to model both the increasing transparency of brain tissue and the decreasing diattenuation of type D^- with increasing time after tissue embedding. Molecular birefringence or dichroism are not affected in this model (this explains why the retardation does not depend much on the embedding time of the sample, cf. Fig. 9.7b).

In contrast to the inclination dependence and the time behavior, the simulated dependence of the transmittance and diattenuation on the tissue homogeneity (cf. Secs. 11.2 and 12.2) cannot easily be compared to experimental data. To obtain reliable information about the fiber sizes and myelin sheath thicknesses, microscopy measurements with higher resolution (e. g. electron microscopy studies) are required. The layered structure of the myelin sheath leads to multiple (anisotropic) scattering, which might have a large impact on the resulting transmittance and diattenuation values. In the simulations, the nerve fibers were only modeled with double myelin layers. Simulations of fibers with several myelin layers (see Sec. 10.4.2) have shown that especially the simulated diattenuation values are sensitive to changes in the number of myelin layers. The dependence of the transmittance and diattenuation on the myelin sheath thickness can therefore not be precisely determined. Future simulations should study the impact of the number of myelin layers in more detail, also for inclined nerve fiber configurations. The number of myelin layers in the investigated brain sections could be determined e. g. by means of X-ray diffraction measurements.

Chapter 14

Conclusion and Outlook

Three-dimensional Polarized Light Imaging (3D-PLI) reconstructs the brain's nerve fiber architecture by transmitting polarized light through histological brain sections and measuring their birefringence. Preliminary measurements have shown that the polarization-independent transmitted light intensity (*transmittance*) depends on the out-of-plane angle (*inclination*) of the nerve fibers. Furthermore, the optical anisotropy that causes the birefringence leads to polarization-dependent attenuation of light (*diattenuation*), which might provide additional information about the underlying fiber architecture. The aim of this thesis was to investigate the transmittance and diattenuation effects in more detail, and to develop ideas how these effects can assist the nerve fiber reconstruction with 3D-PLI. For this purpose, analytical considerations, experimental studies, and simulation studies were performed.[1]

In order to study the inclination dependence of the transmittance, brains from different species were cut along different anatomical planes and measured with a high-resolution Polarizing Microscope. The transmittance images obtained from the 3D-PLI measurements were evaluated in combination with Two-Photon-Fluorescence Microscopy to identify the underlying fiber inclinations.

While the transmittance can be obtained from standard 3D-PLI measurements, the measurement of the diattenuation requires a different setup. In this thesis, a measurement protocol has been developed that enables to measure the diattenuation of brain tissue even with a low signal-to-noise ratio: *Diattenuation Imaging (DI)*. In addition to a thorough characterization of the optical components, a complete analytical description of the imaging system was provided, considering non-ideal filter properties and tissue diattenuation, using the Müller-Stokes calculus. To estimate the impact of the tissue diattenuation and the non-ideal system components on the polarimetric measurements, numerical simulations were performed. To estimate the accuracy of the measurement results, a measurement with crossed polarizers was performed in addition to the 3D-PLI and DI measurements.

In order to model and explain the observed transmittance and diattenuation effects, the propagation of the polarized light wave through the brain tissue was simulated by a Maxwell Solver based on the *Finite-Difference Time-Domain (FDTD)* method, which is particularly well suited to study the scattering of light. In this thesis, a simulation procedure has been developed that considers the optical components of the employed polarimeters and models the polarimetric measurements (3D-PLI and DI) by FDTD simulations so that the transmittance and diattenuation of brain tissue can be studied in more detail. To test the simulation procedure and the applicability of the simulation

[1] Parts of this chapter have been published in Menzel *et al.* (2017, 2018a, 2018b) [3, 67, 68].

results, simulated and measured transmitted light intensities were compared for a well-defined sample (USAF resolution target), and the simulation parameters were evaluated in terms of accuracy and computing time.

Following a bottom-up approach (starting from a straight fiber and ending with more complex fiber configurations), the transmittance and diattenuation effects were simulated for various fiber configurations. The simulations were not only used to model and explain the observed effects, but also to make predictions which were then validated on experimental data. The combination of analytical modeling, experimental studies, and FDTD simulations allows to learn more about the structure of brain tissue and to answer neuroscientific questions. The following paragraphs summarize the most important results.

FDTD Simulations The FDTD simulations proved to be a valuable and reliable tool in many aspects: they allow to better understand the interaction of polarized light with brain tissue, to find explanations for the observed transmittance and diattenuation effects, to make general predictions, and to improve the measurement procedure and analysis.

Both the transmittance and the diattenuation effects could be reproduced when modeling the nerve fibers as cylinders with double myelin layers and with slightly different radii and orientations. Thus, a relatively simple fiber model is already sufficient to reproduce the observed effects, but it is necessary to break the symmetry by slightly random variations of the fiber direction.

The dependence of the transmittance and diattenuation on the embedding time of the tissue samples could be reproduced by gradually matching the refractive index of myelin to the refractive index of the surrounding solution. This supports the hypothesis that the embedding solution of the brain tissue soaks into the myelin sheaths with increasing time after tissue embedding.

Transmittance Effect The experimental studies revealed that the transmittance of brain sections in 3D-PLI measurements significantly decreases with increasing out-of-plane inclination angle of the nerve fibers (by more than 50 %). The FDTD simulation studies could model this effect and show that the decrease in transmittance is caused by polarization-independent (isotropic) light scattering and by the limited numerical aperture of the imaging system.

More importantly, the simulations indicated that the transmittance of flat fiber configurations does not depend on the crossing angle between the fibers. In standard 3D-PLI or DI measurements, regions with horizontal crossing fibers, regions with vertical fibers, and regions with low fiber density cannot be distinguished because they all yield low birefringence and diattenuation signals. Applying the predictions obtained from the simulation studies to experimental data, it was demonstrated that a combined analysis of transmittance and retardation images enables to distinguish between these regions. The simulations also revealed that the transmittance can be used to detect vertical fibers in regions with horizontal crossing fibers, which is to date not even possible with a tiltable specimen stage.

As the transmittance image is always generated during a standard 3D-PLI analysis, the classification of horizontal crossing and vertical fiber regions is also possible for past measurements without need for additional measurements. The transmittance effects have been shown to depend mostly on (isotropic) scattering and not on the polarization

of light so that the results are also relevant for other transmission microscopy techniques that use unpolarized light.

Finally, the simulations of the transmittance have demonstrated that the scattering patterns provide unique information about the underlying fiber architecture and could for example be used to determine the crossing angle of in-plane crossing fibers.

Diattenuation Effect The experimental studies revealed that the diattenuation of brain tissue is relatively small (less than 10 %) and has practically no impact on the measured 3D-PLI signal. Nevertheless, the diattenuation measurement proved to be a valuable extension to 3D-PLI: The phase and amplitude of the measured diattenuation signal can be used as complementary imaging modalities providing different contrasts and structural information in addition to those obtained with 3D-PLI. By comparing the fiber directions extracted from 3D-PLI and DI, two different types of diattenuation can be distinguished that are specific to certain fiber structures and configurations: in some brain regions, the transmitted light intensity becomes maximal when the light is polarized parallel to the nerve fibers (D^+), in other brain regions, it becomes minimal (D^-). Measurements with a prototypic polarizing microscope have shown that higher optical resolution and high-quality components lead to a significantly higher signal-to-noise ratio. Thus, a new microscope should allow for a combined measurement of 3D-PLI and DI to reliably determine regions of type D^+ and D^-.

The FDTD simulations could successfully model the diattenuation and show that diattenuation of type D^- is caused by anisotropic scattering of light which decreases with increasing time after tissue embedding, while diattenuation of type D^+ can be caused both by anisotropic scattering and by anisotropic absorption (dichroism). In addition, the simulations confirmed that steep fibers (with inclination angles $> 65°$) only show type D^+, while non-steep fibers show both types D^+ and D^- depending on whether anisotropic scattering or dichroism dominates. The simulations further revealed that the diattenuation depends not only on the fiber inclination, but also on the tissue composition. This makes Diattenuation Imaging a promising imaging technique that reveals different types of fibrous structures which cannot be distinguished with current imaging techniques.

Outlook The transmittance and diattenuation effects were clearly demonstrated in the experimental studies, and could successfully be modeled and explained by the simulation studies. The results can for example be used to classify different brain regions. In future studies, more experimental data should be generated to obtain better statistics and to enable a quantitative description of the observed effects. This would e. g. allow to include the inclination dependence of the transmittance in the correction of the measured birefringence signals. Particularly interesting would be microscopy measurements with higher optical resolution (e. g. electron microscopy studies) that provide information about the inner tissue structure (distribution of fiber radii, myelin sheath thicknesses, fiber orientations, etc.) and help to better understand how the transmittance and diattenuation (D^+ and D^-) depend on the tissue homogeneity. A more detailed knowledge of the structure and the optical properties of brain tissue would also help to create a more realistic fiber model and enable an even better comparison between simulation and experiment.

The simulations suggest that especially the simplified model of the myelin sheath (double myelin layers) might have an impact on the simulated transmittance and diattenuation values. In future simulation studies, it would be interesting to study the

impact of the myelin layers and the myelin sheath thickness (g-ratio) in more detail and to take different fiber inclinations into account.

As the scattering patterns turned out to provide interesting information about the underlying fiber architecture, future simulations should study the scattering patterns of various fiber configurations to find out whether the patterns can for example be used to distinguish between crossing (X) and kissing ($\supset\subset$) fibers or between interwoven and separate crossing fibers. In addition, measurement techniques should be explored that enable to measure the scattering pattern of the brain sections.

To date, the diattenuation of brain tissue can only be partly modeled because the simulations only account for anisotropic scattering outside the substructure of the myelin layers. The molecular diattenuation was effectively described by a simple analytical model of uniaxial dichroism. One possibility to study the impact of dichroism in more detail is to replace the analytical model by a more advanced model in which the optical properties (dichroism and birefringence) of each tissue voxel are described by a matrix (e. g. Jones matrix, cf. [66]). However, dichroism and anisotropic scattering would still be considered separately, neglecting any interdependencies. If the TDME3D software could be further developed to allow the definition of relative permittivity tensors (anisotropic refractive indices), the total diattenuation and birefringence of the brain tissue (including the molecular structure) could be studied.

A more advanced simulation tool that enables a direct comparison between simulated and experimental data could be used to estimate the probability of certain fiber configurations and to assist the fiber reconstruction with 3D-PLI: Simulations of various fiber configurations could help to relate a certain (simulated) measurement output to a certain fiber configuration (e. g. by using machine learning). This knowledge could then be applied to the analysis of experimental data.

The overall aim of future work should be to bring theory, simulation, and experiment together and to integrate the simulation results into the image analysis of 3D-PLI. As a first step, the transmittance should become part of the standard signal analysis to enable the distinction between brain regions with horizontal crossing and vertical fibers. The combined analysis of transmittance and retardation images should also be applied to past 3D-PLI measurements in order to validate and – if necessary – correct the reconstructed fiber orientations.

Bibliography

[1] Jülich Supercomputing Centre. JURECA: General-purpose supercomputer at Jülich Supercomputing Centre. *Journal of large-scale research facilities*, 2, A62, 2016. doi: 10.17815/jlsrf-2-121.

[2] Jülich Supercomputing Centre. JUQUEEN: IBM Blue Gene/Q Supercomputer System at the Jülich Supercomputing Centre. *Journal of large-scale research facilities*, 1, A1, 2015. doi: 10.17815/jlsrf-1-18.

[3] M. Menzel, J. Reckfort, D. Weigand, H. Köse, K. Amunts, and M. Axer. Diattenuation of brain tissue and its impact on 3D polarized light imaging. *Biomedical Optics Express*, 8(7):3163–3197, 2017. doi: 10.1364/BOE.8.003163.

[4] S. Herculano-Houzel. The human brain in numbers: a linearly scaled-up primate brain. *Frontiers in Human Neuroscience*, 3(31):1–11, 2009. doi: 10.3389/neuro.09.031.2009.

[5] E. R. Kandel, J. H. Schwartz, and T. M. Jessell. *Principles of Neural Science*. McGraw-Hill, USA, 4 edition, 2000.

[6] L. R. Squire, F. E. Bloom, N. C. Spitzer, S. du Lac, A. Ghosh, and D. Berg. *Fundamental Neuroscience*. Fundamental Neuroscience Series. Elsevier Science, 3 edition, 2008.

[7] A. Longstaff. *Neuroscience*. BIOS Instant Notes. Garland Science, Taylor & Francis Group, LLC, 3 edition, 2011.

[8] S. F. Gilbert. *Developmental Biology*. Sinauer Associates, 6 edition, 2000.

[9] K. Amunts, C. Ebell, J. Muller, M. Telefont, A. Knoll, and T. Lippert. The Human Brain Project: Creating a European research infrastructure to decode the human brain. *Neuron*, 92(3):574–581, 2016. doi: 10.1016/j.neuron.2016.10.046.

[10] T. E. J. Behrens and O. Sporns. Human connectomics. *Current Opinion in Neurobiology*, 22(1):144–153, 2012. doi: 10.1016/j.conb.2011.08.005.

[11] Y. Shi and A. W. Toga. Connectome imaging for mapping human brain pathways. *Molecular Psychiatry*, 22:1230–1240, 2017. doi: 10.1038/mp.2017.92.

[12] S. Mori and J. Zhang. Principles of diffusion tensor imaging and its applications to basic neuroscience research. *Neuron*, 51(5):527–539, 2006. doi: 10.1016/j.neuron.2006.08.012.

[13] C. Beaulieu. The basis of anisotropic water diffusion in the nervous system – a technical review. *NMR in Biomedicine*, 15(7–8):435–455, 2002. doi: 10.1002/nbm.782.

[14] D. S. Tuch, T. G. Reese, M. R. Wiegell, and V. J. Wedeen. Diffusion MRI of complex neural architecture. *Neuron*, 40(5):885–895, 2003. doi: 10.1016/S0896-6273(03)00758-X.

[15] S. Mori and P. C. M. van Zijl. Fiber tracking: principles and strategies – a technical review. *NMR in Biomedicine*, 15:468–480, 2012. doi: 10.1002/nbm.781.

[16] T. E. Conturo, N. F. Lori, T. S. Cull, E. Akbudak, A. Z. Snyder, J. S. Shimony, R. C. McKinstry, H. Burton, and M. E. Raichle. Tracking neuronal fiber pathways in the living human brain. *Proceedings of the National Academy of Sciences*, 96 (18):10422–10427, 1999. doi: 10.1073/pnas.96.18.10422.

[17] P. Hagman, J. P. Thiran, L. Jonasson, P. Vandergheynst, S. Clarke, P. Maeder, and R. Meuli. DTI mapping of human brain connectivity: statistical fibre tracking. *NeuroImage*, 19:545–554, 2003. doi: 10.1016/S1053-8119(03)00142-3.

[18] H.-C. Chang, M. Sundman, L. Petit, S. Guhaniyogi, M.-L. Chu, C. Petty, A. W. Song, and N. Chen. Human brain diffusion tensor imaging at submillimeter isotropic resolution on a 3 Tesla clinical MRI scanner. *NeuroImage*, 118:667–675, 2015. doi: 10.1016/j.neuroimage.2015.06.016.

[19] K. L. Miller, C. J. Stagg, G. Douaud, S. Jbabdi, S. M. Smith, T. E. J. Behrens, M. Jenkinson, S. A. Chance, M. M. Esiri, N. L. Voets, N. Jenkinson, T. Z. Aziz, M. R. Turner, H. Johansen-Berg, and J. A. McNab. Diffusion imaging of whole, post-mortem human brains on a clinical MRI scanner. *NeuroImage*, 57:167–181, 2011. doi: 10.1016/j.neuroimage.2011.03.070.

[20] E. A. Susaki, K. Tainaka, D. Perrin, F. Kishino, T. Tawara, T. M. Watanabe, C. Yokoyama, H. Onoe, M. Eguchi, S. Yamaguchi, T. Abe, H. Kiyonari, Y. Shimizu, A. Miyawaki, H. Yokota, and H. R. Ueda. Whole-brain imaging with single-cell resolution using chemical cocktails and computational analysis. *Cell*, 157(3):726–739, 2014. doi: 10.1016/j.cell.2014.03.042.

[21] M. D. Zhang, G. Tortoriello, B. Hsueh, R. Tomer, L. Ye, N. Mitsios, L. Borgius, G. Grant, O. Kiehn, M. Watanabe, M. Uhlén, J. Mulder, K. Deisseroth, T. Harkany, and T. G. M. Hökfelt. Neuronal calcium-binding proteins 1/2 localize to dorsal root ganglia and excitatory spinal neurons and are regulated by nerve injury. *PNAS*, 111(12):E1149–E1158, 2014. doi: 10.1073/pnas.1402318111.

[22] I. Costantini, J.-P. Ghobril, A. P. Di Giovanna, A. L. A. Mascaro, L. Silvestri, M. C. Müllenbroich, L. Onofri, V. Conti, F. Vanzi, L. Sacconi, R. Guerrini, H. Makram, G. Iannello, and F. S. Pavone. A versatile clearing agent for multi-modal brain imaging. *Scientific Reports*, 5:9808, 2015. doi: 10.1038/srep09808.

[23] H. Lee, J. H. Park, I. Seo, S.-H. Park, and S. Kim. Improved application of the electrophoretic tissue clearing technology, CLARITY, to intact solid organs including brain, pancreas, liver, kidney, lung, and intestine. *BMC Developmental Biology*, 14:781, 2014. doi: 10.1186/s12861-014-0048-3.

[24] R. D. Spence, F. Kurth, N. Itoh, C. R. L. Mongerson, S. H. Wailes, M. S. Peng, and A. J. MacKenzie-Graham. Bringing CLARITY to gray matter atrophy. *NeuroImage*, 101:625–632, 2014. doi: 10.1016/j.neuroimage.2014.07.017.

[25] B. Yang, J. B. Treweek, R. P. Kulkami, B. E. Deverman, C-K. Chen, E. Lubeck, S. Shah, L. Cai, and V. Grandinaru. Single-cell phenotyping within transparent intact tissue through whole-body clearing. *Cell*, 158(4):945–958, 2014. doi: 10.1016/j.cell.2014.07.017.

[26] J. Mertz and J. Kim. Scanning light-sheet microscopy in the whole mouse brain with HiLo background rejection. *Journal of Biomedical Optics*, 15(1):016027, 2010. doi: 10.1117/1.3324890.

[27] M. Stefaniuk, E. J. Gualda, M. Pawlowska, D. Legutko, P. Matryba, P. Koza, W. Konopka, D. Owczarek, M. Wawrzyniak, P. Loza-Alvarez, and L. Kaczmarek. Light-sheet microscopy imaging of a whole cleared rat brain with Thy1-GFP transgene. *Scientific Reports*, 6:28209, 2016. doi: 10.1038/srep28209.

[28] L. Silvestri, A. L. Allegra Mascaro, I. Costantini, L. Sacconi, and F. S. Pavone. Correlative two-photon and light sheet microscopy. *Methods*, 66(2):268–272, 2014. doi: 10.1016/j.ymeth.2013.06.013.

[29] J. Men, Y. Huang, J. Solanki, X. Zeng, A. Alex, J. Jerwick, Z. Zhang, R. E. Tanzi, A. Li, and C. Zhou. Optical Coherence Tomography for brain imaging and developmental biology. *IEEE Journal of Selected Topics in Quantum Electronics*, 22(4), 2016. doi: 10.1109/JSTQE.2015.2513667.

[30] C. Magnain, J. C. Augustinack, E. Konukoglu, M. P. Frosch, S. Sakadžić, A. Varjabedian, N. Garcia, V. J. Wedeen, D. A. Boas, and B. Fischl. Optical coherence tomography visualizes neurons in human entorhinal cortex. *Neurophotonics*, 2(1): 015004, 2015. doi: 10.1117/1.NPh.2.1.015004.

[31] J. Ben Arous, J. Binding, J. F. Léger, M. Casado, P. Topilko, S. Gigan, A. C. Boccara, and L. Bourdieu. Single myelin fiber imaging in living rodents without labeling by deep optical coherence microscopy. *Journal of Biomedical Optics*, 16 (11):116012, 2011. doi: 10.1117/1.3650770.

[32] K. Wang, N. G. Horton, and C. Xu. Going deep: Brain imaging with multiphoton microscopy. *Optics & Photonics News*, 24(11):32–39, 2013. doi: 10.1364/OPN.24.11.000032.

[33] W. Zong, R. Wu, M. Li, Y. Hu, Y. Li, J. Li, H. Rong, H. Wu, Y. Xu, Y. Lu, H. Jia, M. Fan, Z. Zhou, Y. Zhang, A. Wang, L. Chen, and H. Cheng. Fast high-resolution miniature two-photon microscopy for brain imaging in freely behaving mice. *Nature Methods*, 14(7):713–719, 2017. doi: 10.1038/nmeth.4305.

[34] S. P. Amato, F. Pan, J. Schwartz, and T. M. Ragan. Whole brain imaging with serial two-photon tomography. *Frontiers in Neuroanatomy*, 10(31), 2016. doi: 10.3389/fnana.2016.00031.

[35] R. Kawakami, K. Sawada, A. Sato, T. Hibi, Y. Kozawa, S. Sato, H. Yokoyama, and T. Nemoto. Visualizing hippocampal neurons with in vivo two-photon microscopy using a 1030 nm picosecond pulse laser. *Scientific Reports*, 3:1014, 2012. doi: 10.1038/srep01014.

[36] A. J. Schain, R. A. Hill, and J. Grutzendler. Label-free in vivo imaging of myelinated axons in health and disease with spectral confocal reflectance microscopy. *Nature Medicine*, 20(4):443–449, 2014. doi: 10.1038/nm.3495.

[37] A. L. A. Mascaro, I. Costantini, E. Margoni, G. Iannello, A. Bria, L. Sacconi, and F. S. Pavone. Label-free near-infrared reflectance microscopy as a complimentary tool for two-photon fluorescence brain imaging. *Biomedical Optics Express*, 6(11): 4483–4492, 2015. doi: 10.1364/BOE.6.004483.

[38] H. J. Waldvogel, M. A. Curtis, K. Baer, M. I. Rees, and R. L. Faull. Immunohistochemical staining of post-mortem adult human brain sections. *Nature Protocols*, 1(6):2719–2732, 2006. doi: 10.1038/nprot.2006.354.

[39] E. Jurrus, M. Hardy, T. Tasdizen, P. T. Fletcher, P. Koshevoy, C.-B. Chien, W. Denk, and R. Whitaker. Axon tracking in serial block-face scanning electron microscopy. *Medical Image Analysis*, 13(1):180–188, 2009. doi: 10.1016/j.media.2008.05.002.

[40] R. Erni, M. D. Rossell, C. Kisielowski, and U. Dahmen. Atomic-resolution imaging with a sub-50-pm electron probe. *Physical Review Letters*, 102(9):096101–1–4, 2009. doi: 10.1103/PhysRevLett.102.096101.

[41] S. Mikula, J. Binding, and W. Denk. Staining and embedding the whole mouse brain for electron microscopy. *Nature Methods*, 9(12):1198–1201, 2012. doi: 10.1038/nmeth.2213.

[42] G. Knott, H. Marchman, D. Wall, and B. Lich. Serial section scanning electron microscopy of adult brain tissue using focused ion beam milling. *Journal of Neuroscience*, 28(12):2959–2964, 2008. doi: 10.1523/JNEUROSCI.3189-07.2008.

[43] R. H. Quarles, W. B. Macklin, and P. Morell. Myelin formation, structure and biochemistry. In G. Siegel, R. W. Albers, S. Brady, and D. Price, editors, *Basic Neurochemistry: Molecular, Cellular and Medical Aspects*, pages 51–71. Elsevier Academic Press, Burlington, MA, 7 edition, 2006.

[44] M. Catani, I. Bodi, and F. Dell'Acqua. Comment on 'The geometric structure of the brain fiber pathways'. *Science*, 337(6102):1605, 2012. doi: 10.1126/science.1223425.

[45] M. Axer, K. Amunts, D. Grässel, C. Palm, J. Dammers, H. Axer, U. Pietrzyk, and K. Zilles. A novel approach to the human connectome: Ultra-high resolution mapping of fiber tracts in the brain. *NeuroImage*, 54(2):1091–1101, 2011. doi: 10.1016/j.neuroimage.2010.08.075.

[46] M. Axer, D. Grässel, M. Kleiner, J. Dammers, T. Dickscheid, J. Reckfort, T. Hütz, B. Eiben, U. Pietrzyk, K. Zilles, and K. Amunts. High-resolution fiber tract reconstruction in the human brain by means of three-dimensional polarized light imaging. *Frontiers in Neuroinformatics*, 5(34):1–13, 2011. doi: 10.3389/fninf.2011.00034.

[47] K. Zilles, N. Palomero-Gallagher, D. Gräßel, P. Schlömer, M. Cremer, R. Woods, K. Amunts, and M. Axer. High-resolution fiber and fiber tract imaging using polarized light microscopy in the human, monkey, rat, and mouse brain. In Kathleen S. Rockland, editor, *Axons and Brain Architecture*, chapter 18, pages 369–389. Elsevier Acadamic Press, San Diego, 2015.

[48] M. Zeineh, N. Palomero-Gallagher, M. Axer, D. Gräßel, M. Goubran, A. Wree, R. Woods, K. Amunts, and K Zilles. Direct visualization and mapping of the spatial course of fiber tracts at microscopic resolution in the human hippocampus. *Cerebral Cortex*, 2016. doi: 10.1093/cercor/bhw010.

[49] G. F. Göthlin. Die doppelbrechenden Eigenschaften des Nervengewebes – ihre Ursachen und ihre biologischen Konsequenzen. *Kungl. Svenska Vet. Akad. Handlingar.*, 51(1):1–91, 1913.

[50] F. O. Schmitt and R. S. Bear. The ultrastructure of the nerve axon sheath. *Biological reviews of the Cambridge Philosophical Society*, 14:27–50, 1939.

[51] M. Menzel, K. Michielsen, H. De Raedt, J. Reckfort, K. Amunts, and M. Axer. A Jones matrix formalism for simulating three-dimensional polarized light imaging of brain tissue. *Journal of the Royal Society Interface*, 12:20150734, 2015. doi: 10.1098/rsif.2015.0734.

[52] M. Dohmen, M. Menzel, H. Wiese, J. Reckfort, F. Hanke, U. Pietrzyk, K. Zilles, K. Amunts, and M. Axer. Understanding fiber mixture by simulation in 3D Polarized Light Imaging. *NeuroImage*, 111:464–475, 2015. doi: 10.1016/j.neuroimage.2015.02.020.

[53] J. Reckfort. *New Approaches to the Interpretation of 3D-Polarized Light Imaging Signals for an Advanced Extraction of Fiber Orientation.* PhD thesis, University of Wuppertal, 2015.

[54] H. Wiese, D. Grässel, U. Pietrzyk, K. Amunts, and M. Axer. Polarized light imaging of the human brain: a new approach to the data analysis of tilted sections. In D. B. Chenault and D. H. Goldstein, editors, *SPIE Proceedings, Polarization: Measurement, Analysis, and Remote Sensing XI*, volume 9099, 2014. doi: 10.1117/12.2053305.

[55] H. Wiese. *Enhancing the Signal Interpretation and Microscopical Hardware Concept of 3D Polarized Light Imaging.* PhD thesis, University of Wuppertal, 2016.

[56] I. Costantini, M. Menzel, L. Silvestri, N. Schubert, M. Axer, K. Amunts, and F. S. Pavone. Polarized Light Imaging and Two-Photon Fluorescence Microscopy correlative approach for 3D reconstruction of the orientation of myelinated fibers. *Optics in the Life Sciences Congress, OSA Technical Digest (online), paper BrW4B.5*, 2017. doi: 10.1364/BRAIN.2017.BrW4B.5.

[57] D. B. Chenault and R. A. Chipman. Measurements of linear diattenuation and linear retardance spectra with a rotating sample spectropolarimeter. *Applied Optics*, 32(19):3513–3519, 1993. doi: 10.1364/AO.32.003513.

[58] S. B. Mehta, M. Shribak, and R. Oldenbourg. Polarized light imaging of birefringence and diattenuation at high resolution and high sensitivity. *Journal of Optics*, 15:1–13, 2013. doi: 10.1088/2040-8978/15/9/094007.

[59] O. K. Naoun, V. L. Dorr, P. Allé, J.-C. Sablon, and A.-M. Benoit. Exploration of the retinal nerve fiber layer thickness by measurement of the linear dichroism. *Applied Optics*, 44(33):7074–7082, 2005. doi: 10.1364/AO.44.007074.

[60] P. Westphal, J. M. Kaltenbach, and K. Wicker. Corneal birefringence measured by spectrally resolved Mueller matrix ellipsometry and implications for non-invasive glucose monitoring. *Biomedical Optics Express*, 7(4):1160–74, 2016. doi: 10.1364/BOE.7.001160.

[61] N. Ghosh and I. A. Vitkin. Tissue polarimetry: concepts, challenges, applications, and outlook. *Journal of Biomedical Optics*, 16(11):110801, 2011. doi: 10.1117/1.3652896.

[62] J. Soni, H. Purwar, H. Lakhotia, S. Chandel, C. Banerjee, U. Kumar, and N. Ghosh. Quantitative fluorescence and elastic scattering tissue polarimetry using an Eigenvalue calibrated spectroscopic Mueller matrix system. *Optics Express*, 21 (13):15475–15489, 2013. doi: 10.1364/OE.21.015475.

[63] S. Jiao, W. Yu, G. Stoica, and L. V. Wang. Contrast mechanisms in polarization-sensitive Mueller-matrix optical coherence tomography and application in burn imaging. *Applied Optics*, 42(25):5191–5197, 2003. doi: 10.1364/AO.42.005191.

[64] M. H. Smith. Interpreting Mueller matrix images of tissues. *Proceedings of SPIE*, 4257:82–89, 2001. doi: 10.1117/12.434690.

[65] X.-R. Huang. Polarization properties of the retinal nerve fiber layer. *Bulletin de la Société belge d'ophtalmologie*, 302:71–88, 2006.

[66] M. Menzel, M. Axer, H. De Raedt, and K. Michielsen. Finite-Difference Time-Domain Simulation for Three-Dimensional Polarized Light Imaging. In K. Amunts, L. Grandinetti, T. Lippert, and N. Petkov, editors, *Brain-Inspired Computing. BrainComp 2015. Lecture Notes in Computer Science*, volume 10087, chapter 6, pages 73–85. Springer International Publishing, Cham, 2016. doi: 10.1007/978-3-319-50862-7_6.

[67] M. Menzel, M. Axer, H. De Raedt, I. Costantini, L. Silvestri, F. S. Pavone, K. Amunts, and K. Michielsen. Transmittance assisted interpretation of 3D nerve fibre architectures. *arXiv:1806.07157v2*, 2018.

[68] M. Menzel, M. Axer, K. Amunts, H. De Raedt, and K. Michielsen. Diattenuation Imaging reveals different brain tissue properties. *arXiv:1806.07712v3*, 2018.

[69] M. Born and E. Wolf. *Principles of Optics – Electromagnetic Theory of Propagation, Interference and Diffraction of Light*. Cambridge University Press, 7 edition, 2011.

[70] W. Demtröder. *Experimentalphysik 2 – Elektrizität und Optik*. Springer-Verlag Berlin Heidelberg, 5 edition, 2009.

[71] E. Hecht. *Optik*. Oldenburg Verlag, München, 5 edition, 2009.

[72] A. Taflove and S. C. Hagness. *Computational Electrodynamics: The Finite-Difference Time-Domain Method*. Artech House, MA USA, 3 edition, 2005.

[73] D. H. Goldstein. *Polarized Light*. CRC Press, Taylor & Francis Group, 3 edition, 2011.

[74] C. Akcay, P. Parrein, and J. P. Rolland. Estimation of longitudinal resolution in optical coherence imaging. *Applied Optics*, 41(25):5256–5262, 2002. doi: 10.1364/AO.41.005256.

[75] F. R. S. Lord Ralyeigh. XXXI. Investigations in optics, with special reference to the spectroscope. *The London, Edinburgh, and Dublin Philosophical Magazine and Journal of Science*, 8(49):261–274, 1879. doi: 10.1080/14786447908639684.

[76] L. Bergmann and C. Schäfer. *Lehrbuch der Experimentalphysik Band 3 – Optik: Wellen- und Teilchenoptik*. De Gruyter, Berlin, 10 edition, 2004.

[77] L. D. Landau and E. M. Lifshitz. *Electrodynamics of Continuous Media – Course of Theoretical Physics, Volume 8*. Pergamon Press, 1960.

[78] F. Pedrotti, L. Pedrotti, W. Bausch, and H. Schmidt. *Optik für Ingenieure – Grundlagen*. Springer-Verlag, Berlin Heidelberg, 3 edition, 2005.

[79] O. Wiener. Die Theorie des Mischkörpers für das Feld der stationären Strömung. *Abhandlungen der Sächsischen Akademie der Wissenschaften*, 32(6):507–604, 1912.

[80] R. P. Hemenger. Birefringence of a medium of tenuous parallel cylinders. *Applied Optics*, 28(18):4030–4034, 1989. doi: 10.1364/AO.28.004030.

[81] G. Scheuner and J. Hutschenreiter. *Polarisationsmikroskopie in der Histophysik*. VEB Georg Thieme Leipzig, 1972.

[82] I. Richter, P.-C. Sun, F. Xu, and Y. Fainman. Design considerations of form birefringent microstructures. *Applied Optics*, 34(14):2421–2429, 1995. doi: 10.1364/AO.34.002421.

[83] A. J. Waddie, R. Buczynski, F. Hudelist, J. Nowosielski, D. Pysz, R. Stepien, and M. R. Taghizadeh. Form birefringence in nanostructured micro-optical devices. *Optical Society of America*, 1(7):1251–1261, 2011. doi: 10.1364/OME.1.001251.

[84] R. A. Chipman. Polarization analysis of optical systems. *Optical Engineering*, 28 (2):280290–280290–, 1989. doi: 10.1117/12.7976914.

[85] R. A. Chipman. Polarimetry. In *Handbook of Optics, Vol. 2: Devices, Measurements, and Properties*, chapter 22, pages 22.1–22.37. McGraw-Hill, New York, 2 edition, 1994.

[86] C. Fan and G. Yao. Imaging myocardial fiber orientation using polarization sensitive optical coherence tomography. *Biomedical Optics Express*, 4(3):460–465, 2013. doi: 10.1364/BOE.4.000460.

[87] E. Collett. *Field Guide to Polarization*. SPIE – The International Society for Optical Engineering, Washington, 2005.

[88] R. C. Jones. A new calculus for the treatment of optical systems. *Journal of the Optical Society of America*, 31:488–503, 1941. doi: 10.1364/JOSA.31.000488.

[89] R. C. Jones. A new calculus for the treatment of optical systems. IV. *Journal of the Optical Society of America*, 32:486–493, 1942. doi: 10.1364/JOSA.32.000486.

[90] H. Müller. Memorandum on the polarization optics of the photoelastic shutter. *Report No. 2 of the OSRD project OEMsr-576*, 1943.

[91] G. G. Stokes. On the composition and resolution of streams of polarized light from different sources. *Transaction of the Cambridge Philosophical Society*, 9:399–416, 1852.

[92] M. Schuenke, E. Schulte, and U. Schumacher. *THIEME Atlas of Anatomy – Head and Neuroanatomy*. Georg Thieme Verlag, Stuttgart, Germany, 2007.

[93] K. Zilles and B. N. Tillmann. *Anatomie*. Springer Medizin Verlag, Heidelberg, 2010.

[94] S. Aggarwal, L. Yurlova, and M. Simons. Central nervous system myelin: structure, synthesis and assembly. *Trends in Cell Biology*, 21(10):585–593, 2011. doi: 10.1016/j.tcb.2011.06.004.

[95] R. E. Martenson. *Myelin: Biology and Chemistry*. CRC Press, USA, 1992.

[96] P. Morell, R. H. Quarles, and W. T. Norton. Formation, structure, and biochemistry of myelin. In G. J. Siegel, editor, *Basic Neurochemistry – Molecular, Cellular, and Medical Aspects*, pages 109–136. Raven Press, New York, 4 edition, 1989.

[97] C. Hildebrand, S. Remahl, H. Persson, and C. Bjartmar. Myelinated nerve fibers in the CNS. *Progress in Neurobiology*, 40:319–384, 1993.

[98] M. Schuenke, E. Schulte, and U. Schumacher. *THIEME Atlas of Anatomy – Head, Neck, and Neuroanatomy*, volume 3. Thieme Medical Publishers, 2 edition, 2016.

[99] A. Schüz and V. Braitenberg. The human cortical white matter: Quantitative aspects of cortico-cortical long-range connectivity. In Schüz A. and V. Braitenberg, editors, *Cortical Areas: Unity and Diversity, Conceptual Advances in Brain Research*, pages 377–385. Taylor Francis, London, UK, 2002.

[100] D. Liewald, R. Miller, N. Logothetis, H.-J. Wagner, and A. Schüz. Distribution of axon diameters in cortical white matter: an electron-microscopic study on three human brains and a macaque. *Biological Cybernetics*, 108:541–557, 2014. doi: 10.1007/s00422-014-0626-2.

[101] F. Aboitiz, A. Ide, and R. Olivares. Corpus callosum morphology in relation to cerebral asymmetries in the postmortem human. In E. Zaidel and M. Iacoboni, editors, *The Parallel Brain: The Cognitive Neuroscience of the Corpus Callosum*, chapter I.2, pages 33–46. Massachusetts Institute of Technology, 2003.

[102] F. Aboitiz, A. B. Scheibel, R. S. Fisher, and E. Zaidel. Fiber composition of the human corpus callosum. *Brain Research*, 598(1-2):143–153, 1992. doi: 10.1016/0006-8993(92)90178-C.

[103] J. Kwon, M. Kim, H. Park, B.-M. Kang, Y. Jo, J.-H. Kim, O. James, S.-H. Yun, S.-G. Kim, M. Suh, and M. Choi. Label-free nanoscale optical metrology on myelinated axons in vivo. *Nature Communications*, 8:1832, 2017. doi: 10.1038/s41467-017-01979-2.

[104] T. Chomiak and B. Hu. What is the optimal value of the g-ratio for myelinated fibers in the rat CNS? A theoretical approach. *PLoS ONE*, 4(11), 2009. doi: 10.1371/journal.pone.0007754.

[105] N. Baumann and D. Pham-Dinh. Biology of oligodendrocyte and myelin in the mammalian central nervous system. *Physiological Reviews*, 81(2):871–927, 2001. doi: 10.1152/physrev.2001.81.2.871. URL `https://doi.org/10.1152/physrev.2001.81.2.871`. PMID: 11274346.

[106] C. H. Fox, F. B. Johnson, J. Whiting, and P. P. Roller. Formaldehyde fixation. *The Journal of Histochemistry and Cytochemistry*, 33(8):845–853, 1985. doi: 10.1177/33.8.3894502.

[107] D. W. Lee, X. Banquy, K. Kristiansen, Y. Kaufman, J. M. Boggs, and J. N. Israelachvili. Lipid domains control myelin basic protein adsorption and membrane interactions between model myelin lipid bilayers. *Proceedings of the National Academy of Sciences*, pages E768–E775, 2014. doi: 10.1073/pnas.1401165111.

[108] K. J. Chang, S. A. Redmond, and J. R. Chan. Remodeling myelination: implications for mechanisms of neural plasticity. *Nature Neuroscience*, 19(2):190–197, 2016. doi: 10.1038/nn.4200.

[109] D. K. Hartline. What is myelin? *Neuron Glia Biology*, 4(2):153–163, 2008. doi: 10.1017/S1740925X09990263.

[110] A. Longstaff. *Neuroscience*. Springer-Verlag, 2000.

[111] J. Sun, S. J. Lee, L. Wu, M. Sarntinoranont, and H. Xie. Refractive index measurement of acute rat brain tissue slices using optical coherence tomography. *Optics Express*, 20(2):1084–1095, 2012. doi: 10.1364/OE.20.001084.

[112] B. de Campos Vidal, M. L. Silveira Mello, A. C. Caiseiro-Filho, and C. Godo. Anisotropic properties of the myelin sheath. *Acta Histochemica*, 66:32–39, 1980.

[113] C. L. Curl, C. J. Bellair, T. Harris, B. E. Allman, P. J. Harris, A. G. Stewart, A. Roberts, K. A. Nugent, and L. M. Delbridge. Refractive index measurement in viable cells using quantitative phase-amplitude microscopy and confocal microscopy. *Cytometry A*, 65(1):88–92, 2005. doi: 10.1002/cyto.a.20134.

[114] W. Choi, C. Fang-Yen, K. Badizadegan, S. Oh, N. Lue, R. R. Dasari, and M. S. Feld. Tomographic phase microscopy. *Nature Methods*, 4(9):717–719, 2007. doi: 10.1038/NMETH1078.

[115] H.-J. van Manen, P. Verkuijlen, P. Wittendorp, V. Subramaniam, T. K. van den Berg, D. Roos, and C. Otto. Refractive index sensing of green fluorescent proteins in living cells using fluorescence lifetime imaging microscopy. *Biophysical Letters*, 94(8):L67–69, 2008. doi: 10.1529/biophysj.107.127837.

[116] F. A. Duck. *Physical Properties of Tissue: A Comprehensive Reference Book*. Academic Press, San Diego, 1990.

[117] M. Daimon and A. Masumura. Measurement of the refractive index of distilled water from the near-infrared region to the ultraviolet region. *Applied Optics*, 46 (18):3811–3820, 2007. doi: 10.1364/AO.46.003811.

[118] M. J. O'Neil, editor. *The Merck Index – An Encyclopedia of Chemicals, Drugs, and Biologicals*. Merck & Co., INC., 14 edition, 2006.

[119] H.-J. Schwarzmaier, A. Yaroslavsky, I. Yaroslavsky, T. Goldbach, T. Kahn, F. Ulrich, P. C. Schulze, and R. Schober. Optical properties of native and coagulated human brain structures. *SPIE*, 2970:492–499, 1997. doi: 10.1117/12.275082.

[120] A. N. Yaroslavsky, P. C. Schulze, I. V. Yaroslavsky, R. Schober, F. Ulrich, and H.-J. Schwarzmaier. Optical properties of selected native and coagulated human brain tissues in vitro in the visible and near infrared spectral range. *Physics in Medicine and Biology*, 47:2059–2073, 2002. URL `http://stacks.iop.org/PMB/47/2059`.

[121] R. Smith and K. S. Baker. Optical properties of the clearest natural waters (200–800 nm). *Applied Optics*, 20(2):177–184, 1981. doi: 10.1364/AO.20.000177.

[122] F. M. Sogandares and E. S. Fry. Absorption spectrum (340–640 nm) of pure water. I. Photothermal measurements. *Applied Optics*, 36(33):8699–8709, 1997. doi: 10.1364/AO.36.008699.

[123] M. Johns, C. Giller, and H. Liu. Computational and in vivo investigation of optical reflectance from human brain to assist neurosurgery. *Journal of Biomedical Optics*, 3(4):437–445, 1998.

[124] H. R. Eggert and V. Blazek. Optical properties of human brain tissue, meninges, and brain tumors in the spectral range of 200 to 900 nm. *Neurosurgery*, 21(4): 459–464, 1987.

[125] A. Yuan, M. V. Rao, V. Nixon, and R. A. Nixon. Neurofilaments at a glance. *Journal of Cell Science*, 125:3257–3263, 2012. doi: 10.1242/jcs.104729.

[126] J. E. Darnell, H. F. Lodish, and D. Baltimore. *Molecular Cell Biology*. Scientific American Medicine, New York, 1990.

[127] X.-R. Huang and R. W. Knighton. Microtubules contribute to the birefringence of the retinal nerve fiber layer. *Investigative Ophthalmology & Visual Science*, 46 (12):4588–4593, 2005. doi: 10.1167/iovs.05-0532.

[128] H. Ambronn. Das optische Verhalten markhaltiger und markloser Nervenfasern. *Berichte der königlichen sächsischen Gesellschaft der Wissenschaften zu Leipzig, Mathematisch-physische Classe*, 42:419–429, 1890.

[129] R. S. Bear. The structure of the myelin sheath. Optical studies. *Neurosciences Research Program bulletin*, 9(4):507–510, 1971.

[130] J. Beuthan, O. Minet, J. Helfmann, M. Herrig, and G. Müller. The spatial variation of the refractive index in biological cells. *Physics in Medicine and Biology*, 41(3): 369–382, 1996.

[131] K. M. Hebeda, T. Mensovsky, J. F. Beek, J. G. Wolbers, and M. J. C. van Gemert. Light propagation in the brain depends on nerve fiber orientation. *Neurosurgery*, 35(4):720–724, 1994.

[132] P.-C. Chen, Y.-L. Lo, T.-C. Yu, J.-F. Lin, and T.-T. Yang. Measurement of linear birefringence and diattenuation properties of optical samples using polarimeter and Stokes parameters. *Optics Express*, 17(18):15860–15884, 2009. doi: 10.1364/OE.17.015860.

[133] M. K. Swami, S. Manhas, P. Buddhiwant, N. Ghosh, A. Uppal, and P. K. Gupta. Polar decomposition of 3×3 Mueller matrix: a tool for quantitative tissue polarimetry. *Optics Express*, 14(20):9324–9337, 2006. doi: 10.1364/OE.14.009324.

[134] S. Jiao and L. V. Wang. Quantification of polarization in biological tissue by optical coherence tomography. *Proceedings of SPIE*, 4617:200–203, 2002. doi: 10.1117/12.472525.

[135] B. Hyle Park, M. C. Pierce, B. Cense, and J. F. de Boer. Jones matrix analysis for a polarization-sensitive optical coherence tomography system using fiber-optic components. *Optics Letters*, 29(21):2512–2514, 2004. doi: 10.1364/OL.29.002512.

[136] M. Todorović, S. Jiao, L. V. Wang, and G. Stoica. Determination of local polarization properties of biological samples in the presence of diattenuation by use of Mueller optical coherence tomography. *Optics Letters*, 29(20):2402–2404, 2004. doi: 10.1364/OL.29.002402.

[137] S. Makita, M. Yamanari, and Y. Yasuno. Generalized Jones matrix optical coherence tomography: performance and local birefringence imaging. *Optics Express*, 18(2):854–876, 2010. doi: 10.1364/OE.18.000854.

[138] L. Martin, G. Le Brun, and B. Le Jeune. Mueller matrix decomposition for biological tissue analysis. *Optics Communications*, 293:4–9, 2013. doi: 10.1016/j.optcom.2012.11.086.

[139] W. Wang, L. G. Lim, S. Srivastava, J. S. Yan, A. Shabbir, and Q. Liu. Roles of linear and circular polarization properties and effect of wavelength choice on differentiation between ex vivo normal and cancerous gastric samples. *Journal of Biomedical Optics*, 19(4):046020, 2014. doi: 10.1117/1.JBO.19.4.046020.

[140] X.-R. Huang and R. W. Knighton. Diattenuation and polarization preservation of retinal nerve fiber layer reflectance. *Applied Optics*, 42(28):5737–5743, 2003. doi: 10.1364/AO.42.005737.

[141] X.-R. Huang and R. W. Knighton. Theoretical model of the polarization properties of the retinal nerve fiber layer in reflection. *Applied Optics*, 42(28):5726–5736, 2003. doi: 10.1364/AO.42.005726.

[142] S.-Y. Lu and R. A. Chipman. Interpretation of Mueller matrices based on polar decomposition. *Journal of the Optical Society of America A*, 13(5):1106–1113, 1996. doi: 10.1364/JOSAA.13.001106.

[143] N. Ghosh, M. F. Wood, and I. A. Vitkin. Mueller matrix decomposition for extraction of individual polarization parameters from complex turbid media exhibiting multiple scattering, optical activity, and linear birefringence. *Journal of Biomedical Optics*, 13(4):044036, 2008. doi: 10.1117/1.2960934.

[144] N. Ghosh, J. Soni, M. F. G. Wood, M. A. Wallenberg, and I. A. Vitkin. Mueller matrix polarimetry for the characterization of complex random medium like biological tissues. *Pramana – Journal of Physics*, 75(6):1071–1086, 2010.

[145] M. R. Hee, D. Huang, E. A. Swanson, and J. G. Fujimoto. Polarization-sensitive low-coherence reflectometer for birefringence characterization and ranging. *Journal of the Optical Society of America B*, 9(6):903–908, 1992. doi: 10.1364/JOSAB.9.000903.

[146] M. Pircher, C. K. Hitzenberger, and U. Schmidt-Erfurth. Polarization sensitive optical coherence tomography in the human eye. *Progress in Retinal and Eye Research*, 30(6):431 – 451, 2011. ISSN 1350-9462. doi: 10.1016/j.preteyeres.2011.06.003.

[147] R. D. Lillie. *Histopathologic Technic and Practical Histochemistry*. Blakiston, 1954. URL `https://books.google.de/books?id=sM5OAAAAMAAJ`.

[148] D. Wagner and D. Schmalstieg. ARToolKitPlus for pose tracking on mobile devices. In *Proceedings of the 12th Computer Vision Winter Workshop*, pages 139–146, 2007.

[149] M. Schober, P. Schlömer, M. Cremer, H. Mohlberg, A.-M. Huynh, N. Schubert, M. E. Kirlangic, K. Amunts, and M. Axer. Reference volume generation for subsequent 3D reconstruction of histological sections. In *Proc. of Bildverarbeitung für die Medizin (BVM), Lübeck, Germany*, pages 143–148, 2015.

[150] I. G. Wood and A. M. Glazer. Ferroelastic phase transition in $BiVO_4$. I. birefringence measurements using the rotating-analyser method. *Journal of Applied Crystallography*, 13:217–223, 1980. doi: 10.1107/S002188988001196X.

[151] A. M. Glazer, J. G. Lewis, and W. Kaminsky. An automatic optical imaging system for birefringent media. *Proceedings of the Royal Society A*, 452:2751–2765, 1996. doi: 10.1098/rspa.1996.0145.

[152] J. Reckfort, H. Wiese, U. Pietrzyk, K. Zilles, K. Amunts, and M. Axer. A multiscale approach for the reconstruction of the fiber architecture of the human brain based on 3D-PLI. *Frontiers in Neuroanatomy*, 9(118):1–11, 2015. doi: 10.3389/fnana.2015.00118.

[153] J. Dammers, M. Axer, D. Grässel, C. Palm, K. Zilles, K. Amunts, and U. Pietrzyk. Signal enhancement in polarized light imaging by means of independent component analysis. *NeuroImage*, 49(2):1241–1248, 2010. doi: 10.1016/j.neuroimage.2009.08.059.

[154] J. Dammers, L. Breuer, M. Axer, M. Kleiner, B. Eiben, D. Grässel, T. Dickscheid, K. Zilles, K. Amunts, N. J. Shah, and U. Pietrzyk. Automatic identification of gray and white matter components in polarized light imaging. *NeuroImage*, 59(2): 1338–1347, 2012. doi: 10.1016/j.neuroimage.2011.08.030.

[155] A. Lührs, O Bücker, and M. Axer. Towards large-scale fiber orientation models of the brain – automation and parallelization of a seeded region growing segmentation of high-resolution brain section images. In K. Amunts, L. Grandinetti, T. Lippert, and N. Petkov, editors, *Brain-Inspired Computing. BrainComp 2015. Lecture Notes in Computer Science*, volume 10087, pages 28–42, Cham, 2016. Springer International Publishing. doi: 10.1007/978-3-319-50862-7_3.

[156] S. Klein, M. Staring, K. Murphy, M. A. Viergever, and J. P. W. Pluim. elastix: A toolbox for intensity-based medical image registration. *IEEE Transactions on Medical Imaging*, 29(1):196–205, 2010. doi: 10.1109/TMI.2009.2035616.

[157] D. P. Shamonin, E. E. Bron, B. P. F. Lelieveldt, M. Smits, S. Klein, and M. Staring. Fast parallel image registration on CPU and GPU for diagnostic classification of Alzheimer's disease. *Frontiers in Neuroinformatics*, 7:50, 2013. doi: 10.3389/fninf.2013.00050.

[158] B. B. Avants, C. L. Epstein, M. Grossman, and J. C. Gee. Symmetric diffeomorphic image registration with cross-correlation: Evaluating automated labeling of elderly

and neurodegenerative brain. *Medical Image Analysis*, 12(1):26–41, 2008. doi: 10.1016/j.media.2007.06.004.

[159] B. B. Avants, N. J. Tustison, G. Song, P. A. Cook, A. Klein, and J. C. Gee. A reproducible evaluation of ANTs similarity metric performance in brain image registration. *NeuroImage*, 54(3):2033–2044, 2011. doi: 10.1016/j.neuroimage.2010.09.025.

[160] National library of medicine insight segmentation and registration toolkit (ITK), `https://itk.org/`.

[161] D. Schmitz, K. Amunts, T. Lippert, and M. Axer. A least squares approach for the reconstruction of nerve fiber orientations from tiltable specimen experiments in 3D-PLI. In *2018 IEEE 15th International Symposium on Biomedical Imaging (ISBI 2018)*, pages 132–135, Washington, DC, USA, 2018. doi: 10.1109/ISBI.2018.8363539.

[162] L. A. Pajdzik and A. M. Glazer. Three-dimensional birefringence imaging with a microscope tilting-stage. I. Uniaxial crystals. *Journal of Applied Crystallography*, 39:326–337, 2006. doi: 10.1107/S002188980604009X.

[163] M. Dohmen. *Towards the Reconstruction of Fiber Tracts in the Human Brain by Means of 3D Polarized Light Imaging*. PhD thesis, University of Wuppertal, 2013.

[164] N. Schubert, M. Axer, U. Pietrzyk, and K. Amunts. 3D Polarized Light Imaging portrayed: Visualization of fiber architecture derived from 3D-PLI. In A. M. Halefoğlu, editor, *High-Resolution Neuroimaging – Basic Physical Principles and Clinical Applications*, chapter 03. InTech, Rijeka, 2018. doi: 10.5772/intechopen.72532.

[165] H. Axer, S. Beck, M. Axer, F. Schuchardt, J. Heepe, A. Flücken, M. Axer, A. Prescher, and O. W. Witte. Microstructural analysis of human white matter architecture using polarized light imaging: views from neuroanatomy. *Frontiers in Neuroinformatics*, 5(28):1–12, 2011. doi: 10.3389/fninf.2011.00028.

[166] P. T. So. Two-photon Fluorescence Light Microscopy. *Encyclopedia of Life Sciences*, 2011. doi: 10.1038/npg.els.0002991.

[167] I. Costantini, L. Silvestri, G. Mazzamuto, E. Baria, E. Lazzeri, R. Cicchi, L. Sacconi, M. Axer, M. Menzel, K. Amunts, and F. S. Pavone. Myelin autofluorescence imaging by glycerol induced contrast enhancement. *(in preparation)*.

[168] A. Bria and G. Iannello. TeraStitcher - a tool for fast automatic 3D-stitching of teravoxel-sized microscopy images. *BMC Bioinformatics*, 13(1):316, 2012. ISSN 1471-2105. doi: 10.1186/1471-2105-13-316.

[169] A. R. Khan, A. Cornea, L. A. Leigland, S. G. Kohama, S. N. Jespersen, and C. D. Kroenke. 3D structure tensor analysis of light microscopy data for validating diffusion MRI. *Neuroimage*, 111:192–203, 2015. doi: 10.1016/j.neuroimage.2015.01.061.

[170] H. De Raedt. Advances in unconditionally stable techniques. In A. Taflove and S. C. Hagness, editors, *Computational Electrodynamics: The Finite-Difference Time-Domain Method*, chapter 18. Artech House, MA USA, 3 edition, 2005.

[171] H. De Raedt, K. Michielsen, J. S. Kole, and M. T. Figge. Solving the Maxwell equations by the Chebyshev method: A one-step finite-difference time-domain algorithm. *IEEE Transactions on Antennas and Propagation*, 51:3155–3160, 2003. doi: 10.1109/TAP.2003.818809.

[172] H. De Raedt and K. Michielsen. Unconditionally stable perfectly matched layer boundary conditions. *Physica Status Solidi (b)*, 244(10):3497–3505, 2007. doi: 10.1002/pssb.200743148.

[173] S. Kole. *New Methods for the Numerical Solution of Maxwell's Equations*. PhD thesis, University of Groningen, 2003.

[174] C. Shen. *Wave Propagation through Photonic Crystal Slabs: Imaging and Localization*. PhD thesis, University of Groningen, 2006.

[175] B. D. Wilts. *Brilliant biophotonics: physical properties, pigmentary tuning & biological implications (Chapter 3)*. PhD thesis, University of Groningen, 2015.

[176] K. S. Yee. Numerical solution of initial boundary value problems involving Maxwell's equations in isotropic media. *IEEE Transactions on Antennas and Propagation*, 14:302–307, 1966. doi: 10.1109/TAP.1966.1138693.

[177] M. Suzuki. Generalized Trotter's formula and systematic approximants of exponential operators and inner derivations with applications to many-body problems. *Communications in Mathematical Physics*, 51(2):183–190, 1976. URL `http://projecteuclid.org/euclid.cmp/1103900351`.

[178] K. Michielsen, H. De Raedt, and D. G. Stavenga. Reflectivity of the gyroid biophotonic crystals in the ventral wing scales of the Green Hairstreak butterfly, *Callophrys rubi*. *Journal of the Royal Society Interface*, 7:765–771, 2010. doi: 10.1098/rsif.2009.0352.

[179] B. D. Wilts, K. Michielsen, H. De Raedt, and D. G. Stavenga. Sparkling feather reflections of a bird-of-paradise explained by finite-difference time-domain modeling. *Proceedings of the National Academy of Sciences*, 111(12):4363–4368, 2014. doi: 10.1073/pnas.1323611111.

[180] L. Chapelle, M. Lévesque, P. Brøndsted, M. R. Foldschack, and Y. Kusano. Generation of non-overlapping fiber architecture. In *Proceedings of the 20th International Conference on Composite Materials ICCM20 Secretariat*, 2015.

[181] H. Altendorf and D. Jeulin. Random walk based stochastic modeling of 3D fiber systems. *Physical Review E : Statistical, Nonlinear, and Soft Matter Physics, American Physical Society*, 83(4), 2010. doi: 10.1103/PhysRevE.83.041804.

[182] K. Zilles. *The Cortex of the Rat – A Stereotaxic Atlas*. Springer, Berlin Heidelberg, 1985. doi: 10.1007/978-3-642-70573-1.

[183] G. Paxinos and C. Watson. *The Rat Brain in Stereotaxic Coordinates*. Academic Press, 6 edition, 2007.

[184] E. A. Papp, T. B. Leergard, E. Calabrese, G. A. Johnson, and J. G. Bjaalie. Waxholm Space atlas of the Sprague Dawley rat brain. *NeuroImage*, 97:374–386, 2014. doi: 10.1016/j.neuroimage.2014.04.001.

[185] R. P. Woods, S. C. Fears, M. J. Jorgensen, L. A. Fairbanks, A. W. Toga, and N. B. Freimer. A web-based brain atlas of the vervet monkey, chlorocebus aethiops. *NeuroImage*, 54(3):1872–1880, 2011. doi: 10.1016/j.neuroimage.2010.09.070.

[186] `http://www.loni.usc.edu/Research/Atlases/Data/vervet/vervetatlas/vervetatlas.html`. University of Southern California, Laboratory of Neuro Imaging. January 2018.

[187] T. E. Oliphant. Python for scientific computing. *Computing in Science & Engineering*, 9:10–20, 2007. doi: 10.1109/MCSE.2007.58.

[188] S. van der Walt, S. C. Colbert, and G. Varoquaux. The NumPy array: A structure for efficient numerical computation. *Computing in Science & Engineering*, 13:22–30, 2011. doi: 10.1109/MCSE.2011.37.

[189] J. W. Cooley and J. W. Tukey. An algorithm for the machine calculation of complex Fourier series. *Mathematics of Computation*, 19(90):297–301, 1965.

[190] M. Rubin. Optical properties of soda lime silica glasses. *Solar Energy Materials*, 12(4):275–288, 1985. ISSN 0165-1633. doi: 10.1016/0165-1633(85)90052-8.

[191] A. D. Rakić, A. B. Djurišić, J. M. Elazar, and M. L. Majewski. Optical properties of metallic films for vertical-cavity optoelectronic devices. *Applied Optics*, 37(22): 5271–5283, 1998. doi: 10.1364/AO.37.005271.

[192] F. Xie, P. Liang, H. Fu, J.-C. Zhang, and J. Chen. Effects of normal aging on myelin sheath ultrastructures in the somatic sensorimotor system of rats. *Molecular Medicine Reports*, 10:459–466, 2014. doi: 10.3892/mmr.2014.2228.

[193] R. Storn and K. Price. Differential evolution – a simple and efficient heuristic for global optimization over continuous spaces. *Journal of Global Optimization*, 11: 341–359, 1997. doi: 10.1023/A:1008202821328.

[194] M. Abramowitz and I. A. Stegun. *Handbook of Mathematical Functions with Formulas, Graphs, and Mathematical Tables*. United States Department of Commerce, National Bureau of Standards, 1964.

List of Publications

In the following, the publications that have been produced within the scope of this doctoral thesis are listed in chronological order. Apart from a brief summary, the author's contributions are specified and the places where parts of the publications have been used in this thesis. The author's contributions were adapted from the respective publications, where available.

[52] Understanding Fiber Mixture by Simulation in 3D Polarized Light Imaging: M. Dohmen, **M. Menzel**, H. Wiese, J. Reckfort, F. Hanke, U. Pietrzyk, K. Zilles, K. Amunts, and M. Axer. *NeuroImage*, 111:464–475, 2015.

- The paper introduces the simulation method simPLI which computes synthetic 3D-PLI image series by representing each tissue voxel by the Jones matrix of a wave retarder.
- M. M. wrote the majority of the manuscript with contributions from M. D. and M. A. (The study was performed by M. D. and others.)
- The measurements of the optic chiasm of a hooded seal (Figs. 1 and 5B) were used in this thesis to study the transmittance of horizontal crossing fibers in Fig. 13.2.

[51] A Jones matrix formalism for simulating three-dimensional polarized light imaging of brain tissue: **M. Menzel**, K. Michielsen, H. De Raedt, J. Reckfort, K. Amunts, and M. Axer. *Journal of the Royal Society Interface*, 12:20150734, 2015.

- The paper uses the Jones matrix formalism to model the birefringent myelin sheaths and to demonstrate that the nerve fiber orientations in 3D-PLI can be estimated assuming that the optic axis is oriented along the fibers.
- M. M. substantially contributed to the conception and design of the study as well as to the acquisition, analysis and interpretation of the simulated data, carried out the simulations and analytical calculations, created the figures, and wrote the manuscript. (K. M. participated in the design of the study, contributed to theoretical considerations and to the interpretation of the simulated data, and helped draft the manuscript. H. D. R. contributed to the interpretation of the simulated data, to the theoretical considerations and to the revision of the manuscript. J. R. conducted experimental measurements, helped transfer the measurement results to the simulation and revised the manuscript. K. A. contributed to the anatomical content of the study and to the revision of the manuscript. M. A. coordinated the study, participated in the conception and design, contributed to the analysis and interpretation of the simulated data, and helped draft the manuscript.)
- The derivation of the phase shift (Appx. A) was used in this thesis in Appx. A.4.1. The result that the optic axis is oriented along the nerve fiber direction was used in Secs. 3.2.3 and 3.2.4 to model the birefringence and diattenuation of brain tissue.

[66] Finite-Difference Time-Domain Simulation for Three-Dimensional Polarized Light Imaging: **M. Menzel**, M. Axer, H. De Raedt, and K. Michielsen. In K. Amunts, L. Grandinetti, T. Lippert, and N. Petkov, editors, *Brain-Inspired Computing. BrainComp 2015. Lecture Notes in Computer Science*, volume 10087, chapter 6, pages 73–85. Springer International Publishing, Cham, 2016.

- The book chapter introduces a 3D Maxwell Solver that is based on a Finite-Difference Time-Domain algorithm and can be used to model the light propagation through brain tissue in 3D-PLI measurements.
- M. M. substantially contributed to the study, carried out the simulations and analytical calculations, created the figures, and wrote the manuscript. (H. D. R. and K. M. developed the Maxwell Solver algorithm and contributed to the analytical considerations. M. A., H. D. R., and K. M. contributed to the interpretation of the results and to the revision of the manuscript.)
- The description of the FDTD algorithm and the TDME3D software (Sec. 4.1) were used in Chap. 6. Some figures (Figs. 3b and 5) were reused in this thesis in Figs. 6.1 and D.2. The simulation of the polarimetric setup (Sec. 4.1) was used in Sec. 10.1.2 to describe the computation of the transmitted light intensities from FDTD simulations.

[56] Polarized Light Imaging and Two-Photon Fluorescence Microscopy correlative approach for 3D reconstruction of the orientation of myelinated fibers: I. Costantini, **M. Menzel**, L. Silvestri, N. Schubert, M. Axer, K. Amunts, and F. S. Pavone. *Optics in the Life Sciences Congress, OSA Technical Digest (online), paper BrW4B.5*, 2017.

- The conference proceeding introduces the combined measurement of 3D-PLI and Two-Photon Fluorescence Microscopy (TPFM) on the same brain section: myelinated axons are made autofluorescent so that they can be measured with TPFM.
- M. M. assisted in evaluating the data and helped draft the manuscript. (I. C. and others conducted the measurements, developed the technique, and wrote the manuscript.)
- The TPFM technique was introduced in Chap. 5. The combined measurement of 3D-PLI and TPFM was used in Sec. 8.3 to determine the nerve fiber inclinations in a brain section measured with 3D-PLI in order to study transmittance vs. inclination.

[3] Diattenuation of brain tissue and its impact on 3D polarized light imaging: **M. Menzel**, J. Reckfort, D. Weigand, H. Köse, K. Amunts, and M. Axer. *Biomedical Optics Express*, 8(7):3163–3197, 2017.

- The paper introduces Diattenuation Imaging which enables to measure the diattenuation of brain tissue even with a low signal-to-noise ratio. Numerical and experimental studies show that there exist two types of diattenuation (D^+ and D^-).
- M. M. contributed to the conception and design of the study, provided the theoretical background, carried out the analytical calculations and the numerical study, computed the polarization-independent inhomogeneities and polarization properties of the optical system, performed the calibration of the XP measurement, participated in the evaluation and interpretation of the experimental data, and wrote the majority of the manuscript. (J. R. contributed to the conception and design of the study, conducted the experimental measurements and the calibration of the 3D-PLI and DI measurements, performed the quality assurance of the experimental data,

participated in the characterization of the optical system, carried out the analysis and evaluation of the experimental results, and wrote the experimental parts of the manuscript. D. W. contributed to the characterization of the optical system, provided the optimization algorithm for fitting the polarization properties, and revised the manuscript. H. K. developed the measurement protocol for the DI measurement and performed the tissue measurements and part of the filter measurements. K. A. contributed to the anatomical content and the interpretation of results, and helped draft the manuscript. M. A. oversees the study, participated in the conception and design, contributed to the interpretation of the numerical and experimental results, and helped draft the manuscript.)

- The theoretical background (Sec. 2) was used in this thesis in Secs. 2.4 and 2.5.2, the measurement setups and signal analysis (Sec. 3) were used in Sec. 4.4, the results of the numerical and experimental studies (Secs. 4–6, Appx. B and D) were used in Chap. 9 (Secs. 9.1, 9.2 and 9.4 and Appx. C.1 to C.3), and the characterization of the optical system (Appx. A) was used in Sec. 7.2 and Appx. B.3.

[67] Transmittance assisted interpretation of 3D nerve fibre architectures: **M. Menzel**, M. Axer, H. De Raedt, I. Costantini, L. Silvestri, F. S. Pavone, K. Amunts, and K. Michielsen. *arXiv:1806.07157v2*, 2018.

- The paper shows in experimental and FDTD simulation studies that the transmittance of brain sections decreases with increasing nerve fiber inclination and can be used to distinguish between horizontal crossing and vertical fibers.
- M. M. substantially contributed to the conception and design of the study as well as to the analysis and interpretation of the experimental and simulated data and to the theoretical considerations, analyzed the measurements, carried out the simulations, created the figures, and wrote the manuscript. (M. A. participated in the conception and design of the study, contributed to the analysis and interpretation of the data, and to the revision of the manuscript. H. D. R. contributed to the interpretation of the simulated data, to the theoretical considerations, and to the revision of the manuscript. I. C., L. S., and F. S. P. produced the TPFM measurements. K. A. contributed to the anatomical content of the study. K. M. participated in the design of the study, contributed to the interpretation of the simulated data, to the theoretical considerations, and to the revision of the manuscript. The polarimetric measurements were performed in the laboratory of INM-1 at Forschungszentrum Jülich.)
- The experimental and simulation results were shown in Chaps. 8, 11, 13 and 14 in this thesis, the methods and supplementaries were partly used in Sec. 5.2, Chap. 10, and Appx. D.11

[68] Diattenuation Imaging reveals different brain tissue properties: **M. Menzel**, M. Axer, K. Amunts, H. De Raedt, and K. Michielsen. *arXiv:1806.07712v3*, 2018.

- The paper shows that the diattenuation of brain sections depends on nerve fiber inclination and time after tissue embedding (diattenuation of type D^- decreases) and explains this behavior by FDTD simulations.
- M. M. substantially contributed to the conception and design of the study as well as to the analysis and interpretation of the experimental and simulated data and to the theoretical considerations, analyzed the measurements, carried out the simulations,

created the figures, and wrote the manuscript. (M. A. participated in the conception and design of the study, contributed to the analysis and interpretation of the data, and to the revision of the manuscript. K. A. contributed to the anatomical content of the study. H. D. R. contributed to the interpretation of the simulated data, to the theoretical considerations, and to the revision of the manuscript. K. M. participated in the design of the study, contributed to the interpretation of the simulated data, to the theoretical considerations, and to the revision of the manuscript. The measurements were performed in the laboratory of INM-1 at Forschungszentrum Jülich.)

- The experimental and simulation results were shown in this thesis in Chaps. 9 and 12 to 14. The analytical model of dichroism (Note 1) was used in Appx. A.4.2 and A.4.3.

List of Figures

List of Tables

List of Acronyms

3D-PLI	Three-Dimensional Polarized Light Imaging
ac	anterior commissure
aci	anterior commissure intrabulbar part
ARDM	absolute relative difference of means
a. u.	arbitrary units
CAB	cellulose acetate butyrate
Cb	cerebellum
cc	corpus callosum
CCD	charge-coupled device
Cd	caudate nucleus
cg	cingulum
CNS	central nervous system
CPu	caudate putamen
cu	cuneate fasciculus
df	dorsal fornix
DI	Diattenuation Imaging
dMRI	diffusion magnetic resonance imaging
DMSO	dimethyl sulfoxide
DTI	diffusion tensor imaging
EMBD	European Marketing and Business Development
EP	elliptical polarization
f	fornix
FDTD	Finite-Difference Time-Domain
FFT	Fast Fourier Transform
FGA	Fiber Growing Algorithm
fi	fimbria
FOM	fiber orientation map
FWHM	full width at half maximum
FZJ	Forschungszentrum Jülich GmbH
GB	gigabyte
GM	gray matter
HBP	Human Brain Project
Hi	hippocampus
HLP	horizontal linear polarization
HSV	color coding scheme (hue $= 2\varphi$, saturation $= 1$, value $= 1 - \alpha/90°$)
ICA	Independent Component Analysis
INM	Institute of Neuroscience and Medicine
LAP	Large-Area Polarimeter
LCP	left-handed circular polarization
LED	light emitting diode
LENS	European Laboratory for Non-Linear Spectroscopy
lo	lateral olfactory tract
lp	line pair

LP linear polarization

MB megabyte

MBP myelin basic protein

MPI Message Passing Interface

NA numerical aperture

OCT Optical Coherence Tomography

opt optic tract

PBC periodic boundary condition

PBS phosphate-buffered saline

PLI Polarized Light Imaging

PLP proteolipid protein

PM Polarizing Microscope

PMMA polymethyl methacrylate

PMT photomultiplier tube

px pixel

RCP right-handed circular polarization

RGB color coding scheme (red = x, green = y, blue = z)

RMAD relative mean absolute difference

RNFL retinal nerve fiber layer

RWTH Rheinisch-Westfälisch Technische Hochschule

SI International System of Units

sm stria medularis

Th thalamus

TPFM Two-Photon Fluorescence Microscopy

UPML uniaxial perfectly matched layer

USAF United States Air Force (resolution test chart)

VCS Volume Colliding Solver

VLP vertical linear polarization

WM white matter

XP crossed polars

List of Symbols

Latin-based symbols (lower case)

a_m	Fourier coefficient associated with cosine functions
$a_{0,\mathrm{N}}$	$\propto I_{\mathrm{T,N}}$ (used to compute simulated transmittance image)
b_m	Fourier coefficient associated with sine functions
c	velocity of light (in vacuum)
d	sample/section thickness;
Δd	distance between two points
f	focal length of a lens
i, j	$i \in \{1, 2, 3\}$, $j \in \{x, y, z\}$
(i, j, k)	coordinates of discrete point in space
$\vec{k}$	wave vector
k	wave number ($\lvert\vec{k}\rvert = 2\pi/\lambda$)
k'	complex wave number
k_{xy}	$= \sqrt{k_{\mathrm{x}}^2 + k_{\mathrm{y}}^2}$
l	line width in USAF chart
m	proportionality factor between retardation and dichroism; index
$\vec{n}$	surface normal vector
n	refractive index (real part)
n'	complex refractive index $(n + i\kappa)$
n_{ax}	axon refractive index (1.35)
$n_{\mathrm{e}}(\theta)$	extraordinary refractive index, depending on the angle $\theta \sphericalangle (\vec{k}$, optic axis)
n_{E}	principal extraordinary refractive index $\left(n_{\mathrm{e}}(\theta = 90°)\right)$
n_{g}	glycerin refractive index (1.37)
n_{m}	myelin refractive index (1.47)
n_{o}	ordinary refractive index
Δn	birefringence $(n_{\mathrm{E}} - n_{\mathrm{o}})$
$\Delta n(\theta)$	$= n_{\mathrm{e}}(\theta) - n_{\mathrm{o}} \approx \Delta n \sin^2\theta$
p	degree of polarization; $= \sin\theta_k - \sin\theta$
$\vec{r}$	point in space
r	radial coordinate; (fiber) radius
r_0	radius of detector microlens
r_{ax}	axon radius
r_{P}	retardation ($\lvert\sin\delta_{\mathrm{P}}\rvert$)
$\vec{s}$	unit wave vector ($\vec{k}/\lvert\vec{k}\rvert$)
s	helix stride
t	time
t_{g}	glycerin layer thickness
t_{m}	myelin layer thickness
t_{sheath}	myelin sheath thickness
Δt	time step
u	arbitrary function
v	phase velocity in medium (c/n)
$v_{\mathrm{e}}(\theta)$	phase velocity of extraordinary wave, depending on the angle $\theta \sphericalangle (\vec{k}$, optic axis)
v_{E}	principal phase velocity of extraordinary wave $\left(v_{\mathrm{e}}(\theta = 90°)\right)$
v_{o}	phase velocity of ordinary wave
w	weighting of diffuse light
x, y, z	coordinate in x,y,z-direction
Δx	pixel size
$\Delta x, y, z$	spatial discretization in x, y, z

Latin-based symbols (upper case)

$\vec{A}_k$	wave vector component describing cosine term ($\vec{E}_{0,k}\cos\phi$)
$\vec{B}$	magnetic flux density
$\vec{B}_k$	wave vector component describing sine term ($\vec{E}_{0,k}\sin\phi$)
C	Courant factor ($c\sqrt{3}\Delta t/\Delta$)
$\mathcal{C}$	image contrast $= (I_{\max} - I_{\min})/(I_{\max} + I_{\min})$
$\vec{D}$	electric flux density
D	diattenuation of brain tissue
$\lvert D\rvert$	strength of the diattenuation
$\lvert\mathscr{D}\rvert$	measured diattenuation
D^+	diattenuation with $\varphi_{\mathrm{D}} \approx \varphi_{\mathrm{P}}$
D^-	diattenuation with $\varphi_{\mathrm{D}} \approx \varphi_{\mathrm{P}} + 90°$
D_{D}	amplitude of diattenuation signal
D_{K}	diattenuation caused by anisotropic absorption (dichroism)
D_{S}	approx. amplitude and phase of sim. diattenuation signal $= (I_{\mathrm{x}} - I_{\mathrm{y}})/(I_{\mathrm{x}} + I_{\mathrm{y}})$
$D_{\mathcal{S}}$	diattenuation caused by anisotropic scattering
$\lvert\mathscr{D}_{\mathrm{S}}\rvert$	strength of the simulated diattenuation signal
D_{x}	diattenuation of polarizer
D_{y}	diattenuation of analyzer
$\vec{E}$	electric field
E	element number in USAF chart
$\vec{E}_0$	direction and amplitude of the electric field vector
E_{p}, E_{s}	electric field amplitude for p- or s-polarized light
F	focal ratio (f/D)
$\mathcal{F}$	Fourier transform
G	group number in USAF chart
$\vec{H}$	magnetic field
I	intensity of light
$I_{\lvert\rvert}$	transmitted intensity of extraordinary wave
$I_{\perp}$	transmitted intensity of ordinary wave
I_0	intensity of the incident light
$I_{\mathrm{D}}(\rho)$	intensity profile from DI
I_{N}	normalized transmitted intensity
$I_{\mathrm{P}}(\rho)$	intensity profile from 3D-PLI
$I_{\mathrm{T,P}}$	polarization-independent transmitted light intensity ("transmittance")
$I_{\mathrm{T,N}}$	normalized transmittance
I_{x}, I_{y}	transmitted intensity for light polarized in the x- or y-direction
$I_{\mathrm{X}}(\rho)$	intensity profile from XP meas.
$\vec{J}$	electric current density; Jones vector (2.46)
J	Jones matrix
$J_n(x)$	Bessel function of the first kind of order n
$\vec{J}_{\mathrm{source}}$	electric current density acting as independent source of the electric field energy
K	absorption coefficient ($4\pi\kappa/\lambda$)
$K_{\mathrm{e}}(\theta)$	absorption coefficient of extraordinary wave, depending on the angle $\theta \sphericalangle (\vec{k}$, optic axis)
K_{E}	principal absorption coefficient of extraordinary wave
K_{o}	absorption coefficient of ordinary wave
ΔK	$= K_{\mathrm{E}} - K_{\mathrm{o}}$
$\Delta K(\theta)$	$= K_{\mathrm{e}}(\theta) - K_{\mathrm{o}} \approx \Delta K \sin^2\theta$
$\mathcal{L}$	matrix (6.9) representing Maxwell's equations

L	number of myelin layers
L_c	coherence length
ΔL	distance between sample and camera lens / detector
$\vec{M}$	magnetic current density
M	Müller matrix representing a section of brain tissue
$\mathcal{M}$	Müller matrix (2.56)
M_ret	Jones matrix of retarder (2.50)
$\vec{M}_\mathrm{source}$	magnetic current density acting as independent source of the magnetic field energy
N	number of fibers / slits
$N_\mathrm{x,y}$	number of grid points
P_x	Jones/Müller matrix of linear horizontal polarizer
P_y	Jones/Müller matrix of linear vertical polarizer
R_p, R_s	reflection amplitude for p- or s-polarized light
$R(\xi)$	Jones (2.52) or Müller (2.57) matrix describing counter-clockwise rotation by ξ
$\vec{S}$	Stokes vector (2.53)
$\mathcal{S}$	scattering coefficient
$\vec{S}_\mathrm{c}$	Stokes vector of camera
$\vec{S}_\mathrm{E}$	Poynting vector ($\vec{E} \times \vec{H}$)
$\vec{S}_\mathrm{L}$	Stokes vector of light source
$\vec{S}_\mathrm{unpol}$	Stokes vector of unpolarized light
T_p, T_s	transmission amplitude for p- or s-polarized light
U	complex wave amplitude
$\mathcal{U}(t)$	time evolution operator ($\mathrm{e}^{t\mathcal{L}}$)
$\mathcal{V}$	fiber volume fraction
W	diameter of the entrance pupil; object size

Greek-based symbols (lower and upper case)

α	out-of-plane inclination angle
α_P	fiber inclination angle obtained from 3D-PLI
$\tilde{\alpha}_\mathrm{P}$	modified inclination angle (4.20)
γ	retardance of quarter-wave retarder ($\approx \pi/2$)
δ	retardance ($\frac{2\pi}{\lambda} d\Delta n(\theta)$), of brain tissue
δ_K	dichroism ($\frac{2\pi}{\lambda} d\Delta\kappa(\theta)$)
δ_P	phase retardation obtained from 3D-PLI measurement
Δ	voxel/mesh size
ϵ	electric permittivity
ϵ_0	permittivity of free space
ϵ_r	relative permittivity
$\tilde{\epsilon}_\mathrm{r}$	relative permittivity tensor
η	number of angles of incidence
$\eta \mathbin{\ast} \Delta\varphi$	diffuse light with $\{\theta = 0°\}$, $\{\theta = 3°, \varphi = \eta \times \Delta\varphi\}$, cf. Eq. (10.2)
θ	polar angle (of incidence); angle between wave vector $\vec{k}$ and optic axis
θ_c	critical angle of total internal reflection
θ_i	angle of incidence
θ_k	angle of incidence for certain wave vector $\vec{k}$
θ_max	max. angle of incidence
θ_r	angle of reflection
θ_t	angle of refraction

Δ_θ	polar angular distance
κ	imaginary part of the refractive index
$\hat{\kappa}$	$= \kappa/n$
$\kappa_\mathrm{e}(\theta)$	imaginary part of the extraordinary refractive index, depending on the angle $\theta \sphericalangle (\vec{k}$, optic axis)
κ_E	imaginary part of the principal extraordinary refractive index
κ_o	imaginary part of the ordinary refractive index
$\Delta\kappa$	$= \kappa_\mathrm{E} - \kappa_\mathrm{o}$
$\Delta\kappa(\theta)$	$= \kappa_\mathrm{e}(\theta) - \kappa_\mathrm{o} \approx \Delta\kappa \sin^2\theta$
λ	wavelength (in vacuum)
$\hat{\lambda}$	peak wavelength (in vacuum)
λ_m	wavelength in a medium
$\Delta\lambda$	spectral width of wavelengths
$\mathit{\Lambda}$	Müller matrix of wave retarder
μ	magnetic permeability; mean of Gaussian distribution
μ_0	permeability of free space
μ_att	attenuation coefficient $(K + \mathcal{S})$
μ_max	max. attenuation coefficient
μ_min	min. attenuation coefficient
μ_r	relative permeability
ξ	rotation angle in counterclockwise direction
$\mathit{\Xi}$	maximum displacement of initial coordinates in the VCS
ρ	rotation angle of filters in the polarimetric measurements
ρ_e	electric charge density
ρ_m	magnetic charge density
σ	standard deviation; mode value of Rayleigh distribution
σ_e	electric conductivity
σ_m	equivalent magnetic loss
$\mathit{\Delta}_\Sigma$	sum of squared differences (B.2)
τ	average transmittance
τ_Λ	average transmittance of retarder
τ_x	average transmittance of polarizer
τ_y	average transmittance of analyzer
ϕ	phase
$\Delta\phi$	phase difference
φ	azimuthal angle (of incidence); in-plane fiber direction angle
φ_D	direction angle of maximum transmittance; direction angle obtained from DI meas.
$\varphi_\mathrm{D,S}$	direction angle obtained from simulated DI signal
φ_P	direction angle obtained from 3D-PLI measurement
φ_X	direction angle obtained from XP measurement
Δ_φ	azimuthal angular distance
χ	crossing angle of fiber bundles; spherical angle of Stokes vector
ψ	spherical angle of Stokes vector
$\mathit{\Psi}(t)$	state of electromagnetic field (6.9)
ω	angular frequency $(2\pi v/\lambda_\mathrm{m})$

APPENDICES

Appendix A

Supplementary Material for Polarization Optics

This chapter provides supplementary derivations and analytical considerations for the theoretical background on polarization optics presented in Chap. 2.

A.1 Derivation of the Wave Equation

The following derivation can be found in [69] (Sec. 1.2) and [70] (Sec. 7.1).

For a homogeneous medium with no free charges or currents, it follows from Maxwell's equations (with $\rho_\mathrm{e} = \rho_\mathrm{m} = 0$ and $\vec{J} = \vec{M} = 0$):

$$\vec{\nabla} \times (\vec{\nabla} \times \vec{E}) \overset{(2.1),(2.6)}{=} -\mu \frac{\partial}{\partial t}(\vec{\nabla} \times \vec{H}) \overset{(2.2),(2.5)}{=} -\epsilon\mu \frac{\partial^2}{\partial t^2}\vec{E} \overset{(2.10)}{=} -\frac{1}{v^2}\frac{\partial^2}{\partial t^2}\vec{E}. \tag{A.1}$$

Using $\vec{\nabla} \cdot \vec{E} = 0$ and the vector identity $\vec{\nabla} \times (\vec{\nabla} \times \vec{E}) = \vec{\nabla}(\vec{\nabla} \cdot \vec{E}) - \nabla^2\vec{E}$ yields:

$$\vec{\nabla} \times (\vec{\nabla} \times \vec{E}) = -\nabla^2\vec{E} \overset{(A.1)}{=} -\frac{1}{v^2}\frac{\partial^2}{\partial t^2}\vec{E}. \tag{A.2}$$

A similar equation can be derived for the magnetic field vector, starting from $\vec{\nabla}\times(\vec{\nabla}\times\vec{H})$. Thus, the electric and magnetic field vectors obey the wave equation (2.9) of the form:

$$\nabla^2 u = \frac{1}{v^2}\frac{\partial^2 u}{\partial t^2}. \tag{A.3}$$

A.2 Plane Waves in Homogeneous Materials

The explanations follow Born·Wolf [69] (Sec. 1.4.1).

Plane waves are functions of the variable $u = \vec{s} \cdot \vec{r} - vt$, where $\vec{s} \equiv \vec{k}/k$ is the unit vector in the direction of phase propagation and v the phase velocity of the wave. When the electromagnetic wave is a plane wave (cf. Eq. (2.13)) and propagates through a homogeneous medium with $\vec{J} = \vec{M} = 0$, it follows from Maxwell's equations (2.1) and (2.2) and material equation (2.6):

$$\vec{\nabla} \times \vec{E} = -\mu \frac{\partial \vec{H}}{\partial t} \quad \Leftrightarrow \quad \vec{s} \times \vec{E}' = +\mu v \vec{H}', \tag{A.4}$$

$$\vec{\nabla} \times \vec{H} = \frac{\partial \vec{D}}{\partial t} \quad \Leftrightarrow \quad \vec{s} \times \vec{H}' = -v\vec{D}', \tag{A.5}$$

where the prime denotes differentiation with respect to the variable u.

Integrating with respect to u, neglecting the additive constants of integration (i. e. a field constant in space), and writing $\vec{s} = \vec{k}/k = \vec{k}\,v/\omega$ yields:

$$\overset{(A.5)}{\Rightarrow} \vec{D} = -\frac{1}{\omega}\,\vec{k} \times \vec{H}, \tag{A.6}$$

$$\overset{(A.4)}{\Rightarrow} \vec{H} = \frac{1}{\omega\mu}\,\vec{k} \times \vec{E}. \tag{A.7}$$

Thus, the electric flux density $\vec{D}$ and the magnetic field $\vec{H}$ are oriented perpendicularly to the wave vector $\vec{k}$. In isotropic media (with $\vec{D} \propto \vec{E}$), the electric field $\vec{E}$, the magnetic field $\vec{H}$, and the wave vector $\vec{k}$ form a right-handed orthogonal triad of vectors, as described in Sec. 2.1.3.

A.3 Derivation of the Refractive Index Ellipsoid for Uniaxial Materials

Appendix A.3.1 derives the equations of the refractive index ellipsoid from Sec. 2.3.1 for non-absorbing uniaxial birefringent materials. The case of absorbing uniaxial birefringent (dichroic) materials is considered in Appx. A.3.2.

A.3.1 Uniaxial Non-Absorbing Materials

The explanations follow Born·Wolf [69] (pp. 793, 796, 806) and Pajdzik·Glazer [162] (Sec. A.1).

The electric flux density for a plane monochromatic wave can be written as (see Appx. A.2):

$$\vec{D} \overset{(A.6)}{=} -\frac{1}{\omega}(\vec{k} \times \vec{H}) \overset{(A.7)}{=} -\frac{1}{\mu\,\omega^2}\Big(\vec{k} \times (\vec{k} \times \vec{E})\Big) = \frac{n^2}{\mu\,c^2}\Big(\vec{E} - \vec{s}\,(\vec{s} \cdot \vec{E})\Big), \tag{A.8}$$

defining $\vec{k} \equiv k\vec{s} = \frac{\omega n}{c}\,\vec{s}$ and using the vector identity: $\vec{k} \times (\vec{k} \times \vec{E}) = \vec{k}(\vec{k} \cdot \vec{E}) - \vec{E}(\vec{k} \cdot \vec{k})$. Writing $\mu = \mu_0\,\mu_\mathrm{r}$ and $c = 1/\sqrt{\epsilon_0\mu_0}$ yields:

$$\vec{D} = \frac{\epsilon_0\,n^2}{\mu_\mathrm{r}}\Big(\vec{E} - \vec{s}(\vec{s} \cdot \vec{E})\Big). \tag{A.9}$$

In anisotropic media, the electric flux density $\vec{D}$ and the electric field $\vec{E}$ are connected via $\vec{D} = \epsilon_0\,\tilde{\epsilon}_\mathrm{r}\vec{E}$ (see Sec. 2.3.1). By choosing an appropriate coordinate system in which the coordinate axes coincide with the principal axes of the electric flux density, the three components ($i = 1,2,3$) of $\vec{D}$ can be written as: $D_i = \epsilon_0\,\epsilon_{\mathrm{r},i}E_i$, where $\epsilon_{\mathrm{r},i}$ are the principal relative permittivities. Thus, Eq. (A.9) simplifies to three homogeneous linear equations in E_i:

$$E_i = \frac{n^2\,s_i(\vec{s} \cdot \vec{E})}{n^2 - \mu_\mathrm{r}\epsilon_{\mathrm{r},i}}\,. \tag{A.10}$$

Multiplying the first equation by s_1, the second by s_2, the third by s_3, summing the resulting three equations together, and dividing both sides by $(\vec{s} \cdot \vec{E})$ yields the *Fresnel equation of wave normals* $\vec{s}$:

$$\frac{1}{n^2} = \frac{s_1^2}{n^2 - n_1^2} + \frac{s_2^2}{n^2 - n_2^2} + \frac{s_3^2}{n^2 - n_3^2}\,, \tag{A.11}$$

where $n_i = \sqrt{\mu_\mathrm{r}\,\epsilon_{\mathrm{r},i}}$ are the principal refractive indices.

Multiplying both sides of Eq. (A.11) by n^2 and subtracting ($s_1^2 + s_2^2 + s_3^2 = 1$) yields:

$$0 = \sum_{i=1}^{3} s_i^2 \left(\frac{1}{1 - \frac{n_i^2}{n^2}} - 1 \right) \tag{A.12}$$

$$\Leftrightarrow 0 = \sum_{i=1}^{3} \frac{s_i^2\, n_i^2}{n_i^2 - n^2}. \tag{A.13}$$

Multiplication by n^2/c^2 yields (with $v = c/n$ and $v_i = c/n_i$):

$$\frac{s_1^2}{v^2 - v_1^2} + \frac{s_2^2}{v^2 - v_2^2} + \frac{s_3^2}{v^2 - v_3^2} = 0. \tag{A.14}$$

For uniaxial birefringent media, the principal phase velocities v_i are given by:

$$v_1 = v_2 \equiv v_\mathrm{o}\ , \quad v_3 \equiv v_\mathrm{E}. \tag{A.15}$$

Multiplying Eq. (A.14) by $(v^2 - v_\mathrm{o}^2)^2(v^2 - v_\mathrm{E}^2)$ results in:

$$(s_1^2 + s_2^2)(v^2 - v_\mathrm{E}^2)(v^2 - v_\mathrm{o}^2) + s_3^2(v^2 - v_\mathrm{o}^2)^2 = 0. \tag{A.16}$$

If the wave vector $\vec{k} = k\vec{s}$ makes an angle θ with the optic axis, one can write $s_1^2 + s_2^2 = \sin^2\theta$ and $s_3^2 = \cos^2\theta$, yielding the equation:

$$(v^2 - v_\mathrm{o}^2)\left[(v^2 - v_\mathrm{E}^2)\sin^2\theta + (v^2 - v_\mathrm{o}^2)\cos^2\theta\right] = 0. \tag{A.17}$$

This equation has two solutions for the phase velocity in an anisotropic medium:

$$v^2 = v_\mathrm{o}^2\,, \tag{A.18}$$

$$v^2 = v_\mathrm{o}^2\cos^2\theta + v_\mathrm{E}^2\sin^2\theta. \tag{A.19}$$

Writing $v = c/n$ yields:

$$n^2 = n_\mathrm{o}^2\,, \tag{A.20}$$

$$1 = \frac{n^2\,\cos^2\theta}{n_\mathrm{o}^2} + \frac{n^2\,\sin^2\theta}{n_\mathrm{E}^2}. \tag{A.21}$$

Thus, in uniaxial birefringent media, there are two *refractive index surfaces*: The first is a sphere with radius n_o and corresponds to the ordinary wave; it describes the ordinary refractive index n_o which is independent of the direction of propagation. The second is an ellipsoid with semi-axes of length n_o (parallel to the optic axis) and n_E (perpendicular to the optic axis) and corresponds to the extraordinary wave; it describes the extraordinary refractive index $n_\mathrm{e}(\theta)$ which depends on the angle θ between the optic axis and the wave vector. Equation (A.21) can be transformed into Eq. (2.33).

A.3.2 Uniaxial Absorbing Materials

The explanations follow Born·Wolf [69] (Sec. 15.6.1).

In anisotropic absorbing materials with high symmetry, the principal axes of birefringence and dichroism are aligned (cf. Sec. 2.4.1), i. e. the directions of the principal axes

of the relative permittivity tensor $\tilde{\epsilon}_\mathrm{r}$ (describing refraction) and the conductivity tensor $\tilde{\sigma}$ (describing absorption) are coincident ([69] p. 840). In this case, the real refractive index n can be replaced by a complex refractive index n':

$$n' = n + \mathrm{i}\,\kappa \equiv n(1 + \mathrm{i}\,\hat{\kappa}), \tag{A.22}$$

where $\hat{\kappa} \equiv \kappa/n$. With n', a complex phase velocity v' can be defined:

$$v' = \frac{c}{n'} = \frac{c}{n(1 + \mathrm{i}\,\hat{\kappa})} \approx v(1 - \mathrm{i}\,\hat{\kappa}) \tag{A.23}$$

$$\Rightarrow\ v'^2 \approx v^2(1 - 2\,\mathrm{i}\,\hat{\kappa}), \tag{A.24}$$

assuming weak absorption[1] ($\hat{\kappa} \ll 1$) and performing a first order Taylor expansion in $\hat{\kappa} = 0$. The complex phase velocities of the ordinary and extraordinary wave (v'_o, v'_e, and v'_E) are defined in a similar manner.

Using the formal substitution $v \to v'$ and $v_i \to v'_i$, Fresnel's equation of wave normals can be written in the form of Eq. (A.14). For uniaxial systems, this equation has two solutions for the complex phase velocity, analogous to those related to non-absorbing uniaxial systems (see Appx. A.3.1):

$$v'^2 = v'^2_\mathrm{o} \tag{A.25}$$

$$v'^2 = v'^2_\mathrm{o}\cos^2\theta + v'^2_\mathrm{E}\sin^2\theta. \tag{A.26}$$

Using the approximation defined in Eq. (A.24), the real part of the two solutions yields Eqs. (A.18) and (A.19). The imaginary part yields:

$$\hat{\kappa} = \hat{\kappa}_\mathrm{o}, \tag{A.27}$$

$$v^2\hat{\kappa} = v^2_\mathrm{o}\hat{\kappa}_\mathrm{o}\cos^2\theta + v^2_\mathrm{E}\hat{\kappa}_\mathrm{E}\sin^2\theta. \tag{A.28}$$

The first equation describes the absorption of the ordinary wave ($\hat{\kappa}_\mathrm{o}$), which is independent of the direction of propagation. The second equation describes the absorption of the extraordinary wave ($\hat{\kappa}_\mathrm{e}(\theta)$), which depends on the angle θ between the optic axis and the wave vector.

The absorption coefficient is related to $\hat{\kappa}$ via (cf. Eq. (2.29)):

$$K = \frac{4\pi n}{\lambda}\hat{\kappa} = \frac{4\pi\kappa}{\lambda}. \tag{A.29}$$

A.4 Birefringence and Dichroism for Uniaxial Absorbing Materials

This section studies the birefringence and dichroism for uniaxial systems with small birefringence and absorption ($|\Delta n| \ll n$, $\kappa \ll n$). In this case, the birefringence (anisotropic refraction) and the dichroism (anisotropic absorption) can be described by a complex retardance, where the complex refractive indices of ordinary and extraordinary wave are given by Eqs. (A.20), (A.21), (A.27) and (A.28).

In Appx. A.4.1 and A.4.2, approximate formulas (used for Eqs. (2.37) and (2.45)) are derived which relate the refractive index and absorption of the extraordinary wave to the birefringence and dichroism of the material. Appendix A.4.3 studies the relationship

[1] Brain tissue has small absorption coefficients (see Sec. 3.2.2).

between birefringence and dichroism, in particular the inclination dependence of dichroism and its relation to the retardation signal. Appendix A.4.4, finally, investigates the dichroism of two crossing fiber bundles.

A.4.1 Approximation of Birefringence

The following derivation has been published in Menzel *et al.* (2015) [51] Appx. A.

When light passes through a birefringent medium, it is split into an ordinary and an extraordinary wave which both experience different refractive indices (see Sec. 2.3.1). The refractive index n_e that the extraordinary wave experiences when passing through the medium under an angle θ with respect to the optic axis is given by Eq. (A.21):

$$\frac{1}{n_\mathrm{e}(\theta)^2} = \frac{1}{n_\mathrm{o}^2}\cos^2\theta + \frac{1}{n_\mathrm{E}^2}\sin^2\theta, \tag{A.30}$$

$$\Leftrightarrow \frac{1}{n_\mathrm{o}^2} - \frac{1}{n_\mathrm{e}(\theta)^2} = \left(\frac{1}{n_\mathrm{o}^2} - \frac{1}{n_\mathrm{E}^2}\right)\sin^2\theta, \tag{A.31}$$

where n_o is the ordinary refractive index and $n_\mathrm{E} \equiv n_\mathrm{e}(\theta = 90°)$ the principal extraordinary refractive index of the medium.

If the birefringence $|\Delta n| = |n_\mathrm{E} - n_\mathrm{o}|$ is small[2] compared to the values of the refractive indices n_o and n_E, a Taylor expansion can be applied to the function

$$f(\Delta n) \equiv \frac{1}{n_\mathrm{o}^2} - \frac{1}{n_\mathrm{E}^2} = \frac{1}{n_\mathrm{o}^2} - \frac{1}{(n_\mathrm{o} + \Delta n)^2} \tag{A.32}$$

in $\Delta n = 0$:

$$f(\Delta n) = \sum_{l=0}^{\infty} \frac{f^{(l)}(0)}{l!}(\Delta n)^l = f(0) + f'(0)\,\Delta n + ... = 0 + \frac{2}{n_\mathrm{o}^3}\Delta n + ... \tag{A.33}$$

The same expansion can be done for $\left(1/n_\mathrm{o}^2 - 1/n_\mathrm{e}(\theta)^2\right)$ in $(|\Delta n(\theta)| = |n_\mathrm{e}(\theta) - n_\mathrm{o}| \ll 1)$. Thus, a first order Taylor expansion of Eq. (A.31) yields (after dividing both sides of the equation by the common factor $2/n_0^3$):

$$\Delta n(\theta) \approx \Delta n\,\sin^2\theta. \tag{A.34}$$

Thus, when light passes through a birefringent medium of thickness d, the extraordinary wave experiences a phase shift with respect to the ordinary wave that depends on the angle θ between the wave vector and the optic axis as described in Eq. (2.37).

A.4.2 Approximation of Dichroism

The following derivation has been published in Menzel *et al.* (2018b) [68] Note 1.

In materials with $\kappa \ll n$, the absorption of the extraordinary wave is given by Eq. (A.28). Writing $\hat{\kappa} \equiv \kappa/n$, $v = c/n$, and $\Delta\kappa \equiv \kappa_\mathrm{E} - \kappa_\mathrm{o}$ yields:

$$\kappa_\mathrm{e}(\theta) = \frac{n_\mathrm{e}^3}{n_\mathrm{o}^3}\kappa_\mathrm{o}\cos^2\theta + \frac{n_\mathrm{e}^3}{n_\mathrm{E}^3}\kappa_\mathrm{E}\sin^2\theta \tag{A.35}$$

$$= \underbrace{\frac{(n_\mathrm{o} + \Delta n(\theta))^3}{n_\mathrm{o}^3}}_{f_1(\Delta n(\theta))}\kappa_\mathrm{o}\cos^2\theta + \underbrace{\frac{(n_\mathrm{o} + \Delta n(\theta))^3}{(n_\mathrm{o} + \Delta n)^3}}_{f_2(\Delta n(\theta),\,\Delta n)}(\kappa_\mathrm{o} + \Delta\kappa)\sin^2\theta. \tag{A.36}$$

[2] For brain tissue $|\Delta n| \ll n$ (see Sec. 3.2.3).

Similar to Appx. A.4.1, a first order Taylor expansion (in 2D) can be applied to f_1 and f_2 in $\{\Delta n(\theta) = 0,\, \Delta n = 0\}$:

$$f_1\left(\Delta n(\theta)\right) = f(0) + f'(0)\,\Delta n(\theta) + \ldots \tag{A.37}$$

$$= 1 + \frac{3}{n_\mathrm{o}}\,\Delta n(\theta) + \ldots \tag{A.38}$$

$$f_2\left(\Delta n(\theta),\, \Delta n\right) = f(0,0) + \frac{\partial}{\partial \Delta n(\theta)}\, f(0,0)\,\Delta n(\theta) + \frac{\partial}{\partial \Delta n}\, f(0,0)\,\Delta n + \ldots \tag{A.39}$$

$$= 1 + \frac{3}{n_\mathrm{o}}\left(\Delta n(\theta) - \Delta n\right) + \ldots \tag{A.40}$$

Inserting Eqs. (A.38) and (A.40) into Eq. (A.36) and using Eq. (A.34) yields:

$$\kappa_\mathrm{e}(\theta) \approx \left(1 + \frac{3}{n_\mathrm{o}}\Delta n\, \sin^2\theta\right) \kappa_\mathrm{o} \cos^2\theta + \left(1 - \frac{3}{n_\mathrm{o}}\Delta n\, \cos^2\theta\right)(\kappa_\mathrm{o} + \Delta\kappa)\sin^2\theta \tag{A.41}$$

$$= \kappa_\mathrm{o} + \left(1 - \frac{3}{n_\mathrm{o}}\Delta n\, \cos^2\theta\right)\Delta\kappa\, \sin^2\theta. \tag{A.42}$$

For materials with small birefringence ($|\Delta n| \ll n$), the term in round brackets in Eq. (A.42) becomes close to one[3] so that $\kappa_\mathrm{e}(\theta) \approx \kappa_\mathrm{o} + \Delta\kappa\, \sin^2\theta$.

Thus, in uniaxial absorbing materials with small birefringence ($|\Delta n| \ll n$) and weak absorption ($\kappa \ll n$), the dichroism (anisotropic absorption) depends on the angle θ between the wave vector and the optic axis, just like the birefringence:

$$\Delta\kappa(\theta) \equiv \kappa_\mathrm{e}(\theta) - \kappa_\mathrm{o} \approx \Delta\kappa\, \sin^2\theta, \quad \Delta\kappa \equiv \kappa_\mathrm{E} - \kappa_\mathrm{o}. \tag{A.43}$$

A.4.3 Relationship between Birefringence and Dichroism

This section studies the relationship between birefringence (retardation $|\sin\delta|$) and dichroism in uniaxial absorbing materials: The diattenuation (describing dichroism and anisotropic scattering) is represented in terms of attenuation coefficients (Appx. A.4.3.1). This notation is then used to derive an expression for the inclination dependence of dichroism (Appx. A.4.3.2) and thus to relate dichroism to retardation (Appx. A.4.3.3). Parts of Appx. A.4.3.1 and A.4.3.2 have been published in Menzel *et al.* (2018b) [68] Note 1.

A.4.3.1 Diattenuation in Terms of Attenuation Coefficients

The diattenuation of a material is defined via Eq. (2.39):

$$|D| = \frac{I_\mathrm{max} - I_\mathrm{min}}{I_\mathrm{max} + I_\mathrm{min}}, \tag{A.44}$$

with I_max and I_min being the maximum and minimum transmitted light intensities for light polarized in orthogonal directions. For light propagating through a diattenuating material of thickness d, the maximum and minimum transmitted light intensities can be written as (cf. Eq. (2.28)):

$$I_\mathrm{max} = I_0\, \mathrm{e}^{-d\,\mu_\mathrm{min}}, \tag{A.45}$$

$$I_\mathrm{min} = I_0\, \mathrm{e}^{-d\,\mu_\mathrm{max}}, \tag{A.46}$$

[3] The refractive index of brain tissue ($n \geq 1.3$, see Sec. 3.2.1) is much larger than the birefringence of biological tissue ($|\Delta n| \leq 0.01$, see Sec. 3.2.3). In this case, the term in round brackets is > 0.97.

with I_0 being the ingoing light intensity and $\mu_{\max}$ and $\mu_{\min}$ the maximum and minimum attenuation coefficients of the material. Thus, the diattenuation can be written as:

$$|D| = \frac{\mathrm{e}^{-d\,\mu_{\min}} - \mathrm{e}^{-d\,\mu_{\max}}}{\mathrm{e}^{-d\,\mu_{\min}} + \mathrm{e}^{-d\,\mu_{\max}}} = \frac{\mathrm{e}^{\,d\,(\mu_{\max}-\mu_{\min})/2} - \mathrm{e}^{-d\,(\mu_{\max}-\mu_{\min})/2}}{\mathrm{e}^{\,d\,(\mu_{\max}-\mu_{\min})/2} + \mathrm{e}^{-d\,(\mu_{\max}-\mu_{\min})/2}} \tag{A.47}$$

$$= \tanh\left(d\,\frac{\mu_{\max}-\mu_{\min}}{2}\right). \tag{A.48}$$

In a similar manner, the average transmittance in Eq. (2.40) can be written as:

$$\tau = \frac{I_{\max}+I_{\min}}{2\,I_0} = \frac{\mathrm{e}^{-d\,\mu_{\min}} + \mathrm{e}^{-d\,\mu_{\max}}}{2} \tag{A.49}$$

$$= \mathrm{e}^{-d\,\frac{\mu_{\max}+\mu_{\min}}{2}}\;\frac{\mathrm{e}^{\,d\,(\mu_{\max}-\mu_{\min})/2} + \mathrm{e}^{-d\,(\mu_{\max}-\mu_{\min})/2}}{2} \tag{A.50}$$

$$= \mathrm{e}^{-d\,\frac{\mu_{\max}+\mu_{\min}}{2}}\,\cosh\left(d\,\frac{\mu_{\max}-\mu_{\min}}{2}\right). \tag{A.51}$$

These are the equations given in Eqs. (2.41) and (2.42).

A.4.3.2 Inclination Dependence of Dichroism

In case of no anisotropic scattering, the diattenuation is caused by dichroism (anisotropic absorption). The *dichroism* δ_{K} is defined in analogy to the retardance δ (Eq. (2.36)) as:

$$\delta_{\mathrm{K}} \equiv \frac{2\pi d}{\lambda}\Delta\kappa(\theta) = \frac{2\pi d}{\lambda}\Big(\kappa_{\mathrm{e}}(\theta) - \kappa_{\mathrm{o}}\Big) \overset{(A.43)}{\approx} \frac{2\pi d}{\lambda}\Delta\kappa\,\sin^2\theta \equiv \delta_{\mathrm{K,max}}\,\sin^2\theta. \tag{A.52}$$

Defining the absorption coefficient of the ordinary wave ($K_{\mathrm{o}} \equiv 4\pi\kappa_{\mathrm{o}}/\lambda$) and of the extraordinary wave ($K_{\mathrm{e}} \equiv 4\pi\kappa_{\mathrm{e}}/\lambda$), the diattenuation and average transmittance for dichroic materials ($\mu_{\mathrm{att}} = K$) can be written as (see Eqs. (2.44), (A.48) and (A.51)):

$$D_{\mathrm{K}} = \tanh\left(\frac{d}{2}\big(K_{\mathrm{o}} - K_{\mathrm{e}}(\theta)\big)\right) \overset{(2.29)}{=} \tanh\left(\frac{2\pi d}{\lambda}\big(\kappa_{\mathrm{o}} - \kappa_{\mathrm{e}}(\theta)\big)\right) \overset{(A.52)}{\approx} \tanh\big(-\delta_{\mathrm{K,max}}\,\sin^2\theta\big), \tag{A.53}$$

$$\tau = \mathrm{e}^{-d\left(\frac{K_{\mathrm{o}}+K_{\mathrm{e}}(\theta)}{2}\right)}\cosh\left(\frac{d}{2}\,\big(K_{\mathrm{o}} - K_{\mathrm{e}}(\theta)\big)\right) \overset{(A.53)}{\approx} \mathrm{e}^{-d\left(\frac{K_{\mathrm{o}}+K_{\mathrm{e}}(\theta)}{2}\right)}\,\cosh\big(\delta_{\mathrm{K,max}}\,\sin^2\theta\big). \tag{A.54}$$

To estimate the diattenuation caused by anisotropic absorption (dichroism) for an inclined nerve fiber, a coordinate system is chosen in which the light propagates in the z-direction and the brain tissue lies in the xy-plane. The optic axis (oriented in the direction of the nerve fiber) makes an angle θ with the z-axis, i. e. the out-of-plane inclination angle of the fiber is: $\alpha = 90° - \theta$ (cf. Fig. 2.3a in light blue).

The long-term study of the diattenuation signal in Chap. 9 suggests that diattenuation caused by anisotropic absorption is positive (see Sec. 9.4): $D_{\mathrm{K}} > 0 \Leftrightarrow \delta_{\mathrm{K,max}} < 0$.

Figure A.1 shows the dichroism D_{K} plotted against the fiber inclination angle α for different $\delta_{\mathrm{K,max}} < 0$. The curves were used in Sec. 12.4 to estimate the impact of anisotropic absorption (dichroism) on the diattenuation for different fiber configurations, in addition to simulated anisotropic scattering.

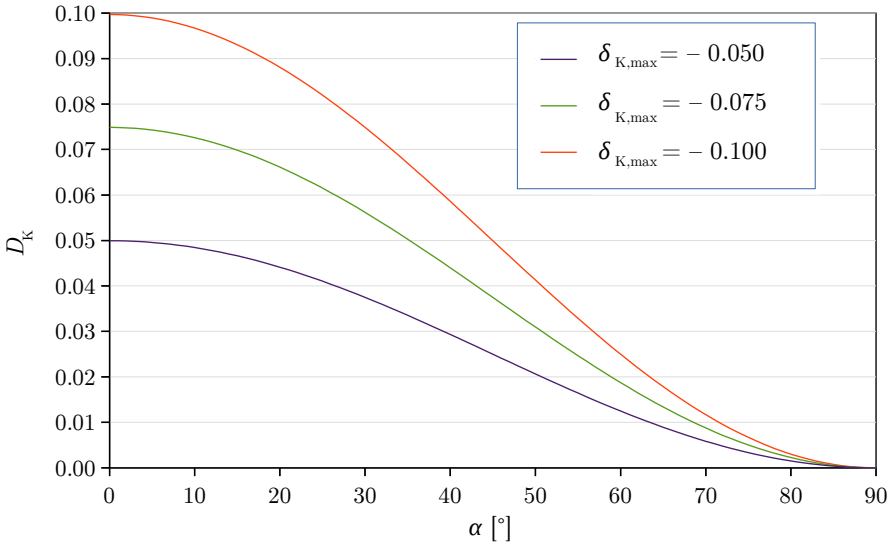

Fig. A.1: Diattenuation caused by anisotropic absorption (dichroism D_K) plotted against the fiber inclination angle α. The curves were computed analytically using Eq. (A.53) with $\theta = (90° - \alpha)$ and assuming different values for $\delta_{K,max}$.

A.4.3.3 Retardation vs. Dichroism

According to Eqs. (A.34) and (A.43), $\Delta n(\theta)$ and $\Delta\kappa(\theta)$ are proportional to each other (for $|\Delta n| \ll n$ and $\kappa \ll n$):

$$\Delta n(\theta) \propto \Delta\kappa(\theta) \quad \overset{(2.36),(A.52)}{\Leftrightarrow} \quad \delta \propto \delta_K. \tag{A.55}$$

Thus, in materials without anisotropic scattering, the retardation $|\sin\delta|$ is related to the diattenuation D_K via:

$$|\sin\delta| \overset{(A.55)}{=} |\sin(m\,\delta_K)| \overset{(A.52),(A.53)}{=} |\sin(m\,\tanh^{-1}(D_K))|, \tag{A.56}$$

$$\Rightarrow |\sin\delta| \approx m\,|D_K|, \quad \text{for small } m\,|D_K|, \tag{A.57}$$

with $m > 0$ being the proportionality factor between retardance δ and dichroism δ_K. In brain tissue, the retardation is usually much larger than the diattenuation ($|\sin\delta| > 0.7$, $|D_K| < 0.1$), yielding proportionality factors $m > 7$.

Figure A.2 shows the retardation plotted against the diattenuation for different proportionality factors $m = \{10, 20, 30, 40, 50\}$. The diattenuation caused by anisotropic absorption is approximately proportional to the retardation for $|\sin\delta| \leq 0.6$ or $|D_K| \leq 0.02$ (see black dotted lines). The curves were used in Sec. 9.4 to explain the increasing correlation between retardation and diattenuation with increasing time after tissue embedding.

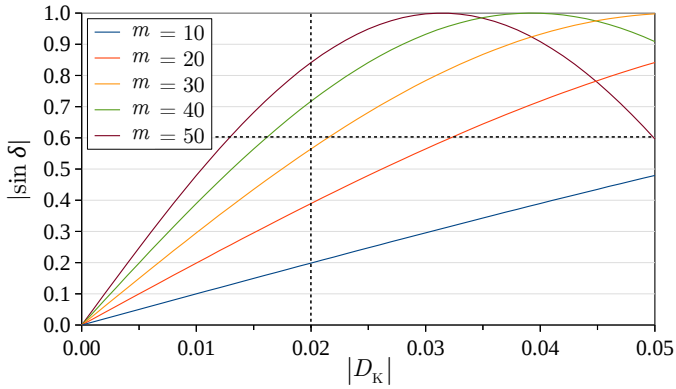

Fig. A.2: Retardation $|\sin\delta|$ plotted against the diattenuation caused by anisotropic absorption (dichroism D_K). The curves were computed analytically using Eq. (A.56) and assuming different proportionality factors m. The dichroism is approximately proportional to the retardation for $|\sin\delta| \leq 0.6$ or $|D_\mathrm{K}| \leq 0.02$ (see black dotted lines).

A.4.4 Dichroism of Crossing Fiber Bundles

To study the diattenuation of crossing fiber bundles, both anisotropic scattering (D_S) and anisotropic absorption (dichroism D_K) need to be considered. In Sec. 12.3, anisotropic scattering was simulated for several crossing fiber bundles.

This section investigates the dichroism of two crossing identical fiber bundles in the xy-plane with crossing angle $\chi \leq 90°$ (see Fig. A.3) in the absence of anisotropic scattering ($D = D_\mathrm{K}$). The fiber bundles are assumed to be uniaxial with the optic axis oriented along the corresponding fiber axis, the principal axes of birefringence and dichroism are coincident. Due to the absence of anisotropic scattering, the attenuation of light can be computed separately and each fiber bundle $i \in \{1, 2\}$ can be represented by a Müller matrix $M_i(\delta, D_\mathrm{K}, \tau)$ with retardance δ, dichroism D_K, and average transmittance τ (see Eq. (2.56)).

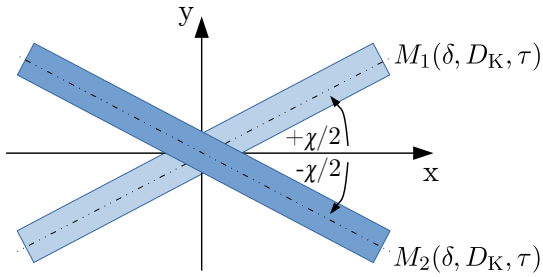

Fig. A.3: Schematic drawing of two crossing fiber bundles (optic axes) in the xy-plane with crossing angle χ. The fiber bundles (with retardance δ, dichroism D_K, and average transmittance τ) are described by Müller matrices M_1 and M_2, as defined in Eq. (2.56).

The transmitted light intensity $I_\mathrm{D}(\rho, \chi)$ was computed as described at the beginning of Sec. 4.4 and Sec. 4.4.3, assuming an ideal linear polarizer ($D_\mathrm{x} = \tau_\mathrm{x} = 1$) and replacing

the tissue matrix $M(\varphi, \delta, D, \tau)$ in Eq. (4.30) by the rotated matrices $M_1(\chi/2, \delta, D_\mathrm{K}, \tau)$ and $M_2(-\chi/2, \delta, D_\mathrm{K}, \tau)$ of the two fibers:

$$\vec{S}'_\mathrm{D}(\rho, \chi) = M_2(-\chi/2, \delta, D_\mathrm{K}, \tau) \cdot M_1(\chi/2, \delta, D_\mathrm{K}, \tau) \cdot P_\mathrm{x}(\rho, 1, 1) \cdot \vec{S}_\mathrm{unpol} \tag{A.58}$$

$$\begin{aligned} \Rightarrow I_\mathrm{D}(\rho, \chi) = \tau^2 \Bigg[1 + D_\mathrm{K}^2 \cos(2\chi) + D_\mathrm{K} \Bigg(\frac{1}{2} \Big(\cos(2\rho - 3\chi) + \cos(2\rho + \chi) \Big) \\ + \cos(2\rho - \chi) - \sqrt{1 - D_\mathrm{K}^2} \cos\delta \sin(2\chi) \sin(2\rho - \chi) \Bigg) \Bigg]. \end{aligned} \tag{A.59}$$

The transmitted light intensity can be written as a Fourier series with Fourier coefficients $a_{0\mathrm{D}}$, $a_{2\mathrm{D}}$, and $b_{2\mathrm{D}}$:

$$\Rightarrow \quad I_\mathrm{D}(\rho, \chi) = a_{0\mathrm{D}}(\chi) + a_{2\mathrm{D}}(\chi) \cos(2\rho) + b_{2\mathrm{D}}(\chi) \sin(2\rho), \tag{A.60}$$

$$a_{0\mathrm{D}}(\chi) = \tau^2 \left(1 + D_\mathrm{K}^2 \cos(2\chi)\right), \tag{A.61}$$

$$a_{2\mathrm{D}}(\chi) = \tau^2 D_\mathrm{K} \left(\frac{1}{2} \cos(3\chi) + \frac{3}{2} \cos(\chi) + \sqrt{1 - D_\mathrm{K}^2} \cos\delta \sin(2\chi) \sin(\chi) \right), \tag{A.62}$$

$$b_{2\mathrm{D}}(\chi) = \tau^2 D_\mathrm{K} \left(\frac{1}{2} \sin(3\chi) + \frac{1}{2} \sin(\chi) - \sqrt{1 - D_\mathrm{K}^2} \cos\delta \sin(2\chi) \cos(\chi) \right). \tag{A.63}$$

To study the dichroism caused by two crossing fiber bundles, the amplitude $|D_{\mathrm{D,K}}|(\chi)$ and the phase $\varphi_{\mathrm{D,K}}(\chi)$ of the intensity profile $I_\mathrm{D}(\rho, \chi)$ were determined using Eqs. (4.36) and (4.37). Figure A.4a,b shows the resulting graphs for fiber bundles with different retardances ($\delta = \{0, \pi/8, \ldots, \pi/2\}$) and $D_\mathrm{K} = 5\,\% > 0$, i. e. the absorption of light was assumed to become maximal when the light is polarized perpendicularly to the fiber axis (in the plane of the lipid molecules). Figure A.4c shows the maximum phase plotted against the retardation $|\sin\delta|$. When the order of the fiber bundles in Fig. A.3 is reversed, the graphs for $\varphi_{\mathrm{D,K}}$ are mirrored about the x-axis.

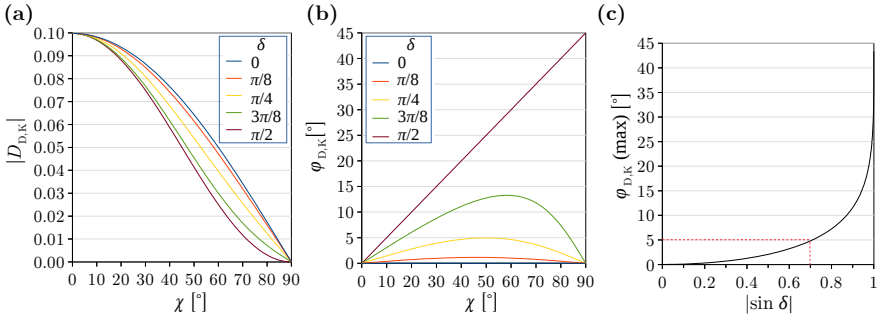

Fig. A.4: Diattenuation caused by anisotropic absorption (dichroism) of two in-plane crossing fiber bundles (see Fig. A.3) with dichroism $D_\mathrm{K} = 5\,\%$, retardance δ, and crossing angle χ. The amplitude $|D_{\mathrm{D,K}}|$ and the phase $\varphi_{\mathrm{D,K}}$ of the transmitted light intensity profile $I_\mathrm{D}(\rho, \chi)$ (see Eq. (A.60)) were computed analytically using Eqs. (4.36) and (4.37): **(a)** $|D_{\mathrm{D,K}}|$ plotted against χ for different δ, **(b)** $\varphi_{\mathrm{D,K}}$ plotted against χ for different δ, **(c)** maximum $\varphi_{\mathrm{D,K}}$ plotted against the retardation $|\sin\delta|$. When the order of the fiber bundles in Fig. A.3 is reversed, the graphs for $\varphi_{\mathrm{D,K}}$ are mirrored about the x-axis.

The resulting dichroism $|D_{\mathrm{D,K}}|$ of the two crossing fiber bundles decreases with increasing crossing angle and reaches zero for 90°-crossing fibers (see Fig. A.4a). Assuming

that one fiber bundle has a maximum thickness of 30 µm, retardation values less than 0.7 are expected (the maximum retardation measured for a 60 µm thin brain sections is less than $|\sin\delta| = 0.9$). In this case ($\delta < \pi/4$), the curves look similar to the curve of $|\mathscr{D}_S|$ for the simulated separate crossing fibers in Fig. 12.8a.

The resulting phase is close to zero for small fiber crossing angles or small retardation values (see Fig. A.4b), i. e. the transmitted light intensity becomes maximal when the light is polarized in the x-direction ($\rho = 0°$). With increasing retardation, the phase is shifted to larger values for larger crossing angles. For 90°-crossing fibers with maximum retardation ($|\sin\delta| = 1$), the phase reaches 45°, i. e. the transmitted light intensity becomes maximal when the light is polarized in the direction of the first fiber bundle (see light blue cylinder in Fig. A.3). For more realistic retardation values ($|\sin\delta| < 1$), the phase for 90°-crossing fibers is always zero. The maximum phase value increases with increasing retardation of the fiber bundles (see Fig. A.4c). For retardation values less than 0.7, the phase is still less than 5° (see red dashed lines).

Thus, the diattenuation signal caused by anisotropic absorption (dichroism) of two crossing fiber bundles is expected to be sinusoidal, with an amplitude that approaches zero with increasing crossing angle and a maximum transmitted intensity for light that is polarized along the mean fiber direction of the two bundles (x-axis in Fig. A.3).

A.5 Total Internal Reflection

Total internal reflection occurs when light propagates from one medium with high refractive index n_1 into another medium with lower refractive index n_2 and if the angle of incidence (θ_i) is larger than the critical angle of total internal reflection (θ_c).

According to Snell's law of refraction (Eq. (2.23)), the critical angle for total internal reflection ($\theta_c = \theta_i$) is given when the exit angle reaches $\theta_t = 90°$ (cf. Sec. 2.2.1):

$$n_1 \sin(\theta_c) = n_2 \sin(90°) \tag{A.64}$$

$$\Leftrightarrow \theta_c = \arcsin\left(\frac{n_2}{n_1}\right). \tag{A.65}$$

In the following, the concept of total internal reflection is applied to a (straight) nerve fiber[4] consisting of an inner axon with lower refractive index ($n_{ax} = 1.35$) and a surrounding myelin sheath (single layer) with higher refractive index ($n_m = 1.47$), embedded in a glycerin solution with lower refractive index ($n_g = 1.37$), cf. Sec. 10.3.1. The fiber is inclined by an angle α with respect to the tissue surface. When the fiber inclination angle α becomes larger than the critical angle θ_c of total internal reflection, light under normal incidence is "guided" within the myelin sheath (see Fig. A.5):

$$\theta_{c1} = \arcsin\left(\frac{n_{ax}}{n_m}\right) = \arcsin\left(\frac{1.35}{1.47}\right) = 66.7°, \tag{A.66}$$

$$\theta_{c2} = \arcsin\left(\frac{n_{surr}}{n_m}\right) = \arcsin\left(\frac{1.37}{1.47}\right) = 68.7°. \tag{A.67}$$

For a reduced myelin refractive index $n_m = 1.39$, the corresponding critical angles of total internal reflection are $\theta_{c1} = 76.2°$ and $\theta_{c2} = 80.3°$, respectively.

[4] As the myelin sheath thickness is smaller than the wavelength, results obtained from geometrical optics do not necessarily hold. However, as discussed in Sec. 11.4, the concept of total internal reflection can still be used to model the observed inclination dependence of the transmittance.

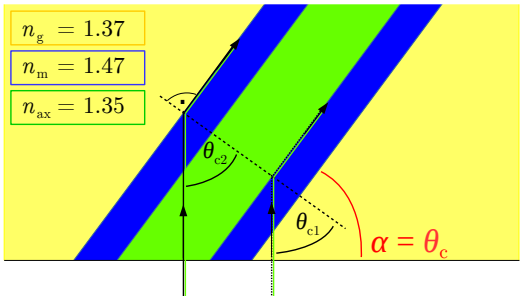

Fig. A.5: Schematic drawing of total internal reflection: Light under normal incidence is "guided" within the myelin layer (blue) when the inclination angle α of the straight fiber becomes larger than the critical angle θ_c of total internal reflection, which is defined by the refractive indices of myelin (n_m), axon (n_{ax}), and the surrounding glycerin solution (n_g).

Figure A.6 shows the critical angle of total internal reflection plotted against the difference in refractive indices $(n_1 - n_2)$, using $n_2 = n_g = 1.37$.

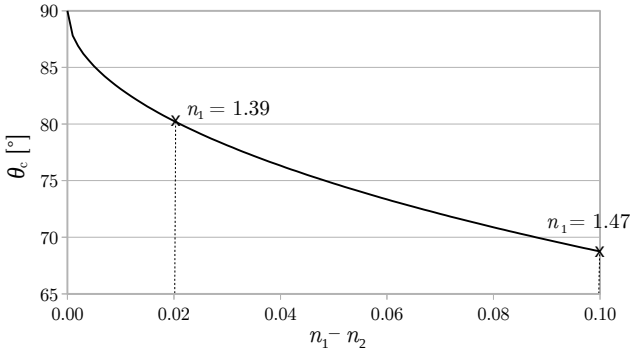

Fig. A.6: Critical angle of total internal reflection θ_c plotted against the difference in refractive indices $(n_1 - n_2)$, where $n_2 = n_g = 1.37$ belongs to the medium with lower refractive index (surrounding glycerin solution) and n_1 to the medium with higher refractive index (myelin)

Appendix B

Optical Properties of the Optical Systems

In this chapter, the optical properties of the optical systems (PM and LAP) are described in more detail. Appendix B.1 provides a detailed description of the optical components. Appendix B.2 shows the line profiles that were obtained from measurements of the USAF resolution target used for determining the optical resolution of the optical systems. Finally, Appx. B.3.1 and B.3.2 describe how the polarization-independent inhomogeneities and the polarization properties were characterized for the LAP.

B.1 Optical Components of the Optical Systems

This section lists all manufacturer information and additional background information for the PM and the LAP. A more detailed characterization of the PM and the LAP can be found in Reckfort [53]. Parts of Appx. B.1.2 have previously been published in Menzel *et al.* (2017) [3] Appx. A.

B.1.1 Polarizing Microscope (PM)

The PM (*LMP-1*) is custom-made by *Taorad GmbH*, Germany. In contrast to the LAP, the filters cannot be removed, only the first polarizer can be rotated, and tilting is not possible. As a consequence, the optical components cannot be characterized individually. However, the components of the PM were thoroughly characterized by the manufacturer and are expected to be of better quality than those of the LAP.

Equipped with a motorized specimen stage in x/y (*Märzhäuser*, Germany) and a motor along the z-axis to change focal position, the PM enables a tile-wise translational scanning of the brain section. Each tile is about $2.7 \times 2.7\,\mathrm{mm}^2$, including an overlap of 0.75–1 mm at the borders for stitching. The pixel size in object space is about 1.33 µm, allowing to map single axons. The measurement of a whole human brain section takes about 24 hours and produces about 800 GB of data.

Figure B.1 shows all optical components that are incorporated in the PM.

Light Source The PM is equipped with a single white LED (*IntraLED 2020+*, operated at 24 W). The light is guided through a bundle of optical fibers, producing a broad angular distribution. To ensure a homogeneous illumination of the sample, a Köhler illumination is used (cf. Fig. 7.2a). Inhomogeneities induced by the light source were determined to be relatively small [53]. The light is filtered by a bandpass filter which is integrated in the rotating linear polarizer and generates wavelengths between 540 and 560 nm. According to manufacturer information, the resulting wavelength spectrum is

$\lambda = (550 \pm 5)$ nm. The wavelength spectrum of the PM was characterized in separate measurements (see Sec. 7.1.1).

Polarizing Filters The filters are high quality, standard filters for polarization microscopy with diameters of about 2.54 cm. The polarization efficiency of the polarizers is indicated as 99.8 %. The employed quarter-wave retarder is optimized for a wavelength of 545 nm, which is similar to the illumination wavelength.

Objective and Tube Lens The objective lens (*TL Plan Fluor EPI P 5x*, manufactured by *Nikon*) has a numerical aperture NA $\approx$ 0.15 and a 5× magnification.

An infinity tube lens unit (*MXA 20696/70g*) for *CFI60* objectives (*Nikon*) is placed between circular analyzer and camera.

Camera The PM is equipped with a *Monochrome Retiga 4000R* camera, manufactured by *QImaging*. The camera is a digital CCD camera with high sensitivity which enables bright-field imaging. It contains a *Kodak KAI-4022-ABA-CD-BA* image sensor with 2048 × 2048 active pixels and an active image size of 15.15 × 15.15 mm^2 with a pixel size of 7.4 µm. The sensor contains an array of telecentric spherical microlenses which focus the light onto subjacent photodiodes (cf. Fig. 7.4b).

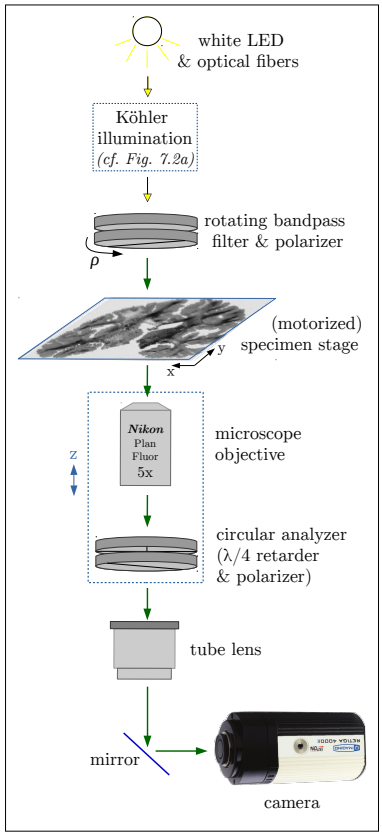

Fig. B.1: Schematic figure (not to scale) of the optical components incorporated in the PM

B.1.2 Large-Area Polarimeter (LAP)

The LAP is an in-house developed system consisting (from bottom to top) of a light source, a linear polarizer, a quarter-wave retarder, a two-axes tiltable specimen stage, and a second rotating linear polarizer (analyzer), cf. Figs. 4.4a and 7.2b. Each filter can be rotated individually or be removed from the imaging system [45, 46], allowing to perform 3D-PLI as well as DI measurements (see Sec. 4.4) and to fully characterize all optical elements.

The LAP enables single-shot imaging of whole human brain sections with a pixel size in object space between 21 µm and 64 µm. A measurement of a whole human brain section (including four tilts) takes about 15 min and produces about 2 GB of data.

Light Source The customized light source (*FZJ SSQ300-ALK-G* provided by *iiM*, Germany) contains a matrix of 36×36 LEDs (*NSPG 510S*, *Nichia corporation*) which illuminates an area of approximately $30 \times 30\,\mathrm{cm}^2$. The emitted light is expected to be incoherent and unpolarized with a wavelength of $(525 \pm 25)\,\mathrm{nm}$ (for an operating temperature of 25°C and a current of 20 mA) [152]. The wavelength spectrum and the polarization of the light source were characterized in separate measurements (see Secs. 7.1.1 and 7.2.2 and Appx. B.3.2).

To create a more uniform illumination, a diffuser plate was placed on top of the LED panel. The plate is 6 mm thick and consists of transparent thermoplastic acrylic glass (PMMA). Despite the diffuser plate, the illumination is not completely homogeneous. The inhomogeneities of the illumination were characterized in separate measurements (see Sec. 7.2.1 and Appx. B.3.1).

To ensure a constant brightness, the LED panel is powered by a constant current source combined with a water-cooling system in order to stabilize the operating temperature.

Polarizing Filters The polarizing filters were manufactured by *ITOS*, Germany. They are large-area circular filters with a diameter of 23.9 cm and consist of polymer foils. Inhomogeneities that might be introduced in the fabrication process and during usage were characterized in separate measurements (see Sec. 7.2.1 and Appx. B.3.1).

The two linear polarizers (*XP38*) are about 0.18 mm thick and consist of dichromatic polymer films, i. e. films containing long chains of polymer molecules that are oriented in the same direction. The filters are covered on both sides with cellulose acetate butyrate (CAB) and laminated between two glass plates for mechanical stabilization. According to the manufacturer, the filters are optimized for a broad wavelength spectrum ($\lambda = 400$–$700\,\mathrm{nm}$), transmit 38 % of the light, and have a polarization efficiency larger than 99.98 %. The degree of polarization was determined in separate measurements (see Sec. 7.2.2 and Appx. B.3.2).

The quarter-wave retarder (*WP140HE*) consists of a 75 µm thin layer of polycarbonate sheet which induces the birefringence. According to manufacturer information, the retarder transmits more than 90 % of the light. The range of use is indicated as $\lambda = 450$–$660\,\mathrm{nm}$ and the induced retardation as $(142 \pm 5)\,\mathrm{nm}$. Thus, the quarter-wave retarder has a working wavelength of 568 nm, which is larger than the wavelength of illumination. The wavelength discrepancy (i. e. the retardance γ of the wave retarder) was determined in separate measurements (see Sec. 7.2.2 and Appx. B.3.2).

Camera The employed RGB-camera (*AxioCam HRc* by *Carl Zeiss AG*, Germany) consists of a 2/3-inch CCD sensor ($8.9 \times 6.7\,\mathrm{mm}^2$) with a pixel size of 6.45 µm and a spectral sensitivity of $\lambda = 400$–$700\,\mathrm{nm}$. The polarization sensitivity of the camera was determined in separate measurements (see Sec. 7.2.2 and Appx. B.3.2).

To achieve a higher sampling resolution, the sensor chip is moved during the measurement (*microscanning procedure*). Without microscanning, $1388 \times 1040\,\mathrm{px}$ are recorded. In a standard 3D-PLI measurement, the scanning rate is increased so that $2776 \times 2080\,\mathrm{px}$ are recorded. In a DI measurement, $4164 \times 3120\,\mathrm{px}$ are recorded to account for the small diattenuation signal.

Depending on the sample size and the desired field of view, different camera objectives with different focal lengths can be mounted (see Tab. 7.1): *Lametar 2.8/25* (*JENOPTIK – Laser, Optik, Systeme GmbH*): $f = 25\,\mathrm{mm}$; *Apo-Rodagon-N50* (*Rodenstock*): $f = 50.2\,\mathrm{mm}$; *Apo-Rodagon-N90* (*Rodenstock*): $f = 90.1\,\mathrm{mm}$. All objective lenses are combined with *Linos Modular Focus*, the focal ratio is chosen to be $F = 8$.

B.2 Contrasts Measured with the USAF Resolution Target

Figure B.2 shows the histograms of the contrast values $\mathcal{C}$ obtained from 25 measurements of the USAF resolution target (see Sec. 7.1.4) for different line widths l.

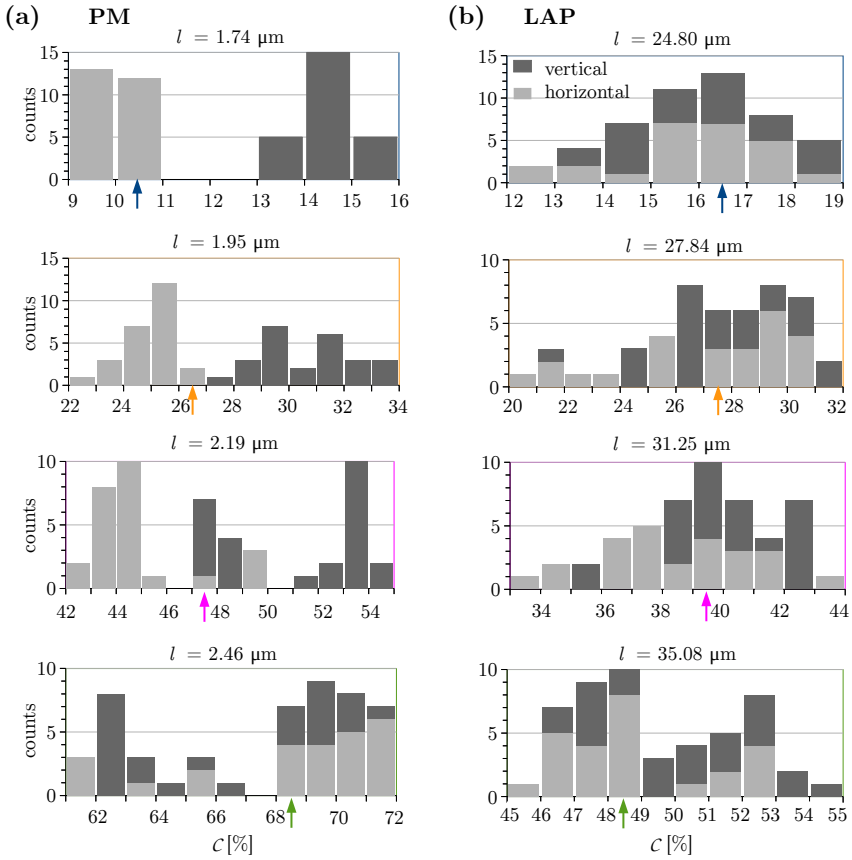

Fig. B.2: Histograms of the contrasts $\mathcal{C}$ obtained from 25 measurements of the USAF resolution target with the PM and the LAP (see Sec. 7.1.4). The contrasts were computed for different line widths l from the horizontal and vertical line profiles of the transmittance images (cf. Fig. 7.5). The arrows mark the columns that contain the median contrast values $\tilde{\mathcal{C}}$ (cf. Fig. 7.6b).

For small line widths in the PM, the vertical line profiles yield larger contrast values than the horizontal line profiles. One possible explanation is that the detector pixels in the camera of the PM are not identical in construction in the x- and y-direction and that this difference becomes visible for structures (line widths) of this size. However, when modeling the optical resolution of the imaging systems for the FDTD simulations (see Sec. 10.1.3), the lateral resolution is assumed to be the same in the horizontal and vertical direction. Therefore, all contrast values (derived from horizontal and vertical line profiles) were considered when comparing simulation and measurement.

B.3 Characterization of the Filter Properties in the LAP

This section describes how the filter properties of the LAP described in Sec. 7.2 were determined. It has previously been published in Menzel *et al.* (2017) [3] Appx. A.

B.3.1 Polarization-Independent Inhomogeneities

To study the polarization-independent inhomogeneities of the LAP (see Sec. 7.2.1), images of the light source and each filter were acquired in separate measurements.[1] For all measurements, the same exposure time was used.

As the effects of light source and camera cannot be separated, they were investigated conjointly. To determine the inhomogeneities caused by an inhomogeneous illumination and a varying sensitivity of the camera pixels, all filters were removed from the setup and an image of the light source was acquired. The photon noise was reduced by repeating the measurement 50 times and averaging the intensity for each image pixel.

The filter inhomogeneities (i. e. the inhomogeneous light absorption of the polymer foils) were measured separately for each filter by removing the other filters from the imaging system and rotating the filter by 18 discrete rotation angles in counter-clockwise direction. To reduce photon noise, each measurement was repeated 20 times. To separate the inhomogeneities caused by light source and camera from the inhomogeneities of the filters, every acquired filter image was divided by the averaged image of the light source. Any remaining pixelated structure was compensated by applying a Gaussian filter with an adequate kernel size. To avoid an influence of a temporal light intensity change of the different LED diodes, the measurement of the light source (as described above) was performed just before every filter measurement.

To separate the light attenuation induced by the filter inhomogeneities from the light attenuation induced by polarization effects (e. g. a partially polarized light source), the images of each image series ($\rho = \{0°, 10°, \ldots, 170°\}$) were digitally rotated in clockwise direction by the corresponding rotation angle ρ so that all images have the same virtual angle position ($\rho = 0°$). For this purpose, the rotation center of the images was determined by identifying in each image series the point that is rotationally invariant. Then, the images were cropped to a circular region around the determined rotation center with a maximum possible diameter of 2914 px and the images were rotated by applying a bilinear interpolation. The resulting 18 images were averaged pixel-wise for each image series.

As a measure for the inhomogeneities of light source and filters, the maximum and minimum intensity values of the averaged images were determined and the image contrast was computed via: $\mathcal{C} = (I_{\max} - I_{\min})/(I_{\max} + I_{\min})$, respectively. The average transmittance of the filters was computed via: $\tau = (I_{\max} + I_{\min})/2$. Note that $I_{\max}$ and $I_{\min}$ are here the maximum and minimum intensity values of the image and should not be confused with the maximum and minimum transmitted light intensities observed in a DI measurement.

It has been observed that a pixelated structure remains in the background when dividing the filter images by the image of the light source. To compensate for this effect, a Gaussian blur was applied to the normalized images with $\sigma = 10\,\mathrm{px}$ (for polarizer and analyzer) and $\sigma = 5\,\mathrm{px}$ (for the retarder).

The resulting images and histograms of light source, polarizer, retarder, and analyzer are shown in Fig. 7.7.

[1] The measurements were performed by Julia Reckfort and Hasan Köse (INM-1, Forschungszentrum Jülich, Germany).

B.3.2 Polarization Properties

To study the polarization properties of the LAP (see Sec. 7.2.2), various filter measurements were performed and the resulting light intensity profiles were fitted by numerically computed intensity profiles to estimate the polarization parameters of the system.

In contrast to the polarization-independent inhomogeneities (Sec. 7.2.1 and Appx. B.3.1), a pixel-wise determination of the polarization parameters is not possible because the polarization effects are non-multiplicative and influence each other. For this reason, the polarization properties of the optical elements could only be determined as an average over the field of view. In principle, the polarization properties could be determined pixel-wise by using a high-quality reference (light source or filters). However, high-quality filters of comparable sizes are commercially not available and illuminating such large-area filters with a highly polarized light source (e. g. laser) is not possible with reasonable experimental effort.

1) Filter Measurements: The filter measurements were performed using different combinations of polarizer, retarder, and analyzer.[2] Some of the filters were rotated by discrete rotation angles $\rho = \{0°, 10°, \ldots, 170°\}$, while other filters were kept at a fixed angle position. Table B.1 lists all executed measurements and the respective angle positions of the filters.

	Polarizer: $P_x(\xi = \rho)$	Retarder: $\Lambda(\xi = \rho - 45°)$	Analyzer: $P_y(\xi = \rho + 90°)$
P_x	$\rho = \{0°, 10°, \ldots, 170°\}$	–	–
$P_x\, P_y$	$\rho = \{0°, 10°, \ldots, 170°\}$	–	$\rho = \{270°, 280°, \ldots, 90°\}$
$P_x\, \Lambda$	$\rho = \{0°, 10°, \ldots, 170°\}$	$\rho = \{0°, 10°, \ldots, 170°\}$	–
$\Lambda\, P_y$	–	$\rho = \{0°, 10°, \ldots, 170°\}$	$\rho = \{270°, 280°, \ldots, 90°\}$
$\Lambda\, P_y(270°)$	–	$\rho = \{0°, 10°, \ldots, 170°\}$	$\rho = 270°$
$P_x\, \Lambda(0°)$	$\rho = \{0°, 10°, \ldots, 170°\}$	$\rho = 0°$	–
$P_x\, \Lambda(10°)$	$\rho = \{0°, 10°, \ldots, 170°\}$	$\rho = 10°$	–
$P_x\, \Lambda(30°)$	$\rho = \{0°, 10°, \ldots, 170°\}$	$\rho = 30°$	–
$P_x\, \Lambda(60°)$	$\rho = \{0°, 10°, \ldots, 170°\}$	$\rho = 60°$	–
$P_x\, \Lambda(80°)$	$\rho = \{0°, 10°, \ldots, 170°\}$	$\rho = 80°$	–
$\Lambda(0°)\, P_y$	–	$\rho = 0°$	$\rho = \{270°, 280°, \ldots, 90°\}$
$\Lambda(10°)\, P_y$	–	$\rho = 10°$	$\rho = \{270°, 280°, \ldots, 90°\}$
$\Lambda(30°)\, P_y$	–	$\rho = 30°$	$\rho = \{270°, 280°, \ldots, 90°\}$
$\Lambda(60°)\, P_y$	–	$\rho = 60°$	$\rho = \{270°, 280°, \ldots, 90°\}$
$\Lambda(80°)\, P_y$	–	$\rho = 80°$	$\rho = \{270°, 280°, \ldots, 90°\}$
$P_x(0°)\, P_y$	$\rho = 0°$	–	$\rho = \{270°, 280°, \ldots, 90°\}$
$P_x\, P_y(270°)$	$\rho = \{0°, 10°, \ldots, 170°\}$	–	$\rho = 270°$
$P_x(0°)\, \Lambda\, P_y(270°)$	$\rho = 0°$	$\rho = \{0°, 10°, \ldots, 170°\}$	$\rho = 270°$

Tab. B.1: Configuration of the filter measurements to determine the polarization properties of the optical components: The angle position ξ of the filters (polarizer/retarder/analyzer) is defined in terms of the rotation angle ρ as described in Sec. 4.4.

All filter measurements were repeated three times, averaged, and divided by the (averaged) image of the light source, which was recorded 50 times before every filter measurement. To avoid fringe effects from absorbing elements at the image border, the intensity was averaged over a circular region with a diameter of 2914 px around the rotation center of the filters for each rotation angle ρ, and the standard deviation $\sigma(\rho)$ was

[2] The measurements were performed by Julia Reckfort and Hasan Köse (INM-1, Forschungszentrum Jülich, Germany).

determined. The resulting intensity values $I(\rho)$ were divided by the averaged intensity $\overline{I}$ over all rotation angles. As the intensities were averaged over the rotation center, the polarization-independent inhomogeneities (described in Sec. 7.2.1) add the same attenuation to the signal for each rotation angle and could therefore be neglected when computing the normalized light intensity profiles.

2) Fitting of Polarization Parameters: As the polarization properties of light source and camera are unknown, they were modeled as generalized, normalized Stokes vectors ($\vec{S}_\mathrm{L}$ and $\vec{S}_\mathrm{c}$) as defined in Eq. (2.55) with $I = 1$:

$$\vec{S}_\mathrm{L} = \begin{pmatrix} 1 \\ p_\mathrm{L}\ \cos(2\,\psi_\mathrm{L})\ \cos(2\,\chi_\mathrm{L}) \\ p_\mathrm{L}\ \sin(2\,\psi_\mathrm{L})\ \cos(2\,\chi_\mathrm{L}) \\ p_\mathrm{L}\ \sin(2\,\chi_\mathrm{L}) \end{pmatrix}, \quad \vec{S}_\mathrm{c} = \begin{pmatrix} 1 \\ p_\mathrm{c}\ \cos(2\,\psi_\mathrm{c})\ \cos(2\,\chi_\mathrm{c}) \\ p_\mathrm{c}\ \sin(2\,\psi_\mathrm{c})\ \cos(2\,\chi_\mathrm{c}) \\ p_\mathrm{c}\ \sin(2\,\chi_\mathrm{c}) \end{pmatrix}. \tag{B.1}$$

The filters (polarizer, retarder, analyzer) were described by the Müller matrices (P_x, Λ, P_y) as defined in Eqs. (4.3), (4.4) and (4.6). To enable a direct comparison with the measured normalized light intensity profiles, the average transmittance of each optical element was set to one ($\tau_\mathrm{x} = \tau_\mathrm{y} = \tau_\Lambda = 1$).

By multiplying the Stokes vectors with the corresponding Müller matrices (using the rotation angles specified in Tab. B.1) and evaluating the first entry of the resulting Stokes vectors, the transmitted light intensity was computed for each filter measurement. The computations were performed using distributed computing on desktop computers consuming about 500 core hours.[3]

The modeled intensity profiles $I_\mathrm{model}(\rho)$ were fitted to the measured intensity profiles $I_\mathrm{meas}(\rho)$ for each rotation angle ($\rho_j = \{0°, 10°, \ldots, 170°\}$) by minimizing the sum of squared differences Δ_Σ between the measured and the modeled intensity profiles. To account for random errors (e. g. read-out noise or a varying sensitivity between camera pixels), the differences were normalized by the determined standard deviation $\sigma(\rho_j)$. To ensure a fair weighting of high and low signal amplitudes, the differences were divided by the measured signal amplitude ($I_\mathrm{meas,max} - I_\mathrm{meas,min}$) for each of the k filter measurements defined in Tab. B.1:

$$\Delta_\Sigma \equiv \sum_{j,k} \left[\frac{\big(I_\mathrm{meas}(\rho_j) - I_\mathrm{model}(\rho_j)\big)^2}{\sigma^2(\rho_j)\ \big(I_\mathrm{meas,max} - I_\mathrm{meas,min}\big)^2} \right]_k . \tag{B.2}$$

To find the global minimum of Δ_Σ, the sum of squared differences was minimized numerically using a differential evolution algorithm [193]. The Stokes parameters of light source $\{p_\mathrm{L}, \psi_\mathrm{L}, \chi_\mathrm{L}\}$ and camera $\{p_\mathrm{c}, \psi_\mathrm{c}, \chi_\mathrm{c}\}$ were fitted for $D_\mathrm{x}, D_\mathrm{y} = \{0.9,\ 0.905,\ \ldots,\ 1\}$ and $\gamma = \{0.4\,\pi, 0.405\,\pi, \ldots, 0.6\,\pi\}$. The parameters D_x, D_y, and γ were not fitted to reduce computing time and to ensure a proper convergence of the algorithm. The parameter ranges were chosen such that the whole range of possible values was enclosed.

Figure B.3 shows the (normalized) light intensity profiles of the filter measurements (solid curves) as well as the modeled light intensity profiles (dashed curves) that were computed for each filter measurement from the determined polarization parameters for which the sum of squared differences Δ_Σ is minimized (see best fit in Tab. B.2). The relative difference between the curves is mostly less than 5 % of the measured signal amplitude, which demonstrates that the fit of the polarization parameters is good.

[3] The computations were performed by Daniel Weigand (Institute of Quantum Information, RWTH Aachen University, Germany).

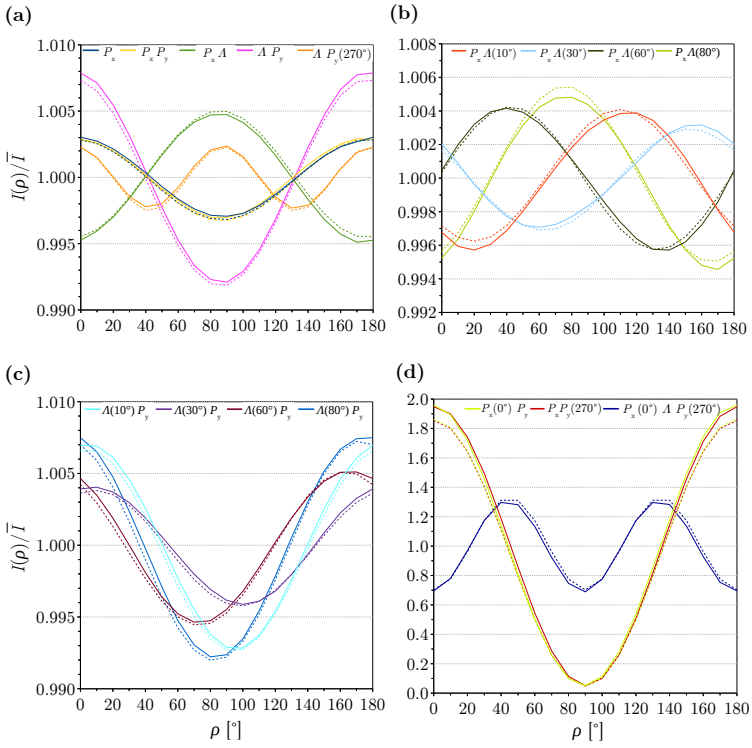

Fig. B.3: Normalized light intensity profiles: The solid curves show the profiles obtained from the filter measurements described in Tab. B.1. The dashed curves show the modeled profiles computed from the polarization parameters defined in Tab. B.2, first row. The angle ρ is the rotation angle of the rotating filters in the measurement. The figure has been published in Menzel *et al.* (2017) [3] Fig. 13.

Table B.2 shows the computed polarization parameters for the best fit ($\Delta_{\Sigma,\min} = 2138.52$) as well as the average, the standard deviation, and the relative standard deviation (divided by the average) of the polarization parameters belonging to the best 20 fits (with $\Delta_\Sigma = 2138.52, \ldots, 2154.68$). The relative standard deviation is mostly less than 1 %, except for χ_L which is consistent with zero. This demonstrates that the fitted polarization parameters are stable and can be used as estimates to describe the polarization properties of light source, filters, and camera.

	D_x	D_y	γ / π	p_L	ψ_L	χ_L	p_c	ψ_c	χ_c
Best Fit	0.98000	0.97000	0.49000	0.00513	1.49472	-5×10^{-5}	0.00822	3.07458	-0.03068
Average	0.98075	0.96900	0.49000	0.00513	1.49469	3×10^{-6}	0.00822	3.07457	-0.03065
Std. Dev.	0.00438	0.00369	0.00284	0.00006	0.00011	8×10^{-5}	0.00006	0.00004	0.00032
Rel. Std. Dev.	0.00446	0.00381	0.00579	0.01234	0.00007	32	0.00738	0.00001	0.01053

Tab. B.2: Fitted polarization properties of filters, light source, and camera: The parameters in the first row minimize the sum of squared differences ($\Delta_{\Sigma,\min} = 2138.52$). The other parameters show the average, standard deviation, and relative standard deviation (divided by the average) for the best 20 fits with $\Delta_\Sigma = 2138.52, \ldots, 2154.68$.

Appendix C

Supplementary Material for Diattenuation Studies

This chapter contains additional material for the diattenuation studies presented in Chap. 9. Appendices C.1 to C.3 have been published in Menzel *et al.* (2017) [3] Secs. 4, B, and D.

C.1 Correction of the 3D-PLI Fiber Orientations

The tissue diattenuation and the non-ideal filter properties influence the fiber orientations derived from a 3D-PLI measurement (cf. Sec. 4.4.1). If the diattenuation of polarizer and analyzer (D_x and D_y), the retardance of the quarter-wave retarder (γ), and the tissue diattenuation (D) were known pixel-wise, the actual retardance δ of the brain tissue could be computed from the Fourier coefficients in Eqs. (4.10) to (4.12):

$$\delta = \arccos\left(\frac{E \pm \sqrt{E^2 + 4(F-G)(H-G)}}{2(G-H)}\right), \tag{C.1}$$

$$E \equiv \frac{a_\mathrm{2P}^2 + b_\mathrm{2P}^2}{a_\mathrm{0P}^2}\,\cos\gamma\;D_\mathrm{x}\,D_\mathrm{y}\,\sqrt{1-D^2}\,\left(1-\frac{1}{2}\cos\gamma\;D_\mathrm{x}\,D_\mathrm{y}\right), \tag{C.2}$$

$$F \equiv \frac{a_\mathrm{2P}^2 + b_\mathrm{2P}^2}{a_\mathrm{0P}^2}\left(1-\frac{1}{2}\cos\gamma\;D_\mathrm{x}\,D_\mathrm{y}\right)^2 - D^2\big(\cos\gamma\;D_\mathrm{x} - D_\mathrm{y}\big)^2, \tag{C.3}$$

$$G \equiv \sin^2\gamma\;D_\mathrm{x}^2\,D_\mathrm{y}^2\,\big(1-D^2\big), \tag{C.4}$$

$$H \equiv -\frac{a_\mathrm{2P}^2 + b_\mathrm{2P}^2}{4\,a_\mathrm{0P}^2}\,\cos^2\gamma\;D_\mathrm{x}^2\,D_\mathrm{y}^2\,\big(1-D^2\big). \tag{C.5}$$

Using the determined value for δ, the actual fiber inclination angle α could be computed via Eqs. (3.8) and (4.20). The actual fiber direction angle φ could be computed using δ and Eqs. (4.11) and (4.12). As a pixel-wise measurement of the filter properties is not feasible (see Sec. 7.2.2), this procedure is not used in the standard 3D-PLI analysis.

C.2 Computation of the Diattenuation Impact on the Polarimetric Measurements

To enable predictions and error estimates for the experimental diattenuation studies in Secs. 9.2 and 9.3, a numerical study was carried out to investigate the influence

of the tissue diattenuation and the non-ideal polarization properties of the LAP on the measured fiber orientation and diattenuation. The main results are presented in Sec. 9.1. This section gives more detailed information on how the numerical study was performed and provides error estimates for all parameters (derived fiber direction, derived fiber inclination, and measured diattenuation) for the whole range of actual fiber orientations and tissue diattenuations. The content of this study has been published in Menzel *et al.* (2017) [3] Sec. 4.

For each measurement setup (3D-PLI, XP, DI), the expected transmitted light intensities were numerically computed by multiplying the corresponding Müller matrices and Stokes vectors (see Sec. 4.4) and considering the polarization properties of the LAP defined in Sec. 7.2.2 ($D_\mathrm{x} = 0.98$, $D_\mathrm{y} = 0.97$, $\gamma = 0.49\,\pi$; $\vec{S}_\mathrm{L}, \vec{S}_\mathrm{c} \neq \vec{S}_\mathrm{unpol}$). For reasons of simplification, the average transmittance of each filter and the intensity of the light source were set to one ($\tau_\mathrm{x} = \tau_\mathrm{y} = \tau_\Lambda = \tau = I_0 = 1$). To account for image calibration (see Sec. 4.3), the resulting intensity profiles of the 3D-PLI and DI measurements were divided by the intensity profiles obtained from a matrix multiplication without tissue matrix M. The image calibration for the XP measurement uses transmittance images of the filters and the light source (cf. Sec. 7.2.1) and is already taken into account by setting the average transmittances and the intensity of the light source to one.

The numerically computed intensity profiles were analyzed as described in Secs. 4.4.1 to 4.4.3, respectively, and the direction angles (φ_P, φ_X, φ_D), the inclination angle (α_P), and the measured diattenuation ($|\mathscr{D}|$) were computed from the determined Fourier coefficients. The inclination angle α_P was derived from δ_P assuming that horizontal fibers (with $\alpha = 0°$) act as an ideal quarter-wave retarder, i. e. $\delta_\mathrm{P} = (\pi/2)\cos^2\alpha_\mathrm{P}$ (cf. Eq. (3.8)). To account for the correction with the maximum retardation value, the modified inclination angle $\tilde{\alpha}_\mathrm{P}$ was computed using Eq. (4.20) with $r_\mathrm{P,max} = \pi/2$.

The impact of the non-ideal polarization properties was estimated by comparing the derived parameters (fiber orientation and diattenuation) to the actual fiber orientation (φ, α) and tissue diattenuation D.

The resulting curves are shown in Appx. C.2.1 to C.2.3. To enable a comparison with the experimental studies in Secs. 9.2 and 9.3, a special focus was placed on the range $|D| \leq 5\,\%$.

As the polarization properties of light source, camera, and filters could only be determined as an average over the field of view (see Sec. 7.2.2 and Appx. B.3.2), local deviations of D_x, D_y, γ, $\vec{S}_\mathrm{L}$, and $\vec{S}_\mathrm{c}$ were not included in the computation. When comparing the numerical results to the results of the experimental study, the curves should therefore only be considered as a reference.

For steep fibers, large deviations of the measured direction angle have only a very small influence on the overall fiber orientation vector and the tissue diattenuation is expected to be very small. Therefore, the curves for steep fibers should only be considered for small diattenuation values. For perfectly vertical fibers, the direction angle is not defined and the tissue diattenuation is expected to be zero due to the radial symmetry. The curves for $\alpha = 90°$ are therefore limiting cases and only shown for reasons of completeness.

C.2.1 Impact on the 3D-PLI Measurement

Figure C.1 shows the predicted impact of the non-ideal polarization properties of the LAP on the measured inclination angles α_P, $\tilde{\alpha}_\mathrm{P}$, and the direction angle φ_P for different tissue diattenuations $D \geq 0$ and fiber inclinations α. As the curves are mostly independent of φ, the curves are only shown for an assumed fiber direction $\varphi = 0°$. For $D < 0$,

the curves for $(\alpha_P - \alpha)$ are mirrored about the y-axis, the curves for $(\varphi_P - \varphi)$ are rotated 180° around the origin.

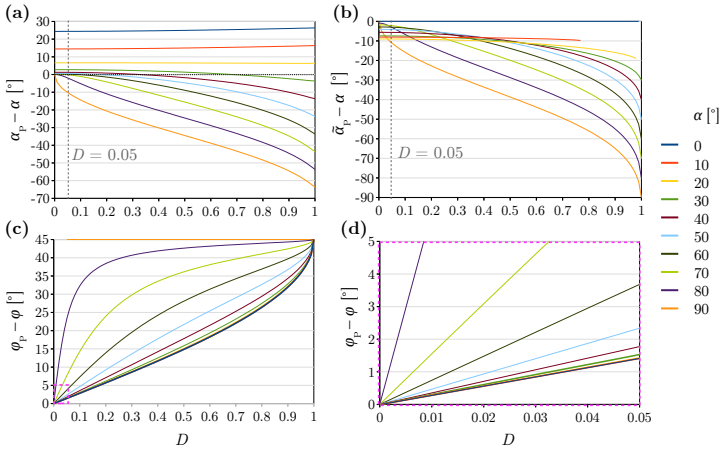

Fig. C.1: Predicted impact of the non-ideal polarization properties of the LAP (specified in Eqs. (7.5) and (7.6)) on the fiber orientation (φ_P, α_P) derived from a 3D-PLI measurement (see Sec. 4.4.1). The plots show the difference between (φ_P, α_P) and the actual fiber orientation (φ, α) for different α and tissue diattenuations $D \geq 0$. In addition to the inclination angle $\alpha_P = \arccos(\sqrt{2\,\delta_P/\pi})$, the modified inclination angle $\tilde{\alpha}_P$ was computed from Eq. (4.20) with $r_{P,max} = \pi/2$. The fiber direction was assumed to be $\varphi = 0°$: **(a)** Difference between α_P and α. **(b)** Difference between $\tilde{\alpha}_P$ and α. **(c)** Difference between φ_P and φ. **(d)** Enlarged view of (c) for $D \leq 5\,\%$. For $D < 0$, the curves for $(\alpha_P - \alpha)$ are mirrored about the y-axis, the curves for $(\varphi_P - \varphi)$ are rotated 180° around the origin. The figure has been published in Menzel *et al.* (2017) [3] Fig. 3.

Figure C.1a shows that for fibers with smaller inclination angles ($\alpha < 30°$), the measured inclination angle α_P is overestimated ($\alpha_P > \alpha$) for all tissue diattenuations. For fibers with larger inclination angles ($\alpha > 30°$), the measured inclination angle is underestimated ($\alpha_P < \alpha$) and the predicted difference between α and α_P increases with increasing absolute tissue diattenuation. For $|D| \leq 5\,\%$, the maximum deviation from the actual fiber inclination is predicted to be about 25° for fibers with $\alpha = 0°$. After correcting with the maximum retardation value, the measured inclination angle $\tilde{\alpha}_P$ is underestimated ($\tilde{\alpha}_P < \alpha$) for all inclination angles (see Fig. C.1b). The difference between α and $\tilde{\alpha}_P$ increases with increasing absolute tissue diattenuation. For $|D| \leq 5\,\%$, the predicted difference is less than 11.2° for all inclinations < 90°. Thus, the correction with the maximum retardation value improves the determination of the inclination angle α_P and should be included in the 3D-PLI analysis.

Figure C.1c shows the predicted influence of the non-ideal system components and the tissue diattenuation on the measured direction angle φ_P. The measured direction angle is expected to be overestimated ($\varphi_P > \varphi$) for all $D > 0$ and underestimated ($\varphi_P < \varphi$) for all $D < 0$. The absolute difference between φ_P and φ increases with increasing absolute tissue diattenuation and fiber inclination. The maximum difference is 45° for $|D| = 1$ or $\alpha = 90°$. For small tissue diattenuations $|D| \leq 5\,\%$, the absolute difference between φ_P and φ increases linearly with $|D|$ (see Fig. C.1d). For fibers with $\alpha \leq 60°$, the maximum absolute difference is less than 3.7°. For steep fibers, the diattenuation

values are expected to be small, resulting in even smaller differences. The impact of the diattenuation is therefore expected to be negligible in the 3D-PLI signal analysis.

C.2.2 Impact on the XP Measurement

Figure C.2 shows the predicted impact of the non-ideal polarization properties of the LAP on the measured direction angle φ_X for different tissue diattenuations $D \geq 0$ and fiber inclinations α. The actual fiber direction was set to $\varphi = 45°$ such that $|\varphi_X - \varphi|$ becomes maximal. For $D < 0$, the curves are rotated 180° around the origin.

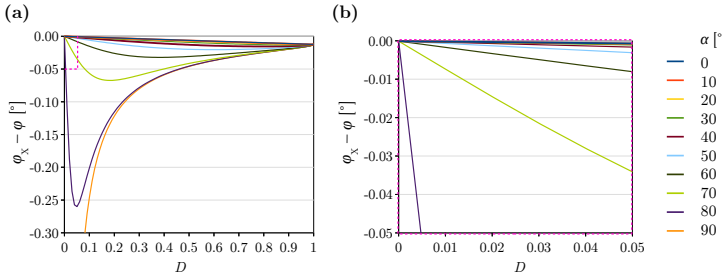

Fig. C.2: Predicted impact of the non-ideal polarization properties of the LAP (specified in Eqs. (7.5) and (7.6)) on the direction angle φ_X derived from an XP measurement (see Sec. 4.4.2). The plots show the difference between φ_X and the actual fiber direction φ plotted against the tissue diattenuation $D \geq 0$ for different fiber inclination angles α. The actual fiber direction was set to $\varphi = 45°$ such that $|\varphi_X - \varphi|$ becomes maximal. **(a)** Difference between φ_X and φ. **(b)** Enlarged view of (a) for $D \leq 5\,\%$. For $D < 0$, the curves are rotated 180° around the origin. The figure has been published in Menzel *et al.* (2017) [3] Fig. 4.

As can be seen in Fig. C.2a, the direction angle φ_X determined from the XP measurement is expected to deviate only slightly from the actual fiber direction φ for all tissue diattenuations and inclinations $< 90°$. For $\alpha \leq 70°$, the difference is less than 0.08°. For $|D| \leq 5\,\%$, it is even less than 0.035° (see Fig. C.2b). As the direction angle φ_X is nearly independent from the diattenuation of the brain tissue and from the polarization properties of the optical components, it is a good reference value for the actual fiber direction φ.

C.2.3 Impact on the DI Measurement

Figure C.3 shows the predicted impact of the non-ideal polarization properties of the LAP on the measured diattenuation $|\mathscr{D}|$ and direction angle φ_D for different tissue diattenuations $D \geq 0$, fiber directions φ, and inclinations α. For $D < 0$, the curves for $(\varphi_D - \varphi)$ are rotated 180° around the origin and shifted by +90° in the y-direction.

As can be seen in Fig. C.3a, the measured diattenuation $|\mathscr{D}|$ depends on the fiber orientation (φ, α) as well as on the diattenuation D of the brain tissue. For regions with no tissue diattenuation (dark blue curve), the measured diattenuation reaches values up to $|\mathscr{D}| = 0.85\,\%$ (for $\alpha = 0°$ and $\varphi \approx 41°$). The measured diattenuation is mostly overestimated for $|D| < 4\,\%$. For larger tissue diattenuations or steep fibers, $|\mathscr{D}|$ is slightly underestimated. For $1\,\% \leq |D| \leq 5\,\%$, the difference between $|\mathscr{D}|$ and $|D|$ lies between $-0.1\,\%$ and $+0.3\,\%$ for all fiber inclinations (see Fig. C.3b). To ensure that the measured diattenuation mostly corresponds to the actual tissue diattenuation, only values $|\mathscr{D}| > 1\,\%$ should be considered.

The measured direction angle φ_D (for $D > 0$) or $\varphi_D - 90°$ (for $D < 0$) corresponds to the actual fiber direction φ for steep fibers, large tissue diattenuations, or $\varphi \approx 88°(\pm 90°)$ (see Fig. C.3c). The maximum absolute difference decreases with increasing absolute tissue diattenuation (see Fig. C.3d): For regions with $|D| = 1\,\%$, the maximum absolute difference is about 21° (for $\alpha = 0°$, $\varphi \approx 41°$). For regions with $|D| = 5\,\%$, it is only about 5°.

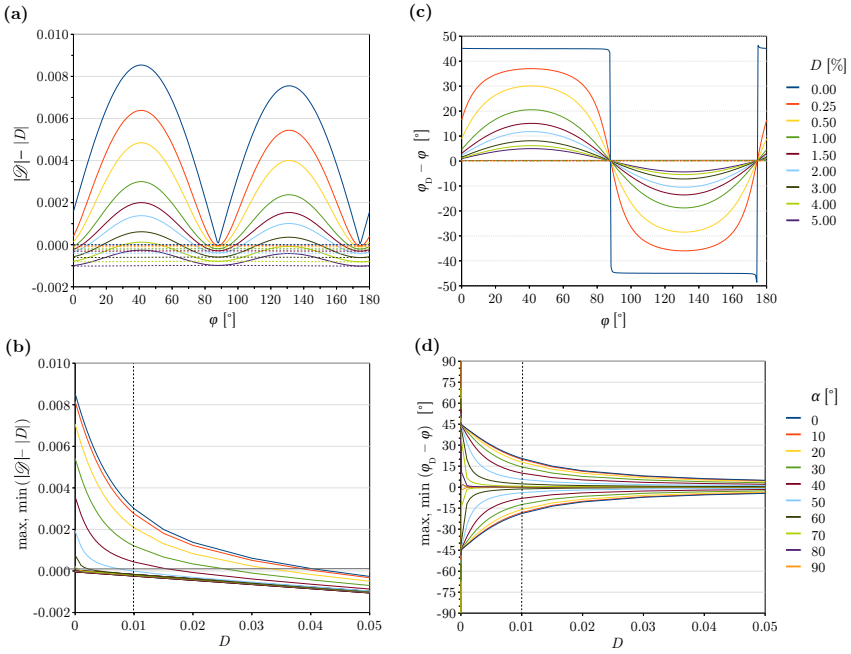

Fig. C.3: Predicted impact of the non-ideal polarization properties of the LAP (specified in Eqs. (7.5) and (7.6)) on the diattenuation $|\mathscr{D}|$ and the direction angle φ_D derived from a DI measurement (see Sec. 4.4.3): **(a)** Difference between $|\mathscr{D}|$ and the strength of the actual tissue diattenuation $|D|$ plotted against the fiber direction φ for different $D \geq 0$. The solid curves correspond to horizontal fibers with inclination $\alpha = 0°$, the dashed curves to vertical fibers with $\alpha = 90°$. The curves for fibers with intermediate inclination angles are not shown and lie in between. **(b)** Maximum difference (pos./neg.) between $|\mathscr{D}|$ and $|D|$ plotted against D for different α. Note that the values $\min(|\mathscr{D}| - |D|)$ correspond to the bottom curve for all α. **(c)** Difference between φ_D and φ plotted against φ for different D. The solid curves correspond to horizontal fibers with inclination $\alpha = 0°$, the curves belonging to vertical fibers with $\alpha = 90°$ and $D > 0$ all lie along the zero line. The curves for fibers with intermediate inclination angles are not shown and lie in between. **(d)** Maximum difference (pos./neg.) between φ_D and φ plotted against D for different α. For $D < 0$, the curves for $(\varphi_D - \varphi)$ are rotated 180° around the origin and shifted by +90°. The figure has been published in Menzel *et al.* (2017) [3] Fig. 5.

C.3 Uncertainties of DI and 3D-PLI Direction Angles as a Function of Retardation

Figure C.4 shows the uncertainties of the direction angles φ_D and φ_P plotted against the measured retardation r_P for regions with a measured diattenuation $|\mathscr{D}| > 1\,\%$. The direction angle φ_X is used as a reference value for the actual fiber direction φ. The direction angles $\{\varphi_D, \varphi_P, \varphi_X\}$ and the retardation were derived from 3D-PLI, XP, and DI measurements with the LAP (as described in Secs. 4.4.1 to 4.4.3) for the five sagittal rat brain sections investigated in Sec. 9.2.1. The content of this section has been published in Menzel *et al.* (2017) [3] Sec. D.

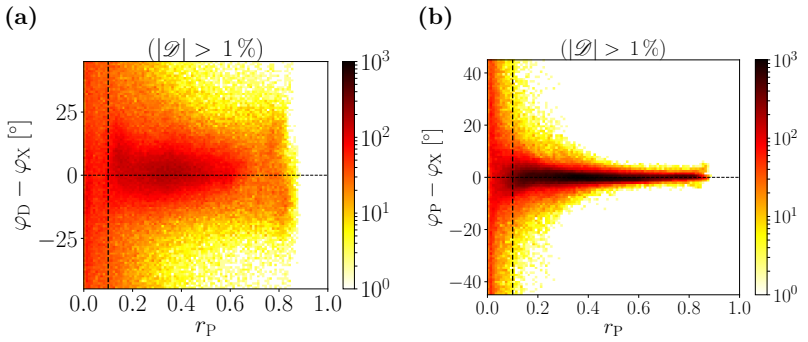

Fig. C.4: (a) 2D histogram showing the difference between the direction angles φ_D and φ_X derived from DI and XP measurements of five sagittal rat brain sections measured one day after tissue embedding (see Sec. 9.2.1) plotted against the measured retardation r_P. **(b)** 2D histogram showing the difference between the direction angles φ_P derived from 3D-PLI measurements of the rat brain sections and φ_X plotted against r_P. The vertical dashed lines mark the regions ($r_P < 0.1$) for which the signal-to-noise ratio of φ_X is low. The number of bins in the 2D histograms is 100 for both axes, respectively. This figure has been published in Menzel *et al.* (2017) [3] Fig. 15.

The distributions of $(\varphi_D - \varphi_X)$ and $(\varphi_P - \varphi_X)$ are broad for $r_P < 0.1$ (marked by the vertical dashed lines). This behavior can be explained by the low signal-to-noise ratio of φ_X for small retardation values: due to the 90°-orientation of the polarizers in the XP measurement, the transmitted light intensity approaches zero for small retardations (cf. Fig. 4.4e). For larger retardation values, the signal-to-noise ratio of φ_X increases and the distribution of φ_D appears to be mostly independent of the retardation (it depends more on the diattenuation, see Fig. 9.3a). The distribution of φ_P is much narrower than for φ_D (in regions with $r_P > 0.1$) and also mostly independent of the retardation.

Based on these observations, $(\varphi_D - \varphi_X)$ and $(\varphi_P - \varphi_X)$ were only evaluated in regions with retardation values $r_P > 0.1$ to avoid misinterpretation.

C.4 Diattenuation Images of Five Sagittal Rat Brain Sections

Figure C.5 shows the diattenuation images of the five sagittal rat brain sections investigated in Sec. 9.2.1. The strength of the diattenuation signal $|\mathscr{D}|$ and the direction angles φ_D and φ_P were determined from DI and 3D-PLI measurements with the LAP as described in Secs. 4.4.1 and 4.4.3. Depending on the angle range of $(\varphi_D - \varphi_P)$ defined in

Fig. 9.2b, two different types of diattenuation are distinguished: D^+ (marked in green) and D^- (marked in magenta), see Fig. C.5b.

The measured diattenuation is relatively small and shows similar patterns for the different brain sections. The type of diattenuation is specific for certain brain regions and consistent across the investigated brain sections: some regions (ac, Cb, cu, opt, fi, part of cc) show diattenuation of type D^+, while other regions (aci, CPu, part of cg) show diattenuation of type D^- (refer to Figs. 8.1a and 9.4a for anatomical labels).

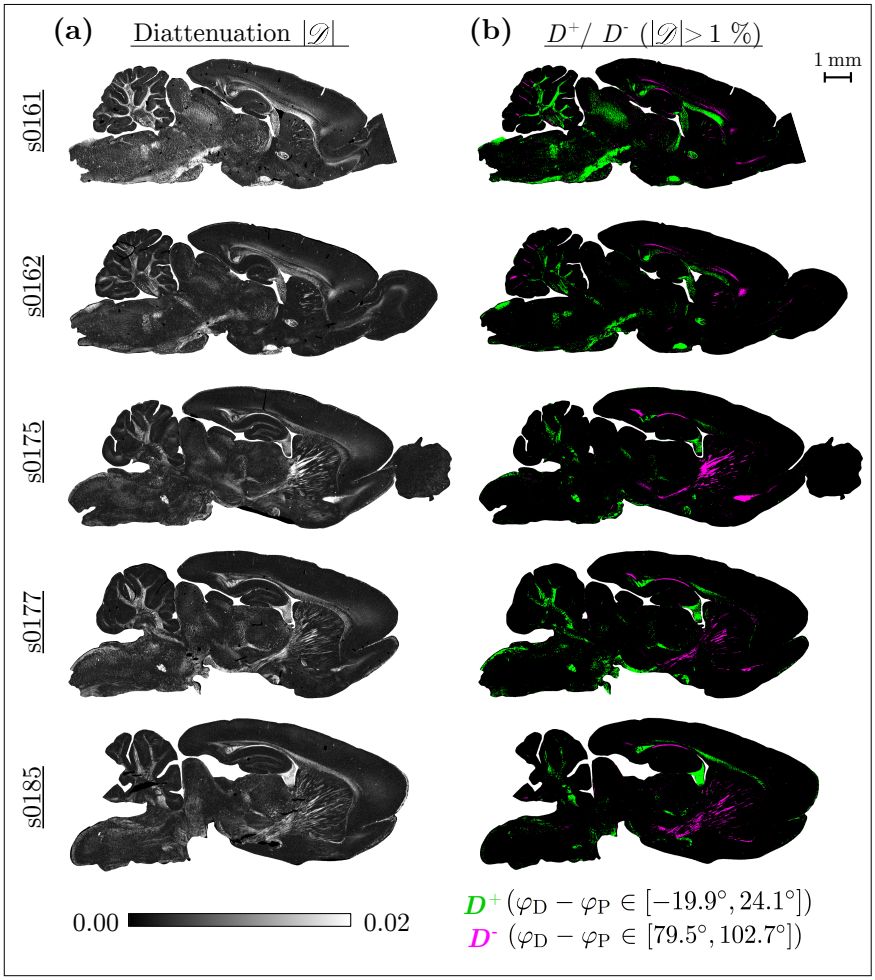

Fig. C.5: Diattenuation images of the five sagittal rat brain sections investigated in Sec. 9.2.1 (measured one day after tissue embedding with an effective object-space resolution of 14 µm/px): **(a)** The strength of the diattenuation signal $|\mathscr{D}|$ was determined from DI measurements with the LAP as described in Sec. 4.4.3. **(b)** Regions with $|\mathscr{D}| > 1\,\%$ that show diattenuation of type D^+ or D^- (cf. Sec. 9.2.1.1) were highlighted in green or magenta, respectively, corresponding to the angle ranges of $(\varphi_D - \varphi_P)$ defined in Fig. 9.2b. The colored images were adapted from Menzel *et al.* (2017) [3] Fig. 9.

Appendix D

Supplementary Material for FDTD Simulations

This chapter contains derivations, lengthly computations, and additional results for the FDTD simulation studies presented in Part IV.

D.1 Finite-Difference Approximation of Maxwell's Curl Equations

In this section, the finite-difference approximation (as described in Sec. 6.1) is shown exemplary for the x-component of the electric field (cf. [72] pp. 63–64).

Using Eqs. (6.3) and (6.4), the Maxwell equation (6.1) for the x-component evaluated at a point $\left((i+\frac{1}{2})\,\Delta x,\ j\,\Delta y,\ k\,\Delta z\right)$ in space and a point $\left((m+\frac{1}{2})\,\Delta t\right)$ in time can be written as:[1]

$$\frac{E_{\mathrm{x}}|_{i+\frac{1}{2},j,k}^{m+1} - E_{\mathrm{x}}|_{i+\frac{1}{2},j,k}^{m}}{\Delta t} = \frac{1}{\epsilon_{i+\frac{1}{2},j,k}} \left(\frac{H_{\mathrm{z}}|_{i+\frac{1}{2},j+\frac{1}{2},k}^{m+\frac{1}{2}} - H_{\mathrm{z}}|_{i+\frac{1}{2},j-\frac{1}{2},k}^{m+\frac{1}{2}}}{\Delta y} - \frac{H_{\mathrm{y}}|_{i+\frac{1}{2},j,k+\frac{1}{2}}^{m+\frac{1}{2}} - H_{\mathrm{y}}|_{i+\frac{1}{2},j,k-\frac{1}{2}}^{m+\frac{1}{2}}}{\Delta z} - J_{\text{source x}}|_{i+\frac{1}{2},j,k}^{m+\frac{1}{2}} - \sigma_{i+\frac{1}{2},j,k}\ E_{\mathrm{x}}|_{i+\frac{1}{2},j,k}^{m+\frac{1}{2}} \right) \tag{D.1}$$

As the electric field values are only stored at an integer time step m, the E_{x} values at time step $\left(m+\frac{1}{2}\right)$ are assumed to be the arithmetic average of the stored values of E_{x} at time step m and the yet-to-be-computed new values of E_{x} at time step $(m+1)$:

$$E_{\mathrm{x}}|_{i+\frac{1}{2},j,k}^{m+\frac{1}{2}} = \frac{E_{\mathrm{x}}|_{i+\frac{1}{2},j,k}^{m+1} + E_{\mathrm{x}}|_{i+\frac{1}{2},j,k}^{m}}{2}. \tag{D.2}$$

Substituting Eq. (D.2) into Eq. (D.1), collecting all terms with $E_{\mathrm{x}}|_{i+\frac{1}{2},j,k}^{m+1}$ and $E_{\mathrm{x}}|_{i+\frac{1}{2},j,k}^{m}$, and solving for $E_{\mathrm{x}}|_{i+\frac{1}{2},j,k}^{m+1}$ yields the explicit time-stepping expression for the x-component of the electric field (cf. [72] p. 64):

[1] For reasons of simplification, the index "e" of σ_{e} has been dropped.

$$E_{\mathrm{x}}\big|_{i+\frac{1}{2},j,k}^{m+1} = \left(\frac{1-\frac{\sigma_{i+\frac{1}{2},j,k}\Delta t}{2\epsilon_{i+\frac{1}{2},j,k}}}{1+\frac{\sigma_{i+\frac{1}{2},j,k}\Delta t}{2\epsilon_{i+\frac{1}{2},j,k}}}\right) E_{\mathrm{x}}\big|_{i+\frac{1}{2},j,k}^{m} + \left(\frac{\Delta t/\epsilon_{i+\frac{1}{2},j,k}}{1+\frac{\sigma_{i+\frac{1}{2},j,k}\Delta t}{2\epsilon_{i+\frac{1}{2},j,k}}}\right) \cdot \left(\frac{H_{\mathrm{z}}\big|_{i+\frac{1}{2},j+\frac{1}{2},k}^{m+\frac{1}{2}} - H_{\mathrm{z}}\big|_{i+\frac{1}{2},j-\frac{1}{2},k}^{m+\frac{1}{2}}}{\Delta y} - \frac{H_{\mathrm{y}}\big|_{i+\frac{1}{2},j,k+\frac{1}{2}}^{m+\frac{1}{2}} - H_{\mathrm{y}}\big|_{i+\frac{1}{2},j,k-\frac{1}{2}}^{m+\frac{1}{2}}}{\Delta z} - J_{\text{source x}}\big|_{i+\frac{1}{2},j,k}^{m+\frac{1}{2}}\right) \tag{D.3}$$

The expressions for the other electric and magnetic field components can be derived analogously. With this system of time-stepping expressions, the new value of the electric field component at time $(m+1)\,\Delta t$ at an arbitrary lattice point can be computed from its previous value at time $m\,\Delta t$ and from the previous values of the magnetic field components at time $\left(m+\frac{1}{2}\right)\Delta t$ at adjacent lattice points, and vice versa, provided that the electric and magnetic current sources are known.

D.2 Modeling Uniform Illumination

To model the incoherent and diffuse light source of the polarimeters, several simulation runs with different angles of incidence (φ, θ) were performed (see Sec. 10.1.1). The illumination of the sample in the measurement is approximately uniform, i. e. the angular distance Δ_θ between neighboring light rays is the same (see Fig. D.1).

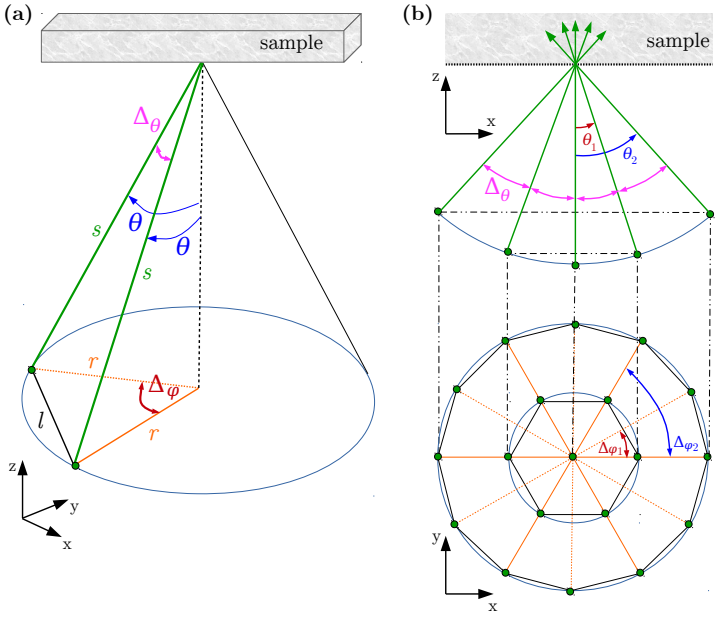

Fig. D.1: Uniform illumination of the light source: **(a)** 3D representation of two neighboring light rays (in green) with polar and azimuthal angular distances Δ_θ and Δ_φ. **(b)** 2D representation of several neighboring light rays (top: xz-plane, bottom: xy-plane)

For light incident at a certain polar angle θ, the corresponding azimuthal angular distance Δ_φ between two neighboring light rays can be computed as follows (using the notation defined in Fig. D.1a):

$$\sin\theta = \frac{r}{s} \tag{D.4}$$

$$\sin\left(\frac{\Delta_\theta}{2}\right) = \frac{l/2}{s} \tag{D.5}$$

$$\sin\left(\frac{\Delta_\varphi}{2}\right) = \frac{l/2}{r} \overset{(D.5)}{=} \frac{s}{r}\sin\left(\frac{\Delta_\theta}{2}\right) \tag{D.6}$$

$$\overset{(D.4)}{=} \frac{\sin(\Delta_\theta/2)}{\sin\theta} \tag{D.7}$$

$$\Leftrightarrow \quad \Delta_\varphi = 2\arcsin\left(\frac{\sin(\Delta_\theta/2)}{\sin\theta}\right). \tag{D.8}$$

D.3 Derivation of the Yee Cell Shift

The Maxwell Solver computes the electromagnetic field components on different positions of the Yee grid (see Fig. 6.1a). Before further processing the electric field vectors $\vec{E}_k(\vec{r},t)$, the vector components $E_{k,i}(\vec{r},t)$ need to be shifted to the middle of the corresponding Yee cell, respectively.

Consider a shift Δj in the direction $j \in \{x,y,z\}$: $j \mapsto j + \Delta j$:

$$\vec{k}\cdot\vec{r} = k_\mathrm{x}\,x + k_\mathrm{y}\,y + k_\mathrm{z}\,z \quad \mapsto \quad k_j\,\Delta j + \vec{k}\cdot\vec{r}. \tag{D.9}$$

Using Eq. (D.9) and trigonometric identities ($\cos(x+y) = \cos x\cos y - \sin x\sin y$, $\sin(x+y) = \sin x\cos y + \cos x\sin y$), the electric field vector components are transformed as:

$$E_{k,i}(\vec{r},t) = A_{k,i}\,\cos(\vec{k}\cdot\vec{r}-\omega t) - B_{k,i}\,\sin(\vec{k}\cdot\vec{r}-\omega t) \tag{D.10}$$

$$\begin{aligned}
\mapsto \quad \check{E}_{k,i}(\vec{r},t) &\overset{(D.9)}{=} A_{k,i}\,\cos\Big(k_j\,\Delta j + (\vec{k}\cdot\vec{r}-\omega t)\Big) - B_{k,i}\,\sin\Big(k_j\,\Delta j + (\vec{k}\cdot\vec{r}-\omega t)\Big) \\
&= \underbrace{\big(A_{k,i}\,\cos(k_j\,\Delta j) - B_{k,i}\,\sin(k_j\,\Delta j)\big)}_{\check{A}_{k,i}}\cos(\vec{k}\cdot\vec{r}-\omega t) \\
&\quad - \underbrace{\big(A_{k,i}\,\sin(k_j\,\Delta j) + B_{k,i}\,\cos(k_j\,\Delta j)\big)}_{\check{B}_{k,i}}\sin(\vec{k}\cdot\vec{r}-\omega t).
\end{aligned} \tag{D.11}$$

To shift the electric field components to the middle of the Yee cell, the following shifts are performed (cf. Fig. 6.1a):

$$E_{k,\mathrm{x}}(\vec{r},t): \quad y \mapsto y + \Delta y/2, \quad z \mapsto z + \Delta z/2, \tag{D.12}$$

$$E_{k,\mathrm{y}}(\vec{r},t): \quad x \mapsto x + \Delta x/2, \quad z \mapsto z + \Delta z/2, \tag{D.13}$$

$$E_{k,z}(\vec{r},t): \quad x \mapsto x + \Delta x/2, \quad y \mapsto y + \Delta y/2. \tag{D.14}$$

The resulting electric field vector is then given by:

$$\vec{E}'_k(\vec{r},t) = \vec{A}'_k\,\cos(\vec{k}\cdot\vec{r}-\omega t) - \vec{B}'_k\,\sin(\vec{k}\cdot\vec{r}-\omega t), \tag{D.15}$$

with vector components $A'_{k,i}$ and $B'_{k,i}$:

$$A'_{k,\mathrm{x}} = \left[A_{k,\mathrm{x}} \cos\left(k_\mathrm{y}\frac{\Delta y}{2}\right) - B_{k,\mathrm{x}} \sin\left(k_\mathrm{y}\frac{\Delta y}{2}\right)\right] \cos\left(k_\mathrm{z}\frac{\Delta z}{2}\right) - \left[A_{k,\mathrm{x}} \sin\left(k_\mathrm{y}\frac{\Delta y}{2}\right) + B_{k,\mathrm{x}} \cos\left(k_\mathrm{y}\frac{\Delta y}{2}\right)\right] \sin\left(k_\mathrm{z}\frac{\Delta z}{2}\right), \tag{D.16}$$

$$B'_{k,\mathrm{x}} = \left[A_{k,\mathrm{x}} \cos\left(k_\mathrm{y}\frac{\Delta y}{2}\right) - B_{k,\mathrm{x}} \sin\left(k_\mathrm{y}\frac{\Delta y}{2}\right)\right] \sin\left(k_\mathrm{z}\frac{\Delta z}{2}\right) + \left[A_{k,\mathrm{x}} \sin\left(k_\mathrm{y}\frac{\Delta y}{2}\right) + B_{k,\mathrm{x}} \cos\left(k_\mathrm{y}\frac{\Delta y}{2}\right)\right] \cos\left(k_\mathrm{z}\frac{\Delta z}{2}\right), \tag{D.17}$$

$$A'_{k,\mathrm{y}} = \left[A_{k,\mathrm{y}} \cos\left(k_\mathrm{x}\frac{\Delta x}{2}\right) - B_{k,\mathrm{y}} \sin\left(k_\mathrm{x}\frac{\Delta x}{2}\right)\right] \cos\left(k_\mathrm{z}\frac{\Delta z}{2}\right) - \left[A_{k,\mathrm{y}} \sin\left(k_\mathrm{x}\frac{\Delta x}{2}\right) + B_{k,\mathrm{y}} \cos\left(k_\mathrm{x}\frac{\Delta x}{2}\right)\right] \sin\left(k_\mathrm{z}\frac{\Delta z}{2}\right), \tag{D.18}$$

$$B'_{k,\mathrm{y}} = \left[A_{k,\mathrm{y}} \cos\left(k_\mathrm{x}\frac{\Delta x}{2}\right) - B_{k,\mathrm{y}} \sin\left(k_\mathrm{x}\frac{\Delta x}{2}\right)\right] \sin\left(k_\mathrm{z}\frac{\Delta z}{2}\right) + \left[A_{k,\mathrm{y}} \sin\left(k_\mathrm{x}\frac{\Delta x}{2}\right) + B_{k,\mathrm{y}} \cos\left(k_\mathrm{x}\frac{\Delta x}{2}\right)\right] \cos\left(k_\mathrm{z}\frac{\Delta z}{2}\right), \tag{D.19}$$

$$A'_{k,\mathrm{z}} = \left[A_{k,\mathrm{z}} \cos\left(k_\mathrm{x}\frac{\Delta x}{2}\right) - B_{k,\mathrm{z}} \sin\left(k_\mathrm{x}\frac{\Delta x}{2}\right)\right] \cos\left(k_\mathrm{y}\frac{\Delta y}{2}\right) - \left[A_{k,\mathrm{z}} \sin\left(k_\mathrm{x}\frac{\Delta x}{2}\right) + B_{k,\mathrm{z}} \cos\left(k_\mathrm{x}\frac{\Delta x}{2}\right)\right] \sin\left(k_\mathrm{y}\frac{\Delta y}{2}\right), \tag{D.20}$$

$$B'_{k,\mathrm{z}} = \left[A_{k,\mathrm{z}} \cos\left(k_\mathrm{x}\frac{\Delta x}{2}\right) - B_{k,\mathrm{z}} \sin\left(k_\mathrm{x}\frac{\Delta x}{2}\right)\right] \sin\left(k_\mathrm{y}\frac{\Delta y}{2}\right) + \left[A_{k,\mathrm{z}} \sin\left(k_\mathrm{x}\frac{\Delta x}{2}\right) + B_{k,\mathrm{z}} \cos\left(k_\mathrm{x}\frac{\Delta x}{2}\right)\right] \cos\left(k_\mathrm{y}\frac{\Delta y}{2}\right). \tag{D.21}$$

D.4 Computation of the Light Intensity in the Image Plane

The output of the Maxwell Solver (TDME3D) is a superposition of monochromatic plane waves with different wave vectors and amplitudes (see Eq. (6.17)):

$$\vec{E}_k(\vec{r},t) = \vec{A}_k \cos(\vec{k}\cdot\vec{r} - \omega t) - \vec{B}_k \sin(\vec{k}\cdot\vec{r} - \omega t). \tag{D.22}$$

To compute the electric field at a certain point $(\vec{r},t)$ in space and time, the corresponding electric field vectors are summed over $\vec{k}$:

$$\vec{E}(\vec{r},t) = \sum_{\vec{k}} \vec{E}_k(\vec{r},t) \overset{(D.22)}{=} \sum_{\vec{k}} \left[\vec{A}_k \left(\frac{\mathrm{e}^{\mathrm{i}(\vec{k}\cdot\vec{r}-\omega t)} + \mathrm{e}^{-\mathrm{i}(\vec{k}\cdot\vec{r}-\omega t)}}{2} \right) - \vec{B}_k \left(\frac{\mathrm{e}^{\mathrm{i}(\vec{k}\cdot\vec{r}-\omega t)} - \mathrm{e}^{-\mathrm{i}(\vec{k}\cdot\vec{r}-\omega t)}}{2\,\mathrm{i}} \right) \right] \tag{D.23}$$

$$= \frac{1}{2} \sum_{\vec{k}} \left[(\vec{A}_k + \mathrm{i}\,\vec{B}_k)\,\mathrm{e}^{\mathrm{i}(\vec{k}\cdot\vec{r}-\omega t)} + (\vec{A}_k - \mathrm{i}\,\vec{B}_k)\,\mathrm{e}^{-\mathrm{i}(\vec{k}\cdot\vec{r}-\omega t)} \right] \tag{D.24}$$

$$= \frac{1}{2} \left[\left(\mathrm{FT}^{-1}\{\vec{A}_k + \mathrm{i}\,\vec{B}_k\}\,\mathrm{e}^{-\mathrm{i}\,\omega t} \right) + \left(\mathrm{FT}^{-1}\{\vec{A}_k + \mathrm{i}\,\vec{B}_k\}\,\mathrm{e}^{-\mathrm{i}\,\omega t} \right)^* \right] \tag{D.25}$$

$$= \Re \left\{ \mathrm{FT}^{-1}\{\vec{A}_k + \mathrm{i}\,\vec{B}_k\}\,\mathrm{e}^{-\mathrm{i}\,\omega t} \right\} \tag{D.26}$$

$$= \Re \left\{ \mathrm{FT}^{-1}\{\vec{A}_k + \mathrm{i}\,\vec{B}_k\} \right\} \cos(\omega t) + \Im \left\{ \mathrm{FT}^{-1}\{\vec{A}_k + \mathrm{i}\,\vec{B}_k\} \right\} \sin(\omega t), \tag{D.27}$$

with $\Re\{f\}$ and $\Im\{f\}$ being the real and imaginary parts and $\mathrm{FT}^{-1}\{f\}$ being the inverse discrete Fourier transform of a function f:

$$\mathrm{FT}^{-1}\{f\} = \sum_{\vec{k}} f_{\vec{k}}\,\mathrm{e}^{\mathrm{i}\,\vec{k}\cdot\vec{r}}. \tag{D.28}$$

Defining $\Re \equiv \Re\left\{\mathrm{FT}^{-1}\{\vec{A}_k + \mathrm{i}\,\vec{B}_k\}\right\}$ and $\Im \equiv \Im\left\{\mathrm{FT}^{-1}\{\vec{A}_k + \mathrm{i}\,\vec{B}_k\}\right\}$, the absolute squared value of Eq. (D.27) is given by:

$$|\vec{E}(\vec{r},t)|^2 = \Re^2 \cos^2(\omega t) + \Im^2 \sin^2(\omega t) + 2\,\Re\,\Im\,\sin(\omega t)\cos(\omega t). \tag{D.29}$$

To compute a stationary solution (independent from time t), the result is averaged over one period ($T = 2\pi/\omega$):

$$|\vec{E}(\vec{r})|^2 = \frac{1}{T} \int_0^T |\vec{E}(\vec{r},t)|^2\,\mathrm{d}t = \frac{1}{2}\left(\Re^2 + \Im^2\right) = \frac{1}{2}\left|\mathrm{FT}^{-1}\{\vec{A}_k + \mathrm{i}\,\vec{B}_k\}\right|^2. \tag{D.30}$$

Thus, the intensity at a certain point $\vec{r}$ in the image plane can be computed from $\vec{A}_k$ and $\vec{B}_k$ via an inverse discrete Fourier transform:

$$I(\vec{r}) \propto |\vec{E}(\vec{r})|^2 \propto \left|\mathrm{FT}^{-1}\{\vec{A}_k + \mathrm{i}\,\vec{B}_k\}\right|^2. \tag{D.31}$$

To derive the expression in Eq. (10.21), $\vec{E}_k(\vec{r},t)$ in Eqs. (D.22) and (D.23) is replaced by $\vec{\tilde{E}}_k(\vec{r},t,\rho) * \mathrm{circ}(r)$. Using the same derivation as above, yields the same expressions as in Eqs. (D.27), (D.30) and (D.31), with $\mathrm{FT}^{-1}\{\vec{A}_k + \mathrm{i}\,\vec{B}_k\}$ being replaced by $\mathrm{FT}^{-1}\left\{\vec{\tilde{A}}_k(\rho) + \mathrm{i}\,\vec{\tilde{B}}_k(\rho)\right\} * \mathrm{circ}(r)$.

D.5 Derivation of the Fourier Transform of circ(r)

The detector microlenses of the PM are modeled by applying a moving average over the area of the microlens, i. e. a convolution with the function:

$$\mathrm{circ}(r) = \begin{cases} \dfrac{1}{\pi\, r_0^2}\,, & r < r_0 \\ 0\,, & r \geq r_0. \end{cases} \tag{D.32}$$

where $\vec{r} = (r_\mathrm{x}, r_\mathrm{y}, 0)^T$ is the radial coordinate in the xy-plane and r_0 the radius of the microlenses.

The corresponding (continuous) Fourier transform is given by:

$$\mathcal{F}\{\mathrm{circ}(r)\} = \int \mathrm{circ}(r)\, \mathrm{e}^{-i\vec{k}\cdot\vec{r}}\, \mathrm{d}\vec{r} = \frac{1}{\pi\, r_0^2} \int_0^{r_0} \int_0^{2\pi} \mathrm{e}^{-\,\mathrm{i}\, k_\mathrm{xy}\, r\, \cos(\varphi-\varphi_k)}\; r\, \mathrm{d}\varphi\, \mathrm{d}r, \tag{D.33}$$

with $k_\mathrm{xy} = \sqrt{k_\mathrm{x}^2 + k_\mathrm{y}^2}$ being the length of the wave vector in the xy-plane and φ_k the azimuthal angle of the wave vector ($\varphi_k = \arctan(k_\mathrm{y}/k_\mathrm{x})$).

Exploiting the periodicity of the cosine, the above integral can be written as:

$$\mathcal{F}\{\mathrm{circ}(r)\} = \frac{1}{\pi\, r_0^2} \int_0^{r_0} \int_0^{2\pi} \mathrm{e}^{\,\mathrm{i}\, k_\mathrm{xy}\, r\, \cos\varphi}\; r\, \mathrm{d}\varphi\, \mathrm{d}r = \frac{2}{r_0^2} \int_0^{r_0} J_0(r\, k_\mathrm{xy})\, r\, \mathrm{d}r\,, \tag{D.34}$$

where the function $J_0(x)$ is the Bessel function of the first kind of order zero (cf. [194] Eq. 9.1.21): $J_0(x) = \frac{1}{2\pi} \int_0^{2\pi} \mathrm{e}^{\,\mathrm{i}\, x \cos\varphi}\, \mathrm{d}\varphi$. Substituting $r\, k_\mathrm{xy} \equiv x$ and using the integral identity $\int_0^{x'} J_0(x)\, x\, \mathrm{d}x = x' J_1(x')$, yields:

$$\mathcal{F}\{\mathrm{circ}(r)\} = \frac{2}{r_0^2\, k_\mathrm{xy}^2} \int_0^{r_0\, k_\mathrm{xy}} J_0(x)\, x\; \mathrm{d}x = \frac{2}{r_0^2\, k_\mathrm{xy}^2}\, r_0\, k_\mathrm{xy}\, J_1(r_0\, k_\mathrm{xy}) = 2\, \frac{J_1(r_0\, k_\mathrm{xy})}{r_0\, k_\mathrm{xy}}. \tag{D.35}$$

In the limit $r_0\, k_\mathrm{xy} \to 0$, i. e. for normally incident light ($k_\mathrm{x} = k_\mathrm{y} = 0$) or no microlenses ($r_0 = 0$), the expression simplifies to:

$$\lim_{x\to 0} \frac{J_1(x)}{x} = \frac{1}{2} \quad \Rightarrow \quad \mathcal{F}\{\mathrm{circ}(r)\} = 1. \tag{D.36}$$

D.6 Representation of the Light Intensity in 3D-PLI Simulations as Fourier Series

This section demonstrates how the light intensity $I(\vec{r}, \rho)$ in 3D-PLI simulations can be represented as a Fourier series. Instead of computing the intensity for a discrete set of rotation angles ρ, the Fourier coefficients are computed, providing a full representation of $I(\vec{r}, \rho)$ as a function of the rotation angle.

The intensity recorded by the camera can be written as (see Eq. (10.27)):

$$I(\vec{r}, \rho) \;\propto\; |\tilde{\mathcal{E}}_\mathrm{x}(\vec{r}, \rho)|^2 + |\tilde{\mathcal{E}}_\mathrm{y}(\vec{r}, \rho)|^2 + |\tilde{\mathcal{E}}_\mathrm{z}(\vec{r}, \rho)|^2. \tag{D.37}$$

The first two terms can easily be represented as a Fourier series (see Eq. (10.28)). In the following, the Fourier series for the third term is derived.

As the vectors $\{\vec{\tilde{A}}_k(\rho) = \vec{\tilde{E}}_{0,k}(\rho)\, \cos\phi,\;\; \vec{\tilde{B}}_k(\rho) = \vec{\tilde{E}}_{0,k}(\rho)\, \sin\phi\}$ are parallel to the electric field vector $\vec{\tilde{E}}_k(\vec{r}, t, \rho)$, they are also perpendicular to $\vec{k}$ and obey Eq. (10.16): $\vec{k} \cdot \vec{\tilde{A}}_k(\rho) = \vec{k} \cdot \vec{\tilde{B}}_k(\rho) = 0$. Thus, Eq. (10.17) also holds for $\tilde{\mathcal{E}}_{k,\mathrm{z}}(\rho) \propto \big(\tilde{A}_{k,\mathrm{z}}(\rho) + \mathrm{i}\, \tilde{B}_{k,\mathrm{z}}(\rho)\big)$:

$$\tilde{\mathcal{E}}_{k,\mathrm{z}}(\rho) = -\frac{k_\mathrm{x} \sin\rho - k_\mathrm{y} \cos\rho}{k_\mathrm{z}} \left(\mathcal{E}'_{k,\mathrm{x}}\, \sin\rho - \mathcal{E}'_{k,\mathrm{y}}\, \cos\rho\right), \tag{D.38}$$

with $\vec{\mathcal{E}}'_k$ being defined as in Eq. (10.26).

The (continuous) inverse Fourier transform of Eq. (D.38) is given by:

$$\tilde{\mathcal{E}}_\mathrm{z}(\vec{r},\rho) \equiv \mathcal{F}^{-1}\left\{\tilde{\mathcal{E}}_{k,\mathrm{z}}(\rho)\right\} = -\int \frac{k_\mathrm{x}\sin\rho - k_\mathrm{y}\cos\rho}{k_\mathrm{z}} \left(\mathcal{E}'_{k,\mathrm{x}}\sin\rho - \mathcal{E}'_{k,\mathrm{y}}\cos\rho\right) \mathrm{e}^{\mathrm{i}\,\vec{k}\cdot\vec{r}}\,\mathrm{d}\vec{k} \tag{D.39}$$

$$\begin{aligned}\Rightarrow \left|\tilde{\mathcal{E}}_\mathrm{z}(\vec{r},\rho)\right|^2 = \iint & \frac{k_\mathrm{x}\sin\rho - k_\mathrm{y}\cos\rho}{k_\mathrm{z}} \; \frac{k'_\mathrm{x}\sin\rho - k'_\mathrm{y}\cos\rho}{k'_\mathrm{z}} \left(\mathcal{E}'_{k,\mathrm{x}}\sin\rho - \mathcal{E}'_{k,\mathrm{y}}\cos\rho\right) \\ & \times \left(\mathcal{E}'^{*}_{k',\mathrm{x}}\sin\rho - \mathcal{E}'^{*}_{k',\mathrm{y}}\cos\rho\right) \mathrm{e}^{\mathrm{i}(\vec{k}-\vec{k}')\vec{r}}\,\mathrm{d}\vec{k}\,\mathrm{d}\vec{k'} \end{aligned} \tag{D.40}$$

$$\equiv e_0(\vec{r}) + e_2(\vec{r})\cos(2\rho) + f_2(\vec{r})\sin(2\rho) + e_4(\vec{r})\cos(4\rho) + f_4(\vec{r})\sin(4\rho). \tag{D.41}$$

The solution of Eq. (D.40) has been computed by Hans De Raedt (University of Groningen, the Netherlands). Defining the inverse Fourier transforms:

$$X_\mathrm{x}(\vec{r}) \equiv \mathcal{F}^{-1}\left\{\frac{k_\mathrm{x}}{k_\mathrm{z}}\mathcal{E}'_{k,\mathrm{x}}\right\} = \int \frac{k_\mathrm{x}}{k_\mathrm{z}}\,\mathcal{E}'_{k,\mathrm{x}}\,\mathrm{e}^{\mathrm{i}\,\vec{k}\cdot\vec{r}}\,\mathrm{d}\vec{k}\,, \tag{D.42}$$

$$X_\mathrm{y}(\vec{r}) \equiv \mathcal{F}^{-1}\left\{\frac{k_\mathrm{y}}{k_\mathrm{z}}\mathcal{E}'_{k,\mathrm{x}}\right\} = \int \frac{k_\mathrm{y}}{k_\mathrm{z}}\,\mathcal{E}'_{k,\mathrm{x}}\,\mathrm{e}^{\mathrm{i}\,\vec{k}\cdot\vec{r}}\,\mathrm{d}\vec{k}\,, \tag{D.43}$$

$$Y_\mathrm{x}(\vec{r}) \equiv \mathcal{F}^{-1}\left\{\frac{k_\mathrm{x}}{k_\mathrm{z}}\mathcal{E}'_{k,\mathrm{y}}\right\} = \int \frac{k_\mathrm{x}}{k_\mathrm{z}}\,\mathcal{E}'_{k,\mathrm{y}}\,\mathrm{e}^{\mathrm{i}\,\vec{k}\cdot\vec{r}}\,\mathrm{d}\vec{k}\,, \tag{D.44}$$

$$Y_\mathrm{y}(\vec{r}) \equiv \mathcal{F}^{-1}\left\{\frac{k_\mathrm{y}}{k_\mathrm{z}}\mathcal{E}'_{k,\mathrm{y}}\right\} = \int \frac{k_\mathrm{y}}{k_\mathrm{z}}\,\mathcal{E}'_{k,\mathrm{y}}\,\mathrm{e}^{\mathrm{i}\,\vec{k}\cdot\vec{r}}\,\mathrm{d}\vec{k}\,, \tag{D.45}$$

the Fourier coefficients in Eq. (D.41) can be written as (omitting the argument $\vec{r}$):

$$e_0 = \frac{1}{8}\left(3X_\mathrm{x}X^*_\mathrm{x} + Y_\mathrm{x}X^*_\mathrm{y} + Y_\mathrm{x}Y^*_\mathrm{x} + X_\mathrm{x}Y^*_\mathrm{y} + Y_\mathrm{y}X^*_\mathrm{x} + X_\mathrm{y}X^*_\mathrm{y} + X_\mathrm{y}Y^*_\mathrm{x} + 3Y_\mathrm{y}Y^*_\mathrm{y}\right), \tag{D.46}$$

$$e_2 = \frac{1}{2}\left(Y_\mathrm{y}Y^*_\mathrm{y} - X_\mathrm{x}X^*_\mathrm{x}\right), \tag{D.47}$$

$$e_4 = \frac{1}{8}\left(X_\mathrm{x}X^*_\mathrm{x} - Y_\mathrm{x}X^*_\mathrm{y} - Y_\mathrm{x}Y^*_\mathrm{x} - X_\mathrm{x}Y^*_\mathrm{y} - Y_\mathrm{y}X^*_\mathrm{x} - X_\mathrm{y}X^*_\mathrm{y} - X_\mathrm{y}Y^*_\mathrm{x} + Y_\mathrm{y}Y^*_\mathrm{y}\right), \tag{D.48}$$

$$f_2 = -\frac{1}{4}\left(Y_\mathrm{x}X^*_\mathrm{x} + Y_\mathrm{y}X^*_\mathrm{y} + Y_\mathrm{y}Y^*_\mathrm{x} + Y_\mathrm{x}Y^*_\mathrm{y} + X_\mathrm{y}X^*_\mathrm{x} + X_\mathrm{x}X^*_\mathrm{y} + X_\mathrm{x}Y^*_\mathrm{x} + X_\mathrm{y}Y^*_\mathrm{y}\right), \tag{D.49}$$

$$f_4 = \frac{1}{8}\left(Y_\mathrm{x}X^*_\mathrm{x} - Y_\mathrm{y}X^*_\mathrm{y} - Y_\mathrm{y}Y^*_\mathrm{x} - Y_\mathrm{x}Y^*_\mathrm{y} + X_\mathrm{y}X^*_\mathrm{x} + X_\mathrm{x}X^*_\mathrm{y} + X_\mathrm{x}Y^*_\mathrm{x} - X_\mathrm{y}Y^*_\mathrm{y}\right). \tag{D.50}$$

D.7 Derivation of the Fraunhofer Diffraction Pattern

In this section, an analytical formula for the Fraunhofer diffraction pattern (cf. Sec. 2.1.3.3) of a one-dimensional grating is derived, which was used in Sec. 10.1.3.3 to model the measurement of the USAF resolution target with the LAP.

Consider a grating with N slits with width l that are centered around $x = 0$. Light with a certain wavelength λ and angle of incidence θ propagates through the grating (cf.

Fig. 10.12 for $N = 3$), yielding a Fraunhofer diffraction pattern on a distant detection plane behind the grating. To simplify notation, the following shorthand is defined:

$$p \equiv \sin\theta_k - \sin\theta, \tag{D.51}$$

where θ is the angle of incidence (in the xz-plane) and θ_k is the polar angle of a distant point in the detection plane.

The complex amplitude of the scalar wave function U behind the grating is then given by (cf. [69] p. 448)[2]:

$$U(p) \propto \frac{1}{\lambda} \int_{-l/2}^{l/2} \mathrm{e}^{-\mathrm{i}kpx}\,\mathrm{d}x \sum_{m=-\frac{N-1}{2}}^{\frac{N-1}{2}} \mathrm{e}^{-2\mathrm{i}kplm} \tag{D.52}$$

$$= \frac{1}{\lambda}\left[\frac{\mathrm{i}}{kp}\,\mathrm{e}^{-\mathrm{i}kpx}\right]_{x=-l/2}^{x=l/2} \sum_{m'=0}^{N-1} \mathrm{e}^{-2\mathrm{i}kpl(m'-(N-1)/2)} \tag{D.53}$$

$$= \frac{\mathrm{i}}{\lambda kp}\left(\mathrm{e}^{-\mathrm{i}kpl/2} - \mathrm{e}^{\mathrm{i}kpl/2}\right) e^{\mathrm{i}kpl(N-1)} \sum_{m'=0}^{N-1} \left(\mathrm{e}^{-2\mathrm{i}kpl}\right)^{m'} \tag{D.54}$$

$$= \frac{2}{\lambda kp}\sin\left(k\,p\,\frac{l}{2}\right) \mathrm{e}^{\mathrm{i}kpl(N-1)} \left(\frac{1-\mathrm{e}^{-2\,\mathrm{i}kplN}}{1-\mathrm{e}^{-2\,\mathrm{i}kpl}}\right), \tag{D.55}$$

where Euler's formula $\left(\sin x = (\mathrm{e}^{\mathrm{i}x} - \mathrm{e}^{-\mathrm{i}x})/2\,\mathrm{i}\right)$ and the geometric series $\left(\sum_{n=0}^{N} z^n = \left(1 - z^{N+1}\right)/(1-z)\right)$ have been used in the last step.

Writing $N = 3$, the complex amplitude for a certain wavelength λ, angle of incidence θ, and line width l is then given by:

$$U(\theta_k)_{\lambda,\theta,l} \propto \frac{2}{\lambda kp}\sin\left(k\,p\,\frac{l}{2}\right) \mathrm{e}^{2\,\mathrm{i}kpl}\left(\frac{1-\mathrm{e}^{-6\,\mathrm{i}kpl}}{1-\mathrm{e}^{-2\,\mathrm{i}kpl}}\right). \tag{D.56}$$

The transmitted light intensity is related to the complex amplitude via: $I(\theta_k) \propto |U(\theta_k)|^2$.

D.8 Fourier Coefficient Maps of Higher Orders

Figure D.2 shows the Fourier coefficient maps (up to order six) computed from a 3D-PLI measurement of a coronal rat brain section. The Fourier coefficients of order four are much smaller than those of order two, but still show the underlying tissue structure. Fourier coefficients of higher orders do not contain valuable information.

[2] The formula for the complex amplitude of the scalar wave function $U(p)$ was adapted from Born·Wolf ([69] Sec. 8.6.1, Eqs. (3) and (4)), with $n = \{-(N-1)/2, \ldots, (N-1)/2\}$, $d = 2\,l$, $\xi = x$, and $F(\xi) = \{1,$ for $-l/2 \leq \xi \leq l/2$ and 0 otherwise$\}$.

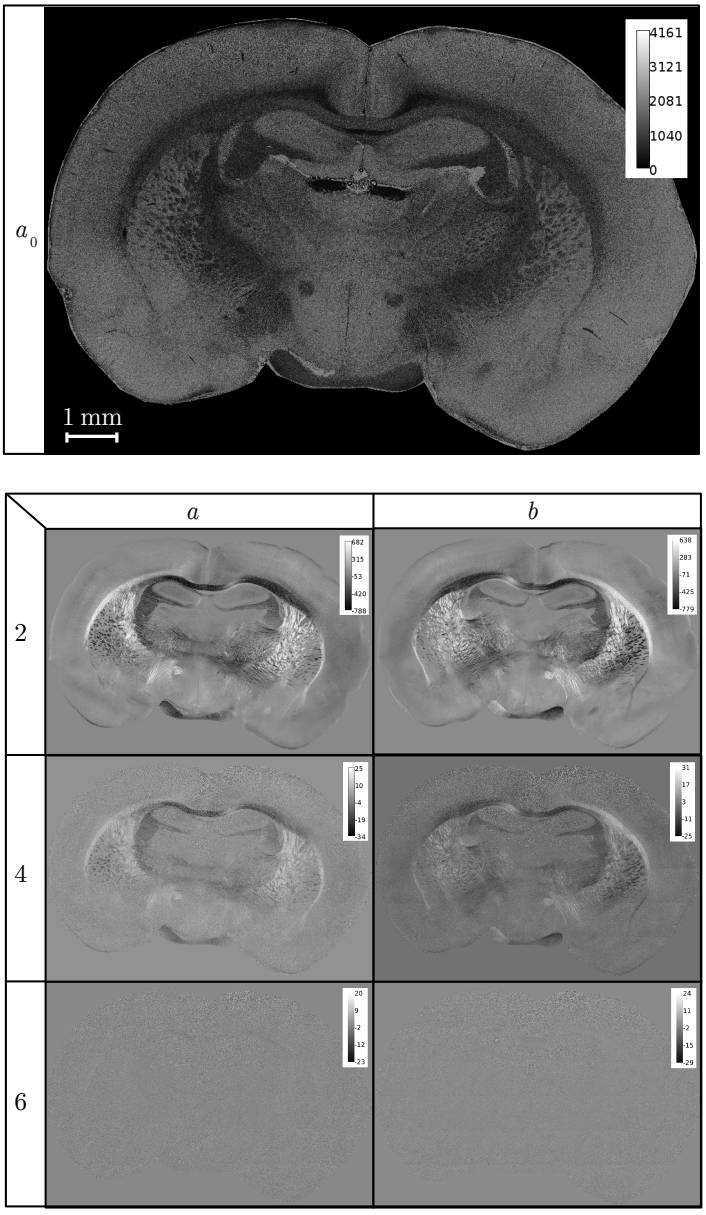

Fig. D.2: Fourier coefficient maps (a_0, a_2, a_4, a_6, b_2, b_4, b_6; cf. Eq. (4.2)) of a coronal rat brain section measured with 3D-PLI. The figure has been published in Menzel *et al.* (2016) [66] Fig. 5.

D.9 Transmittance Profiles of the USAF Resolution Target Simulated for the Polarizing Microscope

Figure D.3 shows the transmittance profiles of the USAF resolution target simulated for the optics of the PM (cf. Figs. 10.6a and 10.7a) for line widths $l = \{1.95, 2.19, 2.46\}$ µm.

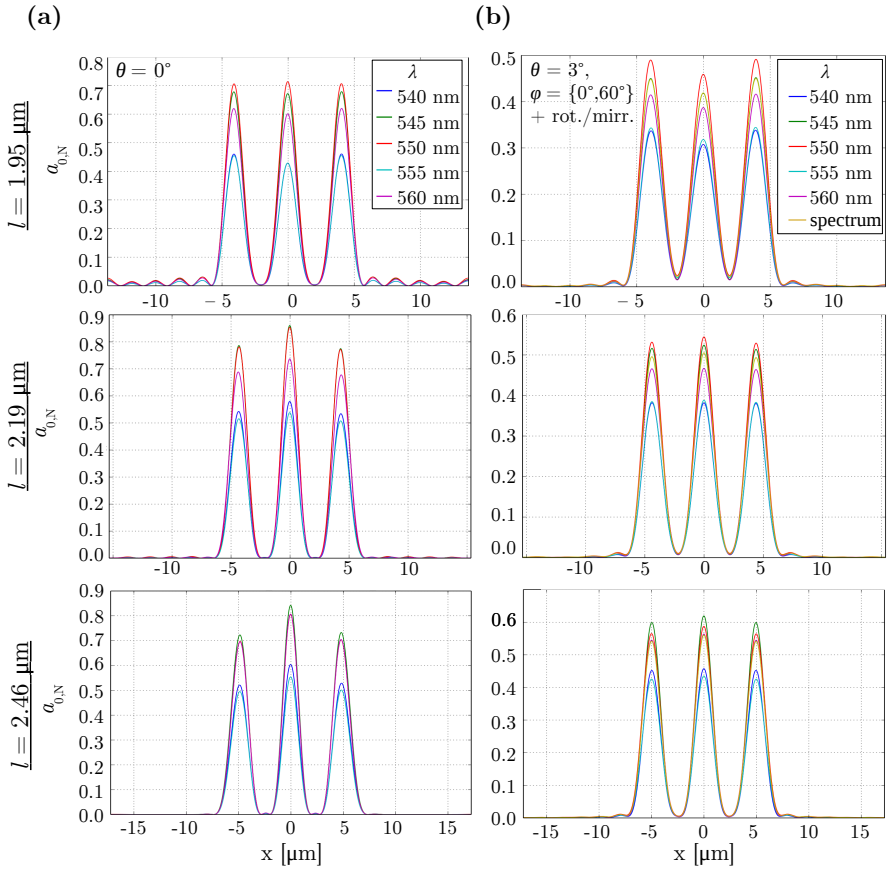

Fig. D.3: Line profiles of the USAF resolution target obtained from 3D-PLI simulations with line widths $l = \{1.95, 2.19, 2.46\}$ µm (cf. Fig. 10.4) for the optics of the PM. The line profiles show the middle pixel in the y-direction evaluated along the x-direction of the resulting transmittance images: **(a)** normally incident light with different wavelengths λ, **(b)** diffuse light with different wavelengths. The transmittance images for diffuse light were computed from three simulation runs with different angles of incidence ($\{\theta = 0°\}$, $\{\theta = 3°$, $\varphi = 0°\}$ $\{\theta = 3°$, $\varphi = 60°\}$), and by 180°-rotation or flipping of the simulated transmittance images. The yellow line profile was obtained from the weighted sum over the wavelength spectrum of the PM light source, according to Fig. 10.5b.

D.10 Transmittance Images and Scattering Patterns for the Hexagonal Grid of Fibers

Figures D.4 to D.7 show the transmittance images ($a_{0,\mathrm{N}}$) and scattering patterns (I_k) for the hexagonal grid of fibers with different geometries: straight fibers, aligned helical fibers, unaligned helical fibers with same strides, and unaligned helical fibers with different strides (cf. Sec. 10.2.1).

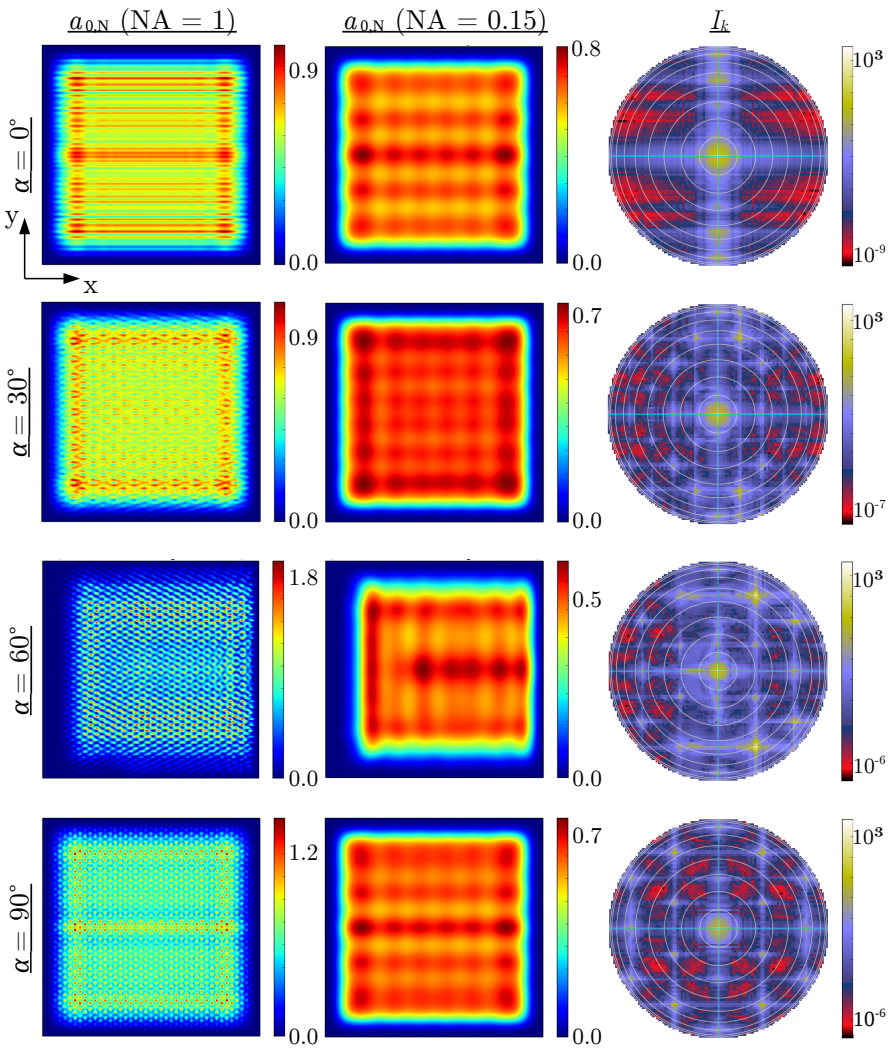

Fig. D.4: Transmittance images ($a_{0,\mathrm{N}}$) and scattering patterns (I_k) computed from a simulated 3D-PLI measurement of a hexagonal grid of straight fibers (see Sec. 10.2.1) for different fiber inclination angles α. The transmittance images were computed for the microscope objective of the PM (numerical aperture: NA = 0.15, microlenses: $r_0 = 0.665\,\mu\mathrm{m}$) and for the case without objective lens (NA = 1, $r_0 = 0\,\mu\mathrm{m}$).

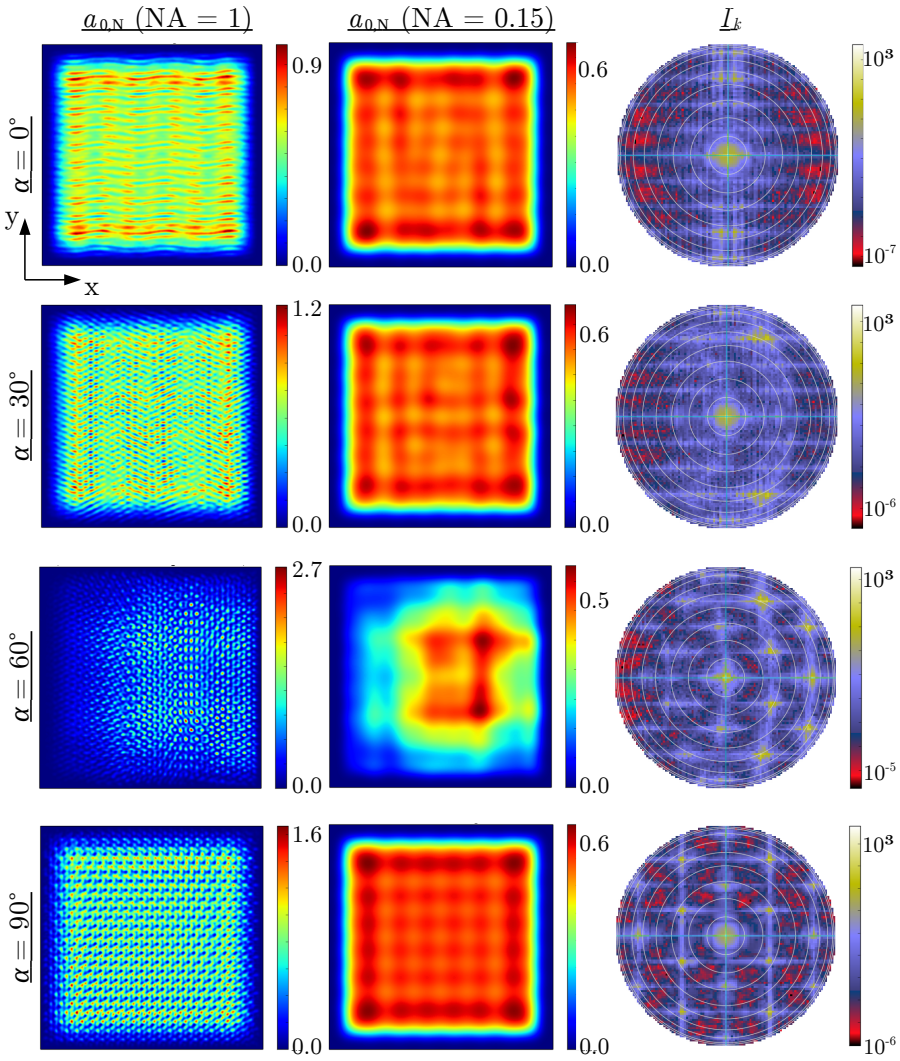

Fig. D.5: Transmittance images ($a_{0,N}$) and scattering patterns (I_k) computed from a simulated 3D-PLI measurement of a hexagonal grid of aligned helical fibers (see Sec. 10.2.1) for different fiber inclination angles α. The transmittance images were computed for the microscope objective of the PM (numerical aperture: NA = 0.15, microlenses: $r_0 = 0.665\,\mu m$) and for the case without objective lens (NA = 1, $r_0 = 0\,\mu m$).

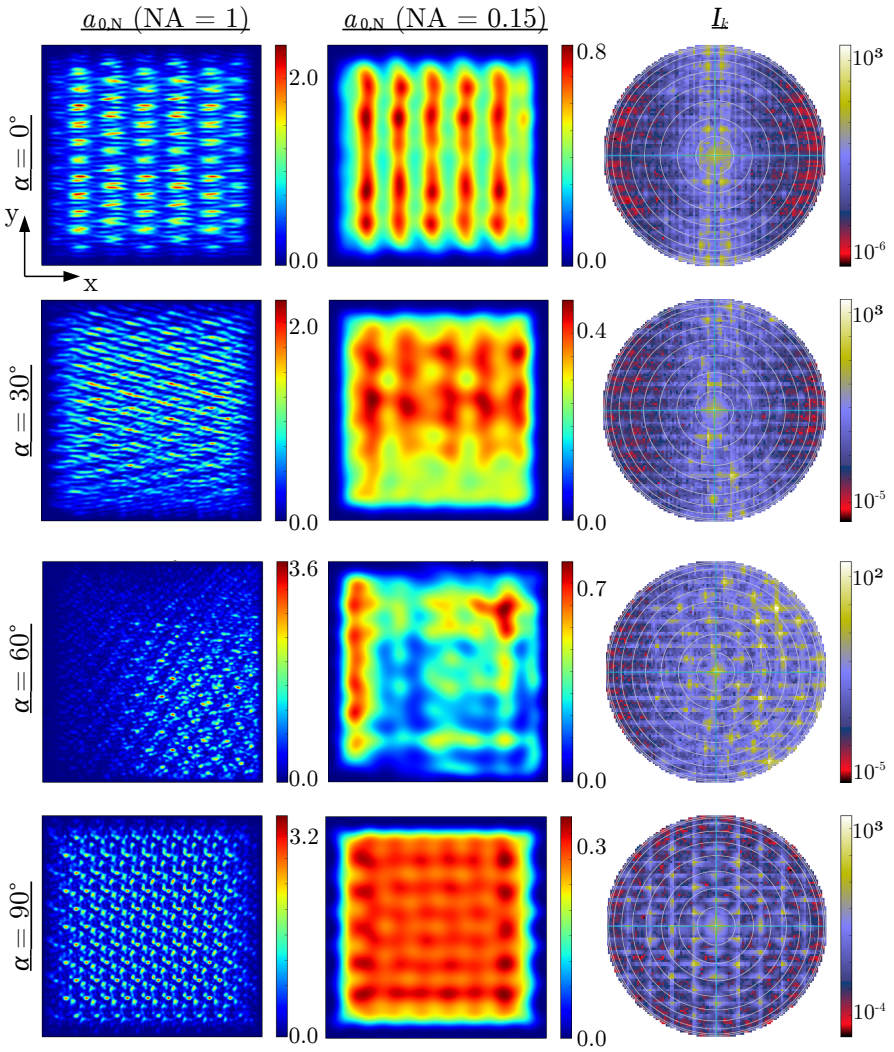

Fig. D.6: Transmittance images ($a_{0,N}$) and scattering patterns (I_k) computed from a simulated 3D-PLI measurement of a hexagonal grid of unaligned helical fibers with same strides (see Sec. 10.2.1) for different fiber inclination angles α. The transmittance images were computed for the microscope objective of the PM (numerical aperture: NA = 0.15, microlenses: $r_0 = 0.665\,\mu m$) and for the case without objective lens (NA = 1, $r_0 = 0\,\mu m$).

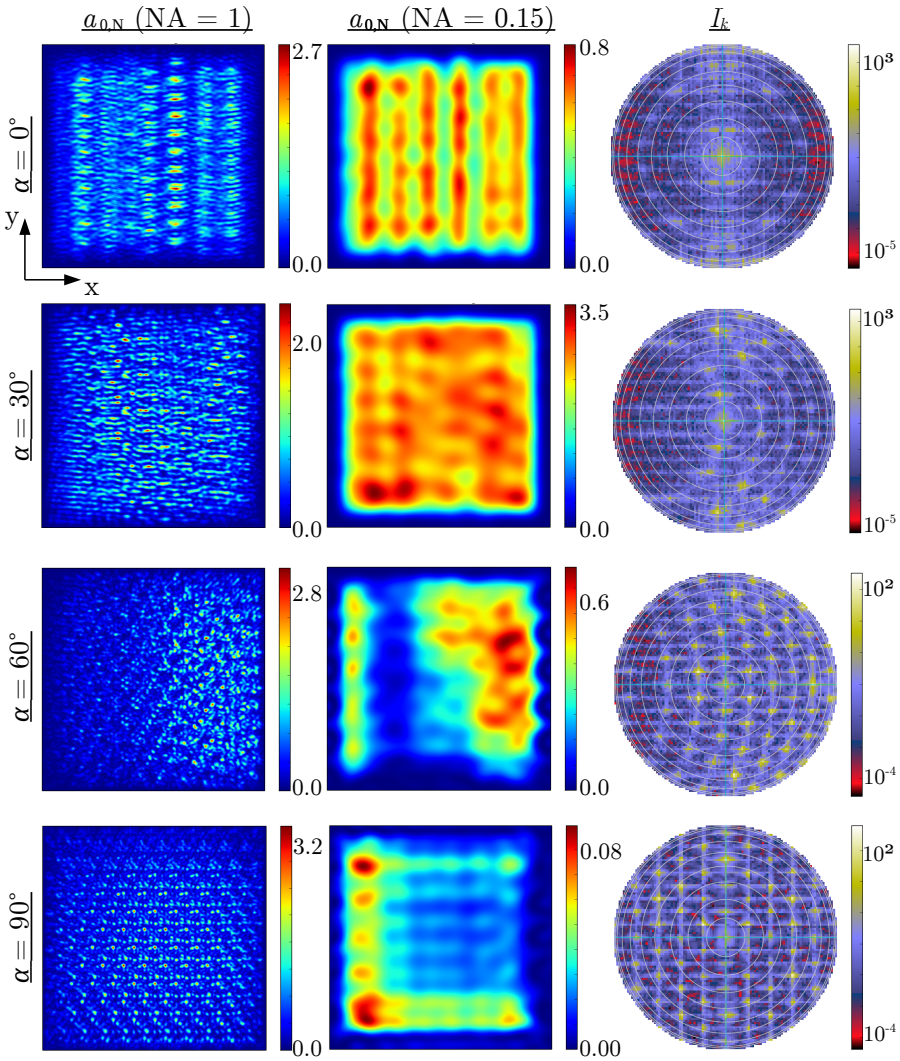

Fig. D.7: Transmittance images ($a_{0,N}$) and scattering patterns (I_k) computed from a simulated 3D-PLI measurement of a hexagonal grid of unaligned helical fibers with different strides (see Sec. 10.2.1) for different fiber inclination angles α. The transmittance images were computed for the microscope objective of the PM (numerical aperture: NA = 0.15, microlenses: $r_0 = 0.665\,\mu m$) and for the case without objective lens (NA = 1, $r_0 = 0\,\mu m$).

D.11 Transmittance and Diattenuation Curves for the Bundle of Densely Grown Fibers Simulated with Different Wavelengths and Smaller Yee Mesh Size

Figure D.8 shows the transmittance (a) and diattenuation (b) curves for the bundle of densely grown fibers (cf. Figs. 11.4a and 12.5a) simulated with normally incident light and different wavelengths $\lambda = \{545, 550, 555\}$ nm. The transmittance and diattenuation curves were obtained from 3D-PLI and DI simulations as described in Chaps. 11 and 12. The solid curves were computed for the microscope objective of the PM (numerical aperture: NA = 0.15, microlenses: $r_0 = 0.665\,\mu$m), the dashed curves were computed for the case without objective lens (NA = 1, $r_0 = 0\,\mu$m). All curves were computed for a Yee mesh size of 25 nm. For some inclination angles ($\alpha = \{0°, 30°, 60°, 90°\}$), the simulations with $\lambda = 550$ nm were repeated for a mesh size of 12.5 nm (black crosses).

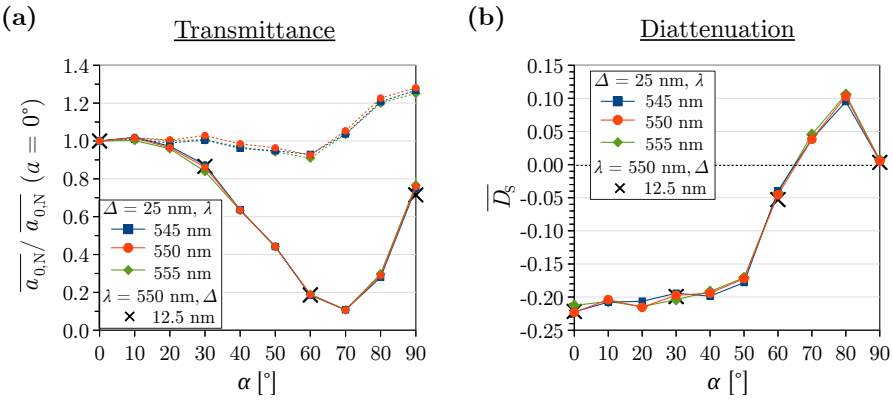

Fig. D.8: Transmittance and diattenuation curves for the bundle of densely grown fibers (cf. Figs. 11.4a and 12.5a) simulated with normally incident light and different wavelengths $\lambda = \{545, 550, 555\}$ nm. The solid curves were computed for the microscope objective of the PM (NA = 0.15, $r_0 = 0.665\,\mu$m), the dashed curves for the case without objective lens (NA = 1, $r_0 = 0\,\mu$m). The transmittance curves show the averaged transmittance $\overline{a_{0,N}}$ (obtained from a 3D-PLI simulation) normalized by the averaged transmittance of the horizontal fiber bundle plotted against the inclination angle α of the fiber bundle. A similar subfigure has been published in Menzel *et al.* (2018a) [67] Fig. 19b. The diattenuation curves show the averaged diattenuation $\overline{D_S}$ (obtained from two DI simulations, cf. Eq. (10.42)) plotted against the fiber inclination. All curves were computed from simulations with a Yee mesh size $\Delta = 25$ nm. The simulation with $\lambda = 550$ nm was repeated for some inclination angles ($\alpha = \{0°, 30°, 60°, 90°\}$) with a mesh size of 12.5 nm, see black crosses.

Simulations with a wavelength of 545 nm and 555 nm yield comparable transmittance and diattenuation curves as simulations with a wavelength of 550 nm. The maximum difference between the normalized transmittance values is about 0.02, the maximum difference between the diattenuation values is about 0.01.

In addition, the simulations with smaller mesh size (black crosses) yield similar results as the simulations with larger mesh size. The maximum difference between the normalized transmittance values is about 0.005, the maximum difference between the diattenuation values is about 0.007.

Thus, all other simulations in Chaps. 11 and 12 were only performed for the peak wavelength of the PM ($\lambda = 550$ nm) and for a mesh size of 25 nm.

D.12 Diattenuation Simulated for the Imaging System of the Large-Area Polarimeter

This section describes how the light source of the LAP was modeled to simulate the diattenuation effect for the bundle of densely grown fibers in Fig. 12.5b.

Due to the broad wavelength spectrum and the large illumination angles of the LAP light source, the Maxwell Solver is less suitable to model the optics of the LAP than the optics of the PM (cf. Secs. 10.1.1 and 10.1.3). The FDTD simulation studies in Chaps. 11 and 12 were therefore only performed for the imaging system of the PM. However, most diattenuation studies in Chap. 9 were performed with the LAP because the PM cannot be used for DI measurements. To investigate whether the diattenuation effects observed in PM simulations are also applicable to the LAP, the DI simulations for the bundle of densely grown fibers (see Sec. 12.1.2) were repeated for the optics of the LAP.

As discussed in Sec. 10.1.1, the imaging system of the LAP was modeled with a numerical aperture NA = 0.0083 and without microlenses ($r_0 = 0\,\mu\text{m}$). The incoherent and diffuse light source was modeled by several simulation runs with different wavelengths ($\lambda = \{496, \ldots, 581\}\,\text{nm}$) and different illumination angles ($\theta_{\max} < 25°$, $\varphi \in \eta \times \Delta\varphi$). To find out how many wavelengths and angles are needed to efficiently model the LAP light source, the diattenuation D_S was computed from Eq. (10.42) for the horizontal bundle of densely grown fibers (see Fig. 10.18a) for different λ and (θ, φ), and the weighted sums over different numbers of wavelengths and angles were compared to each other.[3]

Wavelength Spectrum Figure D.9 (in blue) shows the diattenuation values D_S obtained from simulations with normally incident light and different wavelengths λ which represent the wavelength spectrum of the LAP (see blue numbers in Fig. 10.10a): the diattenuation values become less negative with increasing wavelength ($D_S \approx -27.0\,\%$ for $\lambda = 496\,\text{nm}$, $D_S \approx -23.1\,\%$ for $\lambda = 570\,\text{nm}$).

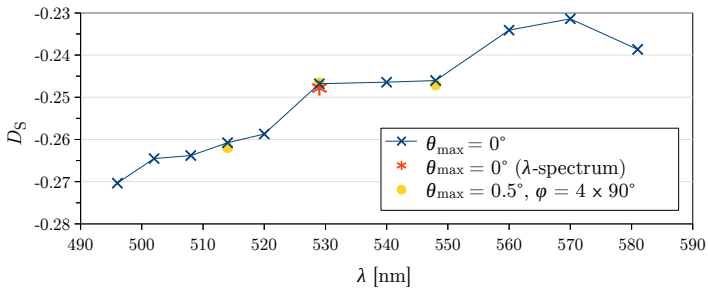

Fig. D.9: Diattenuation values D_S for the horizontal bundle of densely grown fibers (see Fig. 10.18a) simulated for the optics of the LAP (numerical aperture: NA = 0.0083, microlenses: $r_0 = 0\,\mu\text{m}$). The blue values belong to simulations with normally incident light ($\theta = 0°$) and different wavelengths λ, representing the wavelength spectrum of the LAP light source (cf. Fig. 10.10a). The red star marks the diattenuation value obtained from the weighted sum over the wavelength spectrum (cf. Fig. 10.10b). The yellow values belong to simulations with different wavelengths ($\lambda \in \{514, 529, 548\}\,\text{nm}$) and diffuse light ($\{\theta = 0°\}$, $\{\theta = 0.5°, \varphi = \{0°, 90°, 180°, 270°\}\}$) weighted according to Eqs. (10.1) to (10.3).

[3] As the numerical aperture of the LAP is too small to resolve any geometric features, the simulations yield only one diattenuation value per run. For this reason, it is only possible to make a comparison between (averaged) diattenuation values and not between image pixels.

Although the diattenuation depends on the wavelength, the weighted sum over the wavelength spectrum according to Fig. 10.10b (red star) yields a similar diattenuation value ($D_S \approx -24.8\,\%$) as for the peak wavelength $\hat{\lambda} = 529\,\text{nm}$ ($D_S \approx -24.7\,\%$). The absolute relative difference between the mean values is only about 0.4 %. To reduce computing time, the bundle of densely grown fibers was therefore only simulated for $\lambda = 529\,\text{nm}$.

Diffuse Light Figure D.10a shows the averaged normalized transmitted light intensity $\overline{I_N} = (I_x + I_y)/2$ for different angles of incidence (θ, φ).[4] The value in green was computed for normally incident light, the blue (red) values were averaged over $\varphi = 4 \times 90°$ ($8 \times 45°$), cf. Eq. (10.2), for a certain angle $\theta \in \{0.5°, 1°, 1.5°, 3°\}$. More angles of incidence were not simulated due to limited computing resources and because smaller angles of incidence are expected to have the largest contribution to the transmitted light intensity (NA = $0.0083 \Rightarrow \theta_k < 0.48°$, see Sec. 10.1.1).

The averaged transmitted light intensity decreases with increasing θ: from about 0.17 for normally incident light to about 0.09 for $\theta = 0.5°$. For light with larger angles of incidence ($\theta \geq 1°$), the averaged transmitted light intensity is only about 0.008 or less. Averaging over four or eight φ-angles yields similar results. Thus, small angles of incidence ($\theta \leq 0.5°$) contribute the most to the transmitted light intensity as expected.

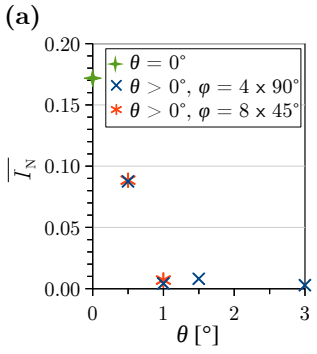

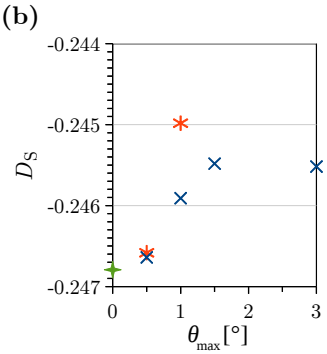

θ [°]	$360°/\Delta_\varphi$
0.5	5.9999
1.0	12.4325
1.5	18.7595
2.0	*25.0620*
2.5	*31.3535*
3.0	37.6383
...	...
25.0	*304.2807*

Fig. D.10: DI simulations of the horizontal bundle of densely grown fibers (see Fig. 10.18a) performed for the optics of the LAP (NA = 0.0083, $r_0 = 0\,\mu\text{m}$, $\lambda = 529\,\text{nm}$) and different angles of incidence (θ, φ): **(a)** Averaged normalized transmitted light intensity $\left(\overline{I_N} = (I_x + I_y)/2\right)$ for different angles of incidence θ, averaged over four φ-angles (blue) and over eight φ-angles (red). **(b)** Diattenuation values D_S obtained from the weighted sum over different angles of incidence $\theta \leq \theta_{max}$ with $\Delta_\theta = 0.5°$. The weighting was performed according to Eqs. (10.1) to (10.3), the values for $360°/\Delta_\varphi$ are given in the above table (the values in italics belong to θ-angles that were used for weighting, but not for the simulations). The blue values were computed from four φ-angles per θ, the red values from eight φ-angles per θ. The green values were computed for normally incident light ($\theta = 0°$).

Figure D.10b shows the diattenuation values D_S obtained from the weighted sum over different angles of incidence $\theta \leq \theta_{max}$ with $\Delta_\theta = 0.5°$. The weighting for the respective angle $\theta \in \{0.5°, 1°, \ldots 3°\}$ was performed according to Eq. (10.3), with $\Delta\varphi = 90°$ (blue) or 45° (red) and Δ_φ computed from Eq. (10.1) with $\Delta_\theta = 0.5°$. The resulting values for

[4] I_x and I_y are the normalized transmitted light intensities obtained from DI simulations with $\rho = 0°$ (x-axis) and $\rho = 90°$ (y-axis). The values were used to compute the diattenuation D_S with Eq. (10.42).

$360°/\Delta_\varphi$ are shown in the table in Fig. D.10b. As the angles $\theta = 2°$ and $2.5°$ were not simulated, the respective weightings were added to the weighting of $\theta = 1.5°$ to compute the weighted sum for $\theta_{\max} = 3°$.

The resulting diattenuation values are similar for normally incident and diffuse light: $D_S \approx -24.68\,\%$ for $\theta_{\max} = 0°$, $D_S \approx -24.55\,\%$ for $\theta_{\max} = 1.5°$ and $3°$ (for $\varphi = 4 \times 90°$). The weighted sum over eight φ-angles yields a diattenuation of about $-24.50\,\%$ for $\theta_{\max} = 1°$. The maximum relative difference is less than $0.74\,\%$.

When taking all angles of incidence into account (by adding the weightings for $\theta = \{3.5°, 4.0°, \ldots, 25°\}$ to the weighting of $\theta = 3°$), the resulting diattenuation ($D_S \approx -25.44\,\%$) is still similar to the one obtained for normally incident light. Note that this value is just a rough estimate because angles $\theta > 3°$ were not simulated.

A comparison of normally incident and diffuse light ($\theta_{\max} = 0.5°$, $\varphi = 4 \times 90°$) for $\lambda \in \{514, 529, 548\}$ nm shows that the diattenuation values are also similar for different wavelengths (cf. blue and yellow values in Fig. D.9).

The simulation results suggest that the light source of the LAP can be modeled by a single simulation run with a wavelength of 529 nm and normally incident light. More extensive studies for the PM (see Sec. 10.4.6), however, have shown that normally incident and diffuse light might yield different diattenuation values for different fiber constellations. To ensure that the simulated diattenuation results are reliable, the bundle of densely grown fibers was simulated for all inclination angles $\alpha \in \{0°, 10°, \ldots, 90°\}$ with $\lambda = 529$ nm and with normally incident as well as with diffuse light ($\{\theta = 0.5°$, $\varphi = \{0°, 90°, 180°, 270°\}\}$), see Fig. 12.5b.

Band / Volume 174
Interfacing EuO in confined oxide and metal heterostructures
P. Lömker (2018), vi, 140 pp
ISBN: 978-3-95806-337-2

Band / Volume 175
Operando Chemistry and Electronic Structure of Electrode / Ferroelectric Interfaces
S. Gonzalez (2018), 172 pp
ISBN: 978-3-95806-341-9

Band / Volume 176
Magnetic Properties of Self-assembled Manganese Oxide and Iron Oxide Nanoparticles
Spin Structure and Composition
X. Sun (2018), ii, 178 pp
ISBN: 978-3-95806-345-7

Band / Volume 177
Model-based reconstruction of magnetisation distributions in nanostructures from electron optical phase images
J. Caron (2018), XXI, 183 pp
ISBN: 978-3-95806-346-4

Band / Volume 178
Simultaneous dual-color imaging on single-molecule level on a Widefield microscope and applications
R. Ledesch (2018), ix, 119 pp
ISBN: 978-3-95806-348-8

Band / Volume 179
Methoden der Leitfähigkeitsuntersuchung mittels Rasterkraftmikroskop und deren Anwendung auf Barium Titanat Systeme
B. Reichenberg (2018), x, 144 pp
ISBN: 978-3-95806-350-1

Band / Volume 180
Manipulation of magnetism in iron oxide nanoparticle / $BaTiO_3$ composites and low-dimensional iron oxide nanoparticle arrays
L. Wang (2018), VI, 151 pp
ISBN: 978-3-95806-351-8

Band / Volume 181
Creating and characterizing a single molecule device for quantitative surface science
M. Green (2018), viii, 142 pp (untersch. Pag.)
ISBN: 978-3-95806-352-5

Band / Volume 182
8th Georgian-German School and Workshop in Basic Science
A. Kacharava (Ed.) erscheint nur als CD (2018)
ISBN: 978-3-95806-353-2

Band / Volume 183
Topological properties of complex magnets from an advanced *ab-initio* Wannier description
J.-P. Hanke (2018), xi, 173 pp
ISBN: 978-3-95806-357-0

Band / Volume 184
Translation Initiation with 70S Ribosomes: A Single Molecule Study
C. Remes (2018), iv, 113 pp
ISBN: 978-3-95806-358-7

Band / Volume 185
Scanning tunneling potentiometry at nanoscale defects in thin films
F. Lüpke (2018), iv, 144 pp (untersch. Pag.)
ISBN: 978-3-95806-361-7

Band / Volume 186
Inelastic neutron scattering on magnetocaloric compounds
N. Biniskos (2018), iii, 92 pp
ISBN: 978-3-95806-362-4

Band / Volume 187
Magnetic Order and Excitation in Frustrated Pyrochlore 5d - Transition Metal Oxides
E. Feng (2018), iv, 182 pp
ISBN: 978-3-95806-365-5

Band / Volume 188
Finite-Difference Time-Domain Simulations Assisting to Reconstruct the Brain's Nerve Fiber Architecture by 3D Polarized Light Imaging
M. Menzel (2018), ix, 296 pp
ISBN: 978-3-95806-368-6

Schlüsseltechnologien / Key Technologies
Band / Volume 188
ISBN 978-3-95806-368-6

Mitglied der Helmholtz-Gemeinschaft

JÜLICH
Forschungszentrum